Quantification of slope deformation behaviour using acoustic emission monitoring

by

Alister Smith

A Doctoral Thesis

Submitted in partial fulfilment of the requirements

for the award of

Doctor of Philosophy of Loughborough University

August 2015

Abstract

Early warning of slope instability will enable evacuation of vulnerable people and timely repair and maintenance of critical infrastructure. However, currently available warning systems are too expensive for wide-scale use or have technical limitations. The acoustic emission (AE) monitoring approach using active waveguides (i.e. a steel tube with granular backfill surround installed in a borehole through a slope), in conjunction with the Slope ALARMS AE measurement system, has the potential to be an affordable early warning system for slope instability. However, the challenge has been to develop strategies to interpret and quantify deformation behaviour from measured AE. The development of an approach to quantify slope deformation behaviour from measured AE will enable the AE monitoring system to provide early warning of slope instability through detecting, quantifying and communicating accelerations in slope movement.

Field monitoring and full-scale physical modelling have been conducted to characterise the AE response from the system to both reactivated slope movements and first-time slope failure. Definitive field evidence has been obtained showing AE monitoring can measure slope movements and generated AE rates are proportional to slope displacement rates, which was confirmed through comparisons with both conventional inclinometer and continuous ShapeAccelArray deformation measurements. A field monitoring case study demonstrated that the AE approach can detect 'very slow' slope movements of 0.075 mm/day. In addition, the concept of retrofitting inclinometer casings with active waveguides to convert the manually read instrument to a real-time monitoring system has been demonstrated using a field trial.

Dynamic strain-controlled shear tests on active waveguide physical models demonstrated that AE monitoring can be used to quantify slope displacement rates, continuously and in real-time, with accuracy to within an order of magnitude. Large-scale first-time slope failure experiments allowed the AE response to slope failure to be characterised. AE was detected after shear deformations of less than a millimetre in previously un-sheared material, and AE rates increased proportionally with displacement rates as failure occurred. The AE rate-displacement rate relationship can be approximated as linear up to 100 mm/hour and shear surface deformations less than 10-20 mm. At greater velocities and larger deformations the gradient of the relationship progressively increases and is best represented using a polynomial. This is because complex pressure distributions develop along the active waveguide analogous to a laterally loaded pile, and the confining pressures increase.

Variables that influence the AE rate-displacement rate relationship have been quantified using physical model experiments and empirical relationships. A framework has been developed to allow AE rate-displacement rate calibration relationships to be determined for any AE system installation. This provides a universal method that can be used by practitioners when installing AE systems, to calibrate them to deliver alarm statuses/warning levels that are related to slope displacement rates. Use of this framework has been demonstrated using a case study example, and decision making protocols have been suggested that use trends in alarms with time to trigger decisions, which could be to send an engineer to inspect the slope, manage traffic, or evacuate people.

Key words: Acoustic Emission (AE); Geotechnical Engineering; Slopes; Landslides; Field Monitoring; Physical Modelling; Deformation; Instrumentation; Early warning

Acknowledgements

I would like to express my gratitude to the Engineering and Physical Sciences Research Council (EPSRC) and Loughborough University for providing the funding and resources necessary to carry out this research.

I am very grateful to my supervisors Professor Neil Dixon and Dr Gary Fowmes. Their unfailing interest and support throughout the project has been a constant source of motivation, and their knowledge and experience has enabled the project to succeed. They have both been good friends, which has made the project extremely enjoyable. I look forward to working with you both in the future. My particular thanks go to Neil for his time and commitment, and for providing the many opportunities that have enabled me to develop and succeed over the last three years.

I would like to express my thanks to the examiners, Dr Joel Smethurst and Dr Paul Fleming, for their very useful insights and interesting discussions.

Colleagues in the School of Civil and Building Engineering have always been supportive and helpful. The experimental work would not have been possible without the support from the technical staff. I would particularly like to thank Lewis Darwin for his excellent technical support in both the laboratory and field work, and whose friendship has made both highly enjoyable. I would also like to thank Dr Matthew Spriggs for his guidance during the early stages of the project.

The field work described in this thesis would not have been possible without the support from numerous individuals and organisations: Steve and Josie Gibson (the Hollin Hill landowners); the British Geological Survey; CH2M (formerly Halcrow); Geotechnical Observations Ltd; Network Rail; Newcastle University; and Scarborough Borough Council. Numerous other individuals and organisations have supported associated work that is not contained within this thesis. Many thanks to you all.

Friends, thank you for always being there and for the constant laughter.

My heartfelt thanks go to my family; they have always been a constant source of support and encouragement. I would particularly like to thank my parents, Lyn and Gary, and my grandparents, Joyce and Eric, for their belief in me and their delight in all of my successes, big or small.

Finally, Efi, thanks for sharing this experience and for being there during both the struggles and the triumphs. Thanks for your constant patience, which I know I challenged, support and encouragement.

List of publications

Parts of the research described in this thesis have been published in the following articles:

Journal articles

Dixon N, **Smith A**, Spriggs MP, Ridley A, Meldrum P and Haslam E (2015) Stability monitoring of a rail slope using acoustic emission. *Proceedings of the Institution of Civil Engineers – Geotechnical Engineering* (in press).

Dixon N, Spriggs MP, **Smith A**, Meldrum P and Haslam E (2015) Quantification of reactivated landslide behaviour using acoustic emission monitoring. *Landslides* 12 (3), 549-560. DOI: 10.1007/s10346-014-0491-z.

Smith A and Dixon N (2015) Quantification of landslide velocity from active waveguide-generated acoustic emission. *Canadian Geotechnical Journal* 52 (4), 413-425. DOI: 10.1139/cgj-2014-0226.

Smith A, Dixon N, Meldrum P, Haslam E and Chambers J (2014) Acoustic emission monitoring of a soil slope: Comparisons with continuous deformation measurements. *Géotechnique Letters* 4(4), 255-261. **Awarded the Institution of Civil Engineers Thomas Telford Premium (Prize for Best Paper in Journal).**

Smith A, Dixon N, Meldrum P and Haslam E (2014) Inclinometer casings retrofitted with acoustic real-time monitoring systems. *GROUND ENGINEERING*, October Issue.

Conference articles

Dixon N, Codeglia D, **Smith A**, Fowmes G, Meldrum P and Haslam E (2015) An acoustic emission slope displacement rate sensor: Case studies. *9th International Symposium on Field Measurements in Geomechanics*. Sydney, Australia (in press).

Dixon N, Moore R, Spriggs MP, **Smith A**, Meldrum P and Siddle R (2014) Performance of an acoustic emission monitoring system to detect subsurface ground movement at Flat Cliffs, North Yorkshire, UK. *IAEG XII Congress - Engineering Geology for Society and Territory 2*, 117-120, Turin.

Smith A and Dixon N (2014) Acoustic emission monitoring of active waveguides to quantify slope stability. *13th BGA Young Geotechnical Engineers' Symposium. University of Manchester*. **Awarded 'best presentation' (oral and paper)**.

Smith A, Dixon N, Berg N, Take A and Proudfoot D (2014) Listening for Landslides: Method, Measurements and the Peace River Case Study. *Geohazards 6*. Ontario, 1-10.

Contents

Abstract i

Acknowledgements ii

List of publications iii

Contents iv

List of figures x

List of tables xxii

Nomenclature xxiv

CHAPTER 1 1

Introduction 1

1.1. Justification of this research 1

1.2. Aim and objectives 4

1.2.1. Aim 4

1.2.2. Objectives 4

1.3. Original contributions to knowledge 4

1.4. Thesis structure 5

CHAPTER 2 7

Literature review 7

2.1. Introduction 7

2.2. Landslides 7

2.2.1. Landslide types and classifications 7

2.2.2. Slope behaviour 11

2.3. Conventional and emerging monitoring instrumentation and techniques 23

2.3.1. Introduction 23

2.3.2. Comparisons of instrumentation and monitoring techniques 25

2.4. Acoustic emission (AE) monitoring 33

2.4.1. Introduction 33

2.4.2. AE monitoring system 35

2.4.3. Soil-generated AE 40

2.4.4. AE monitoring of soil slopes, with particular reference to quantification of deformation behaviour from measured AE 45

2.4.5. Laterally loaded discrete piles 50
2.4.6. AE propagation in waveguides 54
2.5. Summary 62
CHAPTER 3 64
Methodology 64
3.1. Introduction 64
3.2. AE measurement system 64
3.3. Field monitoring 65
3.4. Physical modelling 67
3.4.1. Introduction 67
3.4.2. Active waveguide physical model tests 67
3.4.3. Large-scale first-time slope failure simulation 68
3.4.4. The influence of system variables upon the AE response to applied deformation behaviour 69
3.4.5. Development of a framework for the quantification of slope deformation rates from measured AE 72
3.5. Summary 72
CHAPTER 4 75
Field monitoring case studies 75
4.1. Introduction 75
4.2. Hollin Hill 76
4.2.1. Site description 76
4.2.2. Instrumentation 79
4.2.3. Sample time series measurements 81
4.3. Players Crescent 90
4.3.1. Site description 90
4.3.2. Instrumentation 92
4.3.3. Sample time series measurements 94
4.4. Flat Cliffs 98
4.4.1. Site description 98
4.4.2. Instrumentation 99
4.4.3. Sample time series measurements 100

4.5. Scarborough Spa 102
4.5.1. Site description 102
4.5.2. Instrumentation 103
4.5.3. Sample time series measurements 104
4.6. Nafferton 106
4.6.1. Site description 106
4.6.2. Instrumentation 108
4.6.3. Sample time series measurements 114
4.7. Summary 116
CHAPTER 5 117
Measured AE and deformation behaviour: analysis of field monitoring results 117
5.1. Introduction 117
5.2. Comparisons with conventional inclinometer deformation measurements 117
5.2.1. Introduction 117
5.2.2. Total AE and deformation magnitude comparison 118
5.2.3. Back calculation of velocity-time event profiles 120
5.2.4. Deformation pattern interpretation from AE 125
5.2.5. Application of back calculation method to Flat Cliffs 126
5.3. Comparisons with continuous SAA deformation measurements 127
5.3.1. Introduction 127
5.3.2. AE and deformation comparison 127
5.3.3. Measured AE rate-velocity relationship 130
5.4. Summary 131
CHAPTER 6 133
Measured AE and deformation behaviour: active waveguide physical model tests 133
6.1. Introduction 133
6.2. Experimental design and procedure 133
6.2.1. Introduction 133
6.2.2. Dynamic strain-controlled shear tests 136
6.2.3. Constant strain rate compression tests 138
6.2.4. Quantification of deformation rates during slope failure simulation 140
6.2.5. Comparison of backfill materials 140

6.3. Results and analysis 142
6.3.1. Dynamic strain-controlled shear tests on active waveguide models with gravel aggregate backfill 142
6.3.2. Determination of the coefficient of proportionality 145
6.3.3. Constant strain rate compression tests 147
6.3.4. Quantification of velocity during slope failure simulation 149
6.4. Comparisons of backfill types 153
6.5. Summary 155
CHAPTER 7 156
Measured AE and deformation behaviour: large-scale first-time slope failure simulation 156
7.1. Introduction 156
7.2. Apparatus development and experimental procedure 156
7.3. Results and analysis 169
7.3.1. Deformation and load behaviour 169
7.3.2. AE and deformation behaviour 172
7.4. Summary 188
CHAPTER 8 191
The influence of system variables upon the AE response to applied deformation behaviour 191
8.1. Introduction 191
8.2. Depth to shear surface and attenuation 191
8.2.1. Experimental design 191
8.2.2. Controlled AE source generator 195
8.2.3. Experimental procedure 197
8.2.4. Results and analysis 198
8.2.5. Discussion 205
8.3. Voltage threshold level 209
8.3.1. Experimental procedure 209
8.3.2. Results and analysis 210
8.4. Borehole size 213
8.4.1. Experimental procedure 213
8.4.2. Results and analysis 215
8.5. Waveguide geometry and properties 218

8.5.1. Experimental procedure 218
8.5.2. Results and analysis 220
8.6. Sensor node and transducer combination 222
8.6.1. Experimental procedure 222
8.6.2. Results and analysis 223
8.7. Summary 224
CHAPTER 9 228
A framework for the quantification of slope deformation rates from measured AE 228
9.1. Introduction 228
9.2. Proposed framework and algorithm 228
9.3. Charts for determination of parameters 231
9.4. Example application of method 237
9.5. Framework flow diagram 244
9.6. Error discussion 245
9.7. Decision making protocol 251
9.8. Summary 254
CHAPTER 10 257
Conclusions 257
10.1. Principal findings related to study objectives 257
10.1.1. The aim 257
10.1.2. Objective 1: The AE response from reactivated slope movements 257
10.1.3. Objective 2: The AE response from first-time slope failure 258
10.1.4. Objective 3: The relationship between measured AE and deformation behaviour 258
10.1.5. Objective 4: The influence of system variables upon the AE response to applied deformation behaviour 259
10.1.6. Objective 5: A framework for the quantification of deformation rates from measured AE 262
10.2. Performance of the AE monitoring system 263
10.3. Recommendations for further research 265
References 268
Appendices 280
A1. Field monitoring case study measurements 281
A1.1. Hollin Hill 281

A1.2. Flat cliffs 286
A2. Inclinometer and AE data comparison 287
A3. Active waveguide physical model test results 291
A4. First-time slope failure simulation 295
A5. MISTRAS USB node 301

List of figures

Figure 1.1. Spatial distribution of fatal landslides; each dot represents a single landslide (Petley 2012) . 1

Figure 2.1. Illustrations of the fundamental types of slope movement modified after Varnes (1978) (source: bgs.ac.uk, accessed 10/09/2014)..... 9

Figure 2.2. Factor of safety- and displacement-time behaviour for first-time slope failure after Terzaghi (1950)..... 13

Figure 2.3. a) Shear stress-shear displacement and b) shear strength-normal effective stress relationships for overconsolidated clay in triaxial experiments after Craig (2004)..... 14

Figure 2.4. Development of a shear zone and full shear surface within a slope after Leroueil *et al.* (2012) 14

Figure 2.5. Stages of landslide movement after Leroueil (2001)..... 15

Figure 2.6. Landslide velocity scales taken from; a) Schuster & Krizek (1978) (i.e. Varnes 1978), and b) Cruden & Varnes (1996), Anderson & Holcombe (2013, p92) and Hungr *et al.* (2014) 16

Figure 2.7. Displacement-, velocity- and pore-water pressure-time series for a series of slope movements (Matsuura *et al.* 2008)..... 17

Figure 2.8. Velocity vs. pore-water pressure relationship for a slope movement event (Matsuura *et al.* 2008)..... 18

Figure 2.9. Conceptual model illustrating displacement patterns for the Utiku landslide (Massey *et al.* 2013)..... 18

Figure 2.10. Displacement- and piezometric level-time series for mudslide movement patterns after Allison & Brunsden (1990): a) multiple movement event; b) graded movement event; and c) surge movement event..... 20

Figure 2.11. Displacement-time relationship for four types of landslide movement (Petley *et al.* 2005) . 21

Figure 2.12. Displacement-time data from the Selbourne stability cutting experiment, inset showing geometry of the slope and shear surface and inclinometer locations (after Cooper *et al.* 1989 and Petley *et al.* 2002) 22

Figure 2.13. Linear (a) and asymptotic (b) inverse of velocity vs. time trends of landslide behaviour (after Ng 2007 and Massey 2010)..... 22

Figure 2.14. AE waveform with parameters identified (after Dixon *et al.* 2003) 35

Figure 2.15. The effect of sampling rate on the digital reconstruction of AE: a) 10 samples per unit time; b) 2 samples per unit time (Beattie 1983) 36

Figure 2.16. The effect of voltage threshold level on the number of measured RDC for simulated AE (after Beattie 1983) 37

Figure 2.17. Schematic of AE monitoring system in Koerner *et al.* (1981)..... 38

Figure 2.18. Schematic of an active waveguide installed through a slope deforming on a shear plane, with a sensor connected at the ground surface and protected by a cover (after Dixon *et al.* 2012)..... 39

Figure 2.19. Annotated photograph of the Slope ALARMS AE measurement system from inside the protective surface cover..... 40

Figure 2.20. Schematic of operation of the Slope ALARMS system (including communication and warning system)..... 40

Figure 2.21. AE behaviour of sand and clay undergoing failure (after Koerner *et al.* 1981)..... 43

Figure 2.22. Frequency spectra of AE from clay (a), silt (b) and sand (c) tested in direct shear to near failure (after Koerner *et al.* 1981) 44

Figure 2.23. Number of AE events vs. mean magnitude of AE event from drained triaxial shear tests (after Kavanagh 1997) 45

Figure 2.24. AE behaviour in response to slope failure from a waveguide and sensor installed in the lower part of the Shirasu slope (Fujiwara *et al*. 1999)..... 47

Figure 2.25. Comparison of AE and displacement behaviour during the Shirasu slope failure (Fujiwara *et al*. 1999) 47

Figure 2.26. Comparison of AE and displacement behaviour during movement of a waveguide through a box filled with sand (after Dixon *et al.* 2003) 48

Figure 2.27. Cumulative displacement- and AE energy- time series from the Cowden monitoring experiment after Dixon *et al.* (2003)..... 49

Figure 2.28. AE rate (RDC/min) vs. time (logarithmic scales) from constant strain rate compression tests (after Dixon & Spriggs 2007)..... 50

Figure 2.29. Force diagrams acting on a laterally loaded pile installed through a slope deforming on a shear plane (after Cornforth 2012)..... 51

Figure 2.30. Pile installed through a slope deforming on a shear plane and subjected to lateral loading: a) soil deformations and pile displacement; and b) example qualitative pressures experienced by the pile (after Smethurst & Powrie 2007) 52

Figure 2.31. Deformation, moment, shear and pressure profiles for laterally loaded piles: a) 'flow' mode; b) 'intermediate' mode; and c) 'short-pile' mode (after Poulos 1995)..... 53

Figure 2.32. Difference between deformation profiles of 'rigid' and 'flexible' laterally loaded piles..... 54

Figure 2.33. Attenuation of AE at different frequencies in Toyoura sand (after Shiotani & Ohtsu 1999) 55

Figure 2.34. Attenuation coefficients of different materials after Koerner *et al.* (1981) 55

Figure 2.35. Illustration of a pipe cross-section with internal and external environments 57

Figure 2.36. Exaggerated illustration of Poisson expansion and contraction resulting from longitudinal stress waves after Graff (1975, p79)..... 58

Figure 2.37. a) Thin rod subject to flexural stress wave, and b) an element of the rod subject to various loads (i.e. bending moments and shear forces) after Graff (1975, p141)..... 59

Figure 2.38. Range of diameter, wall thickness and frequency values for which plane longitudinal and shear waves propagate in steel rods/pipes..... 60

Figure 2.39. Incident '0', reflected 'r' and transmitted 't' waves at a connection after Graff (1975, p83) . 62

Figure 4.1. a) Outline of active lobes in the lower part of the slope and the location of the three clusters of instruments; Clusters 1 and 2 on the western lobe and cluster 3 on the eastern lobe (© UKP/Getmapping Licence No. UKP2008/01). b) Illustration of instrumentation cluster locations on the active lobes 77

Figure 4.2. Hollin Hill landslide: a) rotational sliding in the upper part of the slope; and b) materials degrading and forming lobes sliding down the lower part of the slope..... 77

Figure 4.3. Photographs taken from inside a surface cover: a) protruding waveguide with transducer attached; and b) Slope ALARMS sensor powered by a battery..... 79

Figure 4.4. Photograph of instrumentation installation at Cluster 2 at Hollin Hill: surface covers of AEWG In2, AEWG2 and SAA2..... 80

Figure 4.5. Deformed retrofitted inclinometer at Hollin Hill (AEWG In2)..... 81

Figure 4.6. Incremental inclinometer measurements from Cluster 1 for the period 15/10/2009 to 25/10/2012. A-axis is the down-slope direction..... 82

Figure 4.7. Incremental inclinometer measurements from Cluster 2 for the period 28/01/2009 to 13/12/2011. A-axis is the down-slope direction..... 83

Figure 4.8. Incremental inclinometer measurements from Cluster 3 for the period 15/10/2009 to 25/10/2012. A-axis is the down-slope direction..... 84

Figure 4.9. Cumulative RDC, inclinometer measured shear surface deformation and hourly rainfall time series at Cluster 2 at Hollin Hill, with periods of 'S' shaped movement identified 85

Figure 4.10. Cumulative RDC, triggering rainfall event and inclinometer measured shear surface deformation for Event A (highlighted in Figure 4.9) at Cluster 2 87

Figure 4.11. AE rate (RDC/hour), triggering rainfall event and inclinometer measured shear surface deformation for Event A (highlighted in Figure 4.9) at Cluster 2 87

Figure 4.12. AE rate (RDC/hour) and piezometric level for Event A (highlighted in Figure 4.9) at Cluster 2 87

Figure 4.13. Time series for reactivated slope movements at Hollin Hill Cluster 3: a) Rainfall, cumulative AE and cumulative SAA displacement; b) SAA velocity; and c) AE rate..... 89

Figure 4.14. Time series for reactivated slope movements at Hollin Hill Cluster 2 to demonstrate performance of the inclinometer casing retrofitted with an active waveguide: a) SAA measured displacement, AE rate and rainfall vs. time; and b) SAA measured displacement, cumulative RDC and rainfall vs. time 90

Figure 4.15. Photograph of the toe of the Players Crescent slope showing distorted concrete cable trough and toe bulging 91

Figure 4.16. Players Crescent site plan and instrumentation locations, cross-section A-A' is shown in Figure 4.19..... 93

Figure 4.17. Photograph from the bottom of the Players Crescent slope showing surface covers protecting AEWG1, the SAA and housing the communication node..... 93

Figure 4.18. a) Selected inclinometer survey data (initial '0' reading on 21/10/2011) showing the main shear surface at a depth of approximately 6.5 m in the upper part of the slope, and b) selected SAA survey data (initial '0' reading on 11/11/2011) showing the main shear surface at a depth of approximately 3 m in the lower part of the slope. Note deformations increased progressively with time 94

Figure 4.19. Cross-section A-A' (in Figure 4.16) showing the envisaged original slope profile, current slope profile, and the interpreted shear surface (with exaggerated inclinometer and SAA data) (axis units are metres) 95

Figure 4.20. a) Cumulative RDC, displacement and hourly rainfall vs. time for a small magnitude low velocity reactivated deformation event (data from the SAA and AEWG1), and b) AE rate (RDC/hour), displacement and hourly rainfall vs. time (data from the SAA and AEWG1)..... 96

Figure 4.21. AE rate (RDC/hour), inclinometer displacement interpreted for the measurement interval 15/11/2012 to 10/01/2013 and hourly rainfall vs. time for a period of slope movement in response to intensive rainfall (data from AEWG1, AWEG2 and the inclinometer), the timing of the SMS warning messages (Figure 4.22) are superimposed..... 98

Figure 4.22. SMS warning messages AEWG1 (lower waveguide) and AEWG2 (upper waveguide) (Figure 4.21) showing the information contained (e.g. the time stamps and the alarm status) 98

Figure 4.23. Location of active waveguide and inclinometer at Flat Cliffs (Google) (© 2015 Infoterra Ltd & Bluesky) 99

Figure 4.24. Photograph of instrumentation location at Flat Cliffs 100

Figure 4.25. Selected incremental inclinometer measurements at Flat Cliffs, highlighting a period of movement between 17th January 2013 and 22nd March 2013. A-axis is the down-slope direction 101

Figure 4.26. AE rate, rainfall and displacement vs. time behaviour at Flat Cliffs for the period 17th January 2013 to 22nd March 2013 102

Figure 4.27. Location of active waveguide and inclinometer at Scarborough Spa (Google) (© 2015 Infoterra Ltd & Bluesky) 103

Figure 4.28. Photograph of instrumentation installation at Scarborough Spa: waveguide with transducer attached 104

Figure 4.29. Photograph of instrumentation installation at Scarborough Spa: sensor and batteries inside surface cover 104

Figure 4.30. Sample time series measurements from Scarborough: a) AE rate and daily rainfall; and b) Cumulative RDC and cumulative rainfall 105

Figure 4.31. Sample time series measurements from Scarborough: AE rate and daily rainfall (February 2014) 106

Figure 4.32. Sample time series measurements from Scarborough: AE rate and daily rainfall (April to May 2014) 106

Figure 4.33. Location of full-scale embankment at Nafferton (© 2015 Google, map data) 107

Figure 4.34. Photograph of full-scale embankment being constructed at Nafferton, showing sections separated by impermeable membranes (source: Hughes 2007) 108

Figure 4.35. Diagram of full-scale embankment at Nafferton: instrumentation locations are highlighted on the slope being induced to failure (cross-section A-A' is shown in Figure 4.36) (redrawn after Hughes *et al.* 2009; Glendinning *et al.* 2014) 108

Figure 4.36. Cross-section A-A' (from Figure 4.35) of full-scale embankment at Nafferton: instrumentation installations are highlighted through the slope being induced to failure 110

Figure 4.37. Photograph of active waveguide (Leighton Buzzard sand backfill being compacted with tamping rod) and SAA installations at Nafferton 110

Figure 4.38. Photograph of active waveguide and SAA installations (both grouted) at Nafferton 111

Figure 4.39. Photograph of transducer coupled to protruding waveguide at Nafferton 111

Figure 4.40. Photograph showing SAA and Slope ALARMS protected by surface covers at Nafferton 112

Figure 4.41. Photograph of SAA data logger and solar panel, and Slope ALARMS batteries at the top of the slope at Nafferton 112

Figure 4.42. Photograph of Slope ALARMS and SAA surface covers on the slope at Nafferton 113

Figure 4.43. Photograph of Slope ALARMS coordinator system inside the porta cabin at Nafferton ... 113

Figure 4.44. Photograph of Slope ALARMS coordinator GSM and WSN antenna on the wall of the porta cabin at Nafferton 114

Figure 4.45. Selected height vs. resultant horizontal (down-slope direction) displacement surveys taken from the SAA at Nafferton 115

Figure 4.46. Resultant horizontal SAA displacement at 2.3 m depth and AE time series measurements at Nafferton: a) displacement and AE rate; and b) displacement and cumulative RDC 115

Figure 5.1. AE rate, hourly rainfall and inclinometer measured shear surface displacement for an event at Cluster 2 at Hollin Hill 118

Figure 5.2. Relationship between deformation event AE energy (total RDC generated throughout event) and event displacement magnitude for events that occurred in 2010 at Cluster 2 plotted on log-log scales 119

Figure 5.3. Relationship between deformation event AE energy (total RDC generated throughout event) and event displacement magnitude for events that occurred in 2010 at Clusters 1, 2 and 3 plotted on log-log scales 120

Figure 5.4. Total shear surface deformation and total AE generated throughout a deformation event. 121

Figure 5.5. Trapezoidal interrogation of AE rate data to obtain incremental event velocity from the displacement/time relationship 121

Figure 5.6. AE rate and derived velocity time series for the event shown in Figure 5.1 at Cluster 2 122

Figure 5.7. AE rate-velocity calibration relationships for events on different systems over the course of monitoring at the Hollin Hill site 123

Figure 5.8. Comparison of measured slope deformation event velocities and those calculated from the AE rates 124

Figure 5.9. AE rate-, AE derived velocity-, inclinometer measured displacement-, AE derived displacement- and rainfall-time series for a reactivated slope deformation event at Hollin Hill (Cluster 2) 125

Figure 5.10. AE responses of all three clusters to a rainfall event and the derived slope cumulative displacements at each location 126

Figure 5.11. AE rate-, inclinometer measured displacement-, AE derived displacement- and rainfall-time series for a period of slope movement at Flat Cliffs 127

Figure 5.12. Resultant horizontal displacement-, velocity- and smoothed velocity-time measured by SAA3 for a series of reactivated slide events at Cluster 3 at Hollin Hill 128

Figure 5.13. Resultant horizontal SAA3 measured displacement-, cumulative RDC and hourly rainfall-time for the series of slide events at Cluster 3 at Hollin Hill 129

Figure 5.14. Change in shape of SAA3 depth profile at the end of each slope displacement event at Cluster 3 at Hollin Hill 129

Figure 5.15. Resultant measured displacement-, AE rate- and smoothed AE rate-time for the series of slide events at Cluster 3 130

Figure 5.16. Measured (10 hour moving average values taken from AEWG3 and SAA3 during slide events) and back calculated AE rate-velocity relationships 131

Figure 6.1. Photograph of granite gravel aggregate 134

Figure 6.2. Particle size distribution of granite gravel aggregate 135

Figure 6.3. a) Elevation schematic of active waveguide specimen installed in dynamic strain-controlled shear apparatus, b) cross section schematic of active waveguide specimen installed in apparatus, c) photograph of test set up, and d) photograph of active waveguide model with angular gravel aggregate backfill 137

Figure 6.4. Photograph of the active waveguide model installed in the Dixon & Spriggs (2007) constant strain rate compression apparatus 139

Figure 6.5. Photographs of soil samples; a) Gravel Aggregate, b) River Gravel, c) Crushed Glass, d) Leighton Buzzard Sand, and e) Concrete Sand 141

Figure 6.6. Particle size distribution curves for the 5 soil types tested 141

Figure 6.7. Time series from a dynamic strain-controlled shear test; a) displacement- and velocity-time, b) displacement- and AE rate-time, c) velocity- and AE rate-time, and d) force- and AE rate-time 143

Figure 6.8. Measured and calculated AE rate vs. applied velocity relationships determined from one dynamic strain-controlled shear test (2 minute moving average values) 144

Figure 6.9. Force vs. displacement relationship for selected dynamic strain-controlled shear tests of 1 mm, 4 mm and 10 mm total displacements 145

Figure 6.10. Measured AE rate vs. measured velocity relationship using data from 21 dynamic strain-controlled shear tests 146

Figure 6.11. Measured AE rate vs. measured velocity relationship using data from 21 dynamic strain-controlled shear tests; the landslide velocity scale after Cruden & Varnes (1996) is superimposed 146

Figure 6.12. Results from 40 constant strain rate compression tests; AE rate vs. time 148

Figure 6.13. Measured AE rate vs. measured velocity relationship using data from 21 dynamic strain-controlled shear tests and 40 constant strain rate compression tests, the landslide velocity scale after Cruden & Varnes (1996) is superimposed 148

Figure 6.14. Force vs. displacement results from selected rapid constant strain rate compression tests on active waveguides 149

Figure 6.15. Time series from a dynamic strain-controlled failure simulation; a) displacement- and AE rate-time, b) force- and AE rate-time, and c) measured velocity- and calculated velocity (i.e. derived from AE rate 5 second interval values)-time 150

Figure 6.16. Measured and calculated (i.e. derived from AE rate data through application of the coefficient of proportionality) velocity-time behaviour (2 minute moving average values) during a landslide failure simulation using the dynamic strain-controlled shear test apparatus; a) linear velocity scale, b) log velocity scale showing ‘very slow’, ‘slow’ and ‘moderate’ velocity classifications, and c) error (difference between calculated (i.e. derived from AE) and measured velocities (using 2 minute moving average values) 151

Figure 6.17. Calculated velocity (i.e. derived from AE rate data through application of the coefficient of proportionality) vs. measured velocity throughout the slope failure simulation 153

Figure 6.18. Results from dynamic strain-controlled shear tests on active waveguides with different backfill materials 154

Figure 6.19. Linear coefficients of proportionality derived from the AE rate-velocity relationships plotted in Figure 6.18 for the 5 different backfills, showing the magnitude of AE rates generated in response to an applied velocity for each backfill 154

Figure 7.1. a) Concrete block inside mould and b) concrete block outside mould 158

Figure 7.2. Particle size distribution of the clay used as fill in the first-time failure experiments. The distibution was determined from a combination of sieving and a laser diffraction particle size analyser 158

Figure 7.3. Annotated illustration of the first-time slope failure experiment at the start of a test (t = 0). The top block is pulled horizontally to the right of the image by the wire rope during the test. The anchor, wire rope and pulley system are fastened centrally in the horizontal plane and are only shown on cross-section B-B’ for illustrative purposes 159

Figure 7.4. Photograph showing the wire rope fastened to the resin anchor at the front face of the top block. Geomembrane interface fixings are also shown 160

Figure 7.5. Annotated photograph of the first-time failure experiment 161

Figure 7.6. Photographs of the first-time failure experiment: (a) at the start position (i.e. t = 0); and (b) at the final position (i.e. at the end of stage 8), after 50 mm of relative horizontal movement 165

Figure 7.7. Photographs of backfill materials employed in the first-time failure experiments: a) LSG; b) LBS; and c) GG 167

Figure 7.8. Particle size distributions of backfill materials employed in the first-time failure experiments 167

Figure 7.9. Illustrations of selected backfill particles used in the first-time failure tests: a) LSG; b) GG; and c) LBS 168

Figure 7.10. Particle shape determination modified after Krumbein & Sloss (1963) and Cho *et al.* (2006). Diagonal dotted lines correspond to constant particle regularity = (roundness + sphericity)/2 168

Figure 7.11. Ram position, LVDT displacement and resultant horizontal SAA displacement vs. time from Test 3 170

Figure 7.12. Ram position, LVDT displacement and resultant horizontal SAA displacement vs. time during the first 80 minutes of Test 3 171

Figure 7.13. SAA height vs. resultant horizontal deformation from Test 3; data are presented at the end of each stage 171

Figure 7.14. Load vs. displacement data for each first-time failure test. Note that displacement is taken from the SAA MEMS sensor immediately above the shear surface (at a height of 0.9 m) 172

Figure 7.15. Time series of measurements from first-time failure Test 3 at 0.25V threshold level: a) displacement and cumulative RDC vs. time; and b) SAA velocity and AE rate vs. time 173

Figure 7.16. .Time series of measurements from the first 80 minutes of first-time failure Test 3 at 0.25V threshold level: a) displacement and cumulative RDC vs. time; and b) SAA velocity and AE rate vs. time 174

Figure 7.17. Comparison of AE rate-velocity relationships determined from first-time failure Tests 1, 2 and 3 for both 0.1V and 0.25V threshold levels 175

Figure 7.18. Comparison of AE rate-velocity relationships determined from first-time failure Tests 1, 2 and 3 for the 0.25V threshold level 176

Figure 7.19. AE rate and velocity vs. time from first-time failure Tests 3, 4 and 5 at 0.25V threshold level: a) LSG; b) LBS; and c) GG. Note the different AE rate axis scales used 178

Figure 7.20. AE rate and velocity vs. time from first-time failure Tests 3, 4 and 5 at 0.1V threshold level: a) LSG; b) LBS; and c) GG. Note the different AE rate axis scales used 179

Figure 7.21. Time series of measurements from the first 80 minutes of first-time failure Test 5 at 0.1V threshold level: a) displacement and cumulative RDC vs. time; and b) velocity and AE rate vs. time .. 180

Figure 7.22. Comparison of AE rate-velocity relationships determined from first-time failure experiments on each backfill type for the 0.25V threshold level. The insert shows the AE rate-velocity relationships up to a velocity of 100 mm/hour 181

Figure 7.23. Comparison of AE rate-velocity relationships determined from first-time failure experiments on each backfill type for the 0.1V threshold level. The insert shows the AE rate-velocity relationships up to a velocity of 100 mm/hour 181

Figure 7.24. Ratio of AE rates generated by the GG backfill to the other backfills at both 0.1V and 0.25V threshold levels vs. applied velocity 183

Figure 7.25. Ratio of AE rates measured at 0.1V threshold level to AE rates measured at 0.25V threshold level for each backfill type vs. applied velocity 185

Figure 7.26. a), c) and e) show AE rate vs. displacement relationships for each backfill type and voltage threshold level. b), d) and f) show AE rate vs. load relationships for each backfill type and voltage threshold level 186

Figure 7.27. AE rate vs. velocity relationships derived for limestone gravel backfill at both 0.1V and 0.25V voltage threshold levels using the first-time failure experimentation. Error bars show the range of AE measurements recorded at the applied velocity 187

Figure 7.28. AE rate vs. velocity relationships derived for Leighton Buzzard sand backfill at both 0.1V and 0.25V voltage threshold levels using the first-time failure experimentation. Error bars show the range of AE measurements recorded at the applied velocity 188

Figure 7.29. AE rate vs. velocity relationships derived for granite gravel backfill at both 0.1V and 0.25V voltage threshold levels using the first-time failure experimentation. Error bars show the range of AE measurements recorded at the applied velocity 188

Figure 8.1. Photograph of experimentation to measure attenuation in an air-waveguide-air tri-layer system 192

Figure 8.2. Schematic of air-waveguide-air test setup with source generator and sensor positions highlighted 193

Figure 8.3. Schematic of trench experiment, a) plan and dimensions, b) elevation and dimensions, c) running sensor positions and backfill sections, d) running sensor at position 3 with 2 sections backfilled 194

Figure 8.4. Photographs of trench experiment, a) pipe placed at the base of the trench, b) pipe placed on river gravel bed and backfilled with river gravel, c) pipe placed on clay bed and backfilled with clay 194

Figure 8.5. Particle size distribution curves for the two soils used as cover. The distibution for the site won clay was determined from a combination of sieving and a laser diffraction particle size analyser 195

Figure 8.6. Sample AE waveforms generated by soil deforming around a pipe: a) and b) generated by particle-particle and particle-pipe interactions; and c) and d) generated by contact stress release and contact network rearrangement 196

Figure 8.7. Source generator coupled to the pipe 197

Figure 8.8. a) and b) are typical AE waveforms produced by the source generator 197

Figure 8.9. Results of RDC (induced by source generator over 10 second durations) vs. propagation distance from the air-waveguide-air tri-layer system; a) loose couplings, b) tight couplings 199

Figure 8.10. Percentage signal loss over each coupling from the air-waveguide-air tri-layer system experimentation 200

Figure 8.11. a) Exaggerated illustration of screw threaded coupling highlighting the discontinuity in cross-section, and b) photograph of pipe connected with a screw threaded coupling and tightened with chain wrenches 200

Figure 8.12. Results of RDC (induced by source generator over 10 second durations) vs. propagation distance from the air-waveguide-River Gravel tri-layer system; a) signals received by end sensor, b) signals received by running sensor 201

Figure 8.13. Results of RDC (induced by source generator over 10 second durations) vs. propagation distance from the air-waveguide-Clay tri-layer system; a) signals received by end sensor, b) signals received by running sensor 202

Figure 8.14. Attenuation coefficients in RDC per metre derived for each of the tri-layer systems (including losses due to couplings) 203

Figure 8.15. Percentage of source magnitude vs. propagation distance relationship derived using the attenuation coefficient for the air-waveguide-River Gravel system (i.e. including coupling losses) 205

Figure 8.16. Reflection coefficient (at the pipe-external media interface) vs. acoustic impedance of the external media (for the media studied) 207

Figure 8.17. Attenuation coefficient vs. reflection coefficient (at the pipe-external media interface) for the tri-layer systems studied (i.e. steel pipe with screw threaded couplings and air as an internal environment) at a monitoring frequency of 20 to 30 kHz 207

Figure 8.18. Percentage of source magnitude vs. propagation distance relationships for boundary losses due to soil cover (soil cover losses) for the soils examined, demonstrating that soil cover loss varies proportionally with the soil's acoustic impedance 209

Figure 8.19. AE rate vs voltage threshold level relationship obtained from constant strain rate compression tests at a 'rapid' rate of displacement 211

Figure 8.20. AE rate vs voltage threshold level relationship obtained from constant strain rate compression tests at a 'slow' rate of displacement 212

Figure 8.21. Mean AE rate measured at each voltage threshold level and deformation rate, plotted as a factor relative to the mean AE rate obtained at 0.05V 212

Figure 8.22. Mean AE rate measured at each voltage threshold level from both deformation rates combined, plotted as a factor relative to the mean AE rate obtained at 0.05V; error bars represent the standard deviation 213

Figure 8.23. AE rate (presented as a factor relative to a maximum at 0.05V threshold level) vs. voltage threshold level relationship, determined using the data in Figure 8.22 213

Figure 8.24. Photograph of active waveguide physical model employing an inclinometer casing, with Leighton Buzzard sand backfill and 25 mm diameter steel waveguide tube 214

Figure 8.25. AE rate vs. time measurements obtained from constant strain rate compression tests on 130 mm diameter and 59 mm diameter active waveguide models with concrete sand backfill: a) 0.1V, b) 0.25V and c) 0.45V threshold levels 217

Figure 8.26. AE rate vs. time measurements obtained from constant strain rate compression tests on 130 mm diameter and 59 mm diameter active waveguide models with glass aggregate backfill: a) 0.1V, b) 0.25V and c) 0.45V threshold levels 217

Figure 8.27. AE rate vs. time measurements obtained from constant strain rate compression tests on 130 mm diameter and 59 mm diameter active waveguide models with Leighton Buzzard sand backfill: a) 0.1V, b) 0.25V and c) 0.45V threshold levels 218

Figure 8.28. Comparison of mean AE rate measured from each backfill and voltage threshold level. Results from the 59 mm diameter active waveguide are presented relative to the mean AE rate obtained from the 130 mm diameter active waveguide. The error bars represent the standard deviation of the mean derived from each test 218

Figure 8.29. AE rate vs. time measurements obtained from constant strain rate compression tests on 130 mm diameter active waveguide models with angular gravel aggregate backfill employing four different waveguides: a) 0.1V, b) 0.25V and c) 0.45V threshold levels 222

Figure 8.30. Comparison of mean AE rate measured from each waveguide (at all voltage threshold levels) presented relative to the mean AE rate obtained from the standard 50 mm diameter 3 mm wall thickness steel pipe (i.e. the standard waveguide; WG1). The error bars represent the standard deviation of the means derived from each test 222

Figure 8.31. RDC measured by each sensor and transducer combination coupled to a waveguide in response to AE induced by the controlled source generator; measurement systems 1 to 10 received 10s blasts from the motor and measurement systems 11 to 20 received 1s blasts from the motor 224

Figure 9.1. Schematic detailing each of the variables that influence the AE response from the measurement system and the point(s) at which they have influence in the system as AE propagates from the source at the shear surface to the sensor at the ground surface 229

Figure 9.2. AE rate vs. velocity relationships derived for limestone fine-gravel backfill at both 0.1V and 0.25V voltage threshold levels using the first-time failure experimentation (i.e. shallow shear surface) 232

Figure 9.3. AE rate vs. velocity relationships derived for Leighton Buzzard sand backfill at both 0.1V and 0.25V voltage threshold levels using the first-time failure experimentation (i.e. shallow shear surface) 233

Figure 9.4. AE rate vs. velocity relationships derived for granite medium-gravel backfill at both 0.1V and 0.25V voltage threshold levels using the first-time failure experimentation (i.e. shallow shear surface) 233

Figure 9.5. Mean AE rate measured from each waveguide presented relative to the mean AE rate obtained from the standard 50 mm diameter 3 mm wall thickness steel pipe 234

Figure 9.6. Partial factor vs. propagation distance (attenuation) relationships for steel waveguides with no couplings. Relationships for granular backfill, bentonite grout and air external environments are presented. Factor is presented on a linear scale and propagation distance up to 7 m because waveguides any longer typically employ couplings (it is difficult to transport longer lengths to site) 234

Figure 9.7. Partial factor vs. propagation distance (attenuation) relationships for steel waveguides with ~1.0 m lengths connected using screw threaded couplings. Relationships for granular backfill, bentonite grout and air external environments are presented. Factor is presented on a linear scale and propagation distance up to 15 m because waveguides any longer typically employ longer lengths and less frequent couplings 235

Figure 9.8. Partial factor vs. propagation distance (attenuation) relationships for steel waveguides with 3.2 m lengths connected using screw threaded couplings. Relationships for granular backfill, bentonite grout and air external environments are presented. Factor is presented on a log scale and propagation distance up to 30 m. The equations that define the relationships are presented and can be used to quantify factors for longer propagation distances 235

Figure 9.9. Partial factor vs. propagation distance (attenuation) relationships for steel waveguides with 6.4 m lengths connected using screw threaded couplings. Relationships for granular backfill, bentonite grout and air external environments are presented. Factor is presented on a log scale and propagation distance up to 30 m. The equations that define the relationships are presented and can be used to quantify factors for longer propagation distances 236

Figure 9.10. RDC measured by each sensor and transducer combination coupled to a waveguide in response to AE induced by the controlled source generator; measurement systems 1 to 10 received 10s blasts from the motor and measurement systems 11 to 20 received 1s blasts from the motor 236

Figure 9.11. Factor vs. voltage threshold level relationship 237

Figure 9.12. Cross-section of installation at Nafferton embankment with possible failure surfaces superimposed (red lines) 238

Figure 9.13. Schematic of active waveguide installation at Nafferton embankment with an assumed 1 m deep failure surface; lengths of waveguide with different external environments are annotated 239

Figure 9.14. AE rate vs. velocity relationships derived for Leighton Buzzard sand backfill at both 0.1V and 0.25V voltage threshold levels using the first-time failure experimentation (i.e. shallow shear surface). The AE system at Nafferton embankment has Leighton Buzzard sand backfill and a voltage threshold level of 0.25V 239

Figure 9.15. Partial factor vs. propagation distance (attenuation) relationships for steel waveguides with no couplings. Relationships for granular backfill, bentonite grout and air external environments are presented. Factor is presented on a linear scale and propagation distance up to 1 m. The factor derived for 0.3 m of grout cover is superimposed 240

Figure 9.16. RDC measured by each sensor and transducer combination from controlled source generator. Sensor and transducer combination 14 was used to derive the AE rate-velocity relationship for Leighton Buzzard sand at 0.25V (i.e. the base-case relationship used for Nafferton) using the first-time failure experimentation). Sensor and transducer combination 20 was installed at Nafferton 241

Figure 9.17. AE rate vs. velocity relationship derived for Nafferton embankment installation (red line) after application of the quantification framework to the relationship derived from the first-time failure experimentation (grey dashed line) 242

Figure 9.18. AE rate vs. velocity relationship derived for Nafferton embankment installation plotted on log scales with the standard landslide velocity scale superimposed 243

Figure 9.19. AE rate vs. velocity relationship derived for Nafferton embankment installation and an extrapolated relationship 243

Figure 9.20. AE rate vs. velocity relationship derived for Nafferton embankment installation and the extrapolated relationship plotted on log scales with the standard landslide velocity scale superimposed 244

Figure 9.21. Flow diagram of the process required to quantify AE rate-velocity relationships that are calibrated for each specific system installation, and to determine AE rate warning levels that are based on slope displacement rates 245

Figure 9.22. AE rate vs. velocity relationship derived for granite gravel backfill at 0.25V voltage threshold level using the first-time failure experimentation. Error bars show the range of AE measurements recorded at the applied velocity. Percentage errors in derived velocities are shown using the relationship and the error bars 246

Figure 9.23. Factor vs. voltage threshold level relationship with error bars showing possible percentage error using values from the first time failure experiment on granite gravel from both 0.1V and 0.25V threshold levels 247

Figure 9.24. Factor vs. voltage threshold level relationship. The annotations show how to derive a factor from the chart to convert AE rate-velocity relationships from 0.25V to 0.1V 248

Figure 9.25. 'Measured' AE rate vs. velocity relationships derived for granite gravel backfill at both 0.1V and 0.25V voltage threshold levels using the first-time failure experimentation. The black line shows the 'calculated' 0.1V relationship derived from the 0.25V relationship using the conversion factor shown in Figure 9.24. The grey lines show the potential error (+/- 4%) in this 'calculated' relationship 249

Figure 9.26. 'Measured' AE rate vs. velocity relationships derived for granite gravel backfill at both 0.1V and 0.25V voltage threshold levels using the first-time failure experimentation. The black line shows the 'calculated' 0.1V relationship derived from the 0.25V relationship using the conversion factor shown in Figure 9.24. The grey lines show the potential error (+/- 4%) in this 'calculated' relationship. Plotted on logarithmic scales with the landslide velocity superimposed 250

Figure 9.27. AE rate vs. velocity relationship derived for granite gravel backfill at 0.1V threshold level using the first-time failure experimentation. The shaded areas show the maximum error (i.e. increase or decrease by a factor of 10) acceptable when converting from AE rates to slope velocity to prevent incorrect velocity classification 251

Figure 9.28. Conceptual alarm status vs. time relationship for slope failure occurring over 1 to 2 hours 253

Figure 9.29. Conceptual alarm status vs. time relationship for slope failure occurring over several hours 253

Figure 9.30. Conceptual alarm status vs. time relationship for slope reactivation occurring over several hours 254

Figure A.1. Time series measurements from Hollin Hill, comparing AEWG2 measurements with GPS peg displacements and rainfall: a) Cumulative RDC; and b) AE rate 281

Figure A.2. Time series measurements from AEWG2 at Hollin Hill: a) Cumulative RDC, rainfall and GPS peg displacement; b) AE rate and peg displacement; and c) AE rate and piezometric level 282

Figure A.3. Time series measurements from AEWG3 and SAA3 at Hollin Hill (Eastern lobe): a) Cumulative RDC, cumulative displacement and rainfall; b) SAA measured velocity; and c) AE rate 283

Figure A.4. Time series measurements from AEWG2 and SAA2 at Hollin Hill (Western lobe): a) Cumulative RDC, cumulative displacement and rainfall; b) SAA measured velocity; and c) AE rate 284

Figure A.5. Example high magnitude AE contamination/background noise at Hollin Hill: a) time series; b) plotted vs. time of day 285

Figure A.6. Example time series of consistent electronic noise in system AEWG In2 at Hollin Hill, which was removed from time series measurements during analysis 285

Figure A.7. Example high magnitude AE contamination due to electromagnetic interference at Flat Cliffs, which stopped after the coordinator system and solar panel regulator were disconnected (originally they were all housed in the same cover and this caused the interference) 286

Figure A.8. Example periods of movement at AEWG1 (Hollin Hill) during 2010, with inclinometer and AE presented during the period when movement was assumed to have taken place 287

Figure A.9. Example periods of movement at AEWG2 (Hollin Hill) during 2010, with inclinometer and AE presented during the period when movement was assumed to have taken place 288

Figure A.10. Example periods of movement at AEWG3 (Hollin Hill) during 2010, with inclinometer and AE presented during the period when movement was assumed to have taken place 289

Figure A.11. The two inclinometer intervals at Hollin Hill in 2012 with AEWG2 time series measurements 290

Figure A.12. Illustration of wire rope used in first-time slope failure experimentation 295

Figure A.13. Specification of DSRB 270/12 Sheave Block 295

Figure A.14. CAD diagrams used to quantify particle shape parameters 296

Figure A.15. Details of the MISTRAS USB node used to compare the full waveforms of the controlled source generator and soil-generated AE from constant strain rate compression tests 301

List of tables

Table 2.1. Geotechnical modification of Varnes' (1978) landslide material descriptions (after Hungr *et al.* 2014) 10

Table 2.2. Geotechnical landslide classification after Hutchinson (1988) 11

Table 2.3. Comparisons of instrumentation and monitoring techniques 30

Table 2.4. R3a transducer specifications 39

Table 2.5. Influence of soil properties on AE behaviour (summarised after: Koerner & Lord 1972; Koerner *et al.* 1975; Koerner *et al.* 1976; Lord *et al.* 1977; Tanimoto & Noda 1977; Keorner *et al.* 1981; Tanimoto *et al.* 1981; Naemura *et al.* 1991; and Dixon *et al.* 2003) 42

Table 2.6. Standard mechanical properties of steel 59

Table 2.7. Calculated propagation velocity of both longitudinal and flexural wave modes at a frequency of 25 kHz propagating through steel 59

Table 4.1. Summary of field trials detailed in the thesis, highlighting instrumentation installed and parties involved 76

Table 6.1. Tabulated dynamic strain-controlled (DSC) shear tests on active waveguide models with angular gravel backfill and 50 mm diameter 3 mm thick steel pipe contained inside a 130 mm diameter geomembrane cylinder. Voltage threshold level set to 0.25V 138

Table 6.2. Displacement rates, durations and total displacements of constant strain rate compression tests 139

Table 6.3. Number of constant strain rate compression tests conducted at each displacement rate ... 140

Table 6.4. Tabulated dynamic strain-controlled shear tests on active waveguide models with different backfill materials and 50 mm diameter 3 mm thick steel pipe contained inside a 130 mm diameter geomembrane cylinder. Voltage threshold set to 0.25V 142

Table 7.1. Properties of the clay used for fill in the first-time failure experiments 158

Table 7.2. Displacement-controlled function 1: applied to first-time failure simulation Test 1 162

Table 7.3. Displacement-controlled function 2: applied to first-time failure simulation Test 2 162

Table 7.4. Displacement-controlled function 3: applied to first-time failure simulation Tests 3, 4 and 5 162

Table 7.5. Details of the first-time failure (FTF) experiments conducted 163

Table 7.6. Particle size, particle shape and packing properties of the backfills examined in the first-time failure experiments 167

Table 7.7. SAA measured resultant horizontal deformation prior to AE detection for each backfill type and voltage threshold level 180

Table 8.1. Properties of site won clay used as soil cover 195

Table 8.2. Attenuation coefficients determined for the systems tested (i.e. combined losses due to couplings and internal/external environments) 204

Table 8.3. Acoustic velocity, acoustic impedance and reflection coefficients (at the pipe-media interface) for media studied 206

Table 8.4. Tabulated constant strain rate compression tests on active waveguide models and voltage threshold levels set on the AE measurement system 210

Table 8.5. Properties and geometry of the inclinometer casing employed in the constant strain rate compression tests 214

Table 8.6. Tabulated constant strain rate (CSR) compression tests on active waveguide models with different backfill materials, borehole diameters, and voltage thresholds 215

Table 8.7. Geometry and properties of the range of waveguides examined 219

Table 8.8. Tabulated constant strain rate (CSR) compression tests on active waveguide models with different waveguides and voltage thresholds 220

Table 8.9. Tabulated controlled source tests performed on different AE measurement systems 223

Table 9.1. 'Measured' and 'calculated' 0.1V AE rate-velocity relationships shown in Figure 9.25 249

Table A.1. Actual average velocities (using inclinometer measurements and event duration) and calculated average velocities (derived from AE rate measurements) determined for a series of movement events at Hollin Hill 290

Table A.2. Example tabulated results from a dynamic strain controlled shear test of 4 mm amplitude and 0.0003 Hz frequency 291

Table A.3. Example tabulated results from a constant strain rate compression test at a 'rapid' deformation rate 294

Table A.4. Specification of 6 x 36 construction wire rope used in first-time slope failure experimentation 295

Table A.5. Example tabulated results, sampled at 30 second intervals, from first-time failure test 5 296

Nomenclature

AE	Acoustic emission
$\mathrm{AE_{BT}}$	AE rate-velocity function for the active waveguide backfill type
AEWG	Active waveguide
A	AE magnitude (dB) (RDC)
$\mathrm{A_0}$	Source/incident AE magnitude (dB) (RDC)
$\mathrm{A_{air}}$	Attenuation with air surround (parameter)
$\mathrm{A_b}$	Attenuation with granular backfill surround (parameter)
$\mathrm{A_g}$	Attenuation with bentonite-grout surround (parameter)
$\mathrm{A_r}$	Reflected AE magnitude (dB) (RDC)
$\mathrm{A_t}$	Transmitted AE magnitude (dB) (RDC)
$\mathrm{BH_S}$	Borehole size (parameter)
C	Wave velocity (m/s)
$\mathrm{C_l}$	Longitudinal wave mode velocity (m/s)
$\mathrm{C_s}$	Shear wave mode velocity (m/s)
$\mathrm{c'}$	Effective cohesion (kPa)
$\mathrm{C_p}$	Coefficient of proportionality
$\mathrm{C_u}$	Coefficient of uniformity
CPT	Cone penetration test
d	Diameter (mm) (m)
$\mathrm{d_{10}}$	Particle size below which 10% is finer by mass
$\mathrm{d_{60}}$	Particle size below which 60% is finer by mass
dB	Decibels
E	Young's modulus (i.e. modulus of elasticity) (Pa)
e	Euler's/Napier's constant and void ratio
f	Frequency (Hz)
GSM	Global System for Mobile Communications
I	Second moment of area (mm^4) (m^4)
M	Bending moment (Nm)
Np	Nepers
q	Distributed body force (N)
$\mathrm{R^2}$	Correlation factor
$\mathrm{R_c}$	Reflection coefficient
RDC	Ring-down counts
S	Cross-sectional area (mm^2) (m^2)
$\mathrm{S_{S+T}}$	Sensor node and transducer combination (parameter)
$\mathrm{ST\ DEV}$	Standard deviation

SAA	ShapeAccelArray
SPT	Standard penetration test
t	Thickness (mm) (m)
U	Pore pressure (kPa)
V	Shear force and voltage
V_{TL}	Voltage threshold level (parameter)
WSN	Wireless sensor network
W_T	Waveguide type (parameter)
x	Distance (m)
Z	Acoustic impedance (kg/m^{2}s)
α	Attenuation coefficient (RDC/m) (Np/m) (dB/m)
λ	Wavelength (mm)
λ_l	Longitudinal wave mode wavelength (mm)
λ_s	Shear wave mode wavelength (mm)
μ	Shear modulus of elasticity (Pa)
ρ	Density (kg/m^3)
ρ_d	Dry density (Mg/ m^3)
ρ_s	Particle density (Mg/ m^3)
σ	Stress (Pa)
σ_0	Incident stress wave (Pa)
σ_r	Reflected stress wave (Pa)
σ_t	Transmitted stress wave (Pa)
σ'	Effective stress (kPa)
σ_n	Normal stress (kPa)
τ	Shear strength (kPa)
υ	Poisson's ratio
$\emptyset'$	Effective angle of internal friction (°)

CHAPTER 1

Introduction

1.1. Justification of this research

More than 32,000 fatalities resulted from non-seismically induced landslides during the period 2004 to 2010 (Petley 2012). Figure 1.1 shows clusters of fatal landslide locations superimposed on a world map. The dominant global trigger of fatal landslides during this period was rainfall in the northern hemisphere monsoon and the majority of fatalities occurred in Asia, along the Himalayan Arc and in China (Petley 2012). This geographical clustering of fatal landslides was also confirmed by Kirschbaum *et al.* (2012) during the same period. Reasons for such geographical clustering include: the availability of topographical relief upon which a landslide can occur; the frequency and magnitude of precipitation; and the population density (i.e. the probability of a landslide interacting with people). Therefore, areas with high relief, intense rainfall and high population density are most likely to experience fatal landslides.

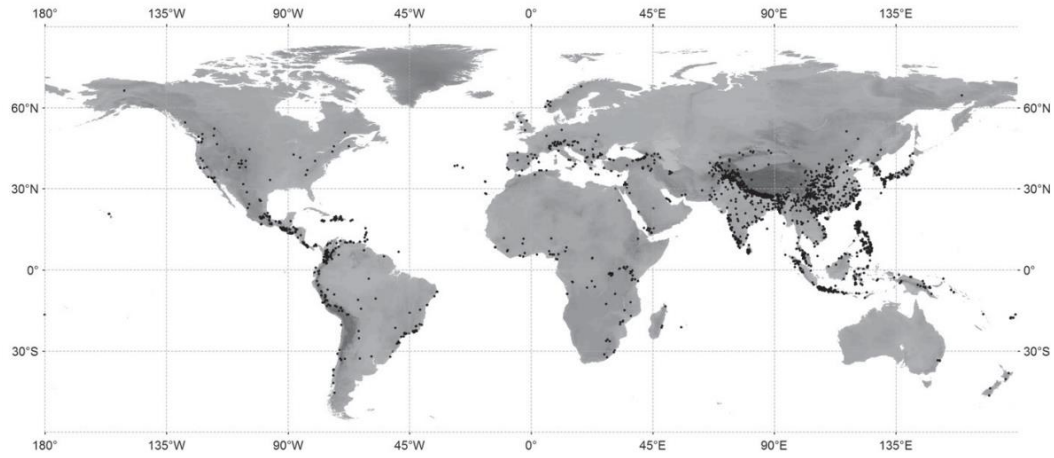

Figure 1.1. Spatial distribution of fatal landslides; each dot represents a single landslide (Petley 2012)

Global population has increased from 1 billion to more than 7 billion over the last 100 years. The majority of this growth has occurred in the developing world over the most recent decades. This has driven the expansion of settlements and infrastructure into land increasingly exposed to natural disasters (Guzzetti *et al.* 1999; Leroueil 2001). Coupled with this is continued deforestation and increased regional precipitation caused by

changing climate patterns. It is therefore not only predicted that the frequency of slope failures will increase, but the number of people exposed to their consequences will also increase (Guzzetti *et al.* 1999; Leroueil 2001).

Fatalities from landslides in the UK are rare, but the cost to maintain and remediate infrastructure and the built environment as a result of slope instability is high. The UK has approximately 20,000 km of infrastructure cuttings and embankments, and many thousands of flood embankments for water retaining earth structures (owned by organisations including: Network Rail, Highways England, British Waterways and London Underground Limited) (Perry *et al.* 2003a,b). The operation of this infrastructure is critically dependent on the performance of the cutting and embankment slopes of which they are constructed. 7% of the main transport network is located in areas with a moderate to significant landslide potential (Dijkstra & Dixon 2010).

The transient elevations in pore-water pressures that occur in response to periods of prolonged and/or intense rainfall are the main trigger of slope instability in the UK. The UK has recently experienced a significant increase in the occurrence of slope instability incidents (e.g. in response to the wet summer and winter of 2012, and winter of 2013). This has had a major impact on geotechnical assets; particularly transport networks (i.e. road and rail). There is evidence that such engineered slopes are deteriorating over time (e.g. through long-term pore-water pressure equilibration). The majority of the rail network was built in the early- to mid-19th century before modern soil mechanics theories, with little or no knowledge of the processes that will occur after construction (Skempton 1996; Perry *et al.* 2003a,b). Motorway earthworks, constructed since the 1960's, were engineered using modern soil mechanics theories and therefore experience major instabilities less often (Loveridge *et al.* 2010). Seasonal cycles of wetting and drying induce cycles of pore-water pressures (positive and negative), effective stress and straining (Smethurst *et al.* 2012; Take & Bolton 2011) (i.e. seasonal ratcheting). This is especially prominent in high-plasticity clays with high shrink-swell potential (Loveridge *et al.* 2010) and can lead to localised strain softening and eventually progressive failure. The significance of this is that slopes are failing in response to rainfall events that they could have survived in the past.

Although reactivated landslides (i.e. slopes with a pre-existing shear surface at or close to residual strength that, therefore, experience little or no further brittle loss of strength) result in small low velocity movements in response to seasonal pore-water pressure oscillations (Hutchinson 1988; Leroueil 2001), they still cause annual expenses over consecutive years in the order of millions of pounds due to structural damage, insurance costs, engineering measures and remediation. These cost estimates relate mostly to direct effects and little information is available on indirect costs associated with disruption to

traffic and the local economy (Glendinning *et al.* 2009; Gibson *et al.* 2013). Changing climate patterns forecast for the UK are expected to result in more intensive rainfall in winter months and therefore a more regular occurrence of extreme rainfall events and more frequent earthwork failures (Clarke & Smethurst 2010; Dijkstra & Dixon 2010; Loveridge *et al.* 2010). Slope instability therefore poses a significant threat and is expected to become more severe in the future. Railway derailments and catastrophic collapse of water retaining earthworks are among the major hazards. The cost of emergency repair in response to slope failures can be ten times greater than the cost of planned maintenance if conducted prior to failure (Glendinning *et al.* 2009). This highlights the growing need for effective real-time monitoring; to detect and communicate slope instability to allow for responsive action to be taken.

Early warning of slope instability will enable evacuation of vulnerable people and timely repair and maintenance of critical infrastructure. However, currently available warning systems are too expensive for wide-scale use or have technical limitations. The acoustic emission (AE) monitoring approach using active waveguides (i.e. a steel tube with granular backfill surround installed in a borehole through a slope), in conjunction with the Slope ALARMS AE measurement system, has the potential to be an affordable early warning system for slope instability. However, the challenge has been to develop strategies to interpret and quantify deformation behaviour from measured AE.

Prior to the research detailed in this thesis, only general qualitative and simple quantitative information could be provided on slope stability from AE measurements. Koerner *et al.* (1981) defined the following qualitative AE guide for slope stability assessment:

- Little or no AE; probably not deforming and therefore stable.
- Moderate levels of AE; deforming slightly but marginally stable. Continued monitoring is necessary.
- High levels of AE; experiencing substantial deformations and considered unstable with immediate remedial measures required.
- Very high levels of AE; undergoing large deformations and probably in a state of failure.

Such a classification cannot be used to provide a quantitative assessment on slope stability. Dixon & Spriggs (2007) found that by applying displacement rates that were separated by orders of magnitude to active waveguide physical models in constant strain rate compression tests, the magnitude of AE rates generated were also separated by orders of magnitude and proportional to the displacement rate applied. This research

demonstrated for the first time that AE monitoring can be used to provide a quantification of slope movement rates.

The development of an approach to quantify slope deformation behaviour from measured AE will enable the AE monitoring system to provide early warning of slope instability through detecting, quantifying and communicating increasing rates of slope movement in real-time (note that the term ‘real-time’ is used to describe the automatic communication of information immediately after it is detected, in contrast to this information being available subsequent to data downloads and analysis).

1.2. Aim and objectives

1.2.1. Aim

To develop an approach to quantify slope deformation behaviour using AE monitoring to enable AE monitoring to provide an early warning of slope instability through detecting, quantifying and communicating accelerations of slope movement.

1.2.2. Objectives

1) To characterise the AE response from reactivated slope movements;
2) To characterise the AE response from first-time slope failure;
3) To establish a relationship between measured AE and deformation behaviour;
4) To investigate the influence of system variables upon the AE response to applied deformation behaviour; and
5) To develop a framework for the quantification of deformation rates from measured AE, which can be used for any Slope ALARMS system installation.

1.3. Original contributions to knowledge

This study has investigated the use of active waveguides and AE measurements in slope stability monitoring. An approach has been developed to provide a quantitative measure of slope stability (i.e. displacement rates) using AE measurements. Both field monitoring and full-scale physical modelling have been performed to achieve this. The following original contributions to knowledge have been generated, large parts of which have been published in journal articles:

i. Definitive field evidence has been obtained demonstrating the ability of AE monitoring using active waveguides to measure slope movements, which has been confirmed through comparisons with both periodic inclinometer and continuous SAA deformation measurements;

ii. Definitive evidence has been obtained from both field trials and physical modelling showing AE rates generated from active waveguides are proportional to slope displacement rates;

iii. Field evidence has been obtained demonstrating that AE monitoring can detect 'very slow' slope movements of 0.075 mm/day, which was confirmed through comparisons with continuous SAA deformation measurements;

iv. The concept of retrofitting inclinometer casings with active waveguides to convert the manually read instrument to a real-time monitoring system and to extend their operating life has been detailed, and performance of the approach has been demonstrated using a field trial;

v. Active waveguide physical model tests have demonstrated that AE monitoring can be used to quantify slope displacement rates, continuously and in real-time, with accuracy better than an order of magnitude and therefore consistent with standard classifications of landslide movements;

vi. The ability of AE monitoring to provide an early warning of slope movements via text messages has been demonstrated using a field trial at a rail cutting slope, and therefore the system can be used by operators and practitioners to make decisions on infrastructure safety;

vii. The AE response from first-time slope failure has been characterised using a large-scale physical model to simulate slope failure, which has conclusively confirmed that the AE monitoring approach can be used to provide an early warning of slope instability; and

viii. A framework has been developed to allow AE rate-slope displacement rate calibration relationships to be determined for any AE system installation. This provides a universal method that can be used by practitioners when installing AE monitoring systems, to calibrate them to deliver alarm statuses/warning levels that are related to slope displacement rates.

1.4. Thesis structure

Chapter 1 is the Introduction and outlines the justification for the project and its aim and objectives.

Chapter 2 provides a review of the existing literature on slope/landslide behaviour, conventional and emerging monitoring instrumentation and techniques, and AE monitoring of slopes.

Chapter 3 provides an overview of the research methodology employed in this study to meet the aim and objectives.

Chapter 4 details field monitoring case studies of the AE approach. Site descriptions, instrumentation details and sample time series measurements are provided for each case study.

Chapter 5 analyses field measurements and compares measured AE with both periodic and continuous deformation measurements in order to identify a relationship between measured AE and deformation behaviour.

Chapter 6 describes an experimental programme performed on active waveguide physical models in order to quantify an empirical relationship between measured AE and deformation behaviour, and to assess the potential to use the empirical relationship to quantify deformation rates from measured AE.

Chapter 7 presents large-scale first-time slope failure experimentation used to characterise the AE response from slope failure, and to quantify the empirical relationship between measured AE and deformation behaviour over a greater range of applied velocities and deformation magnitudes.

Chapter 8 details a series of physical model tests used to investigate the influence of system variables upon the AE response to applied deformation behaviour.

Chapter 9 develops a framework to allow AE rate-slope displacement rate calibration relationships to be determined for any AE system installation, using an amalgamation of the empirical relationships derived in Chapters 7 and 8.

Chapter 10 summarises the principal findings of this study and makes recommendations for further research.

CHAPTER 2

Literature review

2.1. Introduction

This Chapter provides a literature review that was used to identify gaps in existing knowledge and to define the aim and objectives detailed in Chapter 1. The Chapter begins by providing a description of landslide types, classifications and behaviours (Section 2.2). Conventional and emerging slope stability monitoring methods are subsequently described and compared (Section 2.3). Particular attention is then given to the literature on AE monitoring and its application to the monitoring of soil slopes (Section 2.4).

2.2. Landslides

2.2.1. Landslide types and classifications

A standard method for classifying landslide types is critical in understanding and communicating their behaviour amongst professionals throughout the world. It is important that consistency amongst accepted terminology is provided and used with minimal ambiguity. This will allow the user to identify and locate articles that deal with a given phenomenon and describe its characteristics (Hungr *et al.* 2012, 2014). Varnes (1978), Cruden & Varnes (1996) and Hutchinson (1988) are examples of important works conducted in an attempt to provide prescriptive methods for classifying landslide types. The most commonly used classifications of sub-aerial slope movements are based principally on morphology with some account taken of mechanism, material and rate of movement. The type of material is one of the most important factors in the descriptions, due to its influence on the behaviour of a landslide. Figure 2.1 illustrates the various types of movement-material combinations for the fundamental landslide classifications originally defined by Varnes (1978). The following provide brief definitions of the movement types:

- *Fall* – material detaches from a steep slope with little or no shear displacement and descends through the air.
- *Topple* – the resultant vector of applied forces falls through or outside a pivot point causing material to rotate forwards.
- *Rotational slide* – sliding on one or more concave-upward failure surfaces.

- *Translational (planar) slide* – sliding on a planar failure surface running approximately parallel with the slope (i.e. ground surface).
- *Spread* – material fracturing and lateral extension due to liquefaction or plastic flow of subjacent material.
- *Flow* – disaggregation of material with motion comparable to that of a fluid over a rigid bed where the velocity distribution varies with depth (i.e. minimum velocity at the base due to frictional resistance from the basal surface).
- *Complex slide* – slides involving a combination of two or more of the fundamental movement types.

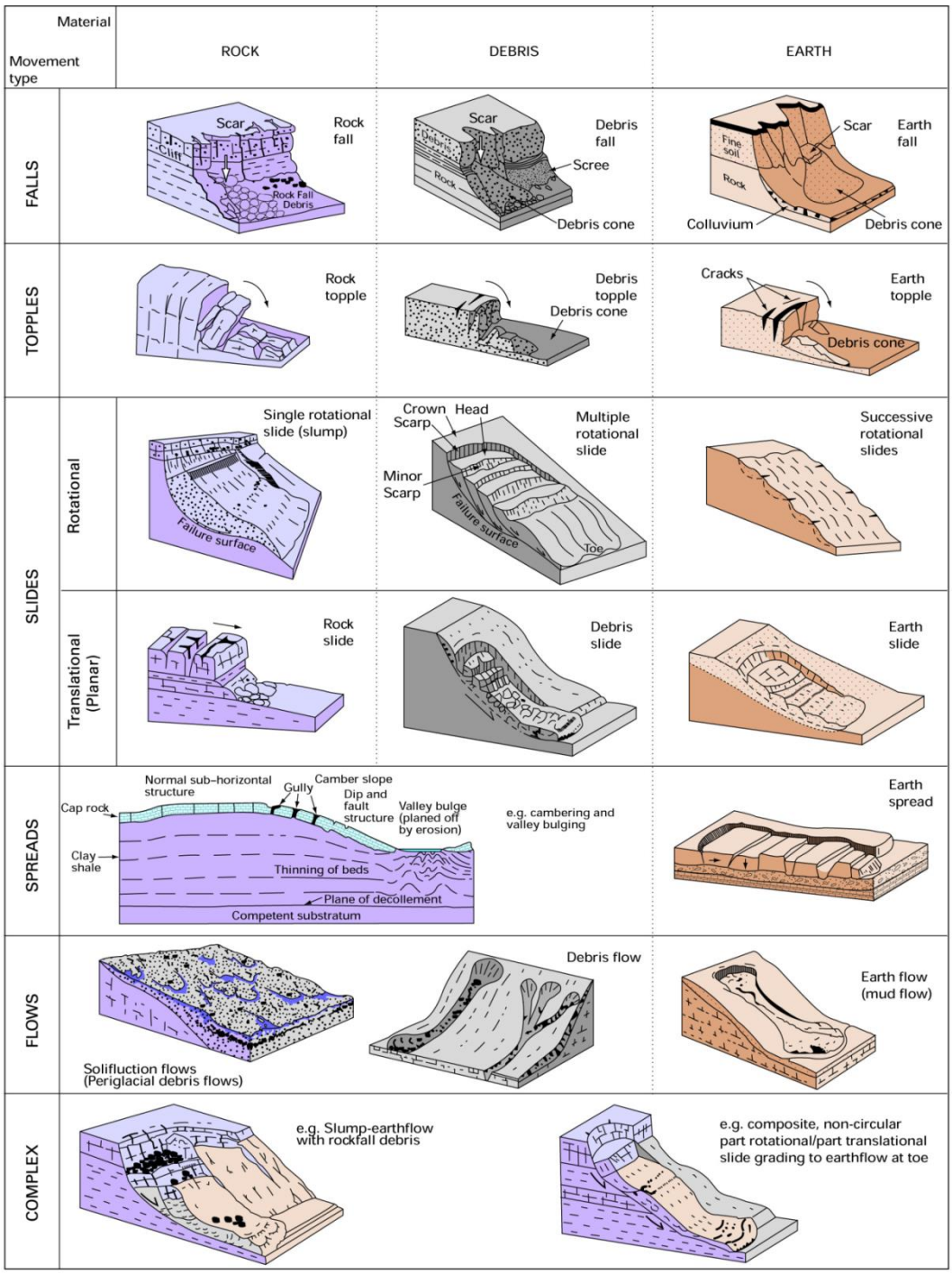

Figure 2.1. Illustrations of the fundamental types of slope movement modified after Varnes (1978) (source: bgs.ac.uk, accessed 10/09/2014)

There are difficulties in attaining discrete classifications of landslide types, such as the following: constant advances in knowledge and landslide science mean that terminology that has been used historically may be technically incorrect and outdated; and the majority of landslides exhibit complex processes and transition between various mechanisms over successive stages. The transformation of a slide into a flow is an example of a mechanism transition: initially a shear surface develops and failure occurs (governed by Mohr-Coulomb criterion) and slide motion initiates, subsequently an energy

increase occurs (e.g. due to an increase in basal surface gradient or an increase in pore-water pressure and liquefaction through infiltration of cracks and pores) and the mass disaggregates and accelerates as a flow (Coussot & Meunier 1996; Malet *et al.* 2005).

The threefold material division proposed by Varnes (1978) (i.e. rock, debris and earth) is not compatible with modern geological or geotechnical terminology and provides minimal information on material mechanical properties (Hungr *et al.* 2012, 2014). Hungr *et al.* (2012, 2014) have developed modifications to the classifications in order to provide geotechnical terminology for material descriptors that allow the user to predict mechanical behaviour (Table 2.1).

Table 2.1. Geotechnical modification of Varnes' (1978) landslide material descriptions (after Hungr *et al.* 2014)

Material name	Character descriptors	Simplified field description for the purposes of classification
Rock	Strong	Strong - broken with a hammer
	Weak	Weak - peeled with a knife
Clay	Stiff	Plastic, can be moulded into standard thread when moist, has dry strength
	Soft	
	Sensitive	
Mud	Liquid	Plastic, unsorted remoulded, and close to Liquid Limit
Silt, sand, gravel, and boulders	Dry	Non-plastic (or very low plasticity), granular, sorted. Silt particles cannot be seen by eye
	Saturated	
	Partly saturated	
Debris	Dry	Low plasticity, unsorted and mixed
	Saturated	
	Partly saturated	
Peat	-	Organic
Ice	-	Glacier

For engineering purposes, particularly the assessment of stability and design of remedial measures, geotechnical classification of landslides is important to predict the shear strength (i.e. pre-peak or post-peak) along shear surface(s). Shear strength of soil is controlled primarily by mineralogy and fabric, and pore-water pressures (Hutchinson 1988). Shear strength is described in terms of effective stress:

$$\tau = c' + (\sigma_n - U)tan\emptyset' = c' + \sigma' tan\emptyset' \quad \textbf{(2.1)}$$

Where τ is the shear strength, c' and $\emptyset'$ are the effective stress shear strength parameters for the soil, σ_n is the total normal stress, U is pore-water pressure, and σ' is the effective stress (Terzaghi 1936; Hutchinson 1988).

The geotechnical classification is therefore concerned with the condition of the soil fabric (i.e. the values of c' and $\emptyset'$) and pore-water pressure conditions local to the shear surface(s) (Hutchinson 1988). Hutchinson (1988) detailed a classification based on these factors (Table 2.2).

Table 2.2. Geotechnical landslide classification after Hutchinson (1988)

Soil fabric conditions (affecting c' and $\emptyset'$)	**Pore-water pressure conditions on shear surface (affecting U)**
1. FIRST-TIME SLIDES IN PREVIOUSLY UNSHEARED GROUND: soil fabric tends to be random (or partly orientated as a result of depositional history) and shear strength parameters are at peak or between peak and residual values. 2. SLIDES ON PRE-EXISTING SHEARS associated with: 2.1. Reactivation of earlier landslides. 2.2. Initiation of landsliding on pre-existing shears produced by processes other than earlier landsliding, i.e: a) Tectonics b) Glacitectonics c) Gelifluction of clays d) Other periglacial process e) Rebound f) Non-uniform swelling In these cases the soil fabric at the slip surface is highly orientated in the slip direction, and shear strength parameters are or about residual value.	A. SHORT-TERM (undrained) – no equalisation of excess pore-water pressure set up by the changes in total stress. B. INTERMEDIATE – partial equalisation of excess pore-water pressures. Delayed failures of cuttings in stiff clay (Vaughan & Walbancke 1973) are usually in this category. C. LONG-TERM (drained) – complete equalisation of excess pore-water pressures to steady seepage values. Note that combinations of A, B and C can occur at different times in the same landslide. A particularly dangerous type of slide is that in which long-term, steady seepage conditions (C) exist up to failure but during failure undrained conditions (A) apply, i.e. a drained/undrained failure.

A focus of the research described in this thesis was to trial the AE monitoring system in translational/rotational/complex slides in both natural and engineered slopes formed predominantly of fine-grained material. In addition, effort was made to monitor both reactivated slopes and first-time slopes failures. These are the types of slopes that present serviceability and ultimate limit state (SLS and ULS) problems to infrastructure within the UK, and they move along discrete shear surfaces (i.e. surfaces where shear strains are localised).

2.2.2. Slope behaviour

2.2.2.1. Instability and failure

The stability of a slope is dictated predominantly by the ratio of two parameters (i.e. using a factor of safety); namely the shear strength (i.e. stabilising forces) and shear stress (i.e. destabilising forces) respectively along the shear surface(s). When the factor of safety approaches unity full mobilisation of shear strength occurs (Dixon & Bromhead 2002). A reduction in stability will therefore occur as a consequence of a reduction in strength or an increase in applied stress. Shear strength in soil will reduce in two main ways: through structural changes as a result of processes such as weathering; or a reduction in inter-particle contact stress (i.e. effective stress), usually due to an increase in pore-water pressure after periods of rainfall. Stress can increase in many ways, such as the following: removal of lateral or underlying supports; surcharge; earthquakes and other

forms of transitory earth stress; altered lateral earth pressures; and volcanic process. The most common causes of slope failure globally are intensive rainfall and earthquakes (Schuster & Krizek 1978).

Shear surfaces can develop in slopes formed of strain-softening materials (e.g. overconsolidated clay) after very small deformations (millimetres) (Skempton & Petley 1985; Bromhead 2004). As a shear surface develops the sliding mass accelerates and first-time failure occurs. When at marginal stability these slopes present a particular threat to buildings and civil infrastructure, in terms of both serviceability and ultimate limit states, as failures can occur suddenly without warning unless adequate monitoring methods are implemented (Dai & Labuz 1996). In its initial state the strain-softening geomaterial is un-sheared and undergoes progressive failure prior to the brittle loss of strength and collapse (Chandler 1984). Figure 2.2 illustrates a conceptual factor of safety- and displacement-time relationship for a first-time slope failure. The slope in Figure 2.2 experienced creep movement prior to the occurrence of a trigger (e.g. a period of intensive rainfall or undrained loading (Hutchinson & Bhandari 1971) leading to elevated pore-water pressures) at time '0', which initiated a gradual reduction in the factor of safety with time. As the factor of safety approached unity, brittle strength loss occurred and a full failure surface developed. Subsequently, the slide mass accelerated and moved along the failure surface, approaching a peak velocity. Resistance was mobilised (e.g. through dissipation of pore-water pressures, remoulding of the landslide toe and/or a reduction in basal surface gradient) and the landslide decelerated and approached equilibrium (Terzaghi 1950; Bishop 1967; Skempton & Petley 1967; Chandler 1984; Leroueil 2001; Hungr *et al.* 2012).

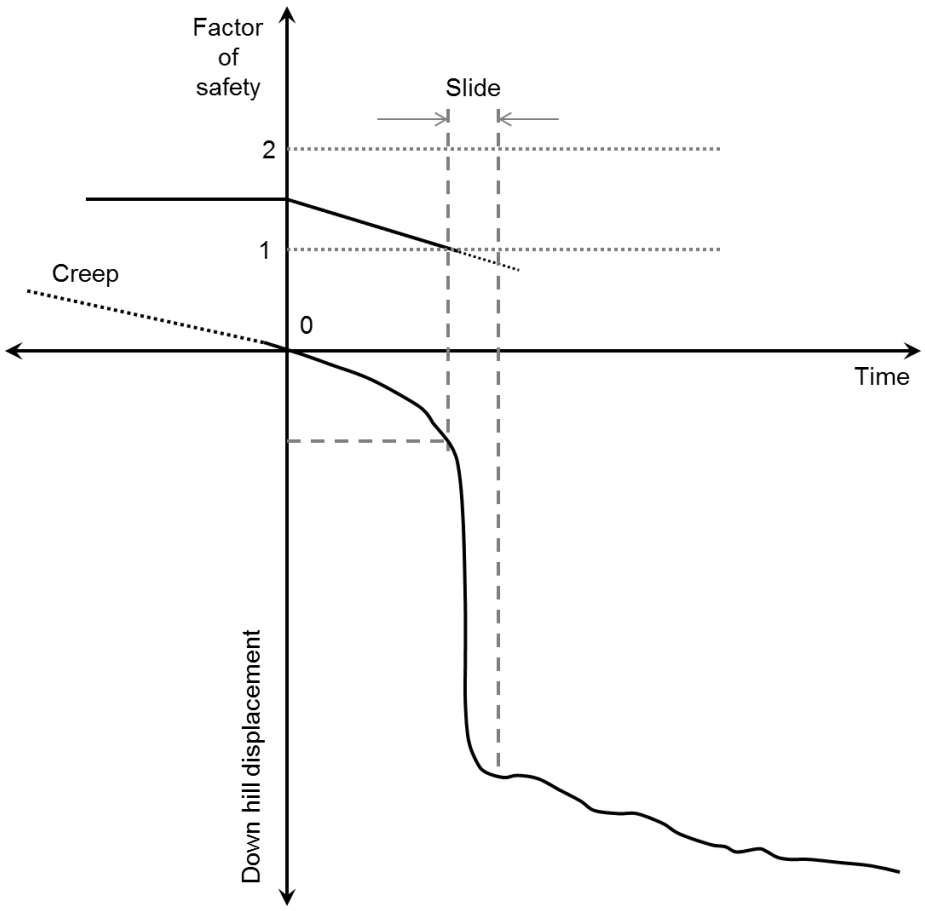

Figure 2.2. Factor of safety- and displacement-time behaviour for first-time slope failure after Terzaghi (1950)

Skempton & Petley (1967) identified the successive stages that occur within a strain-softening clay that is subjected to simple shear. Before the peak strength is reached continuous non-homogeneous straining occurs. As the peak strength is approached, localised shear surfaces are formed 10-30 degrees relative to the direction of movement. When slip along these shears is no longer possible new shear zones are developed parallel to the direction of motion. Further movement causes these shears to propagate through the soil mass to form a full shear surface. The complete shear surface is developed after the clay particles become strongly orientated in a direction parallel to shearing (Skempton & Petley 1967). Figure 2.3 illustrates this process in terms of changes in shear strength, taken from triaxial laboratory testing. After the peak strength is surpassed the strength reduces, as the volume of the soil increases (i.e. dilation occurs). The critical strength is identified by no further volume change (i.e. constant void ratio). The residual strength is reached as the plate-shaped clay particles align to form a slickenside. As the peak strength is surpassed within a localised volume of soil, brittle strength loss occurs and greater stress is therefore sustained throughout the rest of the slope. Peak strength is mobilised in other areas of the slope and subsequently losses in strength occur. Successive reductions in strength propagate throughout the slope and progressive failure occurs; eventually an

entire shear surface develops exhibiting residual strength (or strength close to residual) and the slope fails (Skempton 1964). Figure 2.4 depicts a developed shear surface within a slope and details the shear zone.

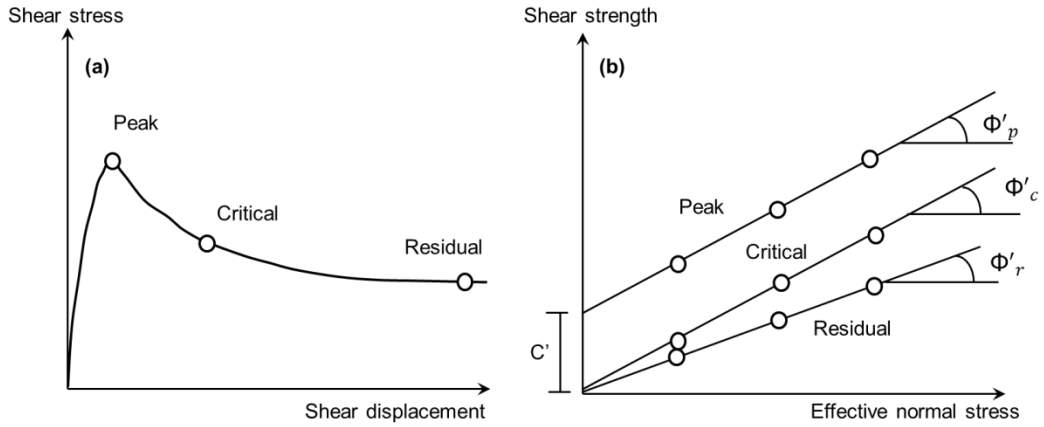

Figure 2.3. a) Shear stress-shear displacement and b) shear strength-normal effective stress relationships for overconsolidated clay in triaxial experiments after Craig (2004)

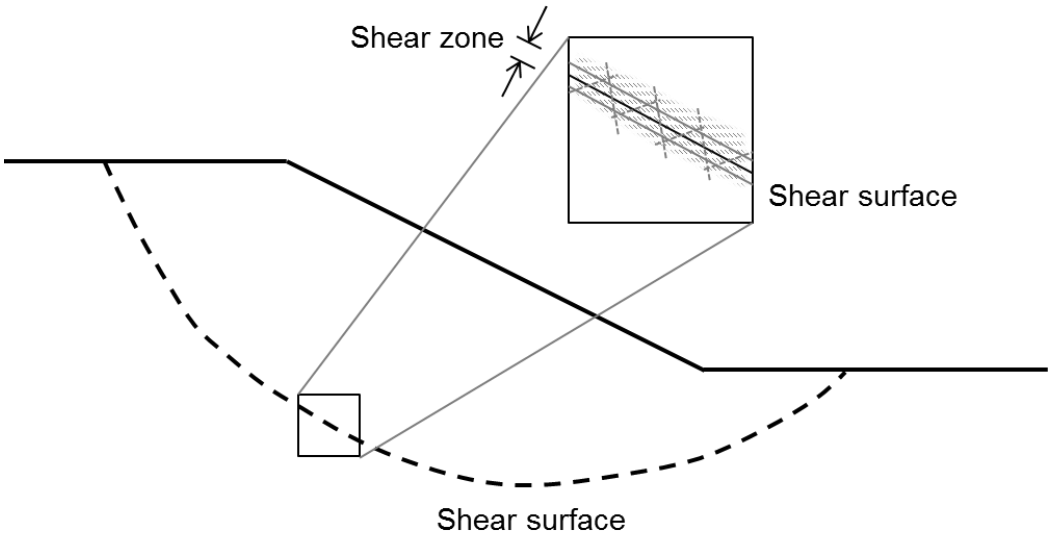

Figure 2.4. Development of a shear zone and full shear surface within a slope after Leroueil *et al.* (2012)

Leroueil (2001) identified four primary conditions required for progressive failure to occur, these include: non-uniformity in the distribution of shear stresses; local shear stresses that exceed the peak shear strength somewhere locally; boundary conditions that allow deformations; and brittleness of the geomaterial. The main factors that can lead to progressive failure include: a change in geometry or shear stress in the system (i.e. through excavation or erosion at the toe, or loading at the head); a reduction in normal effective stress and thus in peak and residual strengths (e.g. pore-water pressure equilibration, intensive rainfall, or any other mechanism that elevates pore-water pressures); and/or a reduction in strength parameters (i.e. lowering of the strength

envelope due to creep, fatigue or weathering). There are various locations within a slope for progressive failure to initiate, such as the following: horizons that exhibit one or a combination of; high pore-water pressures, low peak strength, high brittleness, or shear rigidity that concentrates strain. Another example is at the boundary between two strata where a shear strength discontinuity exists (Bromhead 2004). Bromhead (2004) provided an example of such a shear strength discontinuity where sandstone cap-rock overlies clay. At the interface between the two materials the effective stress is the same, due to equal total stress and pore-water pressures, but the angle of internal friction is greater in the sandstone and therefore shear zones would develop within the clay.

2.2.2.2. Types and rates of movement

The four stages of slope movement defined by Leroueil (2001) are depicted in Figure 2.5: pre-failure; onset of failure; post-failure; and reactivation. It can be seen that the displacement rate (or velocity) vs. time relationship for both first-time failures and reactivations are expected to increase exponentially with time until a peak velocity is reached, and then subsequently decay exponentially until movement ceases and equilibrium is regained.

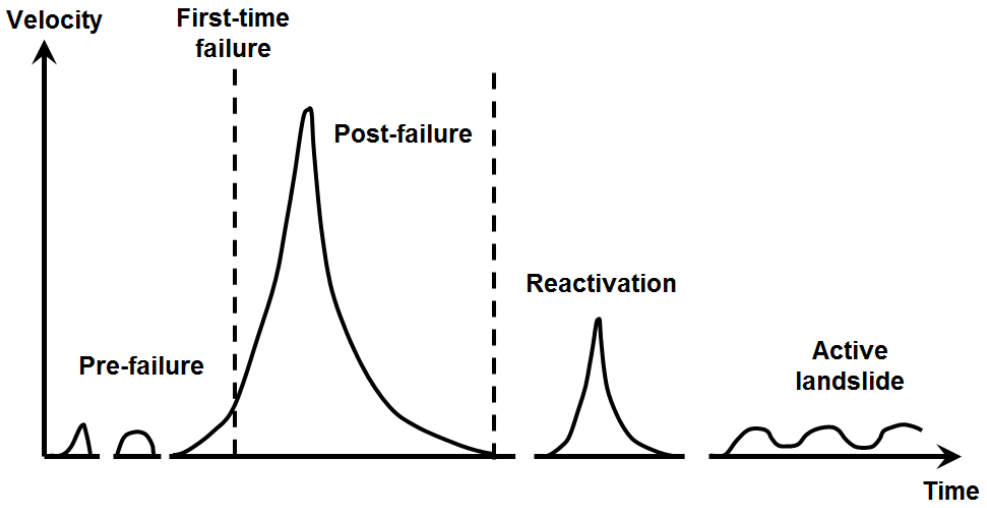

Figure 2.5. Stages of landslide movement after Leroueil (2001)

In reactivated landslides formed in fine-grained soils the shear surface is already at or close to residual strength and therefore no further strain-softening (i.e. brittle loss of strength) can take place and small low velocity movements generally occur (Hutchinson 1988; Leroueil 2001). Movement of such reactivated landslides is generally triggered by periods of rainfall and therefore transient elevations in pore-water pressures (Bjerrum 1967; Bromhead 2004). Rapid movements in reactivated landslides only occur in extreme circumstances, due to: a rapid increase in pore-water pressures and subsequent reduction

in strength; an increased gravitational component of shear stress through excavation or surcharging at the head; and/or earthquakes and other seismic stresses (Leroueil 2001).

A mass movement with high post-failure velocity has the potential to cause significant damage to the built environment and result in fatalities. Post-failure velocity is governed by the magnitude of strength loss (i.e. brittleness) during failure, and high slope velocities are therefore associated with first-time failures. During first-time failure the velocity of the sliding mass is expected to progress over several orders of magnitude; from the gradual development of a defined failure surface producing low velocities, to the subsequent strength loss during brittle failure generating high velocities.

The order of magnitude slope displacement rate classifications initially developed in Schuster & Krizek (1978) (i.e. Varnes 1978) and later modified by Cruden & Varnes (1996), and reported by Anderson & Holcombe (2013, p92) and Hungr *et al.* (2014) are shown in Figure 2.6. The velocity scale varies over several orders of magnitude, from millimetres per year to metres per second.

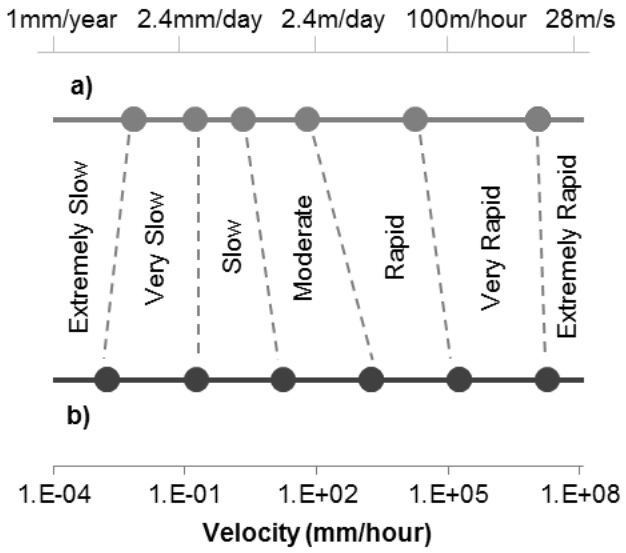

Figure 2.6. Landslide velocity scales taken from; a) Schuster & Krizek (1978) (i.e. Varnes 1978), and b) Cruden & Varnes (1996), Anderson & Holcombe (2013, p92) and Hungr *et al.* (2014)

2.2.2.3. Movement patterns, with particular reference to pore-water pressures

Rainfall is widely recognised as the primary/most common trigger in initiating slope instability. Intense rainfall over short durations has the potential to trigger shallow landslides; however, the triggering of deep-seated landslides generally requires rainfall of longer duration as changes in pore-water pressures at depth are delayed relative to changes at the boundaries (Leroueil 2001). Rainfall intensity-duration relationships, along with antecedent moisture conditions in some cases, have been used to develop thresholds

for landslide failure predictions and early warning systems by various authors (Caine 1980; Zan *et al.* 2002; Guzzetti *et al.* 2008; Crosta *et al.* 2012; Jakob *et al.* 2012).

Matsuura *et al.* (2008) examined the movements of a reactivated landslide formed of weathered mudstone; the landslide's shear surface was at approximately 5 m below ground level. Figure 2.7 shows the displacement (measured using a borehole wire displacement gauge) and pore-water pressure (measured using a piezometer installed at the shear surface) time series for a series of movements. This demonstrates that: movement was triggered by elevated pore-water pressure levels; and movement accelerated with increased pore-water pressure and decelerated with dissipation of pore-water pressure (i.e. the velocity of movement was governed by, and proportional to, the magnitude of pore-water pressures). Figure 2.8 shows the measured relationship between velocity and pore-water pressure throughout an episode of movement, which is non-linear. Non-linear slope velocity vs. pore-water pressure relationships have also been found by other authors (e.g. Skempton 1985 and Massey *et al.* 2013). A non-linear relationship can be explained by changes in shear strength (e.g. caused by behaviour of the particles during shearing) (Skempton 1985; Massey 2010) or changes in shear stress (e.g. caused by an upward curved basal shear surface, and therefore reduction in gradient).

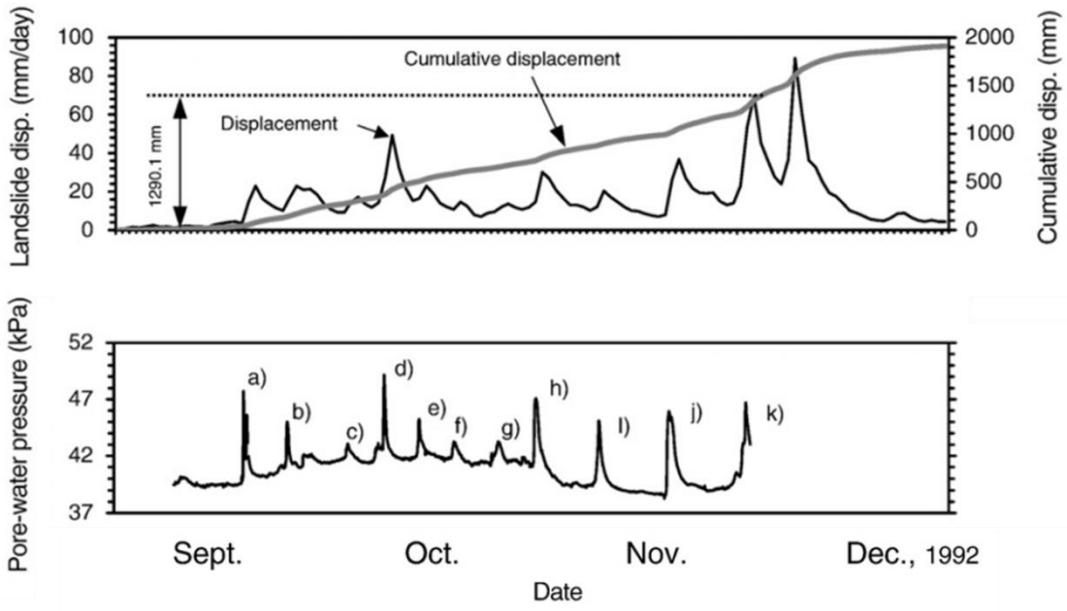

Figure 2.7. Displacement-, velocity- and pore-water pressure-time series for a series of slope movements (Matsuura *et al.* 2008)

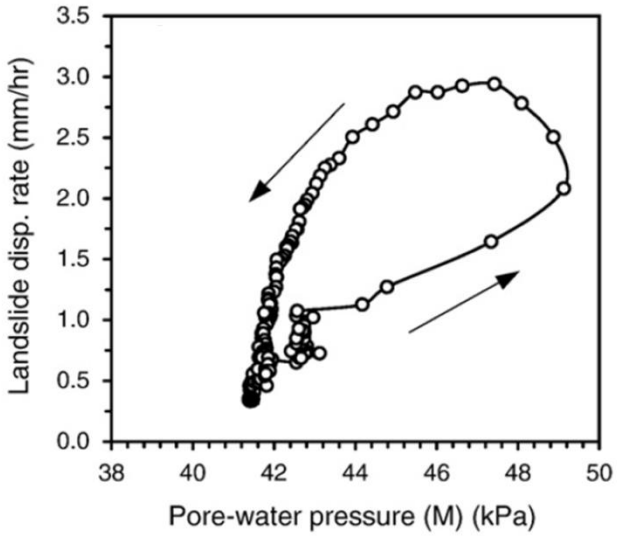

Figure 2.8. Velocity vs. pore-water pressure relationship for a slope movement event (Matsuura *et al.* 2008)

Massey *et al.* (2013) monitored the Utiku landslide, North Island, New Zealand. The landslide is classified as a reactivated, deep-seated, translational slide that moves along a fully developed shear surface within a laterally persistent layer of clay. Surface movement of the landslide was measured using four continuous GPS (cGPS) stations, and pore-water pressures were monitored using vibrating-wire piezometers. Figure 2.9 presents conceptually the movement patterns identified for the Utiku landslide. The landslide experiences slow continuous plastic deformation (e.g. creep) with seasonal accelerations of movement (e.g. triggered by wet weather and elevated pore-water pressures).

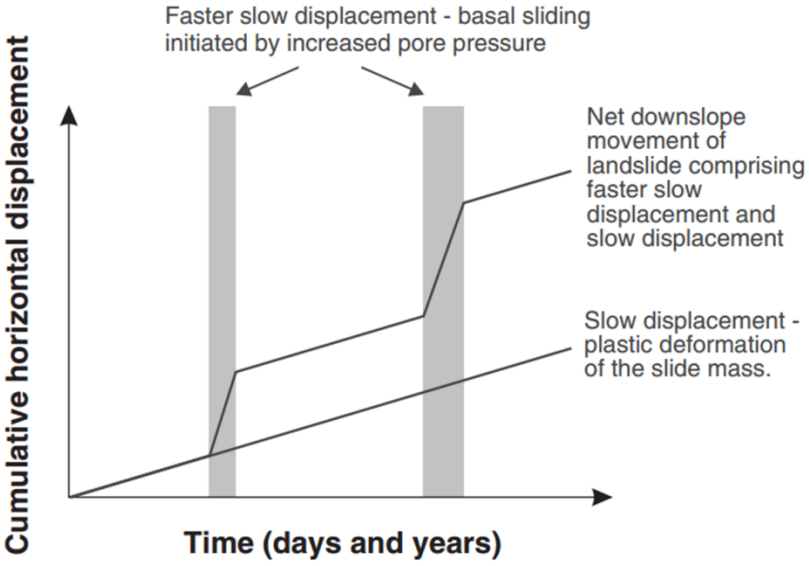

Figure 2.9. Conceptual model illustrating displacement patterns for the Utiku landslide (Massey *et al.* 2013)

Allison & Brunsden (1990) investigated the mechanisms of movement of a reactivated mudslide in the Wealden Beds of the Isle of Purbeck, which had a shallow shear surface at approximately 1 m below ground level. Surface displacements were monitored by measuring the distance between pegs using potentiometers, and pore-water pressures were monitored using pressure transducers and Casagrande standpipe piezometers. Three types of reactivated movements were identified: small, multiple, slip-stick movements (e.g. Figure 2.10a); gradual or graded slip (e.g. Figure 2.10b); and rapid surge events (e.g. Figure 2.10c). The magnitude, duration and pattern of pore-water pressure elevation governed which type of movement occurred.

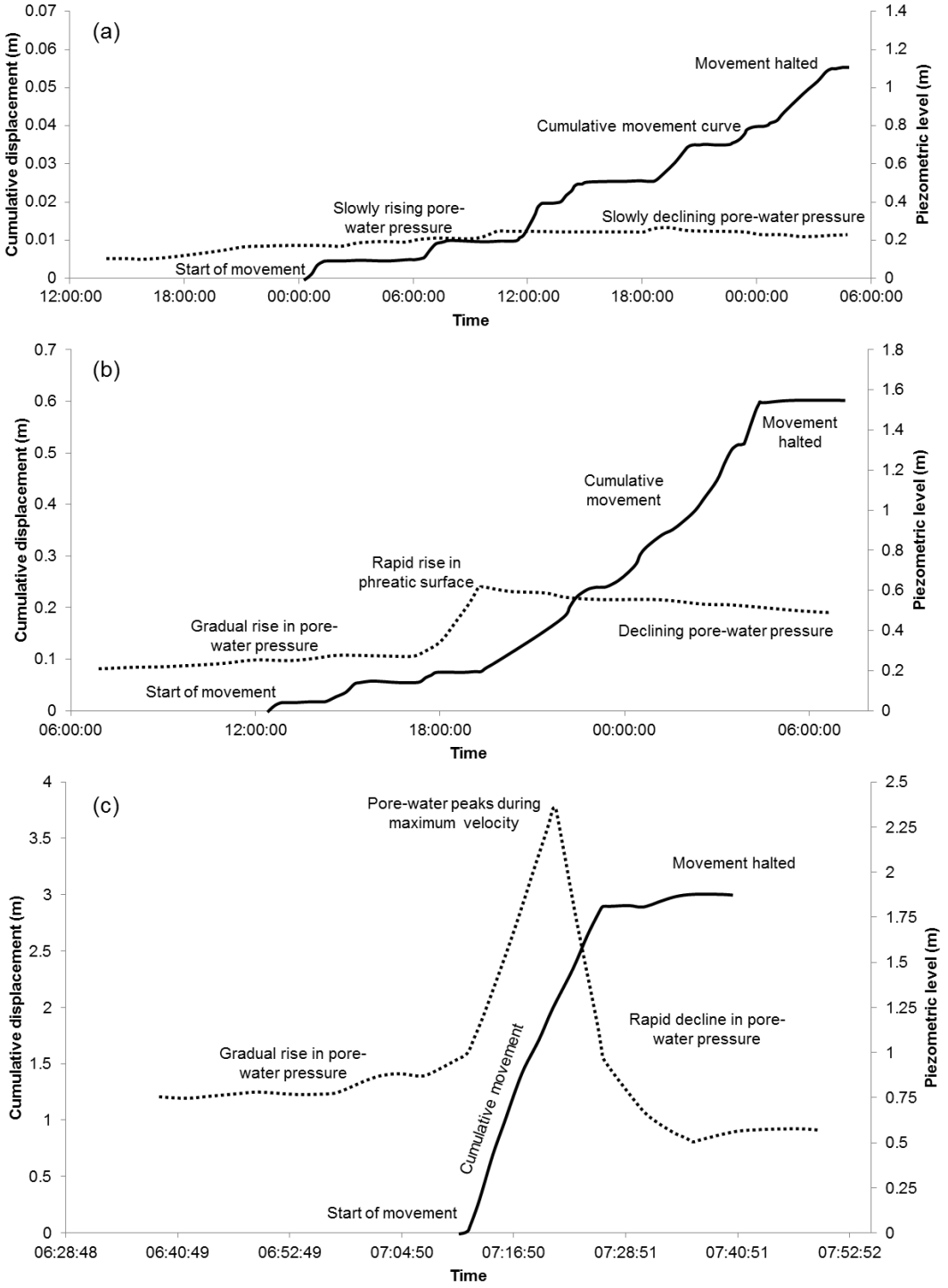

Figure 2.10. Displacement- and piezometric level-time series for mudslide movement patterns after Allison & Brunsden (1990): a) multiple movement event; b) graded movement event; and c) surge movement event.

Petley *et al.* (2005) instrumented the Tessina landslide (a large seasonally active slope failure in north-east Italy). Surface movement monitoring used automated Electronic Distance Measurement (EDM) of a series of reflectors located across the slope, with measurements recorded at 6-hour intervals. This provided surface deformation information with relatively high spatial and temporal resolution. Four types of movement patterns were identified (Figure 2.11), similar to those found by Allison & Brunsden

(1990). Types I and II are associated with pre-failure deformations (i.e. shear surface development) with low velocities, below 2-3 mm/day. Types III and IV relate to reactivated movements along a shear surface at, or near, residual strength, with velocities in the order of millimetres to metres per day (Petley *et al.* 2005; Massey 2010).

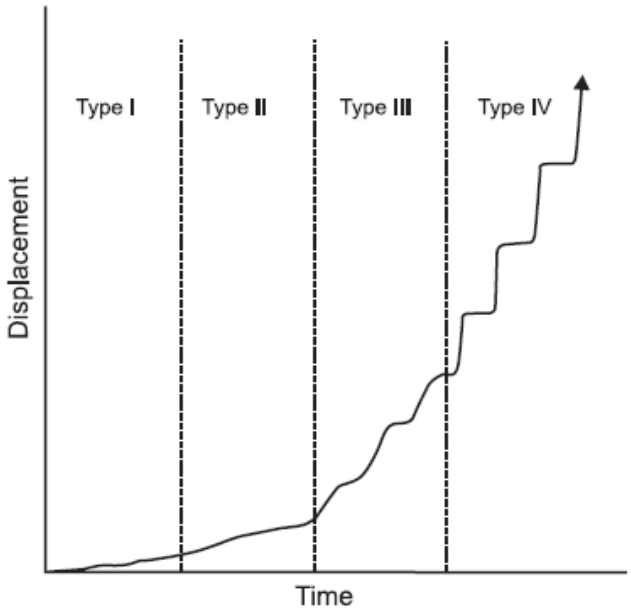

Figure 2.11. Displacement-time relationship for four types of landslide movement (Petley *et al.* 2005)

Cooper *et al.* (1998) detail the behaviour of a first-time slope failure in the Selborne stability cutting experiment. A 9 m deep cut slope was formed in Gault Clay and instability was triggered using pore-water pressure recharge. 1.5 m high steps were cut to form the slope in six sections, after which pore-water pressure equilibration was allowed to occur. Several inclinometers were installed along a cross-section through the slope. A series of 20 recharge wells were installed and pore-water pressure infiltration was initiated on day '0' in Figure 2.12. Figure 2.12 shows the shear surface displacement-time behaviour measured in selected inclinometer casings throughout the experiment. The inset in Figure 2.12 shows the location of the inclinometers, along with the geometry of the slope and shear surface. A near-circular shear surface formed under the upper and middle parts of the slope, with a planar, near-horizontal section in the lower part of the slope, emerging at the toe. Between day 184 and 189 the typical rate of movement measured was 0.6 mm/hour. On day 196 an obvious back scarp formed and the typical rate of movement approached 4 mm/hour. Later on day 196 the rate of movement reached 58 mm/hour, prior to the instruments becoming disrupted and unreadable, and full failure occurred.

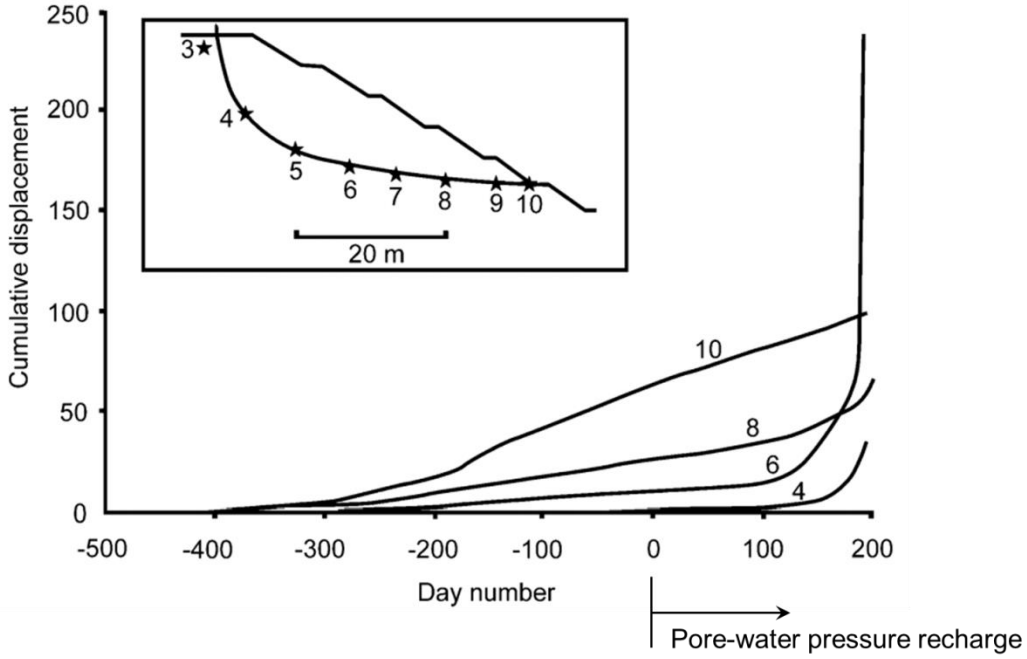

Figure 2.12. Displacement-time data from the Selbourne stability cutting experiment, inset showing geometry of the slope and shear surface and inclinometer locations (after Cooper *et al.* 1989 and Petley *et al.* 2002)

Various authors have examined the inverse of velocity vs. time behaviour of landslides, in an attempt to predict time-to-failure (e.g. Saito & Uezawa 1961; Saito 1965; Saito 1969; Petley *et al.* 2002; Kilburn & Petley 2003; Petley *et al.* 2005; Ng 2007). Petley *et al.* (2002) and Ng (2007) identify two inverse of velocity vs. time trends of behaviour; linear (Figure 2.13a), and asymptotic (Figure 2.13b). Linearity is associated with brittle failure mechanisms and shear surface development (e.g. first-time failure), and asymptotic is associated with movements along an already developed shear surface (e.g. reactivations) (Petley *et al.* 2002; Ng 2007; Massey 2010).

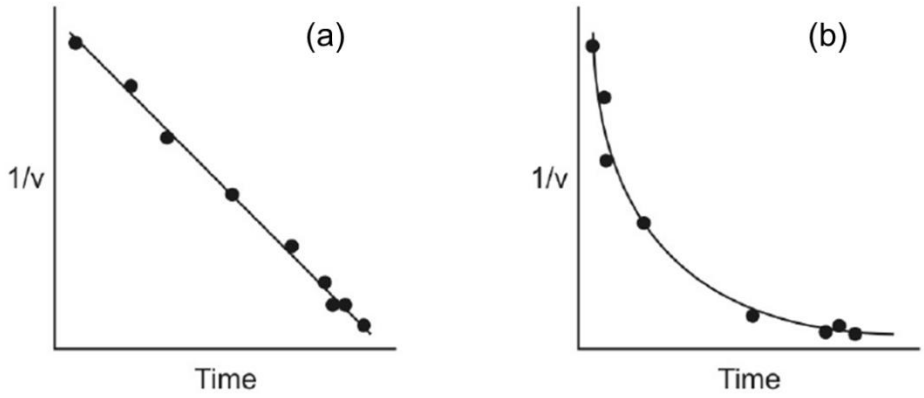

Figure 2.13. Linear (a) and asymptotic (b) inverse of velocity vs. time trends of landslide behaviour (after Ng 2007 and Massey 2010)

2.3. Conventional and emerging monitoring instrumentation and techniques

2.3.1. Introduction

There is a clear need for instrumenting and monitoring marginally stable slopes and landslides in order to: provide early warning of movement and of failure; provide information for input into analysis and remediation design; monitor landslide behaviour in response to and through construction; verify the stability of a landslide subsequent to remediation; and monitor the condition of infrastructure (in terms of serviceability and ultimate limit states) that have the potential to be affected by slope instability (Dunnicliff 1988; Machan & Beckstrand 2012). Examples of important parameters to monitor are: shear surface depths; direction and rate of mass movement; and pore-water pressures, be they positive or negative (i.e. suction), along a shear surface or potential shear surface as this informs of transient changes to effective stress and therefore the stability of the slope. The total magnitude of deformation is also of interest as a few millimetres of displacement can impact on the serviceability limit state of adjacent buildings and infrastructure. Additionally, soils with strain softening characteristics can exhibit a reduction in strength subsequent to the mobilization of peak strength in response to very small deformations, at which point high magnitude and rapid deformations can occur (Skempton 1964).

The cost of remediation subsequent to landslide failure is often an order of magnitude greater than the cost of corrective measures and repairs if conducted prior to failure (Glendinning *et al.* 2009), and this highlights the importance of slope stability monitoring; to detect the onset of instability so that preventative works can be performed. A cost-benefit analysis is usually performed during the design of the monitoring programme to determine the most cost effective monitoring solution. Slope monitoring costs range from inexpensive and short term to costly and long term (Kane & Beck 2000). The labour costs associated with manual readings of instruments is high and is preferentially mitigated by the use of automated data acquisition systems (Machan & Beckstrand 2012). The number of automated monitoring sites is still small, although growing in number, and the large majority of deformation instruments (e.g. inclinometers) are read manually only a few times a year. This method of operation cannot provide real-time information for use in early warning of instability.

There are many different techniques and types of instrumentation commonly used in slope monitoring. No single technique or instrument can provide sufficient information about a landslide, and therefore various combinations are usually used. Each technique or

instrument has associated capital (i.e. product and installation) and operating (e.g. labour and power) costs, along with varying degrees of performance. The performance of monitoring techniques and instrumentation is often measured in terms of accuracy and precision, spatial and temporal resolutions, sensitivity, and reliability.

Surface deformation monitoring methods investigate the change in shape of the ground surface and can provide measurements of the direction and rate of slope movement, and often provide high spatial resolution. Subsurface deformation monitoring methods provide the information necessary for stability assessment and remediation design. Subsurface instruments often yield high levels of accuracy, although with relatively low spatial resolution as the instrument informs only of the soil surrounding the borehole in which it is installed. The traditional manually read inclinometer is the most commonly used instrument for subsurface deformation monitoring and has a reported field accuracy of the order +/- 4 to 8 mm per 30 m (e.g. Mikkelsen 2003; Simeoni & Mongiovì 2007; Abdoun *et al.* 2013). This is a measure of the total error per unit length, which is composed of the random error and systematic error. Random error accumulates with the square root of the number of measurement increments and is reported to be +/- 1.24 mm over 30 m (Mikkelsen 2003). Random error remains after all systematic errors are corrected and removed, and is therefore the limit of precision possible with good practice. If only a single measurement increment is of interest, for example over a localised shear zone, accuracy of the order +/- 0.2 mm is possible (Mikkelsen 2003). Traditional inclinometers provide relatively high resolution with depth as measurements are recorded at 0.5 to 1 m increments, however, it is an interval monitoring instrument and offers relatively low temporal resolution as measurements can only be taken when the casing is manually surveyed.

The advent of in-place inclinometers overcame this problem as a probe-string or an individual probe (installed at the shear surface depth once the depth has been determined from manual surveys) can log data continuously and with high temporal resolution (i.e. at user-defined time intervals ranging from minutes to hours). A recent development is the ShapeAccelArray (SAA) (e.g. Abdoun *et al.* 2013 detail a case history using the SAA), which comprises a string of MEMS (Micro-Electro-Mechanical Systems) sensors installed at regular increments along the length of a borehole (available SAA gauge lengths are 0.2, 0.305 and 0.5 m). The SAA monitors subsurface deformations continuously and with high temporal resolution. The accuracy reported in the literature for the SAA is +/- 1.5 mm per 30 m (e.g. Abdoun *et al.* 2013). In-place inclinometers and SAAs can also provide remote real-time information if connected to a communication system.

Another consideration is the operational life of such subsurface instrumentation. Localised shear surface displacements of the order of 50 mm have been sufficient to induce excessive bending within inclinometer casings and render them unusable (i.e. the torpedo probe can no longer pass the shear surface), although shear surface displacements of the order 100 mm are more typical. In contrast, shear surface displacements in excess of 100's of mm have been recorded using SAA systems (Dasenbrock 2014).

There is a clear need for affordable instrumentation that can provide continuous, remote, real-time information with high temporal resolution on slope movements to provide early warning of instability; for use in the protection of people and infrastructure by practitioners. Current systems are either too expensive for wide-scale use or have technical limitations.

Section 2.3.2 provides descriptions of conventional and emerging slope monitoring instruments and techniques, and Table 2.3 details advantages and disadvantages of each of these, particularly related to the accuracy and spatial and temporal resolution they offer. The general information included in Section 2.3.2 and Table 2.3 amalgamates and builds upon information provided in Pilot 1984, Bhandari 1988, Dunnicliff 1988, Massey 2010, and the EC7 monitoring standard (TC 341 WI 0034 1066: 2011 (E)). Other specific references are provided throughout.

2.3.2. Comparisons of instrumentation and monitoring techniques

2.3.2.1. Surface deformation monitoring

2.3.2.1.1. Global positioning system (GPS)

GPS receivers are used to survey locations of markers on the ground surface in order to produce 3D topographical data. Sequential GPS surveys of marker arrays allow measurement of the change in shape of the ground surface (i.e. slope surface). Signals transmitted from orbiting satellites are detected by GPS receivers, and typically a minimum of 4 satellites are required to determine position (i.e. x, y and z). A Differential Global Positioning System (DGPS) can be implemented to achieve greater accuracy. The DGPS utilises an extra control; a reference station on the ground that has a known location. This reduces error and can yield accuracy of the order of a millimetre, which is often necessary for slope deformation studies (Millis *et al.* 2008).

2.3.2.1.2. Total station

A total station is used to measure angles and distances between target/prism arrays that are installed across the slope surface. Electronic Distance Measurement (EDM) is

employed to measure the distances. Implementation of triangulation/trilateration/ triagnulateration to the measurements allows three-dimensional topographic information to be quantified. The target/prism array can be surveyed at regular time intervals and, using a stable reference point, ground surface displacement vectors (i.e. direction and magnitude) can be quantified (Petley *et al.* 2005; Millis *et al.* 2008).

2.3.2.1.3. Photogrammetry

Slope ground surface measurements can be obtained from photographic images and employing photogrammetry. Overlapping a minimum of two photographs taken from different, known, locations allows accurate reconstruction of the slope ground surface, if sufficient ground control points with known locations are used. Both aerial (e.g. using manned or unmanned aircraft/aerial vehicles) and terrestrial photogrammetry can be employed to conduct each survey. Photogrammetric surveys provide large quantities of data points with spatial measurements that can be used to produce Digital Elevation Models (DEMs). Ground surface displacement vectors (i.e. direction and magnitude) can be quantified by conducting surveys at regular time intervals.

2.3.2.1.4. Remote sensing

Remote sensing uses the reflection of electromagnetic energy from the earth's surface to produce imagery and geometrical measurement. Examples used in slope monitoring are InSAR (Synthetic Aperture Radar Interferometry) and LiDAR (Light Detection and Ranging). Surveys can be performed using terrestrial, aerial and satellite sensors. Remote sensing surveys provide large quantities of data points with spatial measurements that can be used to produce DEMs. Dynamic measurement is also possible (e.g. slope movement measurement) when imagery is taken incrementally through time (Petley *et al.* 2005; Cornforth 2012). The sensor detects electromagnetic energy within the infrared wavelengths in addition to the wavelengths of visible light. This provides greater information about objects and surfaces, which allows classification through knowledge of spectral signatures.

2.3.2.1.5. Tilt meter

Tilt meters are used in slope monitoring as an indirect measurement of deformation. They are particularly useful for monitoring deformation in slopes that move with a large rotational component, however, they do not successfully measure translational movement. Numerous types are available (e.g. electrolytic tilt meter using a spirit level, tilt meter with pendulum sensor, and precision tilt meter with servo accelerometer).

2.3.2.1.6. Extensometer

Extensometers are used to measure localised slope movements along a single axis (i.e. in one-dimension) and therefore provide low spatial resolution, but often high temporal resolution (depending on the logging frequency). The instrument should be installed between two locations of which the relative movement is of interest. Numerous types of extensometer are available (e.g. rod extensometer and magnet extensometer).

2.3.2.1.7. Fibre optics (e.g. Brillouin Optical Time Domain Reflectometry – BOTDR)

Voltage pulses are emitted into fibre optic cables and their reflected signal is measured and characterised. This provides information on straining within the fibre optic cable, due to changes in impedance. In BOTDR, which is useful for monitoring large lengths of the ground surface, the wavelengths of the back-scattered waves are monitored and are related to changes in strain. The location to any deformation along the cable can be determined using the velocity of the transmitted pulse.

2.3.2.1.8. Geophone/accelerometer

Geophones/accelerometers are particularly useful for monitoring ground surface movement accelerations, which could be generated by earthquakes (i.e. a slope destabilisation trigger) or by rapid and brittle slope deformations.

2.3.2.1.9. Movement tracking using electrical resistivity monitoring

Grids of electrodes are installed across the surface of a slope. Resistivity measurements from between the electrodes are related to the separations between them, and the measurements can be inverted to track electrode movements (Wilkinson *et al.* 2010; 2014). Movement tracking of a grid of electrodes offers a potential method of acquiring relatively high spatial and high temporal slope ground surface information. This is an emerging technique and requires further development.

2.3.2.2. Subsurface deformation monitoring

2.3.2.2.1. Inclinometer

Inclinometer casings are installed in a borehole and penetrate stable stratum below any shear surface or potential shear surface that may form beneath a slope (5 to 6 m embedment below the shear surface is typical). The annulus around the casing is backfilled with bentonite-grout that has comparable properties to the surrounding soil. A probe (manual torpedo, in-place or string) measures the inclination of the casing with depth. This allows the horizontal deformation vs. depth profile of the casing to be

determined. If this is plotted through time the magnitude and rate of displacement can be quantified, and the depth to any shear surface(s) can be determined (Simeoni & Mongiovi 2007; Wan & Standing 2014). The conventional manual probe provides measurements at discrete time intervals; however, the in-place or probe-string systems can monitor continuously with high temporal resolution.

2.3.2.2.2. Borehole extensometer

Extensometers are installed inside boreholes to measure localised deformations between two points of interest, in one-dimension. Various types are available (e.g. rod extensometer, mobile extensometer and fibre optic extensometer). See extensometer (surface) for further details (Section 2.3.2.1.6).

2.3.2.2.3. Time domain reflectometry (TDR)

A voltage pulse waveform is sent down a coaxial cable, which is installed in a borehole, using a cable tester. If the pulse encounters a change in the characteristic impedance of the cable then it is reflected; a change in characteristic impedance occurs due to differences in the outer and inner conductors of the cable due to localised deformation. This reflection is shown as a spike in the cable signature and is visualised using an oscilloscope. The size of the spike correlates with the magnitude of movement and the cable tester compares the 'emitted' and 'returned' pulse to determine the reflection coefficient of the cable at that point. By knowing the velocity at which electrical energy propagates along the cable, the distance to the change in characteristic impedance (e.g. shear surface deformation) can be determined. The rate of change of characteristic impedance can be used indirectly to determine the rate of movement (Kane 2000; Kane *et al.* 2001; Millis *et al.* 2008).

2.3.2.2.4. ShapeAccelArray (SAA)

The SAA comprises a string of MEMS (micro-electro-mechanical systems) sensors, which measure three-dimensional displacements continuously and with high temporal resolution (Abdoun *et al.* 2012). SAAs can be installed vertically inside boreholes to provide deformation vs. depth profiles, or horizontally along the ground surface to provide deformation vs. distance (e.g. chainage) measurements.

2.3.2.3. Ground water and pore-water pressure monitoring

2.3.2.3.1. Rain gauge

Rain gauges (e.g. tipping bucket) are used to monitor rainfall within an area of interest. This information is then used, indirectly, to infer the relative stability of the slope(s) due to predicted changes in pore-water pressures. Rainfall intensity-duration relationships, along with antecedent moisture conditions in some cases, have been used to develop thresholds for slope failure predictions and early warning systems by various authors (Caine 1980; Zan *et al.* 2002; Guzzetti *et al.* 2008; Crosta *et al.* 2012; Jakob *et al.* 2012).

2.3.2.3.2. Standpipe

Standpipes are the simplest instrument for ground water level measurement. A borehole is drilled and cased from which the depth to water is measured periodically (e.g. using level gauge) (Wan & Standing 2014). Measurements are usually obtained manually at discrete time intervals.

2.3.2.3.3. Piezometer

The piezometer measures pore-water pressures and various types are available (e.g. pneumatic and vibrating wire). A piezometer tip is installed to depth(s) of interest (e.g. a shear surface) inside a borehole. The annulus around the piezometer is backfilled either with sand or grout (where the permeability of the surrounding soil is less than that of the grout). The remainder of the hole above the piezometer tip is backfilled with grout; to form a closed/sealed system (Wan & Standing 2014). The piezometer is used to monitor positive pore-water pressures and is therefore installed to depths of saturated soil. Piezometers do not typically measure suction (i.e. negative pore-water pressure). Tensiometers or flushable piezometers (for in situ removal of air) are typically used to measure suctions.

2.3.2.3.4. Soil moisture probe

Conventional soil moisture probes derive moisture content based on the relative permittivity of a medium. The two main techniques are: time-domain reflectometry; and capacitance sensors (i.e. employing the medium as a dielectric). Measured relative permittivity is related to the moisture content.

2.3.2.3.5. Electrical resistivity tomography (ERT)

Grids of electrodes are installed across the surface of a slope. Resistivity measurements from between the electrodes are related to soil properties and moisture content. Calibration resistivity-moisture content relationships can be derived by performing tests

on samples in the laboratory. This calibration allows subsurface moisture content models to be developed from resistivity measurements. ERT surveys conducted periodically can be used to assess slope stability (e.g. Chambers *et al.* 2014; Gunn *et al.* 2014).

Table 2.3. Comparisons of instrumentation and monitoring techniques

Instrument/ technique	Advantages/disadvantages
Surface deformation monitoring	
Global positioning system (GPS)	*Accuracy/precision/measurement uncertainty:* • mm to cm. *Temporal resolution:* • Typically low (i.e. week/month/year intervals) due to the time required to conduct each survey of markers and process the data. • Can be high if a receiver is fixed on a specific location and monitored continuously. *Spatial resolution:* • Relatively high depending on the number of locations (i.e. markers) monitored across the site. *Other notes:* • Difficult to use in strong depressions (alpine valleys) and in forests. • Significant time required to install/setup and conduct manual full site surveys. • Instrumentation and software can be high cost.
Total station	*Accuracy/precision/measurement uncertainty:* • 0.5 mm to 5 mm (depending on measured distance). *Temporal resolution:* • Can vary from low (e.g. manual surveys of the site) to high (e.g. an automatic robotic total station taking measurements at user-defined time intervals). *Spatial resolution:* • Relatively high depending on the number of locations (i.e. prisms) monitored across the site. *Other notes:* • Post-processing computations usually required to quantify measurements, however; can be automated with appropriate software packages. • Refraction, poor weather conditions and high levels of vegetation are problematic. • Significant time required to install/setup and conduct manual full site surveys. • Instrumentation relatively high cost.
Photogrammetry	*Accuracy/precision/measurement uncertainty:* • <mm to >m (highly dependent on number/quality of images, flight height, vegetation, weather conditions and ground control points). *Temporal resolution:* • Generally low (i.e. month/year intervals) due to the significant time necessary for photography and processing. *Spatial resolution:* • The technique provides high spatial resolution of deformations and a description (i.e. visual representation) of an entire site, particularly using aerial photogrammetry. *Other notes:* • Time and cost required to conduct each survey is relatively high. • Post-processing of the data is relatively complex.
Remote sensing	*Accuracy/precision/measurement uncertainty:* • <mm to >m (highly dependent on number/quality of images, vegetation, weather conditions and ground control points). *Temporal resolution:* • Generally low (i.e. month/year intervals) due to the significant time necessary for imagery and processing. *Spatial resolution:* • The technique provides high spatial resolution of deformations and a description (i.e. visual representation) of an entire site, particularly using aerial/satellite remote sensing. *Other notes:* • Time and cost required to conduct each survey is relatively high. • Post-processing of the data is relatively complex.
Tilt meter	*Accuracy/precision/measurement uncertainty:* • 0.02% to 1% of measurement range, which can be up to 60 degrees dependent on type. *Temporal resolution:* • High temporal resolution if permanently installed and continuously logging. *Spatial resolution:* • Low spatial resolution (i.e. informs only of the location in which it is installed). *Other notes:* • Robust and relatively low cost. • Sensitive to temperature changes. • Not used to quantify magnitude of ground deformation (i.e. does not measure in mm's of movement). • Translational movements are not detected.
Extensometer	*Accuracy/precision/measurement uncertainty:* • 0.01 mm to 1 mm over a full measurement range of up to 200 mm.

	Temporal resolution: • High temporal resolution with permanent installation and continuous monitoring/logging. *Spatial resolution:* • Low spatial resolution (i.e. informs only of the location in which it is installed). *Other notes:* • Robust and relatively low cost. • Sensitive to temperature changes. • Relatively simple and easy to operate. • One-dimensional measurement only.
Fibre optics (e.g. Brillouin Optical Time Domain Reflectometry – BOTDR)	*Accuracy/precision/measurement uncertainty:* • 0.01% change can be detected (e.g. 1 m over 10 km). *Temporal resolution:* • High temporal resolution with permanent installation and continuous monitoring/logging. *Spatial resolution:* • Relatively high spatial resolution (along the length of the cable(s)). *Other notes:* • Able to identify locations of instability but does not provide total magnitude of deformation at these locations. • Useful for detecting instabilities in long lengths of earthworks. • Relatively high cost. • Sensitive to temperature changes (this needs to be compensated for). • Complex processing often required.
Geophone/ Accelerometer	*Accuracy/precision/measurement uncertainty:* • Acceleration: 0.1m/s^2, Velocity: 0.01 mm/s, Displacement: 10 µm. *Temporal resolution:* • High temporal resolution with permanent installation and continuous monitoring/logging. *Spatial resolution:* • Relatively high spatial resolution with an array of geophones/accelerometers. *Other notes:* • Multiple sensors are required in order to detect, locate and identify slope movement. • Requires relatively complex post-processing. • Difficult to differentiate periods of movement from background noise when monitoring at low frequency. • Difficult to detect low velocity ductile movements (e.g. creep).
Movement tracking using electrical resistivity monitoring	*Accuracy/precision/measurement uncertainty:* • < 5% of the electrode spacing in 2D and < 10% in 3D. *Temporal resolution:* • High to intermediate; resistivity measurements on 2D lines can be repeated several times a day, while 3D grids require more time, usually limiting frequency to daily measurements. *Spatial resolution:* • Small electrode spacing can generate high spatial resolution, but over a small area. Larger spacing is required for large grids in order to cover the extent of a large slope. *Other notes:* • Multiple sensors are needed in order to detect, locate and identify slope movement. • Requires complex installation and post-processing (i.e. expert knowledge), which can also be high cost.

Subsurface deformation monitoring	
Inclinometer	*Accuracy/precision/measurement uncertainty:* • +/- 4 to 8 mm per 30 m. *Temporal resolution:* • Low if manual surveys are conducted using a torpedo probe (i.e. a few times per year). • High if an in-place probe or probe-string is installed permanently with continuous monitoring/logging. *Spatial resolution:* • Relatively low spatial resolution across the slope as informs only of the borehole in which it is installed (and the surrounding soil mass). • Relatively high with depth as measurements are recorded at 0.5 to 1 m depth intervals. *Other notes:* • The quality of the casing is important in order to ensure robustness and that the probe stays within the grooves/keyways during surveys. • Torsion/twisting of the casing at significant depths (>50 m) needs to be controlled. • Excessive localised bending of the casing (e.g. due to shear surface deformations) will render the casings unusable as the probe will no longer be able to pass the shear surface (50 mm of shear surface deformation is often sufficient to render the casing unusable). • It is possible to measure shear surface depths. • Costs range from relatively low (with infrequent manual surveys using a torpedo probe) to relatively high (with frequent manual surveys and in-place probes and probe-strings). • Potential to incorporate a real-time early warning system with regular payments to service provider.
Borehole extensometer	*Accuracy/precision/measurement uncertainty:* • 0.01 mm to 1 mm over a full measurement range of up to 200 mm. *Temporal resolution:* • High temporal resolution with permanent installation and continuous monitoring/logging. *Spatial resolution:* • Low spatial resolution (i.e. informs only of the location in which it is installed). *Other notes:* • Robust and relatively low cost.

	• Sensitive to temperature changes. • Relatively simple and easy to operate. • One-dimensional measurement only.
Time domain reflectometry (TDR)	*Accuracy/precision/measurement uncertainty:* • Able to locate deformation to within mm to cm, although this reduces with depth/length of cable. *Temporal resolution:* • Low if manual surveys are conducted using portable pulse generator (i.e. a few times per year). • High if a continuous in-place pulse generator is used. *Spatial resolution:* • Relatively low spatial resolution as informs only of the borehole in which it is installed (and the surrounding soil mass). *Other notes:* • Does not directly provide measurement of total deformations or rates of deformation. • Able to identify and locate shear surfaces. • Costs range from relatively low (with infrequent manual surveys) to relatively high (with frequency manual surveys or with continuous in-place systems). • Backfill material should have similar properties to the surrounding soil/rock.
ShapeAccelArray (SAA) installed vertically in a borehole	*Accuracy/precision/measurement uncertainty:* • +/-1.5 mm per 30 m length. *Temporal resolution:* • High as monitoring is continuous with measurement intervals ranging from minutes to hours. *Spatial resolution:* • Relatively low spatial resolution across the slope as informs only of the borehole in which it is installed (and the surrounding soil mass). • Relatively high resolution with depth as sensor spacing is typically 0.2, 0.305 or 0.5 m. *Other notes:* • Excessive bending does not render the system unusable (as with inclinometer casing); they continue to operate at larger shear surface displacements than a conventional inclinometer. • It is possible to measure shear surface depths. • The instrumentation and software is relatively high cost. • Potential to incorporate a real-time early warning system with regular payments to a service provider. • Possible to retrieve the SAA string at end of use.

Groundwater and pore-water pressure monitoring	
Rain gauge	*Accuracy/precision/measurement uncertainty:* • Records rainfall as and when it occurs with high precision. Accuracy is dependent on the size of the area for which the rain gauge is being used to represent. *Temporal resolution:* • Relatively high as monitoring is continuous with measurement intervals ranging from minutes to hours; however, resolution can be lower with measurements at daily intervals. *Spatial resolution:* • Relatively high as the information captured using the rain gauge is representative of a wide area. *Other notes:* • Requires heating element at low temperatures. • Not useful for monitoring snow. • Contamination due to dew and hoar frost.
Standpipe	*Accuracy/precision/measurement uncertainty:* • 10 mm. *Temporal resolution:* • Low (read manually at intervals) to high (sensor utilised to log continuously). *Spatial resolution:* • Relatively low spatial resolution as informs only of the borehole in which it is installed (and the surrounding soil mass). *Other notes:* • Simple and robust. • Suitable for permeable soil ($k > 10^{-5}$ m/s). • Only indicative of pore-water pressures within the adjacent soil • Provides information of water level within the hole and not pore-water pressures at locations/depths within the slope that are required for stability quantification. • Simple and relatively low-cost system. • Long term reliability.
Piezometer	*Accuracy/precision/measurement uncertainty:* • 0.1% to 0.5% of measurement range, which can be up to 5 MPa. *Temporal resolution:* • High temporal resolution with permanent installation and continuous monitoring/logging. *Spatial resolution:* • Relatively low spatial resolution as informs only of the borehole in which it is installed (and the surrounding soil mass). *Other notes:* • Robust and reliable. • Barometric compensation required in some cases. • Informs of the pore-water pressure at specific depth in a specific location. • Post processing/calibration required in some cases. • Does not typically measure suction (i.e. negative pore-water pressure); for this a tensiometer or flushable piezometer (e.g. for in situ removal of air) is required.

Soil moisture probe	*Accuracy/precision/measurement uncertainty:* • Moisture content: ± 3% of measurement. *Temporal resolution:* • High temporal resolution with permanent installation and continuous monitoring/logging. *Spatial resolution:* • Low spatial resolution as it provides information representative of the soil immediately adjacent to the probe. *Other notes:* • Robust and reliable. • Site specific calibration is required. • Latest developments include web-based real-time delivery of information.
Electrical resistivity tomography (ERT)	*Accuracy/precision/measurement uncertainty:* • Usually < +/- 5% of moisture content; dependent on the raw resistivity data quality and the representativeness of the laboratory calibration relationship. *Temporal resolution:* • High to intermediate resolution depending on the number of electrodes; measurements can be repeated hourly to daily. *Spatial resolution:* • Dependent on electrode spacing; typical grid cell size ranges from 0.25m to 2.5m. Resolution is sacrificed if coverage over a large area is required, due to larger cells. *Other notes:* • Requires complex installation and post-processing (i.e. expert knowledge), which can also be high cost. • Requires sampling and laboratory testing to determine resistivity-moisture content calibration relationships for each installation.

2.4. Acoustic emission (AE) monitoring

2.4.1. Introduction

Acoustic emission (AE) are relatively high-frequency and low-amplitude (i.e. typically non-audible) elastic stress waves that propagate through materials surrounding the generation source. Example AE generation mechanisms include: leakage; crack initiation and propagation; and frictional phenomena (Beattie 1993; Scruby 1987; Dai & Labuz 1996; Mathiyaparanam 2006). Detection of AE generated by such mechanisms provides useful information on the integrity of assets and structures. AE monitoring is used in many industries to detect and locate: defects and leaks in pipe networks and pressure vessels (e.g. Palmer 1973; Lowe *et al.* 1998; Anastasopoulos *et al.* 2009; Mostafapour & Davoudi 2013); degradation of concrete (and reinforcement) due to straining and corrosion (e.g. Ohtsu 1996; Grosse *et al.* 1997; Yoon *et al.* 2000); instability of rock masses (e.g. Lockner 1993); faults in rail tracks (Bruzelius & Mba 2004); breakages in wire ropes (Casey & Laura 1997); and deterioration of rotating machines (e.g. bearings, engines, gearboxes and pumps) (Mba & Rao 2006).

Successful application of AE monitoring to soil slopes has been hindered, primarily due to: (i) the high level of attenuation that soil generated AE experiences as it propagates through the soil mass in three-dimensions; (ii) the need to filter out background noise (e.g. generated by environmental noise, construction activity and traffic); (iii) the requirement of unitary portable technology that can monitor AE continuously for long-durations in the field environment; and (iv) the need to develop strategies to interpret and quantify

deformation behaviour from the measured AE. Each of these problems has gradually been overcome, to various extents, in recent years:

(i) The use of waveguides (low attenuation AE propagation paths) in soil slope monitoring has allowed AE to be measured from deforming slopes (e.g. Koerner *et al.* 1981; Rouse *et al.* 1991); however, this AE was generated by deformations in the *in situ* soil (i.e. a passive waveguide system) and quantification of deformation behaviour from the measured AE was still not possible due to the significant variability in AE generated by *in situ* soils with highly variable properties.

(ii) Originally, AE monitoring of slopes utilised relatively low-frequency sensors (e.g. Beard 1961; McCauley 1975; Rouse *et al.* 1991), and this resulted in contamination of the measured AE from background noise, which also falls inside this low-frequency range, making interpretation difficult. Koerner *et al.* (1981), Dixon *et al.* (2003) and Spriggs (2005) demonstrated that soil generated AE produces relatively high levels of energy in a higher frequency range (>20 kHz). By filtering out signals with frequency contents below 20 kHz it has been possible to minimise contamination from background noise (Dixon *et al.* 2012a).

(iii) Unitary battery operated AE processing and monitoring sensors (e.g. Slope ALARMS; Dixon & Spriggs 2011) have been developed by Loughborough University in collaboration with the British Geological Survey (BGS). This sensor can monitor relatively high-frequency (>20 kHz) AE continuously in the field environment for long-durations, making continuous field monitoring possible.

(iv) Dixon *et al.* (2003) devised the 'active' waveguide. The active waveguide is installed in a borehole that penetrates any shear surface or potential shear surface that may form beneath the slope; it comprises a metal waveguide rod or tube with a granular backfill surround (i.e. to generate relatively high energy AE as the slope deforms that can propagate along the waveguide). As the slope deforms, the granular backfill also deforms, generating AE. Originally, this concept was developed to introduce material into the slope that generates relatively high energy AE (as opposed to the low energy AE generated by fine-grained soils, which form the large majority of problematic slopes, particularly in the UK). However, because each active waveguide installation utilises similar materials (i.e. are repeatable) it is now possible to develop a universal approach to quantify deformation behaviour of any active waveguide (in response to slope movements)

from the measured AE; development of this approach formed the primary aim of this PhD research project.

2.4.2. AE monitoring system

2.4.2.1. Waveform and processing

Figure 2.14 shows an illustration of an AE waveform obtained from deforming soil (taken from Dixon *et al.* 2003). The raw waveform can be seen as the red line, whose envelope (green) is plotted by treating the crests of the waveform as a series of points. Rise time is the term given to the time interval prior to arrival of the peak amplitude. Ring-down counts (RDC) are the number of times the waveform crosses a pre-determined threshold level.

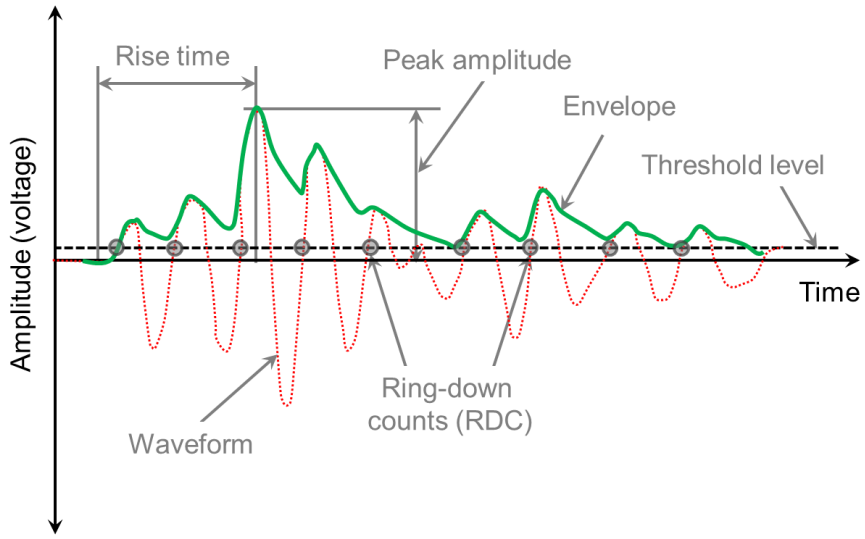

Figure 2.14. AE waveform with parameters identified (after Dixon *et al.* 2003)

2.4.2.2. Transducer

The piezoelectric transducer contains a piezoelectric element that undergoes charge separation when forced to change shape by application of a mechanical stress wave. This charge separation results in the generation of an electrical signal, proportional to the applied stress wave (Beattie 1983; Mathiyaparanam 2006). Broadband-type sensors are designed to acquire signals with a uniform response over a wide range of frequencies and are therefore useful when attempting to investigate the frequency content of a waveform (e.g. using Fourier transform). Resonant-type sensors are designed to respond strongly to waves of a certain frequency range (i.e. corresponding to the resonant frequency of the sensor), and in contrast to broadband-type sensors have comparatively greater sensitivity (Michlmayr *et al.* 2012).

2.4.2.3. Amplifier

The amplifier is used to magnify the amplitude of the electrical signal produced by the transducer. Signal attenuation between transducer and amplifier(s) should be minimal and can be reduced by a short travel distance (i.e. a short cable). The amplifier minimises contamination of the AE signal from electronic noise as it travels through cables and electrical components, and is therefore used to improve the signal-to-noise ratio (SNR) (Scruby 1987; Mathiyaparanam 2006).

2.4.2.4. Band-pass filter

The combination of high-pass and low-pass filters creates a band-pass filter. Utilisation of a band-pass filter allows signals within a certain frequency range to be captured and processed, whilst signals with frequency content outside of the range of interest are significantly attenuated. Filters are therefore used to focus AE detection within a frequency range of interest.

2.4.2.5. Analogue to digital conversion

The analogue-to-digital converter produces a series/sample of digital values, from the original analogue signal, in order to reconstruct the waveform digitally. The sampling rate must be at least twice the Nyquist frequency in order to allow representative reconstruction (Spriggs 2005). Beattie (1983) demonstrated the effect of sampling rate on the digital reconstruction of waves with the example in Figure 2.15. Figure 2.15 shows the difference in quality of reconstruction using different sampling rates.

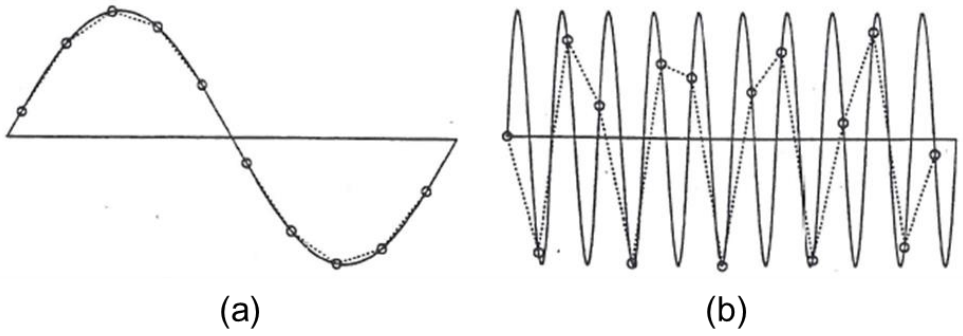

Figure 2.15. The effect of sampling rate on the digital reconstruction of AE: a) 10 samples per unit time; b) 2 samples per unit time (Beattie 1983)

2.4.2.6. Comparator

The comparator is used to register the number of times a signal's amplitude crosses a pre-determined voltage threshold level (e.g. RDC), per unit time. Use of a comparator is an

effective way of minimising contamination from background noise (both electronic and environmental); if the amplitude of the background noise is below the voltage threshold level, it is effectively neglected. Selection of an appropriate voltage threshold can only be done using knowledge of the source AE that will be monitored; a threshold set too high will not register any AE, and a threshold set too low will detect background noise in addition to the AE of interest (Beattie 1983; Mathiyaparanam 2006). Figure 2.16 demonstrates how the number of registered RDC can be influenced by the voltage threshold level (both positive and negative thresholds are used in the example) for a given AE signal. AE increases exponentially with a reduction in threshold level (for the simulated AE in the example), as background noise (both electronic and environmental) begins to significantly contaminate the signal below +/- 0.1V.

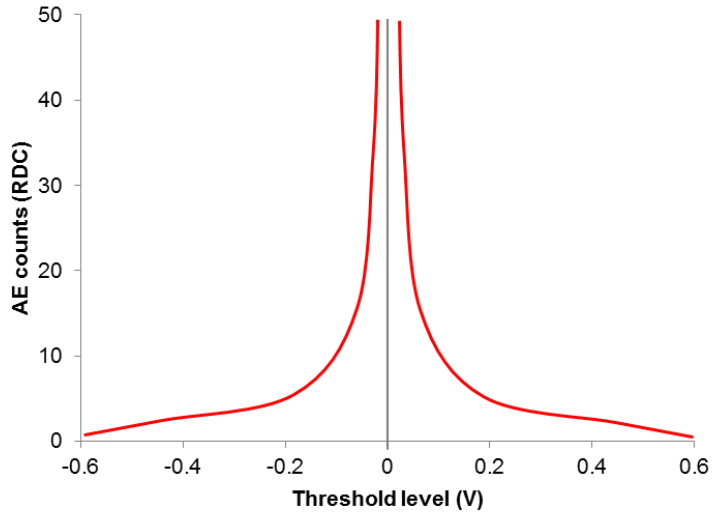

Figure 2.16. The effect of voltage threshold level on the number of measured RDC for simulated AE (after Beattie 1983)

2.4.2.7. AE systems used for monitoring soil slopes

Figure 2.17 shows a diagram of an AE system used for monitoring soil slopes by Koerner *et al.* (1981). The passive waveguide transported the AE from the source within the soil mass to the ground surface where it was detected by the sensor, and sequentially processed through a series of components. The system comprised large components, required significant power supply, and could not monitor continuously (due to insufficient processing power and data storage). The system could not therefore be used for continuous monitoring in the field environment, and monitoring was conducted with infrequent intervals of short duration.

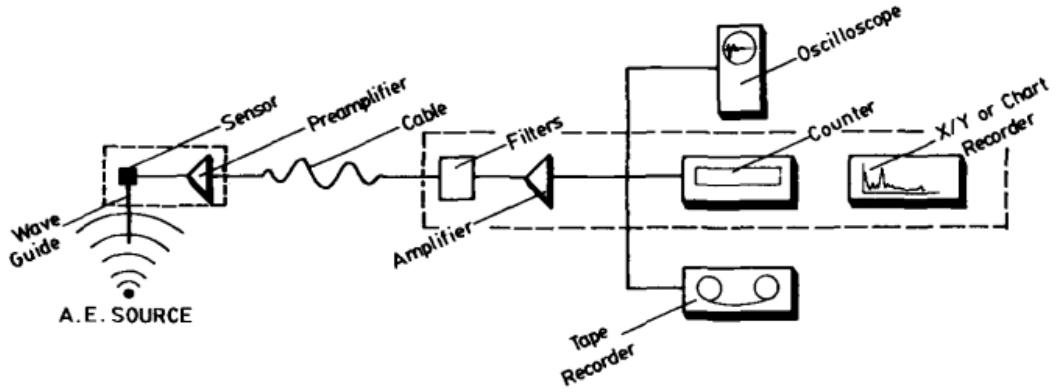

Figure 2.17. Schematic of AE monitoring system in Koerner *et al.* (1981)

Unitary battery operated AE processing and monitoring sensors (e.g. Slope ALARMS; Dixon & Spriggs 2011) have been developed by Loughborough University in collaboration with the British Geological Survey (BGS); in order to monitor active waveguide generated AE continuously in the field. Figure 2.18 shows an active waveguide installed through a soil slope deforming on a shear plane. AE generated by the active waveguide in response to slope movement is detected by a transducer (typical specification in Table 2.4) coupled to the waveguide at the ground surface and is converted to an electrical signal. The transducer is coupled to the outer wall of the pipe with a small layer of silicone gel to increase the surface area of contact and improve acoustic coupling, and held against the wall of the pipe with a consistent compressive contact provided by an elastic band and cable tie. The unitary battery operated Slope ALARMS sensor (Dixon & Spriggs 2011) then amplifies, filters, and processes the signal. In order to reduce the amount of processing power and storage capacity required from a battery operated sensor, which is required to operate continuously in the field environment for months at a time, ring-down counts (RDC) are measured and recorded (i.e. to remove the necessity of processing and recording the entire waveform). RDC are recorded and time stamped for each monitoring period (this can range from 5 seconds to 60 minutes).

Another key design aspect of the Slope ALARMS sensor is the use of filters to focus AE detection within the frequency range of 20 to 30 kHz as this eliminates low frequency (<20 kHz) environmental noise such as generated by wind, traffic and construction activities, leading to a robust system and minimises the potential for false alarms. If a Slope ALARMS sensor detects RDC within a set time period that exceeds a trigger warning level then the sensor transfers this to the communication system through a wireless network link. The communication system subsequently sends an SMS message to responsible persons so that relevant action can be taken (e.g. send an engineer to inspect the slope or immediately stop traffic). Figure 2.19 shows a photograph taken of

the AE measurement system from inside the protective surface cover, and Figure 2.20 shows a schematic of operation of the Slope ALARMS system (including communication and warning system).

Prior to the research described in this thesis, only simple quantitative and general qualitative information could be provided on slope stability from measured AE (e.g. lots of AE indicating instability and no AE indicating stability, and an order of magnitude change in AE rates indicates an order of magnitude change in slope displacement rates). The research described later in this thesis has developed an approach that allows the AE monitoring system to provide a quantitative measure of slope stability (i.e. displacement rates), which can be used to calibrate any AE system to deliver warnings related to slope displacement rates.

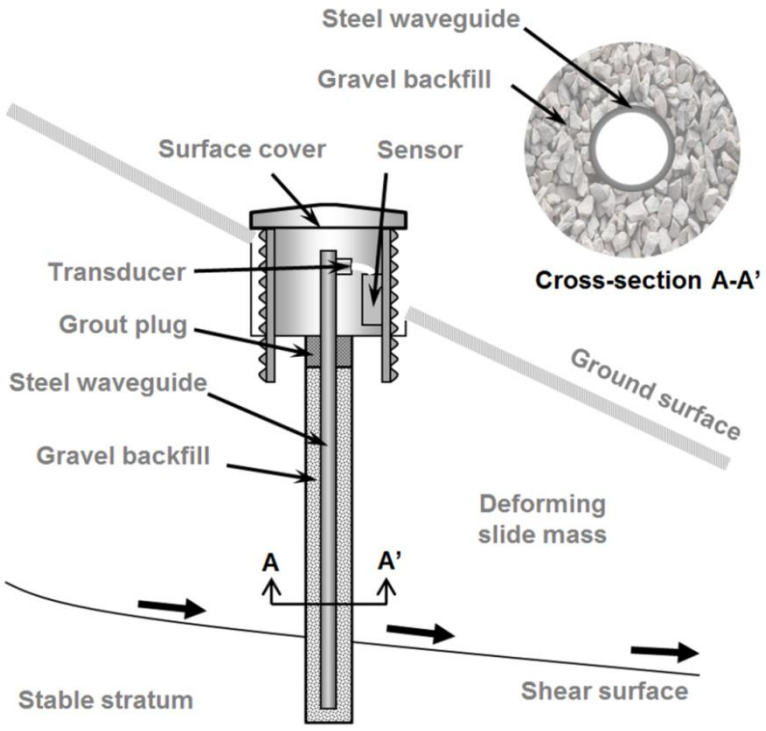

Figure 2.18. Schematic of an active waveguide installed through a slope deforming on a shear plane, with a sensor connected at the ground surface and protected by a cover (after Dixon *et al.* 2012)

Table 2.4. R3a transducer specifications

Manufacturer	Physical Acoustics Corporation
Peak Sensitivity, Ref V/(m/s)	80 dB
Operating Frequency Range	25-70 kHz
Resonant Frequency Ref V/(m/s)	29 kHz
Directionality	±1.5 dB
Mass	41 grams
Case Material	Stainless Steel
Face Material	Ceramic

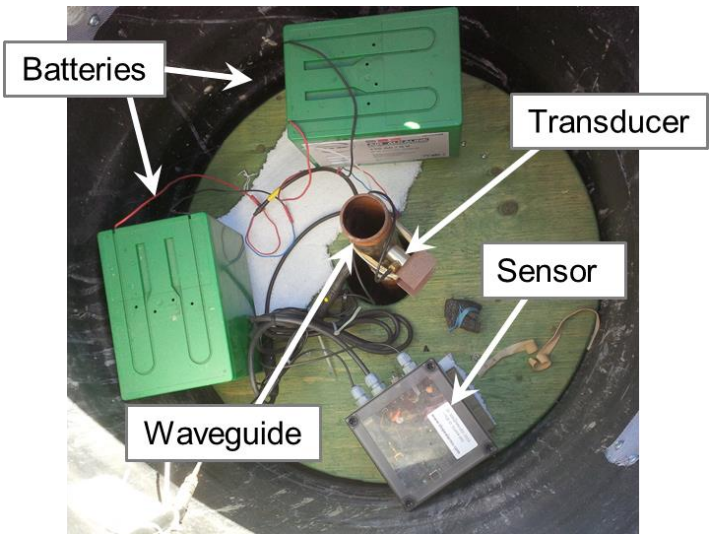

Figure 2.19. Annotated photograph of the Slope ALARMS AE measurement system from inside the protective surface cover

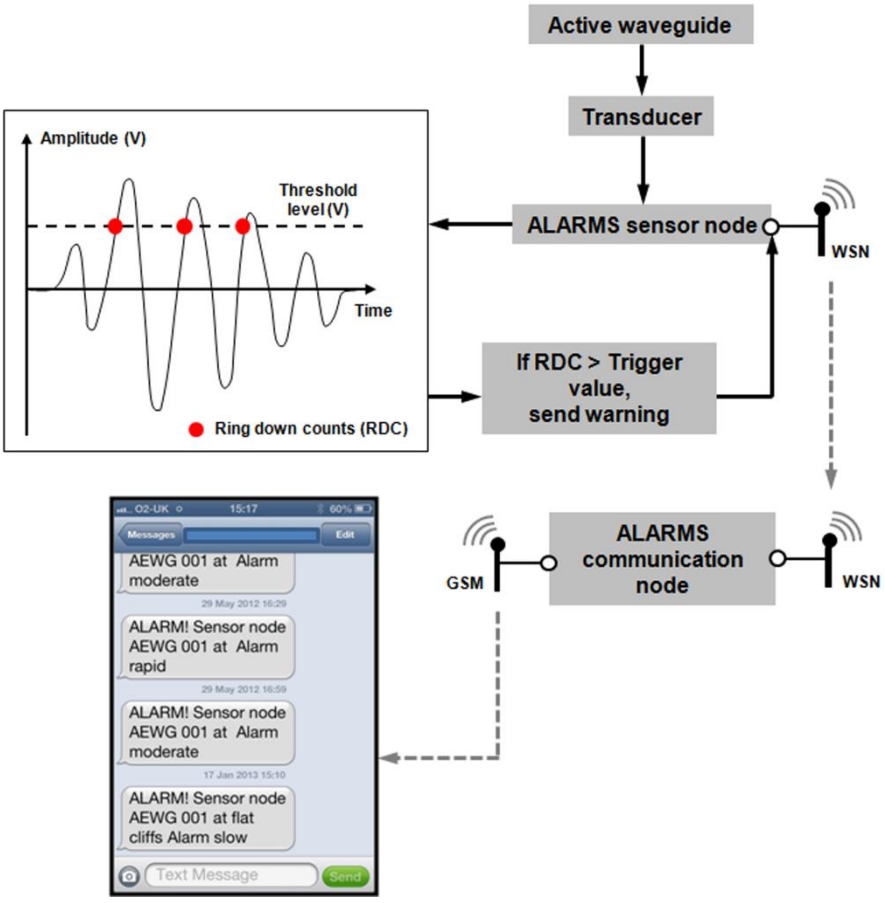

Figure 2.20. Schematic of operation of the Slope ALARMS system (including communication and warning system)

2.4.3. Soil-generated AE

In soil, AE is generated by inter-particle friction and hence the detection of AE is an indication of deformation. The dominant mechanisms for AE generation within soil are

particle-particle interactions such as sliding and rolling friction, and particle contact network rearrangement (e.g. release of contact stress and stress redistribution as interlock is overcome and regained). Other soil generated AE mechanisms include: breakage of adhesive bonds between particles, degradation at particle asperities where contact stresses are very high, and capillary bridge ruptures (Lord & Koerner 1974; Michlmayr *et al*. 2012a; Michlmayr *et al*. 2012b; Michlmayr *et al.* 2013). Research contributions (Koerner *et al.* 1981; Mitchel & Romeril 1984; Garga & Chichibu 1990; Shiotani & Ohtsu 1999; Michlmayr *et al.* 2013) in understanding the fundamental AE behaviour of soil have demonstrated that:

- deforming soil produces detectable AE;
- the characteristics of AE generated are governed by the properties of the soil (e.g. AE from fine grained soils are highly influenced by moisture content and plasticity, and AE events with greatest magnitude are produced in granular soil with large angular particles); and
- the magnitude of AE generated is directly related to the stress state of the soil (e.g. AE events with greater magnitude are generated by deforming soil with high inter-particle contact stresses).

Table 2.5 summarises the influence of soil properties on AE generation, as reported in the literature. The sections that follow provide examples to demonstrate some of these important relationships.

Table 2.5. Influence of soil properties on AE behaviour (summarised after: Koerner & Lord 1972; Koerner *et al.* 1975; Koerner *et al.* 1976; Lord *et al.* 1977; Tanimoto & Noda 1977; Keorner *et al*. 1981; Tanimoto *et al.* 1981; Naemura *et al.* 1991; and Dixon *et al.* 2003)

	Property	**Influence on AE behaviour**
Granular soil	Coefficient of uniformity	Soils with more uniform grading and larger values of coefficient of uniformity produce greater AE. This is because a greater surface area is achieved over which frictional interactions can occur.
	Particle shape	Angular particles generate greater magnitude AE than rounded particles.
	Particle size	Soils with larger particles generate AE with greater magnitude than those with smaller particles; however, smaller particles give rise to a greater number of AE events (due to a greater number of particle-particle interactions per unit volume).
Fine-grained soil	Plasticity index	The higher the plasticity index the lower the AE response of the soil. This is partly due to the higher clay content (i.e. greater proportion of 'quiet' soil grains) found in high plasticity soils. The influence of clay mineralogy is yet to be investigated.
	Water content	The higher the water content, and thus lower the inter-particle contact stresses, the lower the AE response.
General factors	Soil structure	The majority of research has been conducted on remoulded samples and therefore the AE response of samples containing discontinuities (e.g. fissures) has not yet been investigated. It is anticipated that the soil structure will have a significant influence on the AE generated, and therefore understanding the influence of soil structure will be important when interpretation of AE from undisturbed soil is required.
	Stress history	Due to the Kaiser effect*, soils have been shown to exhibit greatly increased AE activity when stress levels exceed the pre-stress/pre-consolidation pressure (e.g. Koerner *et al.* 1984a and Koerner *et al.* 1984b).
*The Kaiser effect is an absence of AE at loads not exceeding the previous maximum load level (e.g. is a clear phenomenon when materials experience repetitive loading)		

Koerner *et al.* (1981) stressed samples of Ottawa sand and Kaolinite clay to failure and monitored the AE produced from both soils. The average AE amplitude varied with an increase in failure stress (%) in both soils (results are shown in Figure 2.21). The AE amplitude generated by sand was consistently greater than clay for the same percentage of failure stress; demonstrating that soils with increased particle size generate AE with greater amplitude. Both curves in Figure 2.21 exhibit an initial increase in AE amplitude with increasing stress; however, as failure occurred, contrasting processes took place in the two different soils. The sand displayed a sudden increase in AE amplitude at failure; likely due to the occurrence of dilation and the relative frictional movement of particles within developed shear zone(s). In contrast, the AE amplitude reduced at failure within the clay sample; this is due to alignment of the clay platelet particles within the shear zone(s), reducing frictional phenomena.

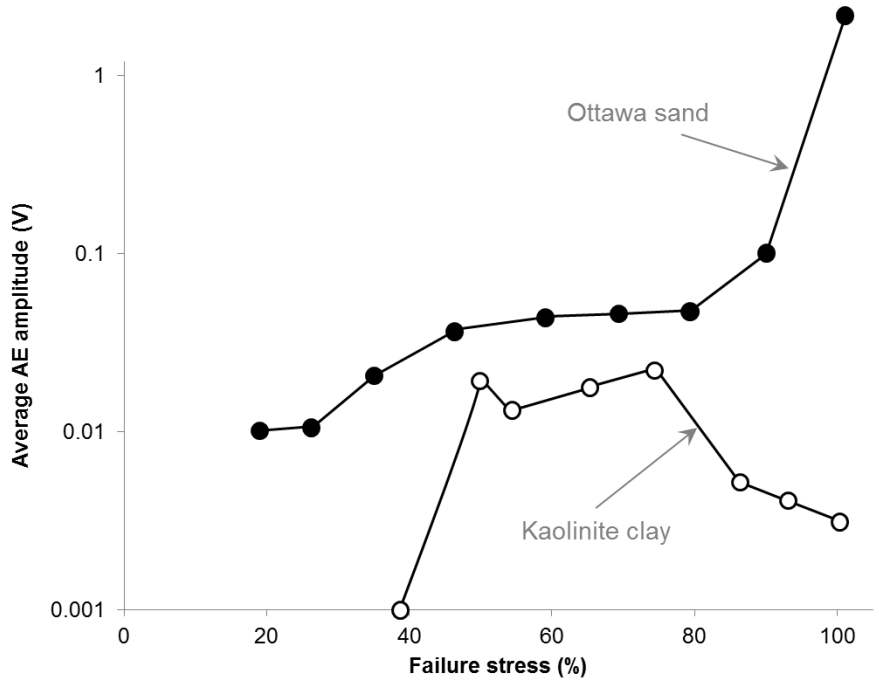

Figure 2.21. AE behaviour of sand and clay undergoing failure (after Koerner *et al.* 1981)

Koerner *et al.* (1981) sheared samples of sand, silt and clay, monitored the AE generated, and plotted the frequency spectra of the AE response (results shown in Figure 2.22). AE energy produced from this experimentation will be bias towards certain frequencies; this is intrinsic to the measurement system used (e.g. resonant frequency of the transducer). However, these results remain important because: they demonstrate that soil generated AE produces high levels of AE in high-frequency ranges (>20 kHz); and the results confirm AE energy generated is proportional to the particle size of the soil. The results also show that soil generated AEs have frequency contents over a wide range, from Hz to 100s kHz, and different soil types have different dominant frequencies. In addition, Mchlimayr & Or (2014) used Fibre Bundle Models (e.g. a model that allows investigation of the stress release mechanisms during shearing of granular assemblies) to simulate AE generated by assemblies of particles and found the dominant frequency spectra generated from stressed and deformed soil bodies is influenced by many other variables, such as: particle assemblies, confining pressures and interaction mechanisms (e.g. inter-particle friction and contact network stress release).

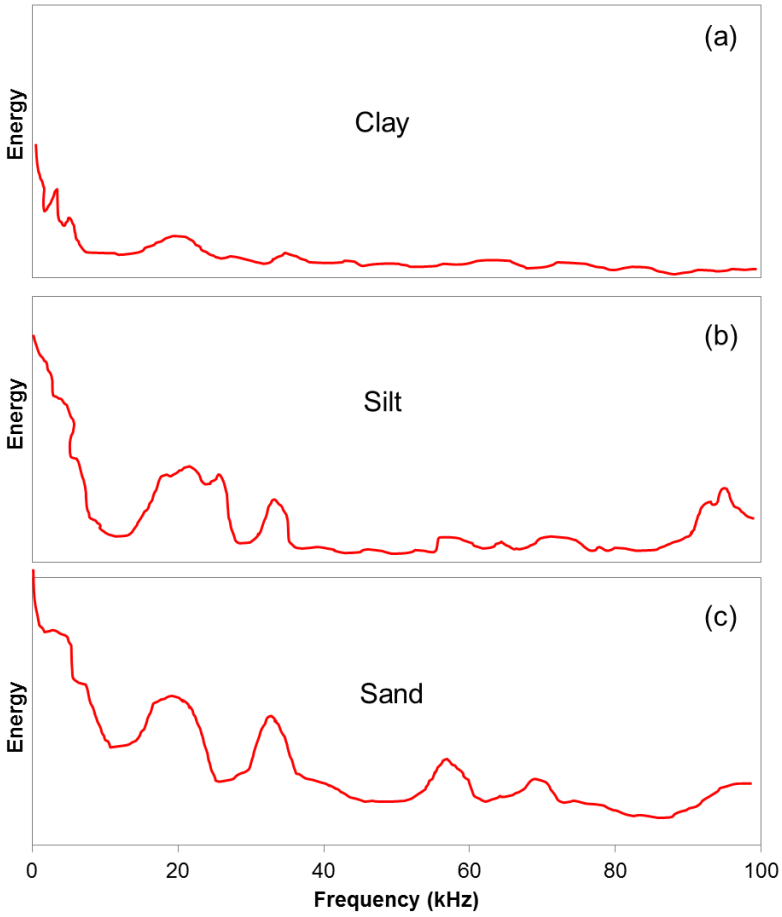

Figure 2.22. Frequency spectra of AE from clay (a), silt (b) and sand (c) tested in direct shear to near failure (after Koerner *et al.* 1981)

Kavanagh (1997) performed drained triaxial shear tests on Leighton Buzzard sand. The results (Figure 2.23) from increasing deviatoric stresses show that, although both the number and amplitude of events increases with increasing stress/strain, the increase in AE can be characterised, principally, by an increase in number of similarly sized events. This confirms that it is appropriate to monitor soil generated AE, in response to deformation, using the number of post-threshold crossings (RDC); provided that an appropriate threshold level, relative to the amplitude of AE generated by the specific soil, is selected. A proportional relationship between soil deformation and RDC rate was also identified by Garga & Chichibu (1990).

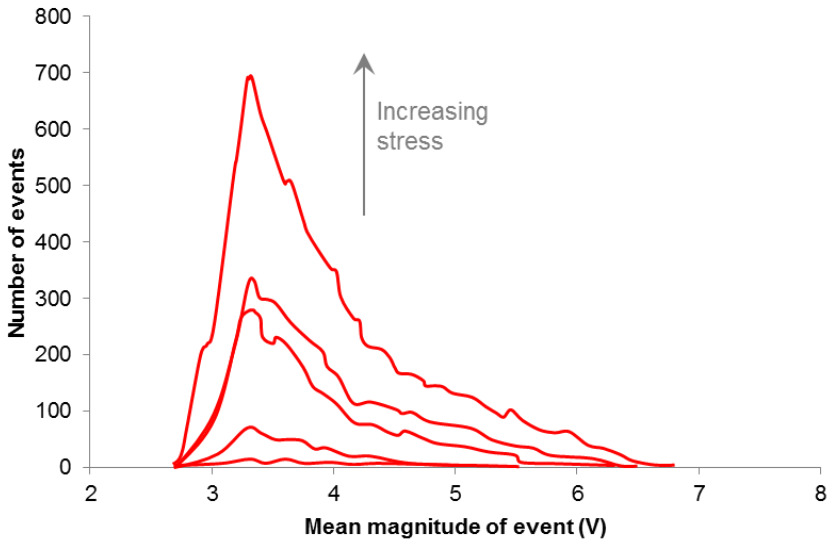

Figure 2.23. Number of AE events vs. mean magnitude of AE event from drained triaxial shear tests (after Kavanagh 1997)

2.4.4. AE monitoring of soil slopes, with particular reference to quantification of deformation behaviour from measured AE

Various authors have used AE monitoring to assess the stability of both natural and constructed slopes (e.g. Beard 1961; Cadman & Goodman 1967; Chichibu *et al*. 1989; Naemura *et al*. 1990; Nakajima *et al*. 1991; Rouse *et al.* 1991; Shiotani *et al.* 1994; Fujiwara *et al.* 1999; Dixon *et al.* 2003). Koerner *et al.* (1981) defined the following qualitative AE guide for slope stability assessment:

- Little or no AE; probably not deforming and therefore stable.
- Moderate levels of AE; deforming slightly but marginally stable. Continued monitoring is necessary.
- High levels of AE; experiencing substantial deformations and considered unstable with immediate remedial measures required.
- Very high levels of AE; undergoing large deformations and probably in a state of failure.

Such a classification cannot be used to provide a quantitative assessment on slope stability, and therefore much research effort has been focused on the development of strategies to interpret and quantify deformation behaviour from the measured AE; as is the focus of this PhD research project.

Nakajima *et al.* (1991) proved that it was possible to quantify deformation behaviour from measured AE using a metal waveguide with a resin and glass fibre composite backfill. When installed in a soil mass and deformation occurred, brittle fracturing of the backfill resulted in high levels of AE. This ‘active’ waveguide was calibrated in the

laboratory to establish an AE rate (frequency of AE events)-displacement rate relationship. Determination of this relationship allowed quantification of the 'coefficient of conversion', for use in quantifying displacement rates from measured AE rates. However, this active waveguide design included two sensors; one at the base of the borehole and one at the ground surface. This approach was utilised in order to determine the depth to the shear plane, using the difference in arrival time of AE between the two sensors. This meant that expensive electronics at the base of the borehole were sacrificial. Additionally, no long-term field trials were conducted to establish performance, reliability and accuracy of this type of active waveguide.

Fujiwara *et al.* (1999) prepared a test slope 5 m wide and 6 m in height, formed of Shirasu, which is widely found in the southern part of Kyushu Island and consists of sediments of pyroclastic origin. Successive excavations from the toe of the slope were made in order to induce instability. From the initiation of the first cut, it took 3.5 hours for collapse to occur. AE was monitored using two 60 kHz resonant frequency sensors coupled to 'passive' waveguides (2 m long and 2 cm diameter), which were installed at the upper and lower parts of the slope. The downward black arrows in Figure 2.24 highlight the timings of excavations. AE activity is shown to reduce exponentially subsequent to each phase of excavation. After cut 5 the AE activity remained elevated, which rapidly increased for a further 15 minutes prior to collapse. The AE sensor installed at the lower part of the slope detected greater AE activity than the one installed at the top of the slope. This suggests that failure initiated at the toe and extended in a retrogressive fashion upslope. Figure 2.25 shows the extensometer displacement-time data and cumulative AE (RDC) data from the experiment. The shapes of both curves resemble each other; changes in the rate of change of the displacement-time curve (i.e. velocity) coincide with rate of change changes in the cumulative AE (RDC)-time curve (i.e. AE rate). This indicates that the AE rates generated throughout the experiment were proportional to the velocity of movement. Also of particular interest is that the curves demonstrate all three stages of creep; primary (decelerating), secondary (steady), and tertiary (accelerating).

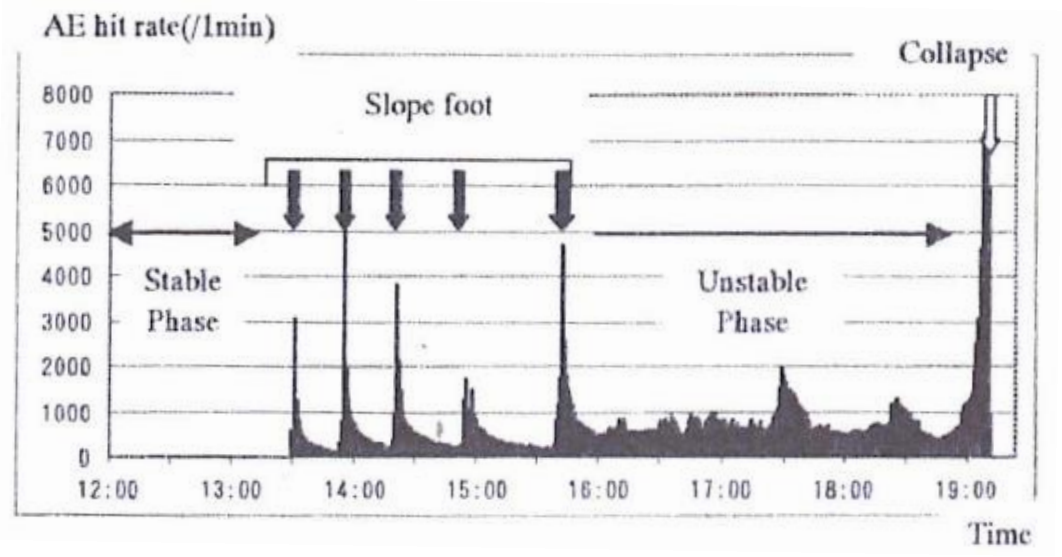

Figure 2.24. AE behaviour in response to slope failure from a waveguide and sensor installed in the lower part of the Shirasu slope (Fujiwara *et al*. 1999)

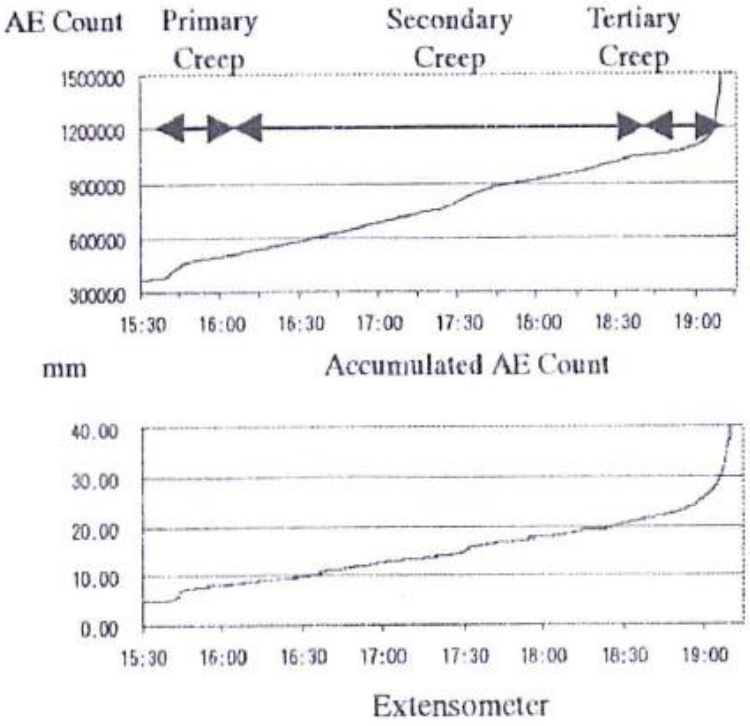

Figure 2.25. Comparison of AE and displacement behaviour during the Shirasu slope failure (Fujiwara *et al*. 1999)

Dixon *et al*. (2003) conducted a series of experiments to displace a waveguide through a box filled with granular soil, and monitored AE induced into the waveguide. Figure 2.26 shows the results obtained; the magnitude and rate of AE production was proportional to the magnitude and rate of waveguide movement.

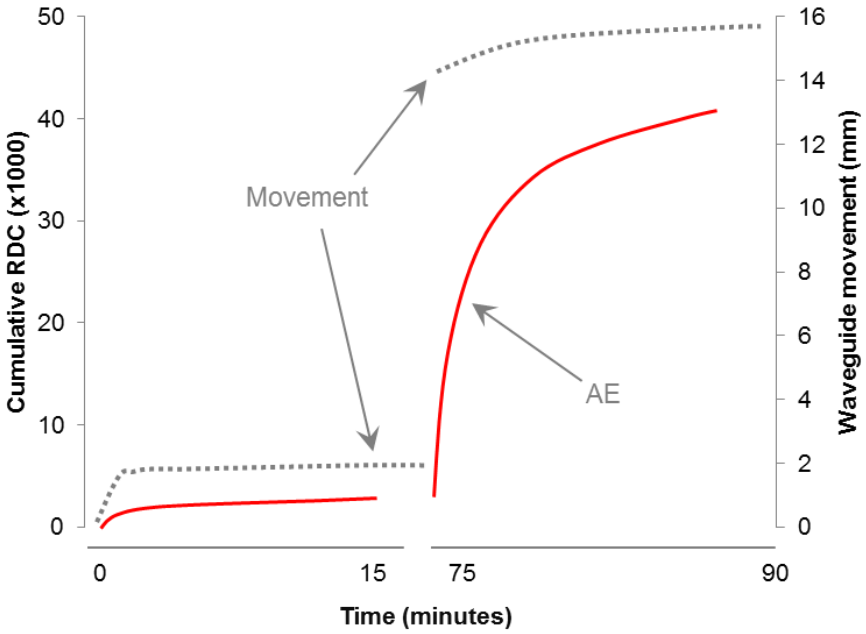

Figure 2.26. Comparison of AE and displacement behaviour during movement of a waveguide through a box filled with sand (after Dixon *et al.* 2003)

Dixon *et al.* (2003) carried out a field trial in a brick pit at Arlesey, Bedfordshire, England. A slope 4.5 m high formed of Gault Clay was instrumented with active waveguides (granular backfill) and inclinometer casings. Slope instability and deformation was induced by stress relief, through excavating successive slices from the toe. Elevated levels of AE measured from active waveguides were detected subsequent to excavation phase 4 while measurements from surveys of the inclinometer casings showed no change until after excavation 5. This work proved that AE monitoring of active waveguides has the potential to detect pre-failure deformations earlier than conventional inclinometers.

Dixon *et al.* (2003) also describe the AE monitoring case study of a coastal slope at Cowden, north-east England, using active waveguides (granular backfill) and conventional inclinometers. The site comprised 20 m high cliffs of stiff glacial till that were experiencing rotational sliding due to toe erosion. Both active waveguides and inclinometers were read at intervals. Each reading from the active waveguide took the form of sampling the AE signal envelope for a 3 minute period, from which the area under the signal was determined (i.e. a measure of AE energy). Figure 2.27 shows the time series of measurements recorded from the study at Cowden. Note that the onset of movement occurred prior to the first readings being taken, however; the displacement- and AE energy- time series show similar behaviour and demonstrate the potential for the AE technique to detect changes in displacement rate during first-time failure. Not only did this case study demonstrate that AE energy increased throughout the failure event as the rate of displacement increased, but that AE continued to generate beyond deformation

magnitudes sufficient to shear off inclinometer casings and render them unusable (the inclinometer casings in this study become unusable after day 160).

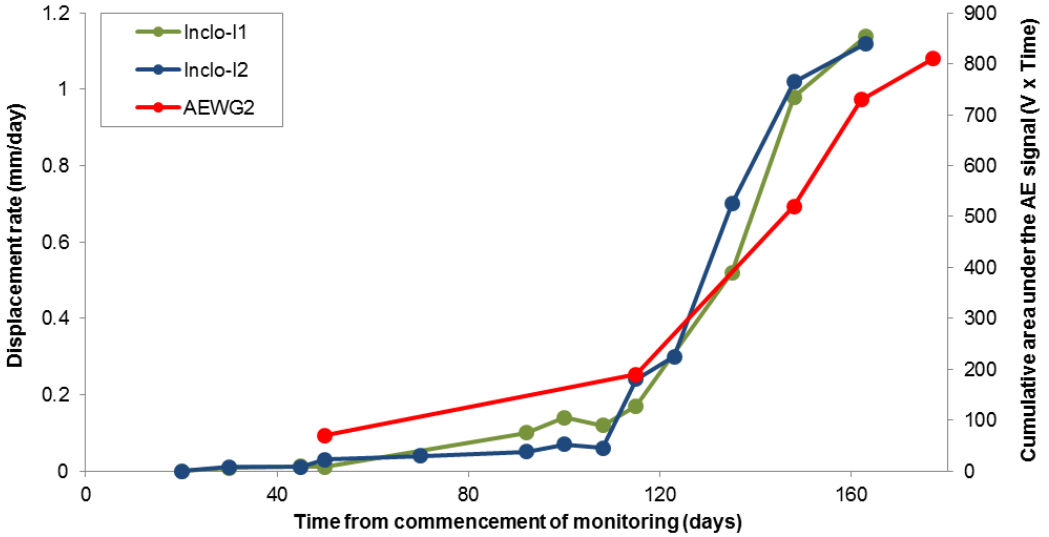

Figure 2.27. Cumulative displacement- and AE energy- time series from the Cowden monitoring experiment after Dixon *et al.* (2003)

Dixon & Spriggs (2007), utilising constant strain rate compression apparatus, found that by applying displacement rates that were separated by orders of magnitude (i.e. very slow, slow, moderate and rapid as in Figure 2.6) to active waveguide models (with angular gravel backfill) in the laboratory, the magnitude of AE rates generated were also separated by orders of magnitude, and proportional to the displacement rate applied. The results from a series of tests reported in Dixon & Spriggs (2007) are shown in Figure 2.28. Note that the AE rates increase under constant rates of deformation because the confining pressures in the system increase; this is described in more detail later in this thesis (in Chapters 6, 7 and 8).

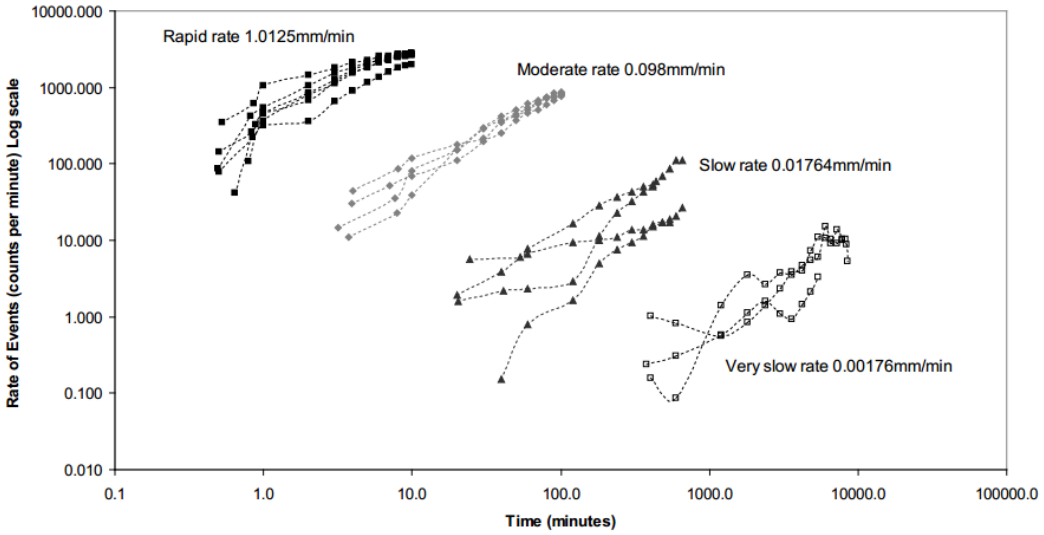

Figure 2.28. AE rate (RDC/min) vs. time (logarithmic scales) from constant strain rate compression tests (after Dixon & Spriggs 2007)

The studies described above demonstrate that determination of a method to quantify deformation behaviour from measured AE, generated by active waveguides in response to slope movements, continuously and in real-time, is attainable. Dixon & Spriggs (2007) demonstrated that displacement rates can be differentiated by orders of magnitude when monitoring AE generated by an active waveguide, which is consistent with standard landslide movement rate classifications (i.e. Schuster & Krizek 1978). Therefore, development of an improved quantification method with a greater level of accuracy was the motivation of this research project.

2.4.5. Laterally loaded discrete piles

The behaviour of laterally loaded discrete piles is relevant to the understanding of how the active waveguide behaves when installed through a deforming slope. Figure 2.29 highlights the stresses exerted on a pile installed through a slope deforming on a shear plane and subjected to lateral loading. This same distribution of stresses is expected to develop within the active waveguide when subjected to slope movements. Figure 2.30 illustrates the deformation behaviour and pressures applied to a discrete rigid pile used stabilise a slope. This pile rotates about a point above the base, which results in a negative deflection at the base of the pile. This behaviour is typical of an ‘intermediate’ soil-pile behaviour mode (Poulos 1995; Chen & Poulos 1997). Poulos (1995) defined three types of pile behaviour when subjected to lateral load, which are governed by the position at which the shear surface intersects the pile; these are illustrated in Figure 2.31. The ‘flow’ mode occurs when the soil deforms plastically around the pile along a shallow shear surface. The ‘short-pile’ mode occurs when the shear surface intersects the pile near the base, and the sliding soil carries the pile through the stable soil layer. The ‘intermediate’

mode occurs between these two extremes and the shear surface intersects the pile in its central region; this mode resulted in a negative deflection at the base of the pile in Figure 2.31. The slenderness ratio (length/diameter) of the pile also governs its behaviour, as illustrated in Figure 2.32. In the example in Figure 2.32 a rigid (low slenderness ratio) pile is subjected a lateral load and negative deformation occurs at the base of the pile (i.e. in the opposite direction to the applied load); however, a flexible (high slenderness ratio) pile, when subjected to the same lateral load, bends and the base of the pile remains stationary.

The active waveguide will behave in a flexible manner because it has relatively small diameter and a relatively high slenderness ratio. During the onset of slope deformation, when small magnitude deformations are taking place (i.e. millimetres), the dominant deformation mechanism within the active waveguide is shearing at the shear surface. At larger displacements however, more complex deformation behaviour occurs and the active waveguide is deformed through the host soil, both above and below the shear surface. This also leads to complex moment, shear and pressure profiles with depth, which will likely influence the AE response from the active waveguide.

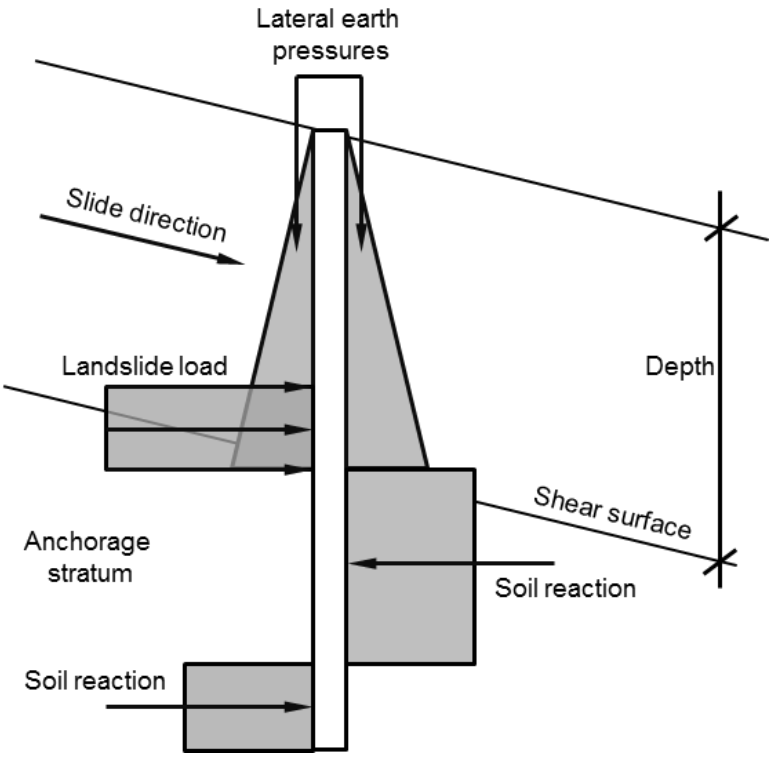

Figure 2.29. Force diagrams acting on a laterally loaded pile installed through a slope deforming on a shear plane (after Cornforth 2012)

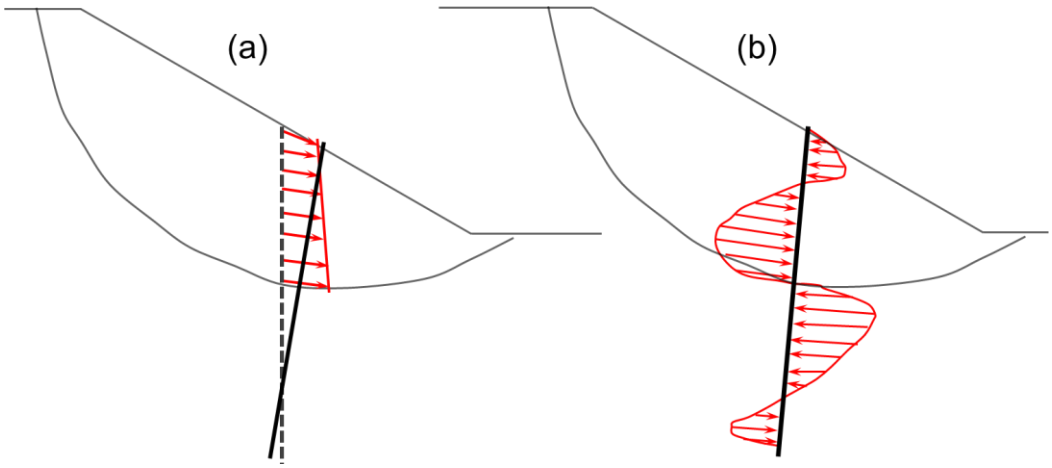

Figure 2.30. Pile installed through a slope deforming on a shear plane and subjected to lateral loading: a) soil deformations and pile displacement; and b) example qualitative pressures experienced by the pile (after Smethurst & Powrie 2007)

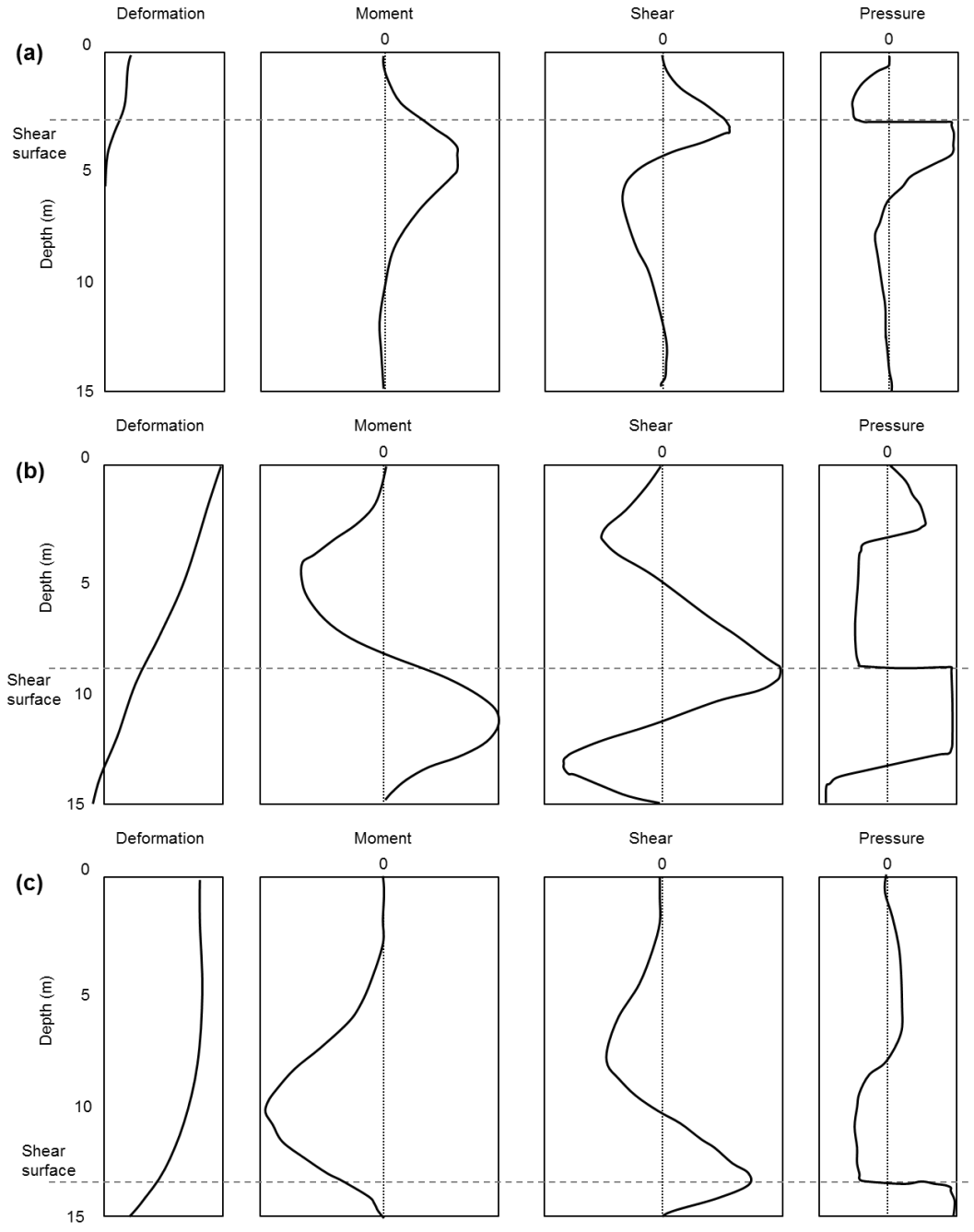

Figure 2.31. Deformation, moment, shear and pressure profiles for laterally loaded piles: a) 'flow' mode; b) 'intermediate' mode; and c) 'short-pile' mode (after Poulos 1995)

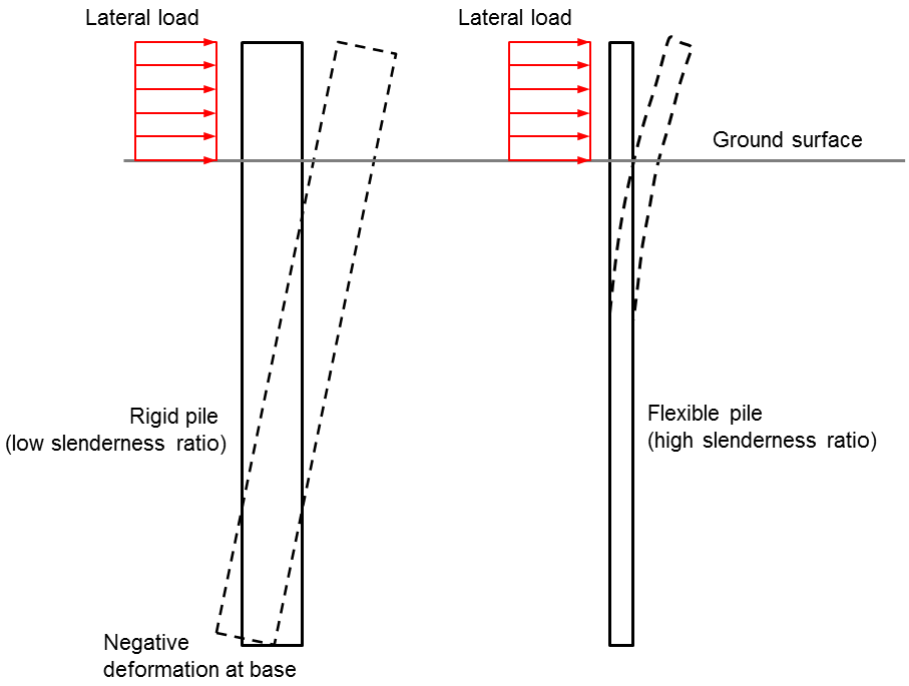

Figure 2.32. Difference between deformation profiles of 'rigid' and 'flexible' laterally loaded piles

2.4.6. AE propagation in waveguides

2.4.6.1. Introduction

Soil generated AE attenuates significantly as it propagates in three-dimensions through the soil mass. This is because in order for a stress wave to propagate through a soil mass, it must travel from particle to particle. When mechanical wave energy reaches the boundary between two particles, a proportion of the energy will be transmitted into the second particle while the rest is reflected back into the original particle (Pollard 1977). This was demonstrated experimentally by Shiotani & Ohtsu (1999) who measured the attenuation of AE with different frequency contents as it propagated through a mass of Toyoura sand. The results are shown in Figure 2.33; attenuation of 1.91 dB/cm was determined at a frequency of 1 kHz, 5.3 dB/cm at 5 kHz, 6.6 dB/cm at 10 kHz, and AE was found to rapidly attenuate at a frequency of more than 30 kHz over less than 8 cm.

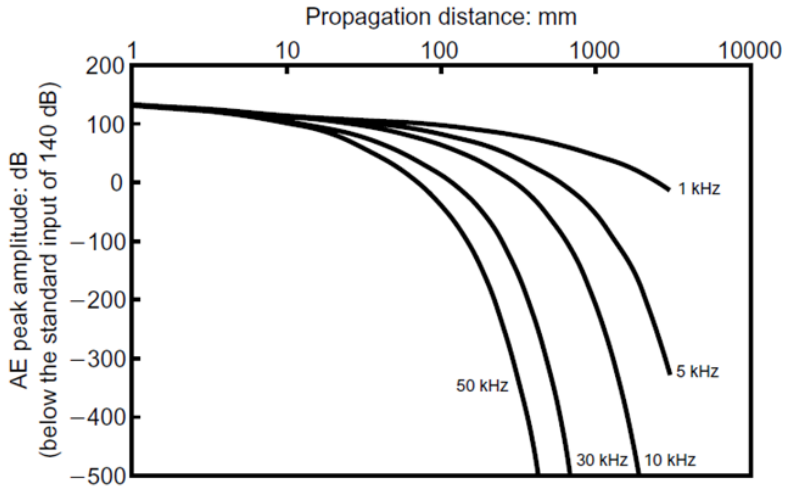

Figure 2.33. Attenuation of AE at different frequencies in Toyoura sand (after Shiotani & Ohtsu 1999)

Koerner *et al.* (1981) determined AE attenuation coefficients for sand and clayey silt and superimposed them upon values determined for other materials by other authors (Figure 2.34). These attenuation coefficients were determined by analysing signal losses over known distances through a box filled with the soil. Figure 2.34 demonstrates that AE suffers significantly less attenuation in metal (by several orders of magnitude) when compared to soil, which is the reason for utilising metal waveguides for AE monitoring of soil slopes.

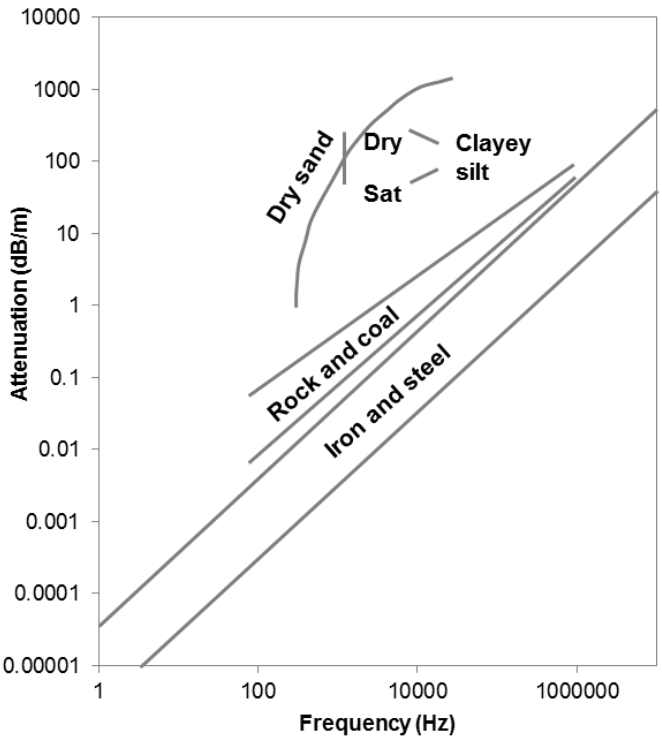

Figure 2.34. Attenuation coefficients of different materials after Koerner *et al.* (1981)

2.4.6.2. Elastic wave propagation in rods and shells

Exact analytical solutions exist for progressive simple harmonic waves of infinite duration propagating in uniform, isotropic, solid circular cylinders of infinite length; one such solution being the Pochhammer-Chree analysis (Wasley 1973, p127). The propagation of elastic stress waves along cylindrical rods and cylindrical shells (i.e. pipes) has been investigated for decades. Gazis (1959) obtained a general solution of harmonic waves in a cylinder surrounded by a vacuum. Studies of wave propagation along submerged fluid filled pipes (e.g. Aristegui *et al.* 2001) and buried water pipes (e.g. Long *et al.* 2003a,b) have demonstrated that the dominant wave modes in each case are dependent on the frequency content of the source, the geometry and properties of the pipe, and the internal and external environments. Long *et al.* (2003a,b) detail an investigation of acoustic wave propagation in buried iron pipes and highlight that significant energy is lost into the surrounding soil if 'leaky' wave modes propagate (i.e. wave induced particle displacements occur on the outer surface of the pipe and are therefore damped by the surrounding media). The magnitude of wave attenuation is dependent on the propagating wave mode, and attenuation generally occurs due to; geometric spreading, leakage (e.g. losses at boundaries), material properties, and scattering at joints (Long *et al.* 2003a,b; Shehadeh *et al.* 2008).

Attenuation in waveguides with air as an external environment (and with air also as an internal environment in the case of a pipe) is predominantly controlled by the material attenuation of the waveguide, which is often steel and in this case attenuation is relatively low and the leakage into the surrounding air is minimal (Aristegui *et al.* 2001). AE propagation in various other waveguide materials and geometries has also been investigated (e.g. Ono & Cho 2004; Sikorska & Pan 2004). This phenomenon has led to pipes and rods being used as low attenuation propagation paths in many non-destructive testing (NDT) and monitoring applications (e.g. Lowe *et al.* 1998; Alleyne & Cawley 1992; Alleyne & Cawley 1997; Maji *et al.* 1997; Demma *et al.* 2005). This function has led to these elements being termed waveguides (Ono & Cho 2004).

Shehadeh *et al.* (2008) understood that waveguide pipes installed in the ground (e.g. active waveguides) have a combination of air and water (e.g. ground water) as an internal environment (i.e. inside the pipe), and soil (saturated, partially saturated or dry) as an external environment (i.e. outside the pipe); therefore forming air-waveguide-soil and water-waveguide-soil tri-layer systems. Figure 2.35 illustrates a cross-section of a pipe with internal and external environments. Shehadeh *et al.* (2008) monitored relatively high frequency (i.e. 100-200 kHz and 300-350 kHz) elastic stress wave propagation in air-steel pipe-air systems and water-steel pipe-wet sand systems. The results demonstrate that the amplitude of the signal detected 5 m from the source in the water-steel pipe-wet sand

system was an order of magnitude less than that in the air-steel pipe-air system. This highlights the potential for significant leakage to occur into the surrounding media when monitoring relatively high frequency signals. Long *et al.* (2003a,b) conducted experimentation on buried iron water pipes (i.e. water-iron pipe-soil tri-layer systems) and monitored in a low frequency range (i.e. < 5 kHz); they found that the signal propagated 175 m and the amplitude reduced by less than a half. Anastasopoulos *et al.* (2009) also found that sensor spacing of 100 m was sufficient to monitor low frequency AE propagation in buried metal pipes for leak detection purposes. These results highlight that the degree of attenuation experienced is significantly dependent on the frequency content of the stress waves, which also governs the wave modes that propagate.

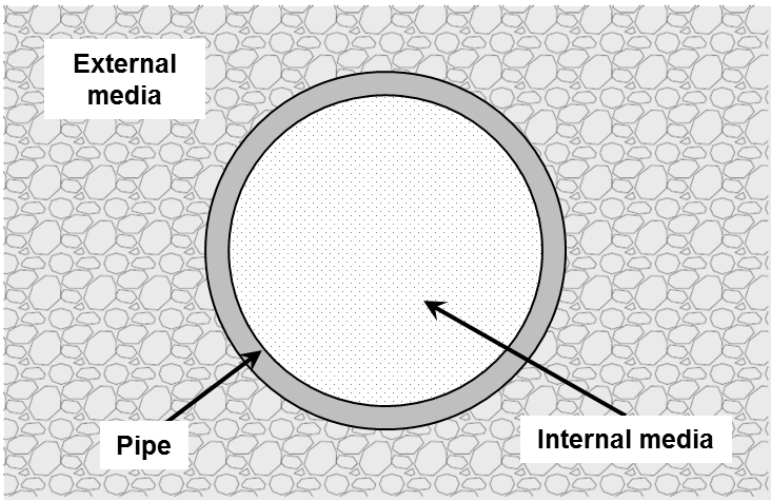

Figure 2.35. Illustration of a pipe cross-section with internal and external environments

2.4.6.3. Relevant theory and equations

2.4.6.3.1. Wave modes

The fundamental relationship between wavelength (λ), frequency (f) and velocity (C) is given by:

$$\lambda = \frac{C}{f} \qquad \textbf{(2.2)}$$

Low-frequency stress waves in thin rods or tubes (where the wavelength 'λ' is much greater than the diameter 'd' and wall thickness 't') propagate as plane longitudinal, flexural (i.e. shear or transverse) and torsional wave modes (Maji *et al.* 1997). The propagation velocity of plane longitudinal (C_l) and shear (C_s) wave modes are given respectively by (Maji *et al.* 1997):

$$C_l = \sqrt{\frac{E}{\rho}} \;;\; C_s = \sqrt{\frac{\mu}{\rho}} \qquad \textbf{(2.3)} \text{ and } \textbf{(2.4)}$$

Where E = Young's modulus, μ = shear modulus of elasticity, and ρ = material density.

High-frequency stress waves ($\lambda << d$, $\lambda << t$) propagate as bulk longitudinal and shear waves inside the material and as Rayleigh waves on the surface. Relatively high-frequency waves propagating through a solid that is bounded by two surfaces (i.e. a plate or tube) where the thickness is of the order of a few wavelengths or less (i.e. $\lambda \sim t$) propagate as Lamb waves (symmetric-extensional and antisymmetric-flexural) (Beattie 1983; Maji *et al.* 1997; Nishino *et al.* 2000; Sikorska & Pan 2004).

Plane longitudinal waves in rods (i.e. where the plane parallel to the cross-section is assumed to remain plane and parallel) induce cycles of positive and negative axial stress which, because of the Poisson effect, results in expansions and contractions of the rod as shown in Figure 2.36. The propagation of plane longitudinal waves along a rod is therefore influenced by the rods stiffness moduli, in addition to the material density and cross-sectional area. An example of a plane flexural wave propagating in a thin rod can be seen in Figure 2.37. The propagation of plane flexural waves induces bending moments and shear forces and is therefore influenced by the rods flexural rigidity; in addition to the cross-sectional area, material density and stiffness moduli.

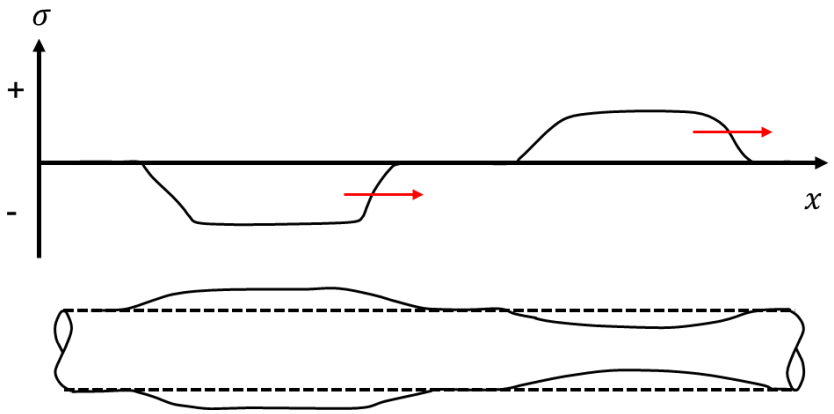

Figure 2.36. Exaggerated illustration of Poisson expansion and contraction resulting from longitudinal stress waves after Graff (1975, p79)

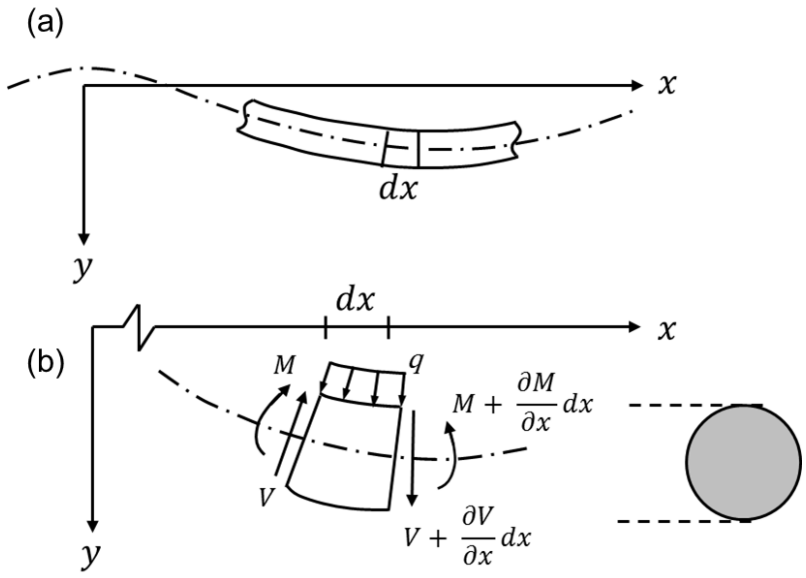

Figure 2.37. a) Thin rod subject to flexural stress wave, and b) an element of the rod subject to various loads (i.e. bending moments and shear forces) after Graff (1975, p141)

The standard material used for waveguides is steel, due to its low attenuation characteristics, and has the standard properties detailed in Table 2.6. The use of Equations 2.3 and 2.4 to determine the propagation velocity of plane longitudinal and flexural wave modes in steel (using the properties in Table 2.6) yields the results in Table 2.7. These values were subsequently input into Equation 2.2 to determine the range of wavelengths (and therefore frequencies), which when compared to the diameter/wall thickness of rod/pipes, satisfy the criteria for plane longitudinal and flexural wave modes to propagate in steel waveguides. The shaded area in Figure 2.38 shows an example range of frequencies and rod/pipe diameters and wall thicknesses for which plane longitudinal and flexural wave modes propagate in steel; this demonstrates that the wave modes we are interested in when monitoring at 20 to 30 kHz (and waveguide diameters less than 100 mm) are plane longitudinal and flexural.

Table 2.6. Standard mechanical properties of steel

Density (kg/m^3)	Modulus of elasticity (Pa)	Poisson's ratio	Shear modulus (Pa)
7850	2.00E+11	0.287	8.00E+10

Table 2.7. Calculated propagation velocity of both longitudinal and flexural wave modes at a frequency of 25 kHz propagating through steel

C_l (m/s)	C_s (m/s)
5048	3192

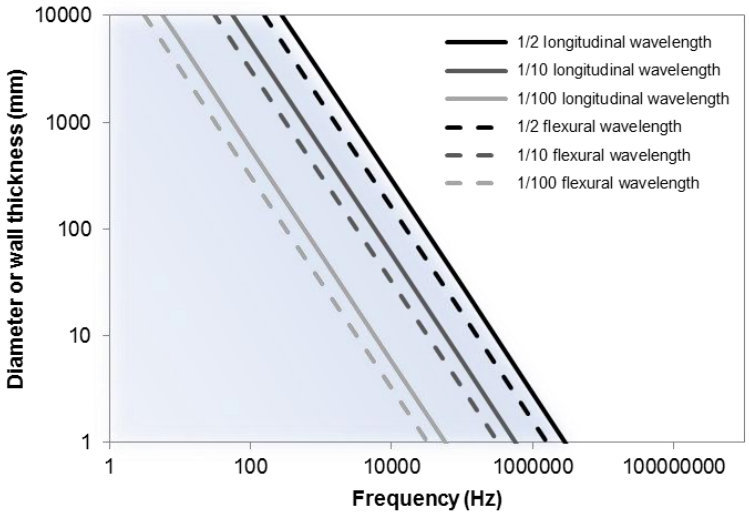

Figure 2.38. Range of diameter, wall thickness and frequency values for which plane longitudinal and shear waves propagate in steel rods/pipes

2.4.6.3.2. Attenuation coefficients

Equation 2.5 details the formula used to derive the attenuation coefficient, α, of a decaying plane wave.

$$A = A_0 e^{-\alpha x} \quad \textbf{(2.5)}$$

Where A represents the magnitude of the wave at some distance, x, from the source, and A_0 represents the magnitude of the signal at the source (i.e. un-attenuated). The term *e* is Euler's (or Napier's) constant. This equation will be used to represent the net effect of all forms of attenuation (e.g. geometrical spreading, internal friction, scattering, diffraction and dispersion) in this study. Rearrangement of Equation 2.5 to make the attenuation coefficient the subject yields:

$$-\alpha = \left(\frac{1}{x}\right) \ln\left(\frac{A}{A_0}\right) \quad \textbf{(2.6)}$$

Note that the units of the attenuation coefficient output from Equation 2.6 are Nepers per metre (Np/m). Decibels per unit length are the units more commonly used; Nepers per metre can be converted to Decibels per metre (dB/m) by dividing by 0.1151 as shown in Equation 2.7.

$$1\ N_p = \frac{1}{20\log_{10} e}\, dB \approx 0.1151\ dB \quad \textbf{(2.7)}$$

Shehadeh *et al.* (2008) quantified the attenuation coefficient for AE in 48 mm outside diameter and 7.4 mm wall thickness steel pipes in the frequency range of 100 to 200 kHz;

the wave modes in this case, according to Figure 2.38, are plane longitudinal and flexural. The coefficient determined was 0.014 Np/m (or 0.12 dB/m). This coefficient is for attenuation in continuous lengths of the steel pipe; however, long lengths are typically connected using joints, which increase the magnitude of attenuation due to greater losses. Hardy (1992) experimentally determined the percentage loss of AE signal amplitude over perpendicularly jointed lengths of rock bolts, using a variety of connection methods (e.g. welding, soldering and clamping); the results demonstrated that welding was the most effective method of connection from those tested with an average signal amplitude loss of 22 %. When welding is used as a method to connect lengths of pipe, the cross-section would remain relatively constant (i.e. continuity) and therefore the acoustic impedance at the joint would remain relatively constant; resulting in reduced reflection and greater transmission.

2.4.6.3.3. Reflection and transmission

Relative proportions of a wave propagating in a rod or pipe will be transmitted and reflected where there is a discontinuity in cross-section or material properties (Graff 1975, p79-141). The transmitted proportion of the wave at a boundary will undergo some form of mode conversion (Sikorska & Pan 2004) (e.g. waves transmitted into water will be converted to compressional waves as water has no shear strength and cannot accommodate shear waves). The relative proportions of reflected and transmitted waves at a boundary between two media (e.g. the pipe-soil interface) are dictated by their relative acoustic impedances (Z) (e.g. Shiotani & Ohtsu 1999). The acoustic impedance and specific acoustic impedance (i.e. per unit area) of a material are shown in Equations 2.8 and 2.9 respectively.

$$Z = \rho CS \;\; and \;\; Z = \rho C \qquad \textbf{(2.8)} \text{ and } \textbf{(2.9)}$$

Where ρ is material density, C is acoustic velocity and S is cross-sectional area. At a boundary where there is a difference in acoustic impedance (e.g. at an interface between two materials or a discontinuity in cross-section), the fraction of the incident wave intensity that is reflected can be determined using Equation 2.10 (i.e. the reflection coefficient - R_c).

$$R_c = \left(\frac{Z_2 - Z_1}{Z_2 + Z_1}\right)^2 \qquad \textbf{(2.10)}$$

Where Z_2 refers to the material occupying the incident wave (e.g. the pipe) and Z_1 refers to the material into which the wave is transmitted (e.g. a coupling or surrounding soil).

Figure 2.39 illustrates the reflected and transmitted portions of an incident wave at a discontinuity in cross-section. The term ‘acoustic impedance’ will be used for the specific acoustic impedance (which has units kg/m^{2}s) where mentioned in the rest of this thesis.

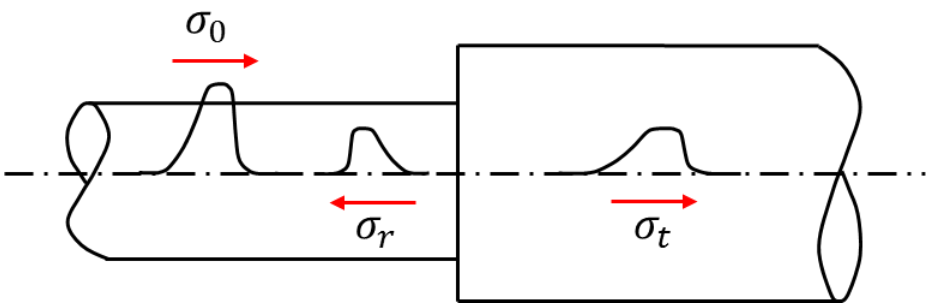

Figure 2.39. Incident ‘0’, reflected ‘r’ and transmitted ‘t’ waves at a connection after Graff (1975, p83)

2.5. Summary

There is an ongoing need to develop new techniques that can provide early warning of slope instability to lessen damage and loss of life. It is important that early warning systems used to detect catastrophic first-time failures are sensitive and can detect accelerations of movement as early as possible. The time lag between the onset of failure being detected and communicated, to full failure taking place needs to be as great as possible in order to enable evacuation of vulnerable people and timely repair and maintenance of critical infrastructure.

AE monitoring using active waveguides (i.e. a metal waveguide with a granular backfill surround installed through a slope) is becoming an established approach to monitor the stability of soil slopes, however, the challenge has been to develop strategies to interpret and quantify deformation behaviour from the measured AE. A method is required to quantify landslide velocity, to better than an order of magnitude (i.e. consistent with standard landslide movement classification), from measured AE, in order for the technique to be capable of providing early warning of slope instability through detecting and quantifying accelerations of slope movement.

Dixon & Spriggs (2007) found that by applying displacement rates that were separated by orders of magnitude to active waveguide physical models in constant strain rate compression tests, the magnitude of AE rates generated were also separated by orders of magnitude and proportional to the displacement rate applied. Based on the understanding of factors controlling the generation of AE as a slope deforms obtained through the literature review, the following Equation (2.11) is therefore proposed by the author as a

method to quantify rates of slope movement from active waveguide generated AE; where C_p is the coefficient of proportionality.

$AE_{rate} \propto$ Velocity

$\therefore AE_{rate} = C_p$ x Velocity

where $C_p = f$(variables) **(2.11)**

An increasing rate of deformation (i.e. in response to increasing slope velocity) within the active waveguide generates an increasing number of particle-particle/particle-waveguide interactions per unit time. Each of these interactions generates a transient AE event. These transient AE events combine and propagate along the waveguide where they are monitored by the sensor at the ground surface. Hence, AE rates produced and measured by the system are proportional to the velocity of slope movement (Equation 2.11).

The coefficient of proportionality is a measure of the systems sensitivity (i.e. the magnitude of AE rates produced in response to an applied velocity) and is dependent on many variables related to the AE measurement system such as:

- the sensor sensitivity controlled by signal amplification and voltage threshold level;
- the depth to the shear surface, which influences the magnitude of AE signal attenuation as it is transmitted from the shear zone to ground surface by the waveguide; and
- active waveguide properties such as the tube geometry, mechanical properties and connections, and backfill properties.

The magnitude of AE rate responses produced by each measurement system will depend on these factors, in addition to the rate of slope displacement. Through knowledge of the coefficient of proportionality it will be possible to convert measured AE rates to rates of slope movement. This forms the aim of this study, as was detailed in Chapter 1.

CHAPTER 3

Methodology

3.1. Introduction

This Chapter provides an overview of the approach used to accomplish the research Objectives defined in Chapter 1. Quantitative research methods (i.e. a positivistic approach) were employed in order to collect numerical data that, subsequent to analysis, allowed phenomena of interest to be explained (Fellows & Liu 2009). Specifically, the behaviour of the AE monitoring system in response to applied slope movements, and the effect certain variables have upon this relationship, were examined. The hypothesis postulated at the close of Chapter 2 (Section 2.5) was tested; that AE rates generated are proportional to slope displacement rates and a coefficient of proportionality can be introduced to define the relationship. Quantitative methods, in the form of parametric regression analyses, were utilised in the identification and quantification of empirical relationships between the variables of interest. The research is not presented in chronological order; rather, work packages have been grouped together based on similarity. Two main methods have been used in order to collect the data required to meet the Objectives; field monitoring and physical modelling. The work undertaken can be grouped into three main areas: determination of an empirical relationship between measured AE and deformation behaviour; an investigation into the influence of system variables upon the AE response to applied deformation behaviour; and development of a framework for the quantification of slope deformation rates from measured AE. The Objectives met by each of the work packages are highlighted throughout.

3.2. AE measurement system

A field-viable AE measurement system was used in this study. This system was used to ensure the results obtained are relevant to field monitoring applications. The system is described as ‘field-viable’ because it includes functionality to remove low-frequency background noise (e.g. generated by construction activity and traffic) and it has low power requirements, which makes continuous monitoring for long durations in the field environment possible. The AE measurement system utilised throughout all of the research was the Slope ALARMS AE measurement system. The Slope ALARMS sensor is the only known available of its type in the world; that is able to monitor AE continuously for

long-durations in the field environment. This is the reason for selection of this measurement system for field monitoring. Use of the same measurement system for all aspects of field monitoring and physical modelling was important in ensuring all data were comparable. Slight changes in measurement system (e.g. differences in amplification gain or filtered range) would make comparisons difficult. It was important that results obtained from both field monitoring and physical modelling could be compared, used to inform each other, and that data obtained from both could be combined to develop the quantification framework (i.e. Objective 5).

The principle of operation of the AE measurement system, as described in Section 2.4.2.7, can be summarised as follows: the R3alpha transducer (specification in Table 2.4) detects the mechanical AE signal and converts this to an electrical signal; the electrical signal is amplified (using 70dB gain) and filtered (to focus within the 20-30 kHz range); and the number of post-voltage threshold crossings (using a comparator) are recorded and time stamped for each measurement interval, which can range from 5 seconds to 60 minutes. The operation of the AE measurement system is therefore described in sufficient detail to allow the reader to reproduce a similar system and observe the same trends in behaviour.

Note that two versions of the AE measurement system were employed in this project: version 1 and version 2. Version 2 is an upgraded version of the original (version 1), and has upgraded hardware and firmware. The principle of operation is the same between the two systems, but the results obtained from both are not directly comparable. Version 1 was used at three of the field trials (the field trials are introduced in the subsequent Section 3.3), two of which were upgraded to version 2 during the project (further details in Table 4.1), and the remainder of the field trials and physical model experiments (the physical model experiments are introduced in Section 3.4) employed version 2.

3.3. Field monitoring

It was important to measure the AE response of the monitoring technique to real slope movements. The measurements obtained from field monitoring were used to achieve Objectives 1, 2 and 3. Five slopes were instrumented and monitored throughout this project:

Slope 1: Hollin Hill - A reactivated natural slope that moves along a shallow shear surface(s) (1 to 4 m deep) in response to rainfall-induced elevations in pore-water pressures;

Slope 2: Players Crescent - A reactivated cutting slope that threatens rail infrastructure and moves along a relatively shallow shear surface (3 to 7 m deep) in response to rainfall-induced elevations in pore-water pressures;

Slope 3: Flat Cliffs - A reactivated coastal slope that threatens a settlement of houses, access roads and utilities, and moves along a relatively deep shear surface (14 m deep) in response to rainfall-induced elevations in pore-water pressures;

Slope 4: Scarborough - A coastal slope with marginal stability that threatens a road and historical building, but had no known shear surfaces at the start of monitoring; and

Slope 5: Nafferton - A research embankment with instability being induced through continuous artificial rainfall, in order to generate a first-time failure.

Active waveguides had been installed in three slopes (Hollin Hill, Players Crescent and Flat Cliffs) prior to the start of this PhD research project, and all of these sites had the potential to provide valuable information on the AE response to real slope behaviour. The author therefore maintained these field trials throughout the course of the research, installed further instrumentation at the sites, and analysed the measurements recorded. The author installed an active waveguide inside an inclinometer casing at Hollin Hill to investigate the possibility of retrofitting inclinometer casings with active waveguides, and installed two SAAs in hand augered holes adjacent to two of the traditional active waveguides at this site, to provide continuous subsurface deformation measurements for comparisons with AE measurements. An active waveguide was installed at Scarborough during the beginning of this PhD research project (November 2012). The author also instrumented Nafferton in November 2014 with an active waveguide and SAA, both in hand augered holes.

Each of these trials had the potential to provide useful information for this study: Hollin Hill is known to experience relatively large displacements after wet winter periods and therefore was the most likely site to provide the AE response to real reactivated slope movements, within the duration of this study; Players Crescent allowed application of the monitoring approach to a typical slope type that is problematic to rail infrastructure in the UK, and to test the system's ability to provide warnings of slope movement; Flat Cliffs allowed assessment of the approach for monitoring slopes with relatively deep shear surfaces; and Scarborough and Nafferton provided the potential for the technique to be assessed in its ability to detect, and provide early warning of, first-time slope failure.

Deformation monitoring instruments were also installed at each of the slopes, adjacent to the active waveguides, in order to provide subsurface deformation measurements for comparison with the AE measurements. This was important in confirming that the AE

was generated by slope movement, and to establish a relationship between measured AE and deformation behaviour (Objectives 1, 2 and 3). Deformation monitoring instrumentation was typically conventional inclinometers, which were read periodically during site visits; however, SAAs were installed at Hollin Hill, Players Crescent and Nafferton to provide continuous subsurface deformation measurements for comparisons with continuous AE measurements. Rainfall data was collected at all sites for comparison with AE and deformation measurements, in order to identify potential triggering pore-water pressure elevations. The field monitoring case studies are detailed in Chapter 4 where descriptions of each site, instrumentation details and sample time series measurements are provided. The AE and deformation measurements obtained from the sites in response to slope movement are analysed further in Chapter 5 in order to establish a relationship between measured AE and deformation behaviour.

3.4. Physical modelling

3.4.1. Introduction

Physical modelling was utilised to control all variables that are uncontrollable within the field environment, and therefore to gain information that would be difficult from the field trials. Full-scale physical modelling was used because it provides information most representative of the behaviour of the real system. Small-scale modelling would require scaling, not only of geometry and material properties, but also of the AE response, and therefore full-scale modelling was deemed the most appropriate approach.

Physical modelling contributed to accomplishment of Objectives 2, 3, 4 and 5: the AE response to first-time slope failure has been characterised; empirical relationships between measured AE and deformation behaviour have been determined; the influence of system variables upon the AE response to applied deformation behaviour have been quantified; and a framework to quantify displacement rates from measured AE has been developed.

3.4.2. Active waveguide physical model tests

Dixon & Spriggs (2007) found that by applying displacement rates that were separated by orders of magnitude to active waveguide models with gravel backfill in constant strain rate compression tests, the magnitude of AE rates generated were also separated by orders of magnitude and proportional to the displacement rate applied. In this study an experimental programme was designed, using active waveguide models comparable to those used by Dixon & Spriggs (2007), to subject active waveguides to simulated slope movements in a controlled environment. Active waveguide models were subjected to

dynamic strain-controlled shear deformations, comparable to those active waveguides experience in response to slope movement, and a calibration AE rate-velocity relationship for the active waveguide model was determined (Objective 3). This experiment differs from that detailed in Dixon & Spriggs (2007) because they used apparatus that could only apply constant rates of strain to the active waveguide models. Dynamic shear apparatus was developed to subject active waveguide models to the simulated slope movements. The Dixon & Spriggs (2007) constant strain rate compression apparatus was also used to validate the results generated from the dynamic shear apparatus. An accelerating displacement-time function was also applied to the active waveguide model, using the dynamic shear apparatus, to simulate slope failure. During this failure simulation the calibration AE rate-velocity relationship was applied to the measured AE rates to assess the performance of the calibration relationship in quantifying deformation rates from measured AE. In addition, a variety of active waveguide backfill materials were tested and their AE responses were compared (Objective 4). This work is detailed in Chapter 6.

3.4.3. Large-scale first-time slope failure simulation

The AE monitoring system was originally developed to provide early warning of instability during first-time slope failure. Thus far the AE system has been trialled in reactivated landslides that move with modest speed and travel, due to seasonal oscillations in pore-water pressures, and experience little or no further brittle loss of strength (due to the shear surface already being at or near residual strength). In order to obtain the response of the AE system to first-time failure and therefore demonstrate its performance in its intended application, a series of options were investigated:

i. To identify a slope with marginal stability, install the system and wait for the slope to fail; however, this approach presented too many uncertainties and yielded little confidence in acquiring the necessary data during the study period.

ii. Construct a full-scale slope and induce it to fail. This option presented more control but it still had many uncertainties, particularly with regards to the mechanism of failure induction, which included options such as: pore-water pressure recharge, comparable to the Selborne experiment (Cooper *et al.* 1998); or stress relief and removal of support through excavations of the toe, comparable to the Arseley experiment (Dixon *et al.* 2003). This option would have significant associated costs.

During the course of this study, Newcastle University and the British Geological Survey began planning to fail a section of the Nafferton (BIONICS) embankment (further details in Section 4.6.1), to investigate pre-failure mechanisms using an ERT array. The author

contributed to this collaborative research through the installation of the AE system, along with an SAA for comparison with continuous deformation measurements, at this embankment to capture the AE response to slope failure. This work is detailed in Chapter 4. Instability was induced in this slope first by steepening it, which increased the gravitational shear stress component, and also through continuous artificial rainfall to increase pore-water pressures. However, the slope was not predicted to fail during the period of study and therefore a large-scale physical model to simulate first-time slope failure was also developed.

A large-scale physical model was selected to minimise uncertainty and ensure failure would occur during this period of research. The experiment designed was a bespoke large shear box through which a full-scale active waveguide could be installed. A significant consideration was the stiffness moduli of the waveguide itself, which when present through a full-scale landslide moving *en mass* is negligible; however, when installed through a shear box in the laboratory is significant. Therefore, the design of the shear box needed to include sufficient strength and mass to represent the host landslide mass, and the method of loading to the box should also be sufficient to replicate this. The final design of the experiment is detailed in Chapter 7. This apparatus also allowed empirical AE rate-slope velocity relationships to be quantified over a greater range of applied velocities and deformation magnitudes than was possible using the results from the active waveguide physical model tests or field trials. Five tests were performed to subject active waveguides to simulated slope failure and large deformations (e.g. 50 mm). Three tests were conducted using the same test conditions and backfill material to assess repeatability (i.e. test-retest reliability). Two subsequent tests were performed using different backfill materials for comparison. This work was conducted to meet Objectives 2, 3 and 4.

3.4.4. The influence of system variables upon the AE response to applied deformation behaviour

3.4.4.1. Introduction

A series of physical model experiments were conducted to develop understanding of the influence of system variables upon the AE response to applied deformation behaviour. The primary variables investigated were depth to shear surface (i.e. attenuation) and sensor sensitivity. This was because they were hypothesised to have the greatest influence upon the systems response. AE generated from a greater shear surface depth would suffer greater attenuation before being measured at the ground surface. The depth to shear surface is uncontrollable and is different for each slope; its influence upon the systems response therefore needed to be quantified. In order to combat signal attenuation from deep shear surfaces, the voltage threshold level (i.e. sensitivity) on the sensor could be

reduced to detect lower amplitude signals. The influence of changing the systems voltage threshold level therefore also needed to be investigated. Due to small changes in manufacture and components used between Slope ALARMS sensor node and transducer combinations, each system has marginally different sensitivity. It was also important therefore to develop an approach to quantify the relative sensitivity between each combined sensor node and transducer system.

When monitoring using the Slope ALARMS system, many variables (e.g. monitored frequency range and signal amplification) are kept consistent between each installation or can be prescribed (e.g. waveguide properties and geometry, number and type of couplings, backfill material, transducer type, and borehole diameter). Investigations were also conducted to quantify the influence of changes to: backfill type; waveguide geometry, mechanical properties and connections; and borehole size. The influence of different backfill materials was investigated in Chapters 6 and 7, and the influence of the other variables stated above was investigated in Chapter 8. This work was conducted to meet Objective 4; however, the empirical relationships that were quantified were also used for inputs in the quantification framework (Objective 5).

3.4.4.2. Depth to shear surface: attenuation

A controlled source generator was developed to produce repeatable AE in the field environment comparable to that produced by deforming soil. A full-scale active waveguide with a length comparable to a deep shear surface was required to quantify the attenuation experienced by AE as it propagates along the active waveguide, including the influence of connections. It was impractical to drill a hole and bury the controlled source generator or AE measurement system to perform this experiment. Therefore, a trench was excavated in order to construct a horizontal active waveguide. Within the trench, a waveguide was buried in backfill and controlled AE, comparable to soil-generated AE, was induced at one end. The AE response was measured at various distances along the waveguide, and with differing lengths of backfill cover. This series of experiments allowed attenuation coefficients to be quantified for the active waveguide, which were then used for inputs into the quantification framework.

3.4.4.3. Voltage threshold level

A series of constant strain rate compression tests (Dixon & Spriggs 2007) were performed on active waveguide models and the AE response was measured with a range of voltage threshold levels set on the AE measurement system. Constant strain rate compression tests were used because they are repeatable and numerous tests could be performed in a comparable way, which meant that the only variable being changed

between each test was the voltage threshold level set on the sensor. This series of experiments was conducted in order to quantify the influence of sensor voltage threshold level on the AE response from the system. An empirical relationship between AE rates and voltage threshold level was generated, which was then used for input into the quantification framework.

3.4.4.5. Borehole size

A series of constant strain rate compression tests (Dixon & Spriggs 2007) were performed on active waveguide models with different diameters. Constant strain rate compression tests were used because they are repeatable and numerous tests could be performed in a comparable way, which meant that the only variable being changed between each test was the diameter of the active waveguide model. Two diameters were selected: 130 mm, which is representative of a standard borehole; and 59 mm, which employed a standard inclinometer casing and is representative of a retrofitted inclinometer and an active waveguide installed inside a hand augered hole. This series of experiments was performed to develop understanding of the difference in AE generated by active waveguides with different borehole diameters. These experiments were designed to answer the question: 'does the borehole diameter influence the magnitude of AE rates generated from the system'. Additionally, this work investigated the performance of active waveguides retrofitted inside inclinometer casings, which is an approach that is very interesting because it would provide relatively low cost real-time monitoring, by employing the existing subsurface infrastructure within a slope (as opposed to the requirement of a new borehole). A quantification of the influence of borehole diameter could then be implemented in the quantification framework.

3.4.4.6. Waveguide properties and geometry

A series of constant strain rate compression tests were also performed on active waveguide models employing different waveguides, with different geometry and mechanical properties. Constant strain rate compression tests were used because they are repeatable and numerous tests could be performed in a comparable way, which meant that the only variable being changed between each test was the waveguide. This work was performed to investigate the influence of different waveguide materials and geometries on the AE response from the active waveguide system. A quantification of the influence of waveguide type could then be implemented in the quantification framework.

3.4.4.7. Sensor node-transducer combination

There are sensitivity differences between each combined sensor node and transducer system, due to slight differences in manufacture and components. A number of tests were

performed for a range of sensor and transducer combinations, using the controlled source generator, in order to measure the variability in this degree of sensitivity. A database of AE responses from 18 different sensor and transducer combinations was compiled, which forms a basis to compare the sensitivity of each system and future systems. Use of the controlled source generator to induce AE, and comparing the measured AE with the database of AE responses, allows the relative sensitivity of the system to be quantified. This was also implemented in the quantification framework.

3.4.5. Development of a framework for the quantification of slope deformation rates from measured AE

Each variable that influences the AE response from the system was quantified using the physical model experiments described above. Each of these was combined in a system schematic to highlight where they have influence upon the system. An algorithm was developed to combine all of these variables within a function that can be used to quantify slope deformation rates from measured AE. Base-case AE rate-slope deformation rate relationships were derived using the large-scale first-time slope failure simulation. These relationships were used because they were derived from the greatest range of applied velocities and displacement magnitudes, when compared to the active waveguide physical model tests and field trials, and the shear mechanism induced was representative of that the real system experiences in response to slope movement in the field. These base-case relationships were representative of slopes with a shallow shear surface (<1 m), and with specific material properties and settings set on the AE measurement system. A series of charts of empirical relationships derived for each of the variables were produced. These charts can be used to obtain partial factors for input into the algorithm, which can be used to modify the base-case relationships to calibrate them for any system installation.

An example application of the framework to quantify a calibration AE rate-slope deformation relationship for the system installation at Nafferton embankment was performed. It was then shown how the calibrated AE rate-slope deformation rate relationships can be used to set alarm status/warning levels on the Slope ALARMS system that are related to rates of slope movement.

3.5. Summary

Field monitoring at five different slopes was used to characterise the AE response to slope movements through comparisons with both conventional periodic deformation measurements and continuous deformation measurements. Three of these field sites are reactivated slopes that move in response to rainfall-induced elevations in pore-water

pressure. Another site, at Scarborough, is a marginally stable coastal cliff that has the potential to fail in the future and provide the AE response to first-time slope failure. The last site, Nafferton embankment, has been steepened and is being induced to failure through artificial rainfall. This slope also presents an opportunity to capture the AE response from first-time slope failure.

Active waveguide physical model tests have been performed to subject active waveguides to simulated slope movements using dynamic shear apparatus. This experimental programme was conducted to quantify an empirical relationship between measured AE and deformation behaviour, which was an AE rate-velocity relationship. This apparatus was then used to subject the active waveguide to simulated slope failure, using an accelerating displacement-time function, and the calibration AE rate-velocity relationship was used to quantify applied velocities from measured AE rates. This apparatus was also used to investigate the AE response from different backfill materials.

Large-scale first-time slope failure apparatus was designed and built to subject elements of soil, through which an active waveguide and SAA was installed, to simulated slope failure. This allowed the AE response from first-time failure to be characterised, and an empirical AE rate-slope velocity relationship to be quantified over a greater range of applied velocities and deformation magnitudes than was possible in the active waveguide physical model tests. This apparatus was also used to investigate the AE response from different backfill materials.

The influence of system variables upon the AE response to applied deformation behaviour was investigated using physical model experiments. Certain variables are kept consistent between each system installation (e.g. monitored frequency range and amplification), certain variables are uncontrollable (e.g. depth to shear surface), and other variables can be prescribed (e.g. voltage threshold level, waveguide properties, geometry and connections, backfill material, and borehole diameter). The influences of variables that are uncontrollable and those that can be prescribed were quantified. The variables investigated include: depth to shear surface (i.e. attenuation); sensor node voltage threshold level; sensitivity of combined sensor node and transducer systems; borehole size; and waveguide geometry, mechanical properties and connections.

A framework was developed that can be used to produce calibration AE rate-slope deformation rate relationships for any Slope ALARMS system installation. This provides a universal method that can be used by practitioners when installing AE systems, to calibrate them to deliver alarm statuses/warning messages that are related to slope displacement rates. The framework comprises an algorithm that includes a function with all of the system variables included. The empirical relationships determined for each of

the variables that have influence upon the systems response were amalgamated using a series of charts. Partial factors can be determined from these charts for input into the algorithm, to modify base-case AE rate-slope deformation rate relationships so that they can be calibrated for each specific system installation.

CHAPTER 4

Field monitoring case studies

4.1. Introduction

Detailed in this Chapter are the field monitoring case studies of slopes that were instrumented with AE monitoring systems and other techniques, as introduced in Chapter 3, in order to capture the AE response from real slope movements. Each of the case studies include: a description of the slope (e.g. classification and typical behaviour); details of the instrumentation and monitoring programme; and example time series measurements collected over the course of monitoring (i.e. measurements that demonstrate the system response to slope movements and comparisons with other periodic/continuous deformation measurements). Table 4.1 provides a summary of the field trials reported in this thesis. The instrumentation installed at each site and the period for which monitoring data is available is detailed. The order in which the field trial case studies are presented in this Chapter is as follows: Hollin Hill; Players Crescent; Flat Cliffs; Scarborough; and Nafferton.

Table 4.1. Summary of field trials detailed in the thesis, highlighting instrumentation installed and parties involved

Site	Description	Location and setting	Instrumentation	Monitoring period	Parties involved
Slope 1: Hollin Hill	Reactivated shallow rotational and translational slides. Material: Whitby Mudstone Formation.	Farmers field near Terrington, North Yorkshire, UK.	Inclo (3), SAA (2), AEWG (3), GPS, TM (2), Piezo (2), RG, ERT. *AE system: Version 1*	Winter 2009/2010 - present.	BGS
Slope 2: Players Crescent	Reactivated rotational slide in cutting. Material: Predominately Barton Clay Formation.	Threatening a freight rail track in Totten, Southampton, UK.	Inclo (1), SAA (1), AEWG (2). *AE system: Version 2.*	February 2011 – April 2014.	GO, NR
Slope 3: Flat Cliffs	Relatively deep-seated (14-m) reactivated coastal slide. Material: Glacial Till.	Threatening a settlement of 50+ homes in Filey, North Yorkshire, UK.	Inclo (1), AEWG (1), Piezo. *AE system: Upgraded from version 1 to version 2 in October 2013.*	September 2011 – present.	CH2M, SBC
Slope 4: Scarboro-ugh	Coastal slope with potential for first-time failure. Material: Glacial Till.	Threatening a road, hotels and spa complex in Scarborough, North Yorkshire, UK.	Inclo (1), AEWG (1), Piezo. *AE system: Upgraded from version 1 to version 2 in February 2014.*	November 2012 – present.	CH2M, SBC
Slope 5: Nafferton	Steepened research embankment with instability induced through continuous artificial rainfall. Material: Glacial Till.	An emankment panel is being induced to failure to develop understanding of pre-failure behaviour. Nafferton Farm, Stocksfield, Northumberland, UK.	AEWG (1), SAA (1), ERT. *AE system: Version 2.*	November 2014 – present.	iSMART

Instrumentation: Inclinometer (Inclo), ShapeAccelArray (SAA), Active waveguide (AEWG), Piezometer (Piezo), Rain gauge (RG), Tilt meter (TM), GPS marker monitoring (GPS), Electrical resistivity tomography (ERT).

Active waveguide installations:

- The standard active waveguide employed in these trials was installed in a borehole with an approximate diameter of 130 mm, and comprised the composite system of a steel tube (50 mm diameter with 3 mm wall thickness, connected in lengths using screw threaded couplings) with a gravel backfill surround (5 to 10 mm angular gravel).
- The active waveguide installed inside the inclinometer casing at Hollin Hill comprised a 25 mm diameter steel tube with 2 mm wall thickness, with Leigthon Buzzard sand backfill (0.6 to 2 mm size range).
- The active waveguide installed inside the hand-augered hole at Nafferton comprised a 21 mm diameter steel tube with 2 mm wall thickness, with Leigthon Buzzard sand backfill (0.6 to 2 mm size range).

Parties: British Geological Survey (BGS), CH2M (CH2M), Geotechnical Observations Ltd (GO), Network Rail (NR), Scarborough Borough Council (SBC), The iSMART Consortium (iSMART).

4.2. Hollin Hill

4.2.1. Site description

An active landslide at Hollin Hill (Figures 4.1 and 4.2) was selected for a trial as in recent years slope deformations have occurred during the winter months and there was confidence that measurable slope deformations would be experienced during the monitoring period. The BGS have used this site to assess performance of other instrumentation developments including ERT and self-potential (SP) geophysical and geotechnical systems for monitoring spatial and temporal behaviour (Chambers *et al.* 2008; Chambers *et al.* 2011; Merritt *et al.* 2013).

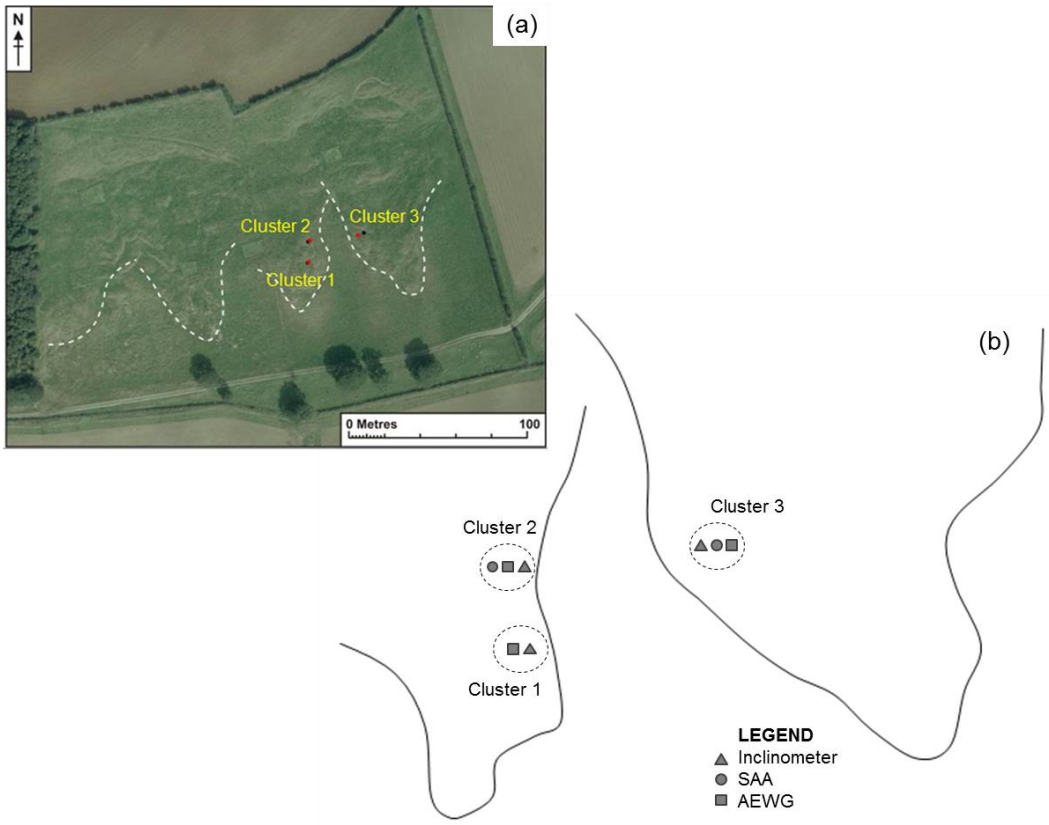

Figure 4.1. a) Outline of active lobes in the lower part of the slope and the location of the three clusters of instruments; Clusters 1 and 2 on the western lobe and cluster 3 on the eastern lobe (© UKP/Getmapping Licence No. UKP2008/01). b) Illustration of instrumentation cluster locations on the active lobes

Figure 4.2. Hollin Hill landslide: a) rotational sliding in the upper part of the slope; and b) materials degrading and forming lobes sliding down the lower part of the slope

The Hollin Hill research site [SE 68122 68852 (UK system), Latitude: 54.111044, Longitude: -0.95948786] lies 11 km to the west of Malton, North Yorkshire, UK, occupying an elevation of between 55 m and 100 m AOD. The site is located on a south facing valley side with a slope of approximately 12°. The bedrock geology, from the base to top of slope, comprises the Lias Group Redcar Mudstone Formation (RMF), Staithes Sandstone Formation (SSF), Cleveland Ironstone Formation (CIF), and Whitby Mudstone Formation (WMF), which are overlain at the top of the hill by the Dogger Sandstone Formation (DF). The bedrock is relatively flat lying with a gentle dip to the north. Slope failure at the site is occurring in the weathered WMF. The landslide can be characterized as shallow rotational failures at the top of the slope that feed into larger-scale slowly moving lobes of slumped material (Figures 4.2a and 4.2b); the rotational features and active lobes extend approximately 150 m down the slope from the top of the hill, and extend laterally more than 1 km along the valley side. In recent years, movement of the lobes has been in the order of tens of centimetres per annum. Movement typically occurs in the winter months (i.e. January and February) when the slope is at its wettest and pore-water pressures in the vicinity of the shear surface(s) are at their greatest magnitude.

Gunn *et al.* (2013) report results from borehole core logging of the lobes at Hollin Hill. Logging from a borehole at the location of Cluster 2 (location shown in Figure 4.1) details the material in the vicinity of the shear surface, which is at approximately 1.5 m below ground level at this location as described in Section 4.2.3.1. The material below the top soil (0.2 m to 1.6 m below ground level) was described as a deposit with a very loose, porous fabric comprising orange–brown, very soft, silty clay with occasional blue–grey streaks. The unit had penetration resistances of 1 MPa or less. The unit from 1.6 m to 3.4 m was described as a matrix of stiff, brown–grey clay with subangular, fine (5 mm) to coarse (40 mm) gravel-sized relic lithoclasts of dark brown, interlaminated claystone and siltstone. The penetration resistance throughout this unit was roughly 2 MPa or less. The unit from 3.4 m to 4.8 m (the depth of the second shear surface on the eastern lobe at Cluster 3 sits at approximately 4 m below ground level as described in Section 4.2.3.1) was described as a compact light orange–brown to red–brown silt matrix with many orange–red, angular, fine to medium (20 mm) gravel-sized ironstone nodules (suspected to be degraded siderite). This unit had relatively high penetration resistances of over 7 MPa. The unit below 4.8 m was described as uncompact clayey silt with occasional subangular fine to coarse gravel of siderite nodules, and this unit had penetration resistances between 3 MPa and 4 MPa.

4.2.2. Instrumentation

Three clusters of active waveguides (AEWG) and inclinometer casings were installed through two of the lobes during winter 2009/2010 (Figures 4.3 and 4.4 show photographs of the instrumentation). The waveguides were installed in 130 mm diameter holes to depths of 5.7 m below ground level. The waveguides comprise two 3 m lengths of 50 mm diameter 3 mm thick steel tubing connected with screw threaded couplings. The annulus around the steel tubing, which is located in the centre of the borehole, is backfilled with angular 5 to 10 mm gravel compacted in nominally 0.25 m high lifts. The top 0.3 m of the borehole is backfilled with a bentonite grout plug to seal against the ingress of surface water. The steel tube extends 0.3 m above ground level, where a transducer is coupled and connected to a monitoring sensor, and all of this is encased in a secure protective chamber. The monitoring systems are powered by batteries and recharged by solar panels. Monitoring is continuous at 30-minute logging intervals. Inclinometer casings were installed approximately 1 m from the waveguides with keyways orientated along the slope dip and strike directions. The inclinometer casings penetrate to depths of 6 to 7 m below ground level and the annulus around the casing is grouted using medium-stiffness cement-bentonite grout (approximate water, cement and bentonite proportions by mass were 1, 0.15 and 0.06 respectively).

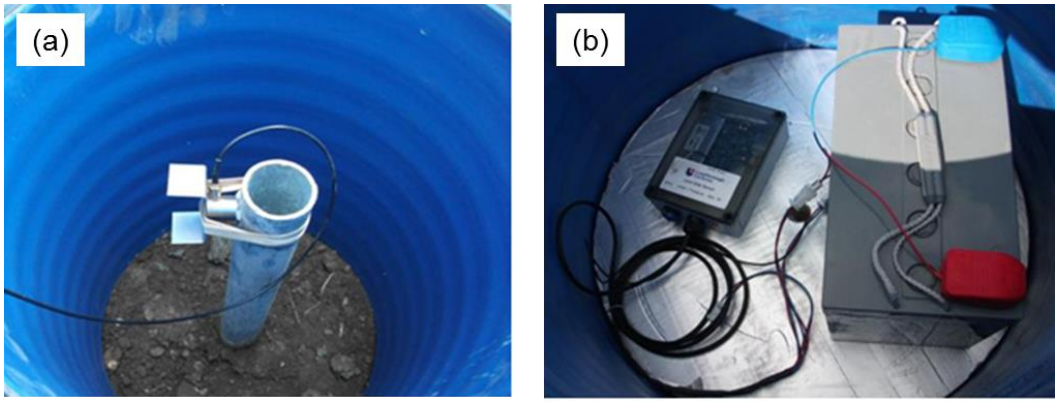

Figure 4.3. Photographs taken from inside a surface cover: a) protruding waveguide with transducer attached; and b) Slope ALARMS sensor powered by a battery

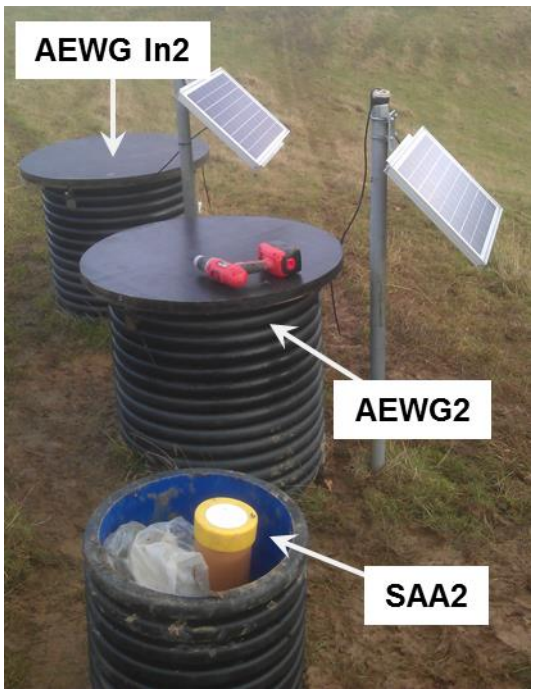

Figure 4.4. Photograph of instrumentation installation at Cluster 2 at Hollin Hill: surface covers of AEWG In2, AEWG2 and SAA2

The author retrofitted an inclinometer casing at Cluster 2 with an active waveguide (AEWG In2) in December 2011; the location of the installation is shown in Figure 4.4 and a photograph taken from inside the surface cover is shown in Figure 4.5. Previous surveys of the inclinometer casing revealed the lobe's shear surface to be at approximately 1.5 m below ground level at this location (as detailed in Section 4.2.3.1). The bottom 2.8 m of the 5.5 m deep inclinometer casing was filled with Leighton Buzzard sand; it was assumed unnecessary for the waveguide to penetrate this depth as the principal zone of AE generation was expected to occur at the shear surface. As the diameter of the inclinometer casing was significantly smaller than the diameter of the borehole used for the traditional active waveguide; waveguide tubing with a smaller diameter and backfill with smaller particle size were required in order to install an active waveguide inside the inclinometer casing. A continuous 3 m long 25 mm diameter and 2 mm thick steel tube was installed vertically into the casing, bearing on top of the already placed Leighton Buzzard sand. The annulus around the waveguide was subsequently backfilled with Leighton Buzzard sand (particle size between 0.6 mm and 2 mm) compacted in nominally 0.25 m high lifts. This column of sand was expected to generate AE in response to slope movements. The steel tube protrudes 0.3 m above ground level, where a transducer is coupled and connected to a monitoring sensor, and all of this is encased in a secure protective chamber. The monitoring system is powered by batteries and recharged by a solar panel. Monitoring is continuous at 30-minute logging intervals.

The author installed ShapeAccelArrays (SAAs) with 0.305 m gauge lengths 1 m west of the traditional active waveguides at Clusters 2 (Figure 4.4) and 3, to a depth of 2.5 m in

May 2013 to provide continuous subsurface deformation measurements for comparison with AE measurements. 60 mm diameter holes were hand augered in order to install the SAAs; the annulus around the SAA and PVC access casing was backfilled with medium-stiffness cement-bentonite grout (approximate water, cement and bentonite proportions by mass were 1, 0.15 and 0.06 respectively). The SAAs are connected to data loggers, which are powered by batteries. Positions of each of the MEMS sensors are logged at 1-hour intervals.

Figure 4.5. Deformed retrofitted inclinometer at Hollin Hill (AEWG In2)

4.2.3. Sample time series measurements

4.2.3.1. Deformation history

The inclinometer surveys show that the shear surface at Clusters 1 and 2 is relatively shallow at 1.0 m and 1.5 m respectively below ground level on the western lobe (Figures 4.6 and 4.7 show the incremental inclinometer measurements). Inclinometer data from Cluster 3 on the eastern lobe (Figure 4.8 shows the incremental inclinometer measurements) shows active shear surface deformation at two depths; 1.5 m and 4.0 m below ground level. A number of deformation events were identified in February 2010 at the end of the winter period. Following 18 months of unusually dry weather in 2010 and 2011 when the slope was stable, deformations were next recorded in 2012 in response to a period of high precipitation during the summer months. Continued precipitation caused further slope movements with the inclinometer casings recording substantial slope deformations in November 2012. These deformations induced significant localised bending of the casings and the probe could no-longer pass the shear surface, and hence

the casings became unusable and inclinometer measurements ceased. A decreased frequency of inclinometer surveys in 2011 and 2012 mean that the deformation measurements have a low temporal resolution for this period. Note that the inclinometer at Cluster 2 (readings shown in Figure 4.7) was converted to an active waveguide as detailed in Section 4.2.2.

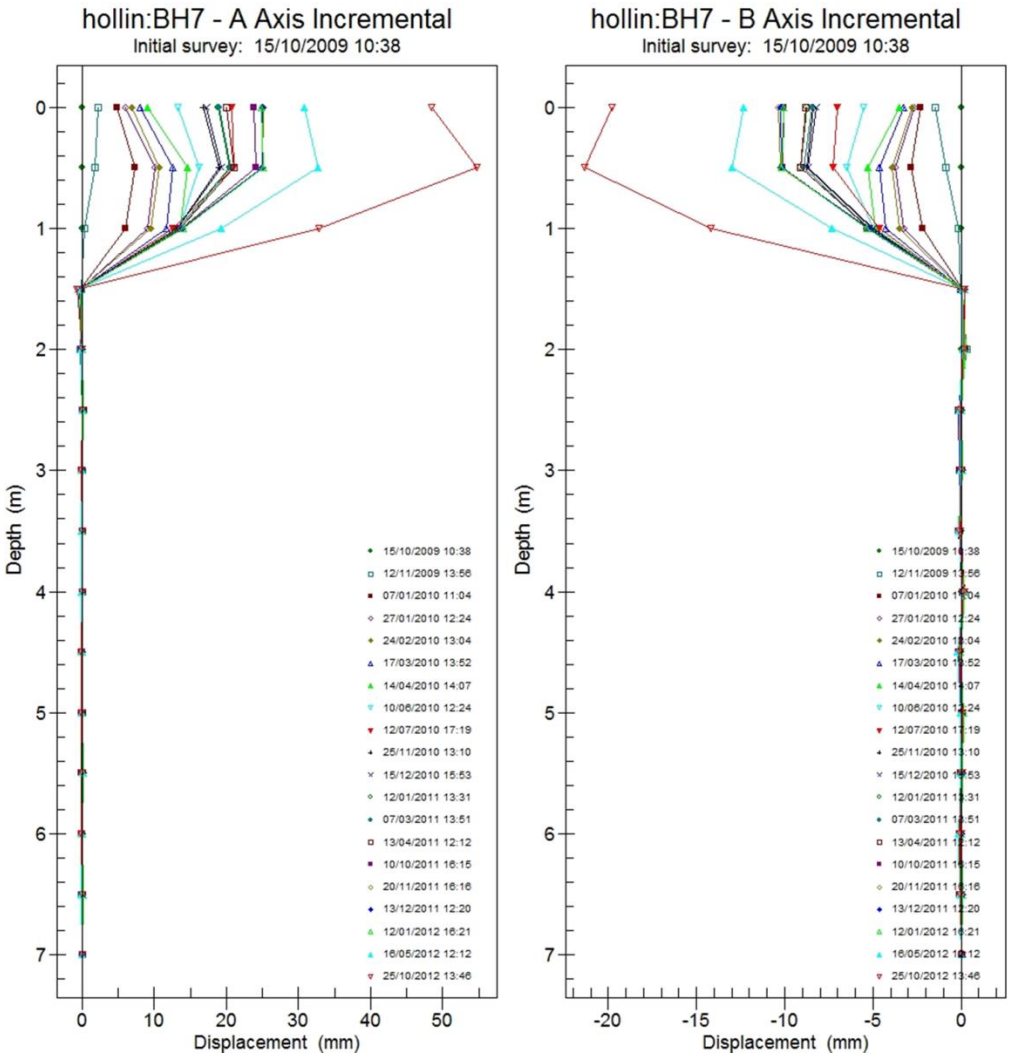

Figure 4.6. Incremental inclinometer measurements from Cluster 1 for the period 15/10/2009 to 25/10/2012. A-axis is the down-slope direction

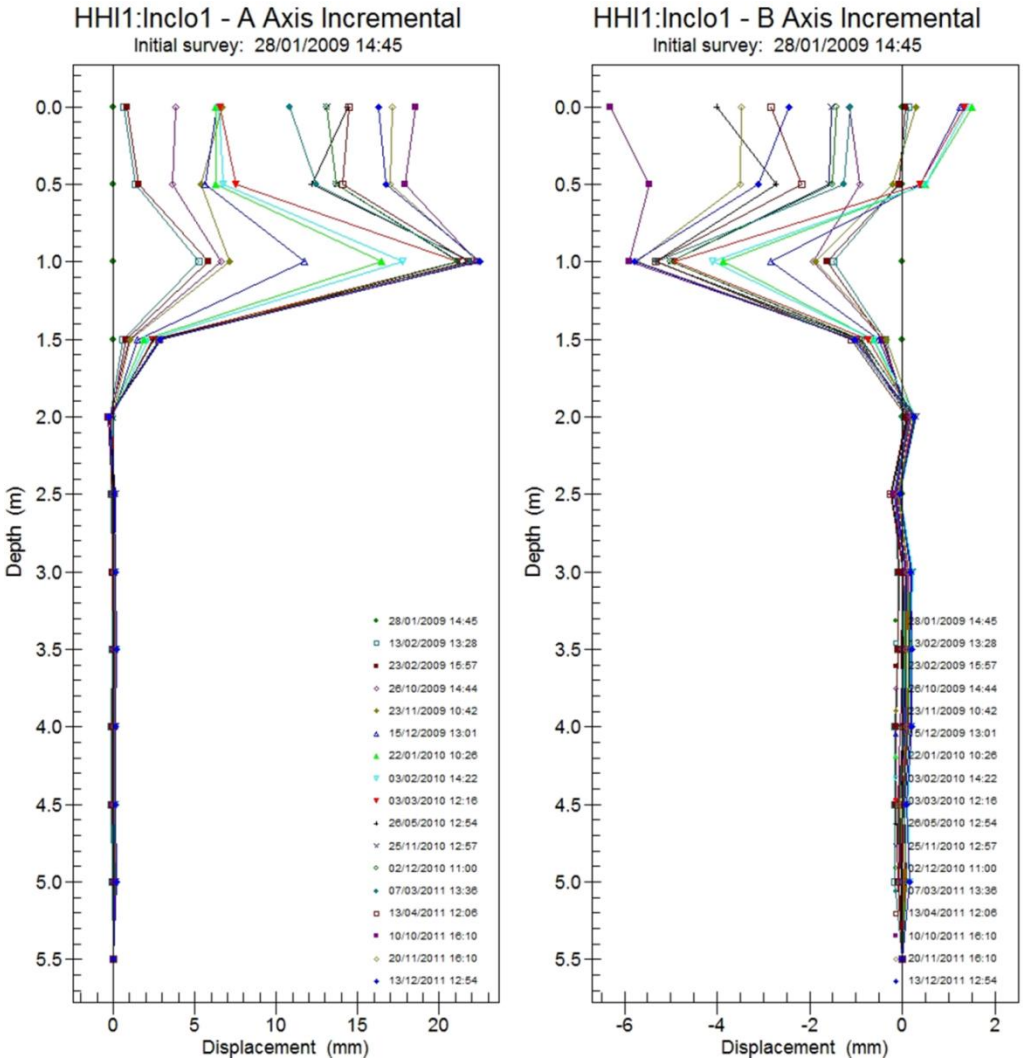

Figure 4.7. Incremental inclinometer measurements from Cluster 2 for the period 28/01/2009 to 13/12/2011. A-axis is the down-slope direction

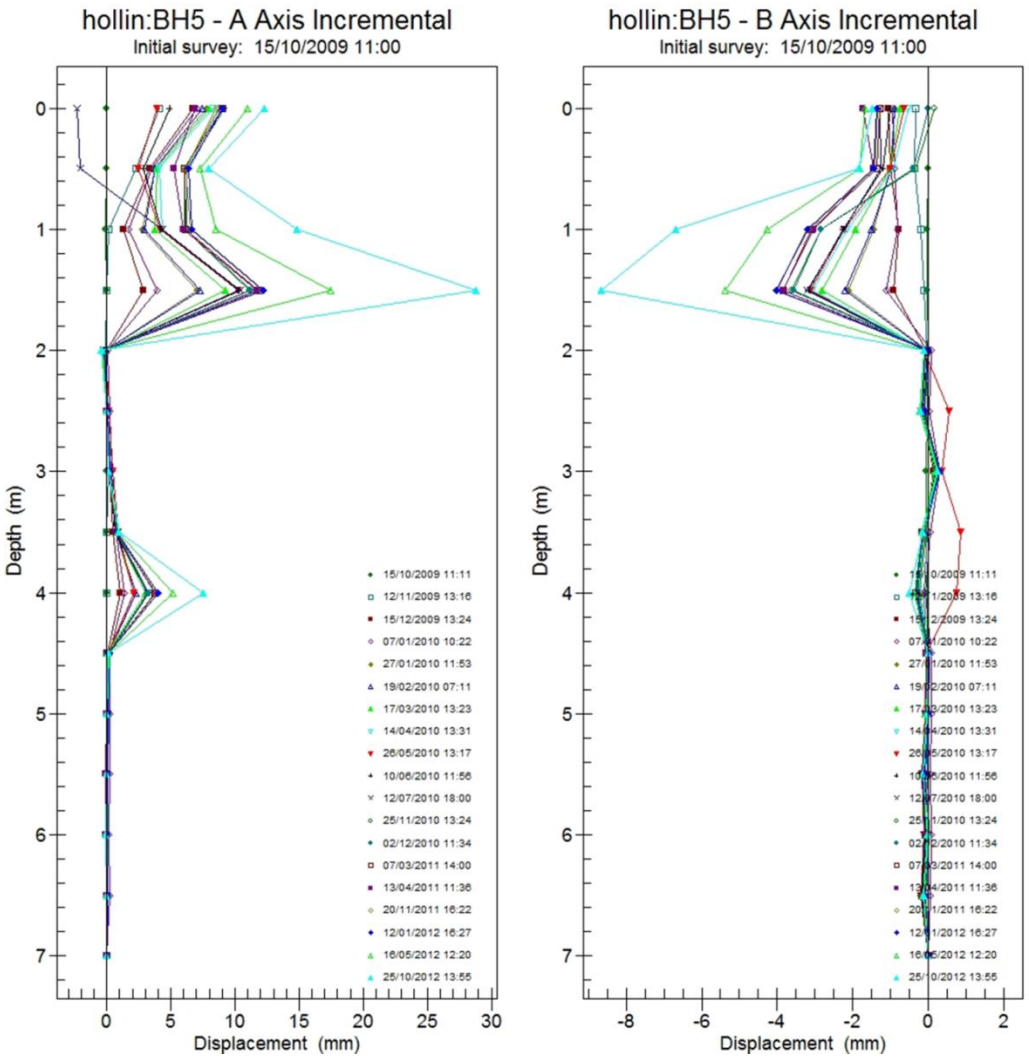

Figure 4.8. Incremental inclinometer measurements from Cluster 3 for the period 15/10/2009 to 25/10/2012. A-axis is the down-slope direction

4.2.3.2. AE and deformation comparisons

4.2.3.2.1. Comparisons with conventional inclinometer measurements

Figure 4.9 shows cumulative RDC, hourly rainfall and cumulative inclinometer measured shear surface deformation time series measurements at Cluster 2 for the first few months of 2010. Of note are the steep increases in the cumulative RDC record, labelled Events A and B, which follow intensive periods of rainfall. The combination of antecedent moisture being accumulated over long periods (i.e. typically during the winter) and a relatively shallow shear surface (1.0 m to 1.5m) mean that short periods of intense rainfall cause a build-up of pore-water pressures in the region of the shear surface, inducing short periods of reactivated slope movements on the existing shear surface. Such renewals of movement on pre-existing shears are expected to be of modest speed and travel as the strength is already at, or close to, the residual value and therefore little further brittle loss of strength can occur (Hutchinson 1988; Leroueil 2001) (Section 2.2.2.2). The ‘S’ shaped increases in cumulative RDC (Figure 4.9) are interpreted as defining periods of slope

deformation and this is validated by the inclinometer measurements. Other similar events recorded at the three clusters are interpreted in the same way and it is hypothesised that AE vs. time relationships can be used as a measure of the timing and rate of slope displacements. As continuous measurements of deformation were not available at this time, it was an assumption that the steps in cumulative RDC gave the timing of the slope movements. This hypothesis has been tested and validated using continuous SAA deformation measurements, which is described later in this Section. Following periods of rainfall, AE measurements at Clusters 1 and 2 generate the characteristic response to slope movement (i.e. 'S' shaped cumulative RDC record) at the same time, which is expected as they are located on the same lobe of the landslide. Events have also been identified to occur on Cluster 3 (eastern lobe) at similar times to Clusters 1 and 2 (western lobe). Merritt *et al.* (2013) also identified simultaneous activations of slope movement from the multiple lobes at this site. This is expected due to the similarity in materials, geometry and boundary conditions between the lobes.

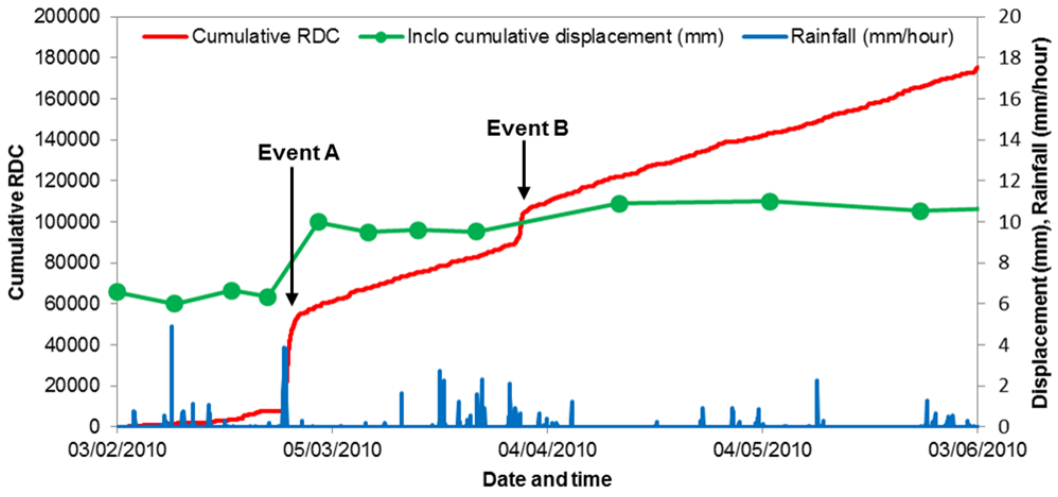

Figure 4.9. Cumulative RDC, inclinometer measured shear surface deformation and hourly rainfall time series at Cluster 2 at Hollin Hill, with periods of 'S' shaped movement identified

Figures 4.10, 4.11 and 4.12 show Event A (identified in Figure 4.9) at a larger scale. The AE generation is triggered by a preceding rainfall event, and consequently an elevation in piezometric level. Note that this piezometer was installed by the BGS and its installation comprises a piezometer tip within a 1 m high active zone (sand pocket) positioned below the shear surface, and therefore the piezometric level shown in Figure 4.12 is only indicative of pore-water pressures at the shear surface. This comparison of AE measurements with piezometric level is presented to confirm that a reduction in strength took place during this period of elevated AE and movement. AE measurements are principally compared with deformation measurements throughout the rest of this thesis, and with rainfall data to identify potential pore-water pressure elevations.

The AE rate measurements rapidly increase and then slowly decrease, giving a characteristic ‘S’ shaped cumulative RDC vs. time curve. This shape is produced by the large majority of events that are generated by reactivated slope deformations at Hollin Hill. Displacement vs. time relationships for reactivated slope movement patterns are reported to exhibit similar ‘S’ shaped curves (e.g. Allison & Brunsden 1990, Petley *et al.* 2005 and Massey *et al.* 2013) (Section 2.2.2.3). Such reactivated slope kinematics are explained by an initial acceleration of the slide mass due to increasing pore-water pressures in the vicinity of the shear surface, and hence reducing shear strength and stability, and a peak velocity is approached. This is followed by a deceleration of movement as pore-water pressures dissipate and due to mobilisation of shear resistance internally in the slide mass and through remoulding at the landslide toe.

The log normal bell shaped AE rate vs. time relationship is typical of the events monitored. The shape of the AE rate-time curve for the deformation event is indicative of an acceleration followed by a deceleration of slope movements and hence it is analogous to a velocity profile. A gradual reduction in AE rate occurs as slope movement and therefore waveguide backfill deformation ceases. Leroueil (2001) presented a conceptual velocity-time profile for the ‘reactivation stage’ of slope movements that possessed the shape of a normal distribution (Section 2.2.2.2), and hence velocity is expected to increase exponentially with time during reactivated slope movements until a peak velocity is reached and the velocity subsequently decays exponentially until movement ceases. AE rate-time relationships for deformation events at Hollin Hill are analogous to such behaviour; however, the AE measurements demonstrate that the velocity profiles for reactivated slope movements at the Hollin Hill site are predominantly log normal in shape. This indicates that 'slip' during the onset of movement accelerates the sliding mass to a peak velocity at a faster rate when compared to the rate at which the sliding mass can mobilise resistance and decelerate to equilibrium. AE monitoring by Fujiwara *et al.* (1999) (Section 2.4.4) of an embankment slope failure also produced log normal AE rate vs. time relationships.

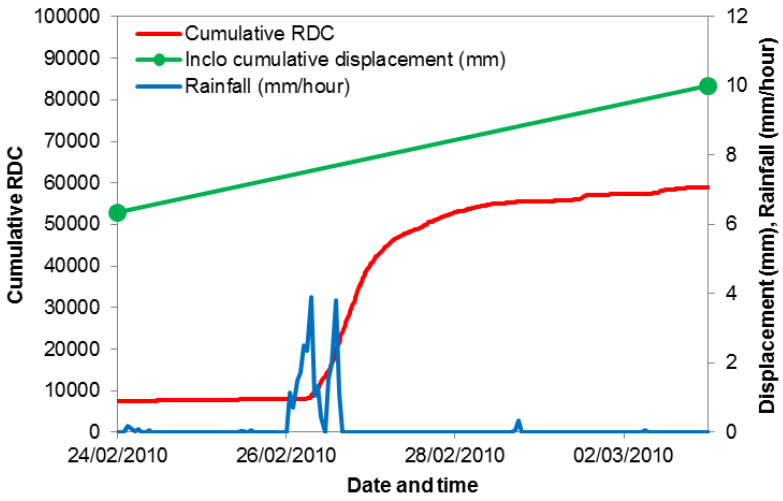

Figure 4.10. Cumulative RDC, triggering rainfall event and inclinometer measured shear surface deformation for Event A (highlighted in Figure 4.9) at Cluster 2

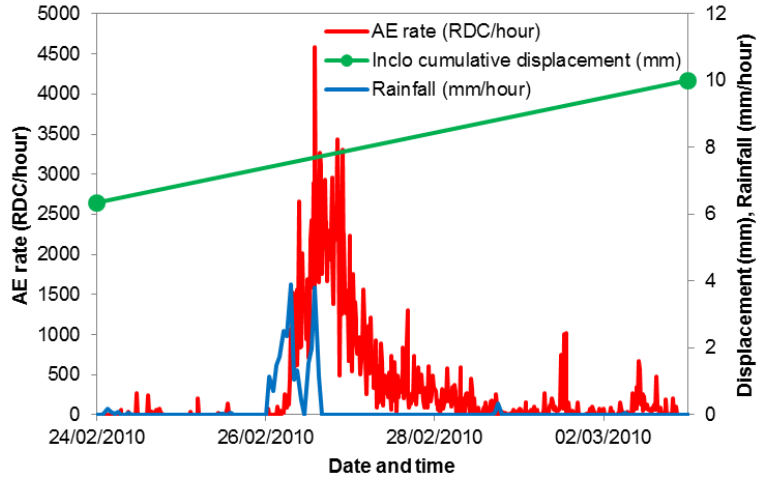

Figure 4.11. AE rate (RDC/hour), triggering rainfall event and inclinometer measured shear surface deformation for Event A (highlighted in Figure 4.9) at Cluster 2

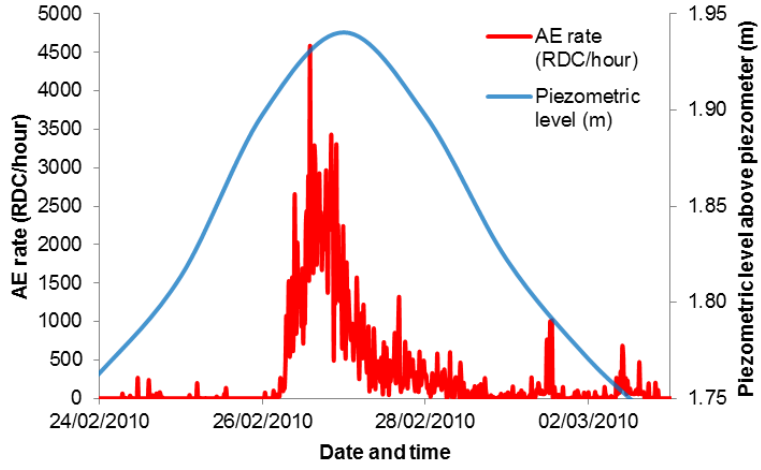

Figure 4.12. AE rate (RDC/hour) and piezometric level for Event A (highlighted in Figure 4.9) at Cluster 2

4.2.3.2.2. Comparisons with continuous SAA deformation measurements

The installation of SAAs at Hollin Hill has allowed the first comparison of continuous AE with continuous subsurface deformation measurements to be conducted. A series of reactivated slope movements occurred in response to periods of rainfall that produced transient elevations in pore-water pressure along the shallow shear surface in January 2014 (Figure 4.13 shows measurements recorded at Cluster 3). The measurements shown in Figure 4.13 comprise: resultant horizontal SAA measured deformation immediately above the shear surface; resultant horizontal SAA measured velocity immediately above the shear surface; AE measurements (both AE rate and cumulative RDC); and hourly rainfall. Note that the smoothed curves shown in Figure 4.13 were produced using 10-hour moving average values, through calculation of the average over the 5 hours preceding and 5 hours succeeding each measurement. This method of smoothing was used because of its simplicity and wide use (Excel software uses this moving averages approach) (further details in Section 5.3.2). These comparisons confirm that: AE rates generated by the system are directly proportional to the rate of deformation; AE monitoring of active waveguides can provide continuous information on slope displacements and displacement rates; and the technique is sensitive to small displacements, displacement rates (i.e. less than 0.5 mm per hour) and changes in displacement rates (i.e. accelerations and decelerations). Note that comparable behaviour was measured at Cluster 2 on the western lobe during the same period; however, to a lesser magnitude (Appendix A1). These measurements are analysed further in Chapter 5.

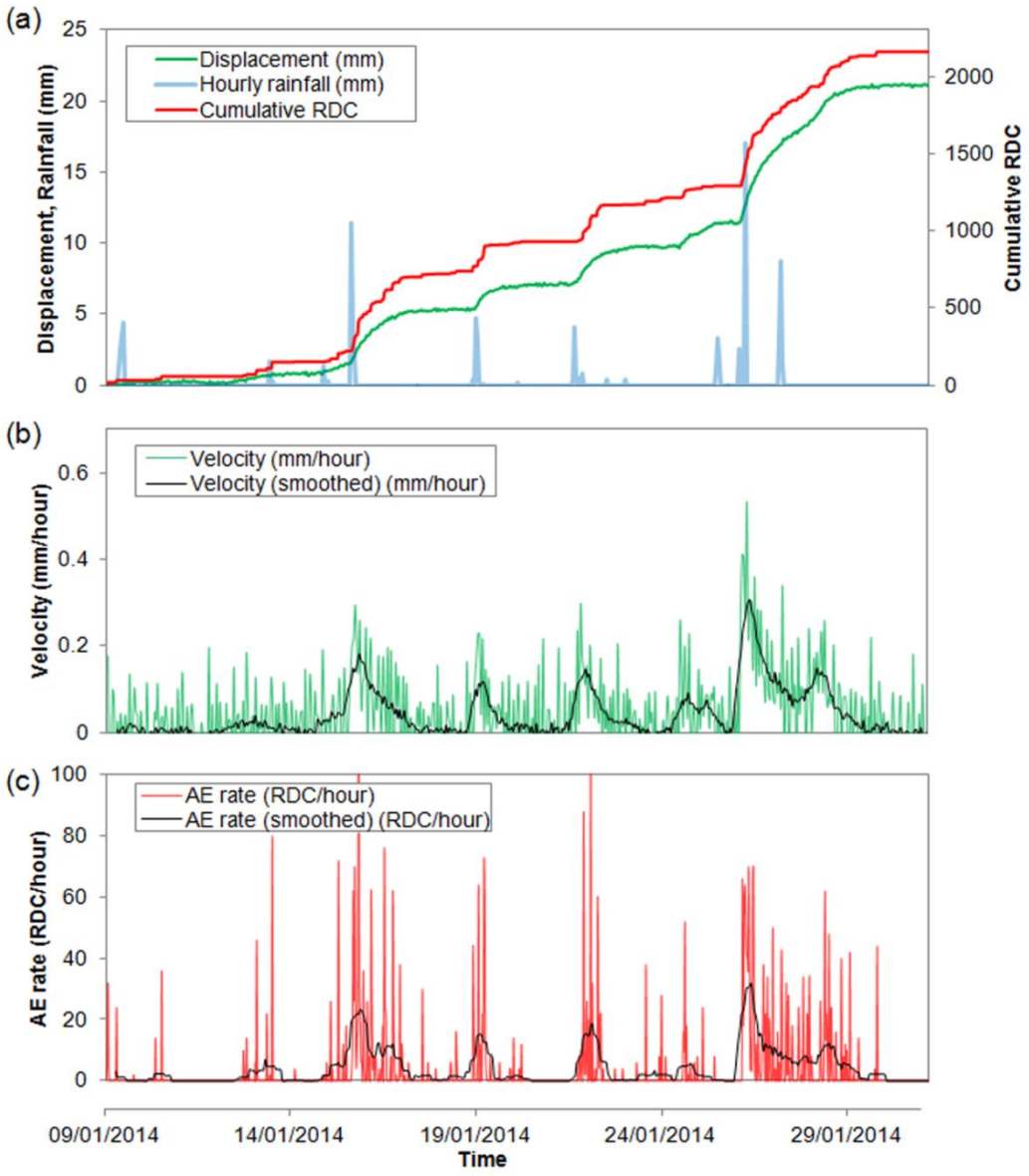

Figure 4.13. Time series for reactivated slope movements at Hollin Hill Cluster 3: a) Rainfall, cumulative AE and cumulative SAA displacement; b) SAA velocity; and c) AE rate

4.2.3.2.3. Performance of the retrofitted inclinometer casing

Figure 4.14a shows the resultant horizontal SAA deformation recorded by SAA2 (western lobe), AE rate measured using AEWG In2 and rainfall time series for a series of reactivated slope movements that occurred at the end of January 2014. Figure 4.14b shows the cumulative RDC trend superimposed on the same time series. The slope movements strained the inclinometer casing along with the active waveguide contained inside and this generated AE. This resulted in a cumulative RDC-time series proportional to the displacement-time series (i.e. confirming that the AE rates generated from the retrofitted active waveguides are proportional to the rate of slope movement). The field trial at Hollin Hill demonstrates that inclinometer retrofitted active waveguides can detect and provide continuous information on slope movements with high temporal resolution. It is important to note that the time series of measurements presented from the retrofitted

inclinometer active waveguide occurred 14 months after the other inclinometer casings at the same site (one on the same lobe) became unusable as the probe could no longer pass the shear surface(s) due to excessive curvature. This is of significance as it demonstrates the ability to not only convert inclinometer casings to continuous real-time monitoring systems, but also to significantly extend their operating life, using the AE technique.

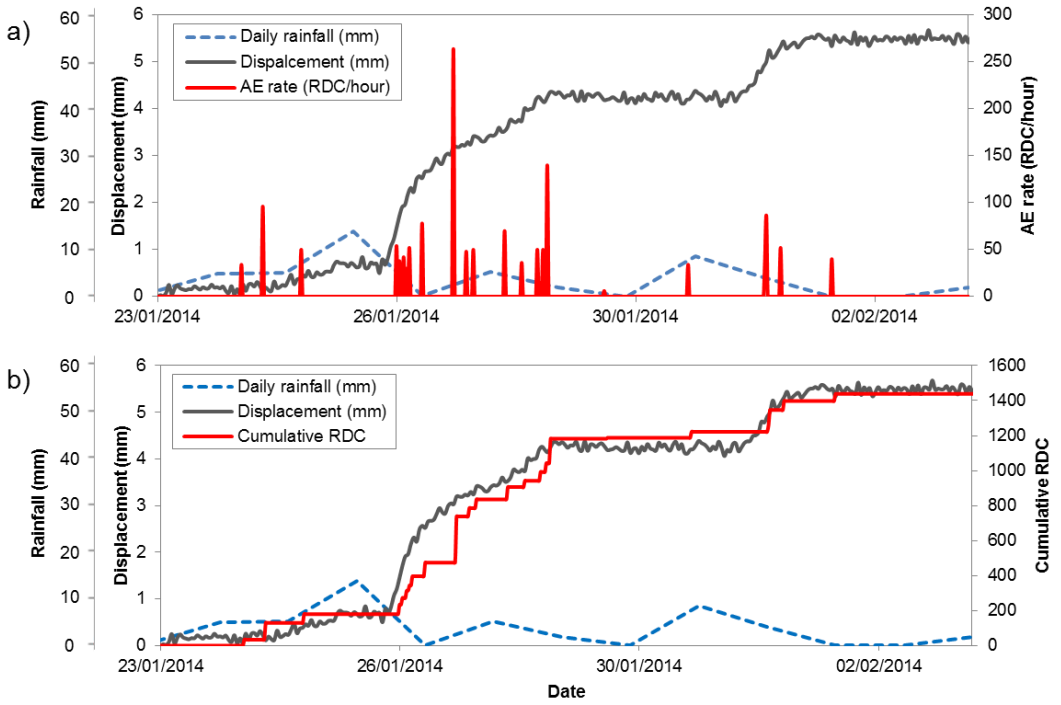

Figure 4.14. Time series for reactivated slope movements at Hollin Hill Cluster 2 to demonstrate performance of the inclinometer casing retrofitted with an active waveguide: a) SAA measured displacement, AE rate and rainfall vs. time; and b) SAA measured displacement, cumulative RDC and rainfall vs. time

4.3. Players Crescent

4.3.1. Site description

In order to evaluate the performance of the AE monitoring system it is important to conduct trials in typical field environments. The Players Crescent field trial was designed to investigate the capability of Slope ALARMS to provide real-time information that could be used by operators to make decisions on transport safety. A reactivated cutting slope at Players Crescent, Totton, Southampton, UK was selected for a field trial as in recent years slope deformations had occurred during the winter months and there was confidence that measurable slope deformations would take place during the planned trial period. A single rail track is located at the toe of the slope servicing the Southampton docks area. It is lightly trafficked (i.e. a few trains per day) by low speed goods trains (limited to 30 miles per hour).

The dominant geology in which the slope at Players Crescent is formed is the Barton Clay Formation (BCF), which is overlain by the Chama Sand Formation (CSF). The CSF terminates at a few metres below ground level at the top of the slope and is not present at the toe of the slope. A site investigation undertaken in March 2009 revealed a soft to firm horizon (in the BCF) at a depth of 6 to 7 m in the borehole in which the upper inclinometer casing was installed (subsequent monitoring has shown this to be the depth of the shear surface at this location, Section 4.3.3.1). During visual inspection at the site it was noted that a previous slope failure had occurred on the opposite side of the rail line where a sheet pile wall had been constructed as part of the remediation effort, demonstrating that multiple earthworks instabilities have occurred along this section of track. The initial visual inspection of the site also revealed the presence of convex young saplings below the crown of the monitored slope, which indicated creep movements were taking place within the over steep surficial CSF. Semi-mature back tilted trees present below the main scarp (on the head) indicate rotational slope movements and therefore a curved shear surface. A possible second scarp present further down-slope suggests that the landslide is possibly compound with multiple failure surfaces.

The reactivated slide mass is interpreted to move along a defined shear surface that is at or close to residual strength. Therefore, rapid and catastrophic failure is not anticipated; however, bulging at the toe of the slope is a concern due to interaction with the adjacent rail infrastructure (i.e. serviceability limit state). A concrete cable trough at the toe of the slope has been deformed indicating continued movement (Figure 4.15).

Figure 4.15. Photograph of the toe of the Players Crescent slope showing distorted concrete cable trough and toe bulging

4.3.2. Instrumentation

The site plan in Figure 4.16 details the locations of the instruments that have been installed along a cross-section of the slope. The current study utilises the central two inclinometer casings that were installed in May 2009 as part of an array of six on this slope, and were typically read twice a year. The inclinometer casing (up-slope) was installed to a depth of 7.5 m below ground level. A SAA string (down-slope) with MEMS sensor spacing of 0.305 m was installed in the lower inclinometer casing to a depth of 5 m below ground level. This converted the manually read instrument into a continuously read system. The annulus around the inclinometer casings and the SAA access tubing were grouted using medium-stiffness cement-bentonite grout (approximate water, cement and bentonite proportions by mass were 1, 0.15 and 0.06 respectively). The SAA was powered by a battery and connected to a data logger (all secured under a protective surface chamber) that logged changes in position of each of the MEMS sensors in the x-, y-, and z-directions at 1 hour intervals. Active waveguides were installed adjacent to both of these subsurface deformation monitoring instruments. The active waveguides were installed in 130 mm diameter boreholes; the down-slope active waveguide (AEWG1) was installed to a depth of 5.7 m adjacent to the SAA, and the up-slope active waveguide (AEWG2) was installed to a depth of 8.9 m adjacent to the inclinometer casing. The waveguides comprise 3.2 m lengths of 50 mm diameter 3 mm thick steel pipe connected with screw threaded couplings. The annulus around the steel pipes was backfilled with angular 5 to 10 mm gravel compacted in nominally 0.25 m high lifts. The top 0.3 m of the boreholes were backfilled with bentonite grout to produce a plug and seal against the infiltration of surface water. The steel pipes extend 0.3 m above ground level so that the transducers can be coupled, and are encased in secure protective chambers. An additional protective chamber was installed to house the communication system. Figure 4.17 shows a photograph of the down-slope surface covers taken from the bottom of the slope. The Slope ALARMS sensors measure AE continuously and log the number of RDC at 30 minute time intervals. The AE sensors and communication system were powered using air-alkaline batteries. AE monitoring commenced in February 2011. Note that the sensors installed at Players Crescent are a later version than those installed at Hollin Hill, and they have updated hardware and firmware (version 2). The AE measurements from Players Crescent are therefore not directly comparable with those obtained from Hollin Hill.

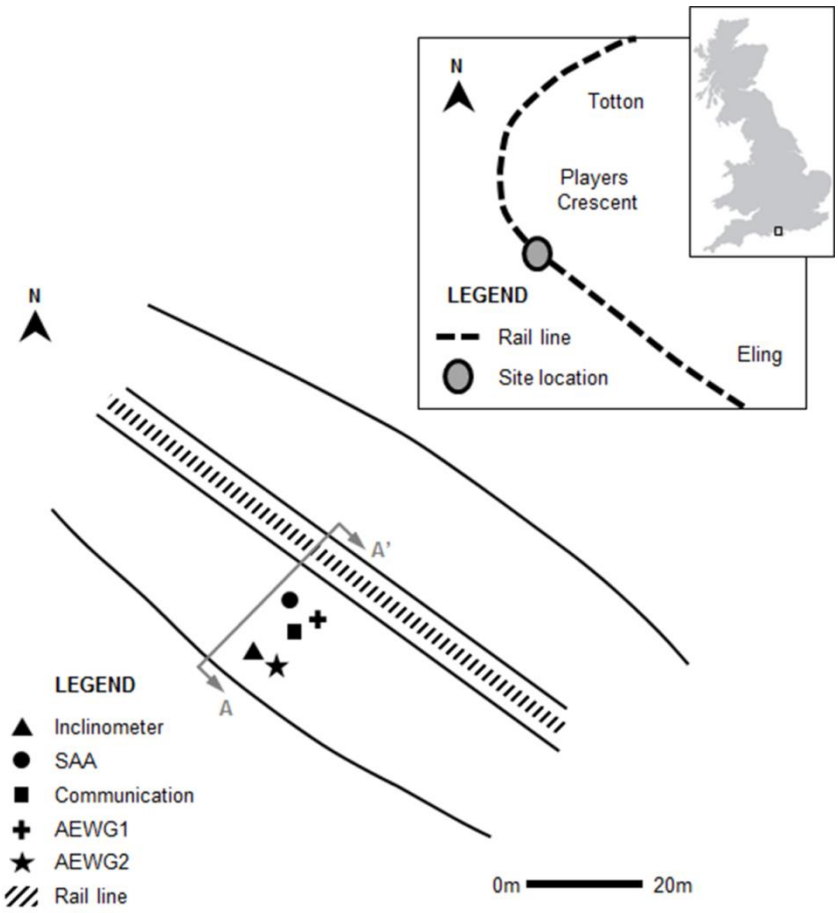

Figure 4.16. Players Crescent site plan and instrumentation locations, cross-section A-A' is shown in Figure 4.19

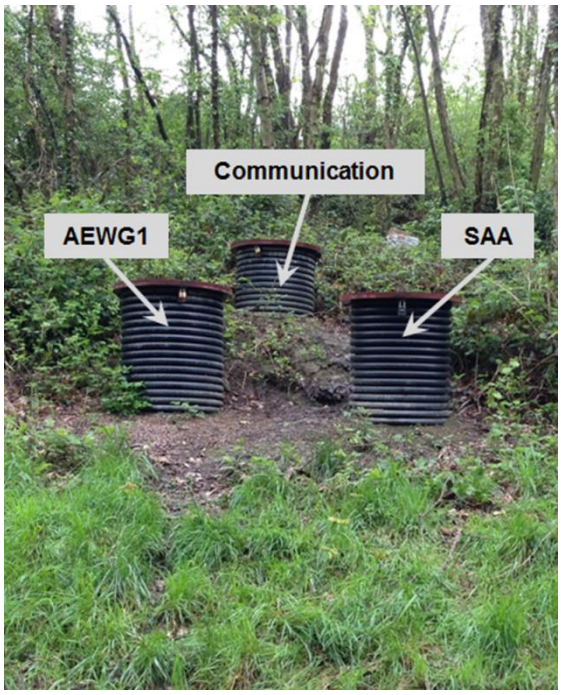

Figure 4.17. Photograph from the bottom of the Players Crescent slope showing surface covers protecting AEWG1, the SAA and housing the communication node

4.3.3. Sample time series measurements

4.3.3.1. Deformation history

Figure 4.18a presents survey data from the inclinometer casing and Figure 4.18b survey data from the SAA. The data shows a shear surface depth at the location of the inclinometer of approximately 6.5 m (agreeing with the location of the soft to firm horizon found in the site investigation as described in Section 4.3.1) and a shear surface depth of approximately 3 m at the location of the SAA. This information was used to produce the cross-section of the slope in Figure 4.19 (Section A-A' in Figure 4.16) and the interpretation of the location and geometry of the shear surface, which was assumed to intersect the rear scarp and the toe.

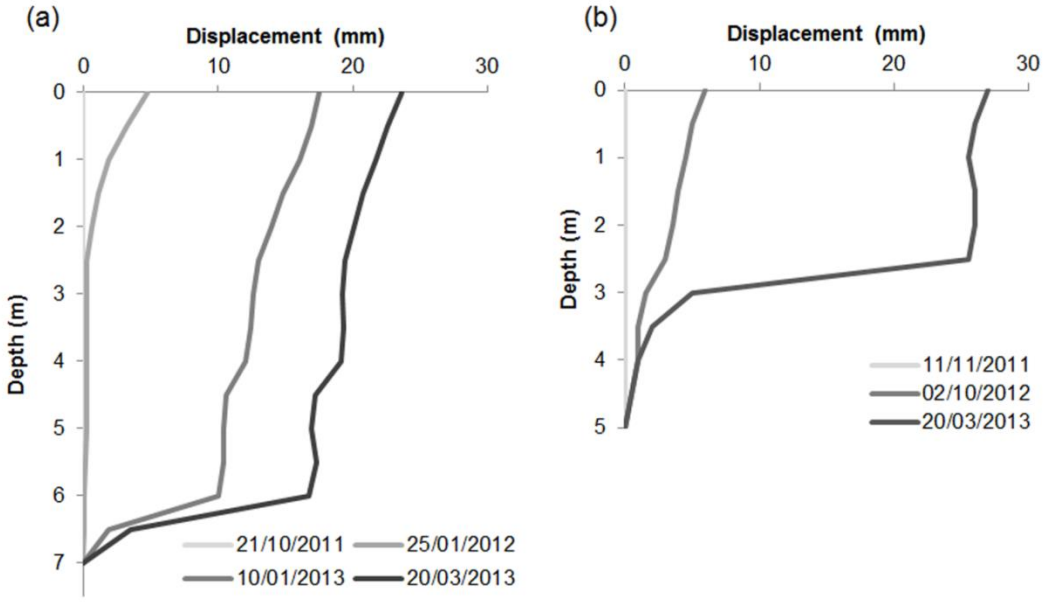

Figure 4.18. a) Selected inclinometer survey data (initial '0' reading on 21/10/2011) showing the main shear surface at a depth of approximately 6.5 m in the upper part of the slope, and b) selected SAA survey data (initial '0' reading on 11/11/2011) showing the main shear surface at a depth of approximately 3 m in the lower part of the slope. Note deformations increased progressively with time

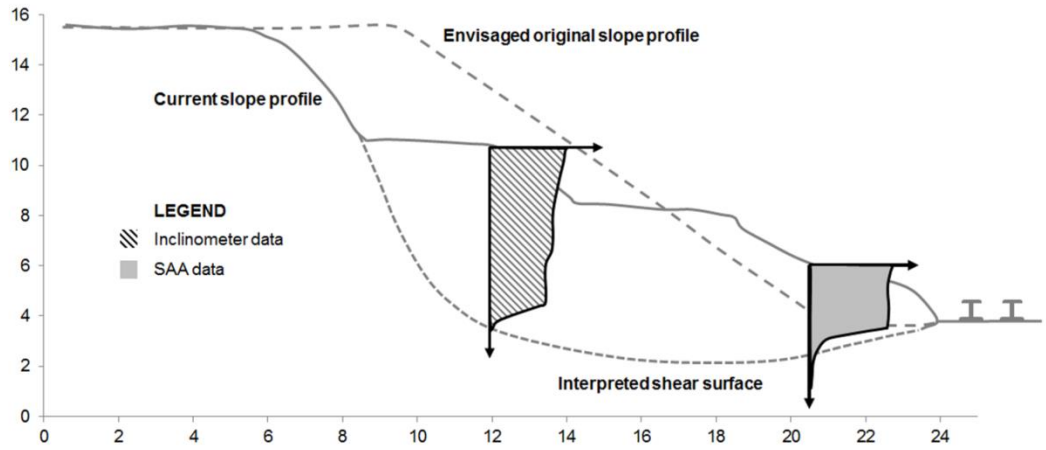

Figure 4.19. Cross-section A-A' (in Figure 4.16) showing the envisaged original slope profile, current slope profile, and the interpreted shear surface (with exaggerated inclinometer and SAA data) (axis units are metres)

4.3.3.2. AE and deformation comparison

Figure 4.20a shows cumulative RDC, deformation and hourly rainfall with time for a period of slope movement that occurred between 19th April 2012 and 5th May 2012. The continuous deformation information was recorded by the SAA installed down-slope (i.e. near the toe). Deformation data was taken from the MEMS sensor immediately above the shear surface depth and the measurements shown are the resultant from both x- and y-directions (i.e. resultant horizontal displacement). The AE data was recorded by the adjacent active waveguide and sensor node (AEWG1). Figure 4.20b shows the AE rate time series superimposed on top of the same deformation event. Approximately 1.2 mm of shear surface deformation occurred during this 16 day period. The gradient of the SAA deformation-time series during the event was relatively constant and therefore the velocity of movement was relatively constant. The velocity can therefore be determined using the displacement/time relation and this generates values of 0.075 mm/day or 0.003 mm/hour; these rates of movement would be classified as 'very slow' according to Cruden & Varnes (1996) (Section 2.2.2.2). Although there are fluctuations of the measured values, this event demonstrates the ability of the SAA to detect and quantify such low velocity and small magnitude movements continuously with high temporal resolution.

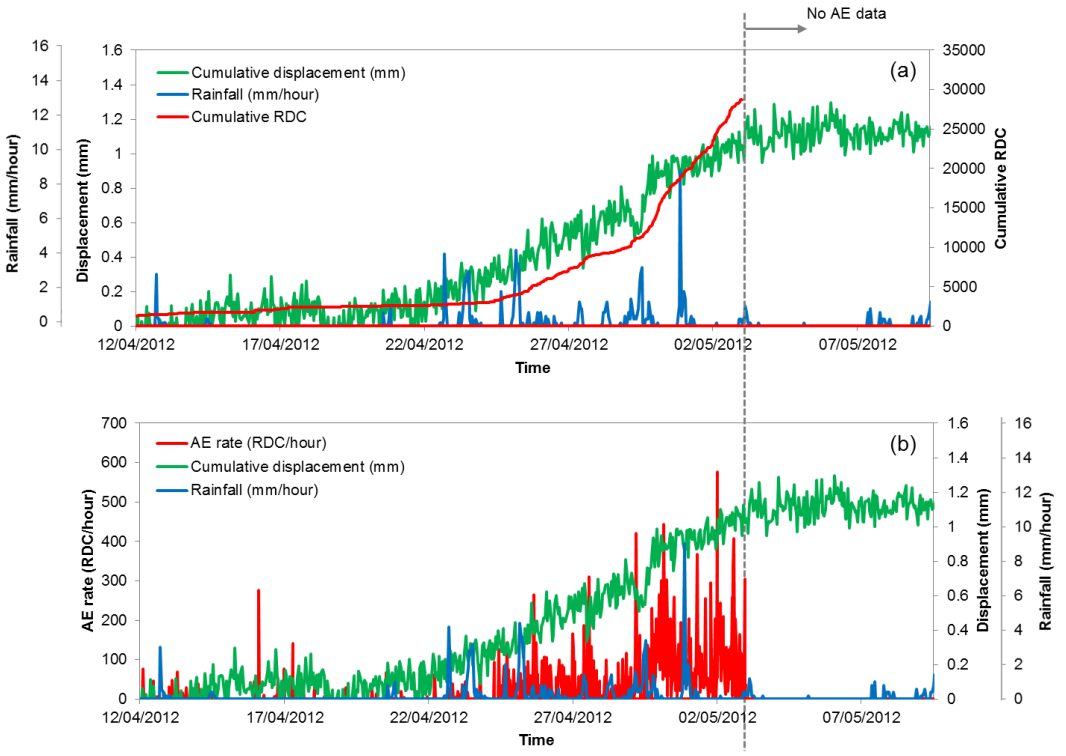

Figure 4.20. a) Cumulative RDC, displacement and hourly rainfall vs. time for a small magnitude low velocity reactivated deformation event (data from the SAA and AEWG1), and b) AE rate (RDC/hour), displacement and hourly rainfall vs. time (data from the SAA and AEWG1)

The AE system also detected this small, low velocity slope movement event. Of particular interest is the dramatic continual increase in AE rates as slope movement initiates and this continues throughout the 'very slow' deformation event. A surge of accelerated movement between April 29th and April 30th occurred in response to a preceding period of intensive rainfall. This period of accelerated movement was detected by the AE system as evidenced by the increased AE rates (Figure 4.20b) throughout this period, and the increased gradient of the cumulative RDC record (Figure 4.20a).

The AE system produced continuous information with high temporal resolution, which demonstrates the potential of the system to provide alternative deformation rate information to detect and provide an early warning of slope movements. The ability of the AE system to detect such small low velocity slope movements highlights its potential for use as an early warning system. Unfortunately the AE data ended on 3rd May 2012 (due to reaching storage capacity on the data logger) and so the final two days of the deformation event was not monitored, however; based on monitoring trends from similar events at other sites (e.g. Hollin Hill; Section 4.2.3.2) it is expected that the AE rates generated by the active waveguide would have reduced as the rate of slope movement reduced, and the gradient of the cumulative RDC curve would gradually decrease and become horizontal as deformation ceased and the column of gravel backfill approached equilibrium (as in the slope movement events monitored at Hollin Hill).

4.3.3.3. Early warning of slope movement

Pre-defined trigger levels were set on the AE system related to deformation rates. The trigger levels were based on the laboratory results obtained by Dixon & Spriggs (2007) from constant strain rate compression tests. The trigger levels are therefore useful in detecting order of magnitude changes, however, the actual values of derived velocity from measured AE rates using this approach may be inaccurate. If the measured RDC in any given monitoring period exceeds one of the trigger levels, a SMS message is generated. The communication system sent a SMS alarm status on 24th November 2012 at 7:00 PM, which stated that AEWG1 had detected 'very slow' movement as the AE rate exceeded 2000 RDC/hour (Figures 4.21 and 4.22). Another SMS was sent on 25th November 2012 at 6:30 AM, which stated that AEWG2 had also detected 'very slow' movement (Figure 4.22). Only one text message was generated at each of the two instrument locations during this period of movement because the AE rates subsequently decreased beneath the lowest trigger threshold in the successive measurement intervals. These warnings were generated by the peaks in the bell-shaped AE rate-time curves shown in Figure 4.21, which are characteristic of deformation events. Figure 4.21 shows the AE rate, inclinometer displacement and hourly rainfall vs. time series for the period in which the deformation events and alarm SMS messages were triggered. The 11.5 hours that separated the warning messages indicated that movement had been detected in the lower part of the slope prior to being detected in the upper section of the slope. Subsequent interrogation of the data shown in Figure 4.21 confirmed that the toe of the slope indeed moved before the head (i.e. AEWG1 generated a bell-shaped AE rate curve prior to AEWG2). An extended period of intense rainfall occurred at the location of the site prior to, and during, the deformation events. This rainfall provided for a build-up of pore-water pressures in the vicinity of the shear surface sufficient to reduce the effective stress and induce movement. This was followed by a deceleration of movements as pore-water pressures dissipated and due to mobilisation of shear resistance internally in the slide mass and through remoulding at the landslide toe. Unfortunately the SAA data logger reached storage capacity prior to this period and therefore continuous deformation data was not available for comparison. However, interpretation of inclinometer measurements made between 15/11/2012 and 10/01/2013 (Figure 4.21) confirmed that deformation had occurred during this period but the rate of movements with time is unknown. This episode has demonstrated the ability of the Slope ALARMS AE monitoring system to detect and communicate warnings of slope movements.

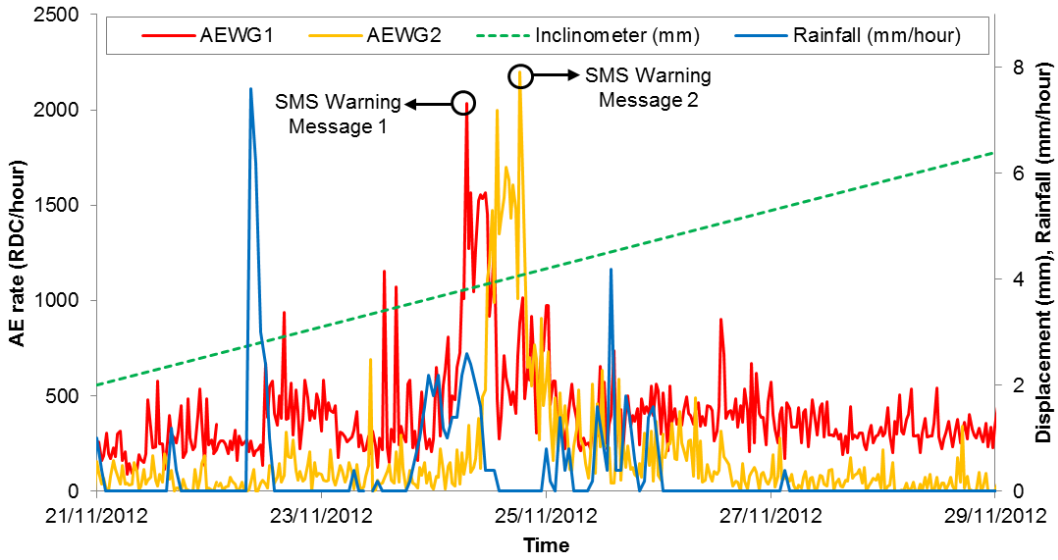

Figure 4.21. AE rate (RDC/hour), inclinometer displacement interpreted for the measurement interval 15/11/2012 to 10/01/2013 and hourly rainfall vs. time for a period of slope movement in response to intensive rainfall (data from AEWG1, AWEG2 and the inclinometer), the timing of the SMS warning messages (Figure 4.22) are superimposed

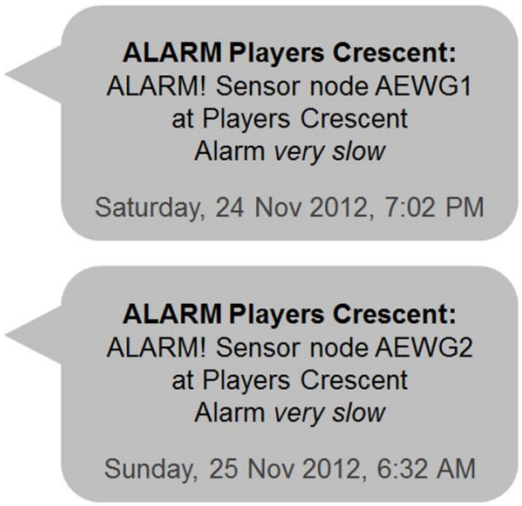

Figure 4.22. SMS warning messages AEWG1 (lower waveguide) and AEWG2 (upper waveguide) (Figure 4.21) showing the information contained (e.g. the time stamps and the alarm status)

4.4. Flat Cliffs

4.4.1. Site description

A large coastal landslide at Flat Cliffs, Filey, UK, was selected for comparison of AE monitoring with a manually read inclinometer (a satellite image of the site is shown in Figure 4.23), principally to test performance of the system in monitoring deep seated slope movements. Periodic slope movements are triggered by rainfall and excess groundwater levels, and due to toe erosion by the sea. Cliff instability is indicated by repeat deformation of an access road that serves a settlement of approximately 50 houses.

The geology at Flat Cliffs has been confirmed by ground investigations commissioned by Scarborough Borough Council in 2001 and 2011; the results have been interpreted by Halcrow (now CH2M). They established that all boreholes terminated within glacial sediments, at depths between 22.5 and 35.0 m below ground level. Despite fragmentary core recovery, the data revealed that the site is underlain by glacial sediments comprising diamicts with localised and discontinuous stratified sands and gravel (meltwater deposits). The glacial sediments have a maximum recorded thickness of 35 m, but could exceed this given that none of the boreholes encountered the underlying Kimmeridge Clay. The contact between the glacial sediment and Kimmeridge Clay at Flat Cliffs is therefore indicated to be an unknown depth beneath the base of the cliffs and beach. Due to the nature of the sediments and problems of core recovery, no pre-existing shear surfaces were logged in either ground investigation.

Figure 4.23. Location of active waveguide and inclinometer at Flat Cliffs (Google) (© 2015 Infoterra Ltd & Bluesky)

4.4.2. Instrumentation

An active waveguide (location shown in Figure 4.24) was installed in a 130 mm diameter borehole to a depth of 25 metres below ground level, with the annulus around the steel tubing backfilled with compacted angular 5 to 10 mm gravel. The steel tube extends 0.3 metres above ground level and is encased in a secure protective chamber. A standard inclinometer casing was installed adjacent to the waveguide to 24.5 m below ground level. The battery powered AE sensor is located inside the protective cover with the piezoelectric transducer coupled to the waveguide and monitoring is continuous with AE recorded and time stamped for each monitoring period. Monitoring commenced at Flat

Cliffs in September 2011 and has been continuous apart from short periods of down-time due to battery failure (e.g. two weeks during November 2012 and four weeks during May-June 2013), with a monitoring interval of 30 minutes.

Figure 4.24. Photograph of instrumentation location at Flat Cliffs

4.4.3. Sample time series measurements

4.4.3.1. Deformation history

Negligible subsurface deformations were recorded from the start of monitoring in September 2011 until the start of 2013. This was anticipated due to the unusually dry weather in 2010/2011 combined with a relatively deep shear surface depth. High winter rainfall intensity and duration are required to increase groundwater (and therefore pore-water pressure along the deep shear surface) to critical levels, reduce the shear strength and hence induce movement (e.g. Moore *et al.* 2010).

A prolonged period of above average precipitation occurred throughout the summer months of 2012 and this was followed by a wet winter in 2012/2013, and this rainfall pattern triggered deformations in early 2013. The inclinometer monitoring interval 17th January 2013 to 22nd March 2013 shows approximately 13 mm of resultant incremental shear surface displacement at 13.5 metres below ground level; inclinometer measurements for this period are shown in Figure 4.25 (incremental inclinometer measurements).

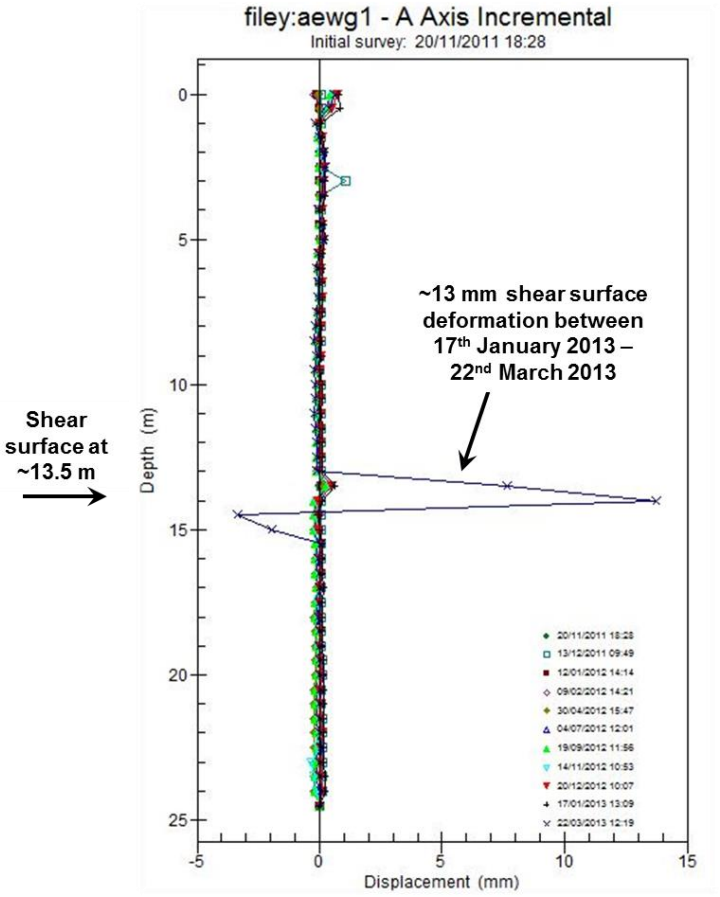

Figure 4.25. Selected incremental inclinometer measurements at Flat Cliffs, highlighting a period of movement between 17th January 2013 and 22nd March 2013. A-axis is the down-slope direction

4.4.3.2. AE and deformation comparison

Figure 4.26 shows AE rate, hourly rainfall and inclinometer measured shear surface displacement for the period January to March 2013. The period of increased AE rates at the end of January 2013, which follows periods of intensive rainfall, is interpreted to define the initiation of landslide movement. The time-lag between the onset of movement and the significantly increased AE rates, and therefore increased velocity of movement, which occurred at the end of February and in the middle of March 2013 (peak of >3000 RDC/hour) is hypothesized to be due to the low permeability characteristics of the landslide mass and the slow rate at which the antecedent rainfall events could infiltrate to the shear surface (this time lag could typically be 2-4 months; e.g. Fort *et al.* 2000 and Moore *et al.* 2010).

The AE rate vs. time curve exhibits periodic surges of movement; such movement patterns cannot be detected using conventional inclinometers. The bell shaped (log-normal) curves are analogous to velocity profiles as demonstrated by the field trials at Hollin Hill and Players Crescent described earlier in this Chapter (Sections 4.2 and 4.3). The fact that negligible AE was produced throughout the extended period of the slopes stability (September 2011 to early 2013) confirms the assumption that these increased

levels of AE produced during the period of landslide movement in early 2013, as evidenced from the inclinometer surveys, were induced by subsurface straining of the active waveguide in response to subsurface ground deformations.

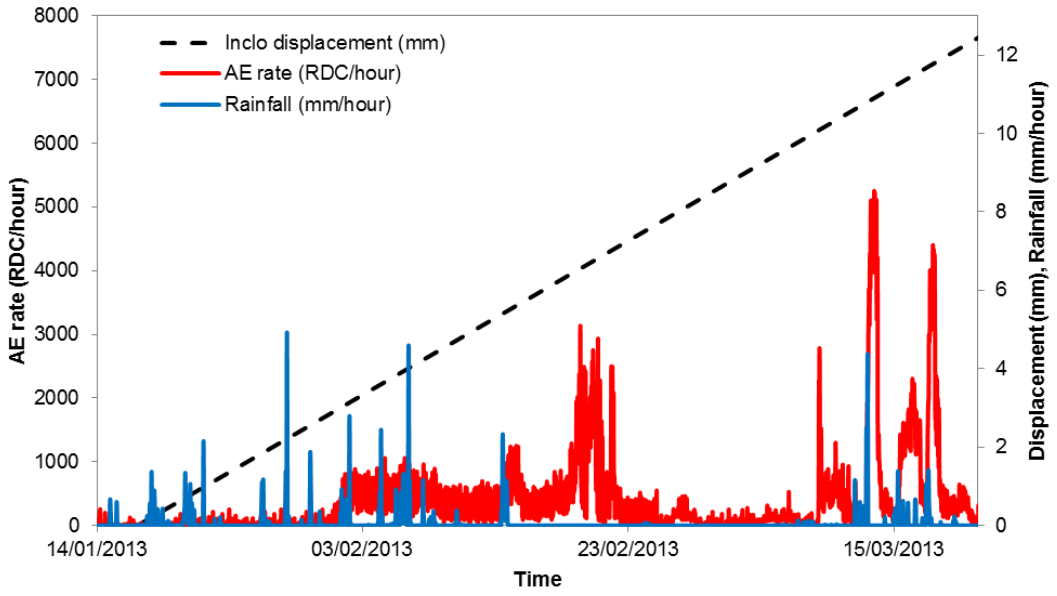

Figure 4.26. AE rate, rainfall and displacement vs. time behaviour at Flat Cliffs for the period 17th January 2013 to 22nd March 2013

4.5. Scarborough Spa

4.5.1. Site description

Cliff instability along the Scarborough coastline triggered Scarborough Borough Council to commission ground investigations in August 2012; to facilitate stability assessments and site risk management. A section of cliff behind the Scarborough Spa, South Bay, Scarborough, North Yorkshire, UK, was identified to have marginal stability. As part of a monitoring programme an array of instruments were installed across the cliff, which included an active waveguide (location in Figure 4.27). This site was selected as a trial for the AE monitoring approach because of the potential for a first-time failure and the ability to assess performance of the system in providing a warning of instability (i.e. the intended application for the monitoring approach). The published geological maps for the site show Glacial Till overlying mudstone and limestone of the Scarborough Formation of Jurassic age. Logs from the borehole in which the active waveguide was installed state that the predominant material down to the bottom of the hole was boulder clay, with bands of sand and gravel from 15 to 18 metres below ground level.

Figure 4.27. Location of active waveguide and inclinometer at Scarborough Spa (Google) (© 2015 Infoterra Ltd & Bluesky)

4.5.2. Instrumentation

An active waveguide was installed in a 130 mm diameter borehole to a depth of 40 m below ground level, with the annulus around the steel tubing (50 mm diameter 3 mm thick) backfilled with compacted angular 5 to 10 mm gravel. The steel tube extends 0.3 metres above ground level and is encased in a secure protective chamber (Figures 4.28 and 4.29). A standard inclinometer casing was installed adjacent to the waveguide to a depth of 43 m below ground level. The battery powered AE sensor is located inside the protective cover with the piezoelectric transducer coupled to the waveguide (Figures 4.28 and 4.29) and monitoring is continuous with AE recorded and time stamped for each monitoring period. Monitoring commenced at Scarborough Spa in November 2012 and has been continuous apart from short periods of down-time due to battery failure (from 22/09/13 to 22/10/13 and 01/12/13 to 10/01/14), with a monitoring interval of 30 minutes.

Figure 4.28. Photograph of instrumentation installation at Scarborough Spa: waveguide with transducer attached

Figure 4.29. Photograph of instrumentation installation at Scarborough Spa: sensor and batteries inside surface cover

4.5.3. Sample time series measurements

Surveys of the adjacent inclinometer casing have not revealed the occurrence of any subsurface deformations thus far during the period of monitoring. However, AE measurements show a distinctive and rapid response to periods of rainfall. It is anticipated that the AE detected at Scarborough is in response to rainfall-induced ground water flow

interacting with the active waveguide backfill column; particularly from rainfall-induced ground water flowing through the high permeability bands of sand and gravel from 15 to 18 metres below ground level. Figure 4.30 shows sample AE and rainfall time series measurements from the Scarborough site for the period February to June 2016. Figures 4.31 and 4.32 focus on certain periods within this period and demonstrate the AE response to rainfall. Note that the rainfall data used was taken from York and therefore is not entirely representative of the rainfall experienced at the Scarborough site.

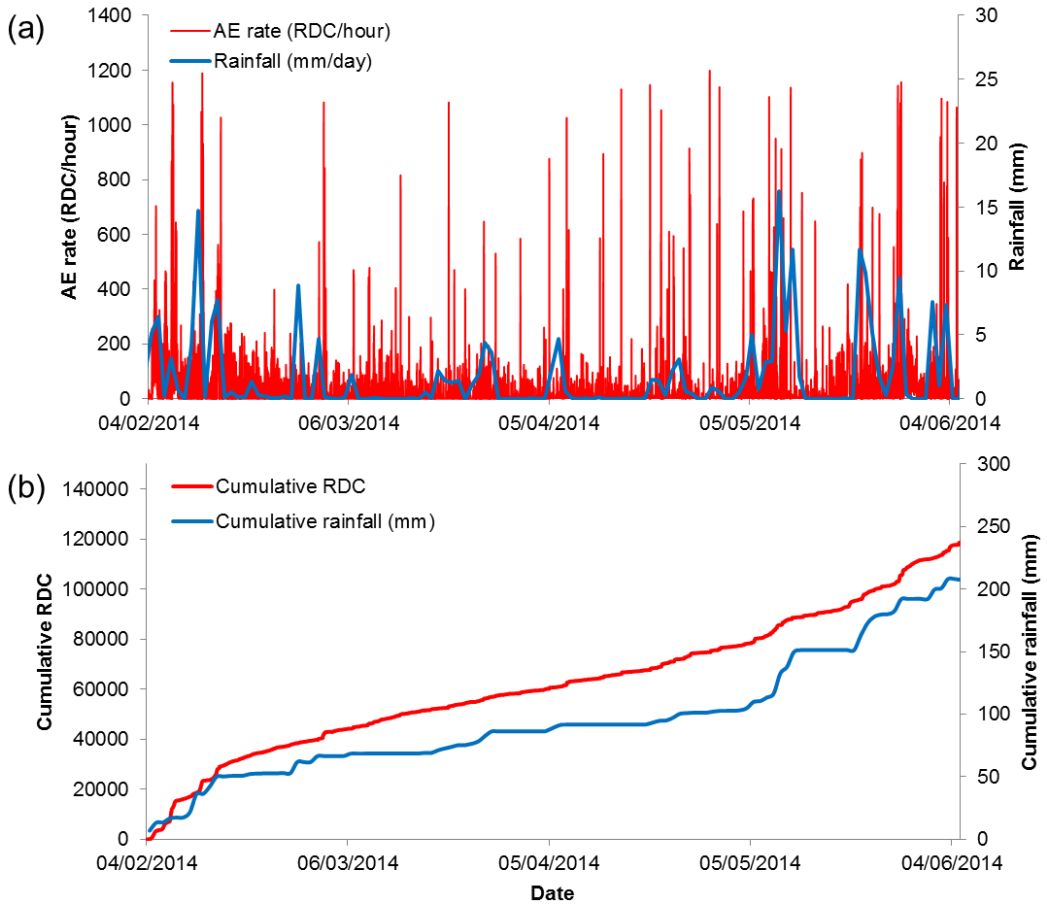

Figure 4.30. Sample time series measurements from Scarborough: a) AE rate and daily rainfall; and b) Cumulative RDC and cumulative rainfall

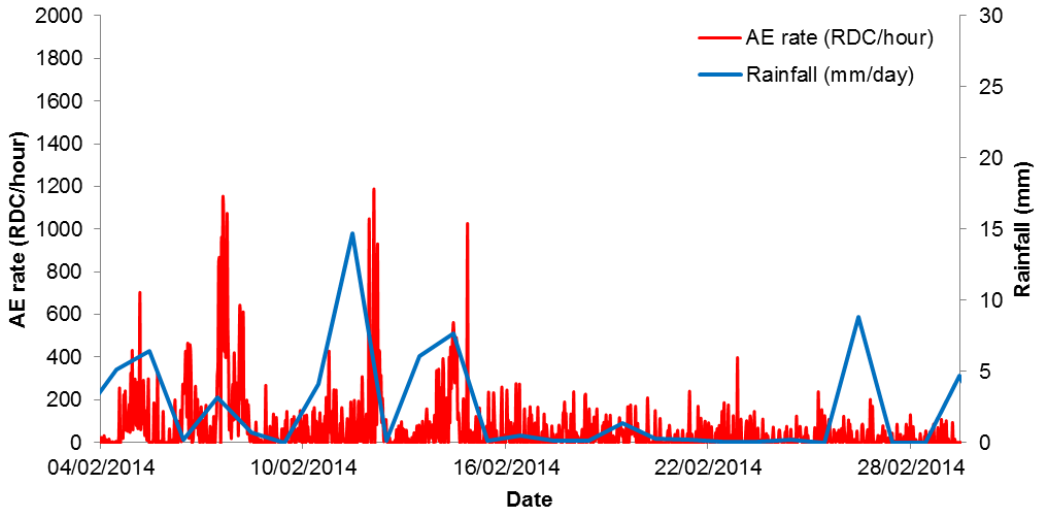

Figure 4.31. Sample time series measurements from Scarborough: AE rate and daily rainfall (February 2014)

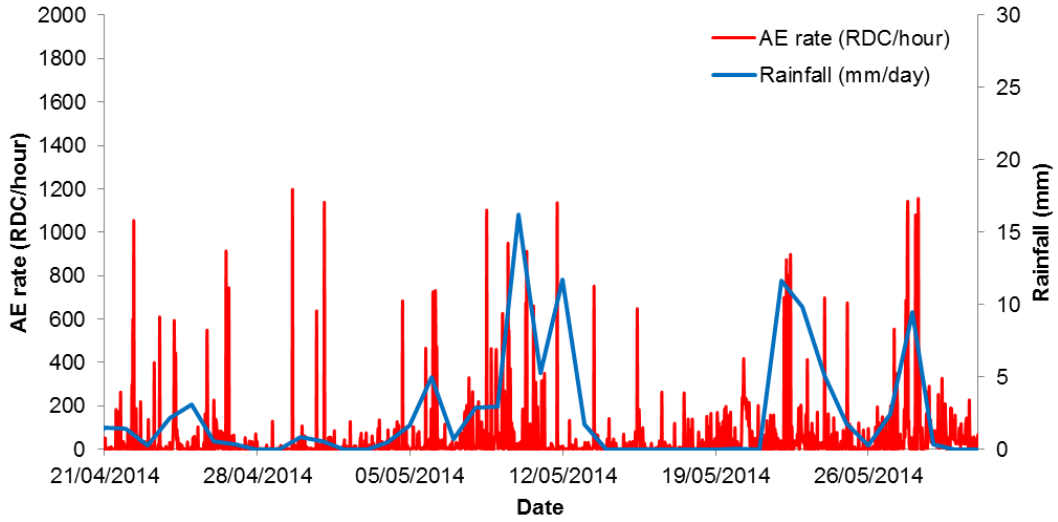

Figure 4.32. Sample time series measurements from Scarborough: AE rate and daily rainfall (April to May 2014)

4.6. Nafferton

4.6.1. Site description

A full-scale embankment (Figures 4.33 and 4.34) was constructed at Nafferton Farm, Stocksfield, Northumberland (OS grid reference NZ 064 657), in 2005 in order to investigate the interactions between hydrological, biological and geotechnical processes within a slope representative of typical UK infrastructure embankments, as part of the BIONICS project. The embankment is 90 m long, 6 m high, 29 m wide and has 1 in 2 slopes. The foundation on which the embankment was constructed was stiff to hard glacial till. The fill material used in the construction of the embankment itself was a locally sourced glacial till. The embankment was constructed in four 18 m long sections

to varying degrees of construction quality: the two central sections were ‘well compacted’ (to UK Highways Agency, now Highways England, specifications); the outer sections were ‘poorly compacted’ (built to represent poorly constructed heterogeneous rail embankments), and the outer most sections were biological test plots (Figures 4.34 and 4.35). Each section was separated by impermeable membrane in order to prevent hydraulic connectivity (Hughes *et al.* 2009; Glendinning *et al.* 2014). It was decided in 2014 that the south facing slope within the western biological plot would be induced to failure, as part of a trial to determine whether pre-failure pore-water pressure triggers could be detected using ERT and other techniques. The slope was steepened, artificial cracks were inserted (to increase vadose zone permeability) and sprinklers were turned on continuously in order to elevate pore-water pressures within the slope, and induce failure. The author installed an active waveguide in November 2014 in order to trial the AE approach in providing a warning of instability prior to, and during, first-time failure. The location of the active waveguide installation is shown in Figure 4.35. The author also installed an adjacent SAA to allow comparisons of AE measurements with continuous subsurface deformation measurements.

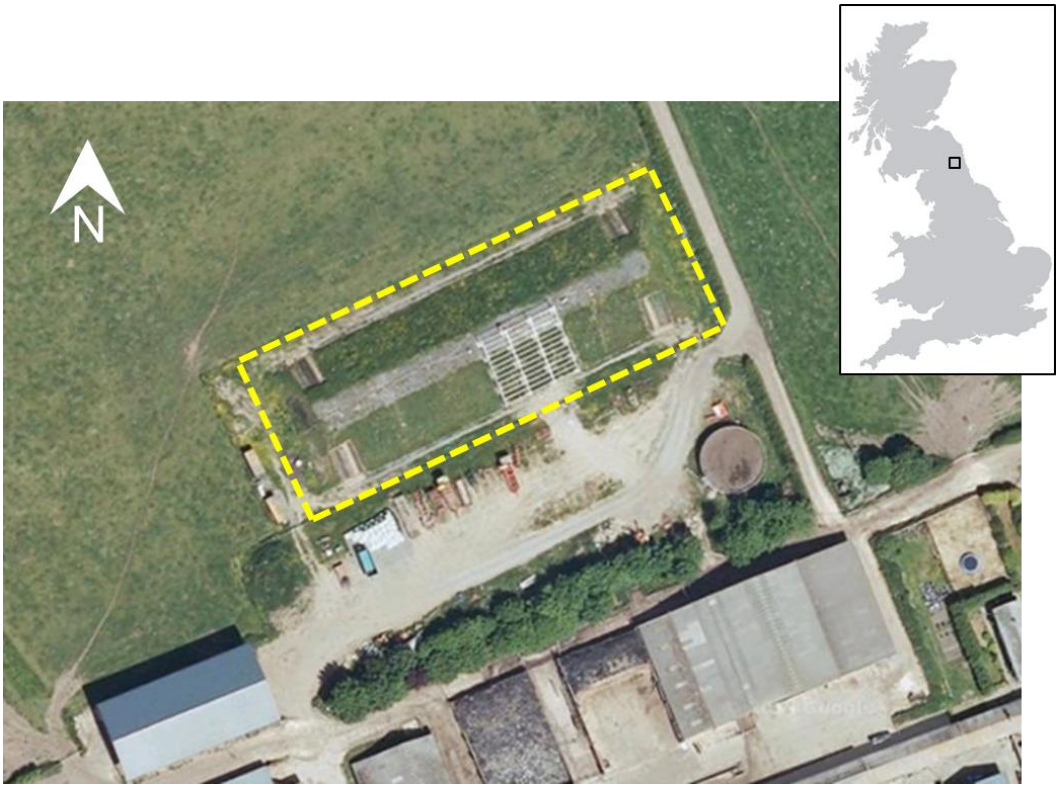

Figure 4.33. Location of full-scale embankment at Nafferton (© 2015 Google, map data)

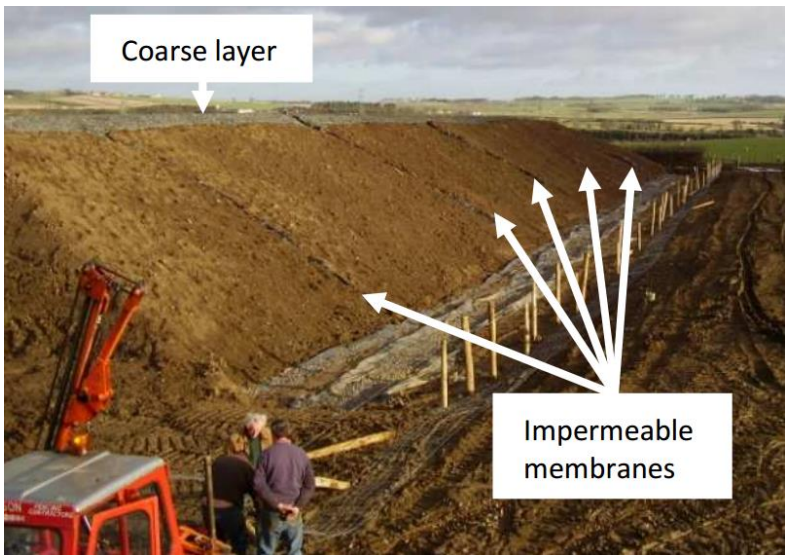

Figure 4.34. Photograph of full-scale embankment being constructed at Nafferton, showing sections separated by impermeable membranes (source: Hughes 2007)

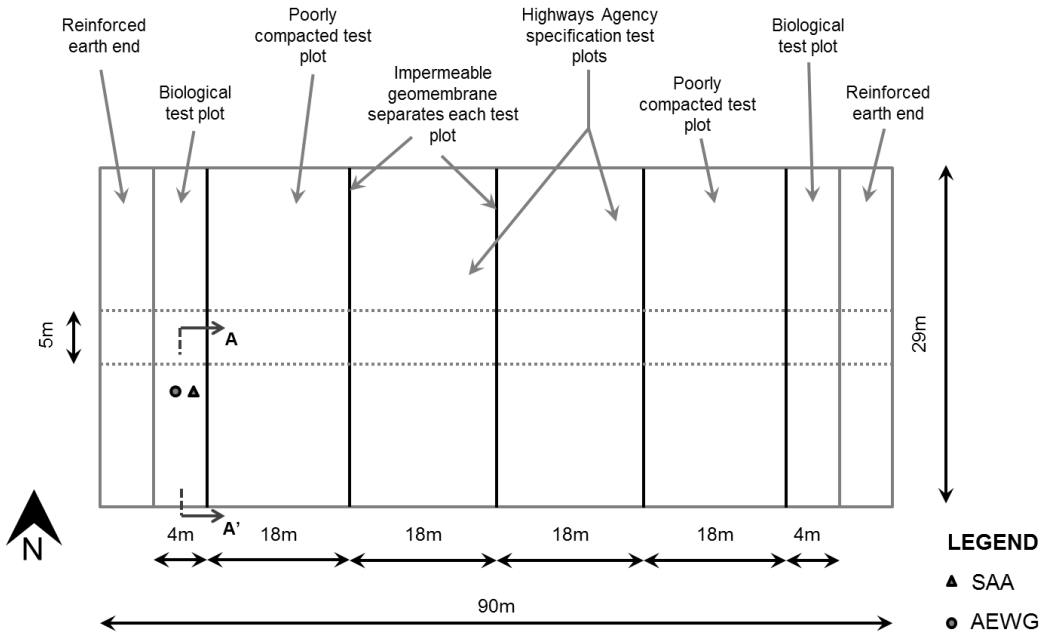

Figure 4.35. Diagram of full-scale embankment at Nafferton: instrumentation locations are highlighted on the slope being induced to failure (cross-section A-A' is shown in Figure 4.36) (redrawn after Hughes *et al.* 2009; Glendinning *et al.* 2014)

4.6.2. Instrumentation

An active waveguide was installed in a hand augered 60 mm diameter hole to a depth of 2.5 metres below ground level (Figure 4.36). The small diameter hand augered hole was selected in order to remove the need for a drilling rig. The estimated depth to any potential shear surface was shallow (i.e. 1 to 2 m) and any shear surface deformation was expected to intersect the 2.5 m deep active waveguide. A 2.2 m long 50 mm diameter PVC downpipe tube was installed inside the hole to contain the active waveguide and

minimise any interaction between the steel waveguide tube and the BGS ERT array. The annulus between the PVC tube and the wall of the augered hole was filled with medium-stiffness cement-bentonite grout (approximate water, cement and bentonite proportions by mass were 1, 0.15 and 0.06 respectively). The waveguide, 2.8 m long 21 mm diameter 2 mm wall thickness steel tube, was installed in the centre of the PVC tube. The annulus around the waveguide was backfilled with Leighton Buzzard sand (particle size between 0.6 mm and 2 mm) compacted in nominally 0.25 m high lifts (Figure 4.37): Leighton Buzzard sand was selected due to the small annulus between the waveguide and the PVC tube. The successful retrofit of an active waveguide within an inclinometer casing at Hollin Hill provided confidence in this small diameter active waveguide to generate AE in response to slope movement. The top 0.3 m of the hole was backfilled with cement bentonite grout to provide a seal against the ingress of surface water (Figure 4.38). The steel tube extends 0.3 metres above ground level to allow the transducer to be coupled, and is encased in a secure protective chamber (Figures 4.39 and 4.40). The Slope ALARMS sensor sits on a shelf within the surface cover and is wired to batteries on the crest of the slope, which provide power (Figures 4.41 and 4.42). A Slope ALARMS coordinator system was setup within the site porta cabin to provide remote access for data downloads and SMS messages (regular health messages and warning messages if RDC thresholds are exceeded) (Figures 4.43 and 4.44). Chapter 9 details how these RDC warning levels were selected using the framework developed in this thesis to relate AE measurements with rates of slope movement.

A second 60 mm diameter hole was hand augered adjacent to the active waveguide to a depth of 5 m. Within this hole a SAA with an active length of 5 m and with MEMS sensor spacing of 0.305 m was installed, within a PVC access casing, and backfilled with cement-bentonite grout (approximate water, cement and bentonite proportions by mass were 1, 0.15 and 0.06 respectively) (Figures 4.36, 4.37, 4.38 and 4.40). A surface cover was installed to protect the SAA protruding at the ground surface (Figures 4.40 and 4.42). The SAA was wired to a datalogger located at the crest of the slope, which was powered by a battery and recharged by a solar panel (Figure 4.41). The SAA is continuously logging at 1-hour intervals. SAA measurements are downloaded during site visits, the first of which took place on 5th February 2015 and the second is scheduled for summer 2015.

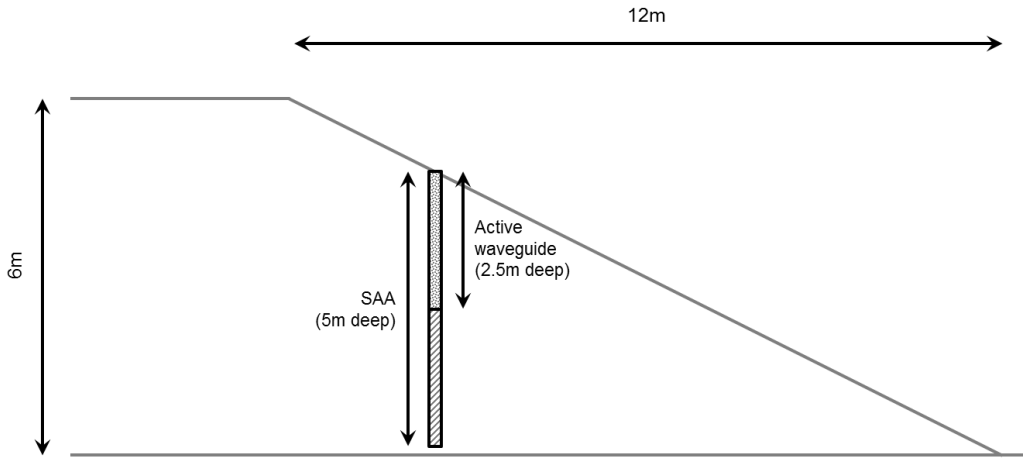

Figure 4.36. Cross-section A-A' (from Figure 4.35) of full-scale embankment at Nafferton: instrumentation installations are highlighted through the slope being induced to failure

Figure 4.37. Photograph of active waveguide (Leighton Buzzard sand backfill being compacted with tamping rod) and SAA installations at Nafferton

Figure 4.38. Photograph of active waveguide and SAA installations (both grouted) at Nafferton

Figure 4.39. Photograph of transducer coupled to protruding waveguide at Nafferton

Figure 4.40. Photograph showing SAA and Slope ALARMS protected by surface covers at Nafferton

Figure 4.41. Photograph of SAA data logger and solar panel, and Slope ALARMS batteries at the top of the slope at Nafferton

Figure 4.42. Photograph of Slope ALARMS and SAA surface covers on the slope at Nafferton

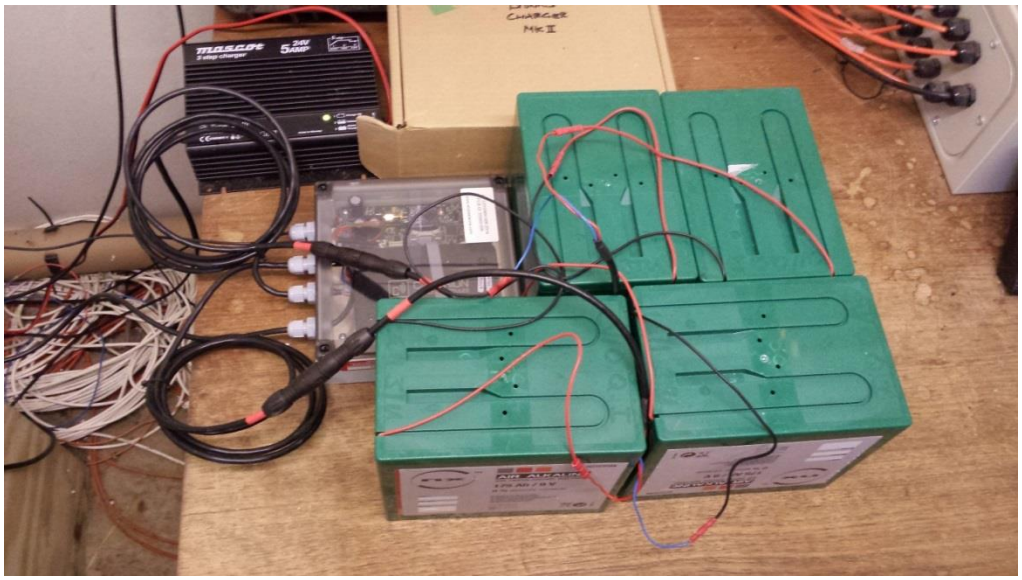

Figure 4.43. Photograph of Slope ALARMS coordinator system inside the porta cabin at Nafferton

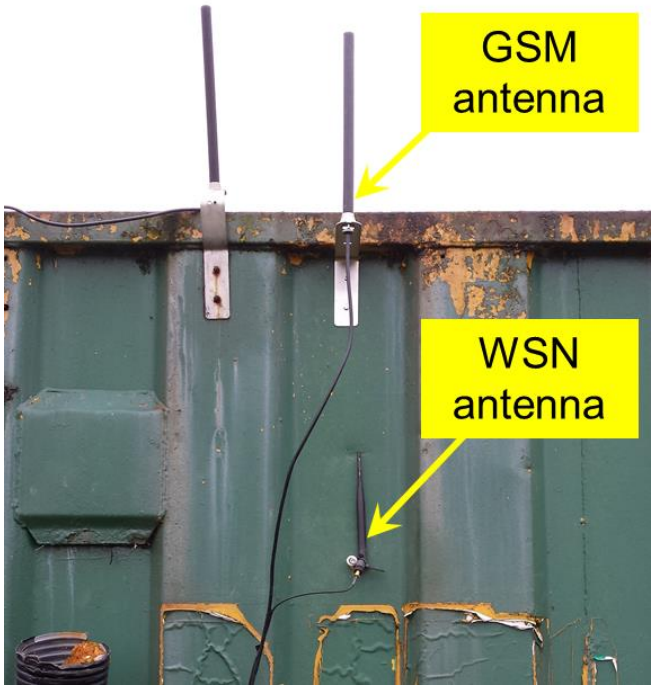

Figure 4.44. Photograph of Slope ALARMS coordinator GSM and WSN antenna on the wall of the porta cabin at Nafferton

4.6.3. Sample time series measurements

Negligible subsurface deformations have been recorded by the SAA during the period of monitoring thus far (Figure 4.45). There appears to be some submillimetre incremental movement; however, nothing indicative of the development of progressive failure in response to the artificial rainfall. Figure 4.46 shows deformation time series measurements taken from 2.3 m depth superimposed on the AE measurements. There appears to be progressive movement at this depth of the order of 0.6 mm over 60 days, with a corresponding average rate of 0.01 mm/day (0.0004 mm/hour) or 'extremely slow'. However, these time series of measurements also show 'rebounding' behaviour (i.e. periods of negative displacement), which can only usually be explained by shrink-swell behaviour. This 'extremely slow' rate of movement is expected to be at the detectable limit from the AE system; however, there appears to be some periods of correlation between the AE and deformation time series. The site at Nafferton will continue to be monitored while artificial rainfall takes place in order to capture the progressive accelerations of movement and the first-time failure.

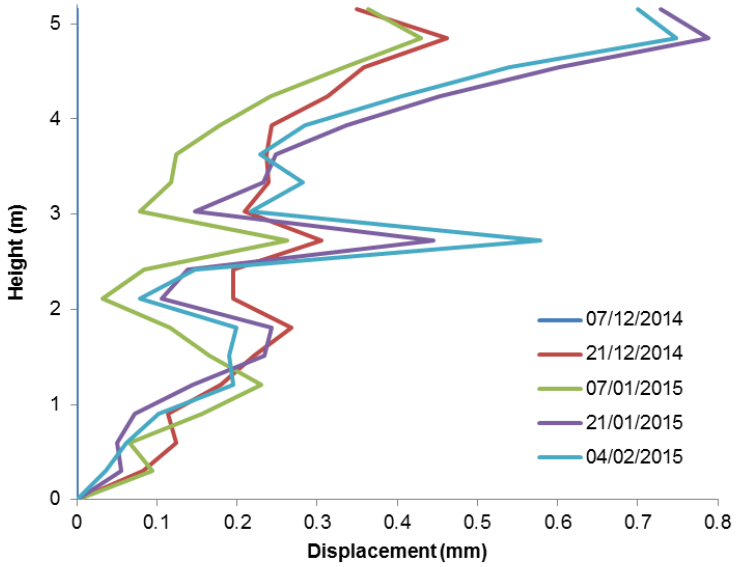

Figure 4.45. Selected height vs. resultant horizontal (down-slope direction) displacement surveys taken from the SAA at Nafferton

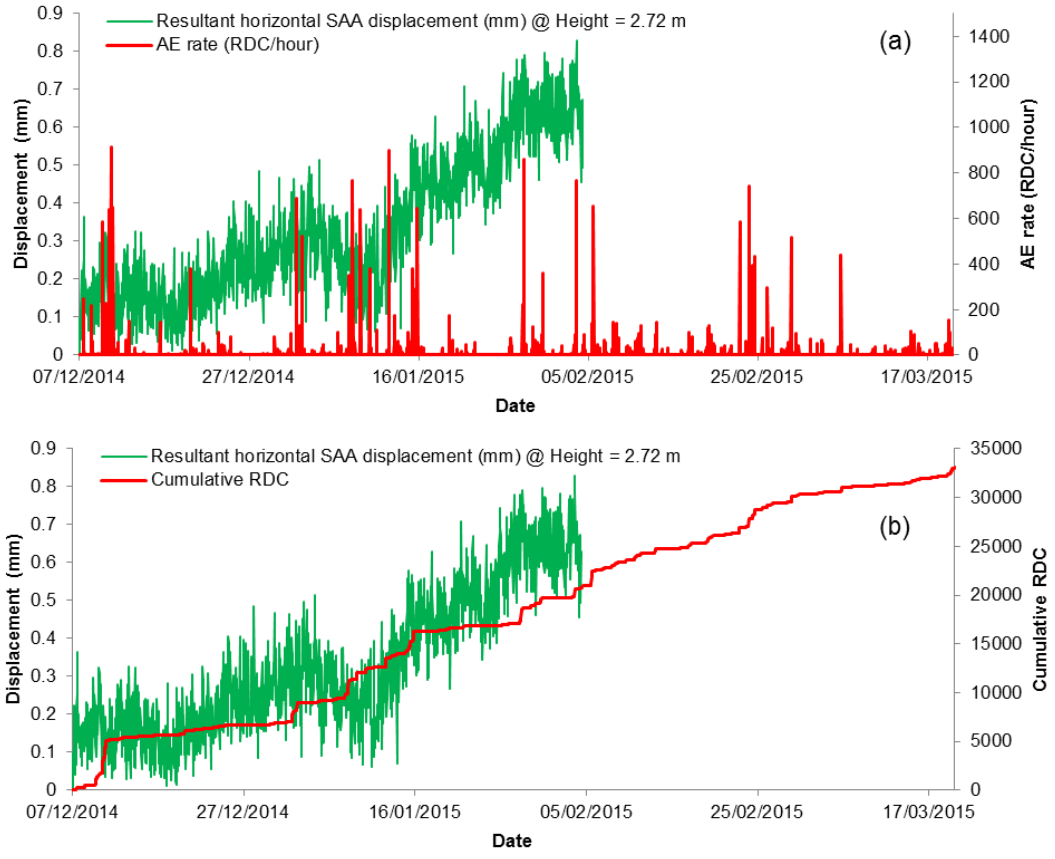

Figure 4.46. Resultant horizontal SAA displacement at 2.3 m depth and AE time series measurements at Nafferton: a) displacement and AE rate; and b) displacement and cumulative RDC

4.7. Summary

A series of field trials of the AE monitoring system have been conducted in order to examine the performance of the system in a range of environments, and to capture the behaviour of the system in a variety of slopes in response to slope movements (Objectives 1 and 2). The field trials have confirmed that AE monitoring using active waveguides is an approach capable of monitoring slope movements. The trial at Hollin Hill allowed the identification of the characteristic 'S' shaped cumulative RDC and log normal bell shaped AE rate vs. time curves generated by reactivated slope movements. These were initially measured and compared with conventional periodic inclinometer measurements, but later with continuous SAA deformation measurements. The trial at Hollin Hill also demonstrated that it is possible to retrofit existing inclinometer casings with active waveguides in order to convert the periodic manually read system into a continuous real-time system, and to also extend the operating life of inclinometer casings. The trial at Players Crescent demonstrated that the system is able to detect and measure 'very slow' rates of movement (e.g. 0.075 mm/day). This trial also demonstrated the performance of the monitoring approach to provide warning SMS messages of slope movements. The trial at Flat Cliffs demonstrated that the AE monitoring system is capable of detecting deep seated slope movements. These trials have provided extensive evidence that AE rates generated by the system are proportional to the rate of slope movement (i.e. velocity); demonstrating that it is possible to establish a relationship between measured AE and deformation behaviour (Objective 3). The trials at Scarborough and Nafferton are ongoing and are likely to be valuable in obtaining the AE response from first-time failure. The trial at Scarborough has revealed that ground water seepage interacting with the active waveguide gravel column generates contaminating AE, which would ideally be isolated or filtered out in order to leave only active waveguide-generated AE in response to subsurface deformation.

CHAPTER 5

Measured AE and deformation behaviour: analysis of field monitoring results

5.1. Introduction

Within this Chapter results from field monitoring case histories are presented and analysed in order to establish a relationship between measured AE and deformation behaviour. The hypothesis detailed in Chapters 1 and 2 is that AE rates are proportional to deformation rates; the analyses conducted in this Chapter have been used to test this hypothesis. Attempts have been made to establish empirical relationships between AE rates and deformation rates from the field monitoring data, using comparisons with both conventional periodic inclinometer measurements and continuous SAA deformation measurements. The Chapter primarily utilises data collected from the trial at Hollin Hill. This trial has the most extensive data set, has experienced numerous episodes of movement, and high quality deformation information is available for comparison. AE measurements are firstly compared with conventional periodic inclinometer deformation measurements. A comparison is subsequently conducted with continuous subsurface SAA deformation measurements, which were available later in this study.

5.2. Comparisons with conventional inclinometer deformation measurements

5.2.1. Introduction

A series of events occurred at all three instrumentation clusters at the Hollin Hill site in 2010 and 2012, as described in Section 4.2, for which inclinometer measurements have confirmed the occurrence of subsurface deformation. Attempts have been made to establish relationships between the measured AE and shear surface displacements measured by the adjacent inclinometer for the periods in which these AE events occurred. Figure 5.1 shows an example of one such event.

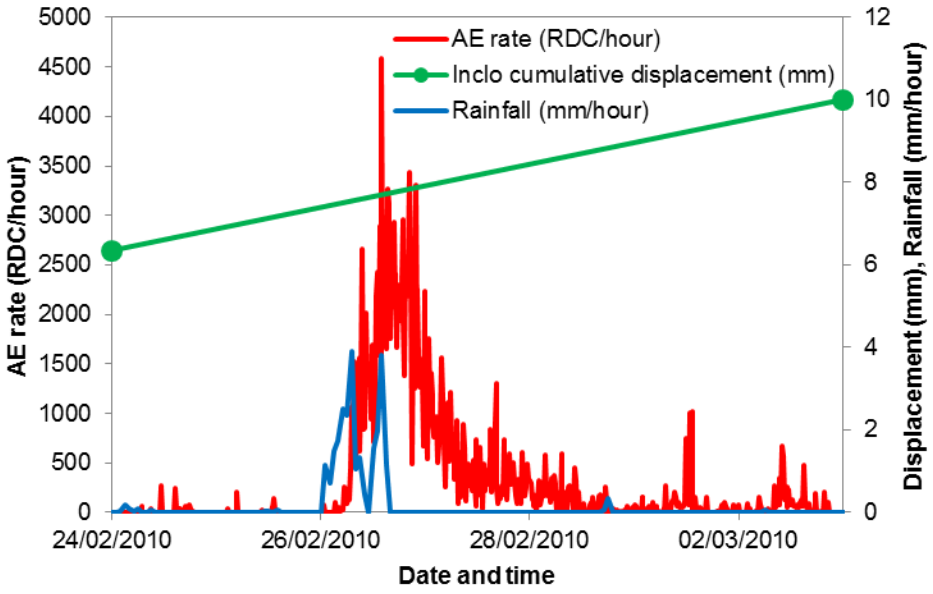

Figure 5.1. AE rate, hourly rainfall and inclinometer measured shear surface displacement for an event at Cluster 2 at Hollin Hill

5.2.2. Total AE and deformation magnitude comparison

As continuous slope deformation data was not available at this time, determination of slope velocity profiles for direct comparison with AE rate profiles was not possible. Therefore, to validate the assumption that AE rates are proportional to slope velocity, relationships between AE event energy and the magnitude of slope movement were investigated. The AE event energy was determined from the area under the AE rate bell shaped curves using trapezoidal integration (Equation 5.1) as the curves are formed of a series of data points, which allows accurate interrogation using trapezoids.

$$Area = \int_a^b f(x)dx \approx \sum(b-a)\frac{f(a)+f(b)}{2} \quad \textbf{(5.1)}$$

The total RDC produced during an event was used as a measure of the deformation event AE energy. These energy values were compared to the magnitude of inclinometer measured shear surface deformation over the same period. Deformation data was taken from 1 m depth on the western lobe (Clusters 1 and 2). The inclinometer data from the eastern lobe (Cluster 3) indicated two shear surfaces at 1.5 m and 4 m depths and therefore the magnitude of deformation used in the analysis of each event was the sum of both shear surface displacements. If AE rates and slope velocities are proportional; the relationship between the AE energy (i.e. total RDC) and the total slope displacement for each event should also be proportional. Differences between system characteristics (e.g. depth to shear surface and sensor voltage threshold level) mean that events produced by each measurement system are not likely to be the same, although trends of behaviour will be comparable. The events analysed and presented were taken from monitoring periods

during which the sensor sensitivity (i.e. voltage threshold level) was constant. Figure 5.2 shows the energy-displacement relationship, plotted log-log, for four events that occurred at Cluster 2 during 2010. Deformation events of greater magnitude produced proportionally greater AE energy.

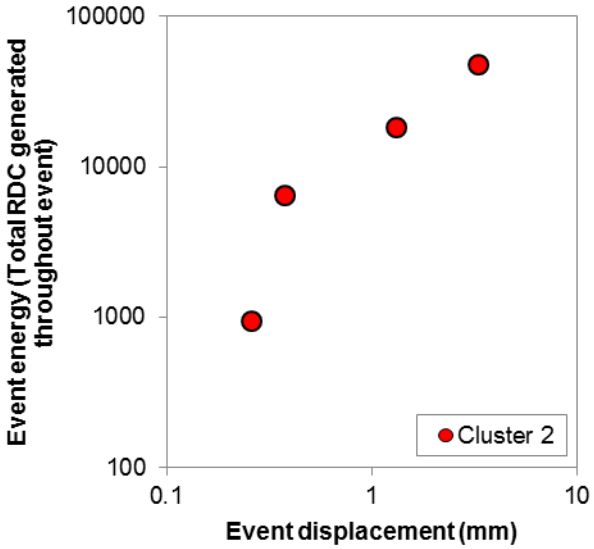

Figure 5.2. Relationship between deformation event AE energy (total RDC generated throughout event) and event displacement magnitude for events that occurred in 2010 at Cluster 2 plotted on log-log scales

The effect of sensor sensitivity changes (i.e. through changes to the voltage threshold level) was investigated during the period of monitoring, the results of which demonstrated that changes in sensitivity can yield order of magnitude changes in output AE rates from the same sensor/waveguide system. Some slope deformation events occurred during such periods of altered sensitivity and therefore the AE data from these were not representative of the energy produced from other events, and are not used in this analysis. The varying sensitivities between the systems on different clusters mean that the results are not directly comparable; however, a general positive relationship is demonstrated in Figure 5.3. The results plotted on logarithmic scales demonstrate that an order of magnitude increase in event deformation yields an order of magnitude increase in the AE event energy produced. It should be noted that the magnitude of events are relatively small due to the slope being a reactivation on an already defined shear surface. This means that the slope velocities experienced are also relatively small. The ability of AE monitoring to detect such small magnitude displacements and displacement rates provides confidence in the technique for use as an early warning system.

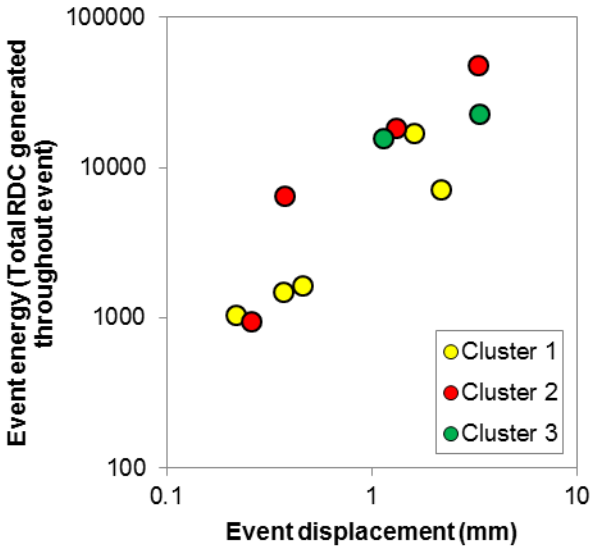

Figure 5.3. Relationship between deformation event AE energy (total RDC generated throughout event) and event displacement magnitude for events that occurred in 2010 at Clusters 1, 2 and 3 plotted on log-log scales

5.2.3. Back calculation of velocity-time event profiles

Demonstration that energy and displacement are proportional to one another supports the hypothesis that AE rates are proportional to slope velocities. AE rates (RDC/hour) are the derivative of energy (RDC) with respect to time (hours), and velocity is the derivative of displacement with respect to time. Therefore, using the shape of the AE rate-time profile it is possible to determine a velocity-time profile for a slope movement event by equating the area under the AE rate-time curve to the magnitude of shear surface displacement measured by an adjacent inclinometer. The total event displacement was then distributed proportionately to each trapezoidal integrand (Equation 5.2 and Figure 5.4).

$$Proportion\ of\ event\ displacement\ in\ trapezoid\ (mm) = Total\ event\ displacement (mm) \times Proportion\ of\ event\ energy\ in\ trapeziod\ (RDC) / Total\ event\ energy\ (RDC) \quad \textbf{(5.2)}$$

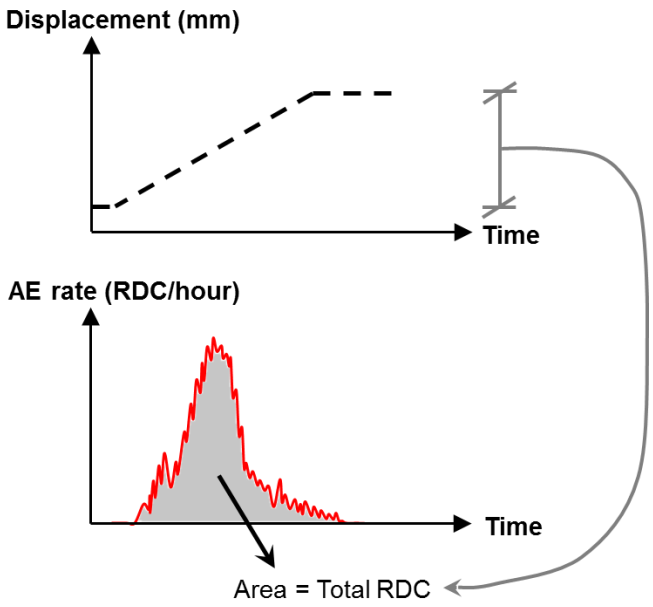

Figure 5.4. Total shear surface deformation and total AE generated throughout a deformation event

This allowed the velocity over each trapezoid under the curve to be determined from the displacement/time relation (Figure 5.5, Equation 5.2 and Equation 5.3).

$$Area\ of\ trapezoid = Displacement\ (mm)$$

$$\therefore\ Velocity\ (mm/hour)\ =\ \frac{Displacement\ (mm)}{T_2 - T_1\ (hour)} \qquad \textbf{(5.3)}$$

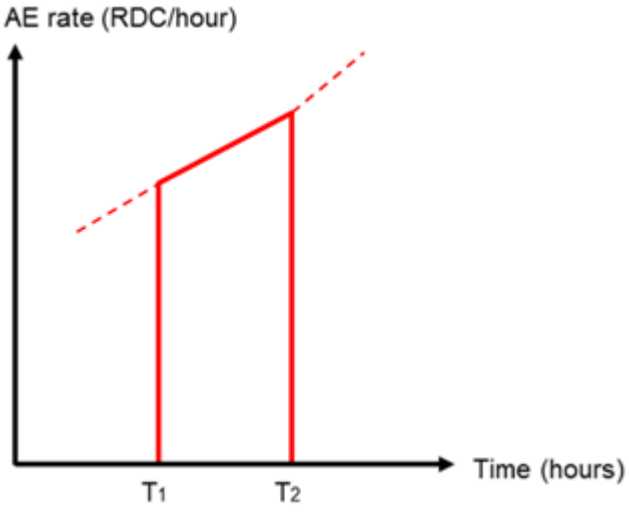

Figure 5.5. Trapezoidal interrogation of AE rate data to obtain incremental event velocity from the displacement/time relationship

This enables a velocity-time curve, proportional to the AE rate-time curve, to be produced for each displacement event by using the magnitude of displacement at the shear surface measured by the inclinometer for the period in which the event occurred. The sporadic nature of the AE rate data is due to slip-stick deformations taking place between the

gravel particles within the backfill as interlock is overcome and regained. Indeed it would be assumed that the velocity-time profile of the slope movement would be a smoother curve of moving averaged values. Interrogation of the velocity profile for Event A in Figure 5.6 yields an event duration of roughly 60 hours, with a peak velocity of 0.16 mm/hour and an average velocity of 0.05 mm/hour. This event would be classified as 'very slow' according to Cruden & Varnes (1996) (Section 2.2.2.2). Of particular interest is the apparent sensitivity of the AE technique to changes in low magnitude slope velocities. As the strength along the slip surface is already at, or close to, the residual value the low magnitude velocities illustrated in Figure 5.6 were expected and are characteristic of a reactivation on an already defined shear surface. For example, Schulz *et al.* (2009) described how the Slumgullion Landslide displayed daily movement patterns where increased velocity seemingly coincided with the diurnal low tides of the atmosphere as changes in air pressure altered the frictional resistance along the shear surface leading to daily velocity cycles that have a peak of roughly 2-3 mm/hour, and Matsuura *et al.* (2008) reported the monitoring of a reactivated landslide under constant creep in Japan that experienced an average hourly displacement of 0.7 mm (Section 2.2.2.3). The ability of the technique to detect small changes of slope velocity demonstrates promise as an early warning system.

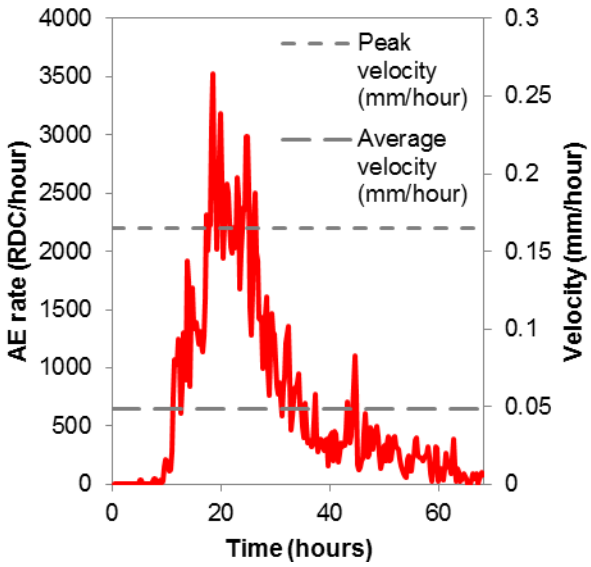

Figure 5.6. AE rate and derived velocity time series for the event shown in Figure 5.1 at Cluster 2

Each point in time throughout the event shown in Figure 5.6 has both a corresponding AE rate and a velocity. Hence a calibration AE rate-velocity relationship (Figure 5.7) can be produced for that specific monitoring system, and this can be used to derive slope movement velocities from the measured AE rates that occur in response to subsequent deformation events. There is the potential to do calculations in real-time if the calibration

relationship is included in an algorithm within the sensor architecture. A generic calibration technique that quantifies the influence of all variables that yield changes in AE rate outputs is developed later in this thesis and is detailed in Chapter 9.

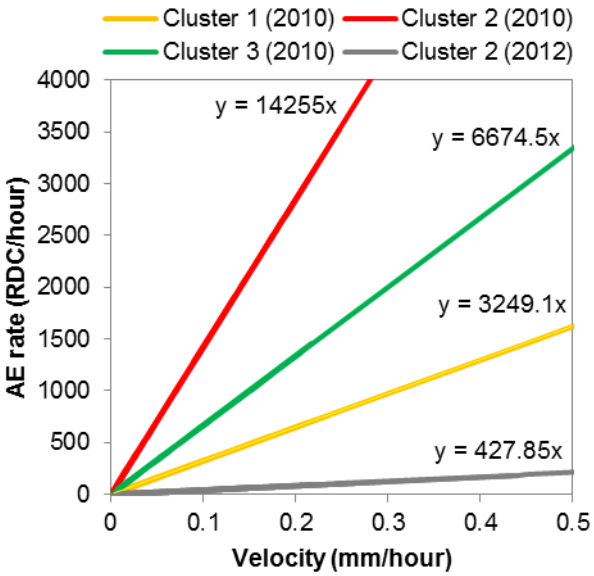

Figure 5.7. AE rate-velocity calibration relationships for events on different systems over the course of monitoring at the Hollin Hill site

Of interest is the coefficient of proportionality, or gradient, 'm' in Figure 5.7. This is dependent on the characteristics of the measurement system used, which dictates the magnitude of AE rates produced in response to an applied velocity (i.e. the systems sensitivity). The coefficient of proportionality is influenced by many different variables as discussed in Section 3.4.3 (i.e. voltage threshold on sensor, depth to the shear surface and attenuation characteristics of the active waveguide etc). In the study at Hollin Hill the coefficient was different for each monitoring system that was used. This is because different voltage threshold levels were set on the sensors during this period, to investigate the influence of the voltage threshold level on the AE response (Section 8.3 demonstrates that changing the voltage threshold level can modify the AE response by more than a factor of 5). The depth to the shear surface(s) and geometry of each active waveguide (after being deformed by numerous reactivated movements) also differed, influencing their response. The calibration relationships for the three clusters and their sensor settings are shown in Figure 5.7. It can be seen that Cluster 2 (2010) has the greatest 'sensitivity', as a greater magnitude of AE rates were produced in response to a given applied slope velocity. Cluster 2 (2012) had the lowest 'sensitivity' by contrast.

The respective relationships shown in Figure 5.7 were used to obtain slope movement velocities from subsequent events that occurred while the systems operated with the same settings and configuration. As continuous deformation data was not available, only

average velocities could be compared. The average AE rate over each deformation event was converted to an average velocity using the calibrations in Figure 5.7 (i.e. 'calculated'). The 'actual' average velocity was determined from inclinometer data and event duration using the displacement/time relationship. The 'calculated' and 'actual' values were compared (tabulated results in Appendix A2) to provide validation and an indication of accuracy of velocity interpretations through the use of the AE rate-velocity calibration approach. Eight events were selected for this part of the analysis, and are numbered in Figure 5.8 in no particular order (event examples are shown in Appendix A2). The results are shown in Figure 5.8 on a logarithmic scale, which demonstrates that the procedure produced errors of less than an order of magnitude (i.e. the difference between 'actual' and 'calculated' velocity). Standard assessment for landslide classification uses order of magnitude accuracy and hence the results presented in Figure 5.8 demonstrate the potential of an AE system to provide this level of information. An example of how the calibration equation was used for interpretation of displacement rates from AE rates is shown in Equation 5.4.

$y = mx, where;$

$y = AE\ rate\ \left(\frac{RDC}{hour}\right), x = Velocity(\frac{mm}{hour}), and\ m =$
$Coefficient\ of\ proportionality$

$$\therefore Velocity = \frac{AE\ rate}{Coefficient\ of\ proportionality} \quad \textbf{(5.4)}$$

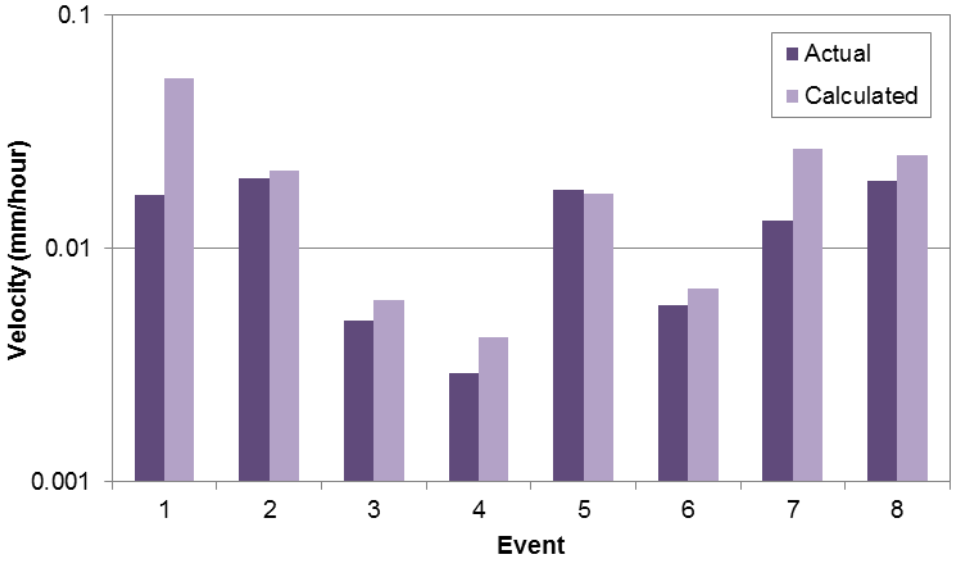

Figure 5.8. Comparison of measured slope deformation event velocities and those calculated from the AE rates

Possible explanations for the error margins produced from the analysis include: underestimation of event duration (when calculated<actual); overestimation of event duration (when calculated>actual); and the occurrence of significant background noise (when calculated>>actual) due to environmental factors (i.e. temperature extremes) or electromagnetic noise. The bell shaped AE rate-time curve for Event No 1 appeared to be superimposed with sporadic background noise; this made it difficult to determine the start and end of the deformation event. Background noise combined with the possible over estimation of event duration could contribute to the 'calculated' average velocity being greater than the 'actual'.

5.2.4. Deformation pattern interpretation from AE

Figure 5.9 illustrates how the AE data can be used to produce continuous cumulative deformation data for Event A on the western landslide lobe based on the calibration at Cluster 2 (2010). The velocity-time profile produced from the AE data was used to determine the cumulative displacement throughout the deformation event. This approach provides temporal resolution for the inclinometer data and demonstrates the potential of continuous AE monitoring using technology such as Slope ALARMS sensors to deliver continuous, real-time deformation rate information, as an alternative to traditional in-place inclinometers or SAA. Figure 5.10 shows the AE rates measured at each of the three clusters in response to a period of rainfall, which have been converted to cumulative displacement using the appropriate calibrations. The results show that all three locations became unstable and experienced similar cumulative displacement magnitudes and rates.

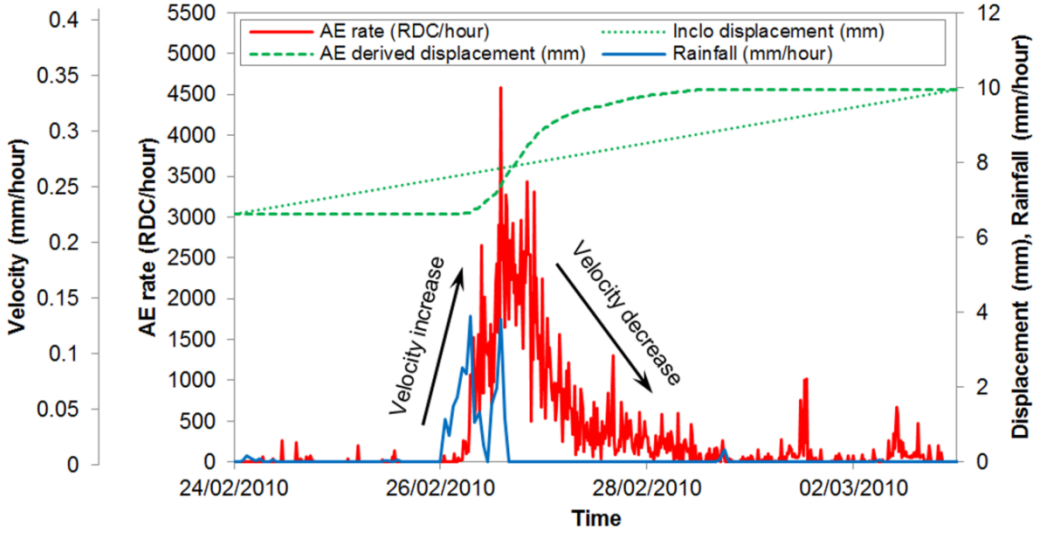

Figure 5.9. AE rate-, AE derived velocity-, inclinometer measured displacement-, AE derived displacement- and rainfall-time series for a reactivated slope deformation event at Hollin Hill (Cluster 2)

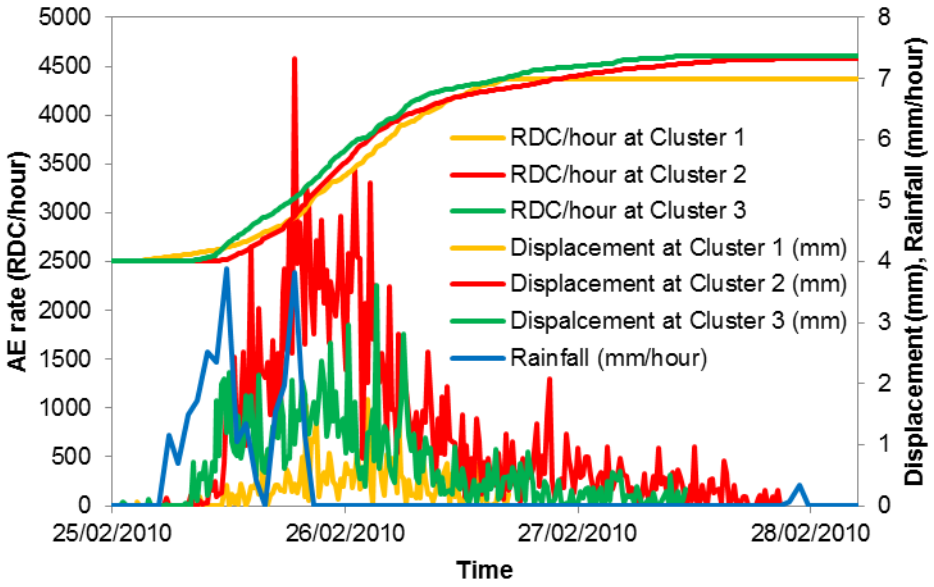

Figure 5.10. AE responses of all three clusters to a rainfall event and the derived slope cumulative displacements at each location

5.2.5. Application of back calculation method to Flat Cliffs

Figure 5.11 shows results from application of the back calculation method to the episode of movement that occurred at Flat Cliffs during the period January to March 2014 (Section 4.4.3.2). The shape of the AE rate-time curves were used to determine the velocity-time profiles for slope movement events by equating the area under the AE rate-time curve to the magnitude of shear surface displacement measured by the inclinometer for the period in which the events occurred. The area under the AE rate-time curve was determined using trapezoidal integration and the total event displacement was distributed proportionately to each trapezoidal integrand under the curve. This allowed determination of the velocity over each trapezoid under the curve from the displacement/time relation. These velocity-time profiles were then used to determine the cumulative displacement profile throughout the inclinometer measurement interval to identify the timings and magnitudes of subsurface deformations with high temporal resolution; the interpreted onset of movement and periodic surges in movement are annotated on Figure 5.11.

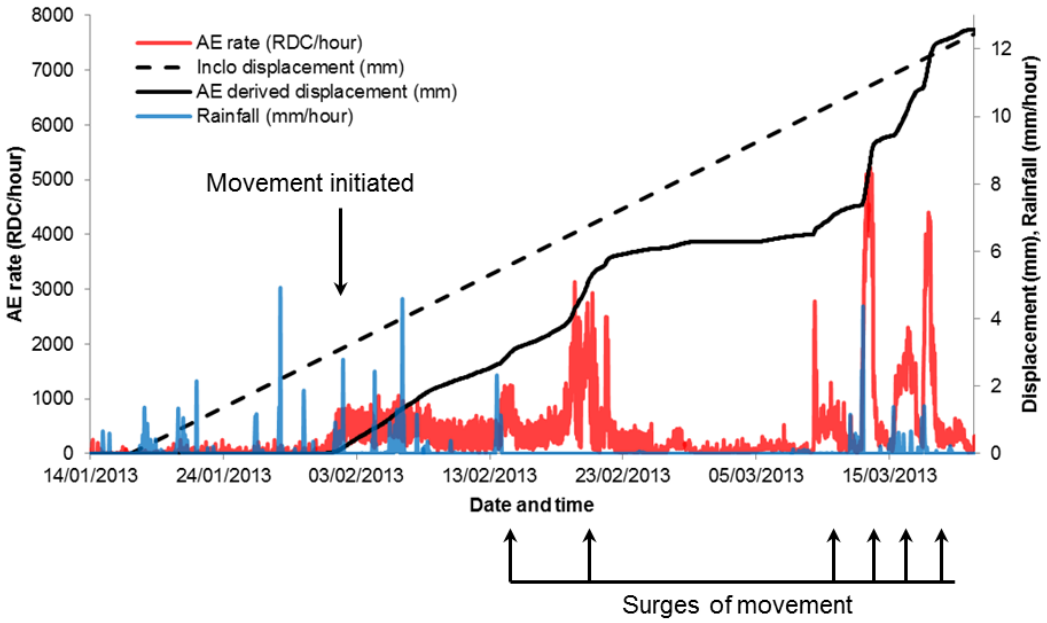

Figure 5.11. AE rate-, inclinometer measured displacement-, AE derived displacement- and rainfall-time series for a period of slope movement at Flat Cliffs

5.3. Comparisons with continuous SAA deformation measurements

5.3.1. Introduction

This Section presents a more detailed analysis of the continuous AE and continuous deformation time series measurements from Hollin Hill that were introduced in Section 4.2.3.2.2, in order to establish an empirical relationship between measured AE rates and slope displacement rates. A series of reactivated slope movements occurred at Hollin Hill in response to periods of rainfall that produced transient elevations in pore-water pressure along the shallow shear surface in January 2014. This series of movement events was measured by both AEWG and SAA systems on both lobes (western and eastern). Results from the eastern lobe (Cluster 3) are analysed in this Section because greater magnitudes of movement occurred on the eastern lobe.

5.3.2. AE and deformation comparison

Figure 5.12 shows the resultant horizontal displacement- and velocity-time series measured from 0.3 m depth in SAA3 (day 0 begins on the 9th of January 2014). Each of the slide events has been allocated an identification number (ID A to F); note that these events are different to those described in Sections 4.2.3.2.1 and 5.2, which occurred in 2010 and 2012. Figure 5.13 highlights the triggering rainfall preceding the slide events. The duration of the movement events varies between 3 and 6 days, with a peak velocity reaching approximately 0.35 mm per hour in Event F. The total displacement (resultant

horizontal) measured over the period of 22 days at 0.3 m depth in SAA3 was approximately 22 mm. The displacement vs. depth profile recorded by SAA3 can be seen in Figure 5.14 with readings presented at the cessation of each event. It is clear that the main shear surface is at a depth between 1.5 m and 2 m at the location of SAA3 and AEWG3, which agrees with inclinometer measurements for the same lobe shown in Section 4.2.3.1. In Figure 5.12 the SAA measured velocity-time data has been superimposed with a smoother curve of 10 hour moving average values; the 10 hour moving average values were determined through calculation of the average of the velocity over the 5 hours preceding and 5 hours succeeding each measurement. 10 hour moving averages were used for smoothing in order to reduce variability in the raw SAA data (60 minute measurement intervals). The variability in the SAA measurements was of a similar magnitude as the slope movement velocities (i.e. < 0.5 mm/hour); such variability would be less significant at greater velocities and therefore the need for smoothing would be reduced. Note that SAA3 did not intersect the deeper shear surface at this lobe, which was identified in inclinometer data detailed in Section 4.2.3.1. Therefore, deformations at this deeper shear surface are unknown and have been ignored in this analysis.

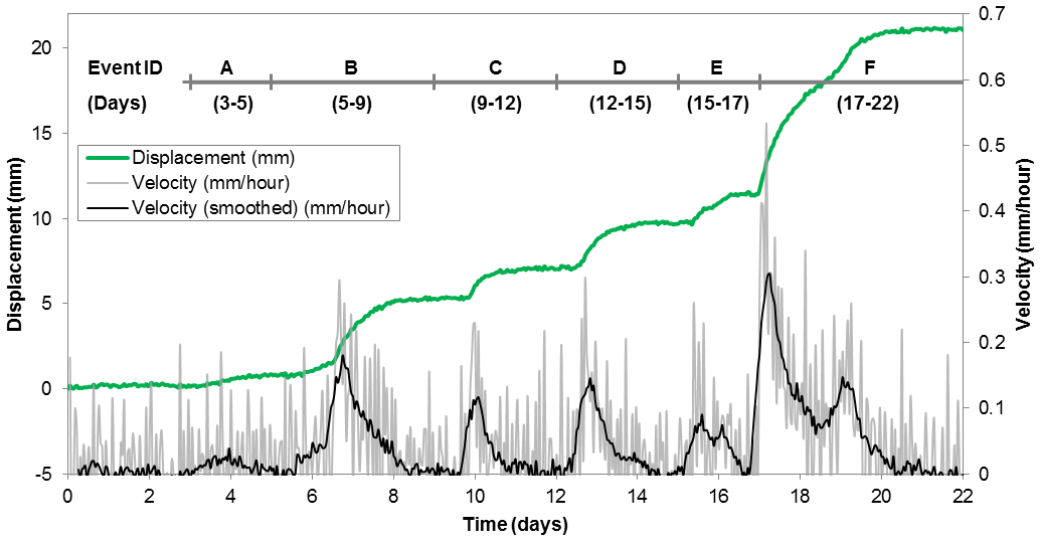

Figure 5.12. Resultant horizontal displacement-, velocity- and smoothed velocity-time measured by SAA3 for a series of reactivated slide events at Cluster 3 at Hollin Hill

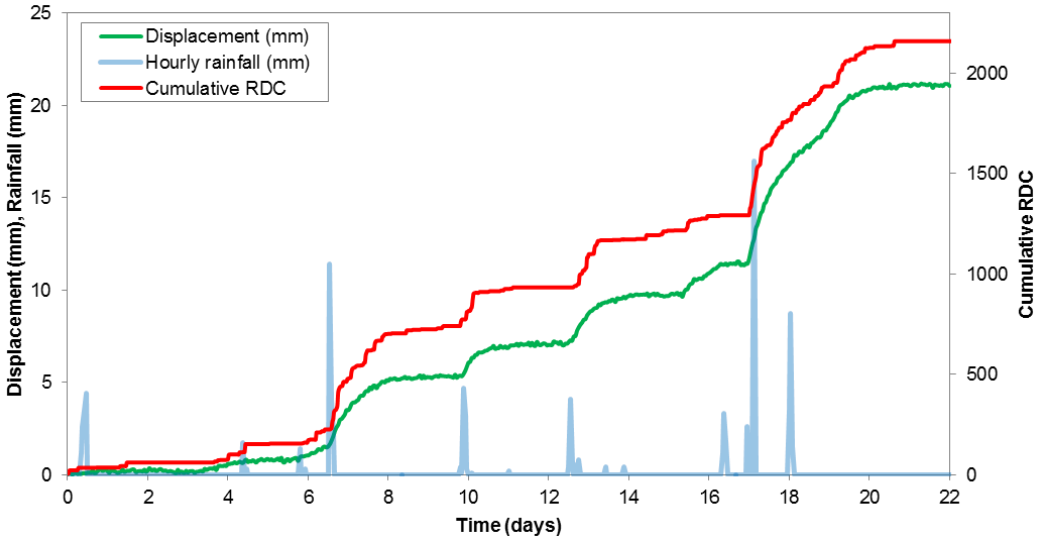

Figure 5.13. Resultant horizontal SAA3 measured displacement-, cumulative RDC and hourly rainfall-time for the series of slide events at Cluster 3 at Hollin Hill

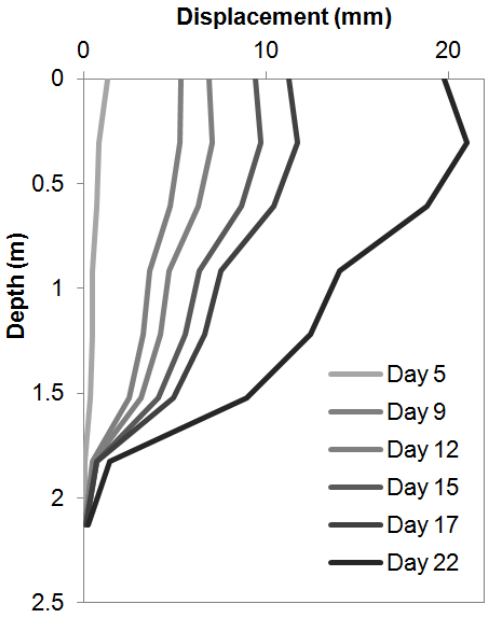

Figure 5.14. Change in shape of SAA3 depth profile at the end of each slope displacement event at Cluster 3 at Hollin Hill

Figure 5.13 shows the cumulative RDC-time relationship recorded by the sensor coupled to AEWG3; the relationship is analogous to the cumulative displacement-time trend recorded by SAA3. Figure 5.15 shows the AE rate-time series superimposed also using a smoothed curve of 10 hour moving average values (the sporadic nature of the raw data is due to slip-stick deformations taking place within the gravel backfill), which is analogous to the velocity-time profiles that are shown in Figure 5.12. These comparisons confirm that: AE rates generated by the system are directly proportional to the rate of deformation (i.e. slope velocity); AE monitoring of active waveguides using a sensor such as Slope ALARMS can provide continuous information on slope displacements and displacement

rates; and the AE monitoring technique is sensitive to small displacements, displacement rates (i.e. < 0.5 mm/hour) and changes in displacement rates (i.e. accelerations and decelerations).

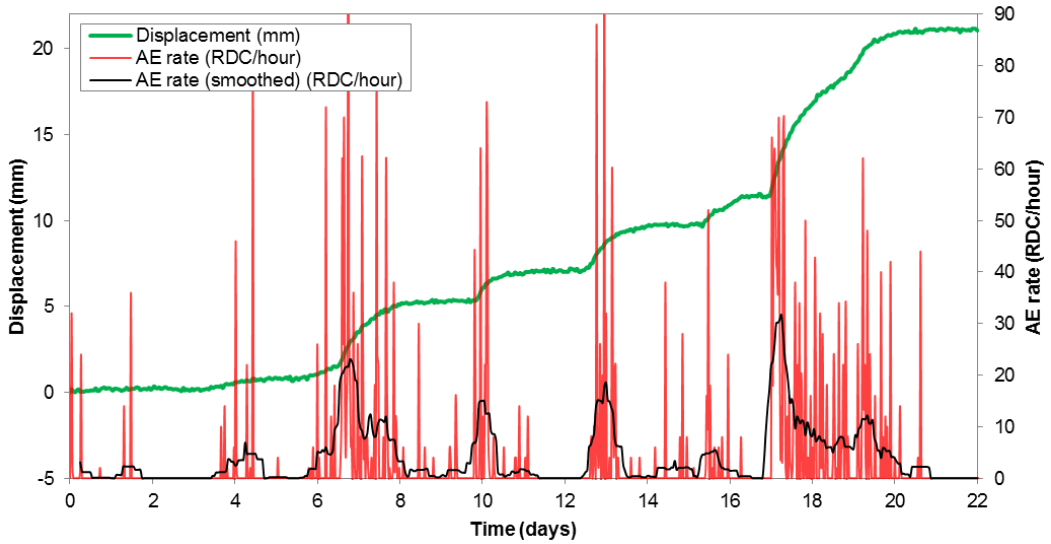

Figure 5.15. Resultant measured displacement-, AE rate- and smoothed AE rate-time for the series of slide events at Cluster 3

5.3.3. Measured AE rate-velocity relationship

To define a measured relationship between AE rates and slope velocity from the continuous time series measurements, the 10 hour moving average values of AE rates and measured slope velocity (i.e. Figures 5.12 and 5.15) were plotted in Figure 5.16. This plot shows for the first time an AE rate-velocity relationship derived from continuous time series measurements. A back calculated relationship was subsequently determined using the method described in Section 5.2; this back calculated linear relationship passes directly through the measured data points (as can be seen in Figure 5.16). A linear regression line was calculated through all of the measured data points and, assuming it passed through the origin, it aligned almost exactly with the back calculated relationship shown; the equation for the trend line is given in Figure 5.16, which produced an R^2 value of 0.8. From the calibration in Figure 5.16 it is now possible to derive slope displacement rates from measured AE rates generated from the system in response to subsequent slide events. Use of the back calculation method to derive AE rate-velocity calibration relationships has therefore been shown to be an appropriate technique for quantifying low velocity (i.e. of the order of mm's per hour or less) slope movements.

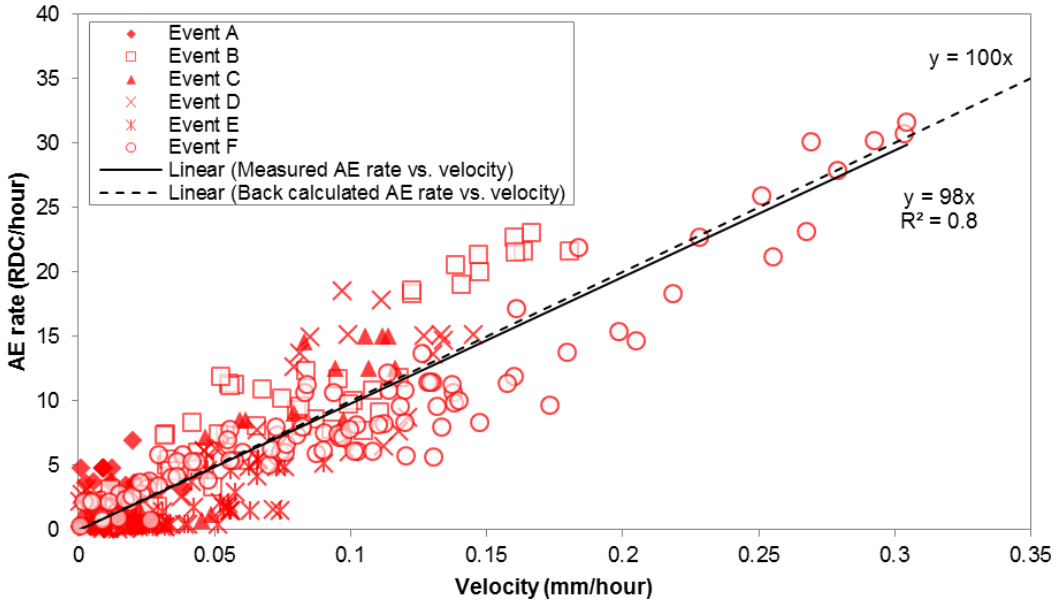

Figure 5.16. Measured (10 hour moving average values taken from AEWG3 and SAA3 during slide events) and back calculated AE rate-velocity relationships

These field measurements have allowed the first comparison of continuous time series AE and slope displacement measurements to be made with relatively high temporal resolution. The study has established that the AE monitoring approach can be used to provide continuous information on slope displacements and displacement rates.

5.4. Summary

Extensive comparisons between measured AE and deformations from real slope movements have been presented and analysed, using results from field trials; principally from Hollin Hill. Evidence has been obtained demonstrating that: AE rates generated by the system are directly proportional to the rate of deformation (i.e. slope velocity); AE monitoring of active waveguides using a sensor such as Slope ALARMS can provide continuous information on slope displacements and displacement rates; and the AE monitoring technique is sensitive to small displacements, displacement rates (i.e. < 0.5 mm/hour) and changes in displacement rates (i.e. accelerations and decelerations). This has been confirmed using comparisons with both conventional periodic inclinometer measurements and continuous SAA deformation measurements, and contributes to meeting Objectives 1 and 3.

The velocity profiles determined using inclinometer data (i.e. using the back calculation method) generated velocity magnitudes comparable to those later evidenced by the SAA measurements (i.e. < 0.5 mm/hour). Additionally, the back calculation method was used to determine a ‘calculated’ AE rate-velocity relationship, which was the same as the

‘measured’ AE rate-SAA measured velocity relationship for a period of slope movements. This demonstrates that the back calculation method is an appropriate technique for quantifying low velocity (i.e. of the order of mm’s per hour or less) slope movements.

The AE rate-velocity calibration relationships differ at each cluster location and they have changed over time, as evidenced by changes from 2010 to 2012 at Cluster 2 and 2010 to 2014 at Cluster 3. This is due to variables that influence the coefficient of proportionality changing (e.g. sensor and transducer combination and voltage threshold level). An investigation into the influence of these variables is discussed in Chapter 8. In addition, change in shape of the active waveguide in response to increased magnitudes of deformation from lateral loading generates complex behaviour and pressure distributions within the active waveguide, and this, combined with the altered geometry, is anticipated to alter the coefficient of proportionality.

The active waveguide-generated AE rate-slope displacement rate relationship was assumed to be linear when the comparisons with periodic inclinometer measurements were performed. The measured AE rate-SAA velocity relationship determined later also appeared to be linear, confirming that this assumption was valid. The linear nature of the AE rate-velocity relationship has been evidenced here from an examination of ‘very slow’ rates of movement (i.e. < 0.5 mm/hour); examinations over greater ranges of displacement rates and magnitudes using physical models are described in Chapters 6 and 7.

CHAPTER 6

Measured AE and deformation behaviour: active waveguide physical model tests

6.1. Introduction

Within this Chapter an experimental programme conducted using active waveguide physical model tests is detailed. The purpose of this series of experiments was to subject active waveguide models to simulated landslide behaviour, and to define an empirical relationship between AE rates and deformation rates for the active waveguide model. In addition, a simulated failure experiment was performed in order to assess the ability of using the empirical calibration AE rate-velocity relationship to quantify deformation rates from measured AE rates. The experimental design and procedure are described, and the commissioning of dynamic strain-controlled shear apparatus that was developed to perform this series of experiments is detailed. A series of tests were also performed using the constant strain rate compression apparatus (developed in Dixon & Spriggs (2007)) to validate the results obtained from the dynamic strain-controlled shear apparatus. A comparison of different active waveguide backfill materials is also presented.

6.2. Experimental design and procedure

6.2.1. Introduction

Two series of experiments were conducted using two types of loading apparatus in order to determine a calibration AE rate-velocity relationship for the active waveguide model. Subsequently, a slope failure simulation was performed to establish the validity of using the relationship to quantify slope velocities from measured AE. First, dynamic (low frequency) strain-controlled shear tests were conducted to subject the active waveguide to realistic slope movement 'S' shaped displacement-time cycles similar to those experienced during reactivated slope movements (e.g. Allison & Brunsden 1990 and Petley *et al.* 2005) (Section 2.2.2.3). Second, constant strain rate compression tests were conducted on the active waveguide model using the same apparatus and procedure as Dixon & Spriggs (2007) in order to validate the results obtained from the dynamic strain-controlled shear tests; the results produced by Dixon & Spriggs (2007) used a different measurement system (i.e. computer system and not the Slope ALARMS sensor) and therefore the results are not directly comparable with the current AE measurement system.

Finally, the dynamic strain-controlled shear test apparatus was used to simulate velocity-time behaviour landslides can experience during first-time failure (i.e. progressively accelerating through order of magnitude changes in velocity) and to assess the proposed method to continuously quantify velocities from monitored AE rates.

The experimental procedure employed was similar to that used by Dixon & Spriggs (2007). The active waveguide was installed in a flexible geomembrane (2 mm thick high density polyethylene) 130 mm diameter cylinder to represent the borehole and support provided by the host soil slope. Geomembrane containment was chosen as it provided sufficient rigidity to hold the gravel in place while allowing deformation of the system in a comparable way to an *in situ* soil surround. The stiffness of the hollow geomembrane cylinder was shown to be negligible over the range of deformations (e.g. up to 10 mm) examined. The ring stiffness of the geomembrane cylinder provided constraint (e.g. restricted volume change) equivalent to the *in situ* surrounding soil (the effects of confinement are discussed later in this Section). A 50 mm outside diameter steel pipe with 3 mm wall thickness was used as the waveguide; the same pipe was used by Dixon & Spriggs (2007) and in the field trials detailed in Chapters 4 and 5 of this thesis because AE stress waves have been shown to propagate along the steel pipe with relatively low attenuation. Crushed granite gravel aggregate (photograph in Figure 6.1) with a nominal particle size of 5 mm to 10 mm (the particle size distribution is shown in Figure 6.2) was used as backfill to produce relatively high energy AE (i.e. relatively large angular particles), and to be consistent with Dixon & Spriggs (2007) and the field trials detailed in Chapters 4 and 5. The backfill was compacted in 0.2 m high lifts to a density of 1520 kg/m^3 before each test (i.e. the model was re-compacted and prepared for each test).

Figure 6.1. Photograph of granite gravel aggregate

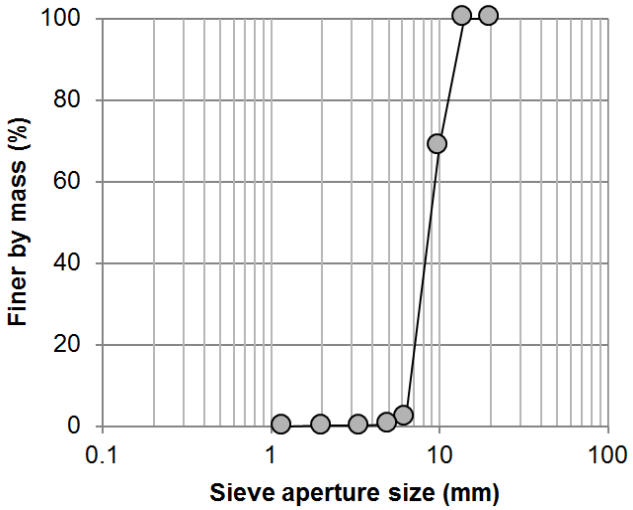

Figure 6.2. Particle size distribution of granite gravel aggregate

The series of experiments described were conducted with dry gravel backfill. This is because the influence of pore-water on the generation of AE in the backfill and propagation of AE through the backfill is anticipated to be minimal. The active waveguide will contain ground water below the water table when installed in the field and the backfill below this depth will be saturated. The influence of water within the granular soil on the generation of AE will be influenced in the same way that particle-particle/particle-waveguide interactions will be influenced and is therefore expected to be minimal unless effective stress is significantly reduced by high water pressures (the influence of moisture content on AE generation in fine grained soil is more significant and is described in Koerner *et al.* 1981). Attenuation of AE propagating through the backfill (prior to transmittance into the waveguide) is increased if the soil contains water (e.g. Oelze *et al.* 2002). However, the maximum distance of AE propagation prior to transmittance into the waveguide is 40 mm (i.e. the distance between 130 mm diameter borehole wall and the 50 mm diameter pipe wall) and the influence of pore-water on the propagation of AE through the backfill prior to transmission into the waveguide is therefore expected to be small. Conducting the experimental programme on dry samples therefore provided results representative of the field system, although potentially overestimated the magnitude of AE rates produced in response to applied deformation rates. Ground water within the active waveguide also increases the attenuation of AE stress waves as they propagate along the steel waveguide to the ground surface. This is due to soil covering loss (AE lost from the waveguide as it is transmitted into the surrounding soil, as described in Shiotani & Ohtsu 1999) increasing with acoustic impedance of the soil (e.g. through increased moisture content) (Section 2.4.5). This is discussed further in Chapter 8. Such losses have been neglected in these experiments because of the short propagation distance from the deformation zone to the sensor (~0.4

m). These experiments focused on developing a methodology to quantify deformation rates from measured AE.

Wooden caps were fitted at each end of the geomembrane cylinder to provide confinement and prevent loss of gravel. Confinement provided to the active waveguide model (i.e. the geomembrane ring stiffness and end caps) will restrict volume change (e.g. the soil will try to dilate inside a relatively constant volume), and will result in increasing confining pressures with the applied load. The increasing confining pressures will result in AE events of greater magnitude in response to deformation (e.g. as discussed in Section 2.4). AE rates generated will remain proportional to the velocity applied; however, the coefficient of proportionality of the AE rate-velocity relationship is expected to increase with increasing confining pressures (i.e. increasing applied force).

6.2.2. Dynamic strain-controlled shear tests

The active waveguide models were oriented horizontally into the loading apparatus and the diameter of the active waveguide was deformed by the loading ram. Figures 6.3a to 6.3d show diagrams and photographs of the test setup. The loading ram bearing and base supports were made of internally concave wooden blocks (Figures 6.3b and 6.3c) to accommodate the cylindrical shape of the active waveguide and to distribute the load (i.e. to avoid unrepresentative point loading). Loading was applied vertically by the ram to the centre of the active waveguide. The underlying supports were positioned either side of the loading ram in order to induce shearing (two shear zones; one at each side of the loading ram) as this mechanism is representative of the shearing mechanism the active waveguide is subject to in response to slope movement, although there is an additional shear zone in the physical model. The additional shear zone has the potential to result in elevated levels of AE rates in response to deformation, relative to those that would be generated by an active waveguide installed through a slope in the field. Based on experience from the field case studies (Chapters 4 and 5) it is not anticipated that the AE rates generated by the modelled system are unrepresentative of the field system and trends of behaviour are comparable. The piezoelectric transducer was consistently coupled to the waveguide 0.4 m from the centre of the loading ram.

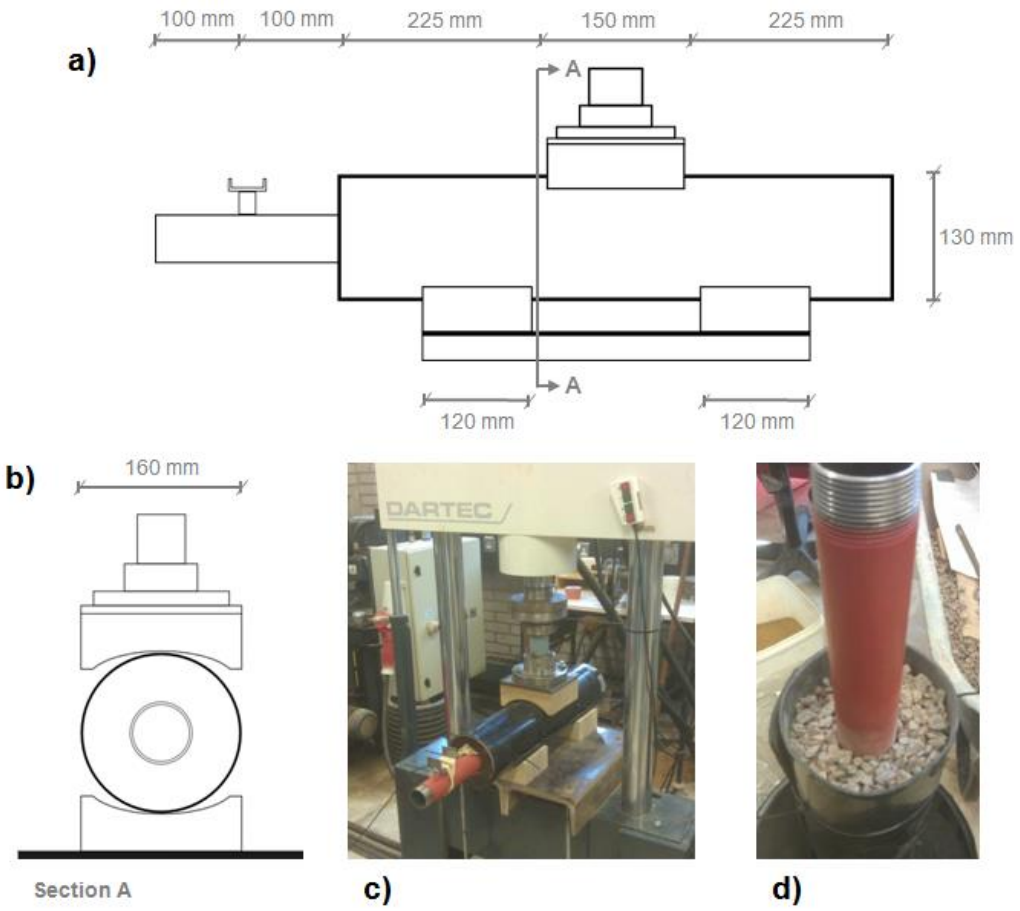

Figure 6.3. a) Elevation schematic of active waveguide specimen installed in dynamic strain-controlled shear apparatus, b) cross section schematic of active waveguide specimen installed in apparatus, c) photograph of test set up, and d) photograph of active waveguide model with angular gravel aggregate backfill

A Dartec hydraulically controlled cyclic loading test machine was adapted in order to apply dynamic strain-controlled loading to the active waveguide model (Figure 6.3). Low frequency cycles (half of a sine wave) of strain-controlled loading with amplitudes (i.e. displacement or stroke) between 1 mm and 10 mm were applied to simulate landslide movements (i.e. bell shaped velocity-time profiles where the velocity increases towards a peak value and then decays towards zero when the slope stabilises). The total deformation during the tests was limited to between 1 mm and 10 mm to avoid damaging of the geomembrane sleeve, allow repeat testing, and to obtain test results for relatively small displacements (i.e. equivalent to the gravel particle size or smaller). Strain-controlled cyclic frequencies between 0.0001 Hz (i.e. the lowest allowable by the Dartec machine) and 0.001 Hz were selected to replicate realistic cycles of movement that soil slopes undergo; up to velocities of approximately 100 mm per hour. LabView was used to record the displacement- and load-time behaviour of the active waveguide throughout the tests and velocity-time was determined later through calculating the rate of change of the displacement-time curve.

The AE rate response of the active waveguide models to the strain-controlled dynamic loading was captured using the Slope ALARMS sensor with a comparator (i.e. voltage threshold) level of 0.25 V to ensure that no mechanical or electrical background noise was recorded (i.e. the amplitude of background noise signals fell below a 0.25 V threshold and were therefore not detected). RDC were recorded and time stamped every 5 seconds throughout each test and these RDC per 5 second AE rates were converted to conventional RDC per hour values. A total of 21 tests were conducted on the active waveguide models with angular gravel backfill; with displacement-time cyclic functions ranging from 1 mm amplitude with 0.0001 Hz frequency to 10 mm amplitude with 0.001 Hz frequency. Table 6.1 provides the details of the displacement-time functions applied in these tests, and the shape of the waveform applied in the tests can be seen in Figure 6.7).

Table 6.1. Tabulated dynamic strain-controlled (DSC) shear tests on active waveguide models with angular gravel backfill and 50 mm diameter 3 mm thick steel pipe contained inside a 130 mm diameter geomembrane cylinder. Voltage threshold level set to 0.25V

	Displacement-time function	
Test no.	**Amplitude (mm)**	**Frequency (Hz)**
DSC-1	1	0.0001
DSC-2	1	0.0003
DSC-3	1	0.001
DSC-4	4	0.0001
DSC-5	4	0.0003
DSC-6	4	0.0003
DSC-7	4	0.0003
DSC-8	4	0.0003
DSC-9	4	0.001
DSC-10	5	0.0001
DSC-11	5	0.0001
DSC-12	5	0.0003
DSC-13	5	0.001
DSC-14	5	0.001
DSC-15	10	0.0001
DSC-16	10	0.0003
DSC-17	10	0.0003
DSC-18	10	0.0003
DSC-19	10	0.001
DSC-20	10	0.001
DSC-21	10	0.001

6.2.3. Constant strain rate compression tests

Constant strain rate compression tests (Figure 6.4) using the same test apparatus as Dixon & Spriggs (2007) were conducted in an attempt to validate the results produced from the dynamic strain-controlled shear tests. Dixon & Spriggs (2007) used a different AE measurement system and therefore it was necessary to conduct an additional series of compression tests using the Slope ALARMS sensor for comparison. The same active

waveguide model used in the dynamic strain-controlled shear tests was used in the constant strain rate compression tests. It should be noted that the mode of deformation of the active waveguide is compression in these tests rather than the double shear mechanism used in the dynamic strain-controlled tests. Figure 6.4 shows a photograph of the active waveguide installed in the test apparatus. 20 tests were conducted at a constant displacement rate of 66.15 mm per hour (rapid), 10 tests were conducted at 5.88 mm per hour (moderate), and 10 tests were conducted at 0.706 mm per hour (slow). The information pertaining to this series of tests is detailed in Tables 6.2 and 6.3. The displacement rates selected were the same as those used by Dixon & Spriggs (2007) and are separated by orders of magnitude.

Figure 6.4. Photograph of the active waveguide model installed in the Dixon & Spriggs (2007) constant strain rate compression apparatus

Table 6.2. Displacement rates, durations and total displacements of constant strain rate compression tests

Classification	Displacement rate (mm/hour)	Duration (hours)	Displacement (mm)
Rapid	66.15	0.25	16.5
Moderate	5.88	2.5	14.7
Slow	0.71	16	11.4

Table 6.3. Number of constant strain rate compression tests conducted at each displacement rate

Number of tests	Displacement rate
20	Rapid
10	Moderate
10	Slow

6.2.4. Quantification of deformation rates during slope failure simulation

The results from both the dynamic strain-controlled shear tests and constant strain rate compression tests were compiled in order to establish an empirical calibration AE rate-velocity relationship for the active waveguide physical model. Subsequently, a slope failure simulation was conducted, using the dynamic strain-controlled shear apparatus, in order to evaluate the ability to quantify deformation rates from measured AE rates, by applying the coefficient of proportionality to measured AE rates. The dynamic strain-controlled shear test apparatus was programmed to apply an accelerating displacement-time function to the active waveguide model similar to those experienced by deforming slopes as they undergo failure. The total displacement applied throughout this test was 10 mm. The first 1 mm of displacement was applied at a frequency of 0.0001 Hz, the second 1 mm of displacement at 0.0002 Hz, the third at 0.0003 Hz and so on. The final (tenth) 1 mm of displacement was applied at a frequency of 0.001 Hz.

6.2.5. Comparison of backfill materials

A series of dynamic strain-controlled shear tests were conducted on active waveguide models with a variety of granular backfill types in order to investigate the influence of granular soil properties on their AE rate response. Principally, the influence of particle size and grading was investigated in these experiments, and it is this basis on which the backfills were selected (i.e. to test backfills with different sizes and gradings). Particle shape and roughness characteristics also influence the AE response; however, this was a preliminary study of the influence of backfill materials. A more detailed investigation of backfill properties (including particle shape) on the AE response from different backfills is provided in Chapter 7 because the apparatus used in Chapter 7 applies a more realistic shear mechanism and a greater range of velocities and deformation magnitudes. Figures 6.5a to 6.5e show photographs of the 5 soil types that were tested and Figure 6.6 shows their particle size distribution curves. The soils examined were: granite gravel aggregate (Figure 6.5a) used in the 21 tests described earlier in Section 6.2.1; Leighton Buzzard sand (Figure 6.5d) used in 4 tests; crushed glass aggregate (Figure 6.5c) used in 3 tests,

concrete sand (Figure 6.5e) in 3 tests; and river gravel (Figure 6.5b) also in 3 tests. The information pertaining to this series of tests is detailed in Table 6.4.

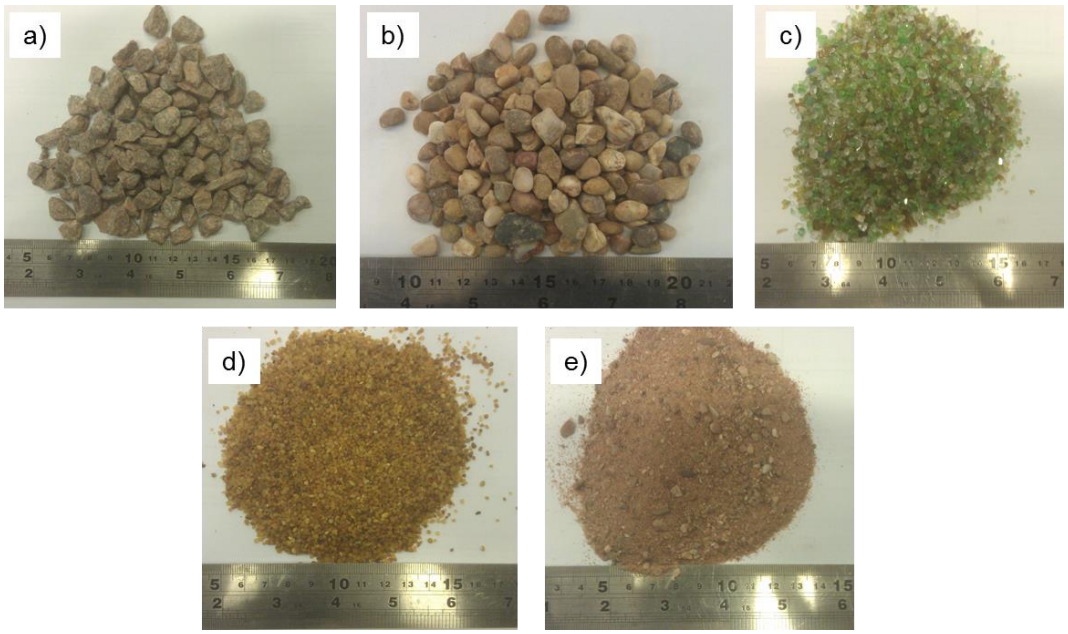

Figure 6.5. Photographs of soil samples; a) Gravel Aggregate, b) River Gravel, c) Crushed Glass, d) Leighton Buzzard Sand, and e) Concrete Sand

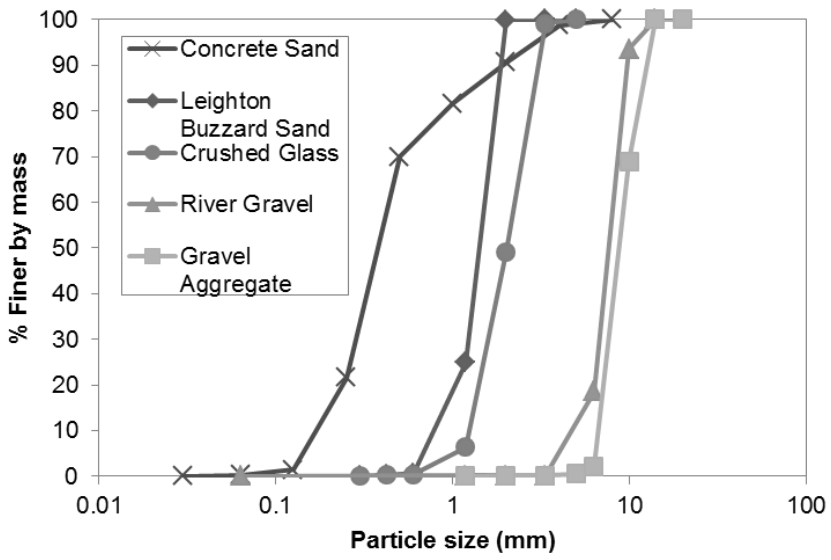

Figure 6.6. Particle size distribution curves for the 5 soil types tested

Table 6.4. Tabulated dynamic strain-controlled shear tests on active waveguide models with different backfill materials and 50 mm diameter 3 mm thick steel pipe contained inside a 130 mm diameter geomembrane cylinder. Voltage threshold set to 0.25V

		Displacement-time function	
Test no.	**Backfill**	**Amplitude (mm)**	**Frequency (Hz)**
DSC-22	LB sand	1	0.0003
DSC-23	LB sand	4	0.0003
DSC-24	LB sand	4	0.0003
DSC-25	LB sand	10	0.0003
DSC-26	Glass	1	0.0003
DSC-27	Glass	4	0.0003
DSC-28	Glass	4	0.0003
DSC-29	Concrete sand	4	0.0003
DSC-30	Concrete sand	4	0.0003
DSC-31	Concrete sand	10	0.0001
DSC-32	River gravel	1	0.0001
DSC-33	River gravel	5	0.0001
DSC-34	River gravel	5	0.001

6.3. Results and analysis

6.3.1. Dynamic strain-controlled shear tests on active waveguide models with gravel aggregate backfill

Figures 6.7a to 6.7d show the results from an applied displacement-time function of 4 mm amplitude and 0.0003 Hz frequency (example tabulated test results are in Appendix A3). Of interest is the AE rate response and its resemblance to the applied velocity throughout the test (Figure 6.7c); suggesting a proportional relationship exists between them. The sensitivity of the AE rate response to changes in applied velocity demonstrates the promise of the system to be able to detect destabilising effects (e.g. slope velocity increasing in response to prolonged rainfall) and stabilising effects (e.g. slope velocity decreasing subsequent to remediation measures), and as an early warning system to detect accelerations of slope movements continuously and in real-time. Note that there is a time lag of roughly 1 minute between the sudden increase in velocity and the initiation of the AE rate response; this is hypothesised to be due to the initial portion (<0.2 mm) of the displacement being taken up by the geomembrane sleeve prior to deformation of the gravel column taking place. The active waveguide model was prepared and compacted vertically and end caps were secured before the specimen was placed horizontally into the test apparatus. Slight lateral displacement of the gravel occurred when placed horizontally as it was difficult to secure the end caps sufficiently to prevent small displacement. This problem does not occur in the field as: the active waveguide is installed vertically through the slope, backfill is compacted sufficiently in lifts and is in direct contact with the host soil slope, and normal stress is provided by the unit weight of the backfill.

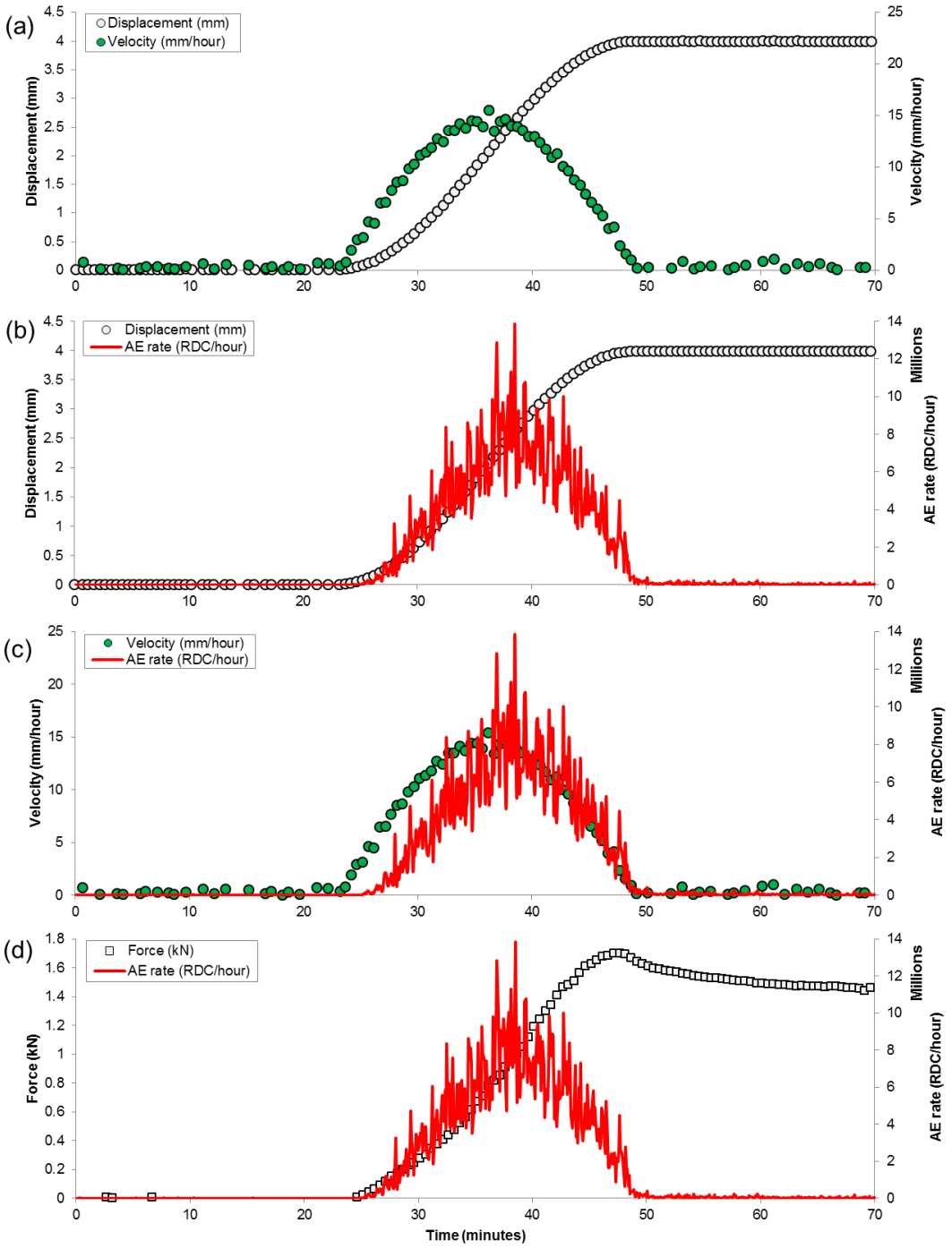

Figure 6.7. Time series from a dynamic strain-controlled shear test; a) displacement- and velocity-time, b) displacement- and AE rate-time, c) velocity- and AE rate-time, and d) force- and AE rate-time

A relationship between the velocity applied and the AE rates produced can be determined from the test example shown in Figure 6.7c. It was possible to produce 'measured' AE rate vs. velocity calibration relationships, such as shown in Figure 6.8, by calculating 2 minute moving average values of velocity and AE rates throughout the test. The lower section of the 'loop' curve in Figure 6.8 is produced from increasing velocity (i.e. the first half of the bell shaped curve in Figure 6.7c) and this approaches the peak velocity that was applied. The upper section of the 'loop' curve is produced from decreasing velocity

(i.e. the second half of the bell shaped curve in Figure 6.7c). The magnitude of AE rates produced in response to increasing velocity was less than those produced from decreasing velocity. This is hypothesised to be due to a combination of: an initial portion of the displacement (<0.2 mm) at the start of the test being taken up by the geomembrane sleeve prior to initiation of deformation of the gravel column; a small magnitude of deformation in the gravel column was required to mobilise particle-particle/particle-waveguide interactions and generate AE during the initial period of the test; the rate of particle-particle/particle-waveguide interactions were sustained (i.e. remained elevated) at the onset of reducing velocity prior to the rate of interactions responding and reducing; and the coefficient of proportionality increased (i.e. AE rates generated in response to an applied velocity increased) with increasing confining pressures throughout the test. The 'calculated' AE rate vs. velocity relationship shown in Figure 6.8 was determined using the back calculation method detailed in Chapter 5 (Section 5.2); the magnitude of total deformation (i.e. 4 mm in this case) was equated to the area under the AE rate-time curve (i.e. the red line shown in Figures 6.7b to 6.7d) and was distributed proportionately to each trapezoidal integrand under the curve and the velocity over each trapezoid was determined using the displacement/time relation. These 'calculated' velocities were then plotted against the measured AE rates to produce the linear AE rate vs. velocity 'calculated' relationship shown in Figure 6.8, which passes directly through the centre of the measured relationship; this validates the back calculation calibration method, although it assumes the relationship to be linear.

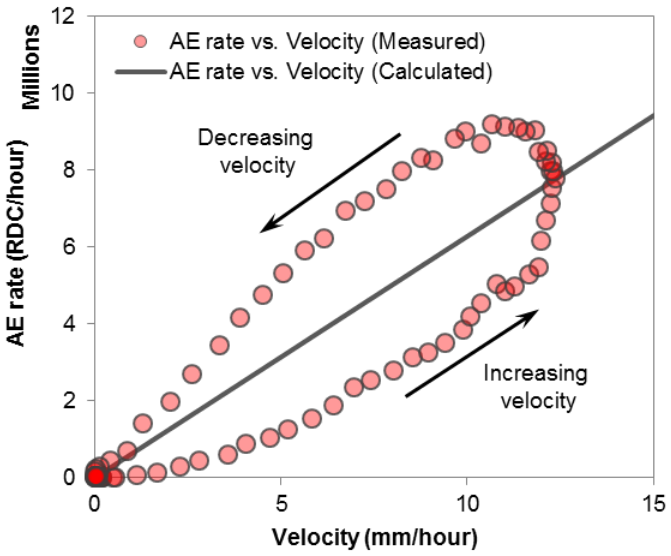

Figure 6.8. Measured and calculated AE rate vs. applied velocity relationships determined from one dynamic strain-controlled shear test (2 minute moving average values)

Figure 6.9 shows the force vs. displacement relationships for selected 1 mm, 4 mm and 10 mm amplitude dynamic strain-controlled shear tests on active waveguide models. The same force-displacement behaviour was experienced in each test demonstrating that each sample was prepared and tested in a consistent manner. The gradual increase in gradient of the relationships in Figure 6.9 is explained by a combination of: increasing confining pressures increasing the shear resistance of the gravel; and at displacements of approximately 4-6 mm the shear resistance of the steel waveguide is gradually introduced within the active waveguide system (i.e. increasing the system stiffness).

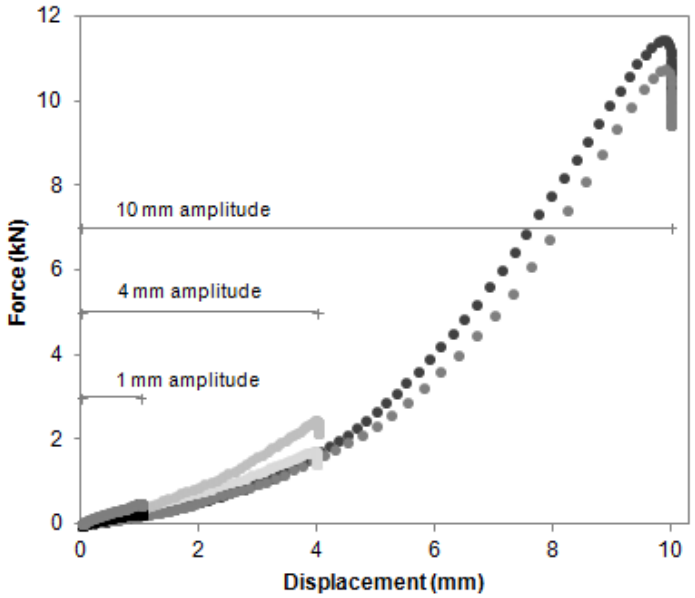

Figure 6.9. Force vs. displacement relationship for selected dynamic strain-controlled shear tests of 1 mm, 4 mm and 10 mm total displacements

6.3.2. Determination of the coefficient of proportionality

Figures 6.10 and 6.11 show the measured AE rate-velocity relationship established using data from the 21 dynamic strain-controlled shear tests on active waveguide models with gravel aggregate backfill. The plots were produced from collating all 'measured' AE rate vs. velocity relationships (i.e. Figure 6.8) from each of the 21 tests. The landslide velocity scale after Cruden & Varnes (1996) is superimposed in Figure 6.11, which is plotted on logarithmic scales, to demonstrate the range of realistic slope displacement rates that have been examined. Determination of an equation to describe the relationship was conducted by plotting a linear regression line through the AE rate-velocity relationship in Figure 6.10. It is anticipated that determination of this relationship will allow measured AE rates to be converted into velocities continuously and in real-time throughout subsequent tests. The equation for the linear relationship is detailed in Equation 6.1; the linear regression produced an R^2 value of 0.82, which indicates a strong positive linear correlation. This

value of C_p is significantly greater than those reported in Chapter 5, which were produced from the field trials. This is expected to be due to a combination of: the AE signals experiencing greater attenuation in the field trials, due to a greater distance of propagation (i.e. from the shear surface); high confining pressures in the physical model; and the double shear loading mechanism in the physical model.

$AE_{rate} = (4.4 \times 10^5) \times \text{Velocity}$

$\therefore C_p = 4.4 \times 10^5$

and $\text{Velocity} = (2.3 \times 10^{-6}) \times AE_{rate}$ **(6.1)**

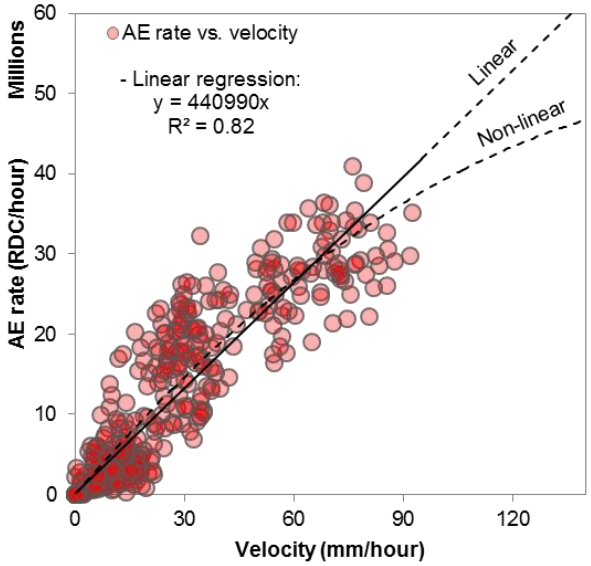

Figure 6.10. Measured AE rate vs. measured velocity relationship using data from 21 dynamic strain-controlled shear tests

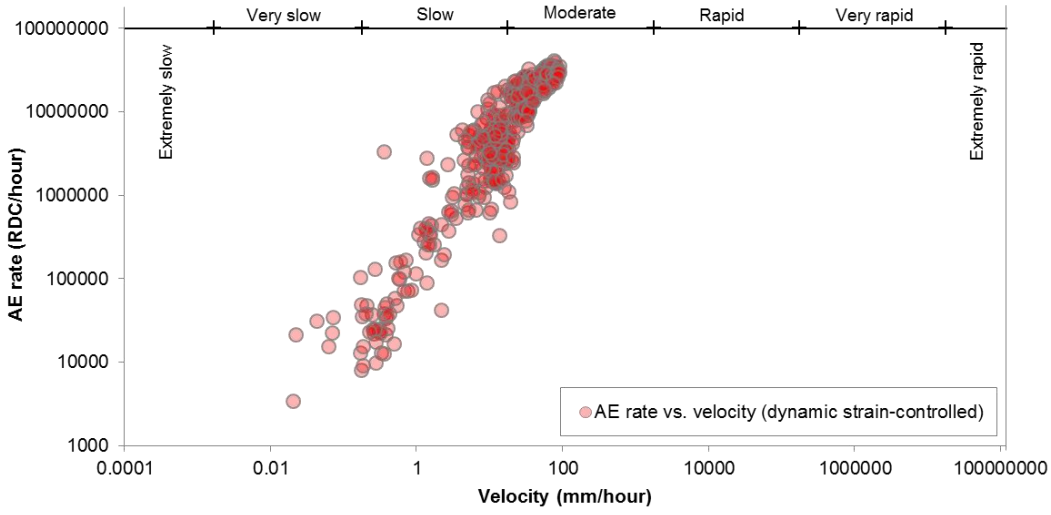

Figure 6.11. Measured AE rate vs. measured velocity relationship using data from 21 dynamic strain-controlled shear tests; the landslide velocity scale after Cruden & Varnes (1996) is superimposed

The AE rate-velocity relationship is influenced by confining pressure and the variability in Figure 6.10 could be a function of this. However, for the purpose of this study, a simple linear regression was selected to define the empirical AE rate-velocity relationship because the aim was to demonstrate that velocity could be quantified to better than an order of magnitude (i.e. for use in a robust AE early warning system). It is anticipated that greater accuracy could be achieved through development of the AE rate-velocity relationship to be a function of confining pressure. The linear relationship was established for the range of velocities examined but it should be noted that the data in Figure 6.10 appears to be slightly non-linear and therefore the AE rate-velocity relationship may become non-linear over a greater range of applied velocities.

6.3.3. Constant strain rate compression tests

The results from the 40 constant strain rate compression tests can be seen in Figure 6.12, and the data sets coalesce into groups governed by the displacement rate that was applied (as detailed in Dixon & Spriggs (2007)). Example tabulated test results can be found in Appendix A3. The average AE rate produced from each test was plotted against the applied velocity in Figure 6.13 (triangle data points). The data fall into the AE rate vs. velocity relationship determined from the dynamic strain-controlled shear tests; this validates the data produced from the dynamic strain-controlled shear tests and suggests that the mechanism of loading (i.e. shear or compression) does not yield a significant difference in the AE rates produced from the model system. Figure 6.14 shows selected force vs. displacement relationships from rapid constant strain rate compression tests, which demonstrate each active waveguide was prepared in a relatively consistent manner.

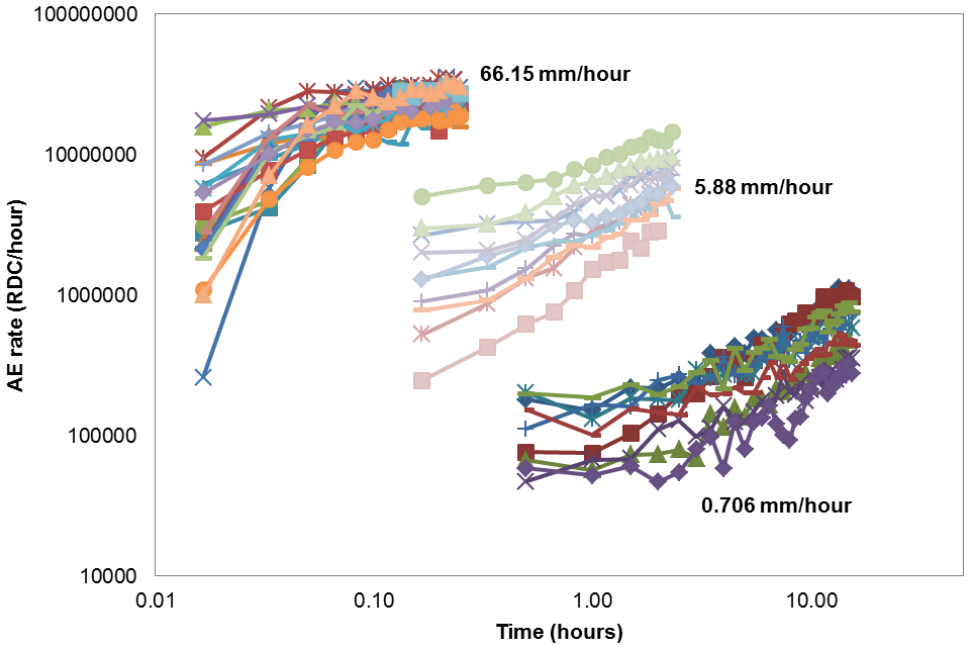

Figure 6.12. Results from 40 constant strain rate compression tests; AE rate vs. time

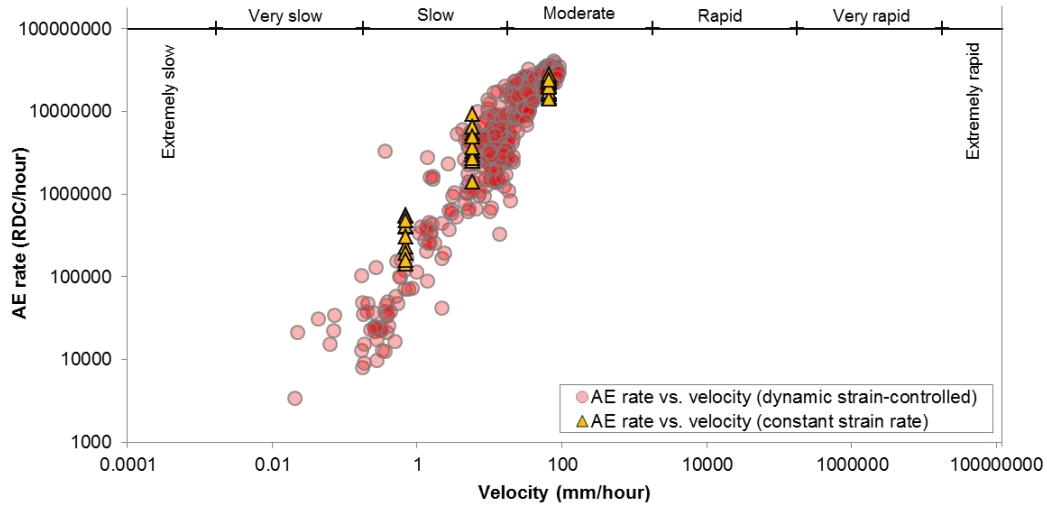

Figure 6.13. Measured AE rate vs. measured velocity relationship using data from 21 dynamic strain-controlled shear tests and 40 constant strain rate compression tests, the landslide velocity scale after Cruden & Varnes (1996) is superimposed

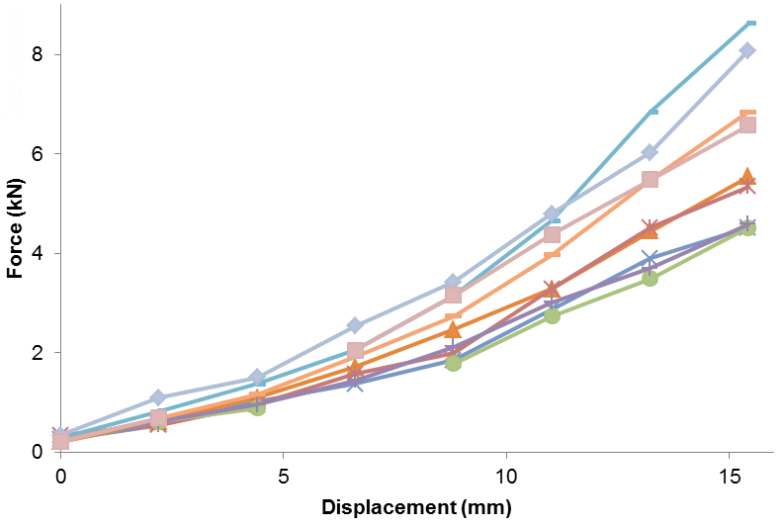

Figure 6.14. Force vs. displacement results from selected rapid constant strain rate compression tests on active waveguides

6.3.4. Quantification of velocity during slope failure simulation

The dynamic strain-controlled shear apparatus, with an accelerating displacement-time function to simulate slope failure behaviour, generated the results shown in Figures 6.15a to 6.15c. The recorded AE rates (recorded over 5 second intervals) were converted to velocity values using Equation 6.1, which has allowed an *a priori* Class A prediction (Lambe 1973) to be made, and are shown in Figure 6.15c as the red line. Figures 6.16a to 6.16c show 2 minute moving average values (i.e. to smooth the sporadic nature of the raw 5 second interval AE data). The results demonstrate that it is possible to quantify applied velocities from measured active waveguide generated AE rates continuously throughout the event with accuracy better than an order of magnitude and in line with standard landslide displacement rate classifications: both calculated and measured velocities fall into the same velocity classification (e.g. 'slow' and 'moderate') throughout the increasing velocity stages of the experiment in Figure 6.16b. The sensitivity of the AE rate response to changes in applied velocity demonstrates promise of the system to be able to detect destabilising and stabilising behaviour, and as an early warning system to detect accelerations of movements continuously and in real-time during progressive failure.

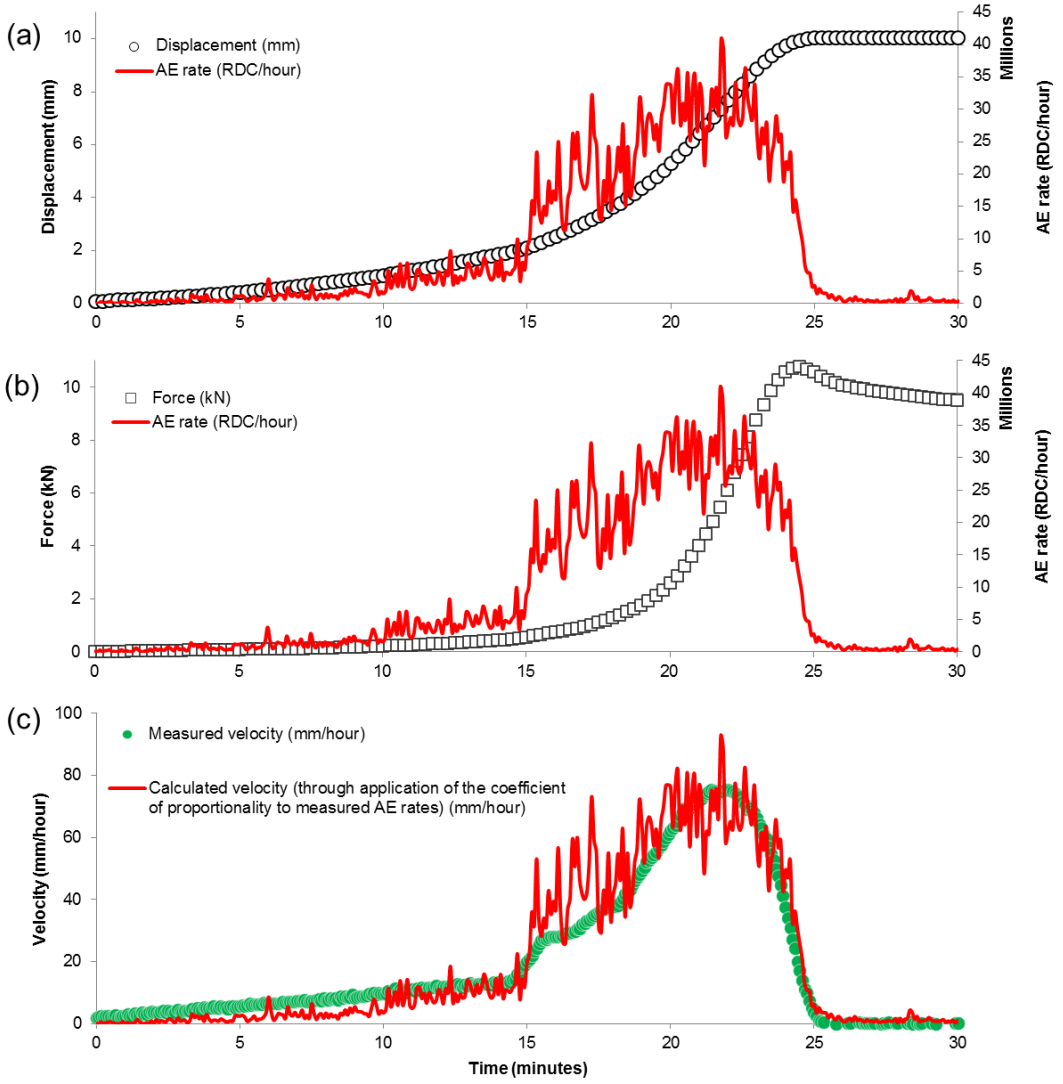

Figure 6.15. Time series from a dynamic strain-controlled failure simulation; a) displacement- and AE rate-time, b) force- and AE rate-time, and c) measured velocity- and calculated velocity (i.e. derived from AE rate 5 second interval values)-time

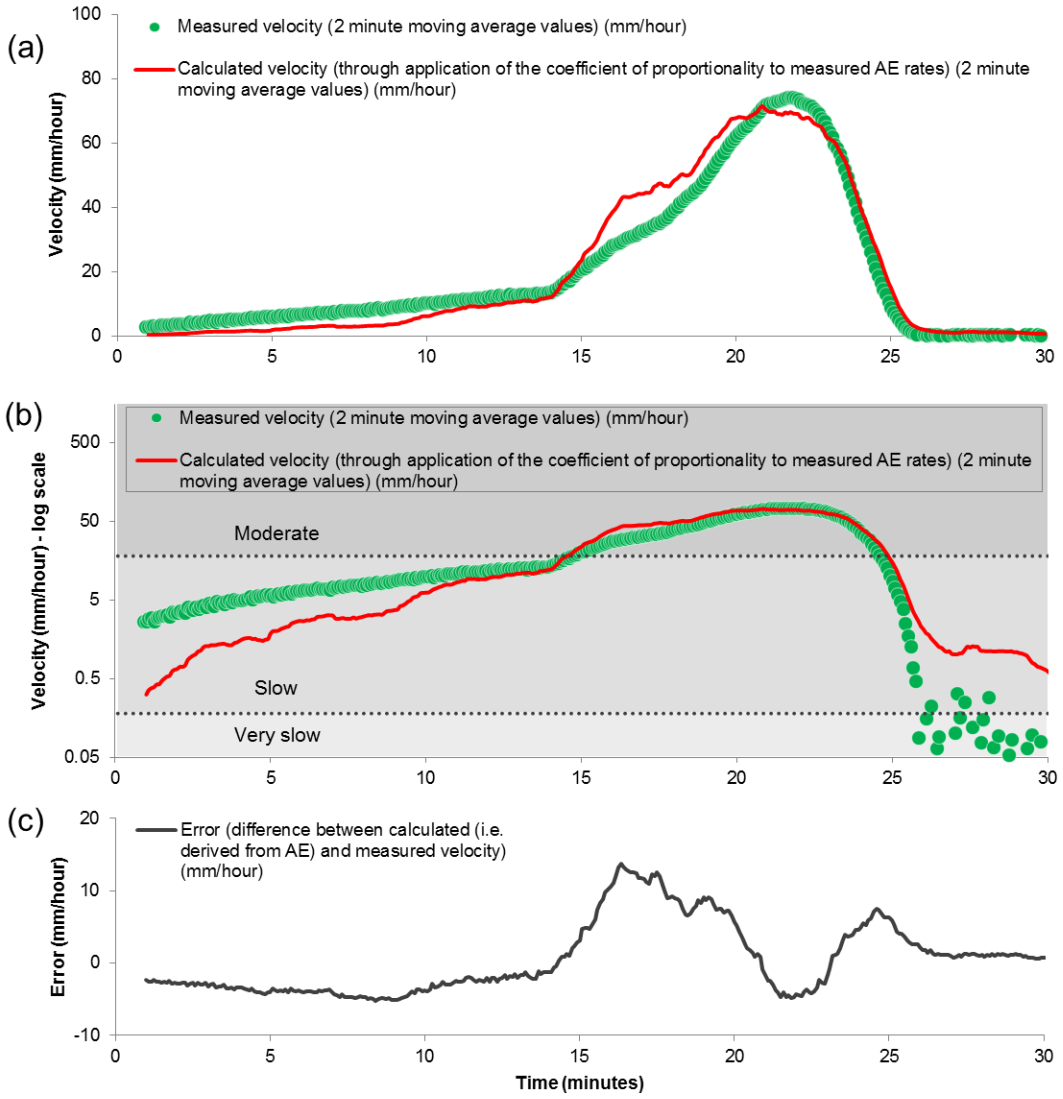

Figure 6.16. Measured and calculated (i.e. derived from AE rate data through application of the coefficient of proportionality) velocity-time behaviour (2 minute moving average values) during a landslide failure simulation using the dynamic strain-controlled shear test apparatus; a) linear velocity scale, b) log velocity scale showing 'very slow', 'slow' and 'moderate' velocity classifications, and c) error (difference between calculated (i.e. derived from AE) and measured velocities (using 2 minute moving average values)

Of particular note is the surge in velocity (i.e. sudden acceleration) that occurred between 14 minutes and 16 minutes as can be seen in Figures 6.15c, 6.16a and 6.16b. The AE rates immediately responded to the increase in velocity and also increased significantly. As the rate of increase in velocity reduced (i.e. gradient of the velocity-time curve reduced) at 16 minutes the AE rates also responded and the rate of increase of AE rates reduced (i.e. gradient of the AE rate-time curve reduced).

Figure 6.16c shows the error (i.e. difference between the calculated and measured velocity) from the 2 minute moving average values throughout the test. The error is consistently less than +/- 5 mm/hour except for the periods in which; the surge in velocity occurred (at approximately 14-16 minutes), and when the velocity suddenly reduced (at 23 minutes) at the end of the test. The calculated values (i.e. derived from AE)

overestimated the velocity for these periods. It is expected that the surge in velocity induced a combination of inter-particle friction, contact stress release and force chain buckling (Michlmayr *et al.* 2013) and therefore resulted in a period of relatively high AE activity and an overestimation in calculated velocity. The overestimation of the calculated velocity at the reduction in measured velocity at the end of the test is anticipated to be due to the same phenomena described in Section 6.3.1: the rate of particle-particle/particle-waveguide interactions were sustained (i.e. remained elevated) at the onset of reducing velocity prior to the rate of interactions responding and reducing; and the applied load began to reduce at approximately 24 minutes, which resulted in changed confining pressures and altered the value of C_p. These error values are considered small and demonstrate the ability of the system and the technique to quantify slope displacement rates from measured AE rates with accuracy in line with standard classification of landslide movements. It is anticipated that these errors could be reduced further if the AE rate-velocity relationship was to be refined through further experimentation. The calculated velocity (i.e. derived through application of the coefficient of proportionality to measured AE rates) is plotted against the measured applied velocity throughout the landslide failure simulation experiment in Figure 6.17. The linear regression in Figure 6.17 produced an R^2 value of 0.96, which demonstrates a very strong linear correlation. The gradient of the linear trend line in Figure 6.17 is 1.05, which highlights that the velocity quantified from measured AE rates (i.e. calculated velocity) was slightly greater than the measured velocity throughout the experiment. This information could be used to refine the value of the coefficient of proportionality for use in subsequent tests.

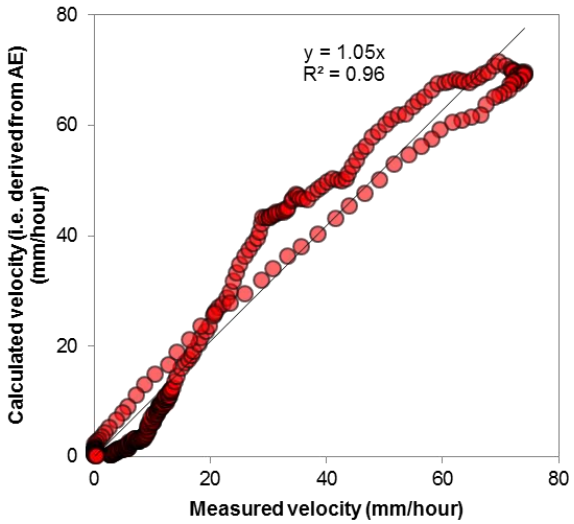

Figure 6.17. Calculated velocity (i.e. derived from AE rate data through application of the coefficient of proportionality) vs. measured velocity throughout the slope failure simulation

6.4. Comparisons of backfill types

A series of dynamic strain-controlled shear tests were performed on active waveguide models with a range of backfills, primarily to investigate the influence of particle size distribution on the AE rate response. The generated AE rates for this range of backfills are plotted against the applied velocity in Figure 6.18 and the results show good agreement with those generated from the angular gravel aggregate. Figure 6.19 shows the gradients from linear regression lines plotted through the data points for each of the backfill materials (i.e. their linear coefficients of proportionality). The greater the value of the coefficient of proportionality, the greater AE rates generated in response to an applied velocity. The results in Figure 6.19 confirm that the angular gravel aggregate generated the greatest AE rates in response to an applied displacement rate. The river gravel appeared to generate the second highest (after the angular gravel aggregate) magnitude AE rates in response to an applied rate of displacement and this is consistent with what would be hypothesised based on the summary of current understanding of soil property influences on AE behaviour detailed in Table 2.5 (i.e. the river gravel had a similar particle size distribution with the gravel aggregate, however, its particles were less angular). Crushed glass and Leighton Buzzard sand generated the lowest AE rate responses of the 5 soils tested. This would fit with the framework proposed as they had smaller particle sizes and were relatively single-sized (i.e. low coefficients of uniformity). Although the concrete sand had the smallest particle size distribution it had a greater AE rate response than the crushed glass and Leighton Buzzard sand. This is hypothesised to be due to its more uniform grading and coefficient of uniformity. These results indicate that in well graded soils (i.e. where the smaller particles fill the pore spaces between the larger particles generating a greater number of particle-particle contacts, and a greater

surface area over which inter-particle friction can take place) generate greater AE rates than poorly graded soils. It could also be expected that well graded angular gravel would yield an even greater AE rate response than the relatively single-sized angular gravel used in this study.

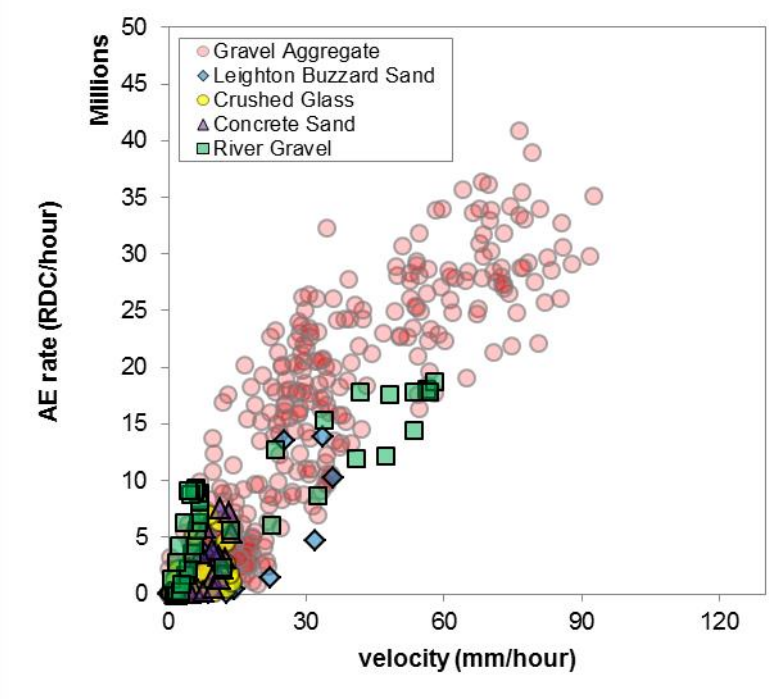

Figure 6.18. Results from dynamic strain-controlled shear tests on active waveguides with different backfill materials

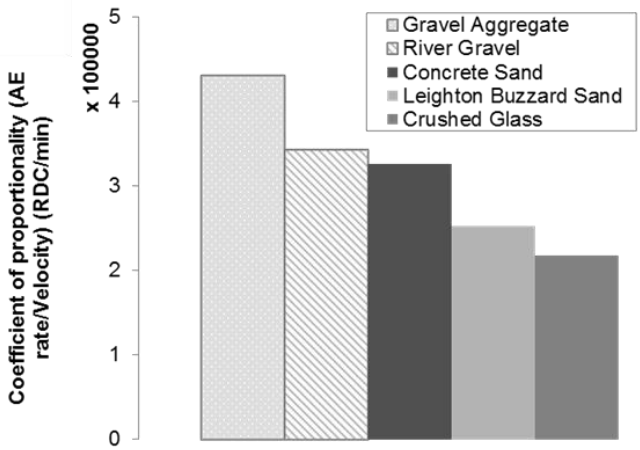

Figure 6.19. Linear coefficients of proportionality derived from the AE rate-velocity relationships plotted in Figure 6.18 for the 5 different backfills, showing the magnitude of AE rates generated in response to an applied velocity for each backfill

A greater number of tests would be required to establish definable AE rate-velocity relationships for each of the backfill materials. It should be noted that a full examination of the AE generation of each of these soils would need analysis of the frequency spectra of the AE and this was not possible with the current system that focuses in the frequency

range of 20 to 30 kHz and discounted any signals with amplitudes below the voltage threshold level of 0.25V. A more detailed investigation of backfill properties and their influence on AE rates generated from the system in response to applied deformation behaviour is provided in Chapter 7.

6.5. Summary

An experimental programme has been conducted to subject active waveguide physical models to deformation, in order to establish an empirical relationship between measured AE and deformation behaviour (Objective 3). Results from dynamic strain-controlled shear loading experiments conducted on active waveguide physical models were presented and the results confirmed that AE rates generated are proportional to the rate of deformation, and the coefficient of proportionality (C_p) that defines the AE rate vs. velocity relationship has been quantified (e.g. 4.4×10^5 for the angular gravel backfill investigated). This value of C_p is significantly greater than those reported in Chapter 5, which were produced from the field trials. This is expected to be due to a combination of: the AE signals experiencing greater attenuation in the field trials, due to a greater distance of propagation (i.e. from the shear surface); high confining pressures in the physical model; and the double shear/compression loading mechanism in the physical model. A large-scale physical model was later developed, which is detailed in Chapter 7, to generate a more realistic slope displacement shear and lateral loading mechanism.

It has been demonstrated that slope velocities can be quantified continuously in real-time through monitoring active waveguide generated AE during a slope failure simulation. The study shows that the technique can quantify landslide velocity to better than an order of magnitude and can therefore be used to provide an early warning of slope instability through detecting and quantifying accelerations of slope movement.

An investigation, using the dynamic strain-controlled shear apparatus, has also been conducted to understand the influence of backfill properties upon the AE response from the system to applied deformation behaviour (Objective 4). Principally, particle size distributions have been examined and 5 different granular soils have been employed. The results suggest that particle size distribution of granular soil does not significantly influence the active waveguide AE rate response over the magnitude of deformations and deformation rates examined. The results do agree with the literature as the greatest AE rates were generated from large angular particles, and soils with more uniform grading generated greater AE than other poorly graded soils with similar particle sizes due to a greater number of particle-particle interactions and a greater surface area of contact over which inter-particle friction can take place.

CHAPTER 7

Measured AE and deformation behaviour: large-scale first-time slope failure simulation

7.1. Introduction

Presented within this Chapter is experimentation conducted to subject active waveguides to first-time slope failure simulations and relatively large deformations. This experimental programme was necessary because the field trials (Chapters 4 and 5) and active waveguide physical model tests (Chapter 6) have not allowed the capability of the AE approach in early detection of first-time slope failures to be assessed. The purposes of this experimental programme were to: obtain the AE response to first-time slope failure (Objective 2); and define an empirical relationship between measured AE and deformation behaviour (Objective 3). The development of the large-scale first-time slope failure apparatus is described and the experimental procedure is detailed. In each test, a shear surface develops and the sliding mass accelerates during failure reaching velocities greater than 300 mm/hr and shear deformations of 50 mm (i.e. greater velocities and deformations than has been examined in the field trials or other physical model experiments). This is the first study to obtain continuous measurements to examine the behaviour of active waveguides subjected to first-time slope failure dynamics. Three tests were performed on the same active waveguide backfill material in order to evaluate repeatability. Subsequently, two further tests were performed with other backfill materials for comparison (Objective 4).

7.2. Apparatus development and experimental procedure

The final design of the large-scale first-time slope failure apparatus was a large shear box, which comprised two concrete blocks (relative proportions of the concrete mix by mass were 4, 2 and 1 for gravel, sand and cement respectively) each with dimensions 1 x 0.7 x 0.7 metre (Figure 7.1a shows the mould used to form the blocks and Figure 7.1b shows a finished block). The bottom box was fixed to a strong floor to prevent movement, and the top box was placed, using a crane/gantry, on top of the bottom box. Through the centre of each box was an open column (with a cross-sectional area of 0.3 x 0.3 m) in which clay

was compacted (details of the clay can be found in Table 7.1 and Figure 7.2). This column was designed to represent an element of the soil slope, through which an active waveguide and SAA were installed. Note that the system being modelled by this apparatus is the active waveguide; there are boundary effects at the interface between the soil column and the shear box wall, however, the boundary effects at the interface between the active waveguide and the soil column are small. The modelled system is therefore representative of the real active waveguide system when installed in a slope.

The column was positioned differently above and below the shear plane, as can be seen in Figure 7.3, to allow for travel of the waveguide through the column of clay during shearing and lateral loading (i.e. a greater volume of clay was behind the active waveguide in the top box and in front of the active waveguide in bottom box). A smooth HDPE geomembrane interface was installed between the two blocks in order to minimise interface friction between the concrete blocks, and allow for reproducible/repeatable interface behaviour. A sheet of 2 mm thick HDPE geomembrane was fixed both to the top of the bottom box, and to the bottom of the top box; the geomembrane sheets were fixed/anchored to the front/rear of each block using steel plate and raw bolts (Figure 7.4).

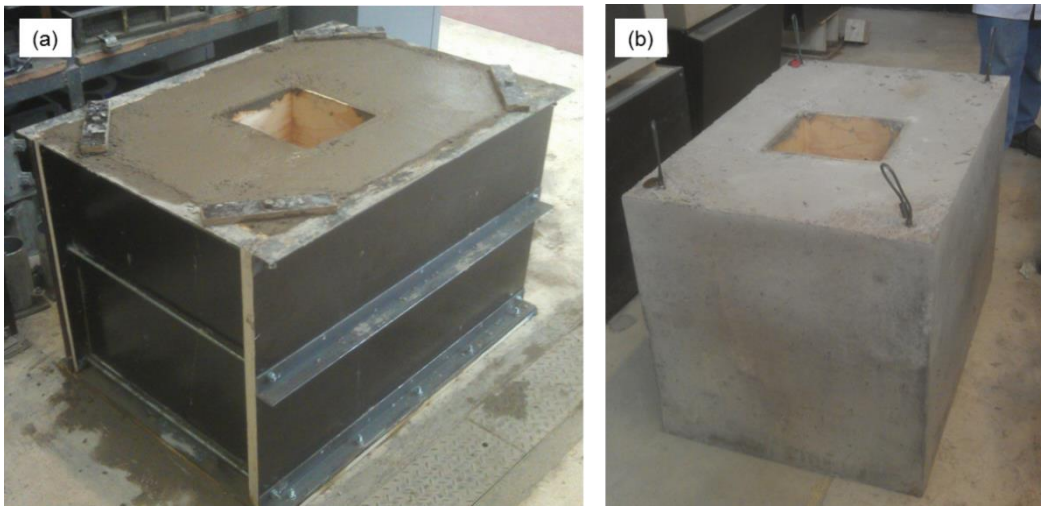

Figure 7.1. a) Concrete block inside mould and b) concrete block outside mould

Table 7.1. Properties of the clay used for fill in the first-time failure experiments

Name	Plastic limit (%)	Liquid limit (%)	Plasticity index (%)	Particle density (Mg/m³)	Optimum moisture content (%)	Maximum dry density (Mg/m³)
Clay	14.8	30.0	15.2	2.54	15.5	1.86

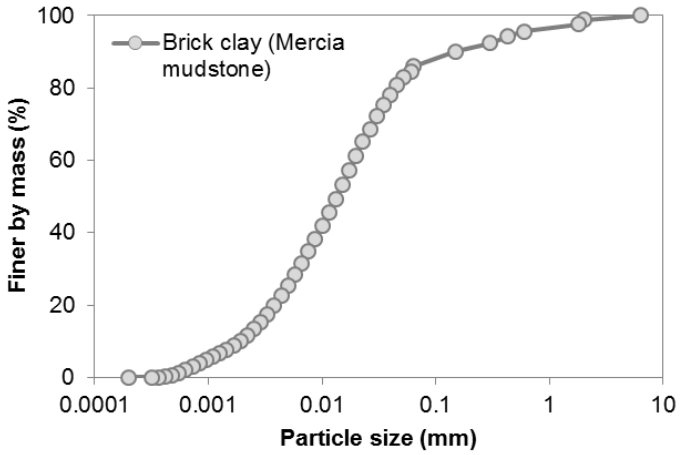

Figure 7.2. Particle size distribution of the clay used as fill in the first-time failure experiments. The distibution was determined from a combination of sieving and a laser diffraction particle size analyser

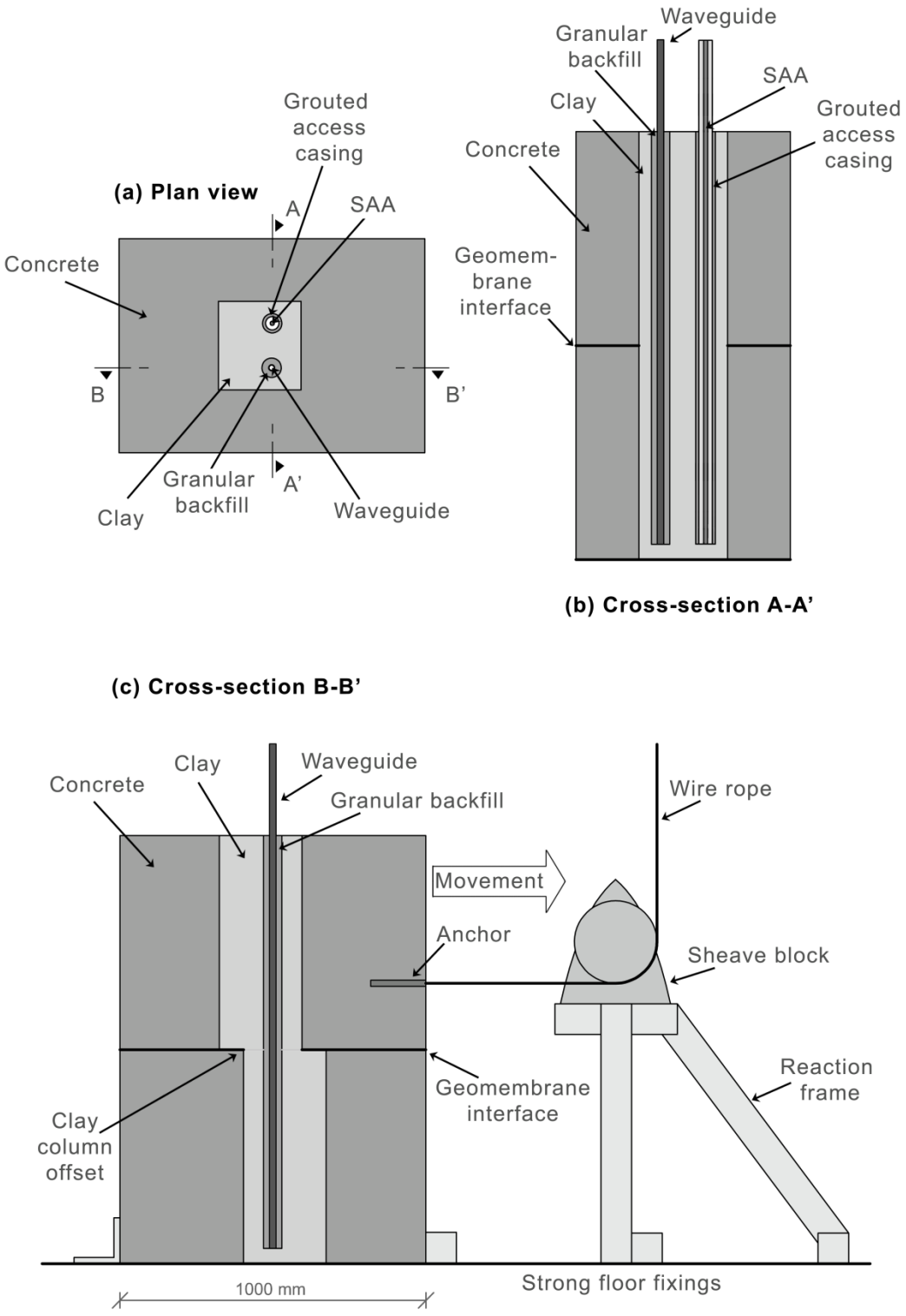

Figure 7.3. Annotated illustration of the first-time slope failure experiment at the start of a test (t = 0). The top block is pulled horizontally to the right of the image by the wire rope during the test. The anchor, wire rope and pulley system are fastened centrally in the horizontal plane and are only shown on cross-section B-B' for illustrative purposes

Figure 7.4. Photograph showing the wire rope fastened to the resin anchor at the front face of the top block. Geomembrane interface fixings are also shown

Figure 7.5 shows an annotated photograph of the apparatus. A large hydraulically controlled loading ram was exploited to provide sufficient load and displacement, and necessary control over the strain-controlled functions that were applied to the top block of the shear box in order to simulate slope failure. In order to move the top block horizontally, and induce shearing within the central soil column, a pulley system was designed. A wire rope (specification in Appendix A4) was fastened to the loading ram and fed around the pulley and fixed to the front of the top block (Figures 7.3, 7.4 and 7.5). The loading ram was programmed to move upwards, which pulled the wire rope around the pulley, and moved the top block horizontally. A 22 mm diameter 18 cm long studded eye anchor was fixed into the front of the top block using a high-strength resin. A d-shackle was used to connect the anchor eye to the 12 mm diameter wire rope. The wire rope was fed horizontally into a sheave block (specification in Appendix A4) and then up 90 degrees to the loading ram. The sheave block was fixed to a table at the appropriate elevation and the table comprised a ‘reaction frame’ that was in turn fixed to the strong floor. Note that the entrance of the wire rope into the sheave block was positioned 2 cm above the elevation of the resin anchor; this was to induce a small vertical component of load to the front of the top block in order to reduce the frictional resistance at the interface of the shear box during the experiment. The wire rope was connected into the bearing on the loading ram using a large d-shackle. As the loading ram moved upwards this pulled the wire rope and the wire rope pulled the top block horizontally, generating the shear box movement.

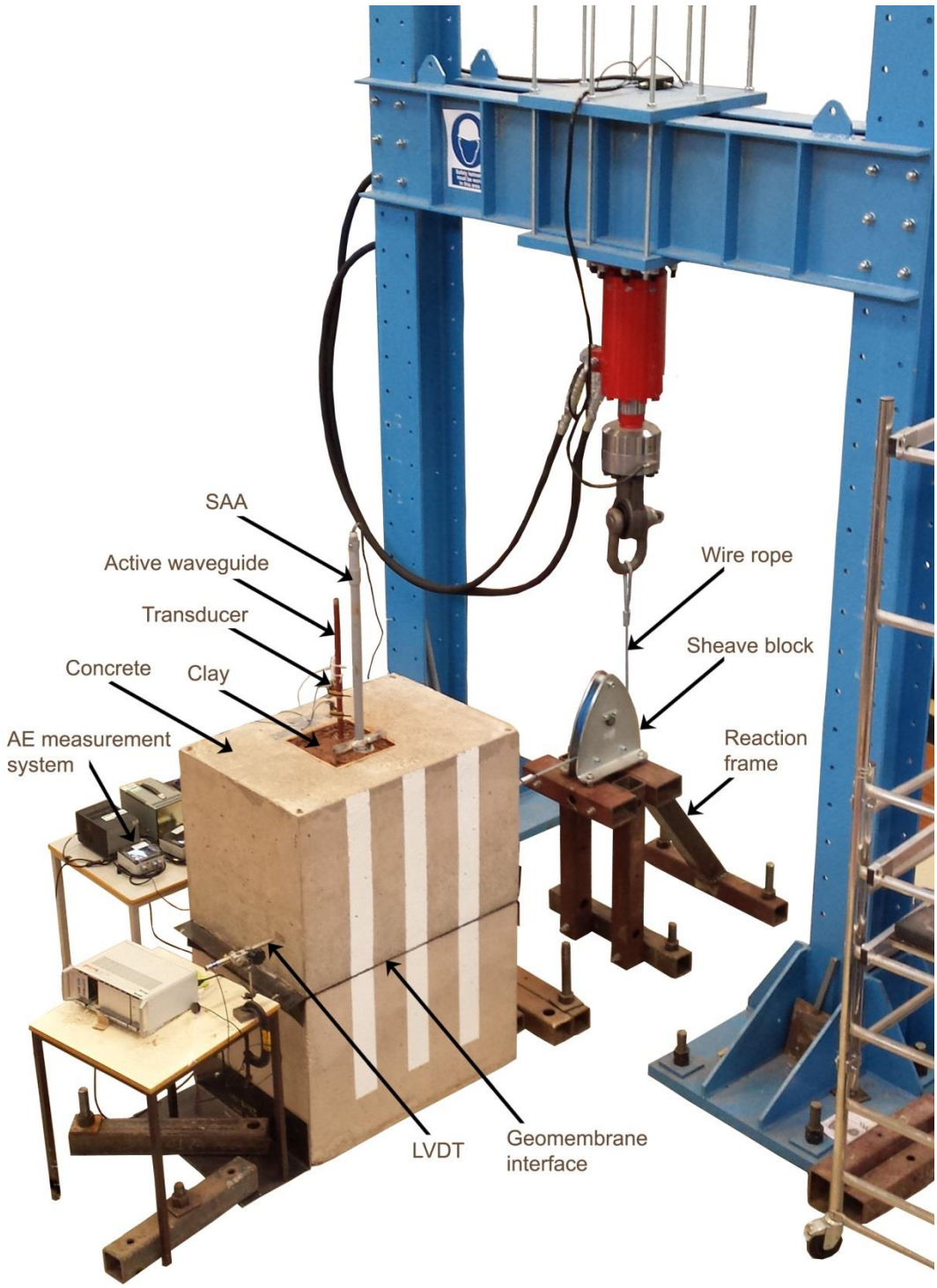

Figure 7.5. Annotated photograph of the first-time failure experiment

Displacement-time functions were designed (Tables 7.2, 7.3 and 7.4) to represent the deformation behaviour that slopes experience as they lose strength rapidly and accelerate during progressive failure. The slowest rate of movement was dictated by the lowest allowable by the loading machine. The duration of the first two stages of the experiment were progressively increased between Test 1 (FTF-1) and Test 3 in order to apply the lowest rates of deformation for greater magnitudes of time and deformation. This was of interest to determine the minimum magnitude of shear deformation in previously un-

sheared soil required to generate detectable AE from the system. The same function was applied in Tests 3, 4 and 5.

Table 7.2. Displacement-controlled function 1: applied to first-time failure simulation Test 1

	Displacement rate				
Stage	mm/minute	mm/hour	Duration (minutes)	Cumulative time (minutes)	Cumulative displacement (mm)
				0	0
1	0.06	3.6	15	15	0.9
2	0.12	7.2	10	25	2.1
3	0.25	15	7	32	3.85
4	0.5	30	6	38	6.85
5	1	60	5	43	11.85
6	2	120	4	47	19.85
7	4	240	3	50	31.85
8	6	360	3	53	49.85

Table 7.3. Displacement-controlled function 2: applied to first-time failure simulation Test 2

	Displacement rate				
Stage	mm/minute	mm/hour	Duration (minutes)	Cumulative time (minutes)	Cumulative displacement (mm)
				0	0
1	0.06	3.6	35	35	2.1
2	0.12	7.2	20	55	4.5
3	0.25	15	10	65	7
4	0.5	30	8	73	11
5	1	60	5	78	16
6	2	120	4	82	24
7	4	240	3	85	36
8	6	360	3	88	54

Table 7.4. Displacement-controlled function 3: applied to first-time failure simulation Tests 3, 4 and 5

	Displacement rate				
Stage	mm/minute	mm/hour	Duration (minutes)	Cumulative time (minutes)	Cumulative displacement (mm)
				0	0
1	0.06	3.6	50	50	3
2	0.12	7.2	25	75	6
3	0.25	15	10	87	9
4	0.5	30	8	95	13
5	1	60	5	100	18
6	2	120	4	104	26
7	4	240	3	107	38
8	6	360	3	110	56

The clay, used to fill the central column and represent an element of the soil slope, was Mercia Mudstone procured from a local brick manufacturer. Although the soil has >80% (by mass) silt sized particles, it plots above the A-line on a plasticity index-liquid limit

plot, and therefore behaves like a clay. The soil can be described as a 'very silty clay'. The clay had an initial moisture content in the range of 25-30% and was therefore close to the liquid limit (Table 7.1). It was subsequently air dried in 10x10x10 cm volumes to achieve moisture contents in the range 16.5-19.9%. This was to ensure that the clay had a moisture content slightly wet of optimum and the plastic limit, and would fail in a brittle manner when sheared. The moisture content of the clay used in each experiment, measured from an average of 6 samples during each experiment setup, are detailed in Table 7.5.

Table 7.5. Details of the first-time failure (FTF) experiments conducted

Test no.	Backfill	Voltage threshold (V)	Clay moisture content (%)	Displacement function
FTF-1	LSG	0.25 and 0.1	18.6	1
FTF-2	LSG	0.25 and 0.1	17.4	2
FTF-3	LSG	0.25 and 0.1	19.9	3
FTF-4	LBS	0.25 and 0.1	18.8	3
FTF-5	GG	0.25 and 0.1	16.6	3

The column of clay was compacted first in the bottom box in layers using vibration from a breaker-hammer with a square foot (16 cm x 16 cm). The top box was subsequently placed on top of the bottom box and the fill was compacted through its central column using the same method. In Test 1 the fill column was compacted in 5 layers in each block, each using 1 minute of vibration. It became apparent during excavation of this test that this method of compaction left numerous voids (these voids became filled with bentonite-grout after the SAA installation; this is described later in Section 7.3.1). Therefore in Test 2, the fill column was compacted in 10 layers in each block, each using 2.5 minutes of vibration; this method resulted in successful compaction with no noticeable voids during excavation. In Tests 3 and 4 the compaction effort required was less due to the material being less stiff (higher moisture content); in these tests 2 minutes of vibration were required for each layer. Test 5 used the same compaction method as Test 2.

Through the central column (vertically through both boxes) two 60 mm diameter holes were subsequently hand augered adjacent to each other (as can be seen in Figures 7.3 and 7.5). Inside one hole a small diameter active waveguide was installed. The active waveguide comprised a 22 mm diameter, 1.8 m long steel tube with 2 mm wall thickness. The annulus around the waveguide was backfilled with granular soil; compacted in 0.25 m high lifts using an 8 mm diameter rebar rod. The waveguide protruded 0.4 m above the top of the box where two Slope ALARMS monitoring systems were coupled to monitor AE generated by the active waveguide. In the second hole a SAA with 0.2 m gauge lengths (total active length of 1.6m) was installed. The bottom SAA MEMS sensor was positioned at a height of 0.1 m above the base of the soil column. The SAA was installed

inside PVC access casing and grouted in place; relative proportions of the bentonite-grout mix in Tests 2 to 5 were 1, 0.17 and 0.07 for water, cement and bentonite respectively. Note that the bentonite-grout mix used in Test 1 was stiffer and had relative mix proportions of 1, 0.19 and 0.085 for water, cement and bentonite respectively. The bentonite-grout mix was refined after Test 1. After each test setup, the grout was left for 4 days to harden prior to test initiation. The SAA provided for continuous subsurface deformation measurements representative of those the active waveguide would experience, and therefore allowed accurate relationships to be made between measured AE and the deformation behaviour. A LVDT (with accuracy greater than +/- 0.1%) was also installed at the rear of the top box to measure horizontal movement of the block; to compare movement of the block with the movement applied by the loading ram and with movement measured within the SAA. Load applied to the ram was also measured using a load cell (with accuracy greater than +/- 0.2%) throughout the experiments.

The author designed the experiment to ensure the sliding mass travelled 50 mm in each test, which required a setup protocol to minimise extension of the wire rope during the tests. Before each test, 1 kN of tension was initially applied, and then a movement rate of 0.1 mm/min was applied until the LVDT detected movement, at which point movement was ceased. After this initial box movement the test was in the start position and the displacement-time function (Tables 7.2 to 7.4) was then applied to the top box. The initial horizontal box movement was 5 mm in Test 1, which demonstrated that when using this setup protocol and after 1 mm of box movement, 95% of the subsequent ram displacement was transferred to the top box and not taken up by extension of the wire rope. Therefore, 1 mm initial displacement was applied during setup of Tests 2 to 5, and ram displacements of >53 mm were applied in each test (shown in Tables 7.2 to 7.4) to ensure the sliding mass travelled 50 mm. Note that the LVDT and SAA measured the actual movement of the top box and the soil column respectively. Figure 7.6a shows a photograph of the test apparatus at the start of a test (t = 0) and Figure 7.6b shows the test apparatus at the end of a test (end of stage 8), after 50 mm of movement. At the end of each test the soil column was excavated and the instruments were removed, prior to setup of the subsequent test.

Two AE measurement systems were used in each test, one set at a voltage threshold level of 0.1V and the other at 0.25V; to investigate the influence of voltage threshold level on the measured AE. AE was logged at 5-second intervals, which were subsequently converted to equivalent RDC/hour AE rate values. The SAA logged at 30-second intervals.

At the end of each test the loading ram was moved downwards to remove tension in the wire rope. The top box was lifted approximately 2 cm upwards, using the crane/gantry,

and moved 50 mm backwards into the start position, then lowered back onto the bottom box. The central column was excavated; both the instrumentation and the soil column were removed. This process was performed at the end of each test prior to the setup of each subsequent test.

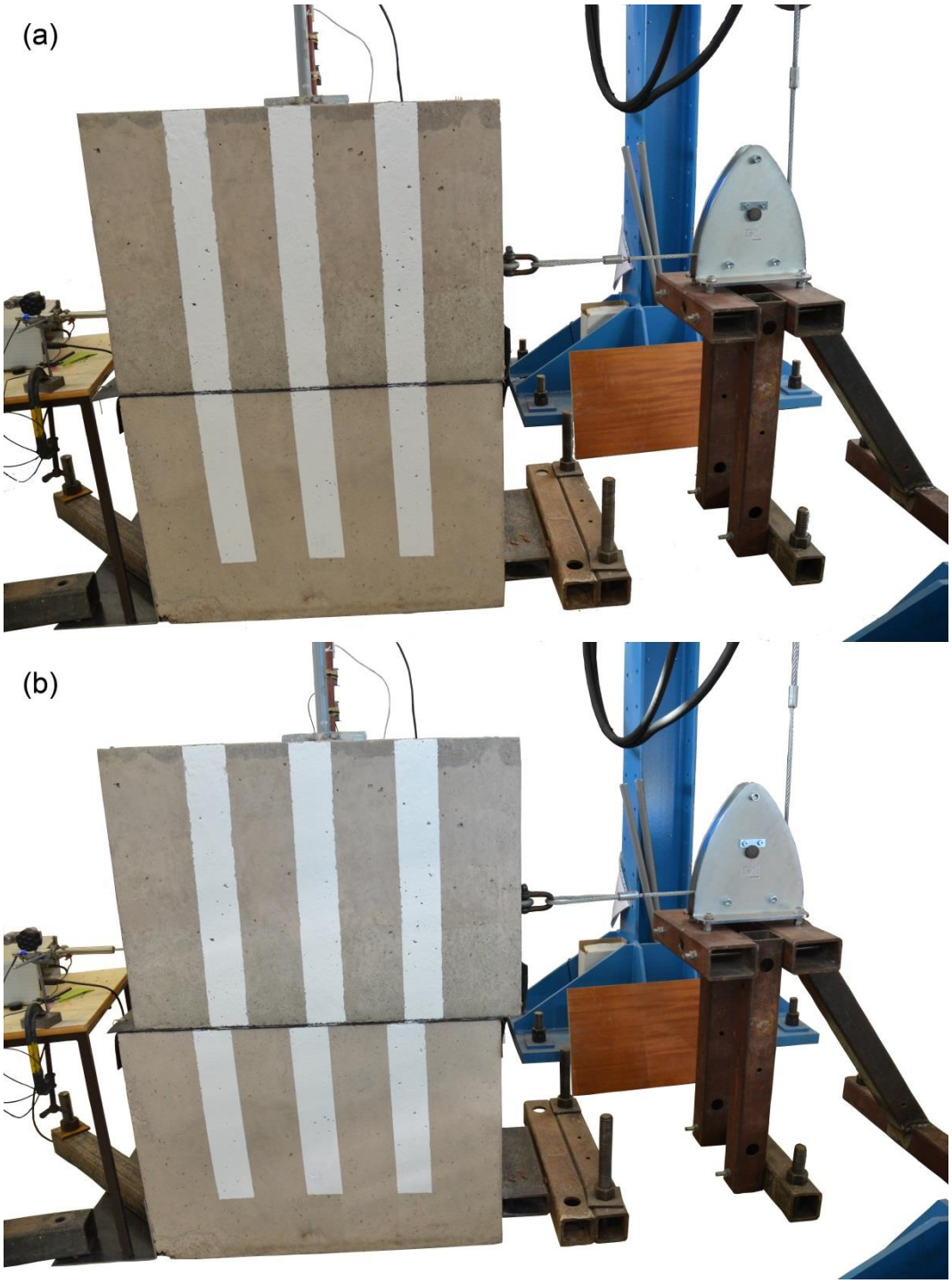

Figure 7.6. Photographs of the first-time failure experiment: (a) at the start position (i.e. t = 0); and (b) at the final position (i.e. at the end of stage 8), after 50 mm of relative horizontal movement

Three granular backfill materials were employed in this experimental programme in order to investigate the influence of their properties on the AE rates generated from the active

waveguide system. The backfill materials were limestone gravel (LSG), Leighton Buzzard sand (LBS), and granite gravel (GG), photographs of which are shown in Figure 7.7. Table 7.5 details which backfill materials were employed in each test. Note that the Leighton Buzzard sand and granite gravel were both used as backfill in the active waveguide physical model tests (Chapter 6). The granite gravel was referred to as angular granite gravel aggregate in Chapter 6; it is referred to as granite gravel here. Figure 7.7 shows the particle size distributions of the three soils. Table 7.6 provides a comparison of the material properties, which includes particle size, particle shape and backfill packing properties. The coefficient of uniformity, C_u, was determined using Equation 7.1 and the compacted void ratio, e, using Equation 7.2.

$$\text{Coefficient of uniformity, } C_u = \frac{d_{60}}{d_{10}} \quad \textbf{(7.1)}$$

$$\text{Void ratio, } e = \left(\frac{\rho_s}{\rho_d}\right) - 1 \quad \textbf{(7.2)}$$

Where ρ_s is particle density, ρ_d is compacted dry density, d_{60} is the particle size below which 60% of the material by mass is finer, and similarly d_{10} is the particle size below which 10% of the material by mass is finer.

Particle shape parameters, namely roundness, sphericity, and regularity, were determined using a selection of 2-dimensional microscopic images (Figure 7.9) and applying the method detailed in Figure 7.10. Roundness is a measure of angularity and is quantified as the average radius of curvature of particle surface features relative to the radius of the maximum sphere that can be inscribed in the particle. Sphericity is a measure of particle ellipticity or platiness and is quantified as the radius ratio between the largest inscribed and the smallest circumscribing sphere. Regularity is the mean of roundness and sphericity (Krumbein & Sloss 1963; Santamaerina & Cho 2004; Cho *et al.* 2006; Cavarretta *et al.* 2010; Siang *et al.* 2012). The microscopic images (illustration in Figure 7.9) were imported to scale in AutoCAD and, using the method detailed in Figure 7.10; circles were fit manually to each particle and feature (Appendix A4). This resulted in the properties detailed in Table 7.6. Particle roughness has not been considered here due to the labour/computationally intensive process required to quantify particle surface roughness parameters (e.g. as described in Cavarretta *et al.* 2010). Particle surface roughness is expected to have influence on AE generation, but is out of scope of this study and is an area for future research.

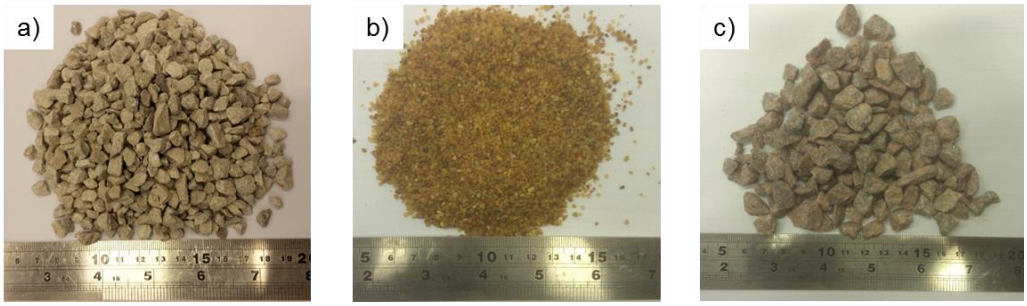

Figure 7.7. Photographs of backfill materials employed in the first-time failure experiments: a) LSG; b) LBS; and c) GG

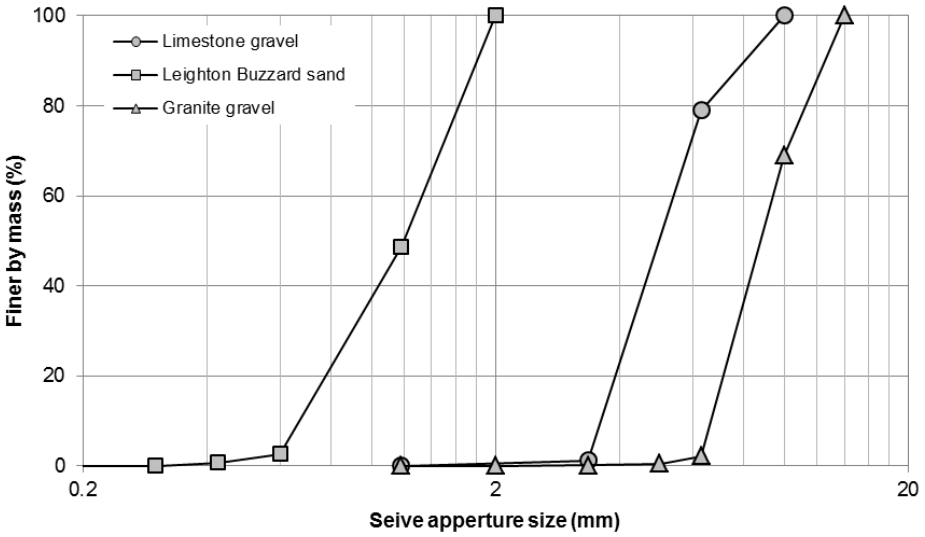

Figure 7.8. Particle size distributions of backfill materials employed in the first-time failure experiments

Table 7.6. Particle size, particle shape and packing properties of the backfills examined in the first-time failure experiments

	Particle size		Particle shape			Packing		
Description	Size range (mm)	Coefficient of uniformity	Roundness	Sphericity	Regularity	Particle density (Mg/m^3)	Dry density (Mg/m^3)	Void ratio
LSG	3.0-8.0	1.51	0.3-0.5	0.5-0.8	0.4-0.6	2.64	1.53	0.730
LBS	0.3-1.8	1.93	0.2-0.5	0.4-0.8	0.3-0.6	2.67	1.70	0.567
GG	5.0-12.0	1.41	0.1-0.3	0.3-0.8	0.2-0.6	2.68	1.58	0.699

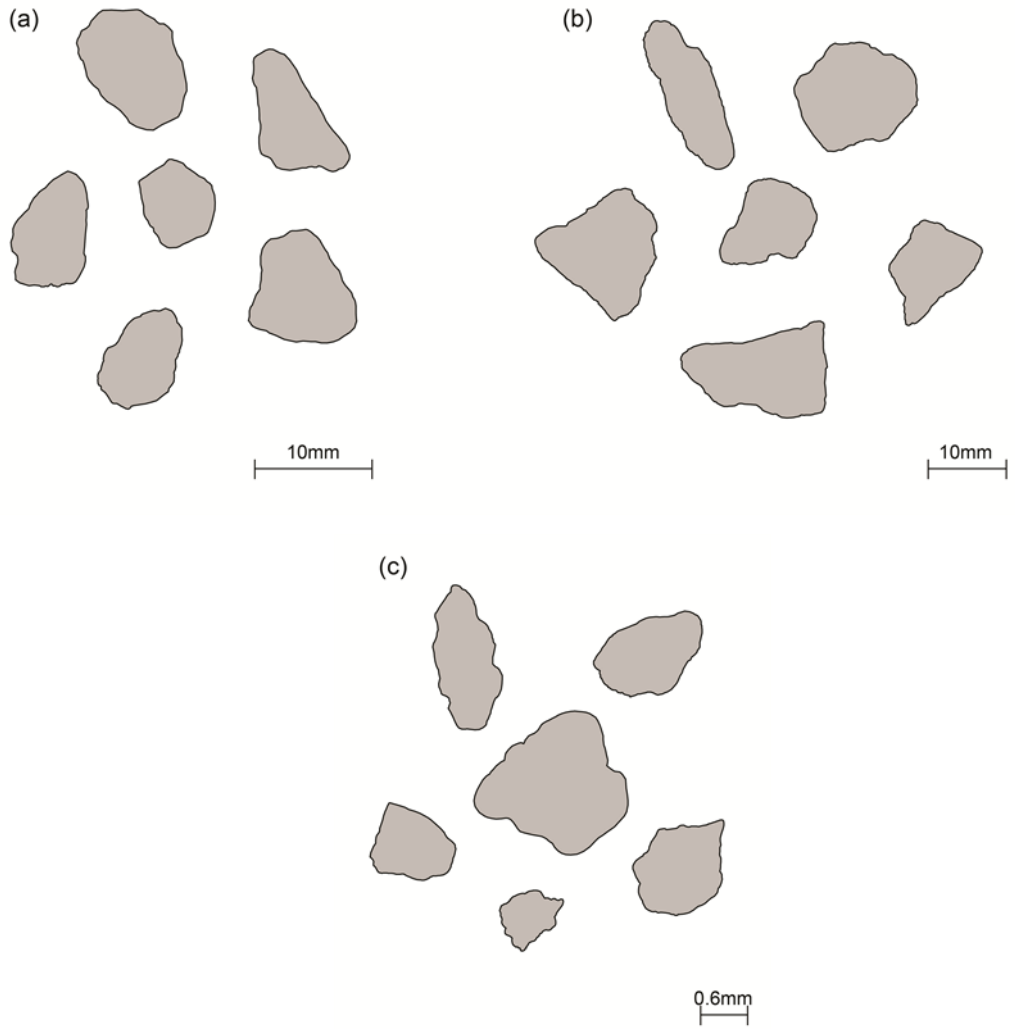

Figure 7.9. Illustrations of selected backfill particles used in the first-time failure tests: a) LSG; b) GG; and c) LBS

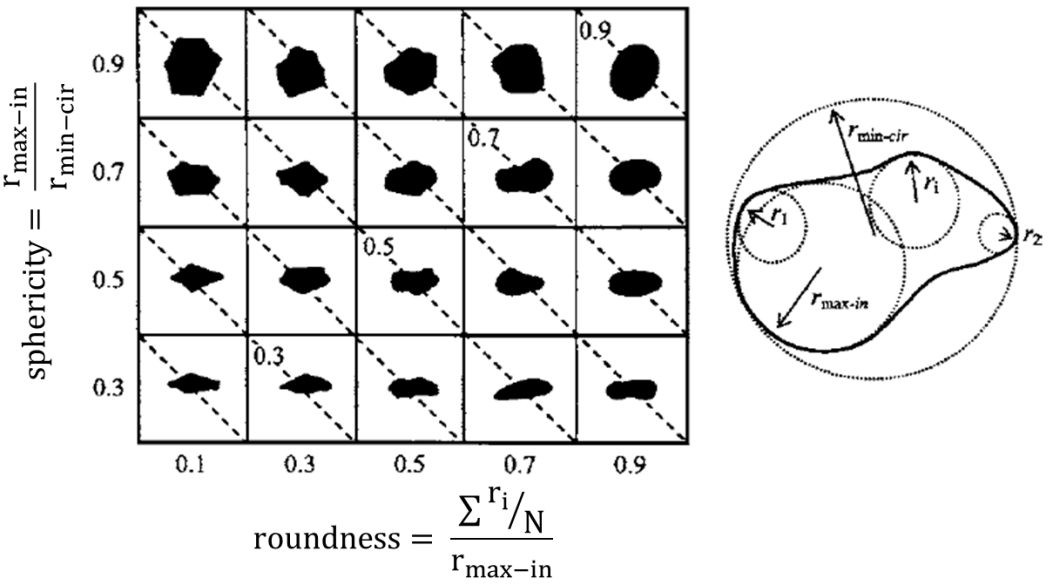

Figure 7.10. Particle shape determination modified after Krumbein & Sloss (1963) and Cho *et al.* (2006). Diagonal dotted lines correspond to constant particle regularity = (roundness + sphericity)/2

7.3. Results and analysis

7.3.1. Deformation and load behaviour

Figures 7.11 and 7.12 show the displacement vs. time measurements recorded from Test 3 by the loading ram, LVDT at the rear of the top block, and the SAA MEMS sensor located immediately above the shear surface (comparable behaviour was measured in each test). A small magnitude of deformation (<3 mm) was taken up by extension in the wire rope throughout each test, which is evident from the difference between the ram position and LVDT displacement throughout the experiments. There was also a small difference (<1 mm) between LVDT measured block displacement and SAA measured horizontal displacement (above the shear surface) during the experiments; this difference was developed during stages 1 and 2 prior to shear surface formation in the fill column (Figure 7.12).

Figure 7.13 shows shear box height vs. resultant horizontal SAA deformation measurements, presented at the end of each stage, experienced by the fill column in Test 3 (comparable behaviour was measured in each test). Height is relative to the base of the bottom block. The first MEMS sensor measurements begin at 0.1 m height and the subsequent MEMS sensors provide measurements at 0.2 m height increments. The interface between the two blocks is at 0.7 m height, which also corresponds to the location of a MEMS sensor. The developed shear surface, identifiable using the SAA measurements, corresponds to this height of 0.7 m. The apparent shear zone is 0.4 m thick (0.2 m above and below the shear surface, between heights of 0.5 m and 0.9 m); however, this is because the adjacent MEMS sensors above and below the shear surface are at a distance of 0.2 m away. In actual fact the real shear zone was significantly thinner and more localised at a height of 0.7 m; this was confirmed by visual inspection during forensic dismantling of each test.

From Figure 7.13 it is clear that no shear surface developed during stage 1; the measurements show the SAA rotating about its base only during this stage (i.e. no relative shear movement between MEMS sensors is identifiable). The load vs. displacement behaviour shown in Figure 7.14 supports this. In each test elastic load-deformation behaviour occurs until 2.3-2.9 mm (stage 2) of deformation is reached, at which point a transition to plastic deformation occurs (i.e. the shear surface forms). This transition is smooth with no significant drop in load in Tests 1, 2 and 5. However, in Tests 3 and 4 a drop in load is identifiable in the load vs. displacement curve. Tests 3 and 4 had the highest moisture contents and a lower degree of compaction (lower stiffness) than Tests 2 and 5. Tests 2 and 5 had the lowest moisture contents and the highest degree of compaction by contrast (highest stiffness). Test 2 had comparable load vs. displacement

behaviour with Test 5, and Test 3 had comparable behaviour with Test 4. This is because their soil columns were comparable; comparable moisture contents and degrees of compaction. Note that the column of active waveguide backfill also has influence on the load vs. displacement behaviour. However, the same active waveguide backfill was installed in Tests 1, 2 and 3, and to the same degree of compaction, and the load vs. displacement behaviour was significantly different between each of these tests, which demonstrates that the column of clay had the greatest influence on the load vs. displacement behaviour. Test 1 experienced noticeably different behaviour to the other tests. The relatively poor degree of compaction achieved in Test 1 left numerous voids, which were subsequently filled with bentonite-grout that infiltrated upon installation of the SAA. This modified the behaviour of the fill column and increased its strength and stiffness, which is evidenced by its load vs. displacement curve. In addition, 5 mm of initial displacement was applied to the top block in Test 1 prior to the initiation of the displacement function. This resulted in larger reactions on the waveguide from the host soil column throughout the test and therefore larger applied loads were necessary to displace the block.

After stage 5, noticeably greater magnitudes of horizontal deformation occur below the shear surface (Figure 7.13). This was due to the SAA being pulled horizontally through the bentonite-grout/clay in the bottom box as a result of the lateral loading applied from the top block, which resulted in behaviour comparable to a laterally loaded 'flexible' pile. This mechanism is likely to have begun earlier, in response to smaller magnitudes of movement, in the active waveguide due to its significantly greater stiffness.

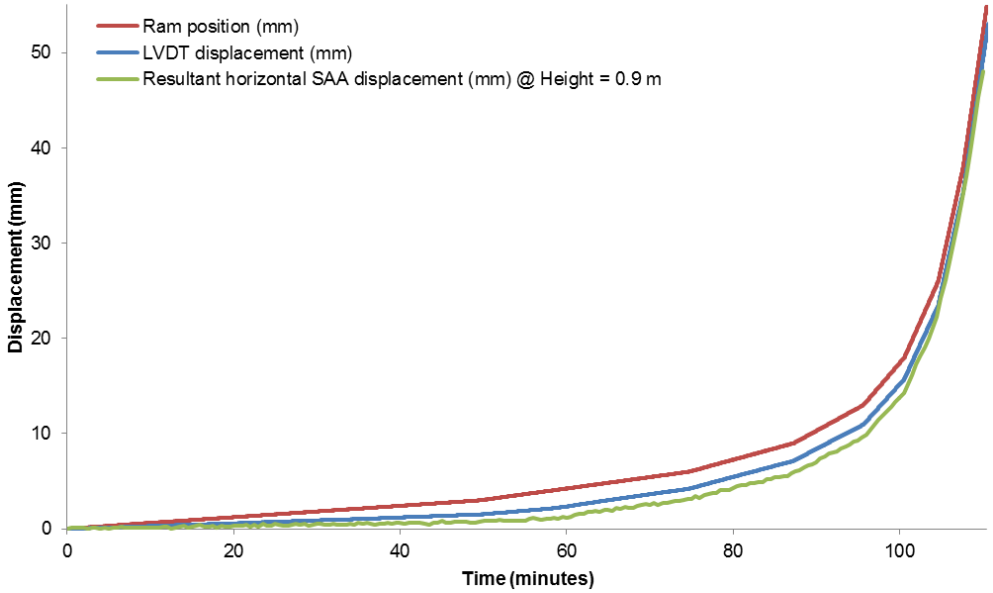

Figure 7.11. Ram position, LVDT displacement and resultant horizontal SAA displacement vs. time from Test 3

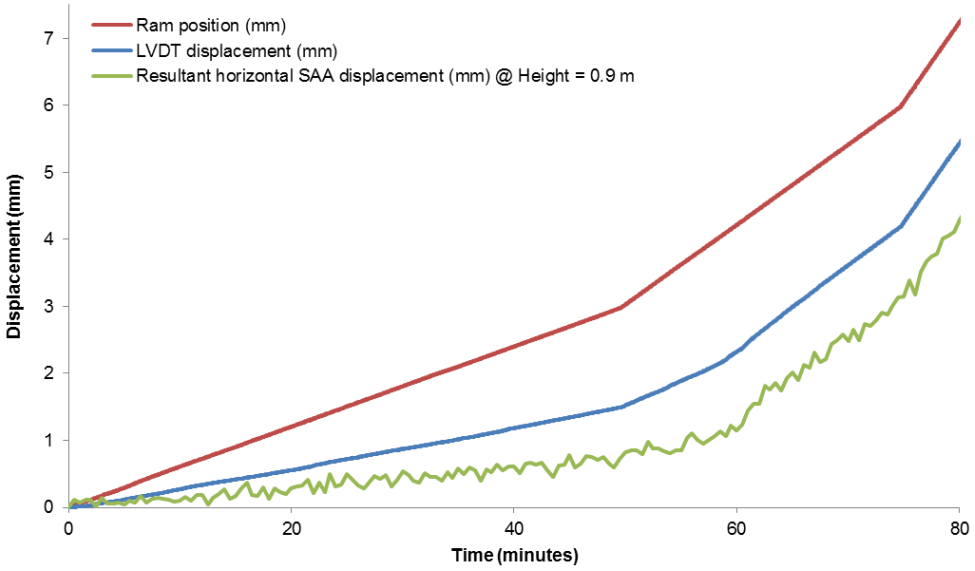

Figure 7.12. Ram position, LVDT displacement and resultant horizontal SAA displacement vs. time during the first 80 minutes of Test 3

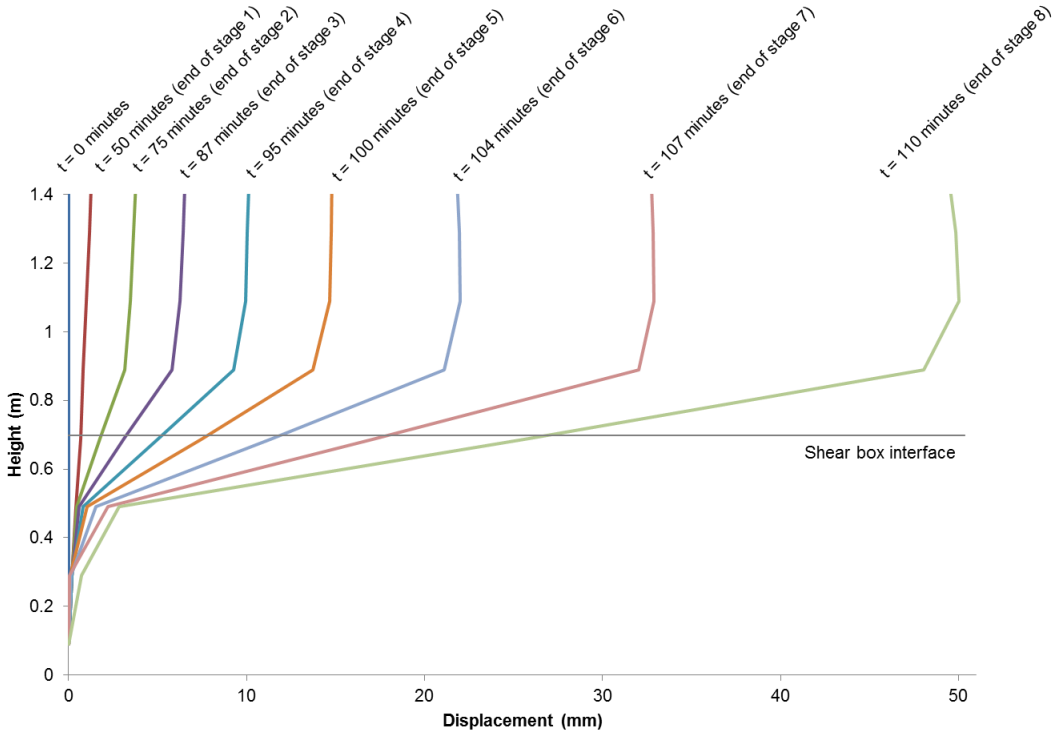

Figure 7.13. SAA height vs. resultant horizontal deformation from Test 3; data are presented at the end of each stage

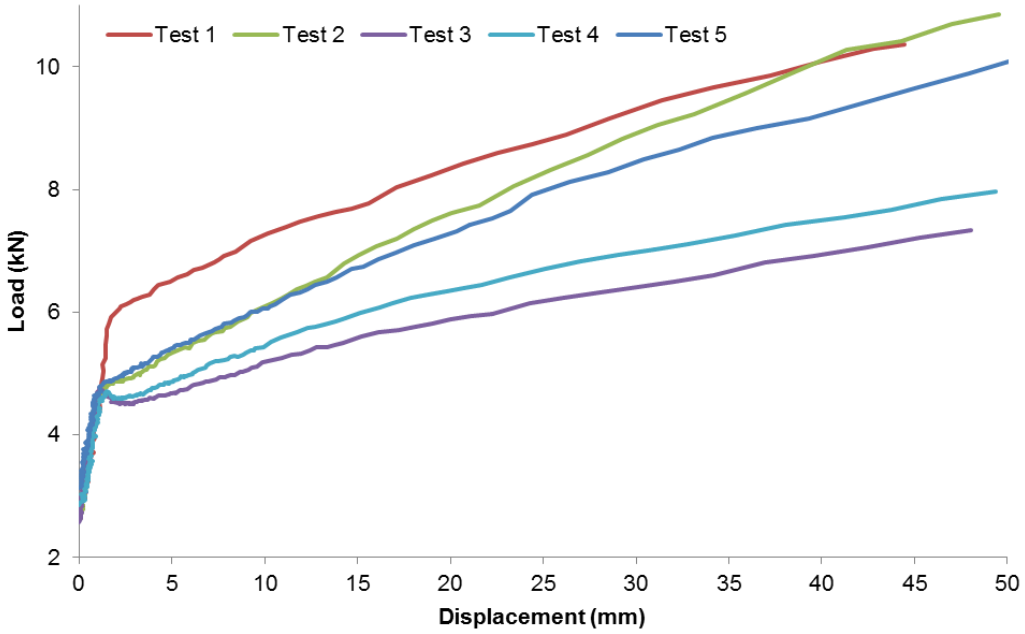

Figure 7.14. Load vs. displacement data for each first-time failure test. Note that displacement is taken from the SAA MEMS sensor immediately above the shear surface (at a height of 0.9 m)

7.3.2. AE and deformation behaviour

7.3.2.1. Tests 1 to 3: limestone gravel backfill and repeatability

Figure 7.15 presents results from Test 3 (limestone gravel backfill) from the AE measurement system set at 0.25V threshold level. It is clear that the cumulative RDC vs. time relationship is proportional to the displacement vs. time relationship, and the AE rate vs. time relationship is proportional to the velocity vs. time relationship. Note that the displacement and velocity measurements were taken from the SAA MEMS sensor at 0.9 m height in the shear box (i.e. immediately above the shear surface). Velocity smoothing was done using 2-minute moving average values; using the average of the velocity over the minute preceding and minute succeeding each measurement. The recorded velocity briefly reduced at the end of each stage before entering the subsequent stage; this same behaviour is identifiable in the AE rate measurements.

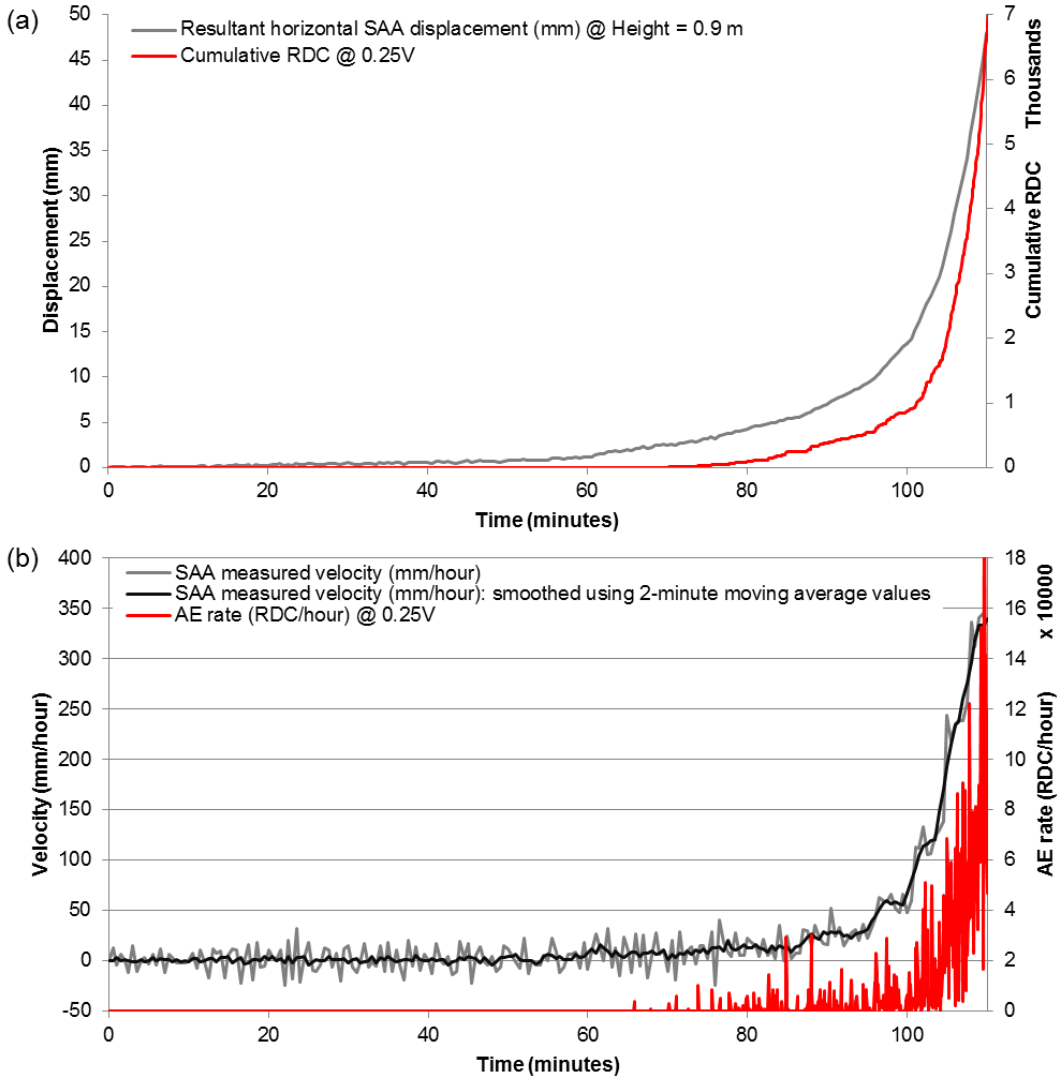

Figure 7.15. Time series of measurements from first-time failure Test 3 at 0.25V threshold level: a) displacement and cumulative RDC vs. time; and b) SAA velocity and AE rate vs. time

Figure 7.16 shows the same time series measurements as those in Figure 7.15, but focuses on the first 80 minutes of the test (up to half way through stage 3). AE detection began after 1.9 mm of deformation and during stage 2, corresponding to the timing of shear surface development, as is identifiable in the SAA height vs. deformation measurements in Figure 7.13. AE detection began after this magnitude of deformation because a shear surface began to develop in the clay column during stage 2, which caused shearing in the active waveguide, generating detectable AE.

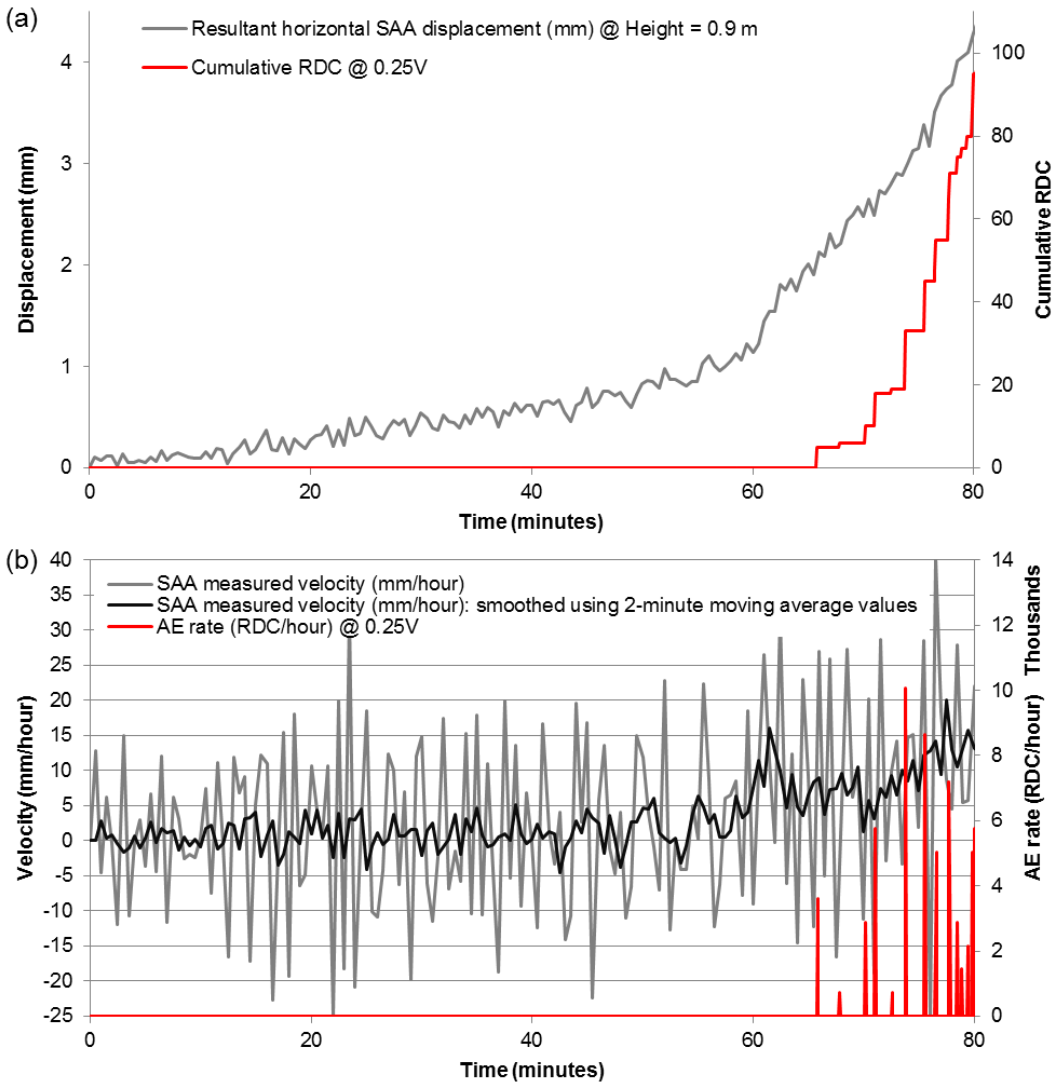

Figure 7.16. .Time series of measurements from the first 80 minutes of first-time failure Test 3 at 0.25V threshold level: a) displacement and cumulative RDC vs. time; and b) SAA velocity and AE rate vs. time

Figure 7.17 shows the AE rate vs. SAA measured velocity relationships defined from Tests 1 to 3 (limestone gravel backfill) for both AE measurement systems (0.1V and 0.25V threshold levels). Each relationship demonstrates strong positive correlation. Although the relationships are not linear, linear trend lines have been plotted through the relationships in Figure 7.17 to define simple measures of the various relationships. The linear gradients plotted through the relationships defined from the 0.25V threshold level results show highly comparable behaviour; the gradients varied from 145 to 158. This demonstrates that AE rate-velocity behaviour experienced by an active waveguide is repeatable; confirming that definition of an empirical AE rate-velocity relationship is attainable. This also demonstrates repeatability of the first-time slope failure experiment (i.e. test-retest reliability). The AE measurement system set at 0.1V threshold level detected greater magnitudes of AE rates, as would be expected due to its greater sensitivity (i.e. lower voltage threshold level). The greater degree of variability in the AE

rate-velocity relationships determined at the 0.1V threshold level (gradients from 507 to 752) is due to the greater sensitivity of the AE measurement system; greater sensitivity to both lower amplitude backfill-generated AE events and background noise.

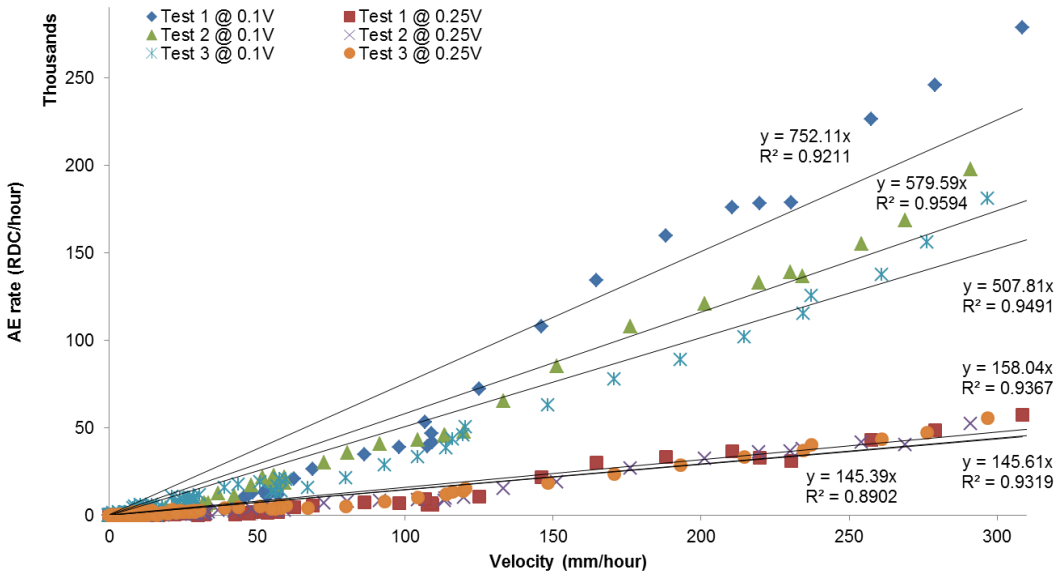

Figure 7.17. Comparison of AE rate-velocity relationships determined from first-time failure Tests 1, 2 and 3 for both 0.1V and 0.25V threshold levels

Figure 7.18 focuses on the AE rate vs. SAA measured velocity relationships defined from Tests 1 to 3 (limestone gravel backfill) for the AE measurement system set at 0.25V threshold level. The results from the three tests overlap, demonstrating that AE generated from active waveguides in response to applied deformation behaviour is highly repeatable. A 3rd order polynomial fits all three relationships almost perfectly (R^2 value of 0.99). A transition in behaviour occurs during stages 5 and 6; causing the gradient of this relationship to increase. As the sliding mass begins to move, granular shearing takes place within the active waveguide at the shear surface. With further displacement, as the waveguide resists shear and bending, the backfill deforms around the waveguide. Analogous to a laterally loaded pile, reactions from the host soil cause the pressures along the active waveguide to increase. Reactions from both the host soil and the waveguide cause the confining pressures in the backfill to increase. Both the volume of backfill being deformed and the confining pressures in the backfill increase with displacement. This behaviour causes the AE rate-velocity relationship gradient to increase.

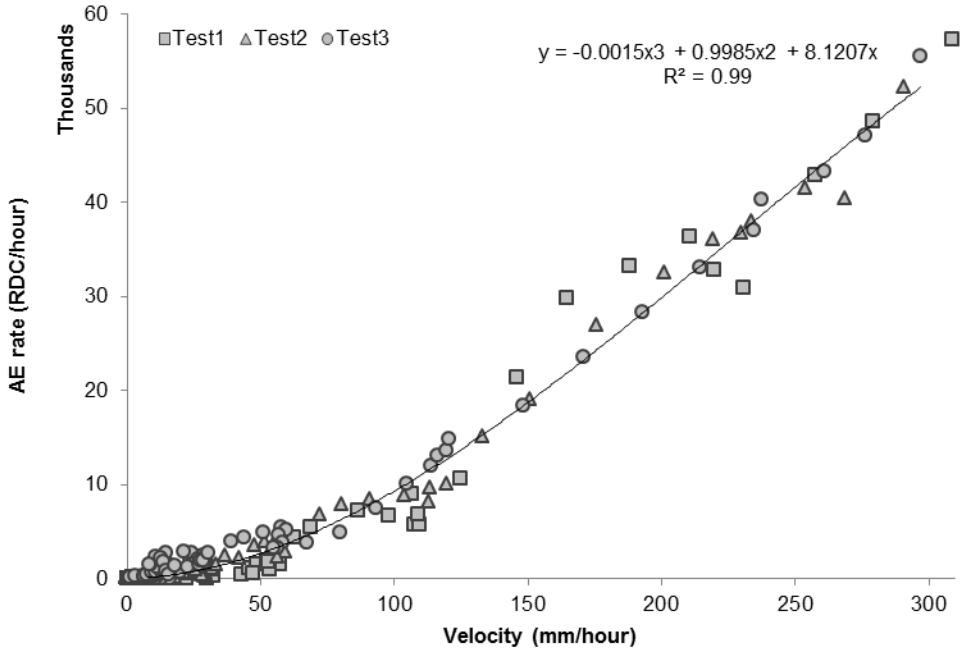

Figure 7.18. Comparison of AE rate-velocity relationships determined from first-time failure Tests 1, 2 and 3 for the 0.25V threshold level

7.3.2.2. Tests 1 to 5: backfill material comparisons

Figure 7.19 presents results from Test 3 (limestone gravel backfill), Test 4 (Leighton Buzzard sand backfill) and Test 5 (granite gravel backfill) from the AE measurement system set at 0.25V threshold level. Tabulated results from Test 5 can be found in Appendix A4. Figure 7.20 presents results from Test 3, Test 4 and Test 5 from the AE measurement system set at 0.1V threshold level. It is clear that the AE rate vs. time relationship is proportional to the velocity vs. time relationship in each test; with each backfill and both voltage threshold levels. All results exhibit a response to sudden changes in velocity (e.g. the brief reductions in velocity prior to the transition into subsequent test stages). Both the Leighton Buzzard sand and granite gravel backfill generated significantly greater AE than the limestone gravel backfill, by more than an order of magnitude. The limestone gravel also generated the greatest variability in AE rates, as is evident in Figures 7.19a and 7.20a and discussed further in Section 7.3.2.3.

AE was detected earliest in Test 5, with granite gravel backfill and the AE measurement system set at 0.1V threshold level, after 0.81 mm of deformation; corresponding to the onset of shear surface development within the fill column. Figure 7.21 shows results from the AE measurement system set at 0.1V from the first 80 minutes of Test 5, which highlights the significant levels of AE detected after 0.81 mm of deformation. The magnitude of AE rates detected during shear surface development in Test 5 with granite gravel backfill (Figure 7.21) are significantly greater than those detected in Test 3 with the limestone gravel backfill (Figure 7.16). Table 7.7 shows the magnitudes of

deformation experienced prior to AE detection in Tests 3, 4 and 5. Note that comparable deformation magnitudes were experienced in Tests 1, 2 and 3. AE detection occurred earliest with the granite gravel backfill, then with the Leighton Buzzard sand, and lastly with the limestone gravel. In all tests a reduced voltage threshold level, from 0.25V to 0.1V, resulted in marginally earlier AE detection.

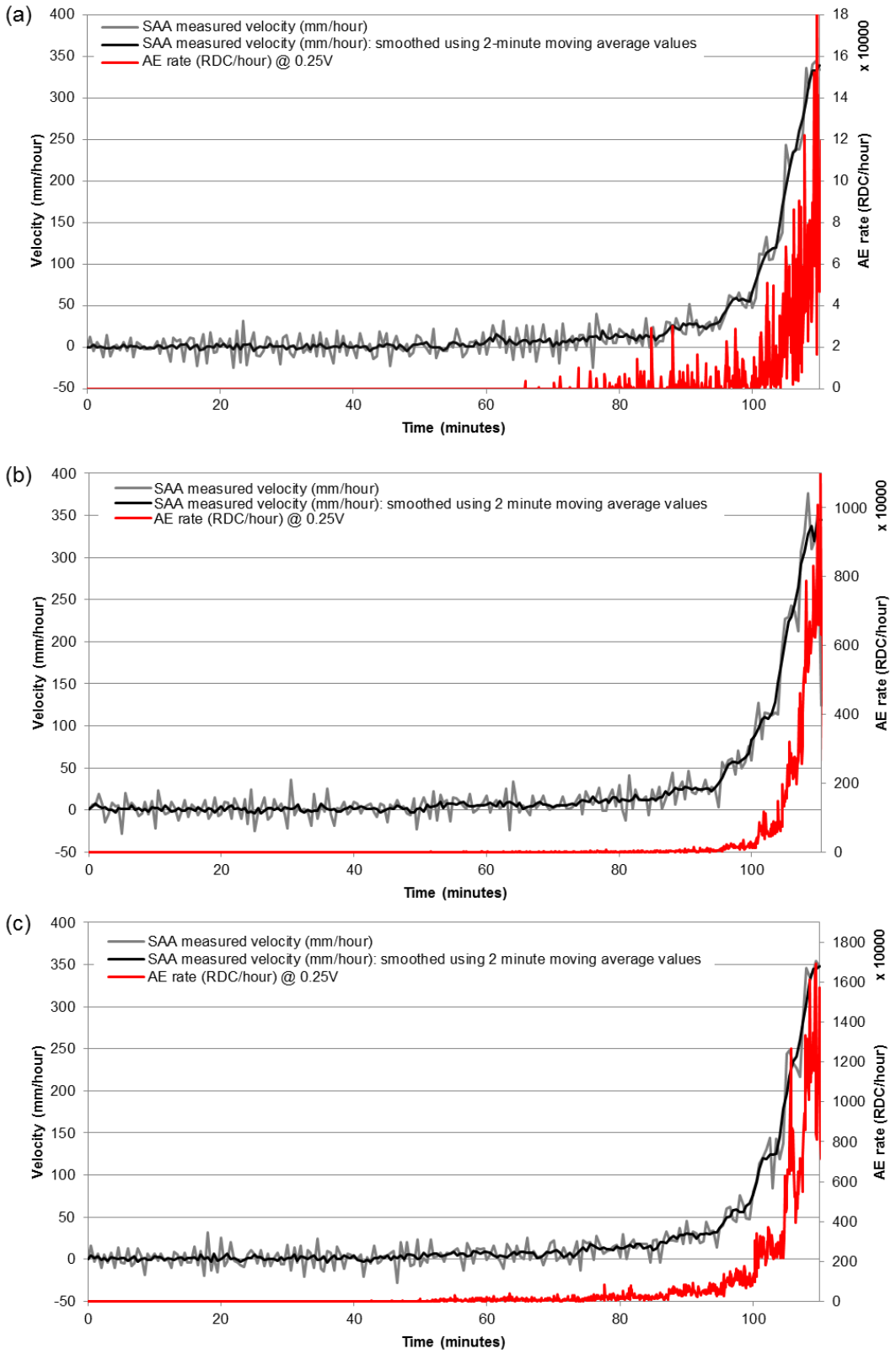

Figure 7.19. AE rate and velocity vs. time from first-time failure Tests 3, 4 and 5 at 0.25V threshold level: a) LSG; b) LBS; and c) GG. Note the different AE rate axis scales used

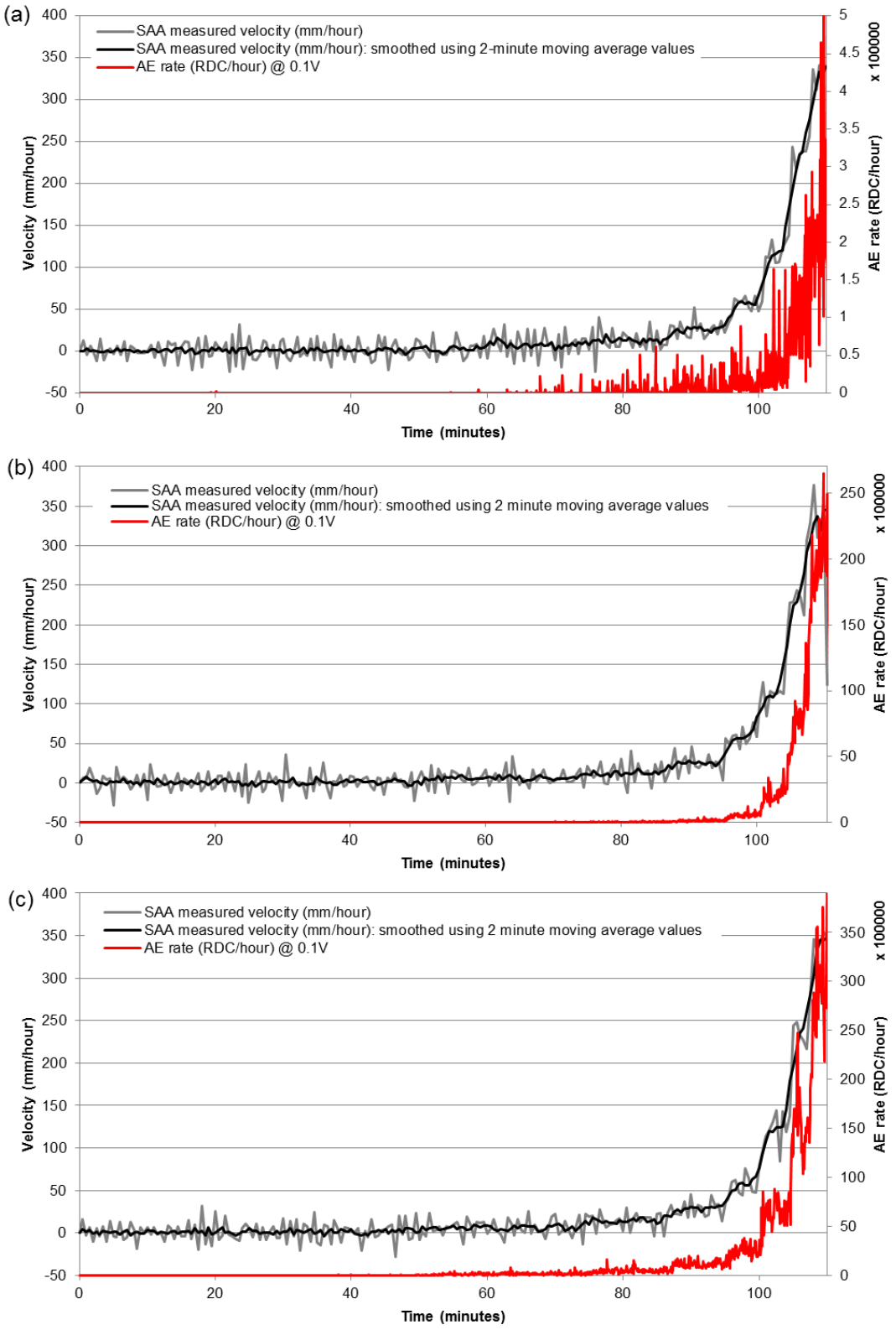

Figure 7.20. AE rate and velocity vs. time from first-time failure Tests 3, 4 and 5 at 0.1V threshold level: a) LSG; b) LBS; and c) GG. Note the different AE rate axis scales used

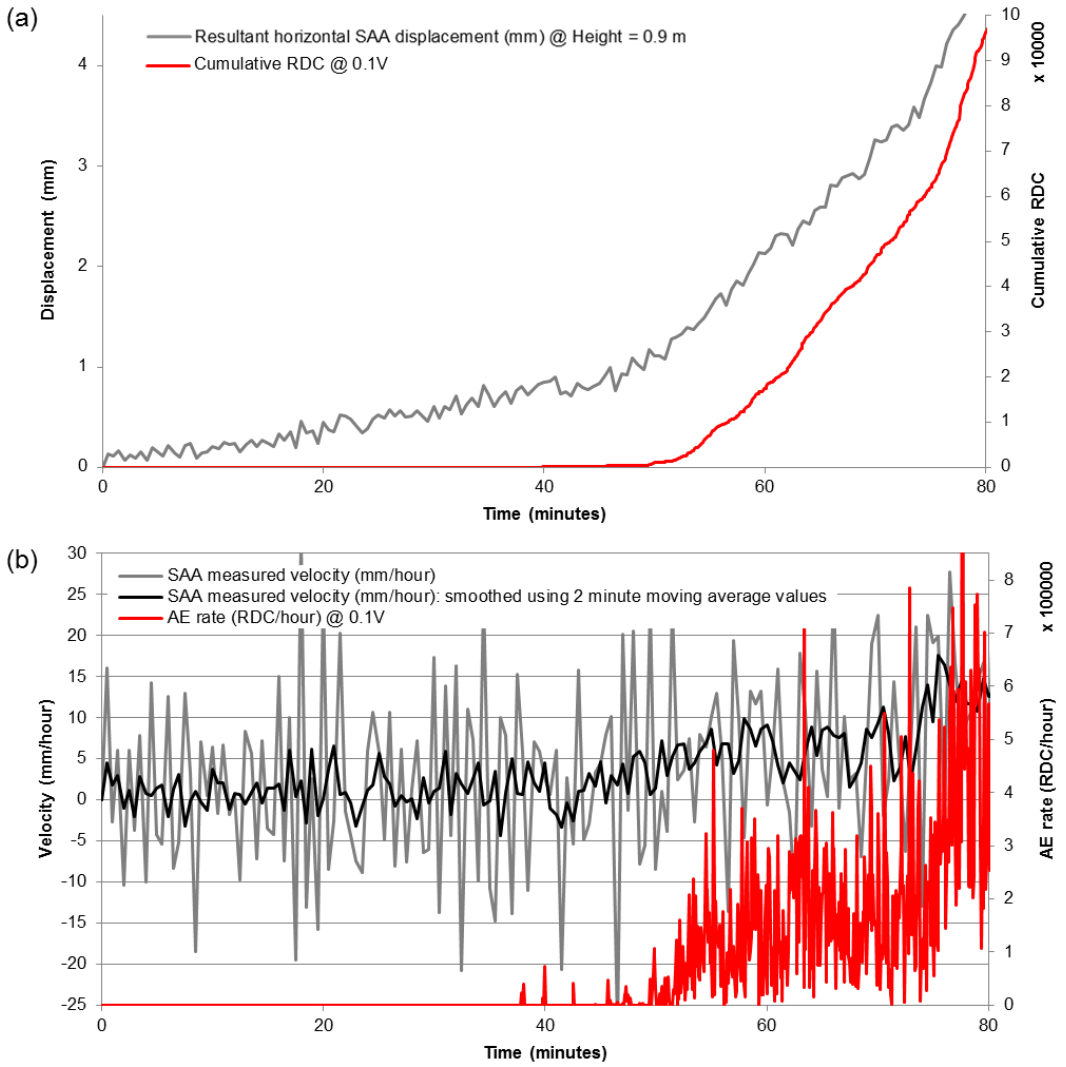

Figure 7.21. Time series of measurements from the first 80 minutes of first-time failure Test 5 at 0.1V threshold level: a) displacement and cumulative RDC vs. time; and b) velocity and AE rate vs. time

Table 7.7. SAA measured resultant horizontal deformation prior to AE detection for each backfill type and voltage threshold level

SAA measured resultant horizontal deformation prior to AE detection (mm)			
	Backfill type		
Voltage threshold level	**LSG**	**LBS**	**GG**
0.1V	1.13	0.94	0.81
0.25V	1.90	0.96	0.84

Figures 7.22 and 7.23 show the AE rate vs. SAA measured velocity relationships defined from Tests 1 to 5; for each backfill material and for both voltage threshold levels. Each relationship demonstrates strong positive correlation. Note that the relationships defined for the limestone gravel use results from Tests 1 to 3, which are shown in detail in Figures 7.17 and 7.18. 3rd order polynomials have successfully been used to define the empirical AE rate-velocity relationships, resulting in R^2 values of greater than 0.99 in

each case, except for the limestone gravel relationship at a 0.1V threshold level that resulted in a marginally weaker correlation with an R^2 value of 0.96.

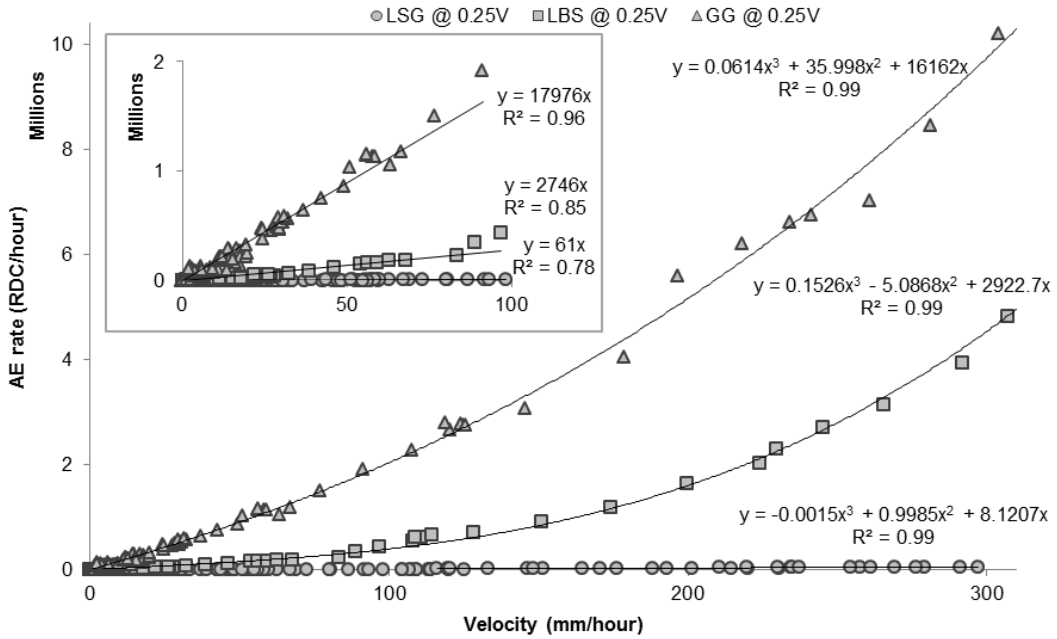

Figure 7.22. Comparison of AE rate-velocity relationships determined from first-time failure experiments on each backfill type for the 0.25V threshold level. The insert shows the AE rate-velocity relationships up to a velocity of 100 mm/hour

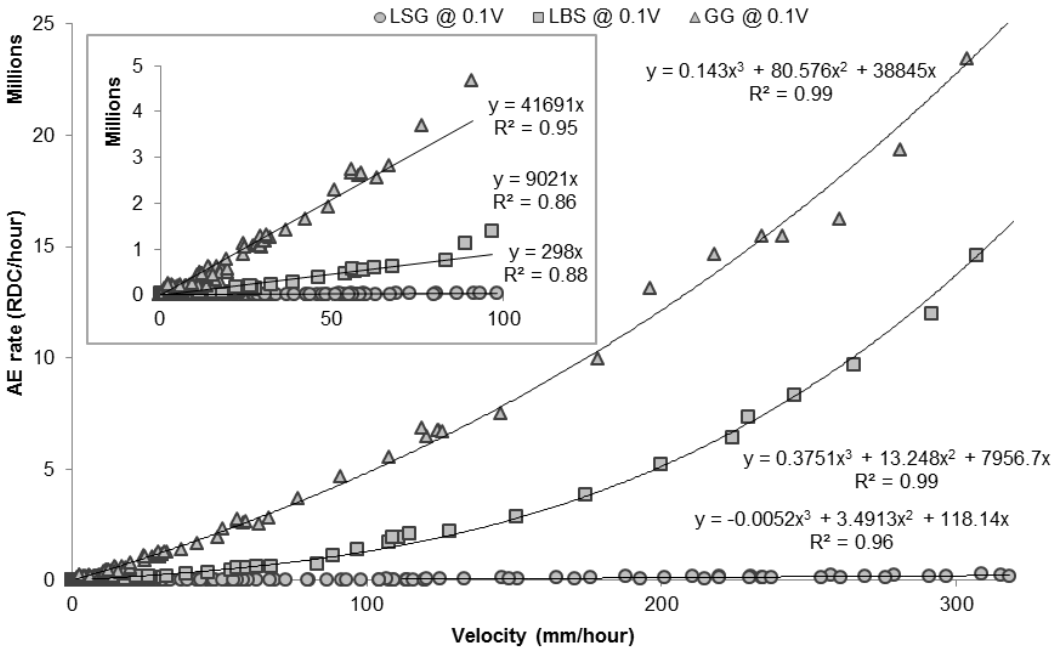

Figure 7.23. Comparison of AE rate-velocity relationships determined from first-time failure experiments on each backfill type for the 0.1V threshold level. The insert shows the AE rate-velocity relationships up to a velocity of 100 mm/hour

The inserts in Figures 7.22 and 7.23 show each of the AE rate vs. SAA measured velocity relationships up to an applied velocity of 100 mm/hour, which can successfully be approximated using linear relationships. The correlation in each linear relationship is very strong, with R^2 values ranging from 0.78 to 0.96, but all are slightly weaker than those determined using the 3rd order polynomials over the full range of applied velocities. AE rate vs. velocity relationships determined from the field measurements (Chapter 5) and active waveguide physical model tests (Chapter 6) were all linear, but were derived from measurements below 100 mm/hour in each case; <0.5 mm/hour in the field and <100 mm/hour in the physical model tests. The correlation is greater in these experiments because the shear mechanism is more realistic and repeatable, and a greater range of velocities have been examined.

The gradients of the linear relationships shown as inserts in Figures 7.22 and 7.23 can be used as a simple measure to compare the AE rate response from each backfill material to an applied velocity. At both voltage threshold levels, the linear AE rate-velocity gradient was an order of magnitude greater for the granite gravel than for the Leighton Buzzard sand. At 0.1V threshold level, the limestone gravel linear AE rate-velocity gradient was an order of magnitude less than that for the Leighton Buzzard sand; at 0.25V the limestone gravel gradient was two orders of magnitude less than that for the Leighton Buzzard sand. Note that the linear AE rate-velocity gradients determined using the active waveguide physical model tests (Chapter 6) were significantly greater than those determined using the first-time slope failure experiment; 1 order of magnitude greater for granite gravel and 2 orders of magnitude greater for the Leighton Buzzard sand. This overestimation in the linear AE rate-velocity gradients determined using the active waveguide physical model tests is because of the reasons outlined in Chapter 6, which include elevated confining pressures and unrepresentative loading mechanisms.

Figure 7.24 provides a comparison of the AE rates generated from each active waveguide backfill material in response to the full range of applied velocities. The curves show a ratio between the AE rates generated by the granite gravel to both the other backfill materials at each voltage threshold level. The Leighton Buzzard sand and limestone gravel are both compared relative to the granite gravel because the granite gravel consistently generated the greatest magnitude of AE rates. The granite gravel generated between 100 and 1960 times greater AE rates than the limestone gravel over the range of applied velocities; the greatest difference was at the lowest velocities (<50 mm/hour). The granite gravel generated between 1.7 and 6 times greater AE rates than the Leighton Buzzard sand over the range of applied velocities.

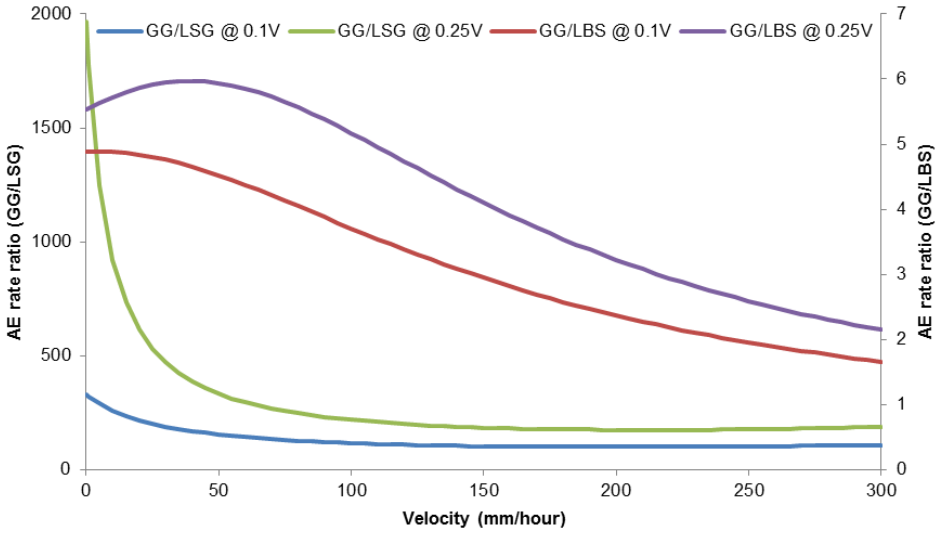

Figure 7.24. Ratio of AE rates generated by the GG backfill to the other backfills at both 0.1V and 0.25V threshold levels vs. applied velocity

Theory states that large angular particles generate AE events with the greatest amplitude and a volume of soil with small particles will generate a greater number of AE events, due to the greater number of particle-particle interactions, but with smaller amplitudes (Koerner *et al.* 1981 and Dixon *et al.* 2003). However, little research has been conducted on the relationship between soil particle shape and the AE it generates. The results from this experimental programme suggest that particles with greater angularity generate a greater number of AE events (i.e. AE rates); the granite gravel had the greatest angularity, and the Leighton Buzzard sand had greater angularity than the limestone gravel. This would be expected due to an increased number of particle surface features at the macroscopic scale generating a greater number of frictional interactions. Particle surface roughness has not been quantified in this study; however, increased roughness would lead to a greater number of particle surface feature interactions at the microscopic scale, and therefore a greater number of AE events (i.e. AE rates). Packing also has a significant influence on the AE rates generated; the limestone gravel had the poorest packing in this series of experiments. Better packing (e.g. reduced void ratio) leads to a greater number of particle-particle contacts, which is of course influenced by particle grading and shape. Particles with more uniform grading (i.e. high coefficients of uniformity) achieve greater density and packing because smaller particles can fill the pore spaces between larger particles, leading to a greater number of particle-particle contacts.

Attenuation of the signal as it propagates from the generation source to the sensor also has influence. Propagation along the waveguide is expected to have little effect on the AE measured from an active waveguide installed through a shallow shear surface, such as the one in this first-time slope failure experiment. However, attenuation is expected to have a significant impact on AE generated from active waveguides installed through a deep

shear surface, due to the greater propagation distance. In this case it is preferable to use backfill with larger angular particles to generate a large number of large amplitude events. Theoretically, well graded angular soils would be used; however, this presents practical issues such as the potential for bridging during installation.

The influence of soil and particle properties on the frequency spectra of the AE generated has been out of scope of this study, which has used an AE measurement system that focuses on the frequency range of 20 to 30 kHz and significantly attenuates any signals outside of this range. Future work will investigate soil generated-AE over a broader frequency range. The differences between the AE rates detected from the backfill materials employed in this study could also be explained by differences in frequency contents of the backfill-generated AE. 20 to 30 kHz is a very narrow frequency band and Koerner *et al.* (1981) show that AEs generated from soils subject to deformation have frequency contents over a wide range, from Hz to 100s kHz, and different soils have different dominant frequencies. In addition, Michlmayr & Or (2014) demonstrate that the dominant frequency response from granular soil subject to deformation can change by more than 10 kHz (the width of the band used in this measurement system) due to, for example, changed particle assemblies, confining pressures and interaction mechanisms (e.g. inter-particle friction and contact stress release).

Figure 7.25 provides a comparison of the AE rates detected at each voltage threshold level, from each backfill material, in response to the full range of applied velocities. The curves show a ratio between the AE rates measured at the 0.1V threshold level to those measured at the 0.25V threshold level. Both the granite gravel and Leighton Buzzard sand measured a relatively consistent ratio across all applied velocities: AE rates detected from the granite gravel at 0.1V were from 2.3 to 2.4 times greater than those detected at 0.25V; and AE rates detected from the Leighton Buzzard sand at 0.1V were from 2.7 to 3.3 times greater than those detected at 0.25V. However, different behaviour was observed from the limestone gravel. At the lowest applied velocities, the AE rates measured at 0.1V were 13.3 times greater than those measured at 0.25V. This ratio reduced rapidly as 50 mm/hour was approached and the ratio eventually became stable at a value of 4.0. This behaviour is partly explained by the greater magnitude of deformation required to initiate detectable AE from the limestone gravel at 0.25V than at 0.1V (0.77 mm greater deformation, as detailed in Table 7.7). The AE rate ratio was consistently greatest from the limestone gravel, while it was consistently the least from the granite gravel. The differences in this ratio between the backfills are explained by differences in the amplitude contents of the generated AE relative to both of the thresholds.

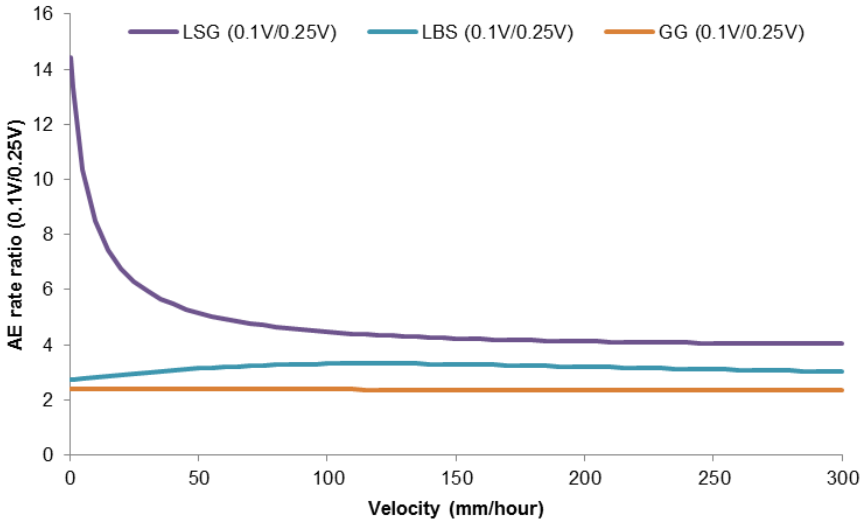

Figure 7.25. Ratio of AE rates measured at 0.1V threshold level to AE rates measured at 0.25V threshold level for each backfill type vs. applied velocity

Figure 7.26 shows the AE rate-displacement and AE rate-load relationships determined from Tests 3, 4 and 5. The shape of the AE rate-displacement and AE rate-load relationships from each test are comparable. AE rates are relatively low until a certain displacement or load, at which point they begin to increase relatively linearly with increasing displacement or load. This transition point corresponds with test stage 6 in each test. The behaviour in Test 5 (granite gravel) is different however, which exhibits obvious periods of elevated AE rates that increase and reduce in cycles, although the overall trend in the relationship is positive. This behaviour is also evident in the time series measurements shown in Figures 7.19 and 7.20. These AE rate cycles are generated by the cycles in measured velocity, which occur during each test stage (i.e. the velocity reduces briefly prior to increasing in the subsequent stage). This behaviour, although not as prominent, can be seen in the AE measurements from the other tests. This demonstrates that the AE rates generated, although increase in a positive manner with increasing displacement and load, are influenced primarily by velocity. This is because an increased rate of deformation generates an increased number of particle-particle/particle-waveguide interactions per unit time, which generates increased AE rates (RDC per unit time); as was hypothesised in the Summary of Chapter 2 (Section 2.5).

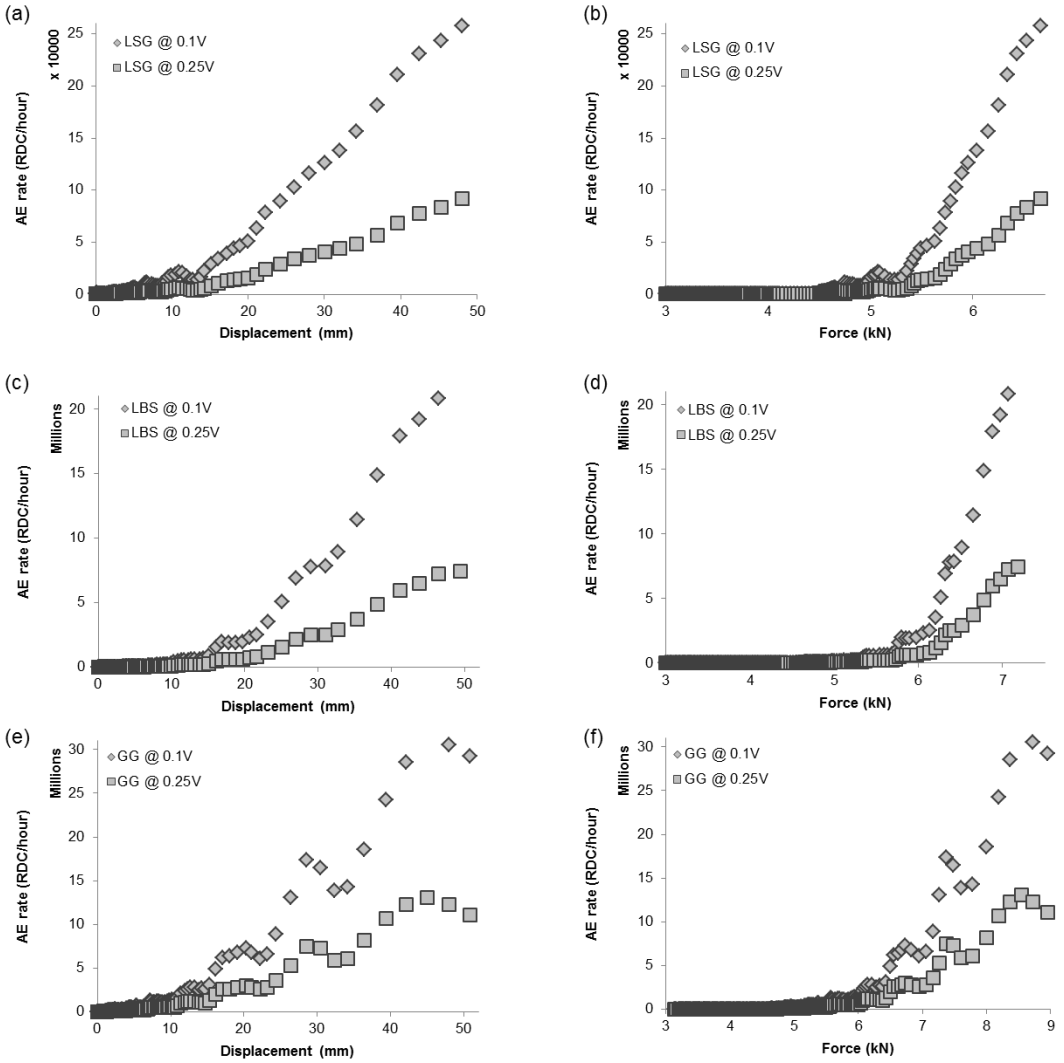

Figure 7.26. a), c) and e) show AE rate vs. displacement relationships for each backfill type and voltage threshold level. b), d) and f) show AE rate vs. load relationships for each backfill type and voltage threshold level

7.3.2.3. AE rate vs. velocity relationships

Figures 7.27, 7.28 and 7.29 present the AE rate vs. velocity relationships derived from the first-time failure experimentation for the three backfill materials, at both voltage threshold levels. The error bars show the range of AE measurements (i.e. AE rates) recorded at that applied velocity. In general, the greatest variability in AE measurements was recorded at the lower velocities (i.e. < 50 mm/hour) and from the sensor set at 0.1V. The variability reduced as the velocity increased, and the error bars became so small that they cannot be presented for velocities above 50 mm/hour in the majority of the relationships (because there is less data at the higher velocities).

Note that the greatest range of AE rates was recorded from the limestone gravel. This is because the relationships combine results from three tests, whereas the relationships for the Leighton Buzzard sand and granite gravel were derived from one test each. The variability in AE measurements from the 0.25V limestone gravel relationship is small

over the full range of applied velocities. However, the variability in the AE measurements from the 0.1V limestone gravel relationship apparently increases with velocity. The 0.1V limestone gravel relationships derived from each of the three tests had significantly less variability than is presented in Figure 7.27, but the three relationships were slightly different to each other (as can be seen in Figure 7.17) so when combined in a single relationship, as in Figure 7.27, the variability is large. This greater variability at 0.1V compared to 0.25V is due to the sensor being more sensitive to low amplitude backfill-generated AE events in addition to low amplitude background noise. Also, the differences in 0.1V limestone gravel AE rate-velocity relationships can be explained by differences between the three tests used to obtain them. Pressure distributions with different magnitudes were set up in the active waveguide in each test, in response to the lateral loading and soil reactions. This resulted in different confining pressures and, therefore, AE events with different amplitude. A significant number of AE events generated from the limestone gravel in the frequency range 20 to 30 kHz clearly had amplitudes comparable to the 0.1V threshold level, which meant in the tests with greater confining pressures a greater number of these events passed the threshold and were detected by the sensor, whereas in the tests with slightly lower confining pressures the amplitudes of these AE events were smaller than the threshold and were not detected.

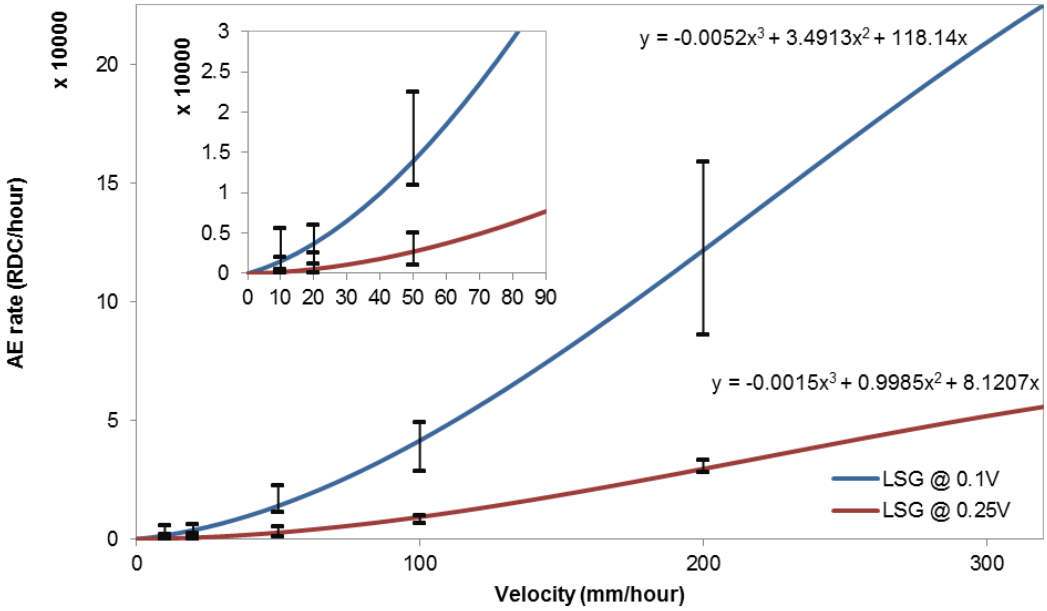

Figure 7.27. AE rate vs. velocity relationships derived for limestone gravel backfill at both 0.1V and 0.25V voltage threshold levels using the first-time failure experimentation. Error bars show the range of AE measurements recorded at the applied velocity

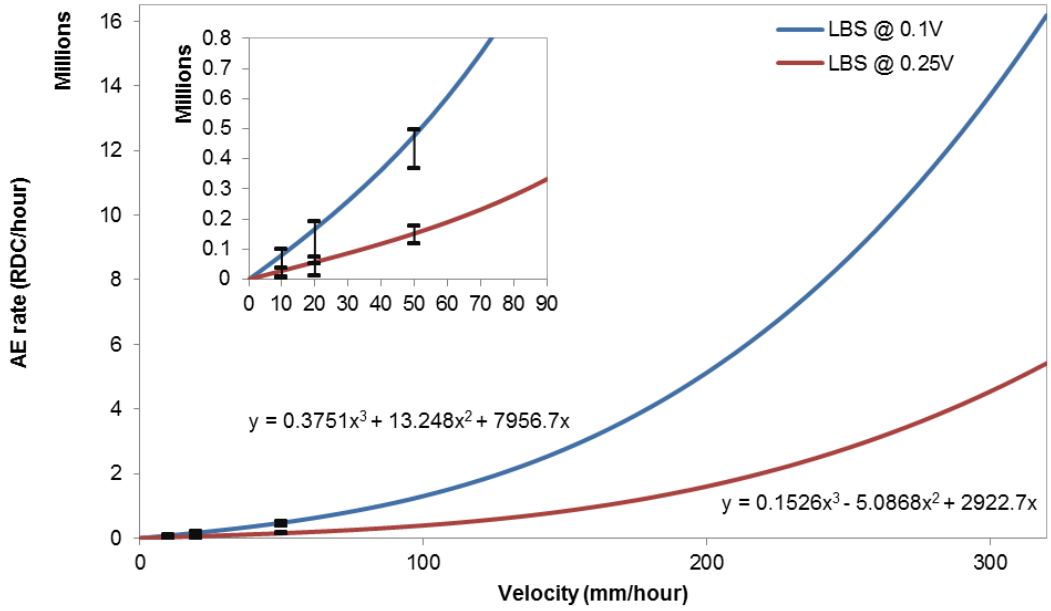

Figure 7.28. AE rate vs. velocity relationships derived for Leighton Buzzard sand backfill at both 0.1V and 0.25V voltage threshold levels using the first-time failure experimentation. Error bars show the range of AE measurements recorded at the applied velocity

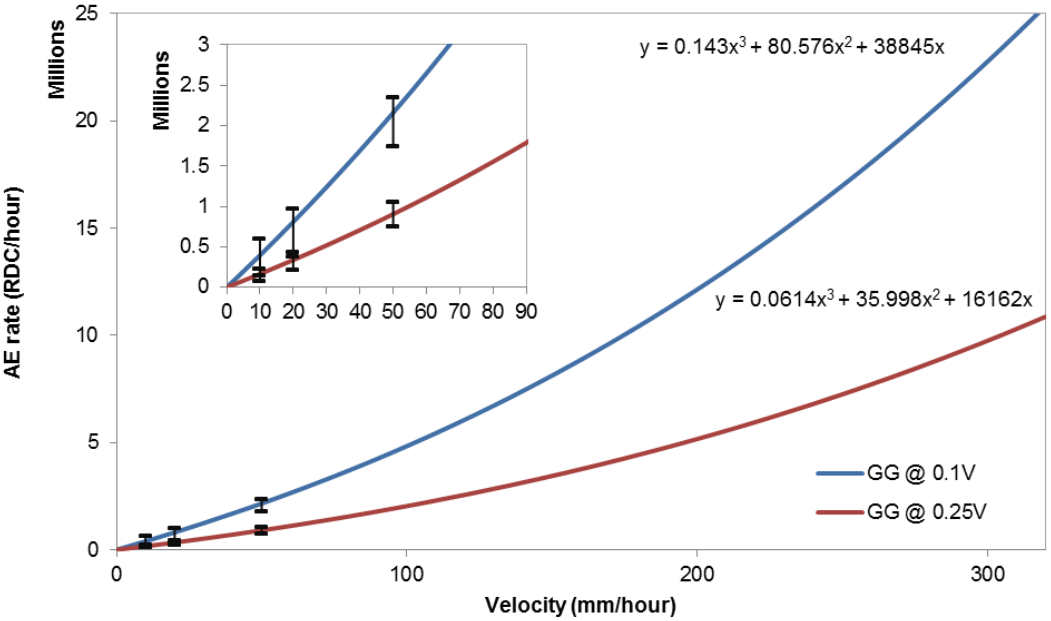

Figure 7.29. AE rate vs. velocity relationships derived for granite gravel backfill at both 0.1V and 0.25V voltage threshold levels using the first-time failure experimentation. Error bars show the range of AE measurements recorded at the applied velocity

7.4. Summary

A large shear box has been developed to perform first-time slope failure simulations on elements of soil, through which 60 mm diameter active waveguides were installed to intersect a shallow shear surface of 0.7 m depth. An SAA was also installed through the element of soil to provide continuous subsurface deformation measurements for

comparison with AE measurements. The findings of this experimental programme have contributed to meeting Objectives 2, 3 and 4. The results have provided conclusive evidence that AE rates are proportional to slope velocity and AE monitoring can be used for early detection of first-time slope failures that progressively develop a shear surface during failure (e.g. AE was detected after as little as 0.81 mm of deformation in previously un-sheared material).

Empirical AE rate-velocity relationships have been established for active waveguides installed in slopes with a shallow shear surface (i.e. <1 m deep) for three different backfill materials; limestone gravel (fine to medium gravel), Leighton Buzzard sand (medium to coarse sand), and granite gravel (medium gravel). Three tests were repeated using the same active waveguide backfill, limestone gravel, to assess repeatability (i.e. test-retest reliability); the three AE rate-velocity relationships determined from these tests overlapped and demonstrated both active waveguide repeatability and first-time slope failure simulation test repeatability. Two further tests were then performed, each employing one of the other active waveguide backfill materials. The empirical AE rate-velocity relationships obtained demonstrate linearity up to applied velocities of 100 mm/hour and displacements of 10-20 mm, which agree with the results obtained from the field trials (Chapter 5) and active waveguide physical model tests (Chapter 6). Over the full range of applied velocities (i.e. >300 mm/hour), 3rd order polynomials best fit the empirical relationships, which produced R^2 values of 0.96 or greater. At larger displacements (> 10-20 mm) more complex interactions occur within the active waveguide, which gradually increases the gradient of the AE rate-velocity relationship leading to a polynomial relationship. These altered mechanisms include: horizontal deformation of the anchored length of the active waveguide below the shear surface through the host soil, in addition to granular shearing at the shear surface that is the dominant mechanism below 100 mm/hour and at smaller deformations (up to 10-20 mm); and increasing confining pressures (i.e. contact stresses) within the backfill and at the backfill-waveguide interface, due to increased lateral loading and soil reactions.

A reduced voltage threshold level (e.g. from 0.25V to 0.1V) produced an increase in measured AE rates by a factor of 2.3 to 4.0, dependent on the backfill material, which was relatively constant over the full range of applied velocities. This reduction in voltage threshold level produced an increase in measured AE rates, from the limestone gravel, up to a factor of 13.3 during the early stages of the test (< 50 mm/hour), which reduced and became relatively constant at 4.0 over greater velocities (>50 mm/hour). This behaviour is partly explained by the greater magnitude of deformation required to initiate detectable AE from the limestone gravel at 0.25V relative to 0.1V (0.77 mm greater deformation).

Limestone gravel backfill generated significantly less, by orders of magnitude, AE rates than both the Leighton Buzzard sand and the granite gravel, and required a greater magnitude of deformation prior to generating detectable AE. The granite gravel generated the greatest AE rates out of the materials examined. The granite gravel had the largest particles and greatest angularity. The Leighton Buzzard sand had the greatest coefficient of uniformity and lowest void ratio (i.e. achieved the best packing). These are the reasons both of these materials performed well. In contrast, the limestone gravel had the lowest angularity and poorest packing (i.e. highest void ratio). The AE measurement system employed in this study has focused on the 20 to 30 kHz range and has ignored AE generated outside of this range. Other research has demonstrated that soil-generated AE has a wide frequency band (Hz to 100s kHz) and its dominant frequency response can change by more than 10 kHz due to changes in particles, assemblies, confining pressures and interaction mechanisms. Another reason for the limestone gravel generating the relatively weaker AE rates, in comparison to the other backfill materials, is the monitoring frequency range used. If using an AE measurement system such as Slope ALARMS (20 to 30 kHz) use of backfill comparable to the granite gravel (comparable properties such as particle size and shape) is recommended, particularly in slopes with deeper shear surfaces as the amplitude of the events generated is greater and this is necessary to combat the greater magnitude of attenuation the signals will experience as they propagate along the waveguide. Backfills comparable to the Leighton Buzzard sand will also perform well, but only in slopes with relatively shallow shear surfaces because their comparatively smaller AE amplitude would attenuate significantly over long propagation distances. The results demonstrate that both macro (e.g. angularity) and micro (e.g. roughness) particle shape/surface properties influence the AE rates generated from soils. Further research is required to understand: the response of backfill materials over a wide range of frequencies using a monitoring system that can capture frequency spectra; and the influence of particle roughness on the AE produced.

CHAPTER 8

The influence of system variables upon the AE response to applied deformation behaviour

8.1. Introduction

In this Chapter an investigation that used a series of physical model experiments in order to quantify the influence of system variables upon the AE response to applied deformation behaviour (i.e. Objective 4) is detailed. Several variables were identified to have influence upon the AE response from the system in response to applied rates of deformation. Empirical relationships are defined between variables using regression analyses, for later input into the quantification framework (i.e. Objective 5 and Chapter 9). The variables hypothesised to have the most significance were; depth to shear surface (i.e. attenuation), and sensor voltage threshold level. Therefore, these are addressed first at the beginning of this Chapter. Subsequently, results from investigations conducted to understand the influence of other variables upon the AE response to applied deformation behaviour are presented: borehole size; waveguide geometry and mechanical properties; and sensor node and transducer combinations.

8.2. Depth to shear surface and attenuation

8.2.1. Experimental design

In order to conduct an investigation into the attenuation of AE in active waveguides (i.e. an air-waveguide-soil tri-layer system), including the influence of screw threaded couplings, which are the typical coupling method employed because of their simplicity and the need to avoid the impracticalities of bringing welding equipment to remote sites; first the attenuation with air as an external environment (i.e. an air-waveguide-air system) was measured for comparison. A photograph of the test setup for the first series of experiments can be seen in Figure 8.1, and a schematic of the test setup is shown in Figure 8.2. A total of 5 x 3.2 m lengths (plus an additional 0.5 m length) of 50 mm outside diameter steel steam pipe with a wall thickness of 3 mm were connected with screw threaded couplings. The properties of the pipe are detailed in Table 2.6 (the same

pipe as used for active waveguides in the majority of the field trials (Chapter 4) and in the active waveguide physical model tests (Chapter 6)). The pipe (total length of 16.5 m) was placed on a series of sponges to elevate the pipe above the stable surface (i.e. tables) and remove any mechanical contact and damp any interaction (as can be seen in Figure 8.1). Sponges were used because they have very low stiffness and density, and therefore the difference in acoustic impedance at the waveguide-sponge interface was high and losses into the sponge were minimal. Additionally, the sponge only covered 0.3% of the surface area of the pipe, which had potential for losses, and therefore the losses into the sponge were assumed negligible by comparison to being surrounded by soil. The screw threaded couplings were hand tightened in the first experiment and subsequently tightened using chain wrenches and lubricated with silicone gel in the second (i.e. to improve connection and increase transmission). This allowed the influence of the quality of the joint on the transmission of the incident source waves to be investigated, and how this affects attenuation.

Figure 8.1. Photograph of experimentation to measure attenuation in an air-waveguide-air tri-layer system

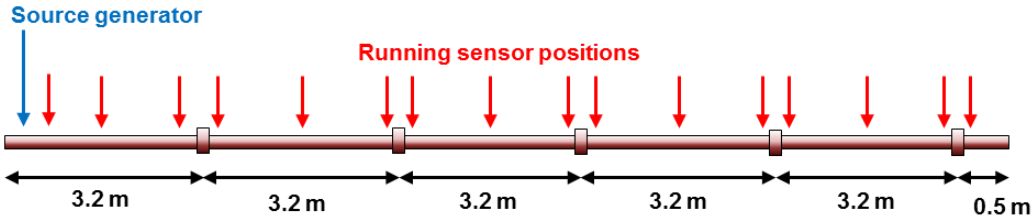

Figure 8.2. Schematic of air-waveguide-air test setup with source generator and sensor positions highlighted

The second series of experiments aimed to investigate the influence of an external environment (i.e. soil) on the attenuation of AE along the pipe. For this series of experiments a 14 m long trench was excavated: a schematic of the phases of the experiment can be seen in Figures 8.3a to 8.3d; and photographs of phases of filling in Figures 8.4a to 8.4c. A total of 4 x 3.2 m lengths of the same pipe detailed in Table 2.6 were connected with screw threaded couplings (lubricated with silicone gel and tightened using chain wrenches), and lowered into the trench. Two soil types were used in this series of experiments; river gravel (granular soil) and site won clay (fine grained soil). River gravel was selected because a large volume was required and large quantities of the river gravel were readily available; the material properties of the river gravel are representative of the gravel used for active waveguide backfill in both the field trials and physical model experiments (Chapters 4, 5, 6 and 7). The clay used was site won material, which had properties representative of bentonite-grout that caps the top of each active waveguide installation to form a plug. In both cases a base layer of the relevant material was placed and compacted on the bottom of the trench, onto which the pipe was placed before the trench was backfilled in sections; this ensured that the soil being tested was in contact with the entire circumference of the pipe. The particle size distribution of the two soils can be seen in Figure 8.5, and Figures 8.4b and 8.4c show photographs of the two soils backfilled over sections of the buried pipe. The river gravel was dry and had a bulk density of 1510 kg/m^3, and Table 8.1 details the properties of the site won clay. Although the site won clay has >65% (by mass) silt sized particles, it plots above the A-line on a plasticity index-liquid limit plot, and therefore behaves like a clay. The soil can be described as a ‘slightly sandy very silty clay’.

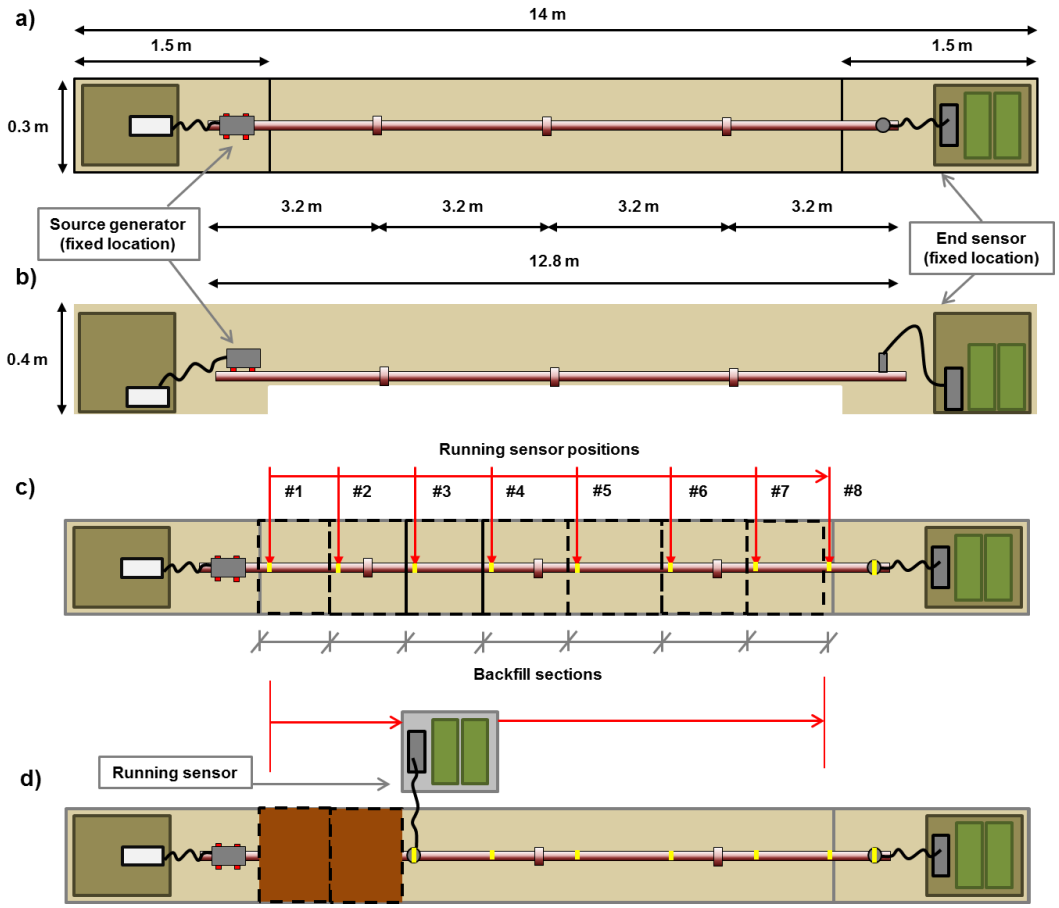

Figure 8.3. Schematic of trench experiment, a) plan and dimensions, b) elevation and dimensions, c) running sensor positions and backfill sections, d) running sensor at position 3 with 2 sections backfilled

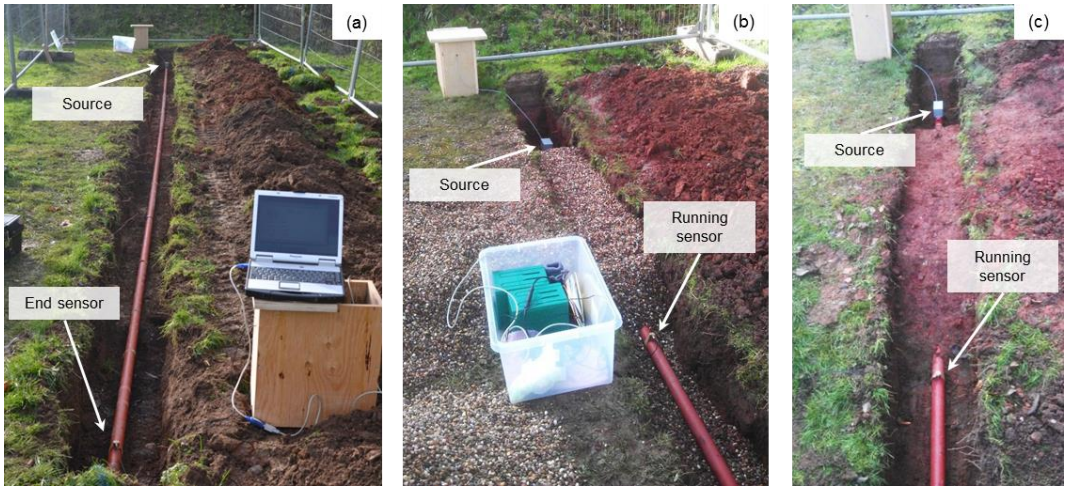

Figure 8.4. Photographs of trench experiment, a) pipe placed at the base of the trench, b) pipe placed on river gravel bed and backfilled with river gravel, c) pipe placed on clay bed and backfilled with clay

Table 8.1. Properties of site won clay used as soil cover

Moisture content (%)	Bulk density (Mg/m^3)	Dry density (Mg/m^3)	Particle density (Mg/m^3)	Liquid limit (%)	Plastic limit (%)	Plasticity index (%)	Liquidity index
30.8	1.86	1.42	2.64	43.6	18.6	25	0.49

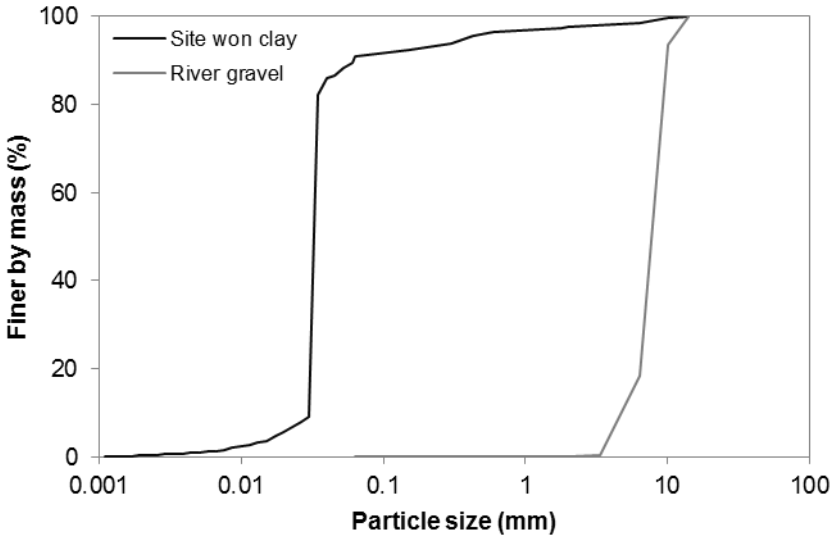

Figure 8.5. Particle size distribution curves for the two soils used as cover. The distibution for the site won clay was determined from a combination of sieving and a laser diffraction particle size analyser

8.2.2. Controlled AE source generator

In order to design a portable generation system that could produce consistent and repeatable AE in the field, comparable to that generated by deforming soil, visualisation of the full AE waveform was required. However, the Slope ALARMS sensor does not record the full waveform and therefore an alternative system was required. To achieve this, the MISTRAS Group Inc. USB AE node was utilised (details can be found in Appendix A5), with the same R3a transducer as described in Table 2.4.

Figure 8.6 shows a series of waveforms recorded from granular soil deforming around the same steel pipe as in Table 2.6, using the constant strain rate compression test apparatus. The typical waveform recorded was consistent with Figures 8.6a,b; and is generated by soil particle-particle and particle-pipe frictional interactions. However, the waveforms with significantly greater energy shown in Figures 8.6c,d occurred occasionally when slip-sitck particle contact network rearrangement occurred (e.g. release of contact stress and stress redistribution as interlock is overcome and regained). These waveforms demonstrate the variability in AE generated by deforming soil due to the various complex mechanisms that occur. It is also important to note that AE generated by deforming soil is continuous throughout the period of deformation, which could be hours or even days or

weeks, as results from field trials demonstrate in Chapters 4 and 5. Because soil generated AE is highly variable and is continuous over long durations, it is not appropriate to attempt to replicate soil generated AE with a single transient source. Continuous vibration over a set time period was therefore investigated as a generation mechanism to produce AE similar to that of particle-particle and particle-pipe interactions (e.g. to approximate/replicate the waveforms shown in Figures 8.6a,b).

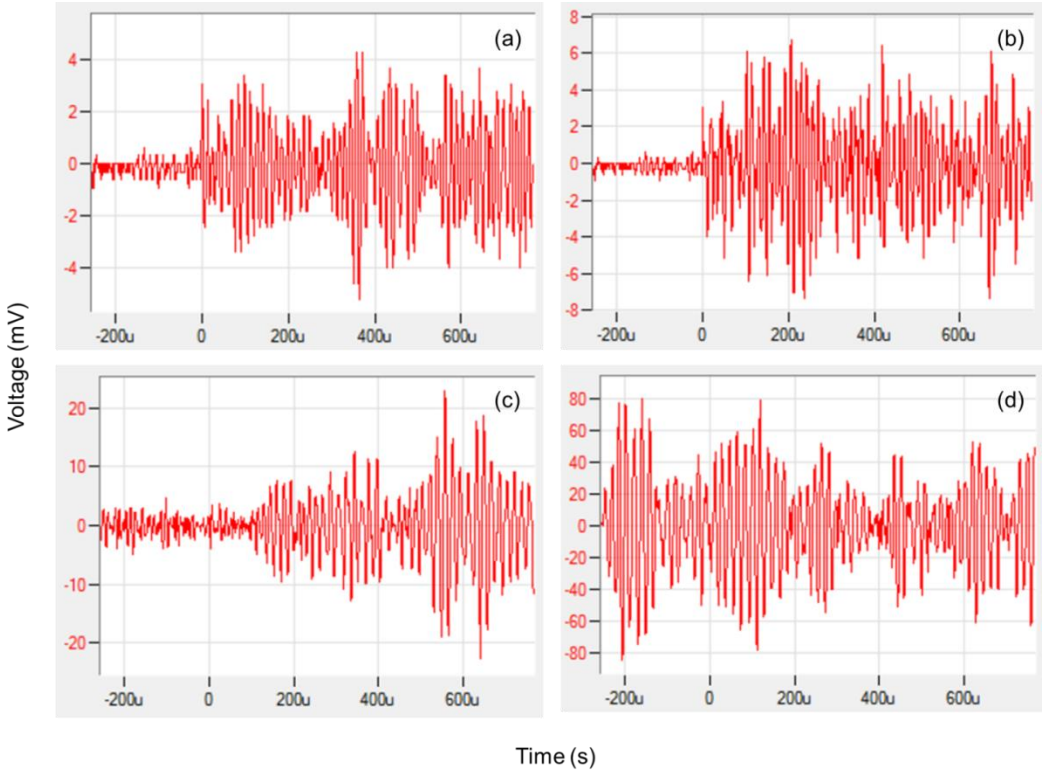

Figure 8.6. Sample AE waveforms generated by soil deforming around a pipe: a) and b) generated by particle-particle and particle-pipe interactions; and c) and d) generated by contact stress release and contact network rearrangement

A photograph of the AE source generator is shown in Figure 8.7. The source is a 26000 rpm (equivalent to 433 Hz oscillating frequency) DC motor with a power input of 6 V. The motor is encased in a water proof metal casing and is connected to the pipe using magnets. The motor is supplied power in 10 second bursts provided by a control box; when the 'on' button is triggered, power is supplied to the motor for a period of 10 seconds and subsequently power is automatically disconnected. This provided a consistent and repeatable source of AE using 10 second bursts of vibration from the DC motor. Figures 8.8a,b show typical waveforms recorded, using the MISTRAS Group Inc. USB AE node and transducer connected to the pipe, by this generation system, which are similar (in terms of amplitude, frequency, pattern etc) to those generated by deforming soil around the pipe in Figures 8.6a,b. Calibration experiments have demonstrated that this source and operation produces repeatable amounts of AE (in RDC using a Slope ALARMS sensor) in the frequency range monitored. It was therefore reasonable to

assume that the attenuation experienced by this AE source was representative of that experienced by deforming soil generated AE.

Figure 8.7. Source generator coupled to the pipe

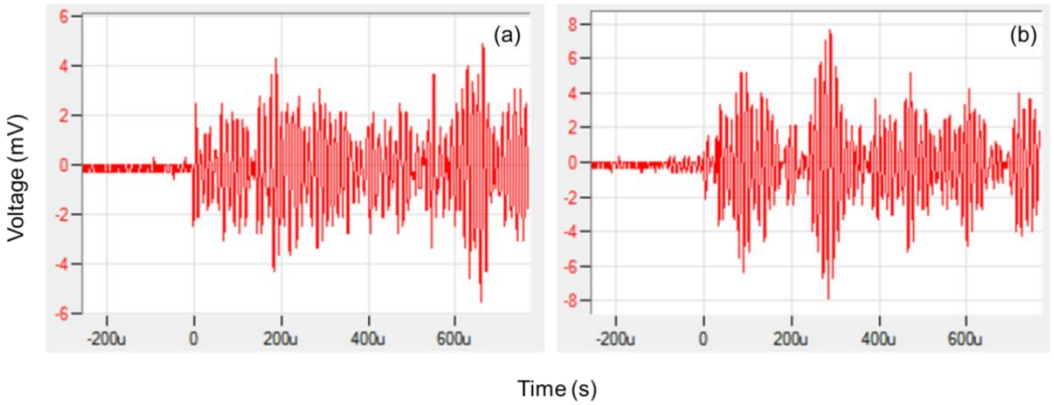

Figure 8.8. a) and b) are typical AE waveforms produced by the source generator

8.2.3. Experimental procedure

The experimental procedure employed in the testing of the air-waveguide-air system is shown in Figures 8.1 and 8.2. The source generator was kept at the same location at one end of the pipe. The AE measurement system was coupled to the pipe at the various locations detailed in Figure 8.2. A minimum of 5 x 10 second bursts of the DC motor (i.e. the AE source) were induced into the pipe while the sensor was coupled at each location. This allowed a minimum of 5 RDC values to be recorded at each location (i.e. various propagation distances along the pipe).

The experimental procedure employed in the testing of the air-waveguide-soil systems (Figures 8.3a to 8.3d and 8.4a to 8.4c) was similar to that adopted for the air-waveguide-air systems. A bed of soil was placed at the bottom of the trench, the pipe was lowered onto the bed, and then the pipe was gradually backfilled in sections as detailed in Figures

8.3a to 8.3d. The pipe was subjected to a minimum of 5 x 10 second bursts of the DC motor inducing AE while the sensor was coupled at each location. In this series of tests two sensors were used; a running sensor (i.e. moved from one location to the next; positions of the running sensor relative to couplings and backfilled sections can be seen in Figures 8.3c and 8.3d) and an end sensor that remained in the same location at the end of the pipe. The running sensor was coupled to the pipe adjacent to each backfilled length. The backfilled sections of the trench had soil compacted to the same conditions (i.e. bulk density) resulting in overburden pressures of 4.4 kPa from the river gravel and 5.5 kPa from the clay. Note that these pressures are generated by the depth of soil above the pipe inside the trench; a discussion as to the effect of increased/decreased pressures is provided later in Section 8.2.5.

The entire experimental procedure for all tri-layer systems was repeated with two different voltage threshold levels set on the sensor. This was conducted to replicate the effects of source signals with different amplitude and energy content (i.e. amplitude relative to the threshold) in order to establish the consistency of the RDC value (i.e. signal magnitude) vs. propagation distance relationship for each tri-layer system with respect to the magnitude of source emissions. Voltage threshold levels of 0.1V and 0.25V were used.

8.2.4. Results and analysis

8.2.4.1. Air-waveguide-air tri-layer systems

The results produced from the air-waveguide-air tri-layer system tests can be seen in Figures 8.9a and 8.9b. Figure 8.9a shows the results from the pipe connected with loose couplings and Figure 8.9b from the pipe connected with tight couplings. It is obvious from the results that the quality of the coupling significantly affects the transmission of the incident wave; the signal significantly attenuated in the pipe with loose couplings after 10 m, whereas the pipe with tight couplings did not result in any significant attenuation after the full distance of 16.5 m. Note that on occasion the RDC detected on the entrance to a coupling was greater than RDC detected at the exit of a coupling; this is assumed to be due to the sensor detecting reflections from the joint in addition to the incident wave. The general trend of RDC detected by the sensors appears to reduce linearly proportionally with the distance of propagation and is therefore assumed to decay linearly proportionally with distance over the pipe length investigated; a linear regression was therefore plotted through the measured data points. The gradient of each of the linear regression lines fitted through the measured data sets gives a value for the attenuation coefficients (i.e. reduction in RDC per metre); these are discussed further in Section 8.2.4.3. It is important to note that the gradient of the RDC vs. propagation distance is

comparable for both 0.1 V and 0.25 V threshold levels, indicating that the attenuation coefficient is independent of source magnitude.

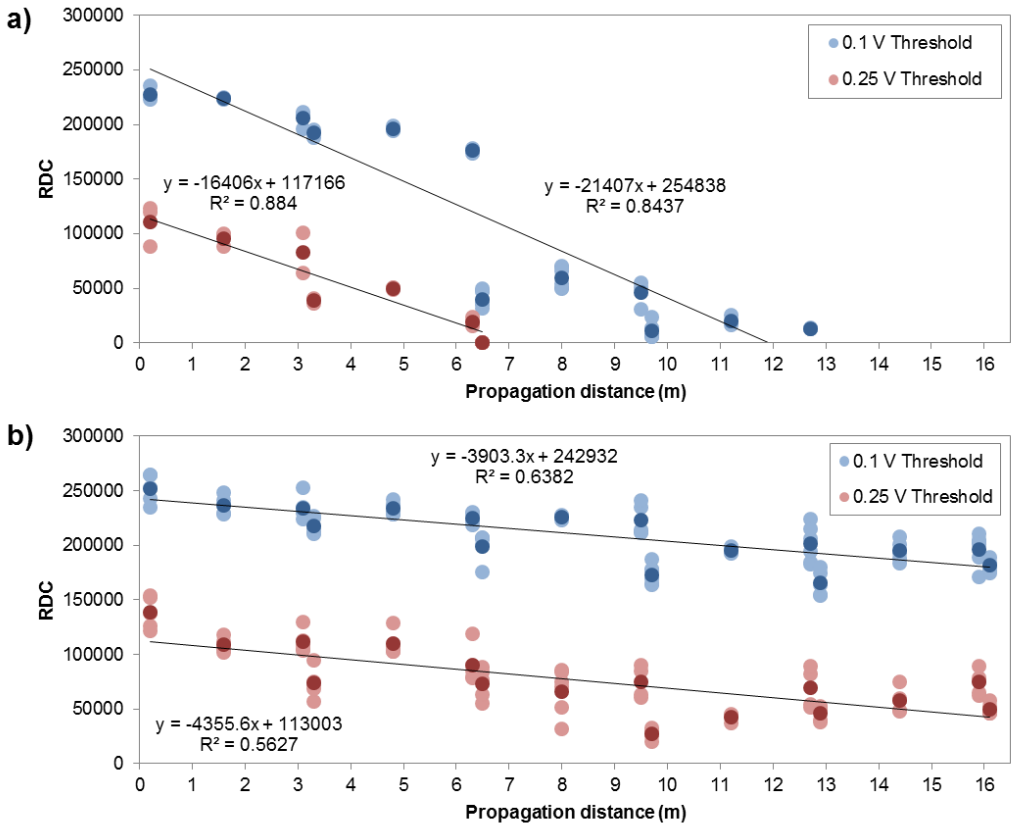

Figure 8.9. Results of RDC (induced by source generator over 10 second durations) vs. propagation distance from the air-waveguide-air tri-layer system; a) loose couplings, b) tight couplings

Figure 8.10 shows the percentage signal loss over each coupling for the series of tests conducted on air-waveguide-air tri-layer systems. The percentage loss was determined from the difference between the average RDC detected in the 3.2 m length of pipe preceding the coupling and the average RDC detected in the 3.2 m length of pipe succeeding the coupling. It can be seen that the signal loss over the couplings was significantly greater for the loose couplings. The average losses over joints in the systems with loose couplings and tight couplings were 76.1% and 9.2% respectively. A negative percentage loss (i.e. an increase) was recorded over the fourth coupling in the results from the tight couplings at 0.25 V. This is hypothesised to be due to significant detected reflections from the end of the pipe in this test. Figure 8.11 illustrates the discontinuities in cross-section at the couplings used, which are the reasons for reflections.

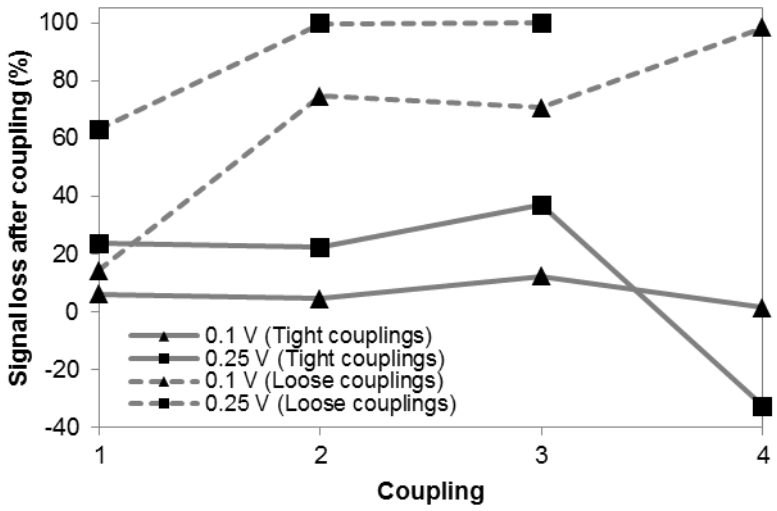

Figure 8.10. Percentage signal loss over each coupling from the air-waveguide-air tri-layer system experimentation

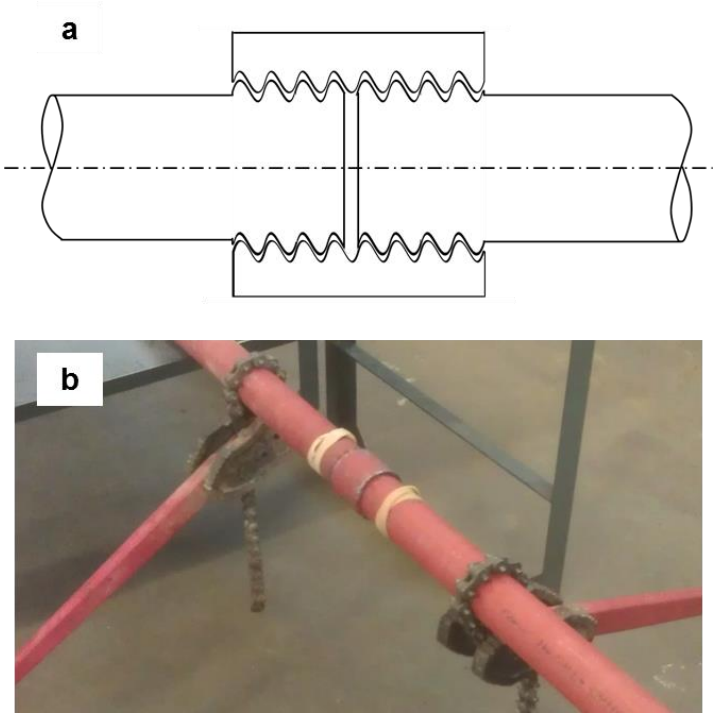

Figure 8.11. a) Exaggerated illustration of screw threaded coupling highlighting the discontinuity in cross-section, and b) photograph of pipe connected with a screw threaded coupling and tightened with chain wrenches

8.2.4.2. Air-waveguide-soil tri-layer systems

The results produced from the air-waveguide-river gravel and air-waveguide-clay tri-layer systems can be seen in Figures 8.12a, 8.12b and 8.13a, 8.13b, respectively. Figures 8.12a and 8.13a show the results detected by the sensor coupled to the end of the pipe (i.e. the furthest distance from the source) while lengths of the pipe were gradually backfilled. Figures 8.12b and 8.13b show the measured results obtained from the running sensor

positioned adjacent to the backfilled lengths as the pipe was progressively covered. The general trend of RDC detected by the sensors appears to reduce linearly proportionally with the distance of propagation and is therefore assumed to decay linearly proportionally with distance over the pipe length investigated; a linear regression was therefore plotted through the measured data points. The gradient of the RDC vs. propagation distance relationship appears to be comparable for both voltage thresholds (i.e. 0.1 V and 0.25 V) and both sensors (i.e. running and end) for each type of soil cover. The results demonstrate that the river gravel cover allowed propagation of the stress waves over 10 m at the lowest threshold level (i.e. highest source magnitude), whereas cover by the clay resulted in severe damping of the signal to below the detection threshold by propagation of less than 4 m from the source.

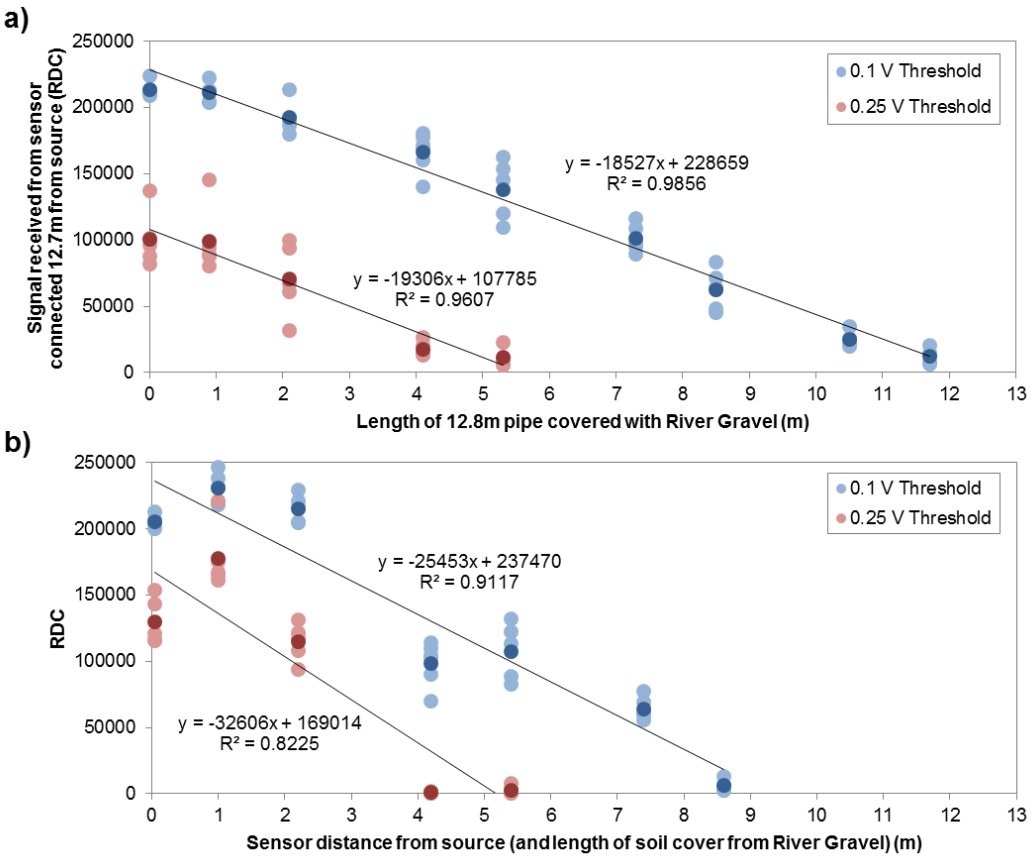

Figure 8.12. Results of RDC (induced by source generator over 10 second durations) vs. propagation distance from the air-waveguide-River Gravel tri-layer system; a) signals received by end sensor, b) signals received by running sensor

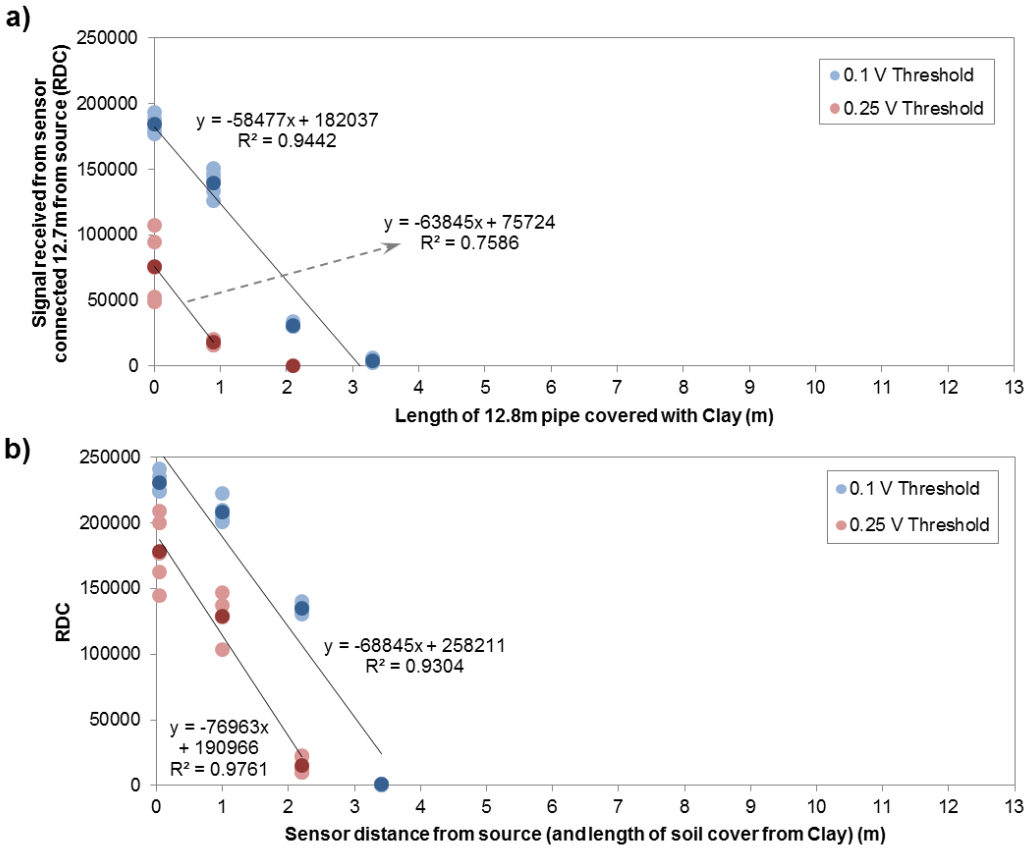

Figure 8.13. Results of RDC (induced by source generator over 10 second durations) vs. propagation distance from the air-waveguide-Clay tri-layer system; a) signals received by end sensor, b) signals received by running sensor

The results detected from the running sensor were more variable than those detected by the end sensor; this is assumed to be due to greater or lesser magnitudes of reflections being detected by the running sensor dependent on its location in relation to a coupling. The running sensor was slightly less sensitive than the end sensor, and therefore detected a slightly smaller RDC magnitude in each experiment than the end sensor. This is particularly evident by the difference in RDC vs. distance relationships for the 0.1 V threshold experiments in Figures 8.12a and 8.12b; RDC ceased to be detected by the running sensor before reaching 9 m, whereas RDC continued to be detected by the end sensor beyond 11 m of cover from river gravel.

8.2.4.3. Attenuation coefficients

As the general trend of RDC detected by the sensors appeared to reduce linearly proportionally with the distance of propagation, a linear regression line was plotted through each of the measured data sets in order to quantify the gradient (or attenuation coefficient) in losses of RDC per metre. These values were grouped for each tri-layer system (i.e. system total losses due to a combined effect of screw threaded couplings and external environments) and are plotted in Figure 8.14. Coefficients determined from both

voltage thresholds (i.e. 0.1 V and 0.25 V) and from both sensor positions (i.e. running and end) show good agreement. The coefficients shown in Figure 8.14 confirm that the greatest attenuation occurred in the air-waveguide-clay tri-layer system while the least attenuation occurred in the air-waveguide-air system with greased and tightened (i.e. high quality) couplings by contrast.

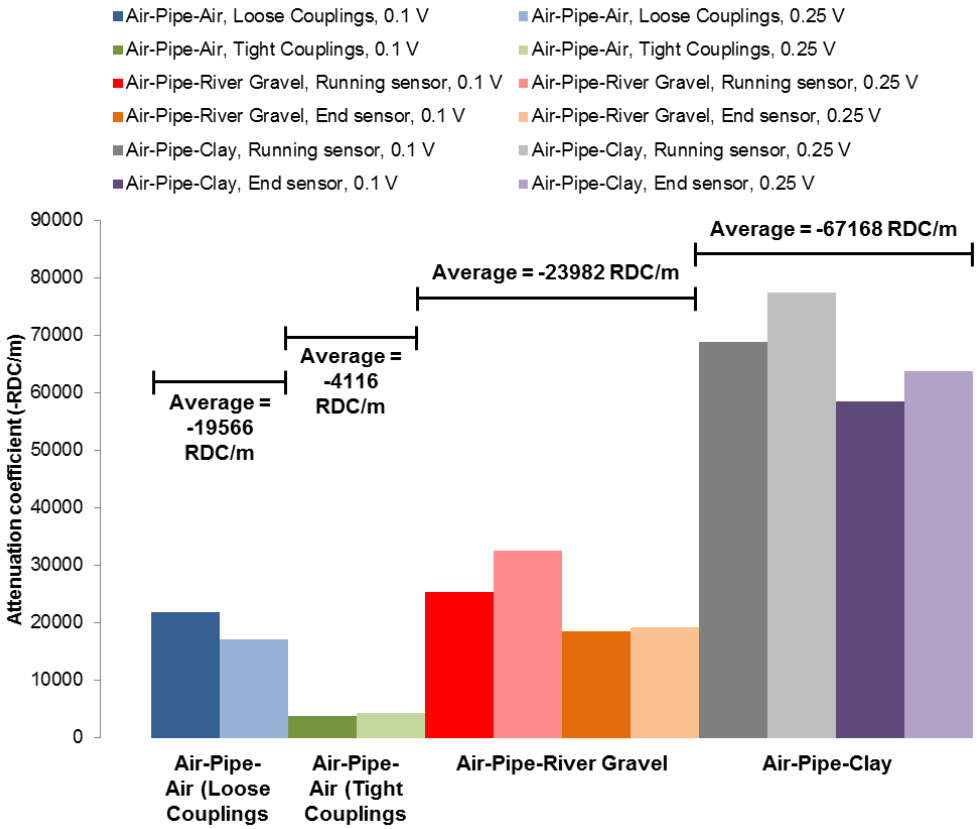

Figure 8.14. Attenuation coefficients in RDC per metre derived for each of the tri-layer systems (including losses due to couplings)

In order to present the results generated in this study in more commonly used units of attenuation coefficients (i.e. decibels per metre) Equations 2.5, 2.6 and 2.7 were used. The equations detail how the attenuation coefficient can be determined in decibels per metre using the ratio of the attenuated and original signal magnitude, and the distance of propagation between them. It is possible to use the ratio of RDC detected some distance from the source and adjacent to the source as values to input into the equations. It is an appropriate assumption that the RDC values measured in this study are proportional to the magnitude of the signal, and therefore the ratio of RDC detected some distance from the source and adjacent to the source will yield an approximate value for the ratio of the attenuated and original signal magnitude. The attenuation coefficients determined for the tri-layer systems (including losses due to couplings) are shown in Table 8.2. The attenuation coefficient determined for plane longitudinal and flexural wave propagation in steel pipes (without couplings) by Shehadeh *et al.* (2008) (Section 2.4.5.3.2) was 0.014

Np/m (or 0.12 dB/m). This demonstrates that approximately 0.006 Np/m (or 0.05 dB/m) of the attenuation in the air-waveguide-air system (with the tight couplings) was due to the losses at couplings (spaced 3.2 m apart). This was calculated by subtracting the coefficient for the waveguide with no couplings away from the coefficient for the waveguide with couplings. This is a slight approximation as the frequency range (100-200 kHz) Shehadeh *et al.* (2008) obtained the attenuation coefficient for was slightly greater than the frequency range monitored at in this study; however, the value is still representative of this system because the same wave modes are propagating. The losses due to high quality screw threaded couplings are therefore very small. The losses due to couplings would reduce if longer lengths (less frequent couplings along the waveguide) were employed. In contrast, the losses due to couplings would increase if shorter lengths (more frequent couplings along the waveguide) were employed.

Table 8.2. Attenuation coefficients determined for the systems tested (i.e. combined losses due to couplings and internal/external environments)

System	Attenuation coefficient	
	(dB/m)	(Np/m)
Air-waveguide-Air (Tight couplings)	0.16	0.02
Air-waveguide-Air (Loose couplings)	2.03	0.23
Air-waveguide-River Gravel	2.78	0.32
Air-waveguide-Clay	4.75	0.55

The percentage of source magnitude vs. propagation distance relationship has been determined using Equation 2.5 and the attenuation coefficient for the air-waveguide-river gravel system (shown in Figure 8.15). The air-waveguide-river gravel system is representative of the waveguide-backfill active waveguide system, and was therefore of particular interest in this study. The results in Figure 8.15 suggest that monitoring of shear surface depths of tens of metres may be possible if the source AE generated at the shear surface is of sufficient magnitude. AE detected from granular shearing at a deep shear surface would be from high amplitude signals, which are typically generated by slip-stick and contact stress release mechanisms, as opposed to sliding and rolling friction behaviour. Consideration should therefore be given to use of backfill with large angular particles when monitoring slopes with deep shear surfaces, and use of a lower voltage threshold level (e.g. 0.1V). Interactions between the waveguide and backfill over the length above the shear surface do generate AE, in addition to the AE generated at the shear surface, and these would experience less attenuation.

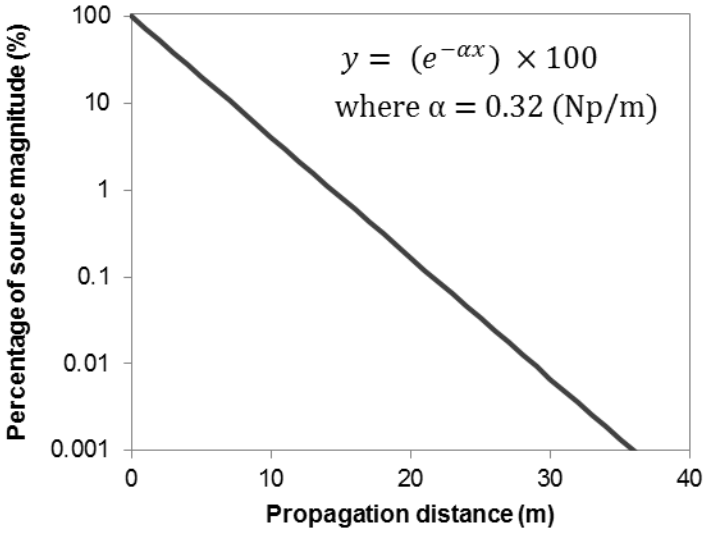

Figure 8.15. Percentage of source magnitude vs. propagation distance relationship derived using the attenuation coefficient for the air-waveguide-River Gravel system (i.e. including coupling losses)

8.2.5. Discussion

8.2.5.1. Effect of different external and internal media on the magnitude of attenuation experienced by the active waveguide system

Table 8.3 details the acoustic velocity, acoustic impedance, and reflection coefficient (at the pipe-media interface) for the media involved in the study. A range of values of acoustic velocity representative of the soils studied (e.g. representative sample depth, particle size distribution, moisture content, degree of compaction and density) were taken from Oelze *et al.* (2002) (mean and standard deviation of the values used are shown in Table 8.3), and the acoustic impedance of the soils was calculated using Equation 2.9 and material bulk density values (i.e. taken from Table 8.1 for the clay and 1510 kg/m^3 for the river gravel as described in Section 8.2.1). The acoustic velocity and acoustic impedance of steel was determined using Equations 2.2, 2.3, 2.4 and 2.9 with values for parameters taken from Table 2.6. The acoustic velocity and acoustic impedance values used for water and air are standard. These values were used to input into Equation 2.10 to determine reflection coefficients at the pipe-external media interface for the media listed in Table 8.3. Figure 8.16 illustrates how the reflection coefficient at the pipe-external media interface varies with the acoustic impedance of the external media. Clay, river gravel and air were the external media studied and their reflection coefficient vs. acoustic impedance relationship can be seen in Figure 8.16. The relationship was also determined for water (shown in Figure 8.16) to demonstrate the magnitude of reflection/transmission at a pipe-water boundary, which is of interest as both the inside of an active waveguide pipe and the gravel soil surround would contain water below the water table.

It is clear from Figure 8.16 that the reflection coefficient varies inversely proportionally to the acoustic impedance of the external media. As the acoustic impedance approaches the same value of the pipe (i.e. steel) the reflection coefficient becomes zero and the full magnitude of the wave entering the boundary will be transmitted. As the acoustic impedance approaches zero (e.g. air) the reflection coefficient approaches 1.0 (i.e. 100% reflection). These results suggest that as the acoustic impedance of the soil at the pipe-soil boundary increases (e.g. through increased density and/or stiffness moduli of the soil) the reflection coefficient at the interface would reduce; resulting in greater transmission, or signal loss, into the surrounding soil. Various scenarios in which the stiffness moduli and/or density of the surrounding soil will increase are described in Figure 8.17. Such scenarios are related to the properties of the surrounding soil (i.e. soil density and stiffness increases proportionally with depth, and hence with effective stress), the moisture content of the soil (i.e. location relative to the water table), and soil grading (i.e. well graded soils are able to achieve greater densities as smaller particles fill the pore spaces between larger particles).

Table 8.3. Acoustic velocity, acoustic impedance and reflection coefficients (at the pipe-media interface) for media studied

Media	**Acoustic velocity (m/s)**		**Acoustic impedance (Z)**		**Reflection coefficient (R_c) at pipe-media interface**	
Steel	5048		3.96E+07		0	
Water	1483		1.48E+06		0.861	
Air	332		4.30E+02		1	
	Mean	Standard deviation (ST DEV)	Mean	Variability (determined from acoustic velocity ST DEV)	Mean	Variability (determined from acoustic velocity ST DEV)
River Gravel	146	59	2.21E+05	8.94E+04	0.978	0.009
Clay	168	60	3.12E+05	1.11E+05	0.969	0.011

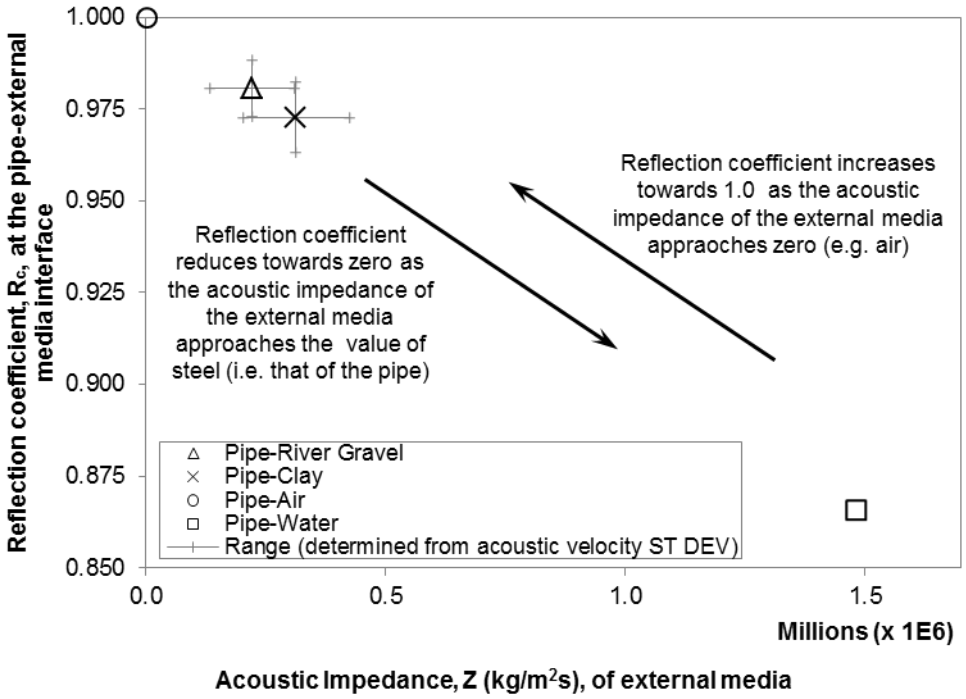

Figure 8.16. Reflection coefficient (at the pipe-external media interface) vs. acoustic impedance of the external media (for the media studied)

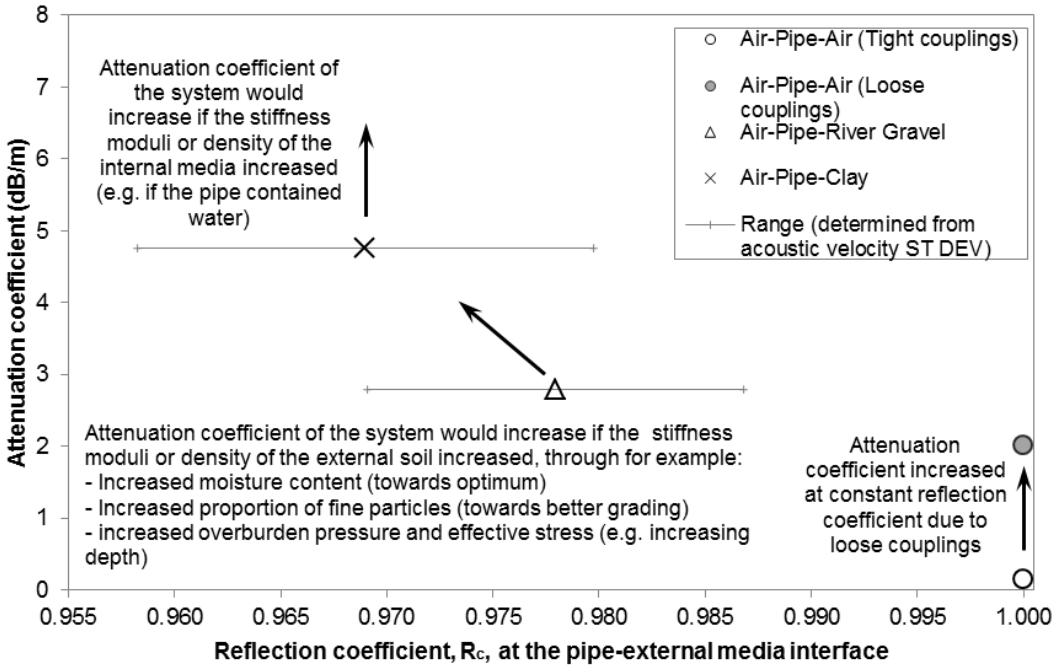

Figure 8.17. Attenuation coefficient vs. reflection coefficient (at the pipe-external media interface) for the tri-layer systems studied (i.e. steel pipe with screw threaded couplings and air as an internal environment) at a monitoring frequency of 20 to 30 kHz

Figure 8.17 demonstrates how the air-waveguide-air and air-waveguide-soil tri-layer system attenuation coefficients (detailed in Table 8.2) vary with the reflection coefficient at the pipe-external media interface. The attenuation coefficient varies inversely proportionally to the reflection coefficient at the pipe-external media interface; this would

be expected because as the reflection coefficient reduces the transmission, or loss, of the wave into the external media increases. There are a variety of scenarios that would result in an increased attenuation coefficient for the tri-layer systems studied while the reflection coefficient at the pipe-external media interface remained the same: if the quality of the couplings were reduced as demonstrated by the difference between 'tight' and 'loose' couplings in Figure 8.17 (the opposite is also true where the attenuation could be reduced by increasing the quality of the couplings); or if the inside of the pipe was filled with media that altered the reflection coefficient at the pipe-internal media interface (e.g. when filled with water) as this will result in increased transmission, or loss, of AE into the internal media. When an AE wave is transmitted into the internal media (e.g. fluid) at the pipe-internal media interface, the wave subsequently propagates through the fluid and some proportion, dictated by the reflection coefficient at the boundary, will then be transmitted back into the pipe. The AE wave will undergo mode conversions as it is transmitted from one media to another, for example; if the internal media within the pipe is water then the waves transmitted from the pipe into the water will be converted to compressional waves as water has no shear strength and cannot accommodate shear waves. The waves will subsequently be converted back into a combination of other modes (e.g. longitudinal, shear and torsional) as they are transmitted back into the pipe.

It is reasonable to assume that boundary losses in the air-waveguide-air tri-layer system (i.e. losses into the surrounding air) are negligible and attenuation in this system is predominantly due to losses at screw threaded couplings and due to the material itself. Therefore, by subtracting the attenuation coefficients determined for the air-waveguide-air (tight couplings) tri-layer system from the air-waveguide-soil tri-layer systems, both of which had the same quality tightened and greased couplings, values that represent boundary losses can be determined per metre of soil cover due to transmission of AE from the pipe into the soil (i.e. soil cover losses). These boundary loss attenuation coefficients due to soil cover were used in conjunction with Equation 2.5 to determine the percentage of source magnitude vs. propagation distance relationships for the two soil types examined (Figure 8.18). As stated earlier in this section, changes in soil acoustic impedance (e.g. through changed density and/or stiffness moduli) will result in greater/lesser losses due to an altered reflection coefficient at the pipe-soil interface. It should also be noted that the soil cover losses presented in Figure 8.18 are for plane longitudinal and flexural waves propagating in steel pipes/rods; if the material of the rod/pipe is changed then the reflection coefficient at the pipe-media interface will also change resulting in greater/lesser attenuation.

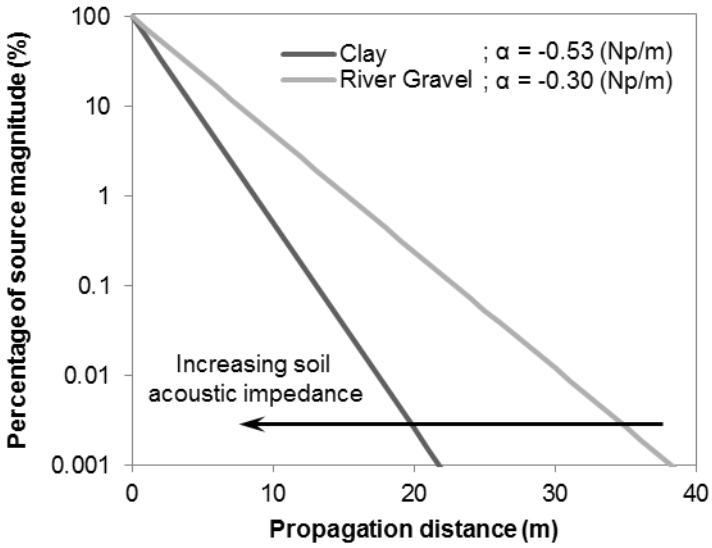

Figure 8.18. Percentage of source magnitude vs. propagation distance relationships for boundary losses due to soil cover (soil cover losses) for the soils examined, demonstrating that soil cover loss varies proportionally with the soil's acoustic impedance

These results confirm that for the tri-layer systems studied, the coefficient of reflection at the internal/external interfaces significantly impact on the propagation of AE (plane longitudinal and flexural waves) along the pipe. An increased acoustic impedance of the internal/external media will result in a reduced reflection coefficient and therefore an increased attenuation coefficient for the internal media-steel pipe-external media tri-layer system.

8.3. Voltage threshold level

8.3.1. Experimental procedure

Constant strain rate compression tests, using the same test apparatus as Dixon & Spriggs (2007) and in Chapter 6, were conducted at both rapid (66.15 mm per hour) and slow (0.706mm per hour) deformation rates with a range of voltage threshold levels set on the AE measurement system (Table 8.4). The minimum possible threshold level setting on the AE measurement system is 0.05V; below this level significant contamination from background (environmental and electronic) noise occurs. This was the reason for selecting 0.05V as the minimum threshold level, as any lower threshold levels would be impractical in the field environment. The maximum allowable threshold setting on the sensor is 0.5V. The number of constant strain rate compression tests conducted at each voltage threshold level and displacement rate are detailed in Table 8.4. Use of constant strain rate compression tests on active waveguide physical models was selected to investigate the influence of voltage threshold level because it was preferable to use backfill-generated AE where possible and the apparatus allowed for large numbers of tests to be performed in a repeatable way. The magnitude of deformation applied in the

tests ranged from 3 mm (in the slow tests) to 12 mm (in the rapid tests). The active waveguide physical models were the same as those used in Chapter 6; 130 mm diameter geomembrane cylinder containing a 50 mm diameter 3 mm thick steel tube with an angular granite gravel backfill surround.

Table 8.4. Tabulated constant strain rate compression tests on active waveguide models and voltage threshold levels set on the AE measurement system

Number of tests	Displacement rate	Voltage threshold (V)
5	Rapid	0.05
15	Rapid	0.1
5	Rapid	0.15
5	Rapid	0.2
25	Rapid	0.25
5	Rapid	0.35
5	Rapid	0.4
10	Rapid	0.45
5	Rapid	0.49
1	Slow	0.05
7	Slow	0.1
1	Slow	0.15
1	Slow	0.2
11	Slow	0.25
1	Slow	0.35
1	Slow	0.4
5	Slow	0.45
1	Slow	0.49

8.3.2. Results and analysis

Figure 8.19 shows the AE rate vs. voltage threshold level relationship obtained from constant strain rate compression tests with a ‘rapid’ rate of deformation. Figure 8.20 shows the AE rate vs. voltage threshold level relationship obtained from constant strain rate compression tests with a ‘slow’ rate of deformation. The compiled results from the numerous tests exhibit an inversely proportional relationship. The variability in AE rates measured at each voltage threshold level is due to a combination of: the variability of backfill-generated AE (e.g. from frictional interactions to slip-stick behaviour); and increasing confining pressures throughout each test with the applied load. Figure 8.21 combines both of these data sets (from Figures 8.19 and 8.20) and presents the mean AE rate measured at each voltage threshold level and deformation rate, plotted as a factor relative to the mean AE rate obtained at 0.05V (i.e. the assumed maximum obtainable as no voltage threshold level below 0.05V can practically be used).

The relationships obtained from both deformation rates are clearly comparable; however, the magnitude of AE rates reduced slightly more rapidly with increasing voltage threshold levels in the results obtained from the ‘slow’ deformation rates. Because both relationships were highly comparable they are combined in Figure 8.22, which presents

the mean AE rate obtained at each voltage threshold level, from both applied deformation rates, relative to the mean AE rate obtained at the 0.05V threshold level; the red error bars on this plot represent the standard deviation. Note that the standard deviation is greater at lower voltage threshold levels and reduces with increasing voltage threshold level. This is due to a greater amount of low amplitude backfill-generated AE and background noise being detected at the lower voltage threshold levels. A power trend line has been plotted through this data in Figure 8.23, which demonstrated that the AE rate-voltage threshold level relationship is a form of $y = 1/x$; the trend line generated an R^2 value of 0.99. This relationship is employed in Chapter 9 in the development of a framework to quantify slope deformation behaviour from measured AE. When this relationship is used to determine a ratio between the factor at 0.1V to the factor at 0.25V (i.e. 0.1V/0.25V), a value of 2.43 is produced. This ratio agrees with the ratio obtained from the same backfill material in Chapter 7 using the first-time failure experimentation, which produced ratios from 2.3 to 2.4 over the full range of applied velocities (this is discussed further in Section 9.6). This demonstrates that this AE rate-voltage threshold level relationship is appropriate for use with comparable backfill materials.

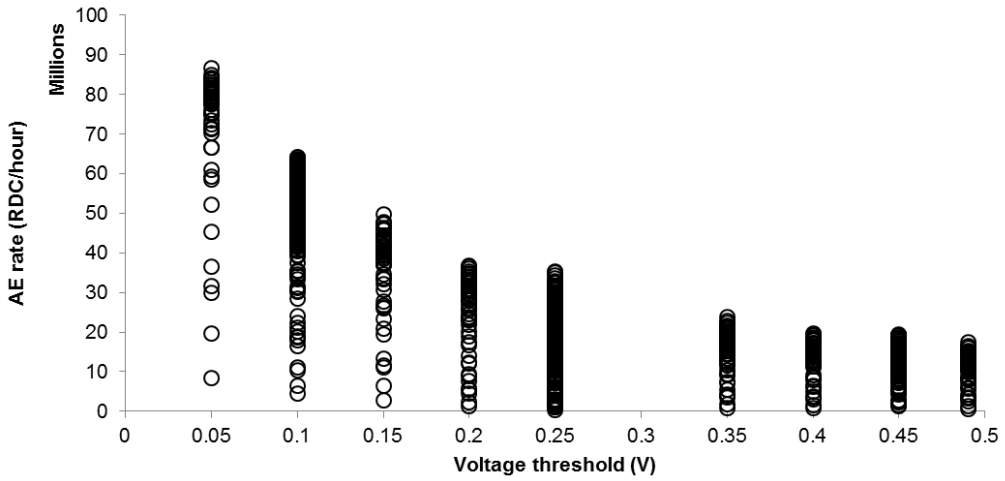

Figure 8.19. AE rate vs voltage threshold level relationship obtained from constant strain rate compression tests at a 'rapid' rate of displacement

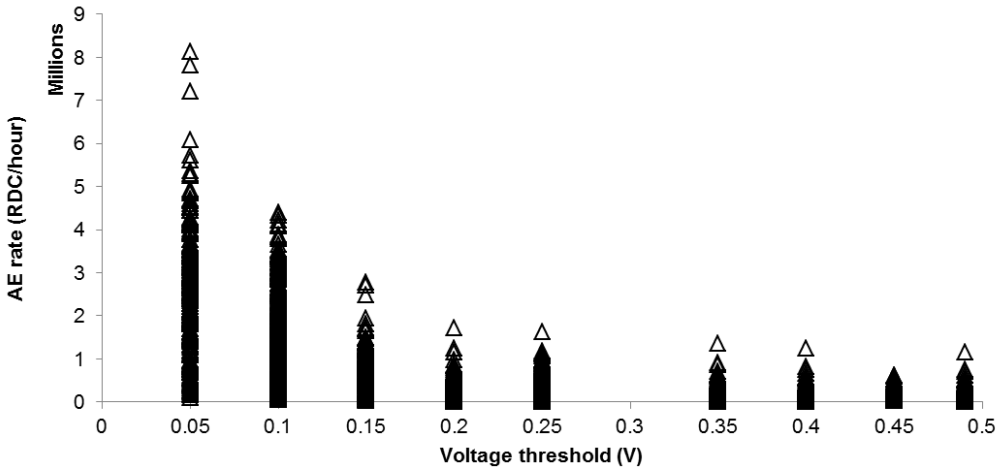

Figure 8.20. AE rate vs voltage threshold level relationship obtained from constant strain rate compression tests at a 'slow' rate of displacement

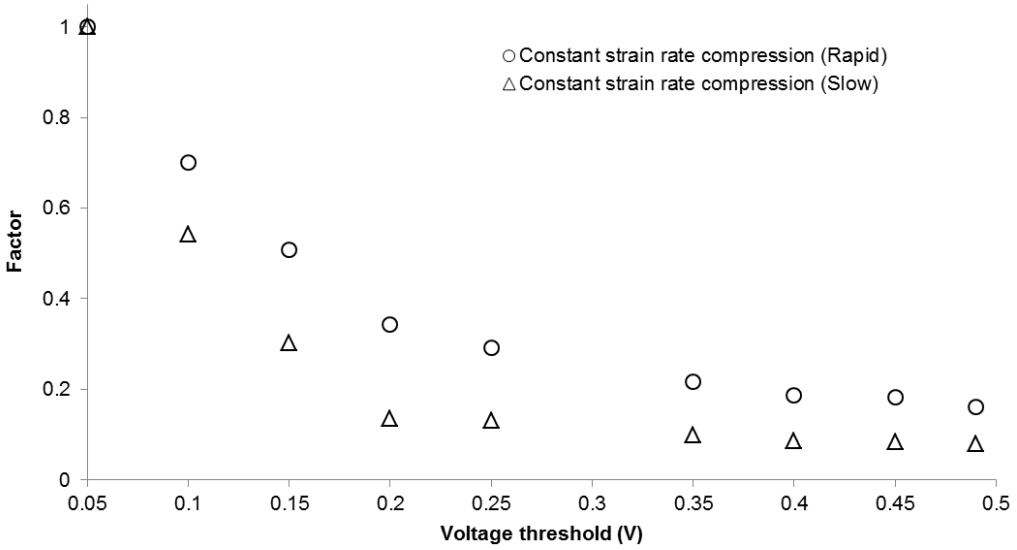

Figure 8.21. Mean AE rate measured at each voltage threshold level and deformation rate, plotted as a factor relative to the mean AE rate obtained at 0.05V

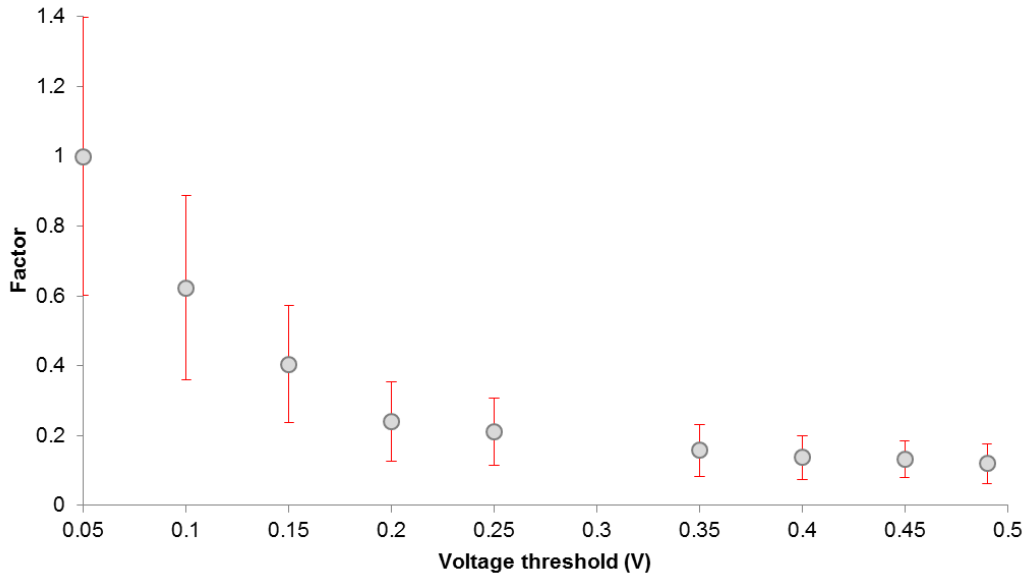

Figure 8.22. Mean AE rate measured at each voltage threshold level from both deformation rates combined, plotted as a factor relative to the mean AE rate obtained at 0.05V; error bars represent the standard deviation

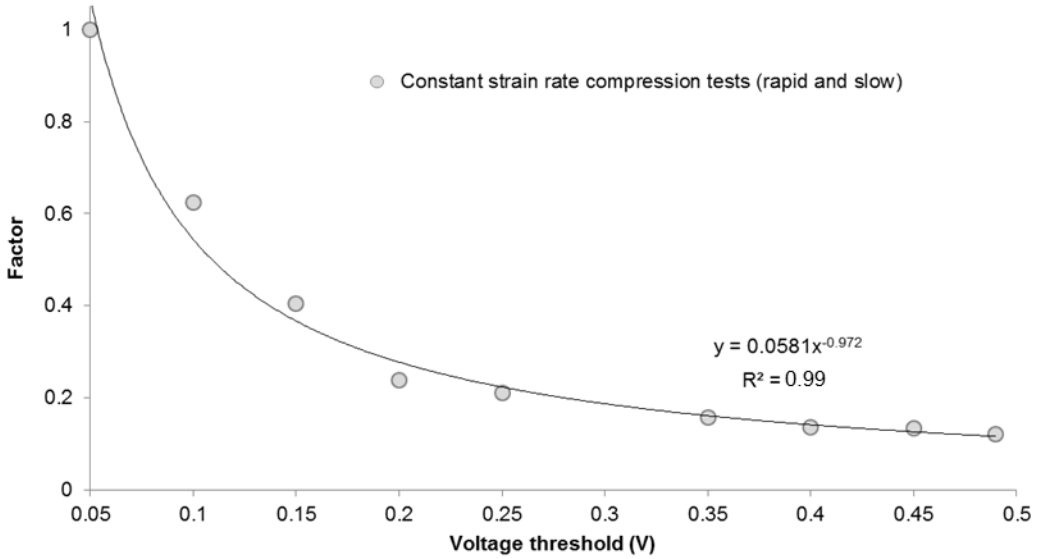

Figure 8.23. AE rate (presented as a factor relative to a maximum at 0.05V threshold level) vs. voltage threshold level relationship, determined using the data in Figure 8.22

8.4. Borehole size

8.4.1. Experimental procedure

Constant strain rate compression tests were performed on active waveguide physical models with different borehole sizes, to investigate the influence of borehole size on the magnitude of AE rates generated in response to applied deformation behaviour. The same 130 mm diameter geomembrane cylinder model as used in Chapter 6 was employed to represent a standard borehole. A 59 mm inside diameter inclinometer casing (Figure 8.24

and Table 8.5) was also employed to represent an active waveguide installed inside a smaller diameter borehole. Both models had wooden end caps to provide confinement, and the same backfill materials and waveguide were employed in each. The waveguide was a 1.3 m long, 25 mm diameter and 2 mm thick steel tube. Three different backfill materials were employed (Leighton Buzzard sand, glass aggregate, and concrete sand; the properties of each are detailed in Section 6.2.5) and three different voltage threshold levels were investigated, to understand the influence of borehole size on a range of backfills and with different voltage threshold levels set on the measurement system. The details of each test are provided in Table 8.6. All tests were performed at a 'rapid' deformation rate for durations of 2.5 minutes and total displacements of 2.8 mm. These tests were limited to <3 mm of deformation because preliminary tests demonstrated that the compression mechanism applied from the apparatus had the potential to permanently damage the inclinometer casing at larger displacements due to its rigidity and brittleness. The backfill materials were compacted in 0.2 m lifts prior to each test using a tamping rod. This experimental programme was conducted in order to establish an empirical relationship between borehole size and measured AE.

Figure 8.24. Photograph of active waveguide physical model employing an inclinometer casing, with Leighton Buzzard sand backfill and 25 mm diameter steel waveguide tube

Table 8.5. Properties and geometry of the inclinometer casing employed in the constant strain rate compression tests

Material	ABS (Acrylonitrile Butadiene Styrene)
Length (mm)	1000
Outside diameter (mm)	70
Inside diameter (mm)	59

Table 8.6. Tabulated constant strain rate (CSR) compression tests on active waveguide models with different backfill materials, borehole diameters, and voltage thresholds

Test no.	Backfill	Borehole diameter (mm)	Voltage threshold (V)
CSR-1	LB sand	130	0.1
CSR-2	LB sand	130	0.25
CSR-3	LB sand	130	0.45
CSR-4	LB sand	59	0.1
CSR-5	LB sand	59	0.25
CSR-6	LB sand	59	0.45
CSR-7	Glass	130	0.1
CSR-8	Glass	130	0.25
CSR-9	Glass	130	0.45
CSR-10	Glass	59	0.1
CSR-11	Glass	59	0.25
CSR-12	Glass	59	0.45
CSR-13	Concrete sand	130	0.1
CSR-14	Concrete sand	130	0.25
CSR-15	Concrete sand	130	0.45
CSR-16	Concrete sand	59	0.1
CSR-17	Concrete sand	59	0.25
CSR-18	Concrete sand	59	0.45

8.4.2. Results and analysis

Figures 8.25, 8.26 and 8.27 show AE rate vs. time series measurements obtained from constant strain rate compression tests on both 130 mm diameter and 59 mm diameter active waveguide models. Figure 8.25 shows results from concrete sand backfill, Figure 8.26 from glass aggregate backfill, and Figure 8.27 from Leighton Buzzard sand backfill. Results from each voltage threshold level are also presented in Figures 8.25, 8.26 and 8.27. The AE rates in each test increase with time under the constant displacement rates because the confining pressures increase with applied load. The 59 mm diameter active waveguide model (with each backfill material and with each voltage threshold level) consistently generated greater AE rates than the 130 mm diameter active waveguide model.

In Figure 8.28 the mean AE rate measured from all tests on the 59 mm diameter active waveguide are presented as a factor relative to the mean AE rate measured from all tests on the 130 mm diameter active waveguide model. These results demonstrate that the 59 mm diameter active waveguide generated an average of 2.2 times greater AE rates than the 130 mm diameter active waveguide. This contradicts the original hypothesis, which was ‘a larger borehole will result in a larger backfill volume and a greater number of particle-particle contacts, and will therefore generate greater AE rates in response to applied deformation behaviour.’ The backfill volume inside the 59 mm diameter active waveguide (1 m long) was 0.0022 m^3 and the volume inside the 130 mm diameter active waveguide (0.6 m long) was 0.0077 m^3. However, the flexural rigidity of the inclinometer

casing was significantly greater than that of the geomembrane cylinder, which led to a greater length of the backfill being deformed in response to the applied load from the ram; because the bulb of stress spread over a greater distance laterally within the 59 mm diameter active waveguide model.

In addition, detected AE from particle-waveguide interactions are typically greater than from particle-particle interactions, because they suffer less attenuation (i.e. the AE does not need to travel through particles before entering the waveguide in particle-waveguide interactions). The small magnitude deformations applied in this test (<3 mm) generated a greater magnitude of particle-waveguide interactions within the smaller diameter active waveguide model; firstly because the deformation applied on the outer wall of the casing was more easily transferred through the backfill to the outer wall of the waveguide, but also because the smaller diameter active waveguide had a greater active length over which particle-waveguide interactions could take place. For these reasons the results obtained from these active waveguide physical model tests are not able to successfully represent differences in active waveguide borehole size, due to the more complex behaviour generated by the differences in both flexural rigidity of the casing and lengths of the active waveguides. However, the results do highlight the significant difference in magnitude of detected AE from particle-waveguide and particle-particle interactions. Also, the results demonstrate that retrofitting inclinometer casings with active waveguides is possible.

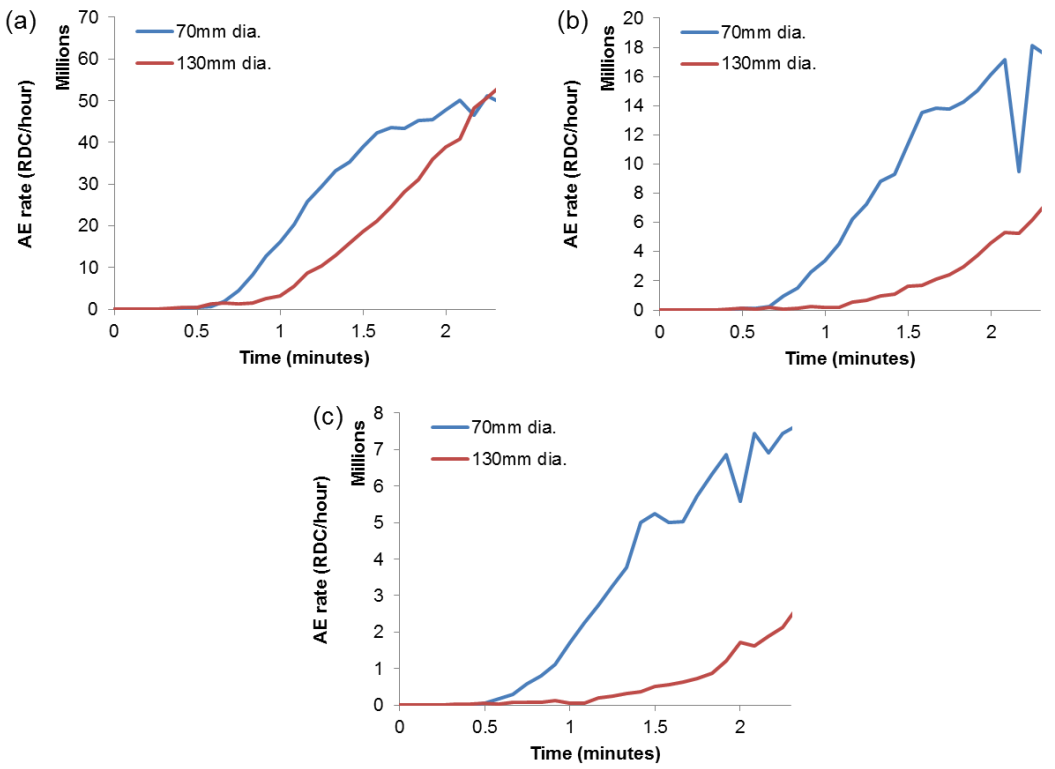

Figure 8.25. AE rate vs. time measurements obtained from constant strain rate compression tests on 130 mm diameter and 59 mm diameter active waveguide models with concrete sand backfill: a) 0.1V, b) 0.25V and c) 0.45V threshold levels

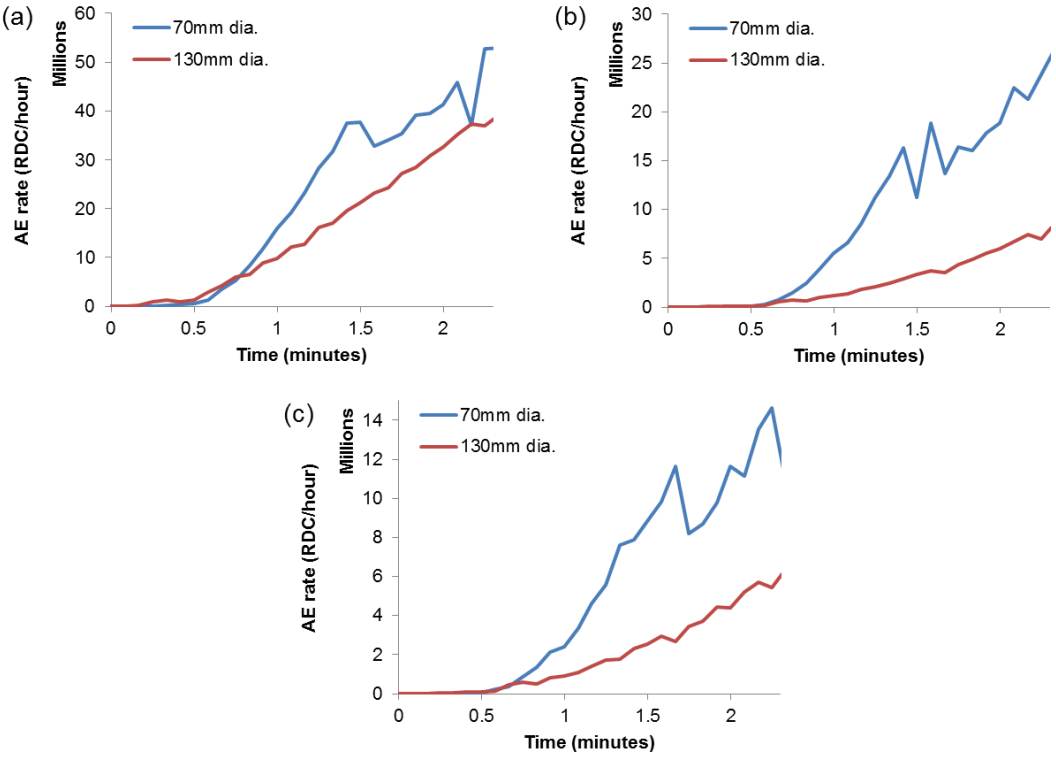

Figure 8.26. AE rate vs. time measurements obtained from constant strain rate compression tests on 130 mm diameter and 59 mm diameter active waveguide models with glass aggregate backfill: a) 0.1V, b) 0.25V and c) 0.45V threshold levels

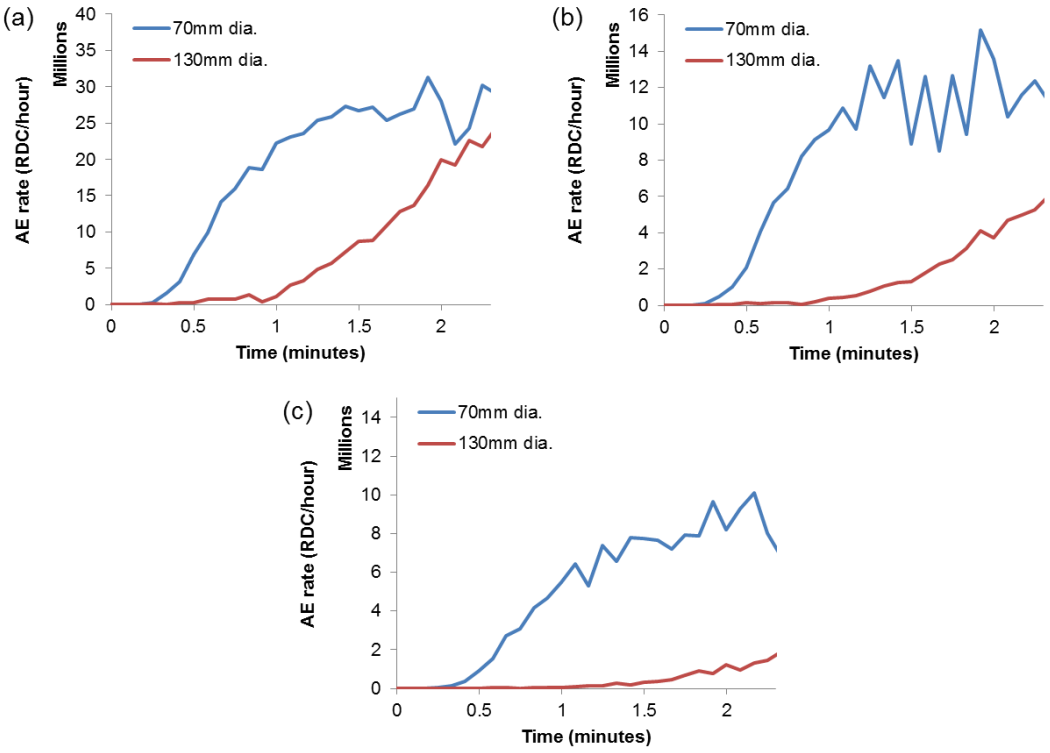

Figure 8.27. AE rate vs. time measurements obtained from constant strain rate compression tests on 130 mm diameter and 59 mm diameter active waveguide models with Leighton Buzzard sand backfill: a) 0.1V, b) 0.25V and c) 0.45V threshold levels

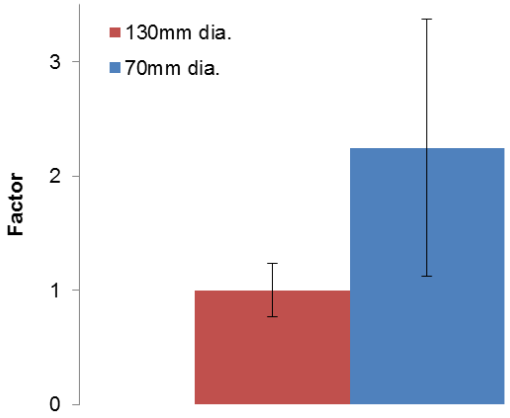

Figure 8.28. Comparison of mean AE rate measured from each backfill and voltage threshold level. Results from the 59 mm diameter active waveguide are presented relative to the mean AE rate obtained from the 130 mm diameter active waveguide. The error bars represent the standard deviation of the mean derived from each test

8.5. Waveguide geometry and properties

8.5.1. Experimental procedure

A series of constant strain rate compression tests have been performed on active waveguide models (130 mm diameter 0.6 m long geomembrane cylinder with angular gravel aggregate backfill) employing four different waveguides, with different geometry

and material properties. Each test was performed at a 'rapid' rate of deformation for a duration of 3 minutes and a total displacement of 3.3 mm. This series of experiments was conducted to investigate the influence of waveguide geometry and properties on the magnitude of AE rates measured in response to applied deformation behaviour. Details of the four waveguides employed are shown in Table 8.7 and details of the tests performed are provided in Table 8.8. Each experiment was repeated three times with a different voltage threshold level set on the AE measurement system (0.1V, 0.25V and 0.45V). Waveguide 1 (WG1) was the standard 50 mm diameter 3 mm wall thickness steel pipe used in the majority of field trials (Chapter 4), in the active waveguide physical model tests (Chapter 6), and in the attenuation tests (Section 8.2). WG2 was a 25 mm diameter steel pipe with 2 mm wall thickness (the same as used in the experiments detailed in Section 8.4). This was selected to investigate to what degree diameter and wall thickness influence the magnitude of backfill generated-AE that is induced into the pipe from applied deformation behaviour, though comparisons with WG1. WG3 was an aluminium tube of 50 mm diameter and 1 mm wall thickness; this was selected to investigate the influence of material properties (i.e. aluminium relative to steel). WG4 was a solid steel rod of 25 mm diameter; this was selected to compare the performance of rods and shells (i.e. pipes) in transmitting AE.

Table 8.7. Geometry and properties of the range of waveguides examined

	Material	Modulus of elasticity (N/m^2)	Outside diameter (m)	Wall thickness (m)	Internal diameter (m)	Cross sectional area (m^2)	Second moment of area (m^4)	Flexural rigidity (EI) (Nm^2)
WG1	Steel	2.00E+11	0.05	0.003	0.044	0.000443	1.228E-07	2.46E+04
WG2	Steel	2.00E+11	0.025	0.002	0.021	0.000145	9.628E-09	1.93E+03
WG3	Aluminium	6.90E+10	0.05	0.001	0.048	0.000154	4.622E-08	3.19E+03
WG4	Steel	2.00E+11	0.025	0	0	0.000491	1.917E-08	3.83E+03

Table 8.8. Tabulated constant strain rate (CSR) compression tests on active waveguide models with different waveguides and voltage thresholds

Test no.	Waveguide	Voltage threshold (V)
CSR-19	WG1	0.1
CSR-20	WG1	0.25
CSR-21	WG1	0.45
CSR-22	WG2	0.1
CSR-23	WG2	0.25
CSR-24	WG2	0.45
CSR-25	WG3	0.1
CSR-26	WG3	0.25
CSR-27	WG3	0.45
CSR-28	WG4	0.1
CSR-29	WG4	0.25
CSR-30	WG4	0.45

8.5.2. Results and analysis

Figure 8.29 shows the AE rate vs. time series measurements obtained from constant strain rate compression tests on the 130 mm diameter active waveguide model employing four different waveguides and with three different voltage threshold levels set on the AE measurement system. The AE rates in each test increase with time under the constant displacement rates because the confining pressures increase with applied load. The AE rates measured from the steel pipe waveguides (both 50 mm and 25 mm diameters; WGs 1 and 2) were consistently the greatest in magnitude, and comparable to each other. The 25 mm diameter steel rod (WG4) produced the least AE rates. The measured AE rates from the 50 mm diameter aluminium pipe (WG3) were between these two extremes, although WG3 performed only slightly better than WG4. In Figure 8.30 the mean AE rate measured from all tests on each waveguide are presented as a factor relative to the mean AE rate measured from all tests on WG1. The error bars in Figure 8.30 were derived from the standard deviation of the data means from the tests. These results demonstrate that both steel pipes performed the best and results from both were comparable, which suggests that diameter and wall thickness, if kept within the practical range (i.e. fit inside a borehole with sufficient annulus for granular soil backfill), have little influence on their performance for use in active waveguides when monitoring AE within the 20 to 30 kHz range.

The AE measured from the aluminium waveguide (WG3) was on average 30% of that measured from the steel pipes, and AE measured from the steel rod (WG4) was on average 6% of that measured from the steel pipes. The predominant wave modes that are measured in the waveguides when monitoring at the 20 to 30 kHz range are plane longitudinal and flexural, as detailed in Section 2.4.5. Propagation of these waves is governed by waveguide stiffness moduli and geometry. However, when comparing the

relative performance of the waveguides with their geometry and properties in Table 8.7, little correlation can be established. WG1 performed the best and it had the greatest flexural rigidity, which influences the propagation of flexural wave modes, however; WG2 had comparable performance with WG1 but had the lowest flexural rigidity of all waveguides examined. In addition, both WG1 and WG4 had the greatest cross-sectional area, along with comparable elastic stiffness, both of which influence the propagation of longitudinal wave modes, however; WG1 performed the best and WG4 performed the worst.

Geometry and properties influence the propagation of AE along the waveguide; however, the transmission (i.e. induction of the AE into the wall of the pipe prior to propagation) of AE into the waveguide from backfill-generated AE cannot be explained by a simple comparison of waveguide properties when monitoring in a narrow frequency band (20-30 kHz). During transmission wave mode conversions take place and depending on the host material properties and geometry, waves with different frequency contents propagate. The AE measurement system used in this series of experiments focused on the frequency range of 20 to 30 kHz, which is a relatively narrow band. Backfill-generated AE propagates with varying frequency contents, after transmission, along waveguides depending on their material properties and geometries. This is an explanation for the differing performances between the different waveguides examined in these tests. Also, it should be noted that the surface characteristics (e.g. roughness) of the waveguides have not been investigated, which influence the AE generated by particle-waveguide interactions.

This experimental programme investigated the relative performance of four different waveguides on their ability to transmit backfill-generated AE. This study did not investigate the attenuation characteristics of the different waveguides within the 20 to 30 kHz range. Theory states that the attenuation characteristics are predominantly due to material properties, and therefore it would be expected that the aluminium waveguide would attenuate the AE by the greatest magnitude. Aluminium waveguides are therefore not recommended for use in active waveguides for monitoring slopes with deep shear surfaces. Based on the results from this experimental programme, the use of steel pipes as waveguides for monitoring slopes using Slope ALARMS (i.e. in the 20-30 kHz range) is recommended. Further work is required to investigate the attenuation characteristics of the different waveguides, and to develop further understanding of their relative performance in transmitting backfill-generated AE, through use of an AE measurement system that allows capture of frequency spectra over a wider band.

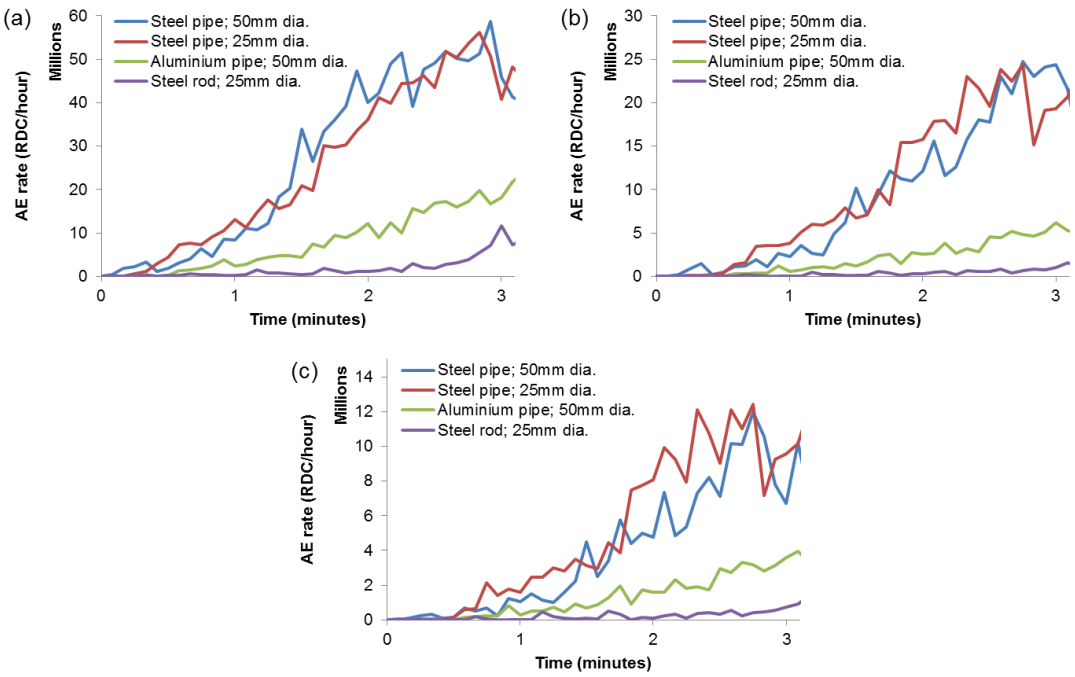

Figure 8.29. AE rate vs. time measurements obtained from constant strain rate compression tests on 130 mm diameter active waveguide models with angular gravel aggregate backfill employing four different waveguides: a) 0.1V, b) 0.25V and c) 0.45V threshold levels

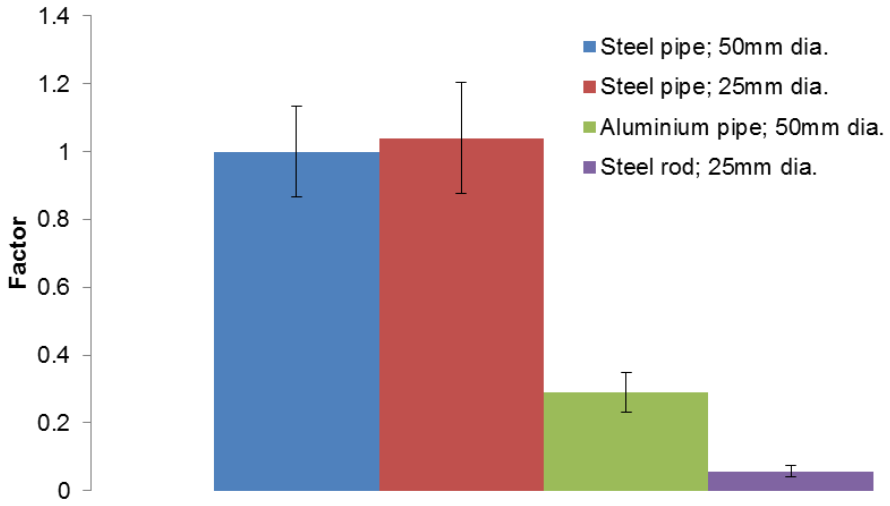

Figure 8.30. Comparison of mean AE rate measured from each waveguide (at all voltage threshold levels) presented relative to the mean AE rate obtained from the standard 50 mm diameter 3 mm wall thickness steel pipe (i.e. the standard waveguide; WG1). The error bars represent the standard deviation of the means derived from each test

8.6. Sensor node and transducer combination

8.6.1. Experimental procedure

There are slight differences in the response from Slope ALARMS sensor node and transducer combinations due to slight differences in components and manufacturing. In order to investigate the variability in the AE measured by different Slope ALARMS

measurement systems (i.e. Slope ALARMS sensor nodes and R3a transducer combinations), due to slight changes in components and manufacture, 18 sensor node and transducer combinations (each with a number ID as detailed in Table 8.9) were employed. The controlled source generator that was developed in Section 8.2 was employed in this series of experiments. A 3.2 m long 50 mm diameter 3 mm thick steel pipe was placed across sponges, comparable to the setup detailed in Section 8.2.1. In each test the AE measurement system was coupled to the waveguide 1.3 m from one end. The controlled source generator was coupled to the waveguide 1.3 m from the opposite end. This resulted in a separation distance of 0.6 m between the AE measurement system and source generator. Each measurement system had a 0.25V threshold level set on the sensor in each test. The first set of 9 measurement systems were examined using minimum of 5 x 10 second bursts from the controlled source generator (i.e. DC motor) and the second set of 9 measurement systems were examined using a minimum of 5 x 1 second bursts.

Table 8.9. Tabulated controlled source tests performed on different AE measurement systems

Sensor node and transducer ID number	Duration of controlled source applied (seconds)
1	10
3	10
4	10
5	10
6	10
7	10
8	10
9	10
10	10
12	1
13	1
14	1
15	1
16	1
17	1
18	1
19	1
20	1

8.6.2. Results and analysis

Figure 8.31 shows the RDC measured from the waveguide by each AE measurement system in response to the applied controlled source. The mean RDC measured in response to the applied 10s bursts was 234843 and the mean RDC measured in response to the applied 1s bursts was 59684. The standard deviation of the RDC measured in response to the applied 10s bursts was 22% of the mean, and the standard deviation of the RDC measured in response to the applied 1s bursts was 13% of the mean. At first inspection this would suggest that greater variability in RDC was recorded from the 10s bursts,

however, at closer inspection it is evident that this variability was due to greater variability in the sensitivity of the AE measurement systems employed. This is because the variability (i.e. spread in measured values) in the measured RDC values from each AE measurement system from both the 1s and 10s bursts was comparable. However, the means of the measured values from the systems tested under 1s bursts were comparable to each other; whereas the means of the measured values from the systems tested under the 10s bursts were more variable. Hence, the sensitivity of the AE measurement systems employed in the 10s burst tests were more variable.

These results demonstrate that slight changes in AE measurement system (i.e. Slope ALARMS sensor node or R3a transducer) can result in quite significant changes in the AE response to applied deformation behaviour. The procedure developed in this series of experiments (i.e. use of the controlled source generator on a waveguide) is expected to serve as a method of calibration of each AE measurement system prior to deployment in the field. Results from each calibration will be compared to the results shown in Figure 8.31 to assess the relative sensitivity of the AE measurement system, so that this can be compensated for when the quantification framework (Chapter 9) is applied during setup and installation.

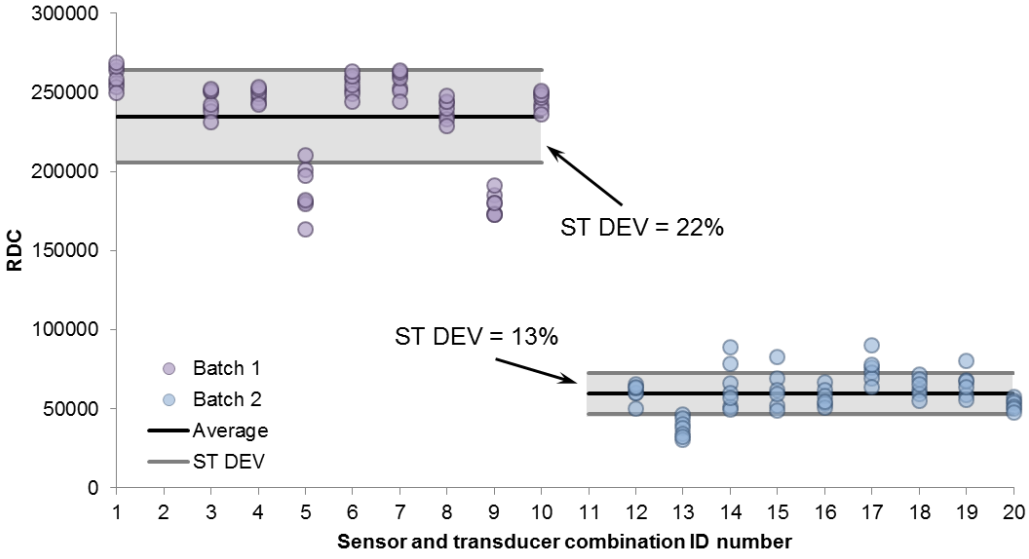

Figure 8.31. RDC measured by each sensor and transducer combination coupled to a waveguide in response to AE induced by the controlled source generator; measurement systems 1 to 10 received 10s blasts from the motor and measurement systems 11 to 20 received 1s blasts from the motor

8.7. Summary

In this Chapter the influence of system variables upon the AE response to applied deformation behaviour (i.e. Objective 4) have been investigated. The results from a series of experimental programmes conducted to understand the influence of each of the

variables are used in the development of a quantification framework (i.e. Objective 5) in Chapter 9.

In order to quantify the influence of attenuation (i.e. depth to shear surface) on the AE measured at the ground surface from an AE system, a series of experiments were conducted to quantify the attenuation coefficients for a waveguide, connected in lengths using screw threaded couplings, with a series of external environments. A controlled source generator that comprised a DC motor was developed to generate easily repeatable AE. Comparisons with constant strain rate compression tests demonstrated that the AE produced from the controlled source was comparable to backfill-generated AE. First, attenuation coefficients for a waveguide connected in 3.2 m lengths with tightened screw threaded couplings and surrounded by air (0.16 dB/m) was determined. This coefficient was compared with results obtained by other authors for a solid length of pipe (i.e. no couplings); this demonstrated that losses due to couplings (spaced 3.2 m apart) along the waveguide could be approximated to 0.05 dB/m. The attenuation due to high quality tightened screw threaded couplings is therefore very small. The losses due to couplings would reduce if longer lengths (less frequent couplings along the waveguide) were employed. In contrast, the losses due to couplings would increase if shorter lengths (more frequent couplings along the waveguide) were employed. Second, a trench was excavated and a waveguide was buried in soil to quantify attenuation coefficients for waveguides surrounded by soil. Attenuation coefficients were determined for a waveguide surrounded by granular soil (2.78 dB/m) (i.e. active waveguide backfill) and fine grained soil (4.75 dB/m) (i.e. the bentonite-grout ground surface plug). The attenuation coefficients are used in Chapter 9 to factor for the AE losses experienced by a system installed in slopes with any shear surface depth.

The influence of sensor voltage threshold level on the magnitude of AE measured was quantified using active waveguide physical model tests (constant strain rate compression tests). The factor vs. voltage threshold relationship was successfully approximated using a $y = 1/x$ relationship (returning an R^2 value of 0.99): $y = 0.0581x^{-0.972}$. This empirical relationship was shown to be consistent with measurements obtained from systems set at different voltage threshold levels in the first-time failure experimentation detailed in Section 7.3.2.2. It should be noted that this empirical relationship was determined using active waveguide physical models that had angular granite medium-gravel aggregate backfill, and results from Section 7.3.2.2 demonstrated that the AE vs. voltage threshold level relationship can be slightly different for different backfill materials. This relationship is therefore representative of that for backfill materials comparable to the medium-gravel employed.

Constant strain rate compression tests on active waveguide physical models were also conducted in an attempt to understand the influence of borehole size on the AE response from an active waveguide. The hypothesis being tested was; 'a larger borehole will result in a larger backfill volume and a greater number of particle-particle contacts, and will therefore generate greater AE rates in response to applied deformation behaviour'. However, the AE measurements from the smaller diameter active waveguide were consistently more than twice the magnitude of AE measurements from the larger diameter active waveguide, which contradicts the hypothesis. These results are expected to be an artefact of the active waveguide physical models employed in the experiments. The smaller diameter active waveguide was longer (1 m) than the larger diameter active waveguide (0.6 m), and the smaller diameter casing had greater flexural rigidity. For both of these reasons a greater magnitude of particle-waveguide interactions took place in the smaller diameter active waveguide in response to the same applied deformation behaviour. The results from these experiments do not allow the influence of borehole size to be quantified; however, they demonstrate the significant difference in AE generated between particle-particle interactions, which must propagate through particles prior to being transmitted into the waveguide, and particle-waveguide interactions. In addition, these results demonstrated that retrofitting inclinometer casings with active waveguides is possible.

An experimental programme was conducted to investigate the influence of waveguide mechanical properties and geometry on their ability to transmit backfill-generated AE. The results demonstrated that when monitoring at a focused frequency range of 20 to 30 kHz, it is not possible to relate the measured AE from various waveguides with their mechanical properties and geometry alone; consideration must also be given to the frequency content of the propagating waves. The results however did demonstrate that when monitoring in the 20 to 30 kHz range using a system such as Slope ALARMS, the greatest backfill-generated AE response is in steel pipes (as opposed to aluminium pipes or steel rods). The AE response (in the 20-30 kHz range) from steel pipes is also comparable irrespective of changes in diameter and wall thickness, as long as they are kept within a practical range (i.e. fit inside a borehole with sufficient annulus for granular soil backfill). The AE measured from the aluminium waveguide was on average 30% of that measured from the steel pipes, and AE measured from the steel rod was on average 6% of that measured from the steel pipes. Results from these experiments therefore demonstrated that steel pipes should preferably be used in active waveguides when using an AE monitoring system such as Slope ALARMS.

An experimental procedure was developed, using the controlled source generator, to calibrate each AE measurement system (i.e. Slope ALARMS sensor node and R3a

transducer combination) prior to deployment in the field. A database of measurements from 18 sensor node and transducer combinations, in response to the applied controlled source generator, has been developed. The sensitivity of each AE measurement system can now be calibrated using this procedure and by comparing the results with the database of results from these 18 systems. The standard deviation of the AE response from the first batch of 9 systems was 22% of the mean, and the standard deviation of the AE response was 13% of the mean from the second batch of 9 systems.

CHAPTER 9

A framework for the quantification of slope deformation rates from measured AE

9.1. Introduction

Each AE system installation is different in that one or more of the variables that influence the AE response to applied deformation behaviour are changed (e.g. depth to shear surface, sensor and transducer combination, sensor voltage threshold level, and backfill material). Results from the field trials (Chapters 4 and 5) and laboratory experiments (Chapters 6 and 7) have demonstrated that a proportional relationship exists between AE rates and slope displacement rates. Within this Chapter a framework is developed for the determination of calibration AE rate-slope displacement rate relationships for any AE system installation. First, the quantification framework and algorithm are proposed. Second, a series of charts are presented that are to be used in the selection of partial factors associated with each variable for input into the quantification algorithm. An example application of the quantification method is then presented using a case study at the Nafferton embankment. This case study demonstrates how the quantification framework can be used to set RDC warning levels on the Slope ALARMS system that are related to rates of slope movement, which allows the AE monitoring approach to provide a quantitative measure of slope stability. This was the overall aim of the PhD and meets Objective 5. The potential error in quantifying slope displacement rates from measured AE rates when using the framework is discussed, and decision making protocols using alarm vs. time behaviour trends are suggested.

9.2. Proposed framework and algorithm

Many variables are kept consistent between each field installation of the AE monitoring system, due to the same specification of sensor node and transducer (e.g. transducer resonant frequency, band pass filter to focus AE within 20 to 30 kHz monitoring range, and 70 dB amplification, etc.). The waveguide mechanical properties and geometry, along with lengths and coupling method, are usually prescribed. The voltage threshold level on the sensor is user definable, although it is usually set to 0.25V in order to capture significant backfill-generated AE from the waveguide but minimal background/

environmental noise. There is also some degree of control over the selection of backfill material as both sand and gravel are usually readily available from a local supplier. The borehole size is often standard at around 130 mm in diameter, which is dictated by the drilling contractor's equipment, but can typically range from 90 mm to 150 mm in diameter. If a shallow active waveguide is installed inside a hand augered hole, these will usually be approximately 60 mm in diameter.

Figure 9.1 shows a schematic detailing each of the variables that influence the AE response from the measurement system and the point(s) at which they have influence in the system as AE propagates from the source at the shear surface to the sensor at the ground surface.

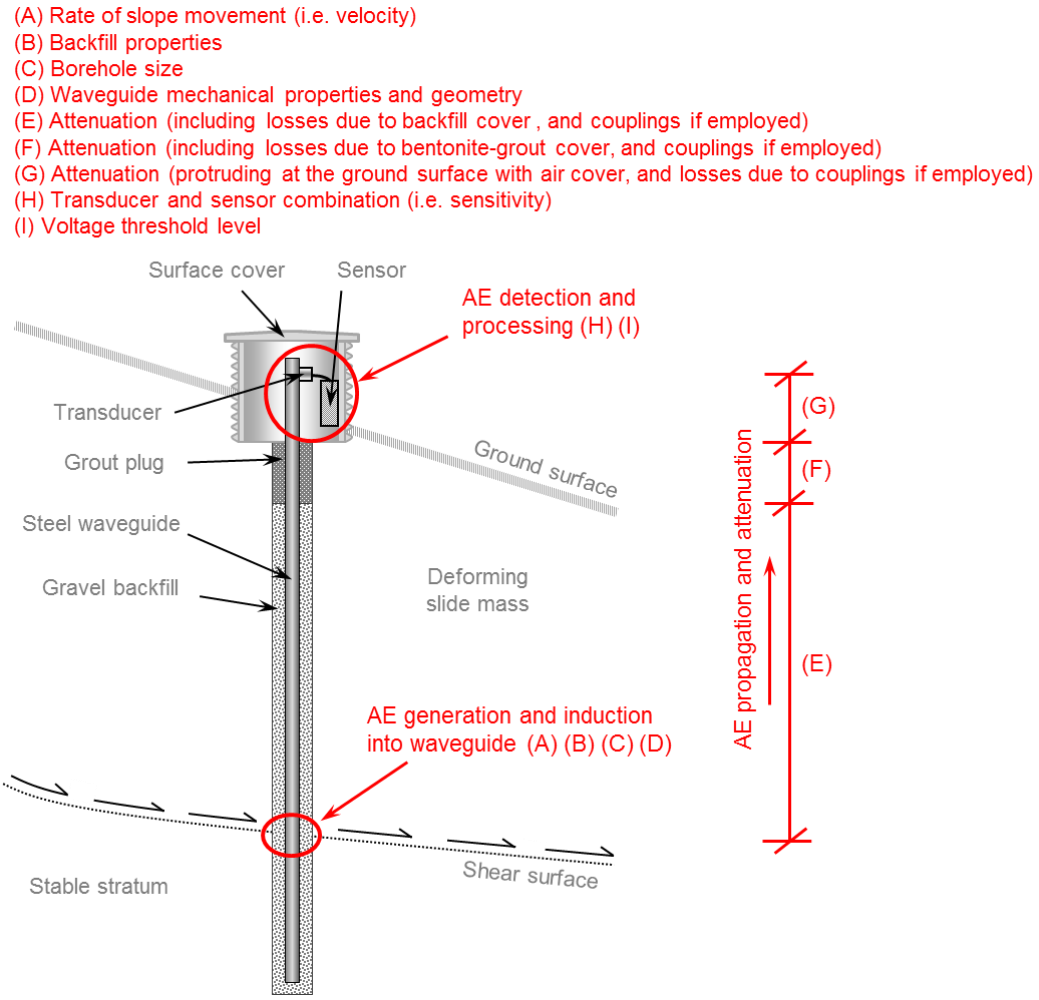

Figure 9.1. Schematic detailing each of the variables that influence the AE response from the measurement system and the point(s) at which they have influence in the system as AE propagates from the source at the shear surface to the sensor at the ground surface

As the slope displaces and deforms the active waveguide, AE rates are generated. The magnitude of AE rates generated from the active waveguide is a function of the applied velocity of slope movement, the backfill material, and the borehole size. These AE rates

are subsequently modified as they are transmitted into the waveguide, due to the waveguide mechanical properties, geometry, and surface characteristics. The magnitude of AE is reduced as it propagates along the waveguide, due to attenuation in the waveguide, at couplings, and at the interface with the granular backfill. The greater this propagation distance (i.e. the greater the depth to the shear surface) is, the greater the reduction in AE. Attenuation also occurs as the AE propagates along the section of waveguide that is surrounded by the bentonite-grout surface plug, and these losses per unit length are greater than those experienced by the granular backfill cover. Further attenuation occurs in the waveguide over the length protruding from the ground surface prior to being detected by the AE measurement system; however, the losses with air cover are significantly less than the losses with granular backfill/bentonite-grout cover. This mechanical AE signal is converted to an electrical signal by the transducer, which is influenced by the quality of the transducer-waveguide coupling. It is important to maximise the surface area of contact at the transducer-waveguide interface and this is done using silicone gel and the compressive contact provided by an elastic band and a cable tie (or similar). The sensor node subsequently processes the signal. At this stage the sensitivity of the sensor node and transducer combination influences the AE measured, along with the voltage threshold level set on the sensor. At each of these stages the AE rates generated by the active waveguide are modified, which can be a magnification or a reduction. If the AE rate-slope displacement rate relationship for the active waveguide is known, partial factors that are derived for each of these AE-magnification or AE-reduction mechanisms can be applied to this relationship, so that slope displacement rates can be derived from measured AE rates for any field installation. This process is presented as an equation in Equation 9.1.

$$\mathrm{AE}_{\mathrm{rate}} = f(\mathrm{C_p}, \mathrm{Velocity})$$

$$\text{where,} \quad \mathrm{C_p} = f(\mathrm{B}, \mathrm{C}, \mathrm{D}, \mathrm{E}, \mathrm{F}, \mathrm{G}, \mathrm{H}, \mathrm{I}) \qquad \textbf{(9.1)}$$

Where factors B to I are defined in Figure 9.1. AE rate-slope displacement rate relationships have been defined for three different backfill materials in Chapter 7. The AE rate-slope displacement rate relationships defined in Chapter 7 are employed here in the development of this framework because they were produced from a realistic slope movement mechanism over the greatest range of applied velocities and for the largest magnitude of applied deformation, out of all of the field and laboratory experiments performed in this study. Equation 9.2 presents the same expression as Equation 9.1, but uses modified notation that is more representative of each of the parameters.

$$AE_{rate} = f(AW_{BT}, Velocity) \times \left(BH_S \times W_t \times A_b \times A_g \times A_{air} \times S_{S+T} \times V_{TL}\right) \quad \textbf{(9.2)}$$

Where $f(AW_{BT}, Velocity)$ = AE rate vs. velocity function (i.e. 3rd order polynomial) for the active waveguide and backfill type, BH_s = borehole size factor, W_t = waveguide transmission factor, A_b = attenuation with backfill surround factor (including coupling effects if employed), A_g = attenuation with bentonite-grout surround factor (including coupling effects if employed), A_{air} = attenuation with air surround factor (including coupling effects if employed), S_{S+T} = sensor node and transducer sensitivity factor, and V_{TL} = voltage threshold level factor.

Note that AE rate in Equation 9.2 is expressed as a function of velocity because it is the rate of deformation that causes the AE rate response. The velocity is the independent variable (i.e. a system input) and AE rates are the dependent variable (i.e. system output). This is also the reason that AE rates are presented on the y-axis and velocity on the x-axis on the charts in this Chapter. The charts are also presented in this way because they are designed to allow the user to select AE rate trigger levels that are based on slope displacement rates, for input into the Slope ALARMS system to trigger text messages when thresholds are exceeded. To quantify velocity values from measured AE rates the user can rearrange the equations to make 'velocity' the subject, or simply plot the charts with velocity on the y-axis and AE rates on the x-axis and plot a new trend line to derive an equation for the relationship with velocity as the subject.

In the following section a series of charts are presented that define empirical relationships for each of these variables, which will allow the user to quantify parameters for input into Equation 9.2 to derive slope displacement rates from measured AE rates from any AE system installation.

9.3. Charts for determination of parameters

The empirical relationships presented in these charts were derived from physical model experiments conducted in Chapters 7 and 8 of this thesis. Note that it has not been possible to successfully quantify the influence of borehole size in this study; therefore charts are not presented for this variable.

Figures 9.2 to 9.4 present the empirical AE rate vs. velocity relationships derived from the first-time failure experimentation detailed in Chapter 7. Figure 9.2 shows the relationships derived for the limestone fine-gravel, Figure 9.3 for the Leighton Buzzard sand, and Figure 9.4 for the granite medium-gravel. Relationships derived from both 0.1V and 0.25V threshold levels are presented on each of these charts. Note that the 3rd order

polynomials used to represent these relationships are only valid over the range of velocities examined and presented (i.e. 0 to ~320 mm/hour). Figure 9.5 shows the relative performance of different waveguide types that can be used if it is not possible to acquire the recommended steel tube, and a steel rod or aluminium tube is used instead. Figures 9.6 to 9.9 show the attenuation (i.e. factor vs. propagation distance) relationships for the granular backfill, bentonite-grout and air external environments. Relationships are presented for waveguides without couplings, and for waveguides connected using ~1.0 m, 3.2 m and 6.4 m lengths. Relationships for waveguides connected in ~1.0 m lengths were determined by multiplying the 3.2 m spaced couplings attenuation coefficient (0.006 Np/m determined in Section 8.2.4.3) by 3, and the relationships for waveguides connected in 6.4 m lengths were determined by dividing the 3.2 m spaced couplings attenuation coefficient by 2. Note that typical pipe lengths are ~1 m, 3.2 m and 6.4 m. Figure 9.10 shows the relative sensitivity of 18 different transducer and sensor node combinations in response to the controlled source. Note that the sensor and transducer combinations used in the first-time failure experiments in Chapter 7, which were used to derive the AE rate-velocity relationships in Figures 9.2 to 9.4, had ID numbers 14 (the system set at 0.25V) and 16 (the system set at 0.1V), both of which exhibit relatively average sensitivity. Figure 9.11 presents the factor vs. voltage threshold level relationship that was derived in Section 8.3.

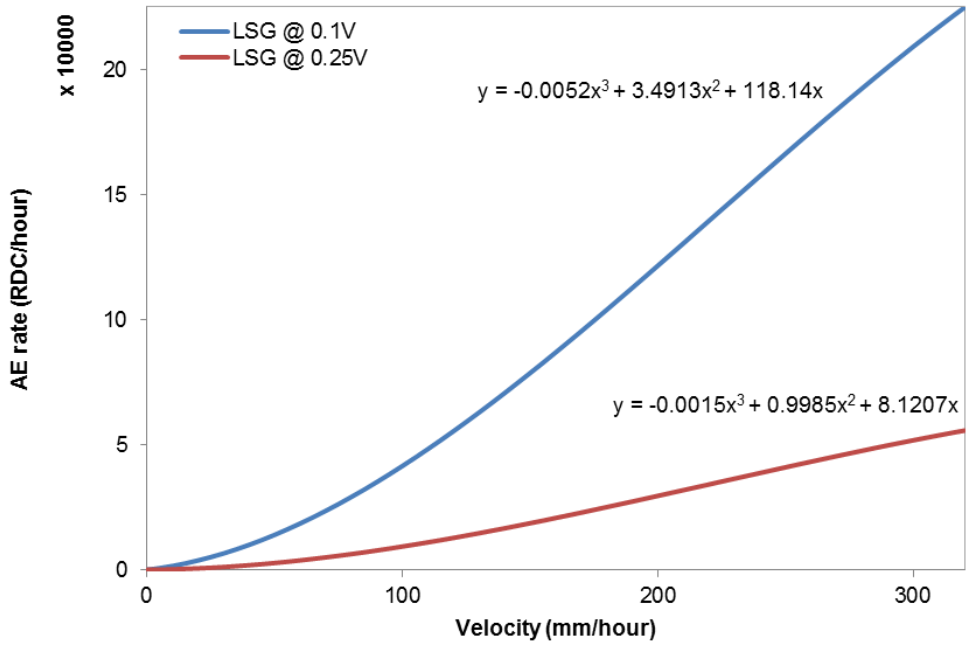

Figure 9.2. AE rate vs. velocity relationships derived for limestone fine-gravel backfill at both 0.1V and 0.25V voltage threshold levels using the first-time failure experimentation (i.e. shallow shear surface)

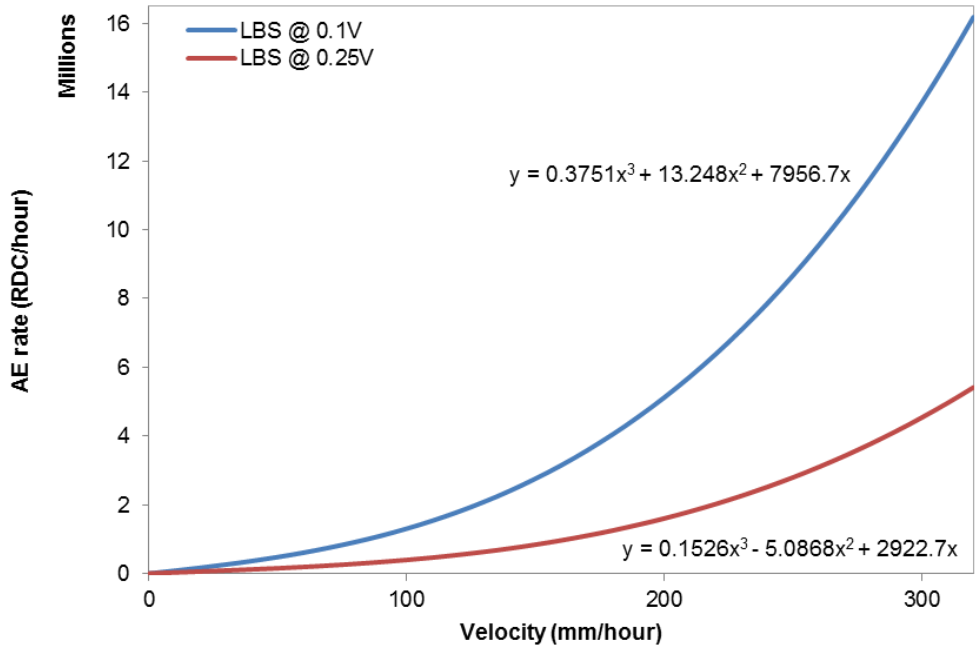

Figure 9.3. AE rate vs. velocity relationships derived for Leighton Buzzard sand backfill at both 0.1V and 0.25V voltage threshold levels using the first-time failure experimentation (i.e. shallow shear surface)

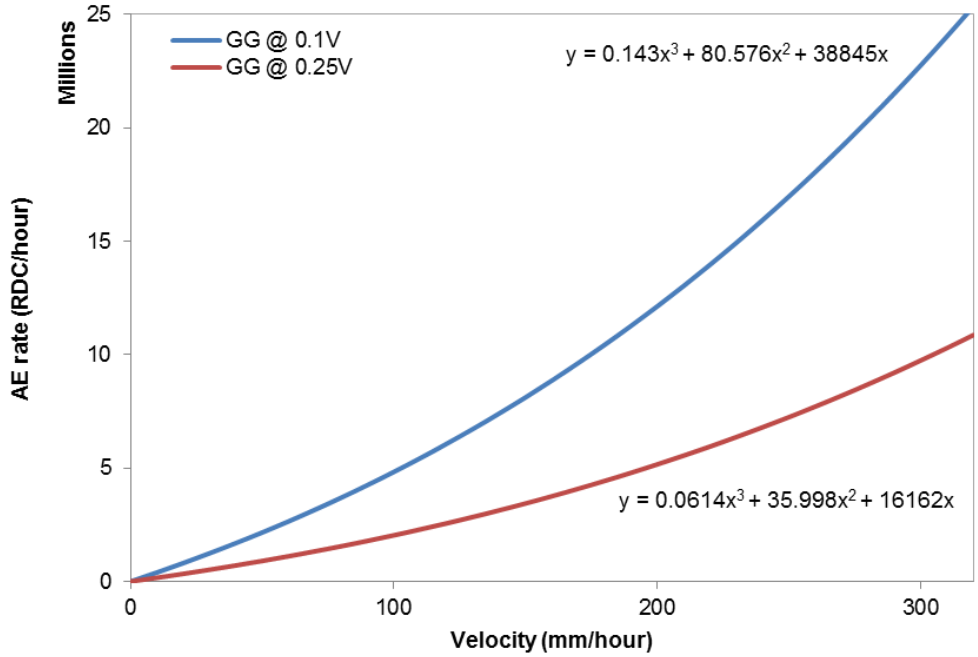

Figure 9.4. AE rate vs. velocity relationships derived for granite medium-gravel backfill at both 0.1V and 0.25V voltage threshold levels using the first-time failure experimentation (i.e. shallow shear surface)

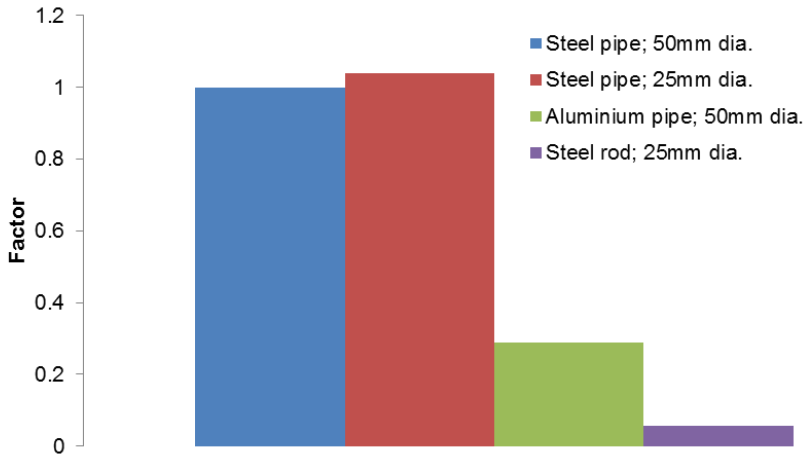

Figure 9.5. Mean AE rate measured from each waveguide presented relative to the mean AE rate obtained from the standard 50 mm diameter 3 mm wall thickness steel pipe

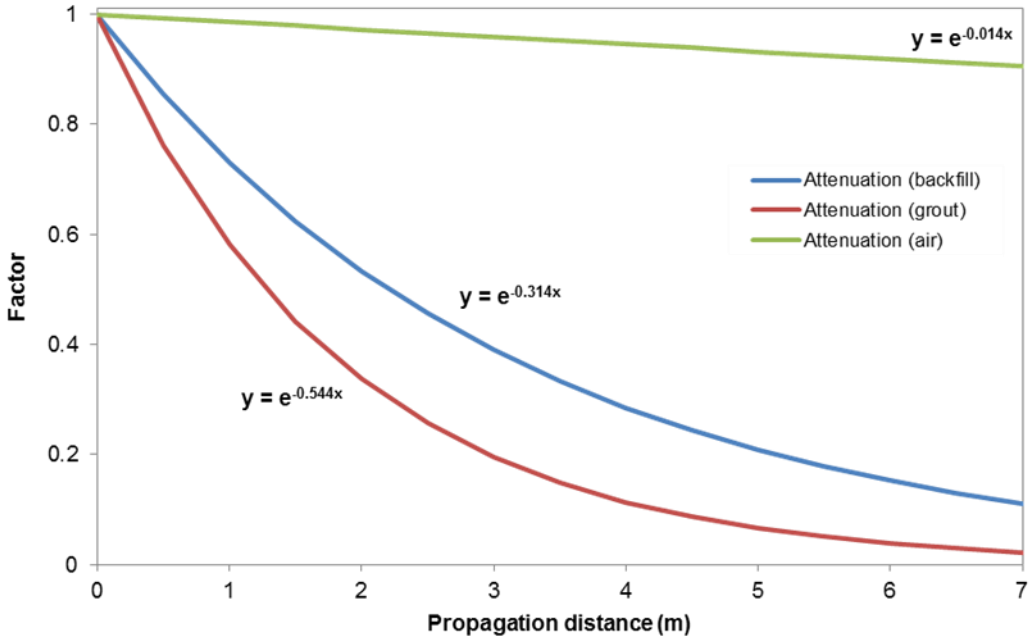

Figure 9.6. Partial factor vs. propagation distance (attenuation) relationships for steel waveguides with no couplings. Relationships for granular backfill, bentonite grout and air external environments are presented. Factor is presented on a linear scale and propagation distance up to 7 m because waveguides any longer typically employ couplings (it is difficult to transport longer lengths to site)

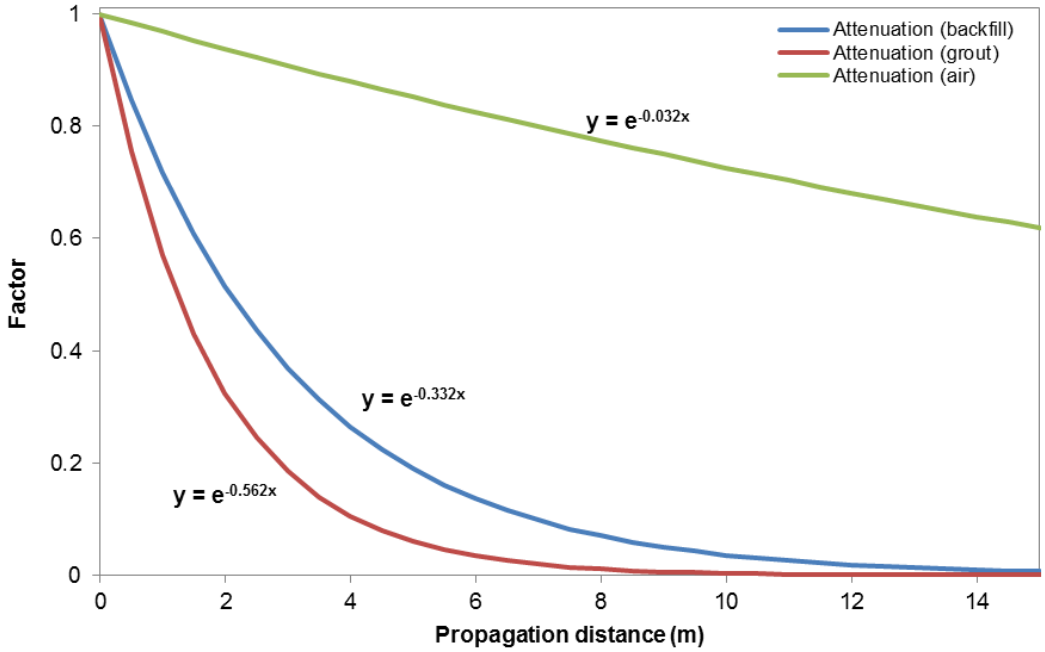

Figure 9.7. Partial factor vs. propagation distance (attenuation) relationships for steel waveguides with ~1.0 m lengths connected using screw threaded couplings. Relationships for granular backfill, bentonite grout and air external environments are presented. Factor is presented on a linear scale and propagation distance up to 15 m because waveguides any longer typically employ longer lengths and less frequent couplings

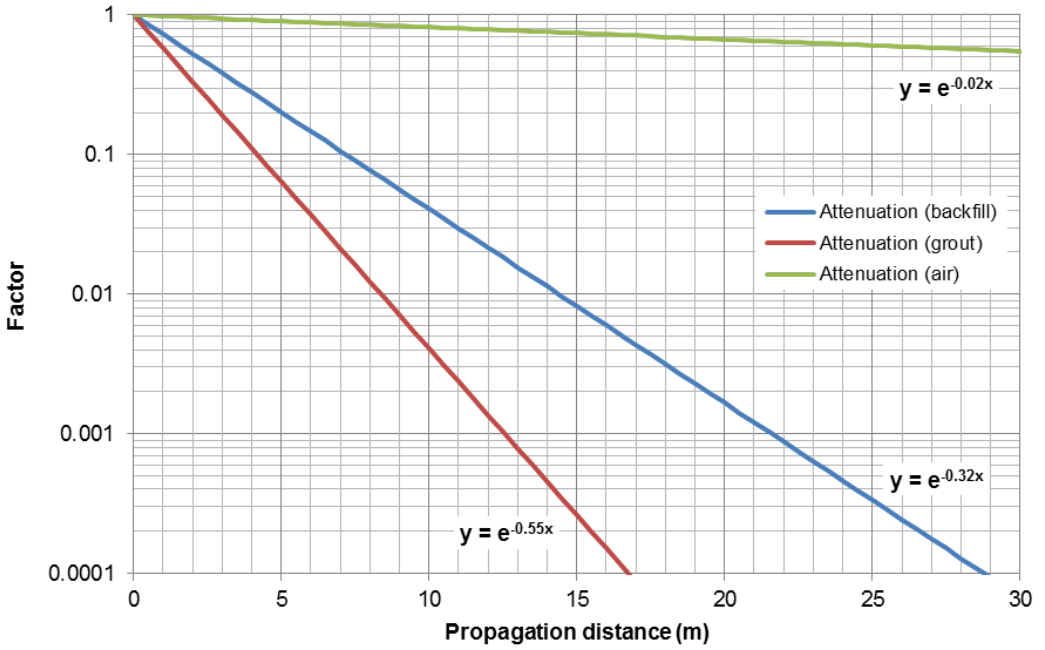

Figure 9.8. Partial factor vs. propagation distance (attenuation) relationships for steel waveguides with 3.2 m lengths connected using screw threaded couplings. Relationships for granular backfill, bentonite grout and air external environments are presented. Factor is presented on a log scale and propagation distance up to 30 m. The equations that define the relationships are presented and can be used to quantify factors for longer propagation distances

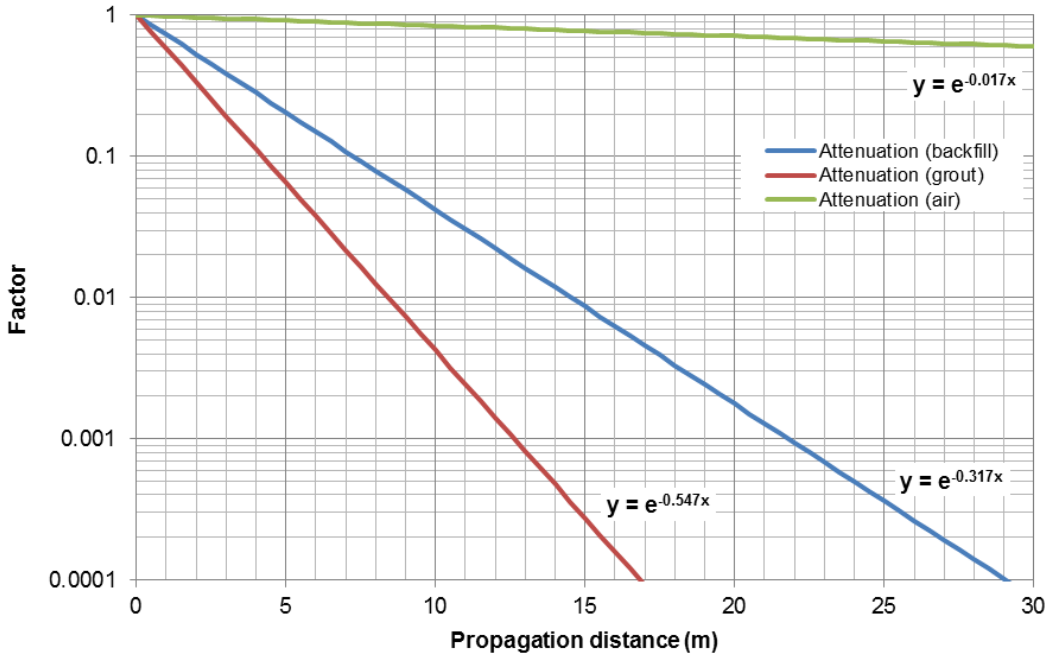

Figure 9.9. Partial factor vs. propagation distance (attenuation) relationships for steel waveguides with 6.4 m lengths connected using screw threaded couplings. Relationships for granular backfill, bentonite grout and air external environments are presented. Factor is presented on a log scale and propagation distance up to 30 m. The equations that define the relationships are presented and can be used to quantify factors for longer propagation distances

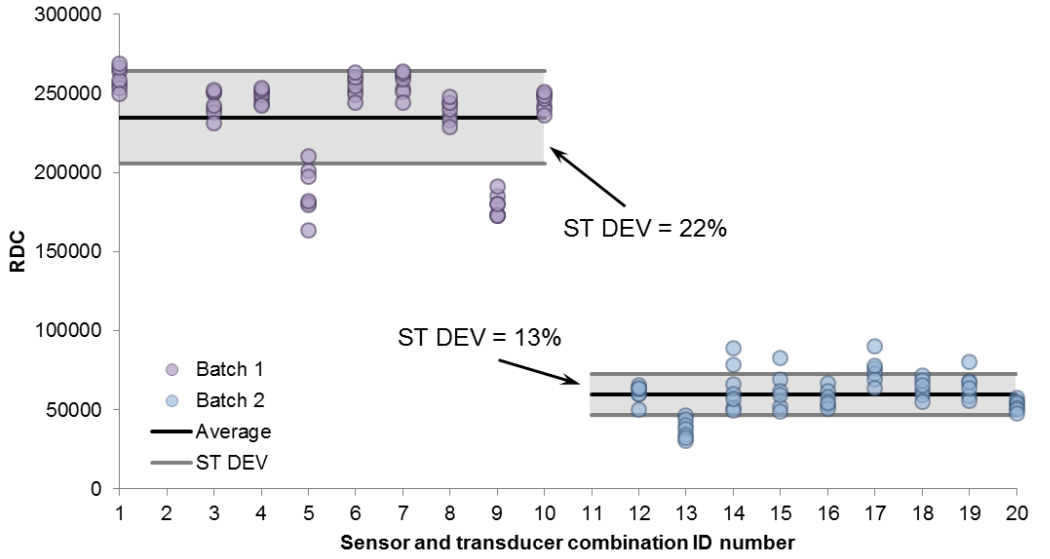

Figure 9.10. RDC measured by each sensor and transducer combination coupled to a waveguide in response to AE induced by the controlled source generator; measurement systems 1 to 10 received 10s blasts from the motor and measurement systems 11 to 20 received 1s blasts from the motor

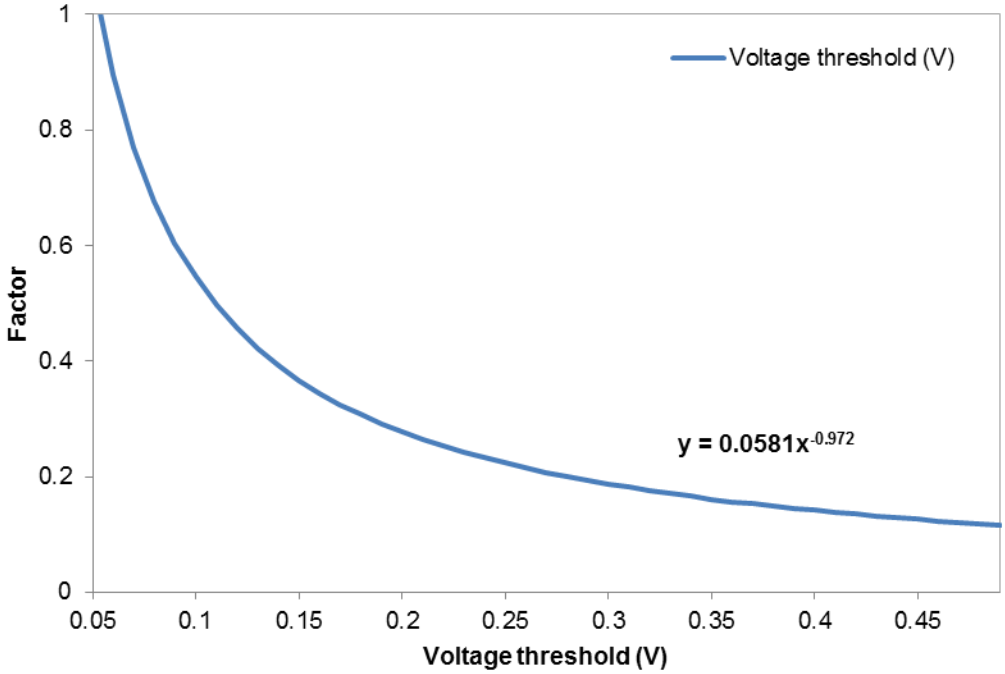

Figure 9.11. Factor vs. voltage threshold level relationship

9.4. Example application of method

In this section an example application of the quantification framework to the installation at Nafferton embankment is presented. Figure 9.12 shows a cross-section of the installation at Nafferton and a series of potential failure surfaces are superimposed. The anticipated failure is shallow. Shear surface development is expected to initiate at the toe of the slope or above. This is because the underlying soil has greater strength. A shallow failure is also expected due to the approach taken to induce failure, which was ground surface water infiltration. Water accumulation in the surficial slope zone will reduce suctions and eventually lead to strength reduction. A shear surface depth at the location of the active waveguide of 1 m was used in this example. Note that shear surface depths can either be determined from other subsurface monitoring instrumentation (e.g. conventional inclinometers where shear surfaces already exist), or predicted using CPT/SPT measurements with depth during drilling, or predicted using information on geometry and as much information on material properties as is available. A sensitivity analysis could then be performed using the range of possible shear surface depths on the variability in AE rate-velocity relationships that would be derived using each shear surface.

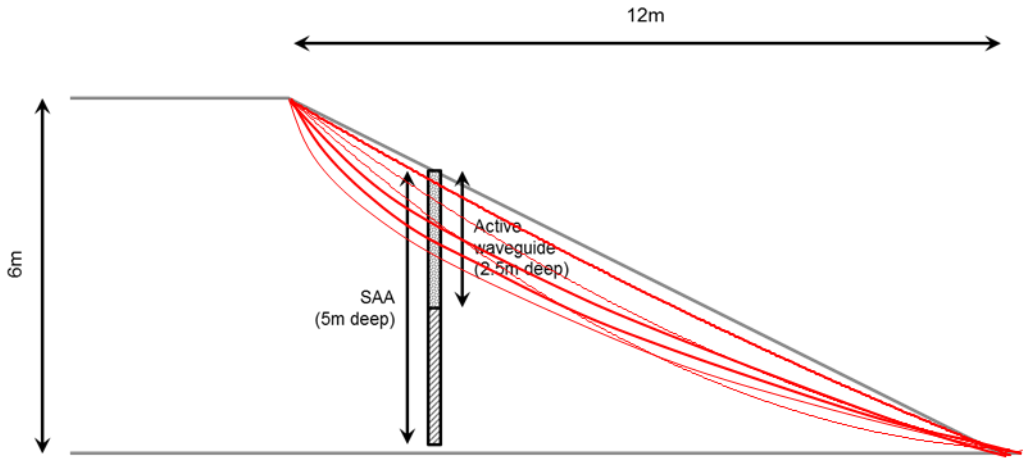

Figure 9.12. Cross-section of installation at Nafferton embankment with possible failure surfaces superimposed (red lines)

Figure 9.13 presents a schematic of the AE system at Nafferton, with a shear surface intersecting the active waveguide at a depth of 1 m. The lengths of waveguide subject to different external environments (i.e. sand, bentonite-grout and air) are annotated; 0.7 m with sand backfill, 0.3 m with bentonite-grout backfill, and 0.3 m exposed to air. Figure 9.14 presents the empirical AE rate-velocity relationships derived for Leighton Buzzard sand, which was the active waveguide backfill used at Nafferton. Note that the sensor node is set to a 0.25V threshold level at Nafferton and so the AE rate-velocity relationship for the 0.25V threshold level will be employed in this example. Because the AE rate-velocity relationship was derived from a physical model that had a shear surface depth of 0.7 m and 0.7 m of the waveguide had granular backfill cover, no attenuation partial factor was derived for this parameter (A_b) and it was set to 1.0. The physical model used to derive the AE rate-velocity relationship had the transducer positioned 0.15 m above the ground surface, which is a comparable distance to that between the transducer and the ground surface at the Nafferton installation; no partial factor was derived for this parameter (A_{air}) in this example and it was set to 1.0. However, the installation at Nafferton had a 0.3 m bentonite-grout plug at the top of the active waveguide and this needed to be accounted for. A partial factor for 0.3 m of grout cover was derived using Figure 9.15, which resulted in a value of 0.85.

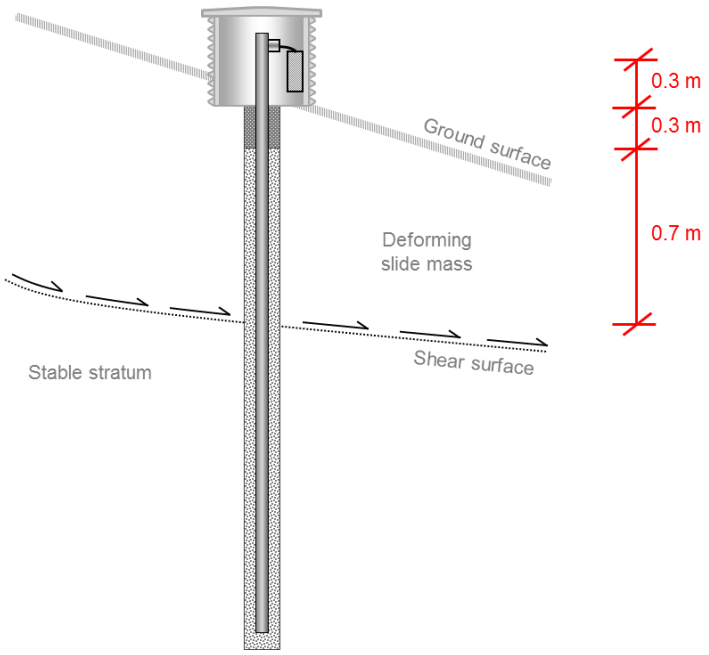

Figure 9.13. Schematic of active waveguide installation at Nafferton embankment with an assumed 1 m deep failure surface; lengths of waveguide with different external environments are annotated

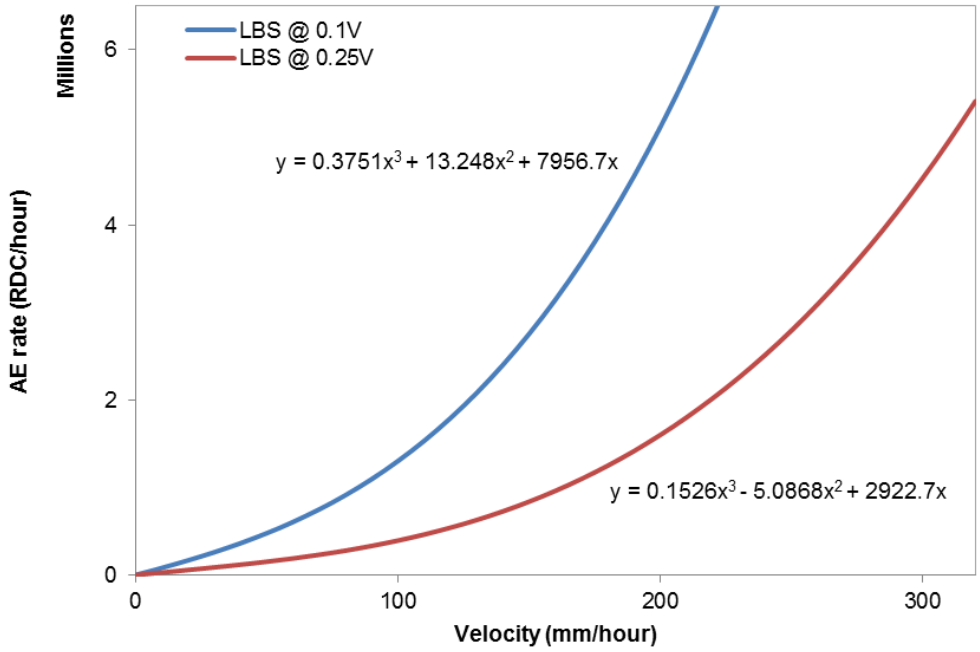

Figure 9.14. AE rate vs. velocity relationships derived for Leighton Buzzard sand backfill at both 0.1V and 0.25V voltage threshold levels using the first-time failure experimentation (i.e. shallow shear surface). The AE system at Nafferton embankment has Leighton Buzzard sand backfill and a voltage threshold level of 0.25V

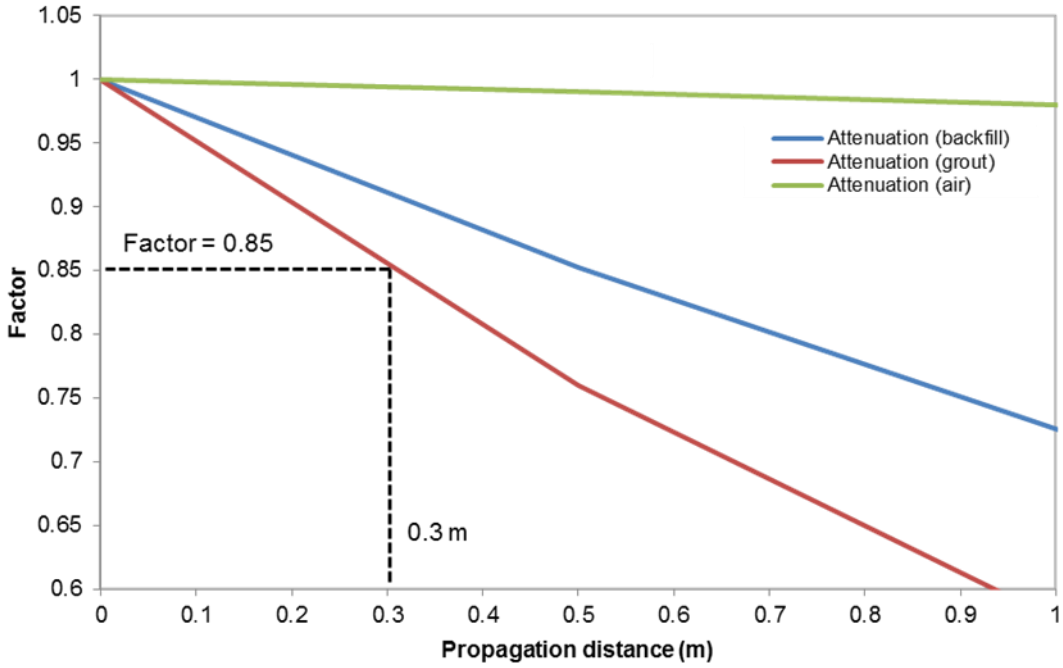

Figure 9.15. Partial factor vs. propagation distance (attenuation) relationships for steel waveguides with no couplings. Relationships for granular backfill, bentonite grout and air external environments are presented. Factor is presented on a linear scale and propagation distance up to 1 m. The factor derived for 0.3 m of grout cover is superimposed

The sensitivity of the transducer and sensor node combination installed at Nafferton (ID 20) needed to be quantified relative to the combination used to derive the AE rate-velocity relationship (ID 14), and this was done using Figure 9.16. The mean RDC recorded in response to the controlled source by system 14 was 64566 and the mean recorded by system 20 was 52531. These measurements were used to quantify the relative sensitivity of the two systems; system 20 was 81% as sensitive as system 14 and therefore a partial factor of 0.81 was used. An additional consideration, which is not included here, is that the active waveguide at Nafferton was installed inside a plastic tube. This will alter how the deforming slope interacts with the active waveguide, and how the slope deformations translate to active waveguide particle-particle and particle-waveguide interactions. Because of the large slide mass in comparison to the stiffness of the plastic tube, the effect is expected to be negligible.

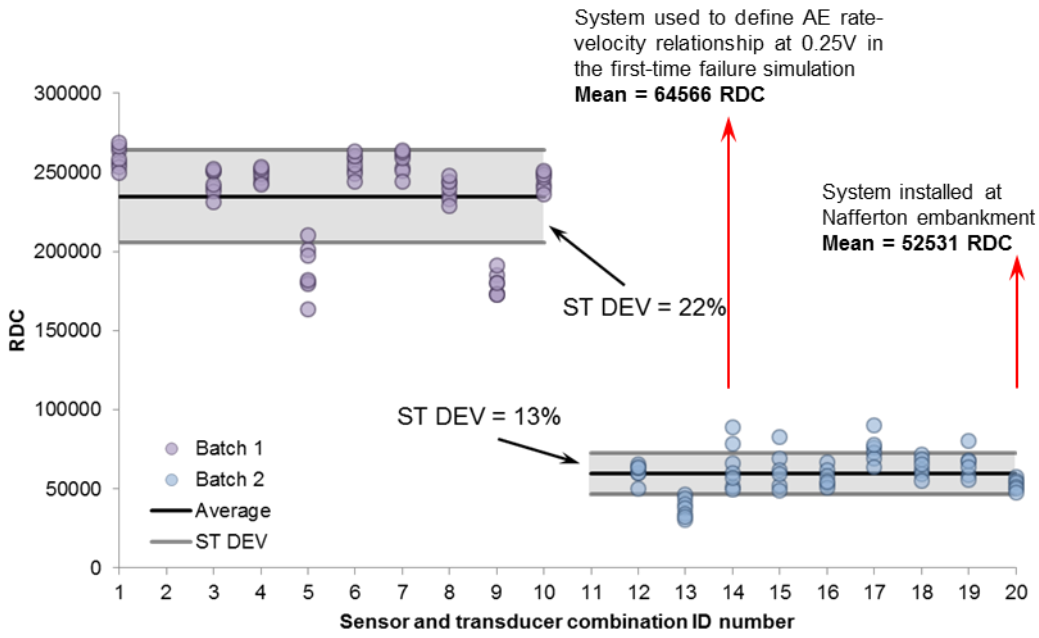

Figure 9.16. RDC measured by each sensor and transducer combination from controlled source generator. Sensor and transducer combination 14 was used to derive the AE rate-velocity relationship for Leighton Buzzard sand at 0.25V (i.e. the base-case relationship used for Nafferton) using the first-time failure experimentation). Sensor and transducer combination 20 was installed at Nafferton

Equation 9.3 demonstrates how all of the parameters derived above can be combined using the quantification algorithm (Equation 9.2) to derive a calibration AE rate-velocity relationship for the AE system installed at Nafferton embankment. Figure 9.17 shows this derived relationship graphically (red line) and the original (base-case) AE rate-velocity relationship that has been modified (grey dashed line).

$$f(\mathrm{AW_{BT}}, \mathrm{Velocity}) = 0.1526(\mathrm{Velocity})^3 - 5.0868(\mathrm{Velocity})^2 + 2922.7(\mathrm{Velocity})$$

$$\mathrm{BH_S} = 1.0$$

$$\mathrm{W_t} = 1.0$$

$$\mathrm{A_b} = 1.0$$

$$\mathrm{A_g} = 0.85$$

$$\mathrm{A_{air}} = 1.0$$

$$\mathrm{S_{S+T}} = 0.81$$

$$\mathrm{V_{TL}} = 1.0$$

$$\therefore \; AE_{rate} = 0.69 \times \left(0.1526(\mathrm{Velocity})^3 - 5.0868(\mathrm{Velocity})^2 + 2922.7(\mathrm{Velocity})\right) =$$

$$0.1053(\mathrm{Velocity})^3 - 3.5098(\mathrm{Velocity})^2 + 2016.7(\mathrm{Velocity}) \qquad \textbf{(9.3)}$$

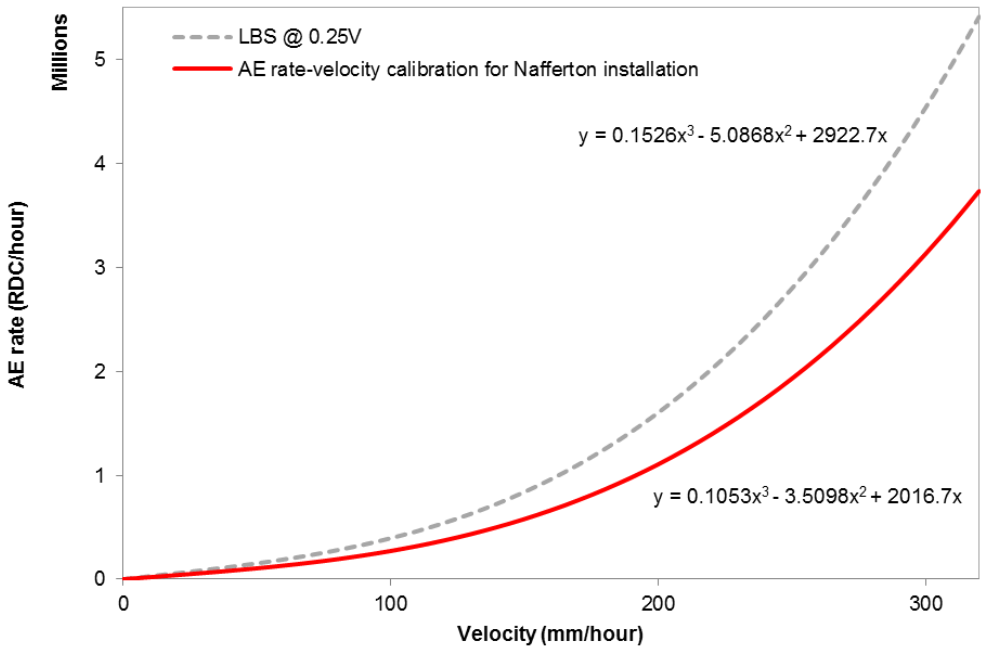

Figure 9.17. AE rate vs. velocity relationship derived for Nafferton embankment installation (red line) after application of the quantification framework to the relationship derived from the first-time failure experimentation (grey dashed line)

Figure 9.18 shows the AE rate-velocity relationship quantified for the Nafferton installation on logarithmic scales, with the standard landslide velocity scale superimposed. This procedure can be used to determine the alarm status/warning threshold levels to be set on the AE monitoring system. For example, using the relationship presented in Figure 9.18, the transition from 'extremely slow' to 'very slow' movement is at a measured AE rate of 3 RDC/hour. Therefore, the 'very slow' threshold should be set on this system at 3 RDC/hour. The 'slow' threshold should be set to 350 RDC/hour, and the 'moderate' threshold should be set to 30,000 RDC/hour. Note that these AE rate thresholds are separated by two orders of magnitude, as are the slope velocity classifications. 'Extremely slow' rates of movement are evidently at the detectable limit of this AE system (< 3RDC/hour). The relationship in Figure 9.18 ends at a velocity of ~320 mm/hour and this is because the applied velocities in the experiments used to derive the relationships did not go beyond this (note that this rate of displacement is significant and the decision maker would be required to take action before this velocity is reached). A hypothesised extrapolation of this relationship is plotted in Figure 9.19. For the purpose of this study the extrapolated relationship has been assumed linear because the actual behaviour at higher velocities is unknown. The derived AE rate-velocity relationship and extrapolated relationship are presented in Figure 9.20 to allow AE rate alarm status/warning threshold levels to be determined over the full landslide velocity scale.

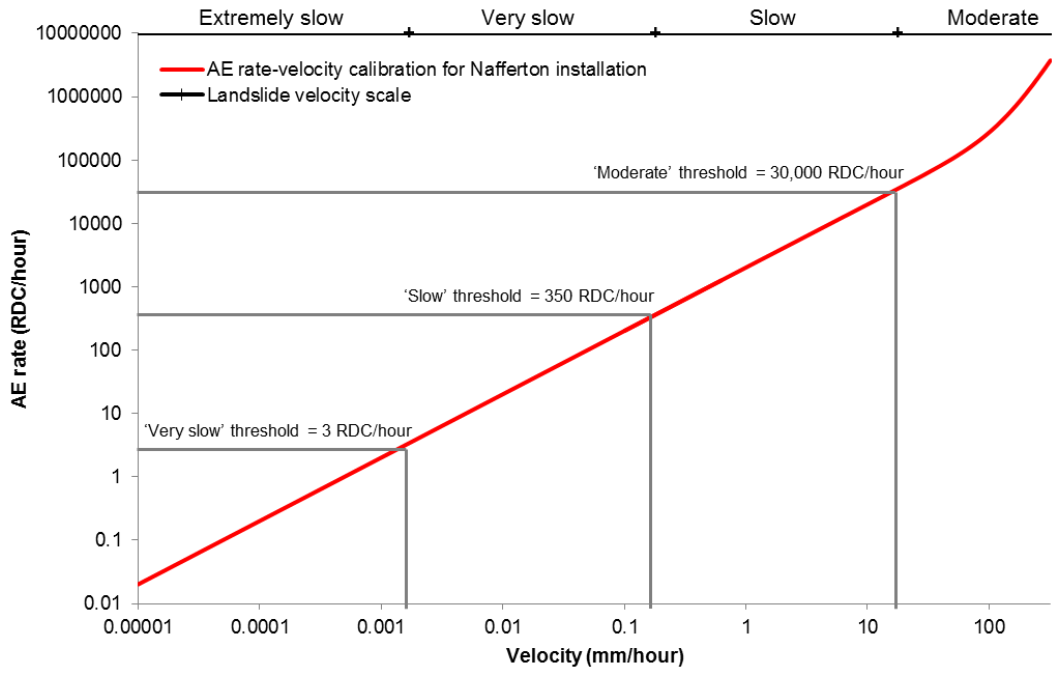

Figure 9.18. AE rate vs. velocity relationship derived for Nafferton embankment installation plotted on log scales with the standard landslide velocity scale superimposed

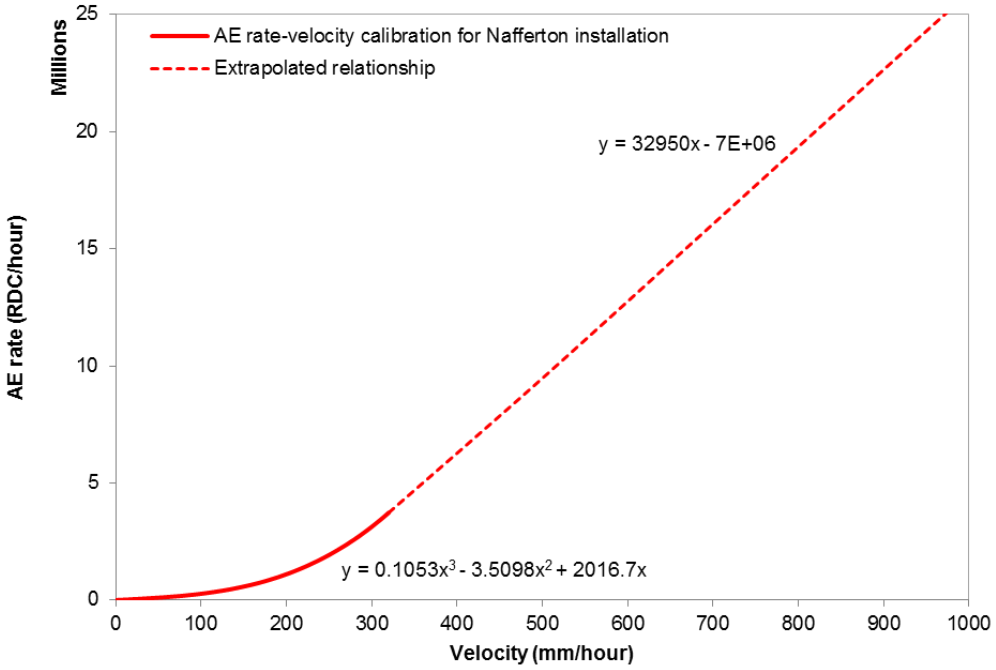

Figure 9.19. AE rate vs. velocity relationship derived for Nafferton embankment installation and an extrapolated relationship

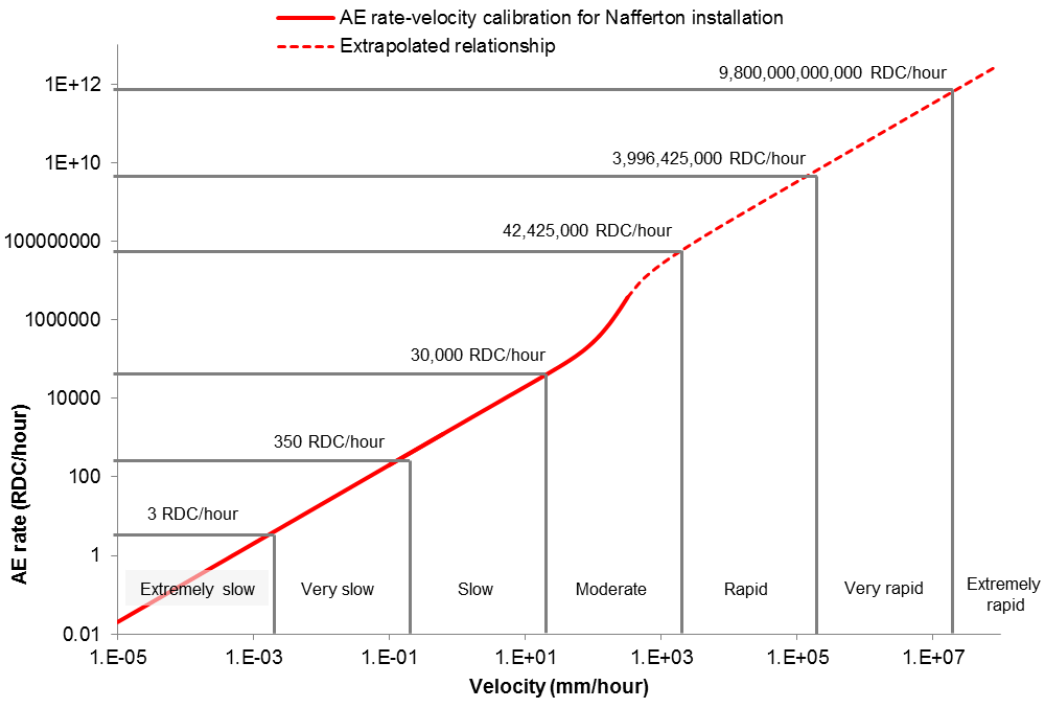

Figure 9.20. AE rate vs. velocity relationship derived for Nafferton embankment installation and the extrapolated relationship plotted on log scales with the standard landslide velocity scale superimposed

9.5. Framework flow diagram

Figure 9.21 summarises the process required to quantify AE rate-velocity relationships that are calibrated for each specific system installation, and to determine AE rate warning levels that are based on slope displacement rates. This is the process that was undertaken in Section 9.4 to determine the calibration relationship and set AE rate warning levels for the Nafferton case study.

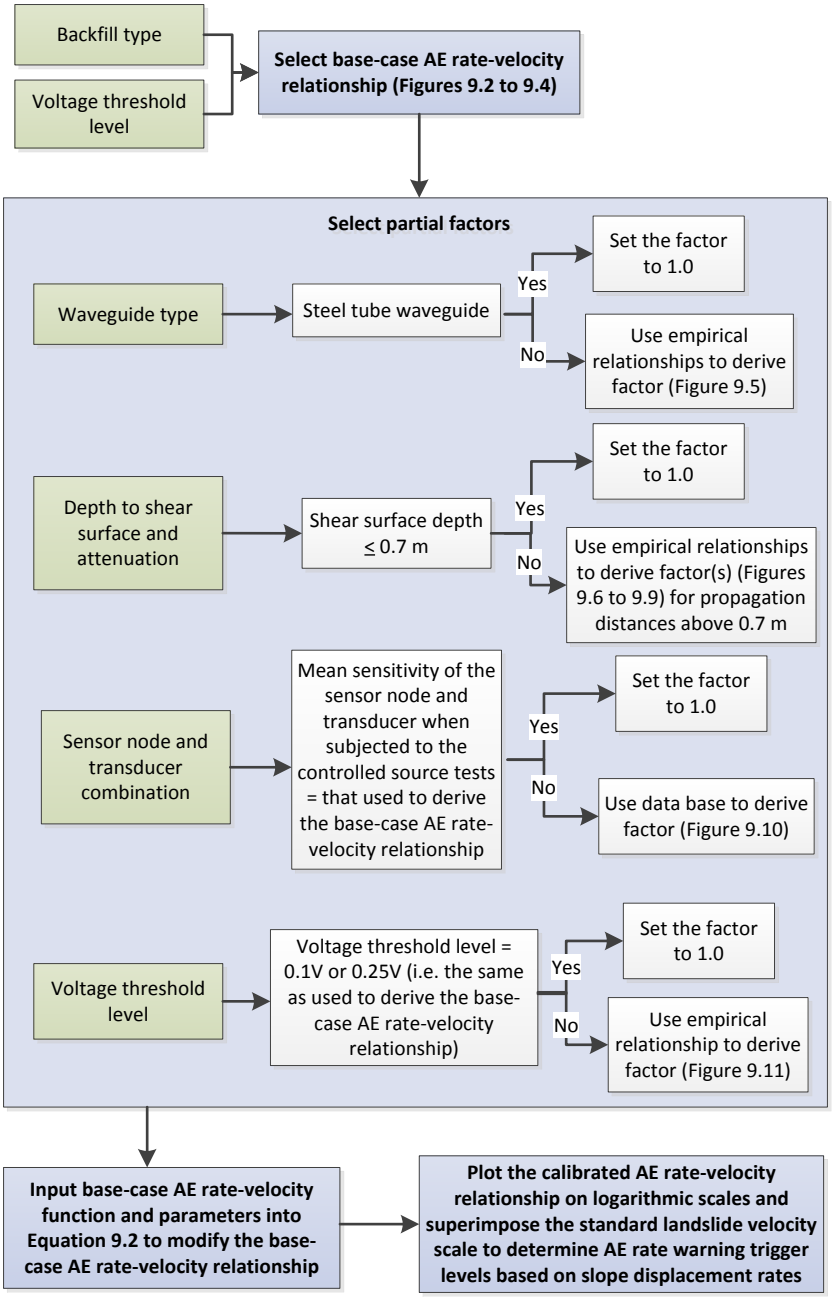

Figure 9.21. Flow diagram of the process required to quantify AE rate-velocity relationships that are calibrated for each specific system installation, and to determine AE rate warning levels that are based on slope displacement rates

9.6. Error discussion

It is important to consider the potential error in deriving displacement rates from measured AE rates when using the quantification framework. Figures 7.27, 7.28 and 7.29 present the AE rate vs. velocity relationships derived from the first-time failure experimentation for the three backfill materials, at both voltage threshold levels. The error bars in these Figures show the range of AE measurements (i.e. AE rates) recorded at that applied velocity. Note that the variability in AE rates at any given velocity is negligible in all relationships except in the 0.1V limestone gravel relationship, and

reasons for the variability in this relationship are discussed in Section 7.3.2.3. Figure 9.22 shows the 0.25V granite gravel AE rate-velocity relationship up to velocities of 70 mm/hour; at greater velocities there was no variability in AE rates (because there is less data for that part of the relationship). In Figure 9.22 the error bars, which represent the range of AE rate measurements recorded at that velocity, have been used to determine the range of potential velocity values that could be quantified using the relationship, taking into account the variability. At a velocity of 10 mm/hour the error could be up to +/- 50%, at 20 m/hour the error could be +/- 25%, and at 50 mm/hour the potential error is +/- 10%. The possible percentage error reduces with increasing velocity.

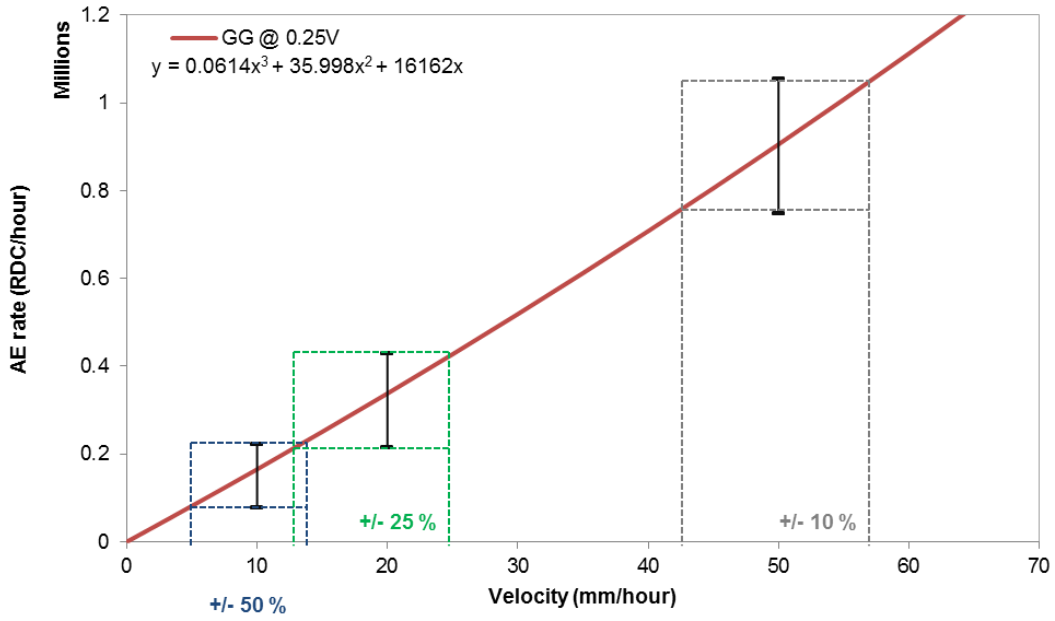

Figure 9.22. AE rate vs. velocity relationship derived for granite gravel backfill at 0.25V voltage threshold level using the first-time failure experimentation. Error bars show the range of AE measurements recorded at the applied velocity. Percentage errors in derived velocities are shown using the relationship and the error bars

When using the quantification framework, factors are applied to the base-case relationship (e.g. Figures 9.2 to 9.4) in order to modify the relationship to be calibrated for any AE system installation. Each modification to the relationship will increase the potential error when deriving displacement rates from measured AE rates. Because the factors are multiplied together within the quantification algorithm, the associated errors will also be magnified. Therefore, the greater the number of variables used in the algorithm, the greater the potential error. Ideally, the potential error associated with each parameter/variable in the framework would be quantified. However, the variability in AE measurements obtained from the active waveguide physical model tests (i.e. dynamic strain-controlled shear and constant strain rate tests) and controlled source tests, which were used to quantify empirical relationships for each of the variables, is not representative of the potential error. The variability measured from the tests includes

variability associated with artefacts from each of the tests, such as: the unrepresentative changes to confining pressures within the active waveguide model tests; and the controlled source generator is not truly representative of soil generated AE. The active waveguide physical model tests and controlled source tests have been appropriate for quantifying trends in behaviour and empirical relationships but the intrinsic variability within the tests cannot be used to quantify the potential error that would be introduced into the calibration relationship when these factors are included. The quantification of potential error associated with each parameter is therefore an area for further work.

It has been possible to quantify the potential error associated with the AE vs. sensor voltage threshold relationship at 0.1V and 0.25V threshold levels using measurements from the first-time failure experiments on granite gravel backfill. This backfill was the same material used to derive the AE vs. voltage threshold relationship in the constant strain rate tests, and the variability associated with AE measurements in the first-time failure experimentation are representative of the real system (i.e. representative backfill generated AE, representative confining pressures, and representative shear loading mechanism). In Section 7.3.2.2 it was shown that the ratio of AE measured at 0.1V to AE measured at 0.25V varied from 2.3 to 2.4 throughout the first-time failure test 5 (granite gravel). This information was used to determine the range of potential values that satisfy this ratio, which resulted in +/- 4% of the 0.1V factor or +/- 2% of the 0.25V factor, as shown in Figure 9.23.

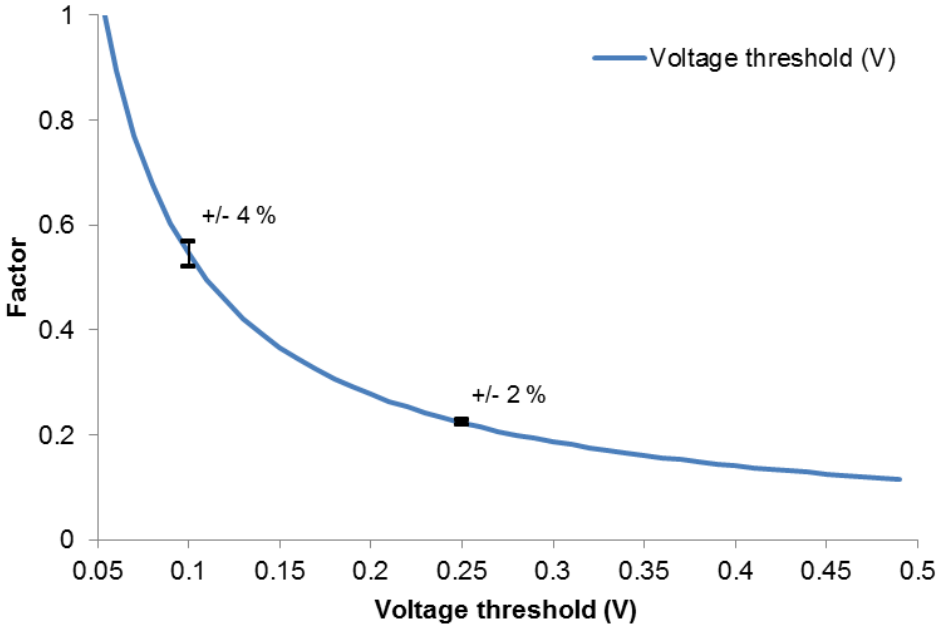

Figure 9.23. Factor vs. voltage threshold level relationship with error bars showing possible percentage error using values from the first time failure experiment on granite gravel from both 0.1V and 0.25V threshold levels

To evaluate the performance of the factor-voltage threshold relationship in modifying base-case AE rate-velocity relationships, results from first-time failure test 5 (granite gravel) were employed. In the following example the 0.25V 'measured' relationship has been modified to achieve a 0.1V 'calculated' relationship, using the voltage threshold relationship to factor for a reduced voltage threshold level, which is then compared to the 'measured' 0.1V relationship. Figure 9.24 shows how the voltage threshold chart can be used to quantify a factor to convert from one voltage threshold level to another (from 0.25V to 0.1V in the example). The conversion factor quantified from the chart was 2.43, which agrees with the 0.1V/0.25V ratio determined from the first-time failure experiments that was described above and varied from 2.3 to 2.4.

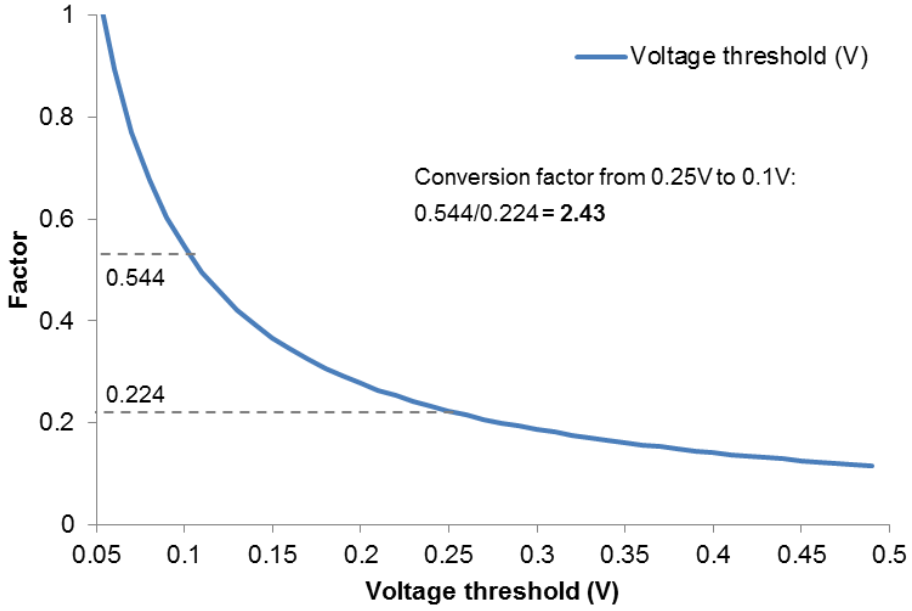

Figure 9.24. Factor vs. voltage threshold level relationship. The annotations show how to derive a factor from the chart to convert AE rate-velocity relationships from 0.25V to 0.1V

The 'measured' 0.25V relationship (red line in Figure 9.25) was then multiplied by this factor to derive the 'calculated' 0.1V relationship (black line in Figure 9.25), which passed directly through the 'measured' 0.1V relationship (blue line in Figure 9.25), although the relationships begin to diverge slightly at velocities above 180 mm/hour. The functions for each of these relationships are shown in Table 9.1. This validates the voltage threshold relationship and proposed framework for calibrating AE rate-velocity relationships for changes in voltage threshold levels. The grey lines in Figure 9.25 are +/- 4% of the 'calculated' 0.1V relationship, to account for the potential error described above. The 'calculated' 0.1V relationship overestimates the AE rates generated in response to an applied velocity above 180 mm/hour, as it diverges from the 'measured' relationship above this velocity. However, the 'calculated' 0.1V relationship minus 4%

aligns perfectly with the 'measured' 0.1V relationship over the full range of applied velocities; demonstrating that the presented error values are realistic.

Note that no factor was introduced for the different sensor and transducer combination (ID 14 at 0.25V and ID 16 at 0.1V) because their sensitivities are comparable, as can be seen by the mean of their corresponding data sets from the controlled source tests in Figure 9.10.

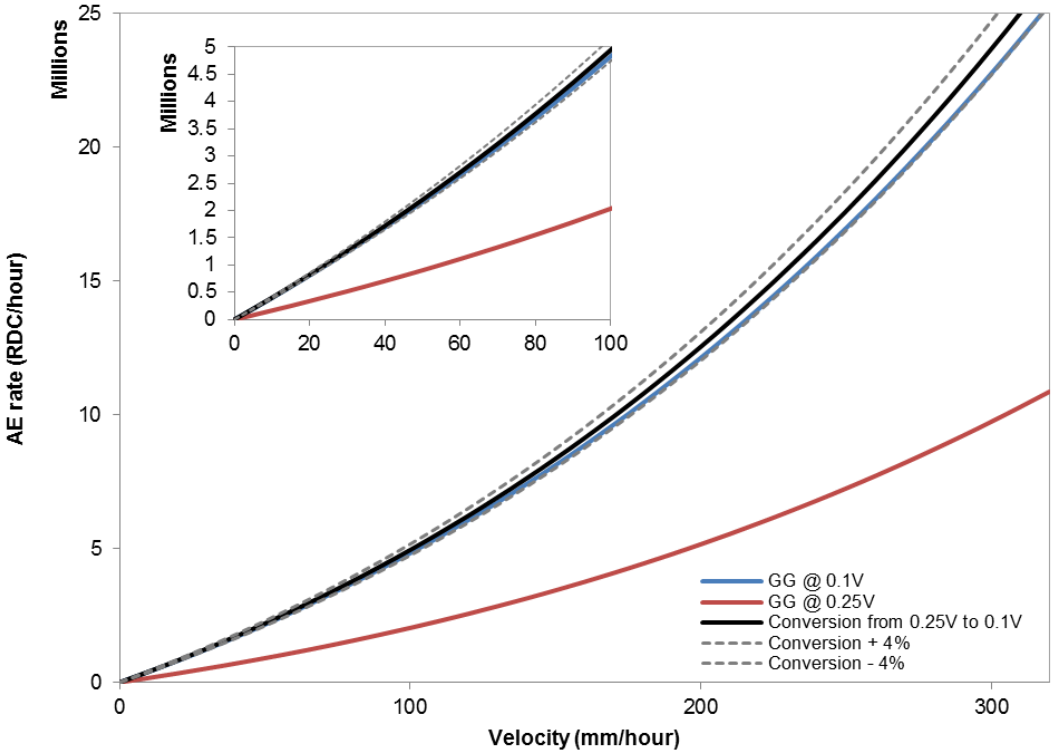

Figure 9.25. 'Measured' AE rate vs. velocity relationships derived for granite gravel backfill at both 0.1V and 0.25V voltage threshold levels using the first-time failure experimentation. The black line shows the 'calculated' 0.1V relationship derived from the 0.25V relationship using the conversion factor shown in Figure 9.24. The grey lines show the potential error (+/- 4%) in this 'calculated' relationship

Table 9.1. 'Measured' and 'calculated' 0.1V AE rate-velocity relationships shown in Figure 9.25

'Measured' 0.25V	$AE_{rate} = 0.0614(\text{Velocity})^3 + 35.998(\text{Velocity})^2 + 16162(\text{Velocity})$
'Calculated' 0.1V	$AE_{rate} = 2.43 \times \left(0.0614(\text{Velocity})^3 + 35.998(\text{Velocity})^2 + 16162(\text{Velocity})\right)$ $= 0.149(\text{Velocity})^3 + 87.475(\text{Velocity})^2 + 39273(\text{Velocity})$
'Measured' 0.1V	$AE_{rate} = 0.143(\text{Velocity})^3 + 80.576(\text{Velocity})^2 + 38845(\text{Velocity})$

Figure 9.26 shows the same relationships as those in Figure 9.25, but they are plotted on logarithmic scales and the landslide velocity scale is superimposed. All 0.1V relationships, including 'measured', 'calculated' and 'calculated' with potential +/- 4% error, align perfectly when plotted on the logarithmic scales. All 0.1V relationships

generate exactly the same RDC warning levels when using the chart in Figure 9.26 because they overlap (i.e. small errors are lost when plotting on logarithmic scales). This reinforces that the voltage threshold relationship and proposed framework for calibrating AE rate-velocity relationships for changes in voltage threshold levels is appropriate, and demonstrates its performance.

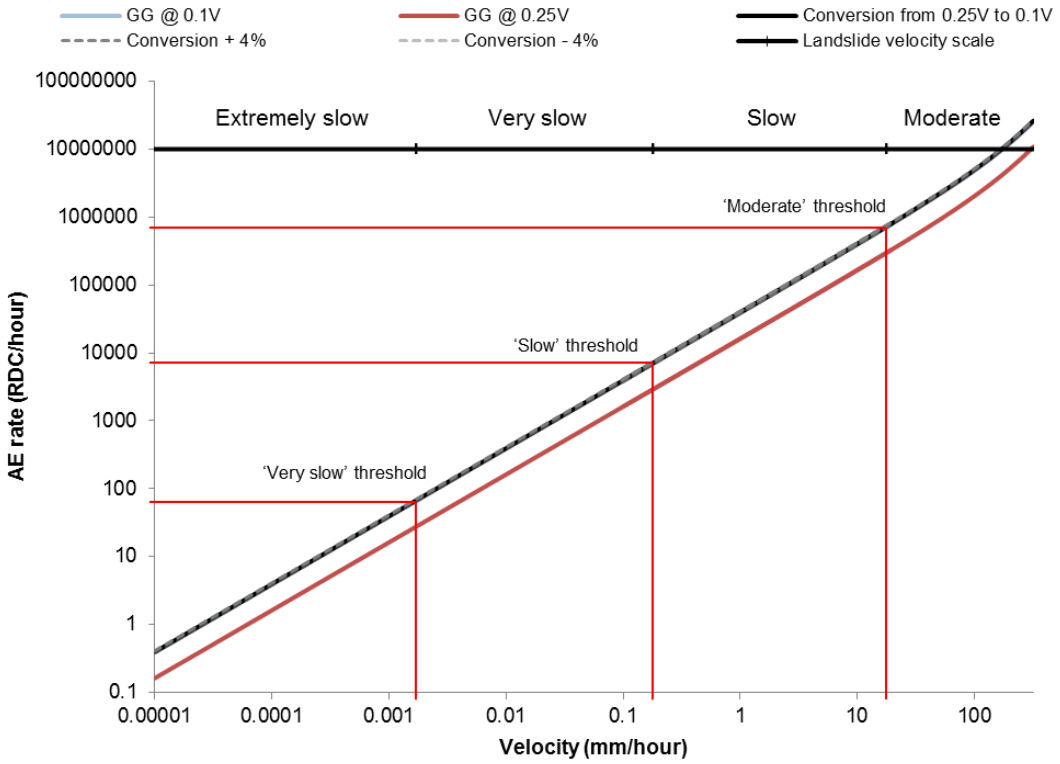

Figure 9.26. 'Measured' AE rate vs. velocity relationships derived for granite gravel backfill at both 0.1V and 0.25V voltage threshold levels using the first-time failure experimentation. The black line shows the 'calculated' 0.1V relationship derived from the 0.25V relationship using the conversion factor shown in Figure 9.24. The grey lines show the potential error (+/- 4%) in this 'calculated' relationship. Plotted on logarithmic scales with the landslide velocity superimposed

Figure 9.27 highlights the maximum possible error acceptable before the quantified velocities fall into an incorrect classification. A velocity value at the centre of its classification (e.g. 'very slow' or 'slow' in the example in Figure 9.27) can be 'calculated' (i.e. from applying the AE rate-velocity relationship to measured AE rates) incorrectly by a factor of 10 (i.e. 10 times larger or 10 times smaller) and still fall into the correct classification.

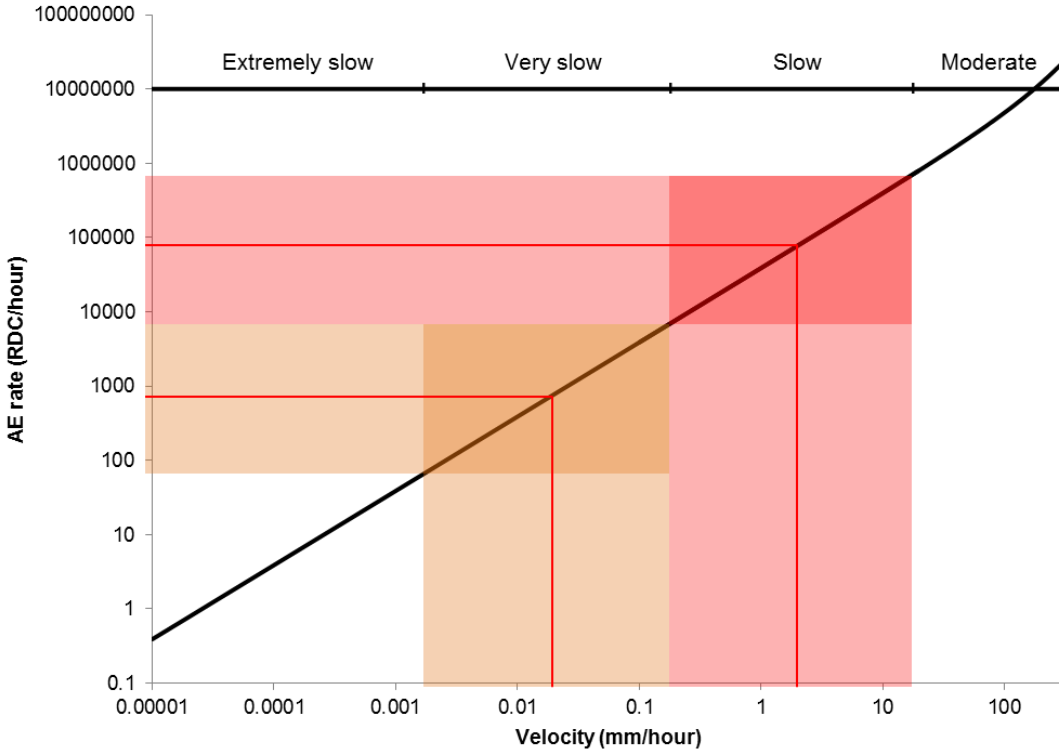

Figure 9.27. AE rate vs. velocity relationship derived for granite gravel backfill at 0.1V threshold level using the first-time failure experimentation. The shaded areas show the maximum error (i.e. increase or decrease by a factor of 10) acceptable when converting from AE rates to slope velocity to prevent incorrect velocity classification

9.7. Decision making protocol

Decision making from slope monitoring information is a difficult topic to cover. Not only does this depend on the severity of the potential hazard, but also predictions of the slopes' stiffness and deformation behaviour should be considered. For example, if a predominantly clay slope has a defined shear surface at residual strength (i.e. reactivated slope) then rapid brittle failure would not be expected, rather, low velocity and small magnitude surges in movement would occur in response to elevated pore-water pressures. However, if the slope comprises stiff material that experiences significant brittle drops in strength during progressive failure, high velocity and large magnitude movements with potentially catastrophic consequences would be expected. Such knowledge should always be included when interpreting slope monitoring information, and no monitoring instrument is a 'magic wand' in that it can tell the user what decision to make.

Figure 9.28 shows a conceptual alarm status vs. time relationship generated by the AE monitoring system in response to a period of slope movement. In each monitoring interval the slope velocity has progressed over two orders of magnitude and triggers the alarm sequence: 'very slow', 'slow', 'moderate' and then 'rapid'. This trend in behaviour would represent a slope failure taking place over the order of minutes to hours depending

on the duration of the monitoring interval, but 30-minute intervals are usually used and in this case Figure 9.28 would represent failure taking place over 2 hours.

Note that the monitoring interval should be selected to acquire temporal resolution necessary to capture slope behaviour: if movement is expected to take place over a period of days (e.g. a reactivated slope moving in response to excess pore-water pressures) monitoring at 1-hour intervals would be satisfactory to capture this behaviour with sufficient temporal resolution; however, if slope failure is expected to occur suddenly over a period of minutes or hours, 1-minute monitoring intervals would be required to capture this behaviour with sufficient resolution to provide early warning.

As soon as the first alarm status was triggered (Figure 9.28), the decision maker should be on alert to monitor the subsequent alarm statuses generated in each monitoring period and relate this information with trends in slope behaviour. In the example shown in Figure 9.28, the slope continued to accelerate in each subsequent monitoring interval. This should trigger the decision maker to take action. Depending on the severity of the potential hazard, this could be to: send an engineer to inspect the slope, stop/manage traffic along the section of road/rail track, or evacuate people. Figure 9.29 shows a similar failure sequence, which takes place over several hours. The slope displacement rate remains at 'very slow' until the 9th monitoring period. Note that at monitoring periods 3 and 6 the slope displacement rate drops below the lowest warning level and no alarm status message was triggered. During monitoring intervals 9 to 12 the slope displacement rate remains at 'slow', and then remains at 'moderate' during monitoring intervals 13 to 14. In monitoring interval 15 a 'rapid' alarm is triggered. This sequence is comparable to that in Figure 9.28 in that the slope accelerates over order of magnitude changes in velocity; however, the process takes longer in Figure 9.29. These sequences are contrasted by that shown in Figure 9.30, which is for a period of reactivated slope movement. In Figure 9.30 the slope accelerated in response to a period of elevated pore-water pressures and reached a 'slow' rate of movement in monitoring interval 3, but subsequently decelerated and became stable again as pore-water pressures dissipated and strength was mobilised. These are the trends in behaviour the decision maker should be aware of and be comparing the alarm statuses with when making decisions.

Another consideration that was not mentioned in the above is false alarms caused by background noise-generated AE. On certain sites AE activity can be generated by preferential ground water flow through high permeability strata in response to rainfall events, which induce AE within the active waveguide (as evidenced by the field trial at Scarborough detailed in Section 4.5). In addition, some sites can be exposed to extreme temperature effects or electromagnetic noise; these factors should also be considered

when making decisions on AE information and therefore decision making protocols should be adapted for each site.

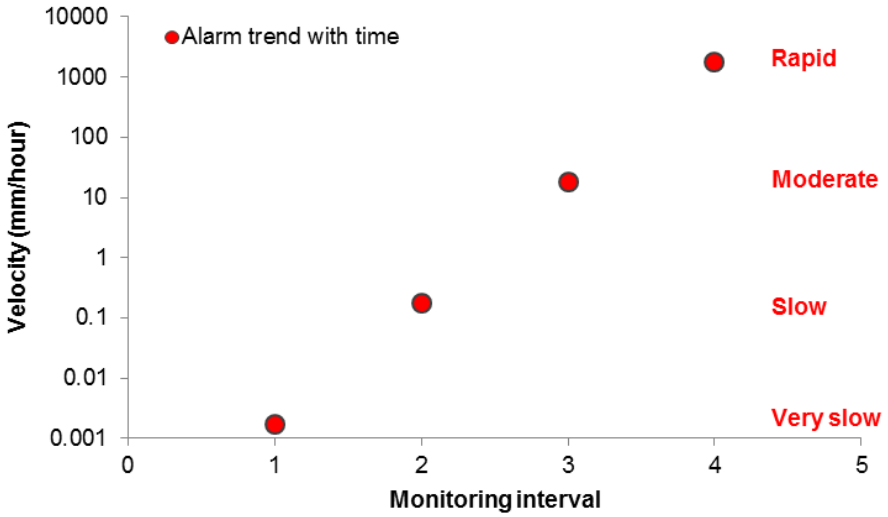

Figure 9.28. Conceptual alarm status vs. time relationship for slope failure occurring over 1 to 2 hours

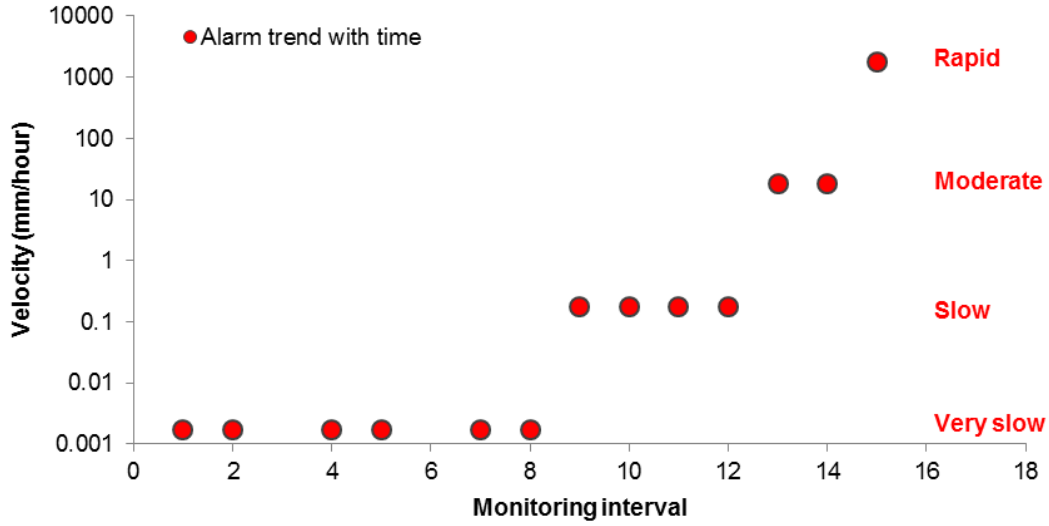

Figure 9.29. Conceptual alarm status vs. time relationship for slope failure occurring over several hours

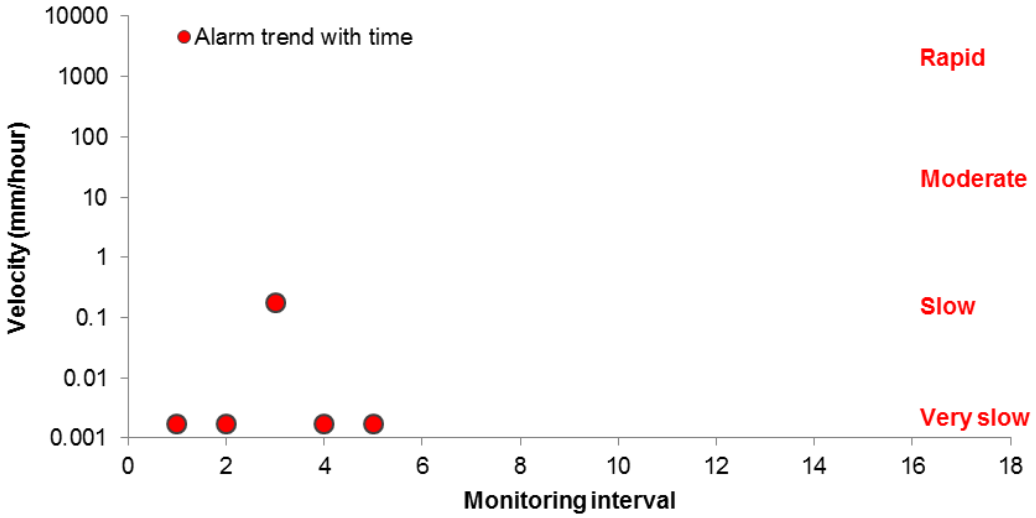

Figure 9.30. Conceptual alarm status vs. time relationship for slope reactivation occurring over several hours

9.8. Summary

In this Chapter a framework has been developed to derive calibration AE rate-slope displacement rate relationships for any AE system installation, so that rates of slope movement can be quantified from measured AE. This Chapter addresses Objective 5 and achieves the overall aim of the thesis. Results from physical modelling performed in Chapters 7 and 8 have been amalgamated to present empirical relationships between variables of interest. The primary contribution to knowledge from this Chapter is a universal method that can be used by practitioners when installing AE monitoring systems, to calibrate them to deliver alarm statuses/warning levels that are related to slope displacement rates. The calibration relationship is used to predict how the active waveguide and AE system will respond in response to an applied velocity of slope movement. This calibration framework therefore allows an *a priori* Class A prediction (Lambe 1973) to be made because it is done before the event taking place.

The framework comprises an algorithm with all variables that influence the AE rate-slope displacement rate defined. Parameters are quantified for each of these variables using a series of charts that present empirical relationships for the variables, which were derived from the physical model experiments detailed in Chapters 7 and 8. A case study example of the framework being applied was provided for the Nafferton embankment installation. The AE rate-slope displacement rate relationship was selected for the appropriate backfill material (i.e. Leighton Buzzard sand). Subsequently, a series of partial factors were determined and input into the algorithm to modify the AE rate-slope displacement rate relationship so that it was calibrated for the specific installation at Nafferton. This required the potential shear surface depth to be predicted, which was done using the predicted failure mechanism and slope geometry. Knowledge of the shear surface depth is

required to generate a calibration AE rate-slope displacement rate relationship for each system, which can be measured using adjacent instrumentation (e.g. conventional inclinometers), or predicted using; CPT/SPT measurements with depth during drilling, or information on geometry and material properties for input into a model that can be used to generate possible failure surfaces.

It was shown how the AE rate-slope displacement rate calibration relationship can be used to set alarm status/warning trigger levels on the AE monitoring system that are related to slope displacement rates using the standard landslide velocity scale. However, the maximum velocity applied during the physical model experiments that were used to derive the empirical relationships was ~320 mm/hour, which corresponds to a 'moderate' displacement rate classification. It was demonstrated how an extrapolated relationship, which was assumed to be linear in this case, can be used to derive alarm status/warning trigger levels for greater rates of movement, up to 'extremely rapid'.

The framework was applied to a base-case 0.25V threshold relationship in order to convert this to a 'calculated' 0.1V threshold relationship. The 'calculated' 0.1V relationship passed directly through the 'measured' 0.1V relationship, although the relationships began to diverge slightly at velocities above 180 mm/hour. In addition, when plotted on logarithmic scales, both the 'calculated' 0.1V and 'measured' 0.1V relationships overlapped perfectly, which meant that exactly the same RDC warning levels would be determined using both relationships. This demonstrates that high levels of accuracy are attainable when using the quantification framework. The potential error in deriving slope displacement rates from measured AE rates when using this framework has been discussed, and it was shown that displacement rate quantifications can be out by a factor of 10 (i.e. multiplied by 10 or divided by 10) before they fall into an incorrect slope displacement rate classification.

The field trial at Nafferton embankment is ongoing and will be used to evaluate the performance of the quantification framework through comparisons with continuous subsurface SAA deformation measurements when the slope fails. Some consideration has been given to the influence of the PVC tube in which the active waveguide was installed at Nafferton upon the interactions between slope deformations and the active waveguide; the effect is expected to be negligible, however, it has not been possible to quantify this and future results from the field trial will be used to develop further understanding.

Evaluation and improvement of the proposed framework and empirical relationships should be done through assessment in field applications and further physical model experiments, particularly to develop confidence in the empirical relationships that have been quantified and demonstrate their applicability to be used in the proposed

quantification framework. Work should also be focused on quantifying the potential error associated with each variable when they are introduced into the algorithm.

Conceptual alarm status vs. time relationships were presented to represent different types of slope behaviour; relationships for both first-time slope failures and reactivations have been presented. It is these trends in behaviour that should be used by decision makers, in addition to knowledge of the slopes stiffness and deformation behaviour, and the severity of the potential hazard. The trends in alarm statuses with time should be used to make decisions such as: send an engineer to inspect the slope, stop/manage traffic, or evacuate people.

CHAPTER 10

Conclusions

10.1. Principal findings related to study objectives

10.1.1. The aim

An approach has successfully been developed to quantify slope deformation behaviour using AE monitoring. AE monitoring can now, therefore, be used to provide an early warning of slope instability through detecting, quantifying and communicating accelerations of slope movement. The aim of the study has therefore been achieved.

10.1.2. Objective 1: The AE response from reactivated slope movements

A series of field trials of the AE monitoring system have been conducted in order to examine the performance of the system in a range of environments, and to capture the behaviour of the system in a variety of slopes in response to slope movements. The field trials have confirmed that AE monitoring using active waveguides is an approach capable of monitoring slope movements. The field trials allowed identification of the characteristic 'S' shaped cumulative AE vs. time and log normal bell shaped AE rate vs. time curves generated by reactivated slope movements. The trial at Flat Cliffs demonstrated that the AE monitoring system is capable of detecting deep seated reactivated slope movements.

Extensive comparisons between measured AE and deformations from real slope movements have been presented and analysed, using results from the field trials; principally from Hollin Hill. Definitive evidence has been obtained demonstrating that: AE rates generated by the system are proportional to the rate of deformation (i.e. slope velocity); AE monitoring of active waveguides using a sensor such as Slope ALARMS can provide continuous information on slope displacements and displacement rates; and the AE monitoring technique is sensitive to small displacements, displacement rates (0.075 mm/day) and changes in displacement rates (i.e. accelerations and decelerations). This has been confirmed using comparisons with both conventional periodic inclinometer measurements and continuous SAA deformation measurements.

10.1.3. Objective 2: The AE response from first-time slope failure

Field trials of the AE monitoring system at Scarborough, a marginally stable coastal cliff, and Nafferton, a research embankment being induced to failure, are ongoing and will be valuable in characterising the AE response from first-time slope failure. Because it was not possible to obtain the AE response from first-time slope failure from these sites during the period of study, a large shear box was developed to perform first-time slope failure simulations on elements of soil, through which active waveguides were installed. A SAA was also installed through the element of soil to provide continuous subsurface deformation measurements for comparison with AE measurements. The results have provided conclusive evidence that AE rates are proportional to slope velocity and AE monitoring can be used for early detection of first-time slope failures that progressively develop a shear surface during failure (e.g. AE was detected after as little as 0.8 mm of shear deformation in previously un-sheared material). AE rates generated by the system continuously increase throughout the failure event proportionally to the velocity of slope movement. Hence, AE monitoring can be used to detect the onset of failure, and subsequently quantify and communicate accelerations of movement throughout the failure event.

10.1.4. Objective 3: The relationship between measured AE and deformation behaviour

A method of back calculating linear AE rate-slope velocity relationships using periodic inclinometer measurements was developed, which was evaluated through comparisons with continuous subsurface SAA deformation measurements for slope displacement rates less than 0.5 mm/hour.

The results obtained from the field trials confirmed that AE rates generated are proportional to the velocity of slope movement; however, the field trials were at reactivated slopes that move with modest speed and travel. An experimental programme was conducted to subject active waveguide physical models to deformation, in order to establish an empirical relationship between measured AE and deformation behaviour over a wider range of velocities. Results from dynamic strain-controlled shear loading experiments conducted on active waveguide physical models confirmed that AE rates generated are proportional to the rate of deformation, and the coefficient of proportionality (C_p) that defines the AE rate vs. velocity relationship was quantified. It was shown that a linear regression was appropriate to represent this relationship over the range of velocities examined; up to 100 mm/hour. Use of this coefficient of

proportionality in a subsequent slope failure simulation demonstrated that slope velocities can be quantified continuously in real-time through monitoring active waveguide generated AE, to better than an order of magnitude, and can therefore be used to provide an early warning of slope instability through detecting and quantifying accelerations of slope movement. The coefficient of proportionality determined from these active waveguide physical model tests were greater than those determined from the field trials and the large-scale first-time slope failure simulation, and this was due to a combination of: a small propagation distance and hence minimal attenuation; unrepresentatively high confining pressures; and unrepresentative loading mechanisms. The trends in behaviour obtained from the active waveguide physical model tests were comparable with real behaviour; however, the actual values were overestimated.

The large-scale first-time slope failure experimentation allowed empirical AE rate-velocity relationships to be established for active waveguides installed in slopes with a shallow shear surface (i.e. <1 m deep) over a greater range of velocities; up to 320 mm/hour. The empirical AE rate-velocity relationships demonstrated linearity up to applied velocities of 100 mm/hour and displacements of 10-20 mm, which agrees with the results obtained from the field trials (Chapter 5) and active waveguide physical model tests (Chapter 6). Over the full range of applied velocities (i.e. ~320 mm/hour), 3rd order polynomials best fit the empirical relationships, which produced R^2 values of 0.96 or greater. At larger displacements (> 10-20 mm) more complex interactions, with pressure distributions comparable to laterally loaded piles installed through deforming slopes, occur within the active waveguide, which gradually increases the gradient of the AE rate-velocity relationship leading to a polynomial relationship. These altered mechanisms include: horizontal deformation of the anchored length of the active waveguide below the shear surface through the host soil, in addition to granular shearing at the shear surface that is the dominant mechanism below 100 mm/hour and at smaller deformations (up to 10-20 mm); and increasing confining pressures (i.e. inter-particle contact stresses) with applied load and deformation due to pressure development over the full length of the active waveguide, due to the landslide load, earth pressures and host soil reactions.

10.1.5. Objective 4: The influence of system variables upon the AE response to applied deformation behaviour

Several physical model experiments have been performed to investigate the influence of system variables upon the AE response to applied deformation behaviour. An experimental programme was conducted to understand the influence of backfill type on their AE response. An initial series of tests using the active waveguide physical model tests demonstrated that large angular soils generated the greatest AE rates and soils with

more uniform grading also generated the greatest AE rates. This series of experiments did not reveal any significant difference in performance between the backfill materials examined. However, more detailed comparisons were performed between three different backfill materials using the large-scale slope failure simulation. These tests demonstrated that the limestone fine-gravel produced AE rates orders of magnitude less than the Leighton Buzzard sand and granite medium-gravel. This could be explained to some extent by the limestone fine-gravels less angular particles and poorer packing; however, it is expected that the primary reason for this is that the dominant frequency response from the backfill fell outside of the monitored range. Backfill comparable to the Leighton Buzzard sand is recommended for active waveguide installations, using Slope ALARMS systems, in small diameter boreholes through slopes with relatively shallow shear surface depths (i.e. < 5 m); however, for deeper shear surfaces backfill comparable to the granite medium-gravel is recommended, because the large energy AE events that they generate are required to combat attenuation.

In order to quantify the influence of attenuation (i.e. depth to shear surface) on the AE measured at the ground surface from an AE system, a series of experiments were conducted to quantify the attenuation coefficients for a waveguide, connected in lengths using screw threaded couplings, with a series of external environments. A controlled source generator that comprised a DC motor was developed to generate easily repeatable AE. Comparisons with constant strain rate compression tests demonstrated that the AE produced from the controlled source was comparable to backfill-generated AE. First, attenuation coefficients for a waveguide surrounded by air (0.16 dB/m), as is the case where the waveguide protrudes from the ground surface, were determined. Second, a trench was excavated and a waveguide was buried in soil to quantify attenuation coefficients for a waveguide surrounded by soil. Attenuation coefficients were determined for a waveguide surrounded by granular soil (2.78 dB/m) (i.e. active waveguide backfill) and fine grained soil (4.75 dB/m) (i.e. the bentonite-grout ground surface plug).

The influence of sensor voltage threshold level on the magnitude of AE measured was quantified using active waveguide physical model tests (i.e. constant strain rate compression tests). This empirical relationship was shown to be consistent with measurements obtained from systems set at different voltage threshold levels in the first-time failure experiments detailed in Chapter 7. It should be noted that this empirical relationship was determined using active waveguide physical models that had medium-gravel backfill, and results from Chapter 7 demonstrated that the AE vs. voltage threshold level relationships can be marginally different for different backfill materials. This

relationship is therefore representative of that for backfill materials comparable to the medium-gravel.

Constant strain rate compression tests on active waveguide physical models were also conducted in an attempt to understand the influence of borehole size on the AE response from an active waveguide. The hypothesis being tested was; 'a larger borehole will result in a larger backfill volume and a greater number of particle-particle contacts, and will therefore generate greater AE rates in response to applied deformation behaviour'. However, the AE measurements from the smaller diameter active waveguide were consistently more than twice the magnitude of AE measurements from the larger diameter active waveguide, which contradicts the hypothesis. These results are expected to be an artefact of the active waveguide physical models employed in the experiments. The smaller diameter active waveguide was longer (1 m) than the larger diameter active waveguide (0.6 m), and the smaller diameter casing had greater flexural rigidity. For both of these reasons a greater magnitude of particle-waveguide interactions took place in the smaller diameter active waveguide in response to the same applied deformation behaviour. The results from these experiments do not allow the influence of borehole size to be quantified; however, they demonstrate the significant difference in AE generated between particle-particle interactions, which must propagate through particles prior to being transmitted into the waveguide, and particle-waveguide interactions. These results also demonstrated that it is possible to successfully retrofit inclinometer casings with active waveguides.

An experimental programme was conducted to investigate the influence of waveguide mechanical properties and geometry on their ability to transmit backfill-generated AE. The results demonstrated that when monitoring at a focused frequency range of 20 to 30 kHz, it is not possible to relate the measured AE from various waveguides with their mechanical properties and geometry alone; consideration must also be given to the frequency content of the propagating waves. The results however did demonstrate that when monitoring in the 20 to 30 kHz range using a system such as Slope ALARMS, the greatest backfill-generated AE response is in steel pipes (as opposed to aluminium pipes or steel rods). The AE response from steel pipes is also comparable for pipes with different diameters and wall thicknesses, as long as they are kept within a practical range (i.e. fit inside a borehole with sufficient annulus for granular soil backfill). Results from these experiments therefore demonstrated that steel pipes should preferably be used in active waveguides when using a monitoring system such as Slope ALARMS.

An experimental procedure was developed, using the controlled source generator, to calibrate each AE measurement system (i.e. Slope ALARMS sensor node and R3a transducer combination) prior to deployment in the field. A database of measurements

from 18 sensor node and transducer combinations, in response to the applied controlled source generator, has been developed. The sensitivity of each AE measurement system can now be calibrated using this procedure and by comparing the results with the database of results from these 18 systems.

10.1.6. Objective 5: A framework for the quantification of deformation rates from measured AE

A framework has been developed to derive calibration AE rate-slope displacement rate relationships for any AE system installation, so that rates of slope movement can be quantified from measured AE. Results from physical modelling performed in Chapters 7 and 8 have been amalgamated to present empirical relationships between variables of interest. This provides a universal method that can be used by practitioners when installing AE monitoring systems, to calibrate them to deliver alarm statuses/warning levels that are related to slope displacement rates.

The framework comprises an algorithm with all variables that influence the AE rate-slope displacement rate defined. Parameters are quantified for each of these variables using a series of charts that present empirical relationships for the variables, which were derived from the physical model experiments detailed in Chapters 7 and 8. A case study example of the framework being applied was provided for the Nafferton embankment installation. The AE rate-slope displacement rate relationship was selected for the appropriate backfill material (i.e. Leighton Buzzard sand). Subsequently, a series of partial factors were determined and input into the algorithm to modify the AE rate-slope displacement rate relationship so that it was calibrated for the specific installation at Nafferton. This required the potential shear surface depth to be predicted, which was done using the predicted failure mechanism and slope geometry. Knowledge of the shear surface depth is required to generate a calibration AE rate-slope displacement rate relationship for each system, which can be measured using adjacent instrumentation (e.g. conventional inclinometers), or predicted using; CPT/SPT measurements with depth during drilling, or information on geometry and material properties for input into a model that can be used to generate possible failure surfaces.

It was shown how the AE rate-slope displacement rate calibration relationship can be used to set alarm status/warning trigger levels on the AE monitoring system that are related to slope displacement rates using the standard landslide velocity scale. However, the maximum velocity applied during the physical model experiments that were used to derive the empirical relationships was ~320 mm/hour, which corresponds to a ‘moderate’ displacement rate classification (note that this rate of displacement is significant and the decision maker would be required to take action before this velocity is reached). It was

demonstrated how an extrapolated relationship, which was assumed to be linear in this case, can be used to derive alarm status/warning trigger levels for greater rates of movement, up to 'extremely rapid'.

The framework was applied to a base-case AE rate-velocity 0.25V threshold relationship in order to convert this to a 'calculated' 0.1V threshold relationship. The 'calculated' 0.1V relationship passed directly through the 'measured' 0.1V relationship, although the relationships began to diverge slightly at velocities above 180 mm/hour. In addition, when plotted on logarithmic scales, both the 'calculated' 0.1V and 'measured' 0.1V relationships overlapped perfectly, which meant that exactly the same RDC warning levels would be determined using both relationships. This demonstrates that relatively high levels of accuracy are attainable when using the quantification framework. The potential error in deriving slope displacement rates from measured AE rates when using this framework has been discussed, and it was shown that displacement rate quantifications can be out by a factor of 10 (i.e. multiplied by 10 or divided by 10) before they fall into an incorrect slope displacement rate classification.

The field trial at Nafferton embankment is ongoing and will be used to evaluate the performance of the quantification framework through comparisons with continuous subsurface SAA deformation measurements when the slope fails. Evaluation and improvement of the proposed framework and empirical relationships should be done through assessment in field applications and further physical model experiments, particularly to develop confidence in the empirical relationships that have been quantified and demonstrate their applicability to be used in the proposed quantification framework. Work should also be focused on quantifying the potential error associated with each variable when they are introduced into the algorithm.

Conceptual alarm status vs. time relationships were presented to represent different types of slope behaviour; relationships for both first-time slope failures and reactivations have been presented. It is these trends in behaviour that should be used by decision makers, in addition to knowledge of the slopes stiffness and deformation behaviour, and the severity of the potential hazard. The trends in alarm statuses with time should be used to make decisions such as: send an engineer to inspect the slope, stop/manage traffic, or evacuate people.

10.2. Performance of the AE monitoring system

AE monitoring of active waveguides using a system such as Slope ALARMS is able to differentiate rates of slope movement to greater than an order of magnitude (e.g. able to

differentiate between 0.001, 0.01, 0.1, 1 and 10 mm/hour etc) and is therefore consistent with standard classification of landslide movements and able to detect changes in rates of movement (i.e. accelerations and decelerations) in response to destabilising (i.e. rainfall) and stabilising (i.e. pore-water dissipation and remediation) effects. The overarching function of the AE monitoring system is to provide an early warning of slope instability through detecting, quantifying and communicating accelerations of slope movement. Conventional inclinometers are unable to provide this level of information because they do not monitor rates of displacement continuously or provide warnings of instability. AE rates increase in response to a decrease in slope stability; they are sensitive to small magnitudes of displacement (e.g. AE was detected after as little as 0.8 mm of shear surface deformation in previously un-sheared material using physical model experiments) and 'very slow' rates of displacement (e.g. the study at Players Crescent confirmed this through comparisons with continuous SAA deformation measurements during a movement event of 0.075 mm/day). In addition, the trial at Hollin Hill demonstrated that it is possible to retrofit existing inclinometer casings with active waveguides in order to convert the periodic manually read system into a continuous real-time system, and to also extend the operational life of inclinometer casings.

The approach provides high temporal resolution as monitoring is continuous at user-defined measurement intervals (of the order of minutes). Resolution with depth provided by the instrumentation is relatively low as it is not currently able to locate shear surfaces; however, if the sensor was able to digitise the entire waveform it would be possible to differentiate arrival times of various AE wave modes (i.e. longitudinal and flexural) propagating along the waveguide in order to locate the shear surface (as described in Spriggs 2005). The system operates at significantly larger shear surface displacements than conventional inclinometers; active waveguides have continued to operate beyond shear surface deformations in excess of 400 mm (e.g. at the Hollin Hill field trial) and are expected to continue to operate at significantly larger deformations.

With regard to reliability, Slope ALARMS installations have continued to operate in the field environment for durations in excess of 5 years without any deterioration of performance. The main cost associated with the AE system, as with most subsurface instrumentation, is with drilling the borehole, and this cost is the same as for other subsurface instrumentation. Installation costs associated with the subsurface materials (i.e. waveguide and backfill) are comparable to those for installing inclinometer casings. The cost of an ALARMS sensor and transducer are comparable to a datalogger and can be re-used at other installations as they are kept above ground level (i.e. are not sacrificial). The provision of a real-time warning system can be incorporated at a monthly cost comparable to a mobile phone SIM contract.

10.3. Recommendations for further research

The field trials at Hollin Hill and Flat Cliffs will continue to enhance field experience and to develop the data base of measured deformation events. The field trials at Scarborough and Nafferton will continue in order to: obtain the AE response from first-time slope failure; and obtain a case study of the AE monitoring approach delivering early warning of slope failure. Additional field trials are also currently in progress. An AE system has been installed through a slope in Peace River, Alberta, Canada, to assess performance of the system in a slope with a relatively deep shear surface (~16 m) undergoing relatively constant creep and ability of the system to operate in temperature extremes (below -30°C). AE systems have also been retrofitted inside standpipe tubes through two slopes in Monmouthshire, Wales, UK, to assess the capability of retrofitting standpipes with AE systems, which should behave in a similar manner to retrofitted inclinometer casings.

The case study at Nafferton will be significant in testing the performance of the quantification framework that has been developed in this study, through comparisons with continuous subsurface SAA deformation measurements during failure. The performance of the proposed framework will also be assessed in future field installations, particularly where continuous deformation information is available for comparison, and using other physical model experiments.

Further work is required to develop understanding of the AE behaviour of different backfill soils, using a monitoring system that is able to capture AE in both time and frequency domains. This work should also take efforts to carefully characterise properties of the soils, including shape parameters, surface roughness, packing, and ultimately their angles of internal friction, which is hypothesised to be key in quantifying the AE response from different soils. Knowledge of the AE generated by different soils will also contribute to the development of an approach to monitor waveguides driven into *in situ* granular material in slopes around the world that are prone to debris flows: this is a future direction to take the AE monitoring approach, which removes the need to drill a borehole. In addition, monitoring in the frequency domain will allow greater understanding of the performance of different waveguide types to be evaluated.

Use of the first-time slope failure experimentation can be used to investigate the influence of borehole size on the AE generated by the system, which was not successfully quantified in this study. A series of tests could be performed that keeps all variables constant, while borehole size is varied; using hand augers with a range of diameters. Note that care should be taken to avoid boundary effects between the active waveguide and the shear box wall with larger diameter hand augered holes in these tests.

The behaviour of the active waveguide when subject to slope movement should be better understood. This study has highlighted that the complex behaviour results in transitions between different mechanisms at different magnitudes of deformation. Initially at small displacements, direct shear takes place within the shear zone, and then stress development propagates along the waveguide both above and below the shear surface, due to landslide loading, reactions within the anchorage stratum, and earth pressures; comparable to a laterally loaded 'flexible' pile. These mechanisms alter the coefficient of proportionality of the AE rate-slope displacement rate relationship, and further understanding of how this behaviour influences the relationship would enable a variable to be introduced within the quantification framework to address this. Currently, the quantification framework can be used to quantify slope velocities from measured AE generated by active waveguides that have been freshly installed and then are subjected to slope failure. However, slopes often experience periods of movement followed by periods of stability, particularly in reactivated slopes, and this leads to periods of stressing and then stress-relaxation, and altered geometry. One particular approach to develop this understanding would be to install strain gauges internally along the length of the active waveguide, and use the measured strains to quantify stress distributions along the active waveguide. This would be particularly useful in the field but it would also be useful to do so in the first-time slope failure experimentation.

The field trial at Scarborough has demonstrated that ground water seepage through the active waveguide can generate contaminative AE. A method to combat this would be to install the active waveguide inside a sealed system, such as a plastic tube. Additionally, if the AE system monitored in the frequency domain, it would be possible to implement an adaptive filter to remove this contamination. On some sites extreme temperatures (hot and cold) have led to contaminative AE from mechanisms such as freezing and solar gain; it may also be possible to filter out these mechanisms if the AE system could monitor in the frequency domain (a new surface cover design might also contribute to minimising these temperature effects). It is currently possible in a lot of cases to filter out this contamination manually through knowledge of time series signatures; however, such filtering methods should be automatic within the system architecture if the approach is to be used in early warning and false alarms are to be minimised.

As a result of the significant evidence obtained from both the field and laboratory work described in this thesis, the concept of using active waveguides and AE monitoring systems to monitor slope stability has been proven. Therefore, significant effort is currently being made to commercialise the AE monitoring approach, particularly through a licence agreement. It is the expectation that future licensees of the technology would take on further development of the system to include some of the functionality mentioned

above, such as: automatic filtering methods; shear surface location using wave mode arrival times; and a more systematic treatment of errors using the quantification framework.

References

Abdoun T, Bennett V, Desrosiers T, Simm J and Barendse M (2013) Asset Management and Safety Assessment of Levees and Earthen Dams Through Comprehensive Real-Time Field Monitoring. *Geotechnical and Geological Engineering*, *31*(3), 833-843.

Alleyne DN and Cawley P (1992) Optimization of Lamb Wave Inspection Techniques. *NDT & E International* 25 (1): 11–22.

Alleyne DN and Cawley P (1997) Long Range Propagation of Lamb Waves in Chemcial Plant Pipework. *Materials Evaluation* 55 (4): 504–507.

Allison RJ and Brunsden D (1990) Some mudslide movement patterns. *Earth Surface Processes and Landforms*, 15(4), 297-311.

Anastasopoulos A, Kourousis D and Bollas K (2009) Acoustic emission leak detection of liquid filled buried pipeline. *Journal of Acoustic Emission*, 27, 27-39.

Anderson MG and Holcombe E (2013) Community-based Landslide Risk Reduction: Managing Disasters in Small Steps. *World Bank Publications.* (p. 92).

Aristegui C, Lowe MJS and Cawley P (2001) Guided Waves in Fluid-Filled Pipes Surrounded by Different Fluids. *Ultrasonics* 39 (5): 367–375.

Beard F D (1961) Predicting Slides in Cut Slopes. *Western Construction*: 72.

Beattie AG (1983) Acoustic Emission, Principles and Instrumentation. *Journal of Acoustic Emission* 2 (1/2): 95–128.

BGS (accessed September 2014) Landslide classification: http://www.bgs.ac.uk/landslides/how_does_BGS_classify_landslides.html

Bhandari RK (1988) Special lecture: Some practical lessons in the investigation and field monitoring of landslides. *Proc 5th International Symposium on Landslides*, Lausanne (pp. 1435–1457).

Bishop AW (1967) Progressive failure - with a special reference to the mechanism causing it. *Proc Geotech Conf Oslo 2* (pp. 142–150).

Bjerrum L (1967) Progressive failure in slopes of overconsolidated plastic clay and clay shales. *Journal of Soil Mechanics and Foundations*, 3–49.

Bromhead EN (2004) Landslide slip surfaces: their origins, behaviour and geometry. *Landslides: evaluation and stabilization. Balkema, Taylor & Francis Group, London. Brunsden D, Prior DB (eds) Slope instability. Wiley, Chichester*, 523-602.

Bruzelius K and Mba D (2004) An initial investigation on the potential applicability of Acoustic Emission to rail track fault detection. *NDT & E International*, 37(7), 507-516.

Cadman J D and R E Goodman (1967) Landslide Noise. *Science* 158: 1182–1184.

Caine N (1980) The rainfall intensity-duration control of shallow landslides and debris flows. *Geogr. Ann.*, 62(A (1-2)), 23–27.

Casey NF and Laura PAA (1997) A review of the acoustic-emission monitoring of wire rope. *Ocean Engineering*, 24(10), 935-947.

Cavarretta I, Coop M and O'Sullivan C (2010) The influence of particle characteristics on the behaviour of coarse grained soils. *Géotechnique*, 60 (6), 413-423. DOI: 10.1680/geot.2010.60.6.413

Chambers J, Gunn D, Wilkinson PB, Meldrum P, Haslam E, Holyoake S, Kirkham M, Kuras O, Merritt A and Wragg J (2014) 4D electrical resistivity tomography monitoring of soil moisture dynamics in an operational railway embankment. *Near Surface Geophysics*, 12, 61-72

Chandler RJ (1984) Recent European experience of landslides in over-consolidated clays and soft rocks. *Proc 4th Int Symp Landslide Toronto* (pp. 61–80).

Chen L and Poulos H (1997) Piles Subjected to Lateral Soil Movements. *Journal of Geotechnical and Geoenvironmental Engineering*, 123(9), 802–811.

Chichibu A, Jo K, Nakamura M, Goto T and Kamata M (1989) Acoustic Emission Characteristics of Unstable Slopes. *Journal of Acoustic Emission* 8 (4): 107–112.

Cho GC, Dodds J and Santamarina JC (2006) Particle shape effects on packing density, stiffness, and strength: natural and ccrushed sands. *Journal of Geotechnical and Geoenvironmental Engineering*, 132 (5), 591-602.

Clarke D and Smethurst JA (2010) Effect of climate change on cycles of wetting and drying in engineered clay slopes in England. *Quarterly Journal of Engineering Geology and Hydrogeology* 43: 473-486.

Cooper MR, Bromhead EN, Petley DJ and Grants DI (1998) The Selborne cutting stability experiment. *Géotechnique*, 48(1), 83-101.

Cornforth DH (2012) Advances in investigation and analysis for soil landslides: Three selected topics. *Landslides and engineered slopes: Protecting society through improved understanding* (pp. 59–71).

Coussot P and Meunier M (1996) Recognition, classification and mechanical description of debris flows. *Earth-Science Reviews*, 40(3-4), 209–227. doi:10.1016/0012-8252(95)00065-8

Craig RF (2004) Craig's soil mechanics. *CRC Press.*

Crosta GB, Frattini P and Di Prisco C (2012) Approaches to rainfall-induced landslides forecasting. *Landslides and engineered slopes: Protecting society through improved understanding* (pp. 15–22).

Cruden DM and Varnes DJ (1996) Landslides: Investigation and Mitigation. *Chapter 3-Landslide types and processes. Transportation research board special report*, (247).

Dai S and Labuz JF (1996) Displacement during progressive failure estimated from microseismic activity. *Transporation Research Record*, (1548), 46–51.

Demma A, Pavlakovic B, Cawley P and Lowe MJS (2005) The Effect of Bends on the Propagation of Guided Waves in Pipes. *Journal of Pressure Vessel Technology* 127 (3): 328–335.

Dijkstra TA and Dixon N (2010) Climate Change and Slope Stability in the UK: Challenges and Approaches. *Quarterly Journal of Engineering Geology and Hydrogeology* 43: 371–385.

Dixon N and Bromhead EN (2002) Landsliding in London Clay coastal cliffs. *Quarterly journal of engineering geology and hydrogeology*, 35(4), 327-343.

Dixon N and Spriggs MP (2007) Quantification of slope displacement rates using acoustic emission monitoring. *Canadian Geotechnical Journal*, 44, 6, 966-976.

Dixon N and Spriggs MP (2011) Apparatus and method for monitoring soil slope displacement rate. UK Patent Application GB 2467419A, Awarded May 2011.

Dixon N, Hill R and Kavanagh J (2003) Acoustic emission monitoring of slope instability: Development of an active wave guide system. *Institution of Civil Engineers Geotechnical Engineering Journal*, 156, 2, 83-95.

Dixon N, Spriggs MP, Meldrum P and Haslam E (2012a) Field Trial of an Acoustic Emission Early Warning System for Slope Instability. In *Landslides and Engineered Slopes: Protecting Society Through Improved Understanding*, 1399–1404.

Dunnicliff J (1988) *Geotechnical instrumentation for monitoring field performance*, John Wiley & Sons.

EC7 - Geotechnical Monitoring Standard - TC 341 WI 0034 1066: 2011 (E)

Fellows RF and Liu AM (2009) Research methods for construction. John Wiley & Sons. pp27.

Fort DS, Clark AR and Cliffe DG (2000) The Investigation and Monitoring of Coastal Landslides at Barton-on-Sea, Hampshire, UK. In: Bromhead, E.N., Dixon, N. & Ibsen, M-L. (eds) *Landslides in Research, Theory and Practice, Vol. 2, pp567-572*. Thomas Telford, London.

Fujiwara T, Ishibashi A and Monma K (1999) Application of Acoustic Emission Method to Shirasu Slope Monitoring. In *Slope Stability Engineering, Yagi, Yamagami & Jiang, Balkema, Rotterdam*, 147–150.

Garga VK and Chichibu A (1990) A Study of AE Parameters and Shear Strength of Sand. *Progress in Acoustic Emission* V: 129–136.

Gazis DC (1959) Three-Dimensional Investigation of the Propagation of Waves in Hollow Circular Cylinders. I. Analytical Foundation. *The Journal of the Acoustical Society of America* 31 (5): 568–573.

Gibson AD, Culshaw MG, Dashwood C and Pennington CVL (2013) Landslide Management in the UK - the Problem of Managing Hazards in a 'Low-Risk' Environment. *Landslides, 10*(5), 599-610.

Glendinning S, Hall J and Manning L (2009) Asset-management strategies for infrastructure embankments. *Proceedings of the Institution of Civil Engineers: Engineering Sustainability*, 162(2), 111-120

Glendinning S, Hughes P, Helm P, Chambers J, Mendes J, Gunn D, Wilkinson P and Uhlemann S (2014) Construction, management and maintenance of embankments used for road and rail infrastructure: implications of weather induced pore water pressures. *Acta Geotechnica*, 9(5): 799-816.

Graff KF (1975) Wave Motion in Elastic Solids. *Courier Dover Publications*: p79–141.

Grosse C, Reinhardt H and Dahm T (1997) Localization and classification of fracture types in concrete with quantitative acoustic emission measurement techniques. *NDT & E International*, 30(4), 223-230.

Gunn D, Chambers J, Uhlemann S, Wilkinson PB, Meldrum PI, Dijkstra TA *et al* (2014) Moisture monitoring in clay embankments using electrical resistivity tomography. *Construction and Building Materials*. In press. DOI: 10.1016/j.conbuildmat.2014.06.007

Guzzetti F, Carrara A., Cardinali M and Reichenbach P (1999) Landslide hazard evaluation: a review of current techniques and their application in a multi-scale study, Central Italy. *Geomorphology*, 31(1-4), 181–216.

Guzzetti F, Peruccacci S, Rossi M and Stark CP (2008) The rainfall intensity-duration control of shallow landslides and debris flows: an update. *Landslides*, 5, 3–17.

Hardy Jr HR (1992) Laboratory Studies Relative to the Development of Mechanical Waveguides for Acoustic Emission Monitoring of Geologic Structures. *Italian Journal of Nondestructive Testing and Diagnostics* 13 (2): 32–38.

Hughes PN, Glendinning S, Mendes J, Parkin G, Toll DG, Gallipoli D and Miller PE (2009) Full-scale testing to assess climate effects on embankments. *Proceedings of the ICE-Engineering Sustainability*, 162(2), 67-79.

Hungr O, Leroueil S and Picarelli L (2012) Varnes classification of landslide types, an update. *Landslides and engineered slopes: Protecting society through improved understanding* (pp. 47–58).

Hungr O, Leroueil S and Picarelli L (2014) The Varnes classification of landslide types, an update. *Landslides*, 11(2), 167-194.

Hutchinson JN (1988) General report: Morphological and geotechnical parameters of landslides in relation to geology and hydrogeology. *Proc 5th International Symposium on Landslides, Lausanne* (pp. 3–35).

Hutchinson JN and Bhandari RK (1971) Undrained loading, a fundamental mechanism of mudflows and other mass movements. *Geotechnique*, 21(4), 353–358.

Jakob M, Owen T and Simpson T (2012) A regional real-time debris-flow warning system for the District of North Vancouver, Canada. *Landslides*, 9, 165–178.

Kane WF and Beck TJ (2000) Instrumentation practice for slope monitoring. *Engineering geology practice in Northern California. Association of engineering geologists Sacramento and San Francisco sections*.

Kane WF, Beck TJ and Hughes JJ (2001) Applications of time domain reflectometry to landslide and slope monitoring. *Second International Symposium and Workshop on*

Time Domain Reflectometry for Innovative Geotechnical Applications, Infrastructure Technology Institute at Northwestern University, Evanston, IL (pp. 305–314).

Kavanagh J (1997) The use of acoustic emission to monitor the deformation of a soil body. PhD Thesis, The Nottingham Trent University, UK.

Kilburn CR and Petley DN (2003) Forecasting giant, catastrophic slope collapse: lessons from Vajont, Northern Italy. *Geomorphology*, 54(1), 21-32.

Kirschbaum D, Adler R, Adler D, Peters-Lidard C and Huffman G (2012) Global Distribution of Extreme Precipitation and High-Impact Landslides in 2010 Relative to Previous Years. *Journal of Hydrometeorology*, 13(5), 1536–1551.

Koerner RM and Lord AE (1972) Acoustic emissions in medium plasticity clayey silt. *Journal of the Soil Mechanics and Foundations Division*, 98(1), 161–165.

Koerner RM, Lord AE and McCabe WM (1975) Acoustic Emission Studies in Soil Masses in the Laboratory and Field. *In Proc. of First Conf. on Acoustic Emission/Microseismic Activity in Geological Structures and Materials, Penn State Univ., University Park, PA* (pp. 244-256).

Koerner RM, Lord AE, McCabe MW and Curran J (1976) Acoustic emission behaviour of granular soils. *Journal of geotechnical engineering division*, 102(GT7), 761–770.

Koerner RM, McCabe WM and Lord AE (1981) Acoustic emission behaviour and monitoring of soils. In *Acoustic Emission in Geotechnical Practice*, ASTM STP 750, pp. 93-141.

Krumbein WC and Sloss LL (1963) Stratigraphy and sedimentation, 2nd Edition. Freeman and Company, San Fransisco.

Lambe TW (1973) Predictions in soil engineering. *Géotechnique*, 23(2), 151-202.

Leroueil S (2001) Natural Slopes and Cuts: Movement and Failure Mechanisms. *Geotechnique* 51 (3): 197–243.

Leroueil S, Locat A, Eberhardt E and Kovacevic N (2012) Progressive failure in natural and engineered slopes. *In: Landslides and Engineered Slopes. Proceedings, 11th International Symposium on Landslides, Banff* (Vol. 1, p. 31).

Lockner D (1993) The role of acoustic emission in the study of rock fracture. *In International Journal of Rock Mechanics and Mining Sciences & Geomechanics Abstracts* (Vol. 30, No. 7, pp. 883-899). Pergamon.

Long R, Cawley P and Lowe MJS (2003a) Acoustic Wave Propagation in Buried Iron Water Pipes. *Proceedings of the Royal Society of London. Series A: Mathematical, Physical and Engineering Sciences* 459 (2039): 2749–2770.

Long R, Lowe MJS and Cawley P (2003b) Attenuation Characteristics of the Fundamental Modes That Propagate in Buried Iron Water Pipes. *Ultrasonics* 41 (7): 509–519.

Lord AE and Koerner RM (1974) Acoustic Emission Response of Dry Soils. *Testing and Evaluation (ASTM)* 2: 159–162.

Lord AE, Koerner RM and Curran JW (1977) Fundamental studies of acoustic emissions in soils. *In Proceedings First Conference on Acoustic Emission/Microseismic Activity in Geologic Structures and Materials: Clausthal, Germany, Trans Tech Publications* (pp. 135-148).

Loveridge F, Spink TW, O'Brien AS, Briggs KM and Butcher D (2010) The impact of climate and climate change on infrastructure slopes, with particular reference to southern England. *Quarterly Journal of Engineering Geology and Hydrogeology 43:461-472.*

Lowe MJS, Alleyne DN and Cawley P (1998) Defect Detection in Pipes Using Guided Waves. *Ultrasonics* 36: 147–154.

Machan G and Beckstrand DL (2012) Practical considerations for landslide instrumentation. *Landslides and engineered slopes: Protecting society through improved understanding* (pp. 1229–1234).

Maji AK, Satpathi D and Kratochvil T (1997) Acoustic Emission Source Location Using Lamb Wave Modes. *Journal of Engineering Mechanics* 123: 154–161.

Malet JP, Laigle D, Remaître A and Maquaire O (2005) Triggering conditions and mobility of debris flows associated to complex earthflows. *Geomorphology*, 66, 215–235.

Massey CI (2010) The dynamics of reactivated landslides: Utiku and Taihape, North Island, New Zealand (Doctoral thesis, Durham University).

Massey CI, Petley DN and McSaveney MJ (2013) Patterns of movement in reactivated landslides. *Engineering Geology*, 159, 1-19.

Mathiyaparanam J (2006) Analysis of acoustic emission in cohesionless soil (Doctoral dissertation, University of South Florida).

Matsuura S, Asano S and Okamoto T (2008) Relationship between rain and/or meltwater, pore-water pressure and displacement of a reactivated landslide. *Engineering Geology*, 101(1), 49-59.

Mba D and Rao RB (2006) Development of Acoustic Emission Technology for Condition Monitoring and Diagnosis of Rotating Machines; Bearings, Pumps, Gearboxes, Engines and Rotating Structures. *The Shock and Vibration Digest*, 2006, Vol 38(1), pp3-16.

McCauley ML (1977) Monitoring slope stability with acoustic emission. *Proceedings of 1st conference "Acoustic emission/microseismic activity in geological structures and materials", Pennsylvania State University* (pp. 257–269).

Michlmayr G and Or D (2014) Mechanisms for acoustic emissions generation during granular shearing. *Granular Matter*, *16*(5), 627-640.

Michlmayr G, Cohen D and Or D (2012a) Sources and characteristics of acoustic emissions from mechanically stressed geologic granular media - A review. *Earth-Science Reviews*, 112, 97–114.

Michlmayr G, Cohen D and Or D (2013) Shear-induced force fluctuations and acoustic emissions in granular material. *Journal of Geophysical Research: Solid Earth*, 118(12), 6086-6098.

Michlmayr G, Or D and Cohen D (2012b) Fiber Bundle Models for Stress Release and Energy Bursts during Granular Shearing. *Physical Review* 86 (061307): 1–7.

Millis SW, Ho ANL, Chan EKK, Lau KWK and Sun HW (2008) Instrumentation and real-time monitoring of slope movement in Hong Kong. The 12th internation conference of internation association for computer methods and advances in geomechanics (IACMAG) (pp. 4563–4576).

Mitchell RJ and Romeril PM (1984) Acoustic Emission Distress Monitoring in Sensitive Clay. *Canadian Geotechnical Journal* 21: 176–180.

Moore R, Carey JM and McInnes RG (2010) Landslide behaviour and climate change: predictable consequences for the Ventnor Undercliff, Isle of Wight. *Quarterly Journal of Engineering Geology and Hydrogeology, Vol. 43, pp447-460.*

Mostafapour A and Davoudi S (2013) Analysis of Leakage in High Pressure Pipe Using Acoustic Emission Method. *Applied Acoustics* 74 (3): 335–342.

Naemura S, Mitugu T, Nishikawa S, Nakamura M, Jo K and Kishishita T (1991) Acoustic Emission of Penetration Experiments to Judge Soil Condition. *Journal of Acoustic Emission* 10 (1-2): 55–58.

Nakajima I, Negishi M, Ujihira M and Tanaba T (1991) Application of the acoustic emission monitoring rod to landslide measurement. *5th conference on acoustic emission / microseismic activity in geologic structures and materials* (pp. 1–15).

Ng KY (2007) Mechanisms of shallow rainfall-induced landslides in residual soils in humid tropical environments (Doctoral thesis, Durham University).

Nishino H, Uchida F, Takashina S, Takemoto M and Ono K (2000) A new method of AE source location in pipes using cylindrical guided waves. *In Proceedings of the 24th European Conference on Acoustic Emission Testing, Senlis* (pp. 139-144).

Oelze ML, O'Brien WD and Darmody RG (2002) Measurement of Attenuation and Speed of Sound in Soils. *Soil Science Society of America Journal* 66 (3): 788–796.

Ohtsu M (1996) The history and development of acoustic emission in concrete engineering. *Magazine of concrete research*, 48(177), 321-330.

Ono K and Cho H (2004) Rods and tubes as AE waveguides. *Journal of Acoustic Emission*, 22, 243-252.

Palmer IG (1973) Acoustic emission measurements on reactor pressure vessel steel. *Materials Science and Engineering*, 11(4), 227-236.

Perry J, Pedley M and Reid M (2003a) Infrastructure embankments – condition appraisal and remedial treatment. C592. London: Construction Industry Research and Information Association.

Perry J, Pedley M and Reid M (2003b) Infrastructure cuttings – condition appraisal and remedial treatment. C592. London: Construction Industry Research and Information Association.

Petley DN (2012) Global Patterns of Loss of Life from Landslides. *Geology, Geological Society of America* 40 (10): 927–930.

Petley DN, Bulmer MH and Murphy W (2002) Patterns of movement in rotational and translational landslides. *Geology*, 30(8), 719-722.

Petley DN, Mantovani F, Bulmer MH and Zannoni A (2005) The use of surface monitoring data for the interpretation of landslide movement patterns. *Geomorphology*, 66, 133–147.

Pilot G (1984) Instrumentation and warning systems for research and complex slope stability problems. *Proc 4th Int Symp Landslides Toronto* (pp. 275–301).

Pollard H (1977) Sound waves in solids. London: Pion. pp6-60.

Poulos HG (1995) Design of reinforcing piles to increase slope stability. *Canadian Geotechnical Journal*, 32(5), 808-818.

Rouse C, Styles P and Wilson SA (1991) Microseismic Emissions from Flowslide-Type Movements in South Wales. *Engineering Geology* 31: 91–110.

Saito M (1965) Forecasting the time of occurrence of a slope failure. *In: Proceedings of the 6th International Conference on Soil Mechanics and Foundation Engineering* (pp. 537–541).

Saito M (1969) Forecasting time of slope failure by Tertiary creep. *In: Proceedings of the 7th International Conference on Soil Mechanics and Foundation Engineering.* Vol. 2. pp 677 – 683.

Saito M and Uezawa H (1961) Failure of soil due to creep. Fifth International Conference of Soil Mechanics and Foundation Engineering.

Santamaerina JC and Cho GC (2004) Soil behaviour: The role of particle shape. Proc. Skempton Conf, March, London, 1-14.

Schuster RL and Krizek RJ (eds.) (1978) *Landslides Analysis and Control, Transportation Research Board Special Report 176*, National Academy of Science, Washington.

Scruby CB (1987) An introduction to acoustic emission. *Journal of Physics E: Scientific Instruments*, 20, 946–953.

Shehadeh M, Abdou W, Steel J and Reuben R (2008) Aspects of Acoustic Emission Attenuation in Steel Pipes Subject to Different Internal and External Environments. *Proceedings of the Institution of Mechanical Engineers* 222 (E): 42–54.

Shiotani T and Ohtsu M (1999) Prediction of slope failure based on AE activity. In Acoustic Emission: Standards and Technology update (Vahaviolos, S.J. (Ed.)), *American Society for Testing Materials*, ASTM STP, Pennsylvania, 1353, pp. 157-172.

Shiotani T, Fujii K, Aoki T and Amou K (1994) Evaluation of progressive failure using AE sources / Improved b-value on slope model tests. *Progress in Acoustic Emission*, VII, 529–534.

Siang AJLM, Wijeyesekera DC, Zainorabidin A and Bakar I (2012) The effects of particle morphology (shape and size) characteristics on its engineering behaviour and sustainable engineering performance of sand. *International Journal of Integrated Engineering. Special issue on ICONCEES*, 4 (2), 27-37.

Sikorska J and Pan J (2004) The effect of waveguide material and shape on acoustic emission transmission characteristics. *Journal of Acoustic Emission*, 22, 264-273.

Simeoni L and Mongiovì L (2007) Inclinometer monitoring of the Castelrotto landslide in Italy. *Journal of Geotechnical and Geoenvironmental Engineering*, 133(6), 653–666.

Skempton AW (1964) Long-term stability of clay slopes. *Geotechnique. Fourth Rankine Lecture*, *14*, 77–101.

Skempton AW (1985) Residual strength of clays in landslides, folded strata and the laboratory. *Geotechnique*, 35(1), 3-18.

Skempton AW (1996) Embankments and cuttings on the early railways. *Construction history*, 11, 33-49.

Skempton AW and Petley DJ (1967) The strength along structural discontinuities in stiff clays. *Proc Geotech Conf Oslo 2* (pp. 29–46).

Smethurst JA and Powrie W (2007) Monitoring and analysis of the bending behaviour of discrete piles used to stabilise a railway embankment. *Géotechnique*, 57 (8), 663–677.

Smethurst JA, Clarke D and Powrie W (2012) Factors controlling the seasonal variation in soil water content and pore water pressures within a lightly vegetated clay slope. *Géotechnique*, 62 (5): 429-446.

Spriggs MP (2005) Quantification of acoustic emission from soils for predicting landslide failure. PhD thesis, Civil and Building Engineering, Loughborough University, UK.

Take A and Bolton MD (2011) Seasonal Ratcheting and Softening in Clay Slopes, Leading to First-Time Failure. *Geotechnique* 61 (9): 757–769.

Tanimoto K and Noda T (1977) A study of acoustic emission from sandy soils. *Proceedings of the 9th International Conference on Soil Mechanics and Foundation Engineering, Tokyo* (pp. 315–318).

Tanimoto K, Nakamura and Fudo R (1981) Application of acoustic emission in in-situ test. *Proc 10th Int Conf Soil Mechanics Engineering, Stockholm* (pp. 573–576).

Terzaghi K (1936) The shearing resistance of saturated soils and the angle between the planes of shear. In: *Proceedings 1st international conference on soil mechanics and foundation engineering* (pp. 54–56).

Terzaghi K (1950) Mechanism of landslides. *The geological society of America, Engineering*, 83–123.

Varnes DJ (1978) Slope movement types and processes. *Transportation Research Board Special Report*, (176).

Vaughan PR and Walbancke HJ (1973). Pore pressure changes and the delayed failure of cutting slopes in overconsolidated clay. *Geotechnique*, 23, 531–539.

Wan MSP and Standing JR (2014) Lessons learnt from installation of field instrumentation. Proceedings of the ICE - Geotechnical Engineering, 167(5): 491-506.

Wasley RJ (1973) *Stress Wave Propagation in Solids: An Introduction*. p127

Wilkinson P, Chambers J, Meldrum P, Gunn DA, Ogilvy RD and Kuras O (2010) Predicting the movements of permanently installed electrodes on an active landslide using time-lapse geoelectrical resistivity data only. *Geophysical Journal International*, 183, 543–556.

Wilkinson P, Uhlemann S, Chambers J and Meldrum P (2014) Development and testing of displacement inversion to track electrode movements on 3D Electrical Resisitivity Tomography monitoring grids. submitted to *Geophysical Journal International.*

Yoon DJ, Weiss WJ and Shah SP (2000) Assessing damage in corroded reinforced concrete using acoustic emission. *Journal of engineering mechanics,* 126(3), 273-283.

Zan L, Latini G, Piscina E, Polloni G and Baldelli P (2002) Landslides early warning monitoring system. *IEEE* (pp. 188–190).

Appendices

A1. Field monitoring case study measurements

A1.1. Hollin Hill

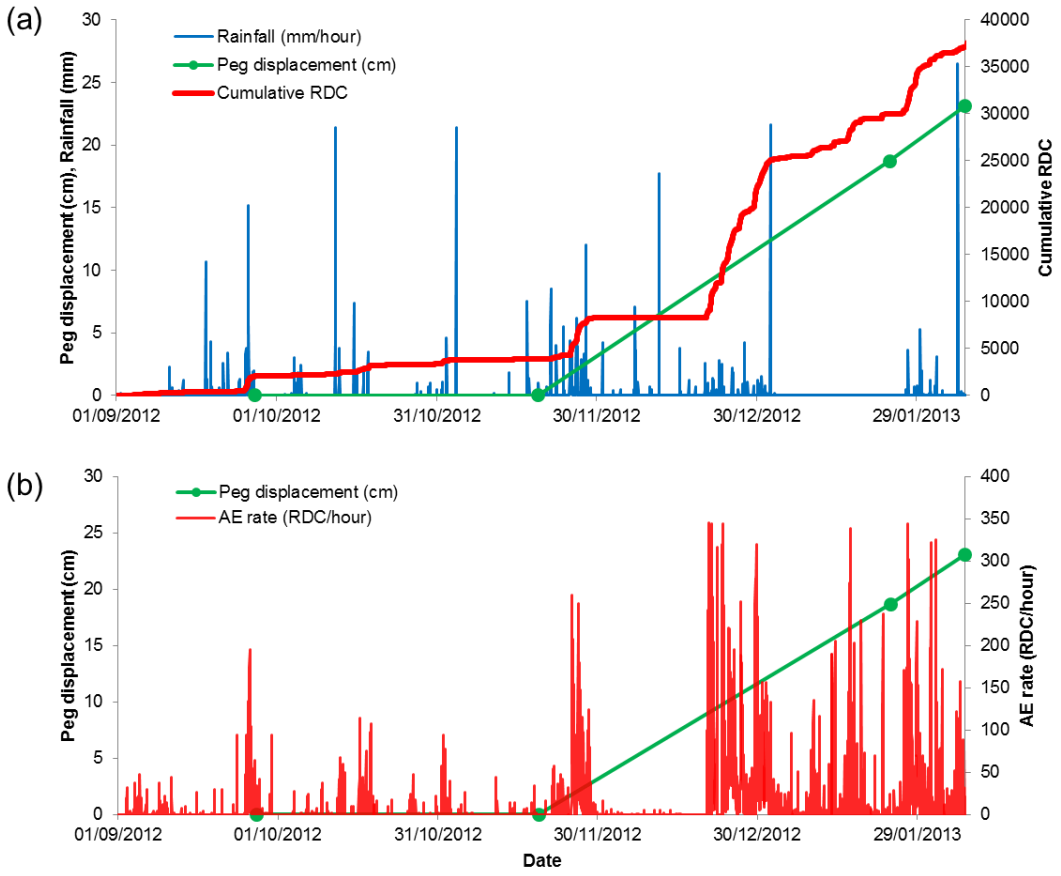

Figure A.1. Time series measurements from Hollin Hill, comparing AEWG2 measurements with GPS peg displacements and rainfall: a) Cumulative RDC; and b) AE rate

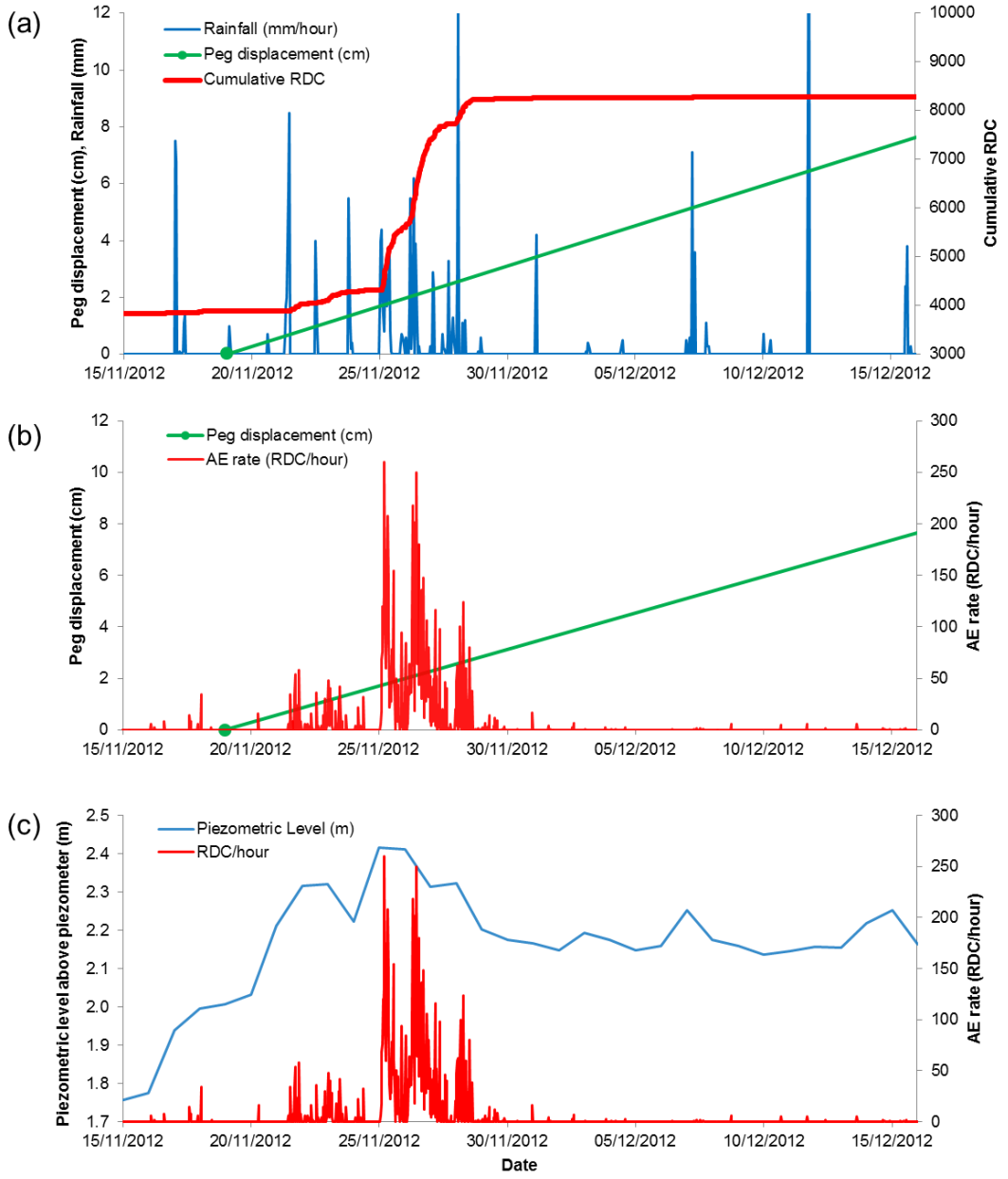

Figure A.2. Time series measurements from AEWG2 at Hollin Hill: a) Cumulative RDC, rainfall and GPS peg displacement; b) AE rate and peg displacement; and c) AE rate and piezometric level

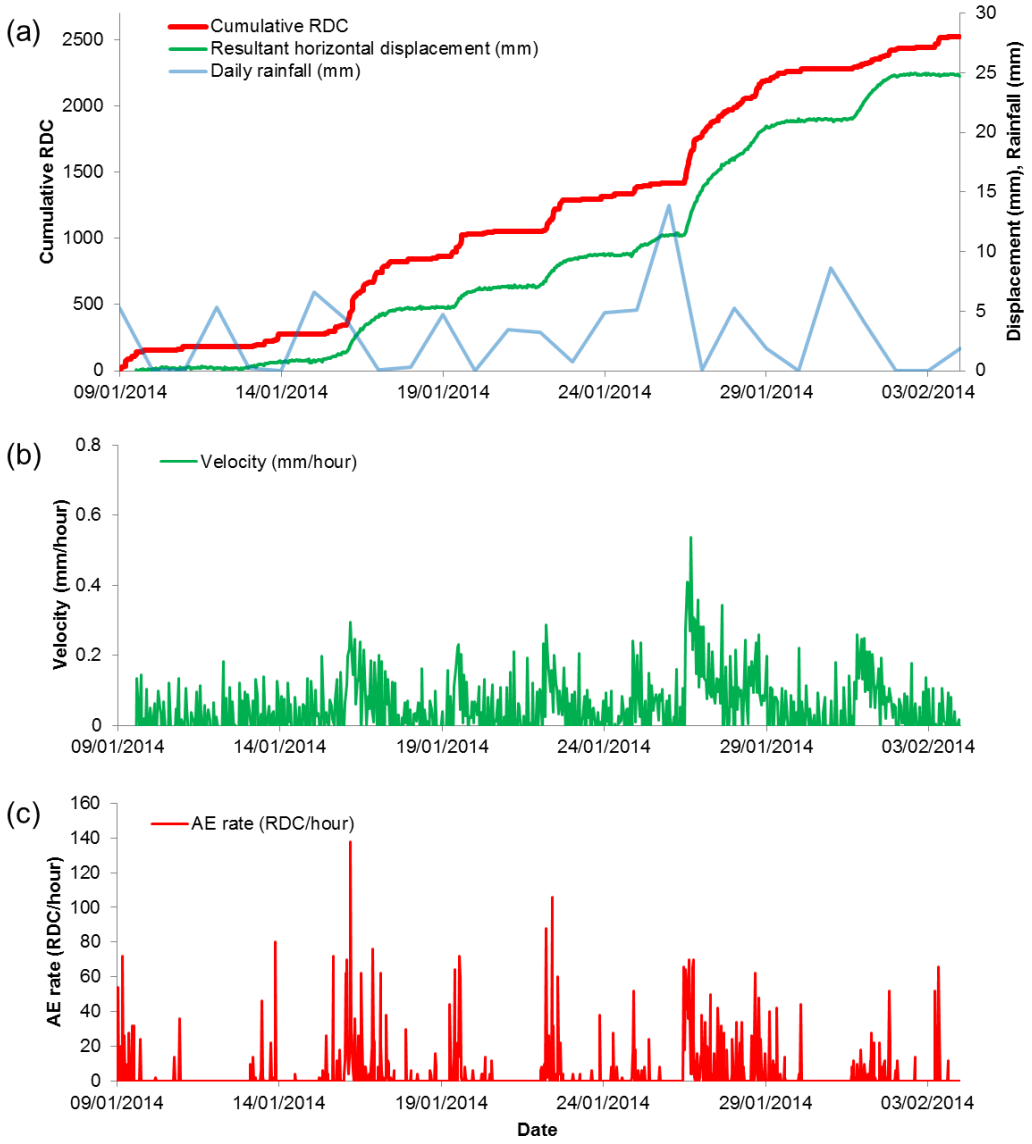

Figure A.3. Time series measurements from AEWG3 and SAA3 at Hollin Hill (Eastern lobe): a) Cumulative RDC, cumulative displacement and rainfall; b) SAA measured velocity; and c) AE rate

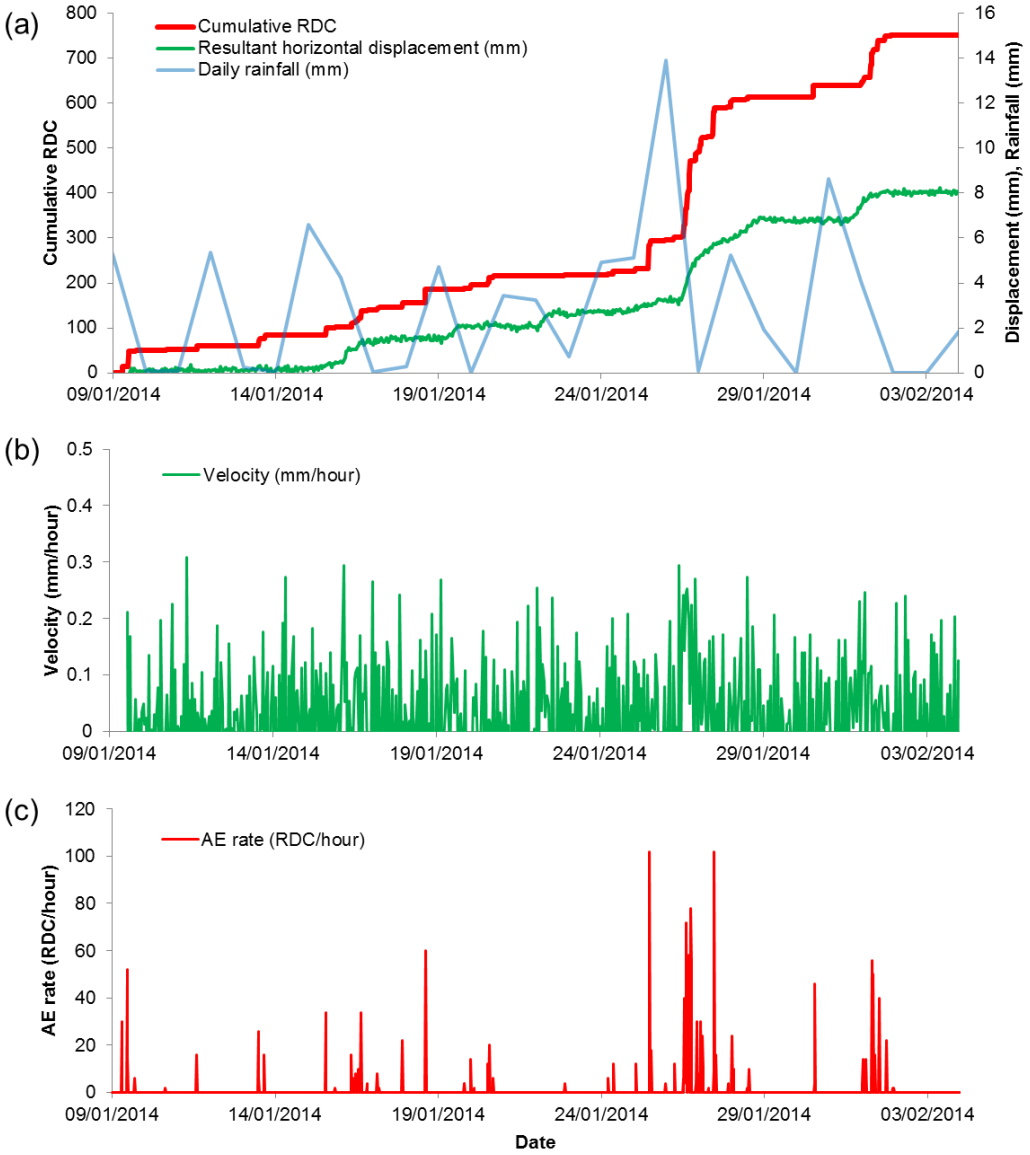

Figure A.4. Time series measurements from AEWG2 and SAA2 at Hollin Hill (Western lobe): a) Cumulative RDC, cumulative displacement and rainfall; b) SAA measured velocity; and c) AE rate

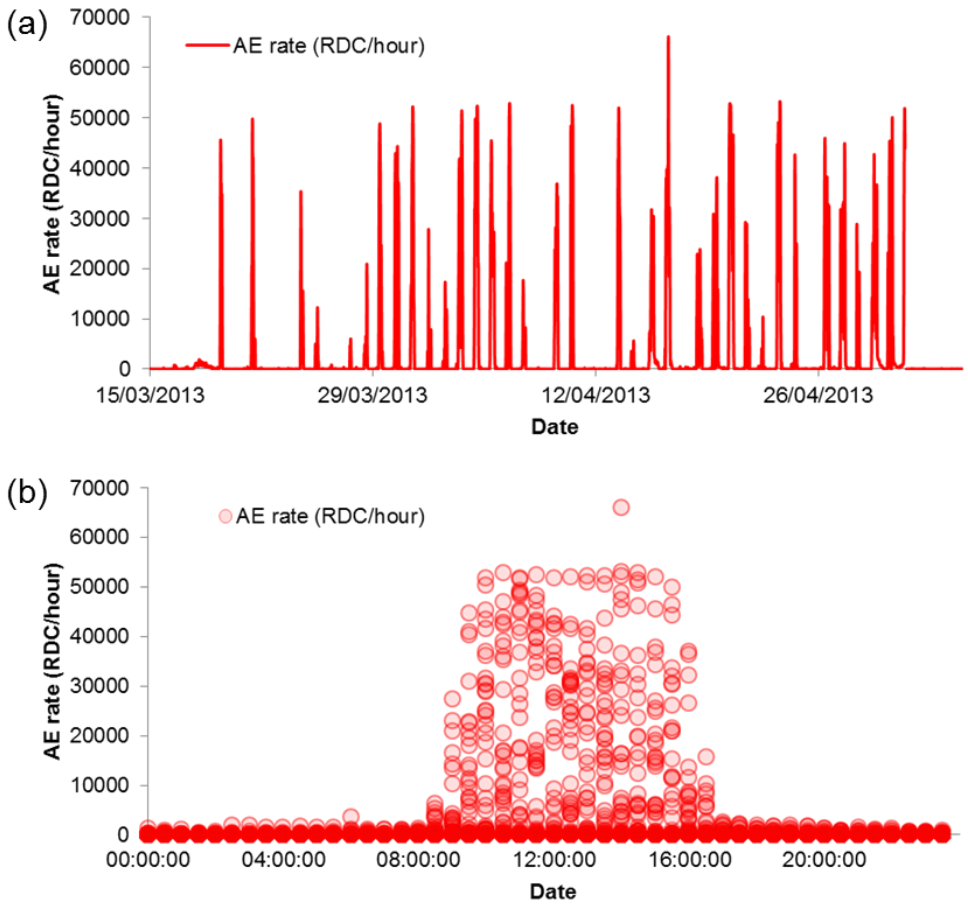

Figure A.5. Example high magnitude AE contamination/background noise at Hollin Hill: a) time series; b) plotted vs. time of day

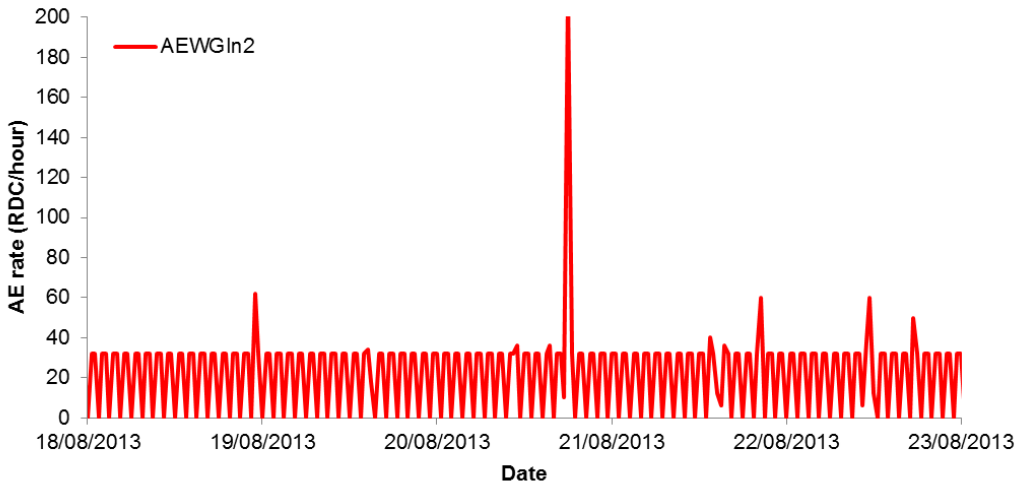

Figure A.6. Example time series of consistent electronic noise in system AEWG In2 at Hollin Hill, which was removed from time series measurements during analysis

A1.2. Flat cliffs

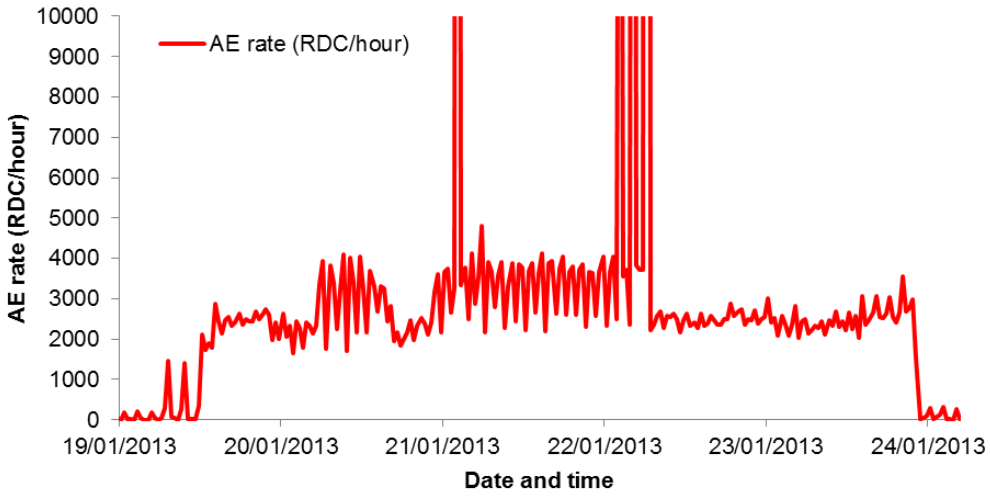

Figure A.7. Example high magnitude AE contamination due to electromagnetic interference at Flat Cliffs, which stopped after the coordinator system and solar panel regulator were disconnected (originally they were all housed in the same cover and this caused the interference)

A2. Inclinometer and AE data comparison

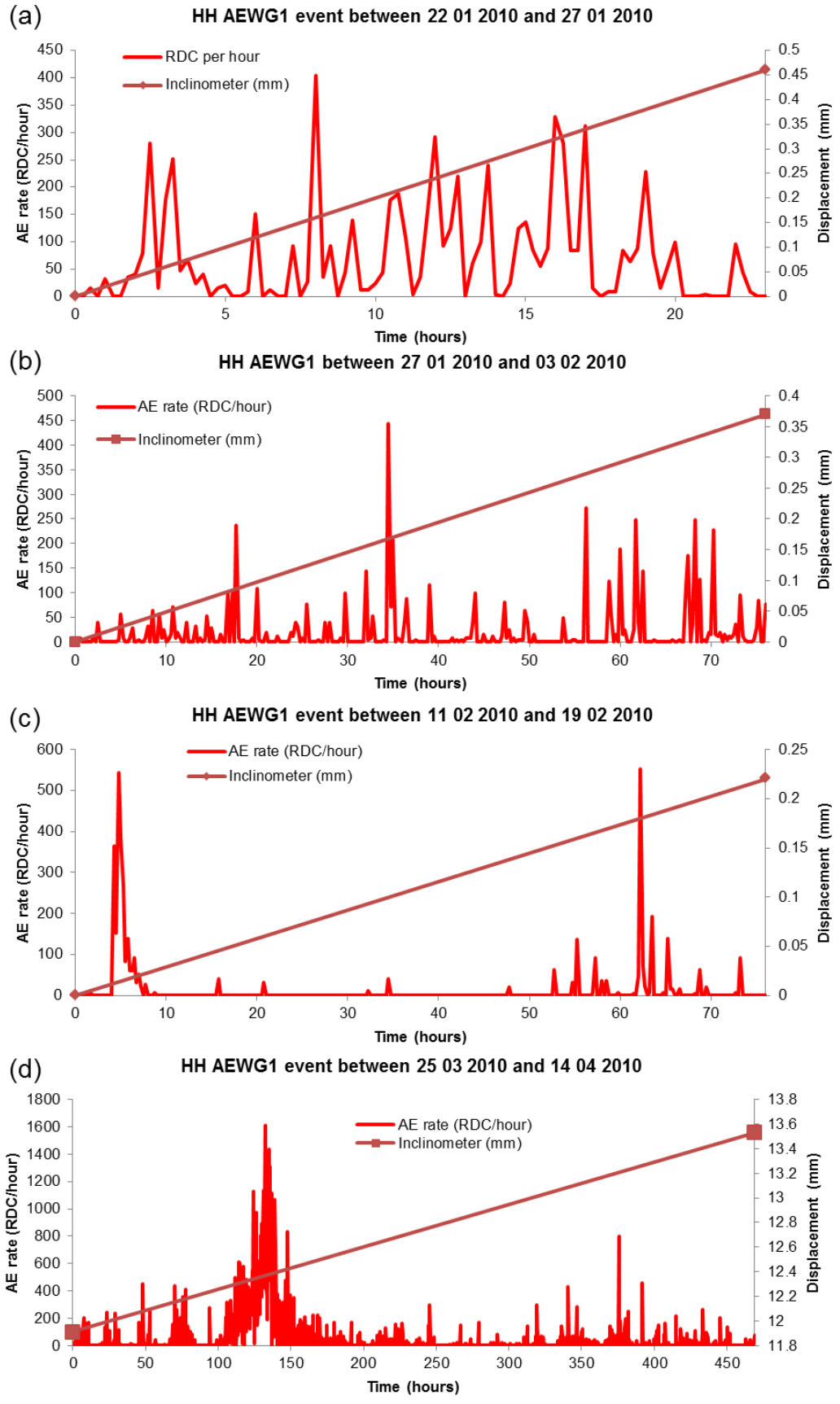

Figure A.8. Example periods of movement at AEWG1 (Hollin Hill) during 2010, with inclinometer and AE presented during the period when movement was assumed to have taken place

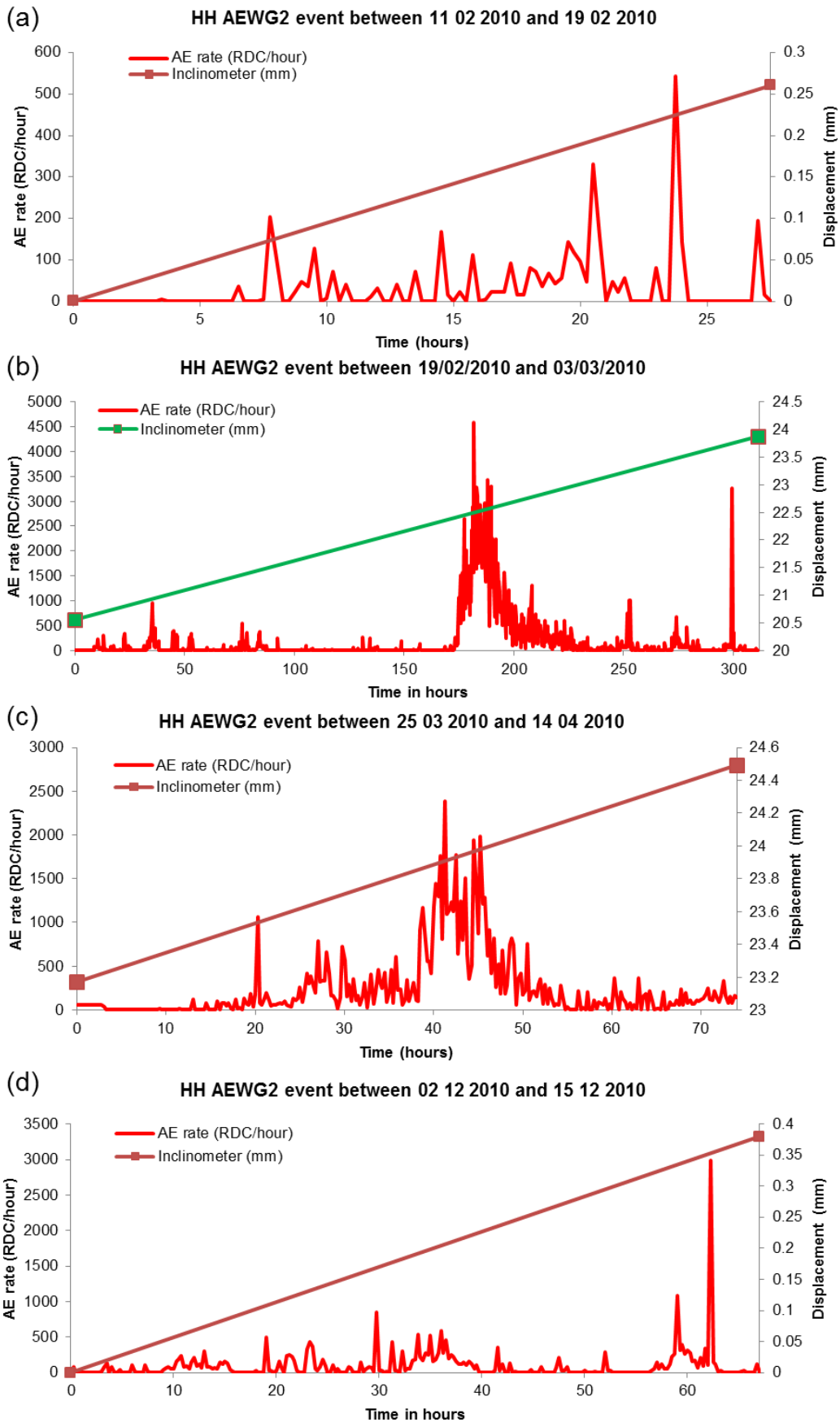

Figure A.9. Example periods of movement at AEWG2 (Hollin Hill) during 2010, with inclinometer and AE presented during the period when movement was assumed to have taken place

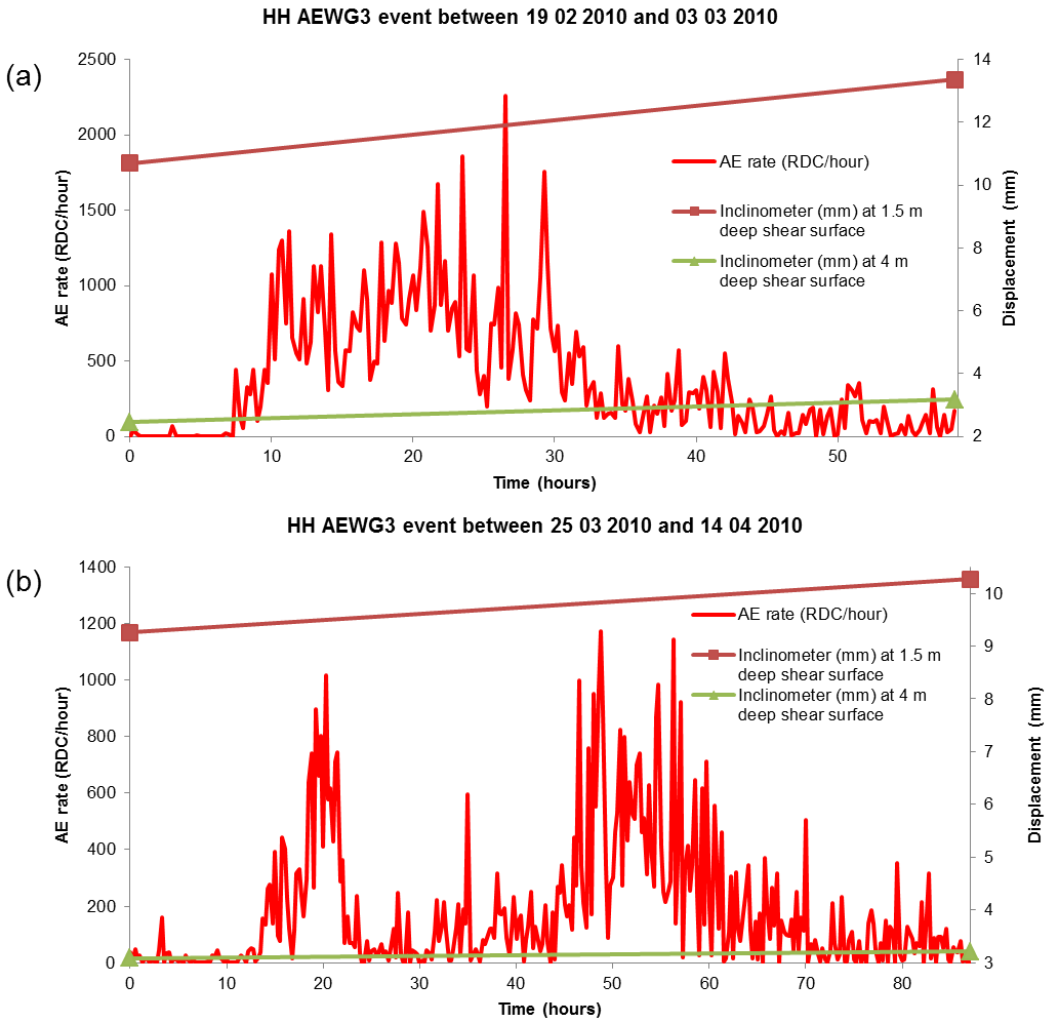

Figure A.10. Example periods of movement at AEWG3 (Hollin Hill) during 2010, with inclinometer and AE presented during the period when movement was assumed to have taken place

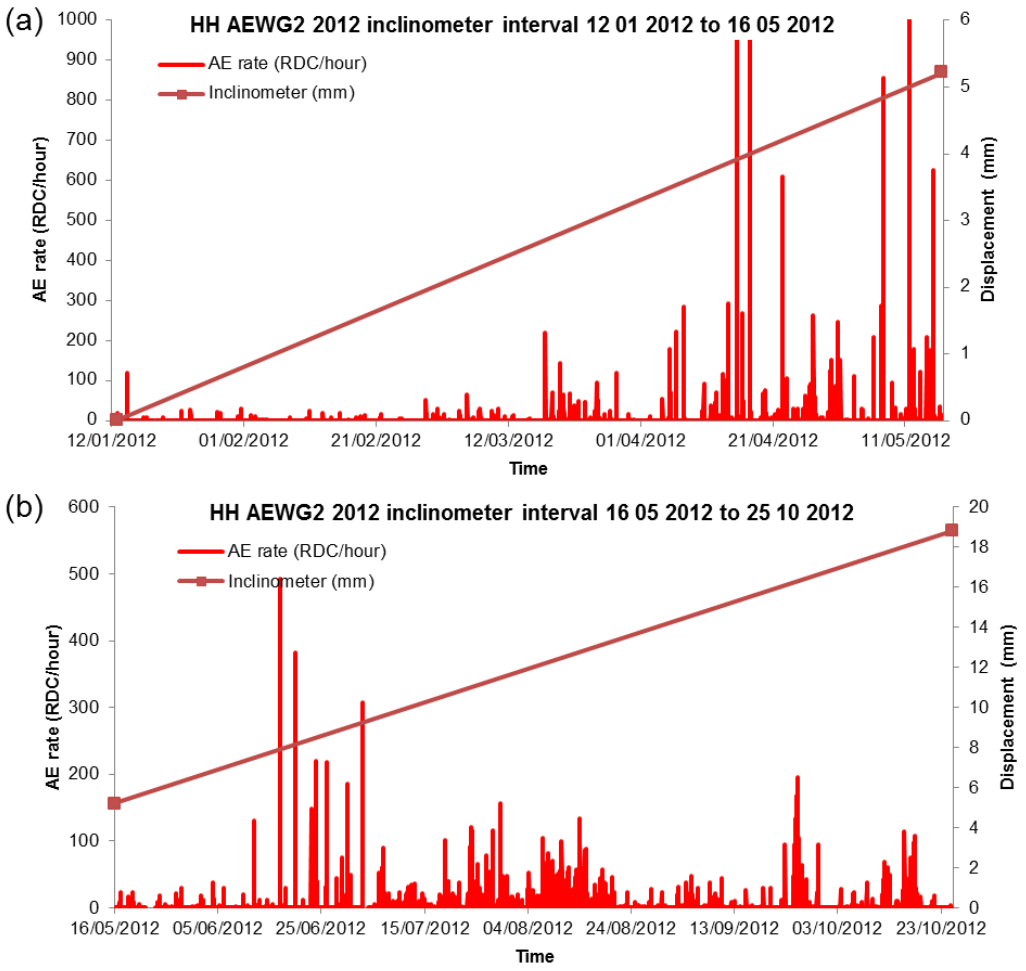

Figure A.11. The two inclinometer intervals at Hollin Hill in 2012 with AEWG2 time series measurements

Table A.1. Actual average velocities (using inclinometer measurements and event duration) and calculated average velocities (derived from AE rate measurements) determined for a series of movement events at Hollin Hill

			Average event velocity (mm/hour)	
No	**Displacement (mm)**	**Duration (hours)**	**Actual velocity (determined from inclinometer data and event duration)**	**Calculated velocity (from AE rate-velocity calibration)**
1	1.62	96	0.0169	0.0537
2	0.46	23	0.0200	0.0217
3	0.37	76	0.0049	0.0060
4	0.22	76	0.0029	0.0042
5	1.32	74	0.0178	0.0171
6	0.38	67	0.0057	0.0068
7	1.14	87	0.0131	0.0268
8	5.21	268	0.0194	0.0251

A3. Active waveguide physical model test results

Table A.2. Example tabulated results from a dynamic strain controlled shear test of 4 mm amplitude and 0.0003 Hz frequency

Time (minutes)	Deformation (mm)	Load (kN)	RDC/5sec	RDC/hour
0.00	0.0058	-0.0097	0	0
0.17	-0.0007	-0.0108	0	0
0.67	0.0054	-0.0097	0	0
1.17	0.0046	-0.0096	0	0
1.67	0.0036	-0.0111	0	0
2.17	0.0040	-0.0032	0	0
2.67	0.0037	0.0084	0	0
3.17	0.0029	0.0026	0	0
3.67	0.0040	-0.0085	0	0
4.17	0.0044	-0.0168	0	0
4.67	0.0034	-0.0169	0	0
5.17	0.0021	-0.0049	0	0
5.67	0.0033	-0.0124	0	0
6.17	0.0060	-0.0106	0	0
6.67	0.0035	0.0066	0	0
7.17	0.0060	-0.0487	0	0
7.67	0.0047	-0.0167	27	19440
8.17	0.0063	-0.0103	0	0
8.67	0.0069	-0.0166	2	1440
9.17	0.0057	-0.0208	0	0
9.67	0.0081	-0.0072	0	0
10.17	0.0007	-0.0164	0	0
10.67	-0.0005	-0.0184	0	0
11.17	0.0041	-0.0174	0	0
11.67	0.0009	-0.0217	0	0
12.17	0.0018	-0.0142	0	0
12.67	-0.0024	-0.0008	0	0
13.17	0.0021	-0.0293	0	0
13.67	0.0010	-0.0203	0	0
14.17	-0.0002	-0.0135	0	0
14.67	-0.0020	-0.0296	0	0
15.17	0.0019	-0.0200	0	0
15.67	0.0016	-0.0275	0	0
16.17	-0.0003	-0.0290	0	0
16.67	0.0009	-0.0298	0	0
17.17	0.0036	-0.0286	0	0
17.67	-0.0001	-0.0297	0	0
18.17	0.0001	-0.0320	0	0
18.67	0.0028	-0.0309	0	0
19.17	0.0024	-0.0304	0	0
19.67	0.0030	-0.0318	0	0
20.17	0.0005	-0.0253	0	0
20.67	-0.0025	-0.0166	0	0
21.17	0.0033	-0.0238	0	0
21.67	-0.0023	-0.0101	0	0
22.17	0.0028	-0.0316	0	0
22.67	-0.0001	-0.0049	0	0
23.17	0.0028	-0.0223	0	0
23.67	0.0091	-0.0064	8	5760

24.17	0.0249	-0.0145	0	0
24.67	0.0492	0.0040	0	0
25.17	0.0754	0.0227	1	720
25.67	0.1138	0.0450	302	217440
26.17	0.1512	0.0634	152	109440
26.67	0.2052	0.0915	692	498240
27.17	0.2598	0.1177	1653	1190160
27.67	0.3237	0.1498	1592	1146240
28.17	0.3945	0.1748	636	457920
28.67	0.4667	0.2004	1706	1228320
29.17	0.5484	0.2269	2454	1766880
29.67	0.6339	0.2476	2969	2137680
30.17	0.7262	0.2776	4942	3558240
30.67	0.8209	0.3018	5387	3878640
31.17	0.9194	0.3434	5799	4175280
31.67	1.0250	0.3736	6611	4759920
32.17	1.1285	0.4042	6879	4952880
32.67	1.2412	0.4358	8637	6218640
33.17	1.3537	0.4733	4983	3587760
33.67	1.4715	0.5226	8625	6210000
34.17	1.5857	0.5640	5231	3766320
34.67	1.7058	0.6121	10002	7201440
35.17	1.8256	0.6736	8692	6258240
35.67	1.9414	0.7073	10865	7822800
36.17	2.0700	0.7777	8993	6474960
36.67	2.1819	0.8183	8863	6381360
37.17	2.3014	0.8548	8014	5770080
37.67	2.4231	0.9077	8192	5898240
38.17	2.5391	0.9610	15693	11298960
38.67	2.6546	1.0015	7145	5144400
39.17	2.7668	1.0515	9093	6546960
39.67	2.8745	1.1163	10554	7598880
40.17	2.9819	1.1916	8535	6145200
40.67	3.0850	1.2437	12159	8754480
41.17	3.1826	1.3012	7500	5400000
41.67	3.2735	1.3424	10673	7684560
42.17	3.3672	1.4103	5376	3870720
42.67	3.4507	1.4659	7761	5587920
43.17	3.5305	1.4793	9433	6791760
43.67	3.6032	1.5101	5950	4284000
44.17	3.6718	1.5639	6354	4574880
44.67	3.7328	1.6118	7109	5118480
45.17	3.7871	1.6270	5515	3970800
45.67	3.8359	1.6546	4283	3083760
46.17	3.8793	1.6802	6548	4714560
46.67	3.9127	1.6860	2301	1656720
47.17	3.9470	1.6974	3416	2459520
47.67	3.9666	1.7021	6199	4463280
48.17	3.9795	1.6924	3831	2758320
48.67	3.9873	1.6706	532	383040
49.17	3.9885	1.6452	404	290880
49.67	3.9868	1.6284	147	105840
50.17	3.9885	1.6130	60	43200
50.67	3.9868	1.5979	62	44640
51.17	3.9855	1.5903	81	58320

51.67	3.9848	1.5818	82	59040
52.17	3.9861	1.5726	242	174240
52.67	3.9843	1.5689	40	28800
53.17	3.9909	1.5581	37	26640
53.67	3.9870	1.5535	26	18720
54.17	3.9876	1.5454	297	213840
54.67	3.9898	1.5380	13	9360
55.17	3.9847	1.5324	111	79920
55.67	3.9878	1.5282	24	17280
56.17	3.9856	1.5269	13	9360
56.67	3.9856	1.5224	0	0
57.17	3.9860	1.5174	0	0
57.67	3.9878	1.5131	342	246240
58.17	3.9837	1.5095	41	29520
58.67	3.9874	1.5057	6	4320
59.17	3.9864	1.5038	77	55440
59.67	3.9831	1.4918	104	74880
60.17	3.9901	1.4932	152	109440
60.67	3.9831	1.4889	69	49680
61.17	3.9917	1.4887	72	51840
61.67	3.9866	1.4826	54	38880
62.17	3.9870	1.4824	0	0
62.67	3.9869	1.4771	4	2880
63.17	3.9915	1.4700	16	11520
63.67	3.9853	1.4739	5	3600
64.17	3.9878	1.4718	2	1440
64.67	3.9849	1.4697	18	12960
65.17	3.9897	1.4704	0	0
65.67	3.9859	1.4676	0	0
66.17	3.9876	1.4712	84	60480
66.67	3.9877	1.4733	0	0
67.17	3.9867	1.4669	0	0
67.67	3.9862	1.4633	110	79200
68.17	3.9858	1.4618	137	98640
68.67	3.9874	1.4553	48	34560
69.17	3.9891	1.4417	4	2880
69.67	3.9882	1.4583	1	720
70.17	3.9843	1.4500	1	720

Table A.3. Example tabulated results from a constant strain rate compression test at a 'rapid' deformation rate

Time (minutes)	Force (N)	Displacement (mm)	RDC/minute	RDC/hour
0	82.14	0	19	1140
1	246.42	1.1025	46356	2781360
2	383.32	2.205	69921	4195260
3	602.36	3.3075	140971	8458260
4	876.16	4.41	246195	14771700
5	1382.69	5.5125	303962	18237720
6	1957.67	6.615	335763	20145780
7	2655.86	7.7175	402017	24121020
8	3408.81	8.82	492908	29574480
9	4312.35	9.9225	440165	26409900
10	5092.68	11.025	448070	26884200
11	6023.6	12.1275	412039	24722340
12	6913.45	13.23	365409	21924540

A4. First-time slope failure simulation

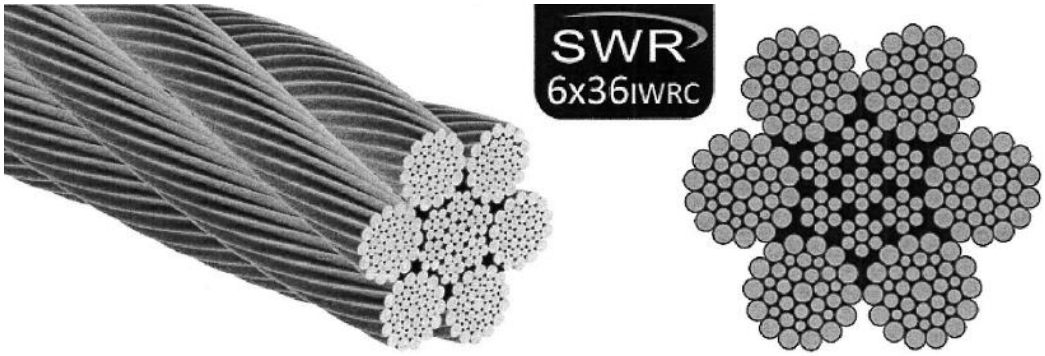

Figure A.12. Illustration of wire rope used in first-time slope failure experimentation

Table A.4. Specification of 6 x 36 construction wire rope used in first-time slope failure experimentation

Nominal diameter (mm)	Mass (kg/m)	Minimum breaking load (kN)	Length (mm)
12	0.573	90.7	1450

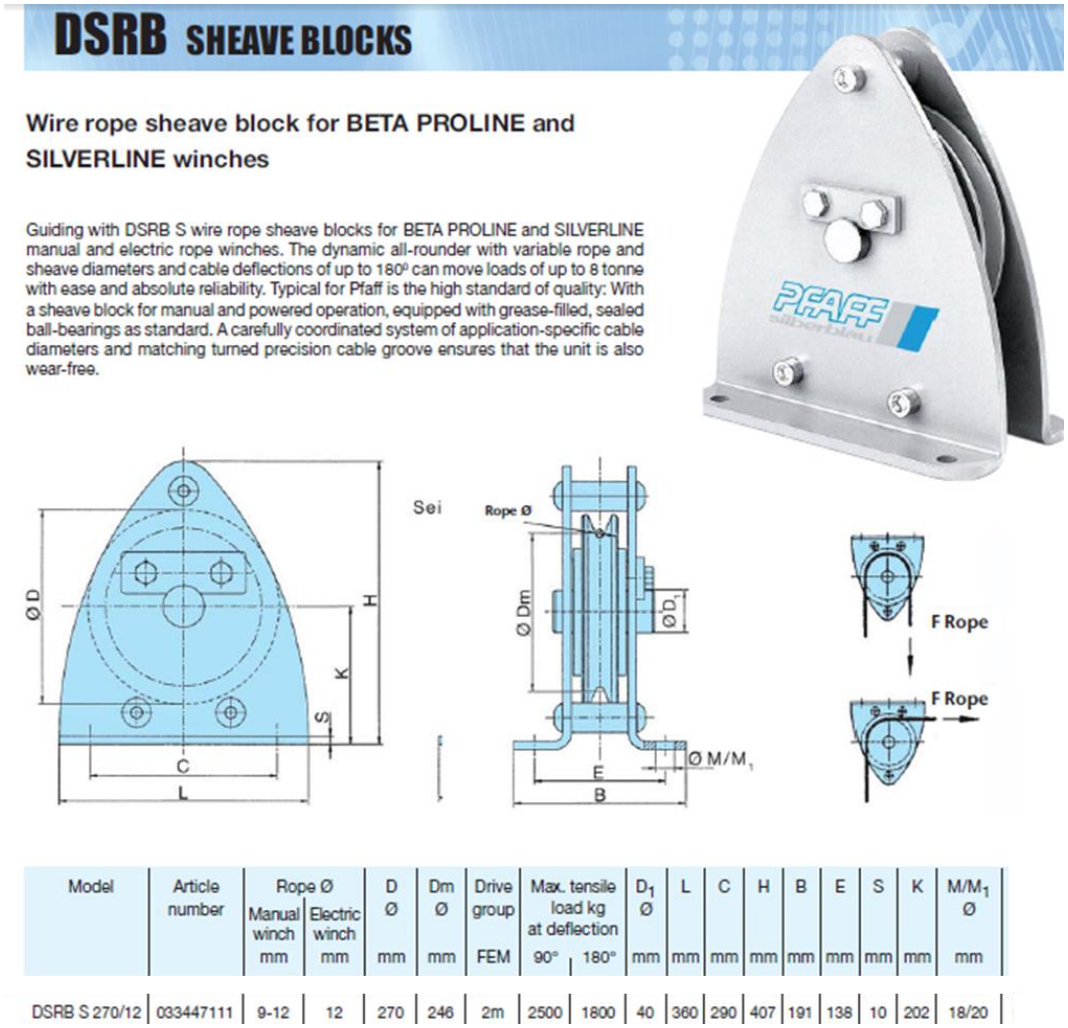

Model	Article number	Rope Ø Manual winch mm	Rope Ø Electric winch mm	D Ø mm	Dm Ø mm	Drive group FEM	Max. tensile load kg at deflection 90°	Max. tensile load kg at deflection 180°	D_1 Ø mm	L mm	C mm	H mm	B mm	E mm	S mm	K mm	M/M_1 Ø mm
DSRB S 270/12	033447111	9-12	12	270	246	2m	2500	1800	40	360	290	407	191	138	10	202	18/20

Figure A.13. Specification of DSRB 270/12 Sheave Block

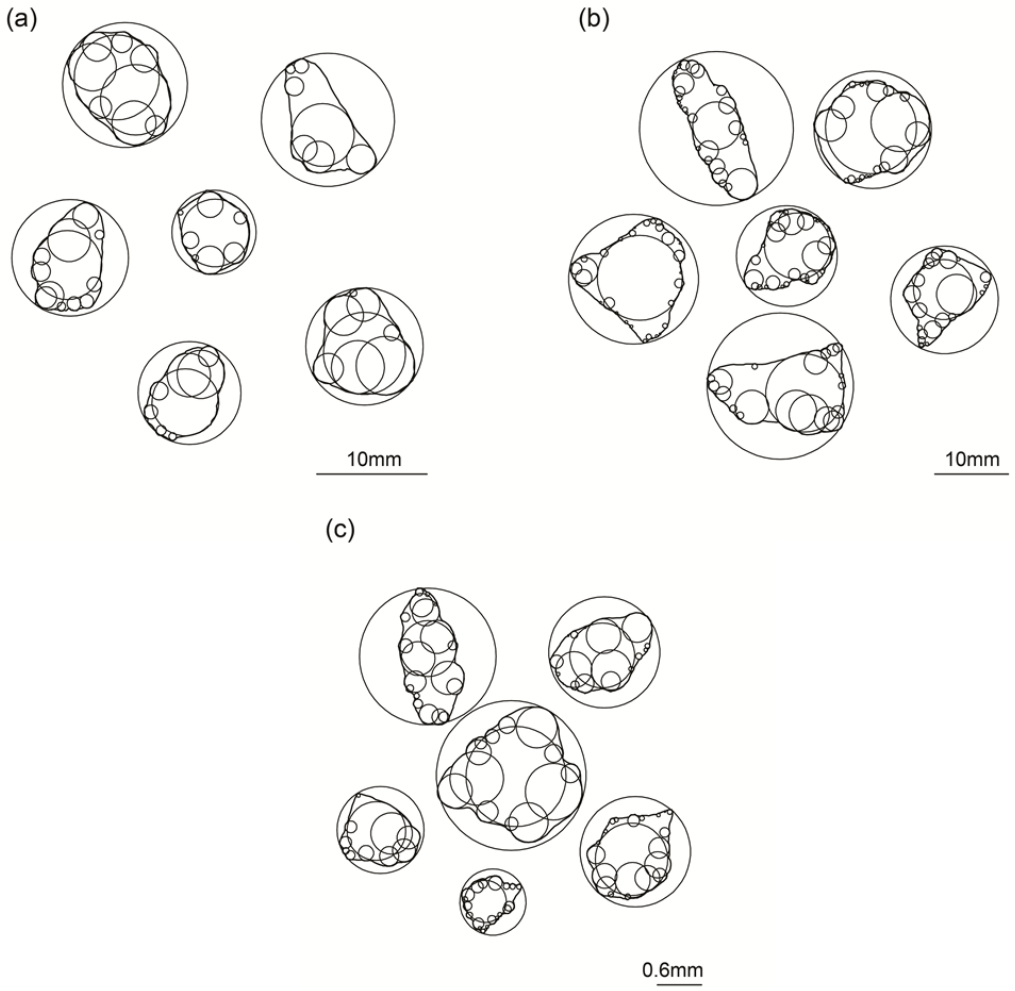

Figure A.14. CAD diagrams used to quantify particle shape parameters

Table A.5. Example tabulated results, sampled at 30 second intervals, from first-time failure test 5

				S016 @ 0.1V		S014 @ 0.25V		
Time (minutes)	Load (kN)	Ram position (mm)	LVDT displacement (mm)	RDC/5sec	AE rate (RDC/hour)	RDC/5sec	AE rate (RDC/hour)	Resultant horizontal SAA displacement (mm) @ Height = 0.9 m
0.00	3.139	0.012	0.001	0	0	0	0	0.000
0.50	3.176	0.04	0.002	0	0	0	0	0.134
1.00	3.179	0.068	0.004	0	0	0	0	0.111
1.50	3.196	0.094	0.016	0	0	0	0	0.162
2.00	3.212	0.125	0.027	0	0	0	0	0.075
2.50	3.252	0.158	0.043	0	0	0	0	0.126
3.00	3.245	0.185	0.057	0	0	0	0	0.094
3.50	3.25	0.211	0.069	0	0	0	0	0.160
4.00	3.279	0.238	0.083	0	0	0	0	0.076
4.50	3.297	0.265	0.093	0	0	0	0	0.196
5.00	3.315	0.294	0.107	0	0	0	0	0.160
5.50	3.327	0.32	0.12	0	0	0	0	0.115
6.00	3.341	0.347	0.135	0	0	0	0	0.221
6.50	3.345	0.376	0.152	0	0	0	0	0.151
7.00	3.373	0.406	0.164	0	0	0	0	0.108
7.50	3.367	0.43	0.178	0	0	0	0	0.217
8.00	3.399	0.459	0.193	0	0	0	0	0.244
8.50	3.401	0.486	0.205	0	0	0	0	0.090
9.00	3.434	0.52	0.223	0	0	0	0	0.148
9.50	3.429	0.547	0.24	0	0	0	0	0.153
10.00	3.444	0.576	0.256	0	0	0	0	0.206
10.50	3.438	0.603	0.27	0	0	0	0	0.192

11.00	3.471	0.633	0.288	0	0	0	0	0.248
11.50	3.496	0.666	0.305	0	0	0	0	0.233
12.00	3.508	0.695	0.325	0	0	0	0	0.237
12.50	3.52	0.726	0.344	0	0	0	0	0.156
13.00	3.538	0.76	0.359	0	0	0	0	0.226
13.50	3.495	0.789	0.384	0	0	0	0	0.273
14.00	3.563	0.82	0.393	0	0	0	0	0.213
14.50	3.587	0.849	0.408	0	0	0	0	0.273
15.00	3.605	0.878	0.426	0	0	0	0	0.244
15.50	3.603	0.91	0.438	0	0	0	0	0.209
16.00	3.631	0.938	0.454	0	0	0	0	0.334
16.50	3.63	0.964	0.472	0	0	0	0	0.272
17.00	3.653	0.992	0.488	0	0	0	0	0.356
17.50	3.667	1.021	0.509	0	0	0	0	0.194
18.00	3.674	1.047	0.527	0	0	0	0	0.460
18.50	3.68	1.077	0.545	0	0	0	0	0.350
19.00	3.725	1.106	0.564	0	0	0	0	0.371
19.50	3.724	1.134	0.584	0	0	0	0	0.240
20.00	3.729	1.163	0.603	0	0	0	0	0.450
20.50	3.739	1.188	0.618	0	0	0	0	0.379
21.00	3.758	1.218	0.634	0	0	0	0	0.358
21.50	3.787	1.25	0.65	0	0	0	0	0.526
22.00	3.782	1.28	0.667	0	0	0	0	0.515
22.50	3.819	1.31	0.688	0	0	0	0	0.478
23.00	3.817	1.337	0.704	0	0	0	0	0.416
23.50	3.836	1.365	0.72	0	0	0	0	0.342
24.00	3.864	1.4	0.737	0	0	0	0	0.392
24.50	3.872	1.425	0.756	0	0	0	0	0.481
25.00	3.891	1.456	0.774	0	0	0	0	0.529
25.50	3.886	1.482	0.79	0	0	0	0	0.489
26.00	3.926	1.513	0.807	0	0	0	0	0.578
26.50	3.932	1.544	0.829	0	0	0	0	0.511
27.00	3.954	1.572	0.852	0	0	0	0	0.562
27.50	3.966	1.6	0.873	0	0	0	0	0.499
28.00	3.998	1.632	0.893	0	0	0	0	0.509
28.50	3.999	1.658	0.908	0	0	0	0	0.569
29.00	4.011	1.687	0.931	0	0	0	0	0.515
29.50	4.049	1.719	0.951	0	0	0	0	0.465
30.00	4.053	1.747	0.968	0	0	0	0	0.610
30.50	4.054	1.775	0.984	0	0	0	0	0.495
31.00	4.093	1.809	1.002	0	0	0	0	0.611
31.50	4.087	1.837	1.021	0	0	0	0	0.575
32.00	4.125	1.868	1.039	0	0	0	0	0.711
32.50	4.126	1.893	1.054	0	0	0	0	0.537
33.00	4.149	1.924	1.07	0	0	0	0	0.630
33.50	4.162	1.957	1.089	0	0	0	0	0.690
34.00	4.173	1.982	1.111	0	0	0	0	0.608
34.50	4.199	2.014	1.126	0	0	0	0	0.816
35.00	4.217	2.042	1.151	0	0	0	0	0.727
35.50	4.235	2.073	1.166	0	0	0	0	0.604
36.00	4.264	2.104	1.185	0	0	0	0	0.687
36.50	4.268	2.132	1.201	0	0	0	0	0.752
37.00	4.283	2.159	1.22	0	0	0	0	0.637
37.50	4.304	2.188	1.239	0	0	0	0	0.764
38.00	4.331	2.214	1.254	1	720	0	0	0.812
38.50	4.34	2.244	1.269	0	0	0	0	0.720
39.00	4.353	2.27	1.29	0	0	0	0	0.779
39.50	4.367	2.302	1.31	0	0	0	0	0.828
40.00	4.379	2.329	1.329	102	73440	0	0	0.851
40.50	4.4	2.361	1.348	0	0	0	0	0.857
41.00	4.419	2.387	1.374	0	0	0	0	0.907
41.50	4.42	2.418	1.391	0	0	0	0	0.734
42.00	4.44	2.447	1.407	0	0	0	0	0.756

42.50	4.482	2.477	1.428	0	0	0	0	0.711
43.00	4.491	2.506	1.445	0	0	0	0	0.842
43.50	4.483	2.534	1.462	0	0	0	0	0.802
44.00	4.502	2.565	1.482	0	0	0	0	0.777
44.50	4.527	2.593	1.5	3	2160	1	720	0.806
45.00	4.551	2.621	1.517	0	0	0	0	0.844
45.50	4.556	2.653	1.537	0	0	0	0	0.911
46.00	4.574	2.68	1.557	0	0	0	0	0.995
46.50	4.613	2.712	1.579	1	720	0	0	0.763
47.00	4.618	2.741	1.596	6	4320	5	3600	0.930
47.50	4.63	2.768	1.614	27	19440	3	2160	0.919
48.00	4.633	2.8	1.636	0	0	0	0	1.091
48.50	4.644	2.828	1.658	4	2880	0	0	1.026
49.00	4.638	2.858	1.682	0	0	0	0	0.981
49.50	4.657	2.89	1.707	68	48960	15	10800	1.178
50.00	4.655	2.918	1.73	45	32400	19	13680	1.108
50.50	4.667	2.944	1.751	50	36000	3	2160	1.117
51.00	4.714	2.98	1.772	68	48960	27	19440	1.084
51.50	4.722	3.037	1.819	0	0	0	0	1.280
52.00	4.753	3.097	1.864	144	103680	57	41040	1.301
52.50	4.776	3.156	1.911	57	41040	17	12240	1.331
53.00	4.8	3.214	1.97	288	207360	182	131040	1.393
53.50	4.806	3.272	2.006	19	13680	0	0	1.371
54.00	4.854	3.332	2.05	160	115200	70	50400	1.437
54.50	4.892	3.394	2.098	448	322560	265	190800	1.491
55.00	4.87	3.452	2.155	111	79920	62	44640	1.576
55.50	4.863	3.509	2.21	165	118800	187	134640	1.683
56.00	4.855	3.568	2.268	101	72720	52	37440	1.729
56.50	4.868	3.627	2.321	57	41040	26	18720	1.615
57.00	4.869	3.686	2.397	153	110160	68	48960	1.776
57.50	4.87	3.744	2.449	213	153360	140	100800	1.857
58.00	4.873	3.799	2.485	51	36720	20	14400	1.819
58.50	4.882	3.856	2.539	143	102960	65	46800	1.929
59.00	4.895	3.916	2.594	198	142560	80	57600	2.027
59.50	4.903	3.978	2.648	301	216720	190	136800	2.137
60.00	4.913	4.033	2.7	31	22320	28	20160	2.132
60.50	4.927	4.093	2.754	150	108000	70	50400	2.179
61.00	4.934	4.151	2.81	442	318240	339	244080	2.311
61.50	4.935	4.21	2.869	247	177840	28	20160	2.329
62.00	4.929	4.266	2.921	403	290160	145	104400	2.316
62.50	4.947	4.326	2.978	329	236880	235	169200	2.219
63.00	4.965	4.385	3.031	440	316800	199	143280	2.368
63.50	4.97	4.442	3.087	147	105840	122	87840	2.457
64.00	4.966	4.503	3.146	96	69120	37	26640	2.430
64.50	4.98	4.562	3.2	397	285840	212	152640	2.560
65.00	4.976	4.62	3.255	293	210960	96	69120	2.591
65.50	5	4.677	3.309	284	204480	165	118800	2.594
66.00	4.995	4.737	3.365	177	127440	110	79200	2.809
66.50	4.999	4.796	3.426	269	193680	111	79920	2.801
67.00	5.006	4.852	3.478	60	43200	68	48960	2.885
67.50	5.021	4.912	3.534	109	78480	55	39600	2.906
68.00	5.033	4.971	3.591	176	126720	58	41760	2.933
68.50	5.063	5.032	3.648	124	89280	65	46800	2.875
69.00	5.061	5.087	3.702	81	58320	38	27360	2.917
69.50	5.067	5.146	3.757	195	140400	123	88560	3.075
70.00	5.073	5.208	3.813	502	361440	167	120240	3.263
70.50	5.077	5.264	3.87	135	97200	49	35280	3.247
71.00	5.088	5.322	3.925	46	33120	21	15120	3.267
71.50	5.104	5.384	3.982	219	157680	118	84960	3.386
72.00	5.121	5.443	4.034	331	238320	140	100800	3.413
72.50	5.112	5.499	4.088	207	149040	55	39600	3.360
73.00	5.111	5.559	4.146	197	141840	260	187200	3.415
73.50	5.123	5.618	4.199	178	128160	90	64800	3.591

74.00	5.148	5.677	4.257	169	121680	23	16560	3.483
74.50	5.152	5.736	4.314	321	231120	180	129600	3.671
75.00	5.125	5.798	4.379	180	129600	79	56880	3.830
75.50	5.164	5.853	4.425	440	316800	258	185760	3.996
76.00	5.163	5.912	4.482	728	524160	477	343440	3.986
76.50	5.178	5.972	4.538	772	555840	405	291600	4.218
77.00	5.208	6.081	4.638	466	335520	322	231840	4.356
77.50	5.239	6.199	4.751	486	349920	283	203760	4.413
78.00	5.248	6.317	4.862	646	465120	333	239760	4.493
78.50	5.273	6.433	4.977	792	570240	289	208080	4.584
79.00	5.301	6.552	5.094	1074	773280	534	384480	4.705
79.50	5.33	6.67	5.204	254	182880	89	64080	4.844
80.00	5.343	6.791	5.322	788	567360	359	258480	4.864
80.50	5.341	6.903	5.436	1368	984960	703	506160	5.111
81.00	5.369	7.02	5.545	725	522000	320	230400	5.110
81.50	5.364	7.14	5.662	246	177120	138	99360	5.263
82.00	5.405	7.259	5.772	951	684720	402	289440	5.454
82.50	5.408	7.375	5.885	550	396000	281	202320	5.560
83.00	5.416	7.495	5.999	867	624240	409	294480	5.708
83.50	5.441	7.615	6.114	634	456480	235	169200	5.859
84.00	5.451	7.73	6.233	548	394560	326	234720	6.006
84.50	5.469	7.849	6.349	437	314640	323	232560	5.974
85.00	5.483	7.968	6.458	566	407520	278	200160	6.161
85.50	5.481	8.083	6.57	1036	745920	470	338400	6.358
86.00	5.5	8.202	6.682	1296	933120	598	430560	6.327
86.50	5.53	8.322	6.792	209	150480	158	113760	6.524
87.00	5.539	8.438	6.907	1192	858240	485	349200	6.798
87.50	5.564	8.557	7.014	1393	1002960	619	445680	6.986
88.00	5.561	8.672	7.127	2326	1674720	1028	740160	7.175
88.50	5.587	8.792	7.237	2202	1585440	880	633600	7.349
89.00	5.596	8.908	7.347	2423	1744560	820	590400	7.658
89.50	5.64	9.072	7.495	1134	816480	415	298800	7.811
90.00	5.699	9.306	7.715	1507	1085040	630	453600	8.190
90.50	5.717	9.536	7.937	1660	1195200	826	594720	8.351
91.00	5.749	9.77	8.152	2801	2016720	1278	920160	8.626
91.50	5.759	10.004	8.375	1174	845280	392	282240	8.880
92.00	5.815	10.235	8.587	1306	940320	614	442080	9.038
92.50	5.837	10.466	8.803	1800	1296000	718	516960	9.219
93.00	5.881	10.697	9.016	1451	1044720	492	354240	9.586
93.50	5.904	10.929	9.228	2189	1576080	1279	920880	9.858
94.00	5.95	11.165	9.45	2433	1751760	1250	900000	10.142
94.50	5.972	11.396	9.67	1685	1213200	952	685440	10.261
95.00	6.01	11.628	9.889	1543	1110960	633	455760	10.558
95.50	6.021	11.861	10.102	1822	1311840	824	593280	10.892
96.00	6.053	12.095	10.325	3473	2500560	1464	1054080	11.397
96.50	6.104	12.334	10.544	4316	3107520	2067	1488240	11.913
97.00	6.126	12.566	10.773	2855	2055600	1111	799920	12.313
97.50	6.14	12.8	10.993	5014	3610080	2300	1656000	12.681
98.00	6.215	13.097	11.263	3017	2172240	1183	851760	13.313
98.50	6.291	13.595	11.737	3237	2330640	1202	865440	13.846
99.00	6.329	14.095	12.217	2551	1836720	998	718560	14.251
99.50	6.368	14.592	12.698	4733	3407760	1968	1416960	14.649
100.00	6.445	15.094	13.19	4777	3439440	1730	1245600	15.317
100.50	6.489	15.595	13.69	4157	2993040	1709	1230480	16.097
101.00	6.548	16.094	14.172	8870	6386400	3067	2208240	17.041
101.50	6.628	16.596	14.656	9793	7050960	4164	2998080	18.049
102.00	6.69	17.098	15.159	7945	5720400	2847	2049840	19.135
102.50	6.717	17.599	15.65	11134	8016480	4517	3252240	20.334
103.00	6.824	18.224	16.279	7458	5369760	3217	2316240	21.040
103.50	6.897	19.202	17.284	8349	6011280	3578	2576160	22.231
104.00	7.059	20.18	18.204	9459	6810480	4103	2954160	23.219
104.50	7.162	21.156	19.116	9558	6881760	4176	3006720	24.369
105.00	7.258	22.131	20.03	17296	12453120	6491	4673520	26.402

105.50	7.371	23.109	20.941	25068	18048960	10783	7763760	28.474
106.00	7.526	24.579	22.298	26349	18971280	11890	8560800	30.415
106.50	8.428	32.76	30.098	17147	12345840	6835	4921200	32.311
107.00	8.59	34.756	32.045	20257	14585040	9085	6541200	34.120
107.50	8.798	37.08	34.255	23032	16583040	10209	7350480	36.449
108.00	9.064	39.597	36.679	34770	25034400	15395	11084400	39.331
108.50	9.341	42.557	39.54	49138	35379360	21446	15441120	42.123
109.00	9.596	45.97	42.835	44025	31698000	18691	13457520	44.973
109.50	9.816	48.905	45.678	38470	27698400	11623	8368560	47.929
110.00	10.076	51.83	48.457	56171	40443120	21833	15719760	50.832

A5. MISTRAS USB node

www.mistrasgroup.com/products/company/publications/2$Acoustic_Emission/USB_AE_Node.pdf

MISTRAS

PRODUCTS & SYSTEMS DIVISION | PRODUCT BULLETIN

FEATURES

- Powered and operated through USB Port
- Rugged surface mount (SMT) construction
- Built-in internal preamplifier and power for external preamplifiers
- 18 bit resolution, 20MHz sampling frequency
- With analog and programmable digital filters
- Waveform and Location Options
- Free LabView/C++ driver available for customer program development

SPECIFICATIONS

AE Input:.....1 Channel/USB node (4 nodes/system)
Sampling Frequency:.....20 MHz
AE Digitizing:.....18 bits
Parametric Inputs:.....CH 1, +/- 10V, 16 bits
CH 2-4, 0-10V, 16 bits
Digital I/O:.....2
Preamplifier:.....Built-in
OS:.....Win XP, VISTA, Win 7, and Win 8
Case Size:.....L 5.25"x W 3.25"x H 1.25"
(133 x 83 x 32mm)
Weight:.....0.5 lbs. (0.23kg)
Power Requirements:.....USB Powered (5V)
< 100 mA/running
Power Consumption:.....< 0.5 watt

Figure A.15. Details of the MISTRAS USB node used to compare the full waveforms of the controlled source generator and soil-generated AE from constant strain rate compression tests